

IFIP AICT 546

Daoliang Li
Chunjiang Zhao
(Eds.)



Computer and Computing Technologies in Agriculture XI

11th IFIP WG 5.14 International Conference, CCTA 2017
Jilin, China, August 12–15, 2017
Proceedings, Part II

2 Part II

 Springer

Editor-in-Chief

Kai Rannenber, Goethe University Frankfurt, Germany

Editorial Board

TC 1 – Foundations of Computer Science

Jacques Sakarovitch, Télécom ParisTech, France

TC 2 – Software: Theory and Practice

Michael Goedicke, University of Duisburg-Essen, Germany

TC 3 – Education

Arthur Tatnall, Victoria University, Melbourne, Australia

TC 5 – Information Technology Applications

Erich J. Neuhold, University of Vienna, Austria

TC 6 – Communication Systems

Aiko Pras, University of Twente, Enschede, The Netherlands

TC 7 – System Modeling and Optimization

Fredi Tröltzsch, TU Berlin, Germany

TC 8 – Information Systems

Jan Pries-Heje, Roskilde University, Denmark

TC 9 – ICT and Society

David Kreps, University of Salford, Greater Manchester, UK

TC 10 – Computer Systems Technology

Ricardo Reis, Federal University of Rio Grande do Sul, Porto Alegre, Brazil

TC 11 – Security and Privacy Protection in Information Processing Systems

Steven Furnell, Plymouth University, UK

TC 12 – Artificial Intelligence

Ulrich Furbach, University of Koblenz-Landau, Germany

TC 13 – Human-Computer Interaction

Marco Winckler, University Paul Sabatier, Toulouse, France

TC 14 – Entertainment Computing

Matthias Rauterberg, Eindhoven University of Technology, The Netherlands

IFIP – The International Federation for Information Processing

IFIP was founded in 1960 under the auspices of UNESCO, following the first World Computer Congress held in Paris the previous year. A federation for societies working in information processing, IFIP's aim is two-fold: to support information processing in the countries of its members and to encourage technology transfer to developing nations. As its mission statement clearly states:

IFIP is the global non-profit federation of societies of ICT professionals that aims at achieving a worldwide professional and socially responsible development and application of information and communication technologies.

IFIP is a non-profit-making organization, run almost solely by 2500 volunteers. It operates through a number of technical committees and working groups, which organize events and publications. IFIP's events range from large international open conferences to working conferences and local seminars.

The flagship event is the IFIP World Computer Congress, at which both invited and contributed papers are presented. Contributed papers are rigorously refereed and the rejection rate is high.

As with the Congress, participation in the open conferences is open to all and papers may be invited or submitted. Again, submitted papers are stringently refereed.

The working conferences are structured differently. They are usually run by a working group and attendance is generally smaller and occasionally by invitation only. Their purpose is to create an atmosphere conducive to innovation and development. Refereeing is also rigorous and papers are subjected to extensive group discussion.

Publications arising from IFIP events vary. The papers presented at the IFIP World Computer Congress and at open conferences are published as conference proceedings, while the results of the working conferences are often published as collections of selected and edited papers.

IFIP distinguishes three types of institutional membership: Country Representative Members, Members at Large, and Associate Members. The type of organization that can apply for membership is a wide variety and includes national or international societies of individual computer scientists/ICT professionals, associations or federations of such societies, government institutions/government related organizations, national or international research institutes or consortia, universities, academies of sciences, companies, national or international associations or federations of companies.

More information about this series at <http://www.springer.com/series/6102>

Daoliang Li · Chunjiang Zhao (Eds.)

Computer and Computing Technologies in Agriculture XI

11th IFIP WG 5.14 International Conference, CCTA 2017
Jilin, China, August 12–15, 2017
Proceedings, Part II

Editors

Daoliang Li
China Agricultural University (CAU)
Beijing, China

Chunjiang Zhao
National Research Center of Intelligent
Equipment for Agriculture (NRCIEA)
Beijing, China

ISSN 1868-4238 ISSN 1868-422X (electronic)
IFIP Advances in Information and Communication Technology
ISBN 978-3-030-06178-4 ISBN 978-3-030-06179-1 (eBook)
<https://doi.org/10.1007/978-3-030-06179-1>

Library of Congress Control Number: 2018965408

© IFIP International Federation for Information Processing 2019

This work is subject to copyright. All rights are reserved by the Publisher, whether the whole or part of the material is concerned, specifically the rights of translation, reprinting, reuse of illustrations, recitation, broadcasting, reproduction on microfilms or in any other physical way, and transmission or information storage and retrieval, electronic adaptation, computer software, or by similar or dissimilar methodology now known or hereafter developed.

The use of general descriptive names, registered names, trademarks, service marks, etc. in this publication does not imply, even in the absence of a specific statement, that such names are exempt from the relevant protective laws and regulations and therefore free for general use.

The publisher, the authors, and the editors are safe to assume that the advice and information in this book are believed to be true and accurate at the date of publication. Neither the publisher nor the authors or the editors give a warranty, express or implied, with respect to the material contained herein or for any errors or omissions that may have been made. The publisher remains neutral with regard to jurisdictional claims in published maps and institutional affiliations.

This Springer imprint is published by the registered company Springer Nature Switzerland AG
The registered company address is: Gewerbestrasse 11, 6330 Cham, Switzerland

Preface

Agricultural information technology has become an important means for developing modern agriculture. In order to promote the academic exchange and cooperation of ICT in Agriculture, from 2000 to 2016, the National Engineering Research Center for Information Technology in Agriculture (NERCITA), China Agricultural University (CAU), and related organizations hosted eight events in the International Symposium on Intelligent Information Technology in Agriculture (ISIITA) series and ten events in the International Conference on Computer and Computing Technologies in Agriculture (CCTA) series, which provided a platform for the exchange of information on and ICT in agriculture between global scholars.

Since 2015, the Internet of Things, big data, robots, and precision farming have entered a stage of agricultural applications. Artificial intelligence (AI) has gradually penetrated the agriculture field and promoted the development of intelligent agriculture, which is characterized by “information perception, quantitative decision-making, intelligent control, precision input, and personalized services.” To exchange experiences and share the state of the art as well as successful application cases of ICT in intelligent agriculture, ISIITA and CCTA were merged into the International Conference on Intelligent Agriculture (ICIA). The ICIA will be held every two years (odd year), and the co-sponsors and conference venue are also selected according to applications.

ICIA 2017 focused on four topics: Internet of Things and Big Data in Agriculture, Precision Agriculture and Agricultural Robot, Agricultural Information Services, and Animal and Plant Phenotyping for Agriculture. The newest theories, viewpoints, technologies, products, and applications were extensively presented. Practical experiences in innovation and applications in intelligent agriculture were shared among experts from different countries.

We selected the 100 best papers among the 282 papers submitted to CCTA 2017 for these proceedings. All papers underwent two reviews by members who are from the Special Interest Group on Advanced Information Processing in Agriculture (AIPA), IFIP. In these proceedings, creative thoughts and inspiration can be discovered, discussed, and disseminated. It is always exciting to have experts, professional, and scholars with creative contributions getting together to share inspiring ideas and to accomplish great developments in the field.

I would like to express my sincere thanks to all authors who submitted research papers to the conference. Finally, I would also like to express my sincere thanks to all speakers, session chairs, and attendees, both national and international, for their active participation and support of this conference.

Organization

Organizers

China National Engineering Research Center for Information Technology in Agriculture (NERCITA), China
China Agricultural University (CAU), China
China National Engineering Research Center of Intelligent Equipment for Agriculture (NERCIEA), China
Branch of Agricultural Information Processing, International Federation for Information Processing (IFIP TC5.14)
Chinese Association of Artificial Intelligence (CAAI), China
Chinese Society of Agricultural Engineering (CSAE), China
Chinese Society for Agricultural Machinery (CSAM), China
Informatization Branch, China Agricultural Mechanization Association (CAMA), China
Committee of Information Technology, China Agro-technological Extension Association (CAEA), China
Technology Innovation Strategic Alliance for Agricultural Internet of Things Industry (TISA-AITI), Beijing, China
Beijing Society for Information Technology in Agriculture (BSITA), China
Key Laboratory of Information Technology in Agriculture, Ministry of Agriculture, China
Sino-US Cooperative Technology Center of Agricultural Aviation, China
Beijing Key Laboratory of Digital Plant, China

Sponsors

Department of Science, Technology and Education, Ministry of Agriculture (MOA), China
Department of Market and Economic Information, Ministry of Agriculture (MOA), China
Department of International Cooperation, Ministry of Science and Technology (MOST), China
Jilin Provincial Agricultural Commission, China
Jilin Provincial Department of Science and Technology, China
Changchun Municipal Government, China
Beijing Association for Science and Technology, China
Beijing Academy of Agriculture and Forestry Sciences, China

Organizing Committee

Chunjiang Zhao	China National Engineering Research Center for Information Technology in Agriculture, China
Nick Sigrimis	Agricultural University of Athens, Greece
Yanbo Huang	Crop Production Systems Research, USDA-ARS
Youhong Sun	Jilin University, China
Zhang Yuejie	Jilin Agricultural University, China

Academic Committee

Maohua Wang	China Agricultural University (CAU) and Chinese Academy of Engineering, China
Jiulin Sun	Institute of Geographic Sciences and Natural Resources Research, Chinese Academy of Sciences and Chinese Academy of Engineering, China
Deyi Li	61st Institute of the General Staff Headquarters of Chinese People's Liberation Army and Chinese Academy of Engineering, China
Xiwen Luo	South China Agricultural University, Chinese Academy of Engineering, China
Xuegeng Chen	Institute of Agricultural Machinery, Xinjiang Academy of Agricultural and Reclamation Science and Chinese Academy of Engineering, China
Yu Li	Jilin Agricultural University, Chinese Academy of Engineering, China
Luquan Ren	Jilin University, Chinese Academy of Sciences, China
Fangquan Mei	Agricultural Information Institute, Chinese Academy of Agricultural Sciences (CAAS), China
Chunjiang Zhao	China National Engineering Research Center for Information Technology in Agriculture, China
Daoliang Li	College of Information and Electrical Engineering, China Agricultural University, China
Xinting Yang	China National Engineering Research Center for Information Technology in Agriculture, China
Liping Chen	China National Engineering Research Center of Intelligent Equipment for Agriculture, China
Yong He	College of Biosystems Engineering and Food Science, Zhejiang University, China
Yan Zhu	College of Agriculture, Nanjing Agricultural University, China
Dongjian He	College of Mechanical and Electronic Engineering, Northwest A&F University, China
Chengliang Liu	Shanghai Jiao Tong University, China
Hanping Mao	Institute of Agricultural Engineering, Jiangsu University, China

Haiye Yu	College of Biological and Agricultural Engineering, Jilin University, China
Shijun Li	College of Information Technology, Jilin Agricultural University, China
Guifen Chen	College of Information Technology, Jilin Agricultural University, China
Nick Sigrimis	Agricultural University of Athens, Greece
Kuanchong Ting	Zhejiang University, China/University of Illinois at Urbana-Champaign, USA
Manuel Berenguel	University of Almeria, Spain
Jose Fernando Bienvenido	University of Almeria, Spain
Rajiv Khosla	Colorado State University, USA
Zhang Qin	Washington State University, USA
Yanbo Huang	Crop Production Systems Research, USDA-ARS
Wesley Clint Hoffmann	Aerial Application Technology Group, USDA-ARS
Jens Leon	University of Bonn, Germany
Thomas Rauschenbach	Fraunhofer-IOSB, Advanced Systems Technology Branch (AST), Germany
Daniela Baganz	Leibniz Institute of Freshwater Ecology and Inland Fisheries, IGB, Germany
Sun-Ok Chung	Chungnam National University, Republic of Korea, Korea
Naoshi Kondo	Kyoto University, Japan
Noboru Noguchi	Hokkaido University, Japan
Ning Wang	Oklahoma State University, USA
Naiqian Zhang	Kansas State University, USA
Frederic Baret	French National Institute for Agricultural Research, France

Additional Reviewers

Chunjiang Zhao	China National Engineering Research Center for Information Technology in Agriculture, China
Daoliang Li	College of Information and Electrical Engineering, China Agricultural University, China
Xinting Yang	China National Engineering Research Center for Information Technology in Agriculture, China
Yong He	College of Biosystems Engineering and Food Science, Zhejiang University, China
Chengliang Liu	Shanghai Jiao Tong University, China
Zhenbo Li	College of Information and Electrical Engineering, China Agricultural University, China
Yingyi Chen	College of Information and Electrical Engineering, China Agricultural University, China
Yaoguang Wei	College of Information and Electrical Engineering, China Agricultural University, China

Qingling Duan	College of Information and Electrical Engineering, China Agricultural University, China
Longqing Sun	College of Information and Electrical Engineering, China Agricultural University, China
Chunhong Liu	College of Information and Electrical Engineering, China Agricultural University, China
Weizhong Yang	College of Information and Electrical Engineering, China Agricultural University, China

Secretary General

Xiaohong Du
Xia Li
Ming Li
Hongru Wang
Han Zhang

Contents – Part II

Research and Application of Spark Platform on Big Data Processing in Intelligent Agriculture of Jilin Province	1
<i>Siwei Fu, Guifen Chen, Shan Zhao, and Enze Xiao</i>	
Summary of Agricultural Drought Monitoring by Remote Sensing at Home and Abroad	13
<i>Meng Wang, Tao Liu, Shouzhen Ling, Xueyan Sui, Huimin Yao, and Xuehui Hou</i>	
Research and Application of 3D Visualization Plug-in Integration with ArcGIS.	21
<i>Yinglun Li, Guifen Chen, and Dongxue Wang</i>	
Growth and Spectral Characteristics of Grassland in Response to Different Soil Textures.	31
<i>Xiaochun Zhong, Junchan Wang, Liu Tao, Chengming Sun, Zhemin Li, and Shengping Liu</i>	
Soil Moisture Estimation by Combining L-Band Brightness Temperature and Vegetation Related Information.	45
<i>Yuanyuan Fu, Chunjiang Zhao, Guijun Yang, and Haikuan Feng</i>	
Study on Precision Fertilization Model Based on Fusion Algorithm of Cluster and RBF Neural Network	56
<i>Shan Zhao, Guifen Chen, Siwei Fu, and Enze Xiao</i>	
Study on Three-Dimensional Data Acquisition of Crop Grains	67
<i>Zetao Yu, Weiliang Wen, Xinyu Guo, and Xianju Lu</i>	
An Agricultural Habitat Information Acquisition and Remote Intelligent Decision System Based on the Internet of Things	75
<i>Ze Lin Hu, Yi Gao, Miao Li, Hua Long Li, Xuan Jiang Yang, and Zhi Run Ma</i>	
Comprehensive Evaluation of Soil Fertility in Yanzhou District Based on Principal Component Analysis	86
<i>Qiuting Zhang and Xia Geng</i>	
Advances in Monitoring Soil Nutrients by Near Infrared Spectroscopy	94
<i>Yan Wang, Bei Cui, Yanhua Zhou, and Xiudong Sun</i>	

Microwave Mixing Technique for Nondestructive Measurement of Moisture Content of Particulate Agricultural Products	100
<i>Chenxiao Li, Yanlei Xu, He Gong, Yuanyuan Liu, and Qian Song</i>	
China's Wine Import Industry: An Economic Analysis of Influencing Trade Factors.	109
<i>Yu Hu, Wei Ma, Ruimei Wang, Huan Song, Weisong Mu, Dong Tian, and Jianying Feng</i>	
Three - Dimensional Visualization of Soil Nutrient Evolution in Maize Precision Operation Area Based on ArcGIS	119
<i>Enze Xiao, Guifen Chen, Shan Zhao, and Siwei Fu</i>	
Characteristics of the Warming Trend During Winter Wheat Growing Seasons in Jiangsu Province of China	127
<i>Xiangying Xu, Xinkai Zhu, Wenshan Guo, Chunyan Li, and Jinfeng Ding</i>	
Estimation of Leaf Nitrogen Concentration of Winter Wheat Using UAV-Based RGB Imagery.	139
<i>Qinglin Niu, Haikuan Feng, Changchun Li, Guijun Yang, Yuanyuan Fu, Zhenhai Li, and Haojie Pei</i>	
New NNI Model in Winter Wheat Based on Hyperspectral Index	154
<i>Wang Jianwen, Li Zhenhai, Xu Xingang, Zhu Hongchun, Feng Haikuan, Liu Chang, Gan Ping, and Xu Xiaobin</i>	
Fruit Trees 3D Data Acquisition and Reconstruction Based on Multi-source	162
<i>Sheng Wu, Boxiang Xiao, Weiliang Wen, Xinyu Guo, and Long Liu</i>	
Comparison of Remote Sensing Estimation Methods for Winter Wheat Leaf Nitrogen Content	173
<i>Chunlan Zhang, Fuquan Tang, Heli Li, Guijun Yang, Haikuan Feng, and Chang Liu</i>	
Design and Implementation of the Wheat Population Nutrition Detection System	185
<i>Lei Shi, Qiguo Duan, Mingyang Xiong, Juanjuan Zhang, Lihong Song, and Xinming Ma</i>	
Hyperspectral Estimation Methods for Chlorophyll Content of Apple Based on Random Forest.	194
<i>Haojie Pei, Changchun Li, Haikuan Feng, Guijun Yang, Mingxing Liu, and Zhichao Wu</i>	
Improving Design of a PVDF Grain Loss Sensor for Combine Harvester.	208
<i>Liming Zhou, Yanwei Yuan, Junning Zhang, and Kang Niu</i>	

Maize Precision Farming Parallel Management Technology and Its Application in Northeast China	218
<i>Xianju Lu, Xinyu Guo, Jiangchuan Fan, Sheng Luo, Yufa Song, and Chunwei Li</i>	
Research on Vegetation Ecologic Quality Index of Rocky Desertification in Karst Area of Guangxi Province Based on NPP and Fractional Vegetation Cover Since 2000	225
<i>Xin Yang, Haihong Huang, Shuan Qian, and Hao Yan</i>	
Estimation of Leaf Nitrogen Content of Winter Wheat Based on Akaike's Information Criterion	231
<i>Haojie Pei, Haikuan Feng, Fuqin Yang, Zhenhai Li, Guijun Yang, and Qinglin Niu</i>	
Monitoring of Winter Wheat Biomass Using UAV Hyperspectral Texture Features	241
<i>Chang Liu, Guijun Yang, Zhenhai Li, Fuquan Tang, Haikuan Feng, Jianwen Wang, Chunlan Zhang, and Liyan Zhang</i>	
Reconstruction and Body Size Detection of 3D Sheep Body Model Based on Point Cloud Data	251
<i>Yanqing Zhou, Heru Xue, Chunlan Wang, Xinhua Jiang, Xiaojing Gao, and Jie Bai</i>	
Research on Irrigation System of Limited Water Supply for Soybean Crops in Shanxi Province	263
<i>Lantao Ye, Yangren Wang, Qing Liu, and Sida Wang</i>	
Development and Application of Hyperspectral Remote Sensing	271
<i>Huimin Xing, Haikuan Feng, Jingying Fu, Xingang Xu, and Guijun Yang</i>	
Study on Spatial Distribution Characters of Rubber Yield and Soil Nutrients in Guangba Farm of Hainai Province	283
<i>Bei Cui, Wenjiang Huang, Huichun Ye, and Qimin Cao</i>	
The Environment Intelligent Monitoring and Analysis for Enclosed Layer House with Four Overlap Tiers Cages in Winter	292
<i>Hualong Li, Miao Li, Junying Li, Kai Zhan, and Xianwang Liu</i>	
Research and Realization of Winter Wheat Yield Estimation Model Based on NDVI Index	301
<i>Zhichao Wu, Changchun Li, Haikuan Feng, Bo Xu, Guijun Yang, Zhenhai Li, Haojie Pei, and Mingxing Liu</i>	
Study on Vegetation Classification Based on Spectral Knowledge Base	310
<i>Peng Liu, Jingcheng Zhang, Bin Wang, Xuexue Zhang, and Kaihua Wu</i>	

Hyperspectral Estimation of Nitrogen Content in Winter Wheat Leaves Based on Unmanned Aerial Vehicles	321
<i>Liu Mingxing, Li Changchun, Feng Haikuan, Pei Haojie, Li Zhenhai, Yang Fuqin, Yang Guijun, and Xu Shouzhi</i>	
Quantification of Root Anatomical Traits in RGP Transgenic Maize Plants Based on Micro-CT	340
<i>Xiaodi Pan, Liming Ma, Ying Zhang, Jinglu Wang, Jianjun Du, and Xinyu Guo</i>	
Effects of Exogenous Gamma-Aminobutyric Acid on Absorption and Regulation of Ion in Wheat Under Salinity Stress	347
<i>Xiaodong Wang, Hongtu Dong, Peichen Hou, Hang Zhou, Lulu He, and Cheng Wang</i>	
Development of Portable Dynamic Ion Flux Detecting Equipment	358
<i>Peichen Hou, Cheng Wang, Xiaodong Wang, Aixue Li, Peng Song, Bin Luo, Ye Hu, and Liping Chen</i>	
Study on Intelligent Monitoring Technology for Composting of Agricultural and Livestock Wastes	368
<i>Hualong Li, Miao Li, Xuanjiang Yang, Zelin Hu, Zhirun Ma, and Xianwang Liu</i>	
Optimization and Simulation of Fertilizer Guide Device Parameters Based on EDEM Software	377
<i>Hai Ding, Xiaofei An, Guangwei Wu, Liwei Li, and Qingzhen Zhu</i>	
Development of an Automated Guidance System for Tracked Combine Harvester	389
<i>Fangming Zhang, Wenbin Wu, and Yunfei Zhu</i>	
Research on the Internet of Things Platform Design for Agricultural Machinery Operation and Operation Management	400
<i>Qian Zhou, Jiandong Jiang, Zhangfeng Zhao, Jiang Zhong, Bosong Pan, Xiao Jin, and Yuanfang Sun</i>	
Understanding the Consumer Satisfaction of the “Last-Mile” Delivery of E-Business Services	411
<i>Shujun Liu, Yan Li, Jingqi Huang, and Xin Zhao</i>	
The State of Motion Stereo About Plant Leaves Monitoring System Design and Simulation	419
<i>Jiangchuan Fan, Xinyu Guo, Chuanyu Wang, Xianju Lu, and Sheng Wu</i>	
Research on Agricultural Scientific and Technological Information Dissemination System Based on Complex Network Technology	432
<i>Hang Chen, Guifen Chen, Ying Zhang, and HongJun Gu</i>	

An Illumination Invariant Maize Canopy Structure Parameters Analysis Method Based on Hemispherical Photography	440
<i>Chuanyu Wang, Xinyu Guo, and Jianjun Du</i>	
Application of DBSCAN Algorithm in Precision Fertilization Decision of Maize	453
<i>Yang Li, Guowei Wang, Yu Chen, Yang Jiao, Haijiao Yu, and Guogang Zhao</i>	
Location and Recognition Fruit Trees Based on Binocular Stereo Vision	460
<i>Xueguan Zhao, Yuanyuan Gao, Songlin Wang, Xiu Wang, Pengfei Fan, and Qingcun Feng</i>	
The Realization of Pig Intelligent Feeding Equipment and Network Service Platform	473
<i>Weihong Ma, Jinwei Fan, Chunjiang Zhao, and Huarui Wu</i>	
Improvement of Regional Spatial Interaction Based on Spatial Traffic System Accessibility: A Case Study in Shandong Province, China	485
<i>Yu Zhang, Shouzhi Xu, Fengguang Kang, and Shihua Yin</i>	
Research on the Key Techniques of Semantic Mining of Information Digest in the Field of Agricultural Major Crops Based on Deep Learning	496
<i>Hao G. J. M. Gong, Yunpeng Cui, and Ping Qian</i>	
COPS: A Real-Time Cross-Domain Object Part Segmentation System	508
<i>Xueqing He</i>	
Author Index	517

Contents – Part I

Quinoa Traceable System Based on Internet of Things.	1
<i>Guowei Wang, Yu Sun, Jing Chen, Yang Jiao, Chuanhong Zhang, Haijiao Yu, Chan Lin, and Guogang Zhao</i>	
Research and Application of Safety Management for Virtual Desktop in Colleges and Universities	9
<i>Haifeng Jia and Guifen Chen</i>	
Philosophical Principles of Data Discovery.	24
<i>Quan Wu, Min Liu, Juanying Sun, Weijie Jiao, Shuanghua Tao, Xiaochen Li, Xue Han, and Lijuan Jia</i>	
Fast Analysis of Maize Kernel Plumpness Characteristics Through Micro-CT Technology	31
<i>Meng Shao, Ying Zhang, Jianjun Du, Xiaodi Pan, Liming Ma, Jinglu Wang, Dennis Böhmer, and Xinyu Guo</i>	
Automated Counting of Sex-Pheromone Attracted Insects Using Trapped Images.	40
<i>Wenyong Li, Meixiang Chen, Ming Li, Chuanheng Sun, and Lin Wang</i>	
Study of Machine Learning Based Rice Breeding Decision Support Methods and Technologies	54
<i>Yun-peng Cui, Jian Wang, Shi-hong Liu, En-ping Liu, and Hai-qing Liu</i>	
A Bayesian Network Model for Yellow Rust Forecasting in Winter Wheat.	65
<i>Xiaodong Yang, Chenwei Nie, Jingcheng Zhang, Haikuan Feng, and Guijun Yang</i>	
Soil Organic Carbon Prediction Using Vis-NIR Spectroscopy with a Large Dataset	76
<i>Yang Shi, Rujing Wang, and Yubing Wang</i>	
Research on High Resolution Remote Sensing Image Classification Based on Convolution Neural Network	87
<i>Wenwen Gong, Zhuqing Wang, Yong Liang, Xin Fan, and Junmeng Hao</i>	
Computer Vision and Feeding Behavior Based Intelligent Feeding Controller for Fish in Aquaculture.	98
<i>Chao Zhou, Kai Lin, Daming Xu, Chuanheng Sun, Lan Chen, Song Zhang, and Qiang Guo</i>	

Multi-scale 3D Data Acquisition of Maize	108
<i>Weiliang Wen, Xinyu Guo, Xianju Lu, Yongjian Wang, and Zetao Yu</i>	
Remote Sensing Monitoring of Drought Based on Landsat8 and NDVI-Ts Characteristic Space Method.	116
<i>Shouzhen Liang, Tao Liu, Zhen Chen, Xueyan Sui, Xuehui Hou, Meng Wang, and Huimin Yao</i>	
Curve Fitting Derivative Method and Its Application in Mouse Growth	126
<i>Zhihua Li and Xin Zhao</i>	
Spatial Structure Change Analysis of Cultivated Soil Nutrients in Urban Fringe of North China	134
<i>Shiwei Dong, Yuchun Pan, and Bingbo Gao</i>	
Evaluation and Mapping of Rice Flood Damage Using Domestic Remotely Sensed Data in China	143
<i>Huifang Wang, Xiaoyi Fang, Wei Guo, Yonghong Liu, Qingzu Luan, Shuo Zhang, and Yanhu Gao</i>	
Estimating Leaf Carotenoid Concentration of Ginger in Different Layers Based on Discrete Wavelet Transform Algorithm	152
<i>Qinhong Liao</i>	
Ecological Footprint Model of Cultivated Land Based on Ecosystem Services in Beijing	159
<i>Hui Guo, Di Wu, Lei Fa, Shunxiang Pei, Xuebing Xin, Shumin Ma, Sha Wu, and Shiwei Dong</i>	
Numerical Simulation of the Effects of Design Parameters on the Performance of Tractor Powered Flail Choppers	170
<i>Zhiqiang Zhang, Hongwen Li, Allen D. McHugh, Jin He, Qingjie Wang, Caiyun Lu, Wenzheng Liu, and Sun Nina</i>	
Design and Implementation of Water Spectrum Observation System for Aquaculture Pond	194
<i>Yinchi Ma, Wen Ding, Yonghua Qu, and Xiande Zhao</i>	
Chlorophyll Fluorescence Measurement: A New Method to Test the Effect of Two Adjuvants on the Efficacy of Topramezone on Weeds	206
<i>Jinwei Zhang, Ortrud Jäck, Alexander Menegat, Gen Li, and Xiu Wang</i>	
Wheat Growth Process 3D Visualization Research Based on Growth Model . . .	217
<i>Hailong Liu, Shuqin Li, Yeping Zhu, Shengping Liu, and Shijuan Li</i>	
Research on Information Integration Method of Agricultural Products Producing and Managing Based on Knowledge Graph.	232
<i>Xiang Sun, Huarui Wu, Peng Hao, and Qingxue Li</i>	

A 3D Canopy Reconstruction and Phenotype Analysis Method for Wheat . . .	244
<i>Boxiang Xiao, Sheng Wu, Xinyu Guo, and Weiliang Wen</i>	
Detection of Young Green Apples in Orchard Environment Using Adaptive Ratio Chromatic Aberration and HOG-SVM.	253
<i>Xia Xue, Zhou Guomin, Qiu Yun, Li Zhuang, Wang Jian, Hu Lin, Fan Jingchao, and Guo Xiuming</i>	
Detection of Overlapped Apples in Orchard Scene Using Improved K-means and Distance Least Square	269
<i>Xia Xue, Zhou Guomin, Qiu Yun, Li Zhuang, Wang Jian, Hu Lin, Fan Jingchao, and Guo Xiuming</i>	
Application of Growth Curve in Agricultural Scientific Research	285
<i>Zeng-hui Wang, Yan-jun Zhao, Yang Liu, and Dong-yan Huang</i>	
The Study of the Work Parameters of the Corn Harvester Cutter.	293
<i>Zeng-hui Wang, Yan-jun Zhao, Yang Liu, and Dong-yan Huang</i>	
Test Device of Soil Outline and Compactness Distribution on Seedbed Based on Sensors	302
<i>Caiyun Lu, Liwei Li, Zhijun Meng, Xiu Wang, and Qingjie Wang</i>	
Study the Spatial-Temporal Variation of Wheat Growth Under Different Site-Specific Nitrogen Fertilization Approaches.	316
<i>Bei Cui, Wenjiang Huang, Xiaoyu Song, Huichun Ye, and Yingying Dong</i>	
Classification Method Research of Fresh Agaricus Bisporus Based on Image Processing	333
<i>Fengyun Wang, Jiye Zheng, Lei Wang, Wenjie Feng, and Luyan Niu</i>	
A Study About Searching Behavior of Scientific Data User Based on Educational Background and Retrieval Capability.	341
<i>Guilan Zhang, Jian Wang, Guomin Zhou, Jianping Liu, Fei Gao, and Caoyuan Wei</i>	
A Review on the Soil Moisture Prediction Model and Its Application in the Information System	352
<i>Wengang Zheng, Lili Zhangzhong, Xin Zhang, Caiyuan Wang, Shirui Zhang, Shijun Sun, and Hongfei Niu</i>	
Application of Image Segmentation Technology in Crop Disease Detection and Recognition	365
<i>Leilei Deng, Zhenghao Wang, and Hui Zhou</i>	

Research and Realization on the Performance Testing Tool of Web Application	375
<i>Huarui Wu and Huaji Zhu</i>	
Operation Area Measurement Based on Trajectories of Agricultural Machinery	384
<i>Chang Ren, Yanwei Yuan, Liwei Yang, Junning Zhang, Yangchun Liu, Chengxu Lv, and Bo Zhao</i>	
Analysis of Influential Factors of Social Satisfaction in Food Industry	395
<i>Zhiyu Lai, Xinyao Zhu, Chenyue Jin, Mingxin Li, and Yan Qi</i>	
Abnormal Identification of Swine Flu Clinical Characteristics Based on Body Temperature and Behavior	404
<i>Duo Wang, Ying Xu, Qifeng Liu, Yue Lou, Chaorong Luo, and Changji Wen</i>	
Hierarchical Denoising Method of Crop 3D Point Cloud Based on Multi-view Image Reconstruction	416
<i>Lei Chen, Yuan Yuan, and Shide Song</i>	
Non-invasive Edge Detection of Leaves Based on Order Morphology	428
<i>Yanlei Xu, Qi Zhang, Chenxiao Li, Xindong Wang, and Xiaotian Meng</i>	
Development and Test of GNSS/IMU-Based Speed Measurement Device for Agricultural Machinery	440
<i>Weiqliang Fu, Shupeng Hu, Changhai Luo, You Li, Shuxia Guo, and Junxiang Zhang</i>	
Farmland Weed Species Identification Based on Computer Vision	452
<i>Shengping Liu, Junchan Wang, Liu Tao, Zhemin Li, Chengming Sun, and Xiaochun Zhong</i>	
Remote Monitoring and Control System for Aquarium Based on Mobile Communication Platform	462
<i>Wen Ding, Yinchu Ma, and Jinjing Zhang</i>	
Effects of the Factors on Maize Yield Under Drip Irrigation Under Film	468
<i>Hongzheng Shen, Yangren Wang, Xinrui Fan, Hao Wang, and Yonglin Li</i>	
An Amperometric Glucose Microbiosensor for Real-Time Measurements in Plants	476
<i>Ye Hu, Cheng Wang, and Aixue Li</i>	
Field Information Recommendation Based on Context-Aware and Collaborative Filtering Algorithm	486
<i>Zhili Chen, Chunjiang Zhao, and Huarui Wu</i>	

Research on the Current Situation and Development of Intelligent Precision Fertilizer Technology	499
<i>Wu Yan and Wang Fan</i>	
The Design and Analysis of Self—Balancing Adjustment Implement Leveling Control System	507
<i>Qingfeng Yang, Yehua Shang, Siyu Liu, Fujie Zhang, Yue Cong, Weiqiang Fu, Rui Pan, and Chunjiang Zhao</i>	
Research on Automatic Steering Control System of Full Hydraulic Steering Tractor	517
<i>Shupeng Hu, Weiqiang Fu, You Li, Yue Cong, Yehua Shang, and Zhijun Meng</i>	
Design of Farmland Information Acquisition System Based on LoRa Wireless Sensor Network	529
<i>Qiulan Wu, Chuanqi Zhao, Yong Liang, Dalei Zhang, and Junmeng Hao</i>	
Multi-sensor Array Based Fire Monitor for Cotton Pile	540
<i>Chenrui Bai, Junning Zhang, Chengxu Lv, Liguang Wei, Liming Zhou, and Bo Zhao</i>	
Author Index	555



Research and Application of Spark Platform on Big Data Processing in Intelligent Agriculture of Jilin Province

Siwei Fu, Guifen Chen^(✉), Shan Zhao, and Enze Xiao

Jilin Agricultural University, Changchun 130118, China
465136727@qq.com, guifchen@163.com

Abstract. Aiming at the demand of real-time massive data processing of Intelligent Agriculture in Jilin Province, this paper studies the big data processing of Intelligent Agriculture in Jilin Province based on Spark platform by acquiring real-time data through monitoring platform. This study first conducted the performance comparison experiment of Hadoop and Spark data processing platform, then used the Spark distributed cluster computing platform, real-time processing the big data of monitoring area. The experimental results show that the Spark platform speeds up 11.4 times faster than the Hadoop platform in the case of 100 million data sizes; and based on the Spark platform for real-time processing of big data intelligent agricultural monitoring network, not only provides memory calculations to reduce IO overhead, but also the results are faster and more accurate. The research results provide strong support for the implementation of precision agriculture technology in intelligent agriculture.

Keywords: Spark · Big data processing · MapReduce
Intelligent Agriculture in Jilin Province

1 Introduction

China is a large agricultural country, facing the ever changing agricultural production technology, Especially the introduction of remote sensing, geographic information technology, precision agriculture and expert system in the field of farmland management. This condition leads to the original variety of agricultural ecosystems turning more complex. Among them, the agricultural data gradually evolved from single quantitative transformation into qualitative transformation. The characteristics of data are massive, dynamic, spatio-temporal, etc., accompanied by structural changes. Thus, if only relying on the existing data mining technology and relational database, it has been unable to meet the current data storage and data analysis needs. It is particular important how to effectively analyze and deal with massive data, and according to the needs of the results back to the user's hands is particular important. One of the starting points in the study of big agricultural data is how to dig out valuable knowledge from complicated agricultural data. Therefore, it is urgent to use a method to classify and extract large amounts of data to find out the correlation and underlying pattern between them [1], establish the platform for analysis and preprocessing data, monitor agricultural production process, and

combine with data mining technology to obtain real-time information, formulate appropriate coordination measures, and finally realize the precise operation of the farmland management area. Improving the quality of agricultural products under the premise of sustainable development provides a good development environment and material basis for other areas and even the whole national economic development [2].

Aiming at demand for real-time processing of massive intelligent agricultural data, this study firstly accesses the soil air temperature and humidity data from intelligent monitoring network of the National Spark Program “Integration and demonstration of corn precise operation technology based on Internet of things” demonstration area at Nong’an county in real time through the intelligent agricultural monitoring platform, proposes the Spark distributed cluster computing platform. Secondly, conducted the performance comparison experiment of Hadoop and Spark data processing platform, then used the Spark distributed cluster computing platform with extended MapReduce computational models, real-time processing the big data of monitoring area. Spark distributing cluster computing platform has efficient supported for multiple computing modes. Spark with the main characteristics of computing in memory can be applied to a wide variety of distributed platform scenarios, including batch processing, iterative algorithms, interactive queries, stream processing, and so on [3, 4]. These different calculations are supported by a unified framework. Spark allows us to integrate various processing processes simply and at a low cost, combined Spark streaming, SQL, MLlib, Graph X and other modules and data mining technology to make appropriate analysis of data processing [5], it provides the basis for the analysis of mass data in the future. The research results provide strong support for the processing of agricultural big data and the implementation of precision agriculture technology in intelligent agriculture. Thus, it contributes to the sustainable development of agriculture, and realize the modern development of intelligent agriculture.

2 Data Sources and Research Methods

2.1 Data Sources

The study area is Nong’an County of Jilin Province, located in the hinterland of Songliao plain, and it is the central part of Jilin Province, attached to the city of Changchun, located 60 km northwest of Changchun City, east longitude $124^{\circ} 31' - 125^{\circ} 45'$, north latitude $43^{\circ} 55' - 44^{\circ} 55'$, the south is adjacent to the suburbs of Changchun, the east borders on Dehui, northeast across the river and to Fuyu, north of the former Guoer Ross Mongolian Autonomous County, west of Changling, southwest border with Gongzhuling City. County 114.7 km long from north to south, east and west 97.7 km wide [6], the total area is 5400 km². In 2013, the county planting area of agricultural land reached 366,000 hectares, the coverage rate of fine varieties is above 98%, it is one of the important commodity grain bases in Jilin Province. Nong’an County annual average temperature of 4.7° , frost free period of 145 days, rainfall of 507.7 mm, the effective accumulated temperature of 2800° . Flat terrain, four distinct seasons, is a temperate continental climate. The soil in Nong’an county is divided into 10 soil types and 20 sub types, 50 genera and 111 species of soil. The zonal soil is black soil, chernozem [7]. This data comes from the seven real-time data monitoring stations located in Nong’an County

Kai'an Town, Hualong Town Chenjiadian Village, real-time monitoring network for intelligent agriculture, monitoring and collection of crop production environment information using wireless sensor networks, thus to realize the real-time processing and analysis of the big data of the intelligent agriculture.

2.2 Research Methods

2.2.1 Spark Cluster Computing Platform

Spark was originally born at the APM laboratory at the University of Berkeley. It is a fast, general purpose engine that can be used in large-scale data processing [8], today is one of the top open source projects under the Apache Software Foundation. Just as its name Spark, such as lightning fast cluster computing platform, the original design goal of Spark was to make data analysis faster—Not only is it fast, but it also has to be able to write programs quickly and easily. In order to make the program run faster, Spark provides memory computing, reducing the IO overhead in iterative computation. In order to make the program run easier, Spark is written in a concise, elegant Scala language [9], Scala provides an interactive programming experience. From enterprise, medical treatment, transportation to retail trade, the big data solutions offered by Spark are pushing ahead with the insights of business that have never been seen before, and thus accelerated decision-making.

The Spark project contains more than one tightly integrated component, the core of Spark is a computing engine that consists of scheduling, distributing, and monitoring applications that are composed of many computing tasks, running on multiple work machines, or a computing cluster. As shown in Fig. 1, Spark is a large and unified software stack, including Spark SQL, Spark Streaming, MLlib, GraphX, Spark Core and Independent scheduler, YARN, Mesos Modules [10]. Spark Core implements the basic functions of Spark, including task scheduling, memory management, error recovery, storage system interaction and other modules [11]; Spark SQL is a program package that

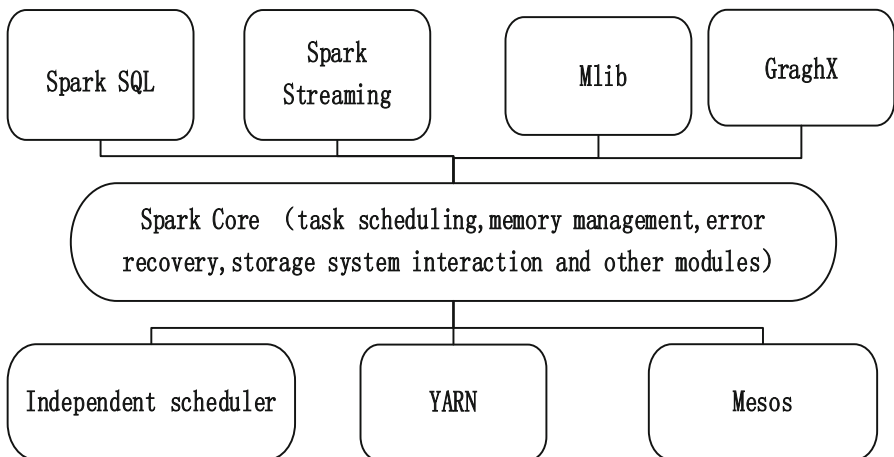


Fig. 1. Spark software stack

Spark used to manipulate structured data; Spark Streaming is a component that Spark provides for streaming computations of real-time data [12]; MLlib provides a variety of machine learning algorithms, all of which are designed to be easily scalable on a cluster [13]; GraphX is a library for operating diagrams, which can be computed in parallel [14].

In a distributed environment, the Spark cluster uses a master/slave architecture. In a Spark cluster, one node is responsible for central coordination, and each distributed work node is scheduled. The central coordination node is called the drive node, and the corresponding work node is called the actuator node. Drive nodes can communicate with a large number of actuator nodes, and they also operate as independent Java processes [15]. The drive node, together with all of the actuator nodes, is called a Spark application, as shown in Fig. 2:

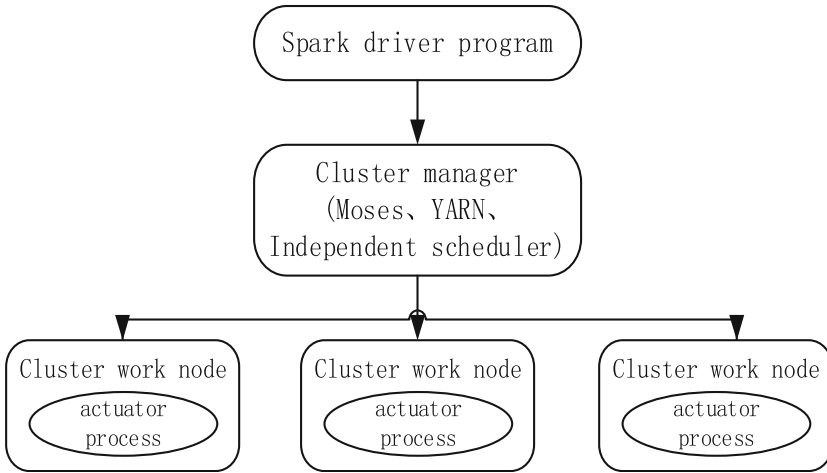


Fig. 2. Calculation framework of Spark cluster

The Spark relies on the cluster manager to start the executor node, but in some special cases it also depends on the cluster manager to start the drive node. The cluster manager is a pluggable component in Spark [16]. In this way, in addition to Spark’s own standalone cluster manager, Spark can also run on other external cluster managers, such as YARN and Mesos [17].

2.2.2 The Characteristics and Advantages of Spark Platform Implementation

Although Hadoop has become the defacto standard of big data, there are still many defects in its MapReduce distributed computing model, Spark draws lessons from the advantages of Hadoop and MapReduce, and solves the problems faced by MapReduce. As shown in Fig. 3, comparing the execution flow of Hadoop and Spark can be seen, The biggest feature of Spark is the introduction of the concept of an elastic distributed data set (Resilient Distributed Dataset, RDD) [18], this allows Spark to cache data set in each node memory in cluster computing, eliminating the need to load multiple times into memory and disk storage [19], and greatly speed up the processing speed.

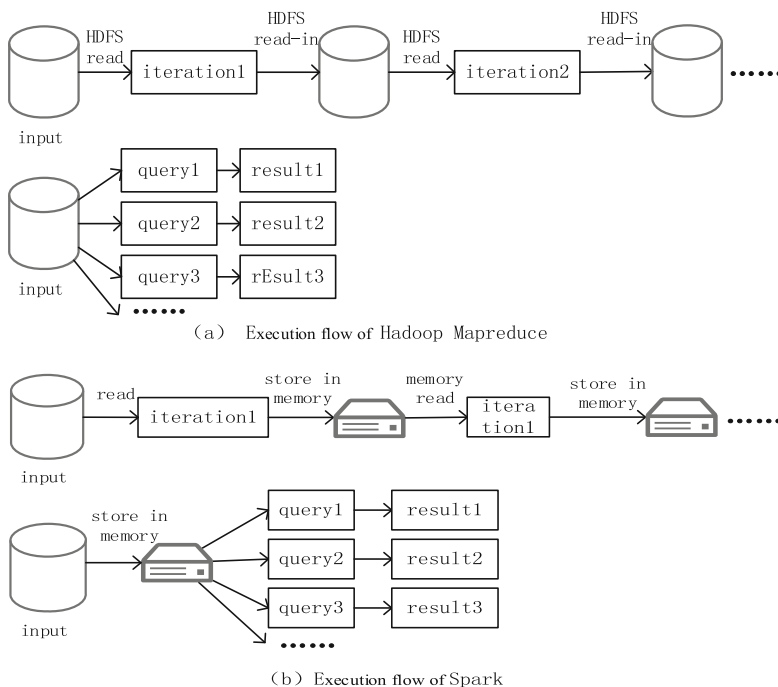


Fig. 3. Comparison of Hadoop and Spark in execution flow

About the advantages of Spark and Hadoop in executing engine, technology stack and so on, As shown in Table 1 [20–22].

Table 1. Comparison table of Hadoop and Spark performance

Type	Spark	Hadoop
Execution engine	DAG task scheduling execution mechanism	MapReduce iteration execution mechanism
Programing language	Scala, Java, Python	Java, Python, C/C++, Ruby
Technology stack	Spark streaming, SQL, MLlib, GraphX	HDFS, MapReduce, HBase, Hive
Operation mode	Independent cluster model	Distributed memory computing
Calculation model	Belong to MapReduce, but not limited to Map and Reduce, multiple data set operation types	Only Map and Reduce two operations

(continued)

Table 1. (continued)

Type	Spark	Hadoop
IO spending	Small, memory calculation	large, disk read write
Implementation of fault tolerance	RDD data storage model	Data replication
Programming code (code quantity)	Real-time interactive programming (1)	Traditional programming (3–6)
Hardware requirements	Requirements for memory and CPU	Cheap, heterogeneous
Suitable application scenarios	(1) Data mining with iterative operations (2) Real time and fast calculation (3) Machine learning operation	Delay is too high, only for offline, batch application scenarios

3 Experimental Results and Analysis

3.1 Comparison of Efficiency Test Between Spark and Hadoop

In performance, the efficiency test compares the time differences between Hadoop and Spark processing large amounts of data when performing logical regressions. This experiment from 2015–2017 intelligent monitoring network in Nong’an County 230 million soil, air temperature and humidity data in the selected 5 groups, respectively 10 thousand, 100 thousand, 1 million, 10 million, 100 million data for execution logistic regression time contrast, the efficiency test results are shown in Table 2 and Fig. 4.

Table 2. Comparison of run time between Hadoop and Spark

Computing platform	10 thousand (1 W)	100 thousand (10 W)	1 million (100 W)	10 million (1000 W)	100 million (10000 W)
Hadoop	8	17	27	255	1755
Spark	10	11	15	27	154

The number in Table 2 is the run time, units are seconds. In Fig. 4, “W” stands for “ten thousand bars”.

3.2 Real Time Processing of Big Data in Intelligent Agriculture

- (1) Build a stream processing framework for Spark platform

The big data analysis platform is designed to have tremendous capabilities and flexibility to meet all these requirements. The major types of processing used in big data analysis are batch processing, stream processing, and iterative processing. Therefore, we need such a platform to store such huge distributed data and perform all of these types of analysis.

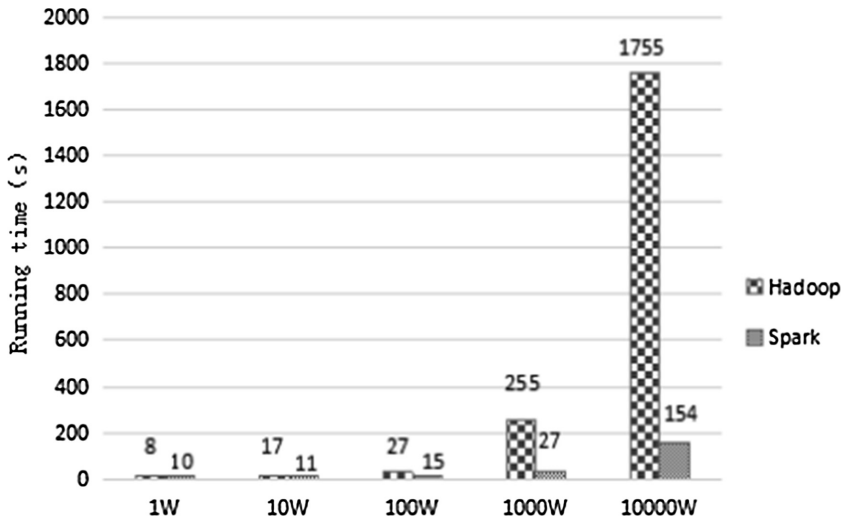


Fig. 4. Comparison of Hadoop and Spark in efficiency test

Before implementing the Spark ecosystem, you need to configure the HDFS distributed file system, build Block data blocks, Name node master nodes and Data node slave nodes; based on the HDFS distributed processing model, create HBase database to achieve high performance, real-time read and write, column storage, scalable functions; with the Thrift software framework, we build seamless and efficient service with Java, Python, C/C++, Ruby and other programming languages.

For the intelligent agriculture monitoring system in Jilin, which requires millisecond real-time response, the processing data is characterized by online, small, dynamic, relative to off-line data processing, because of the high time requirements, it is more suitable for dealing with small amounts of data and running relatively simple algorithms; for the high fault tolerance and high reliability requirement of the system, Spark uses record update to create a record RDD transform sequence, in order to facilitate the recovery of file partitions.

According to the above requirements analysis, the system uses the Spark Streaming stream computing framework with good fault tolerance and easy combination with machine learning and graph computing in the Jilin intelligent agriculture monitoring platform, real-time reception, calculation and delivery of data streams using Spark Streaming; Based on the MLlib machine learning framework, combining the improved particle swarm optimization and the limit learning machine ELM, batch processing the data for the training model; transferred processing data to the distributed file system HDFS and HBase database to store calls; the final results are fed back to the Jilin provincial wisdom agriculture monitoring platform in the form of analytical charts, as shown in Fig. 5.

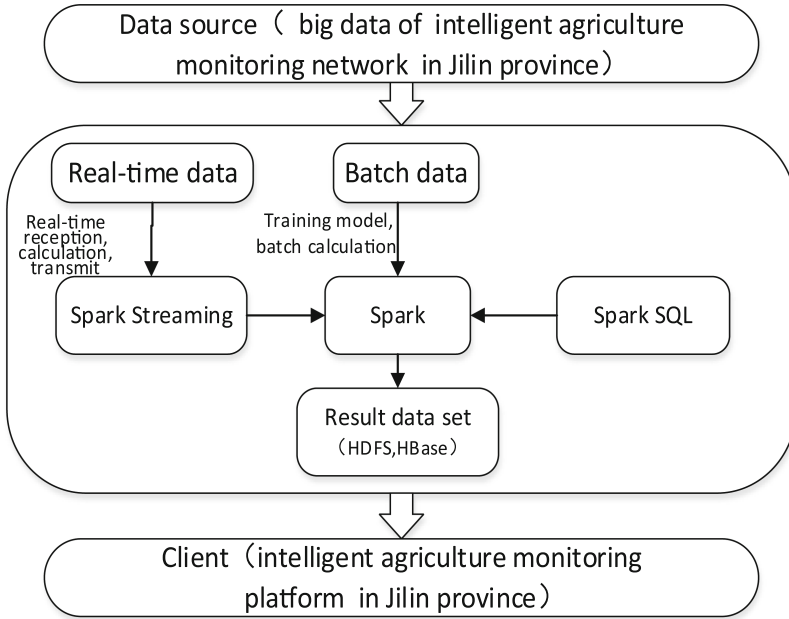


Fig. 5. Stream processing framework of intelligent agriculture monitoring platform in Jilin province

(2) Collecting intelligent monitoring network data

Based on the data comes from seven intelligent monitoring network of the National Spark Program “Integration and demonstration of corn precise operation technology based on Internet of things” demonstration area at Nong’an county, collected from May 1, 2015 to December 31, 2016 crop different dimensions (0–20 cm, 20–40 cm, 40–60 cm, 60–80 cm) soil temperature and humidity data (as shown in Table 3), and import the data into the HBase system.

Table 3. Soil moisture and temperature data of intelligent agricultural monitoring network in Jilin province

Time	Water content				Soil temperature (°C)			
	0–20 cm	20–40 cm	40–60 cm	60–80 cm	0–20 cm	20–40 cm	40–60 cm	60–80 cm
2015.5	8.75%	15.31%	19.47%	17.43%	14.51	12.63	11.18	10.11
2015.6	20.62%	20.62%	29.38%	28.85%	20.46	18.55	17.06	15.94
2015.7	12.04%	20.59%	30.73%	29.81%	24.67	23.07	21.75	20.70
2015.8	14.16%	20.91%	31.41%	30.27%	23.79	23.31	22.79	22.24
2015.9	20.69%	20.69%	30.09%	29.43%	19.02	19.34	19.47	19.41
2015.10	12.61%	19.72%	28.66%	28.13%	9.87	11.36	12.44	13.12
2015.11	5.69%	15.78%	25.63%	26.05%	2.22	4.33	5.93	7.04

(continued)

Table 3. (continued)

Time	Water content				Soil temperature (°C)			
	0–20 cm	20–40 cm	40–60 cm	60–80 cm	0–20 cm	20–40 cm	40–60 cm	60–80 cm
2015.12	3.51%	9.35%	11.63%	21.92%	-2.51	-0.30	1.38	2.48
2016.1	2.70%	7.47%	6.24%	9.91%	-8.06	-5.20	-2.70	-0.99
2016.2	4.70%	7.76%	6.15%	8.50%	-6.35	-5.31	-4.14	-3.17
2016.3	15.33%	13.83%	11.73%	11.12%	-0.75	-1.04	-0.98	-0.80
2016.4	15.85%	20.74%	25.51%	19.71%	3.96	1.39	0.09	-0.02
2016.5	15.05%	20.98%	30.96%	28.80%	12.75	10.86	7.98	8.36
2016.6	14.10%	20.92%	31.23%	29.75%	19.73	18.10	16.80	15.81
2016.7	13.05%	20.60%	31.57%	30.33%	24.08	22.73	21.58	20.68
2016.8	13.91%	22.07%	33.36%	31.36%	24.73	24.25	23.67	23.08
2016.9	18.43%	23.13%	34.19%	31.66%	18.82	19.29	19.61	19.74
2016.10	16.76%	21.51%	31.16%	29.17%	9.77	11.95	12.65	13.56
2016.11	9.18%	18.21%	27.27%	26.54%	1.83	3.79	5.51	6.78
2016.12	7.35%	9.55%	14.36%	21.40%	-2.12	0.18	1.88	3.03

(3) Processing of Soil Moisture Monitoring Data

According to Table 3 data, soil moisture data in different depths were obtained in real time, then to dynamic monitoring and multi angle data processing analysis. The processing results are shown in Fig. 6.

3.3 Results and Analysis

(1) Comparing the efficiency test of Hadoop and Spark platform

By comparing the efficiency test of Hadoop and Spark platform, the experimental results are obtained (Table 2 and Fig. 4): When the amount of monitoring data is 10 thousand, Hadoop running time is lower than Spark platform, at this point, the Hadoop is processing faster than the Spark. When the amount of data reaches 100 thousand or more, Spark takes advantage of its fast memory, computing, and distributed frameworks. In time, it is much better than Hadoop's multiple iteration algorithm. When the test content reaches 100 million, the Hadoop platform is 11.4 times more expensive than Spark. At the same time, it can be seen by the contrast chart: Under the Spark distributed framework, as the amount of data increases, the time difference between the time spent and the total time is getting smaller and smaller, reflects the stability and reliability of the Spark platform.

(2) Real-time monitoring and processing of soil moisture data

As can be seen from Fig. 6, in 2015 and 2016 in May to December year on year, the change of soil temperature at different levels is not obvious. But the soil moisture change is obvious at different levels; soil moisture content was lowest in late seedling stage (at the end of June), and it was the most in early mature (September 4th); soil temperature was lowest in the middle of seedling (June 10th), and highest in late maturing (at the end of September). At the same time, the trend of moisture change of

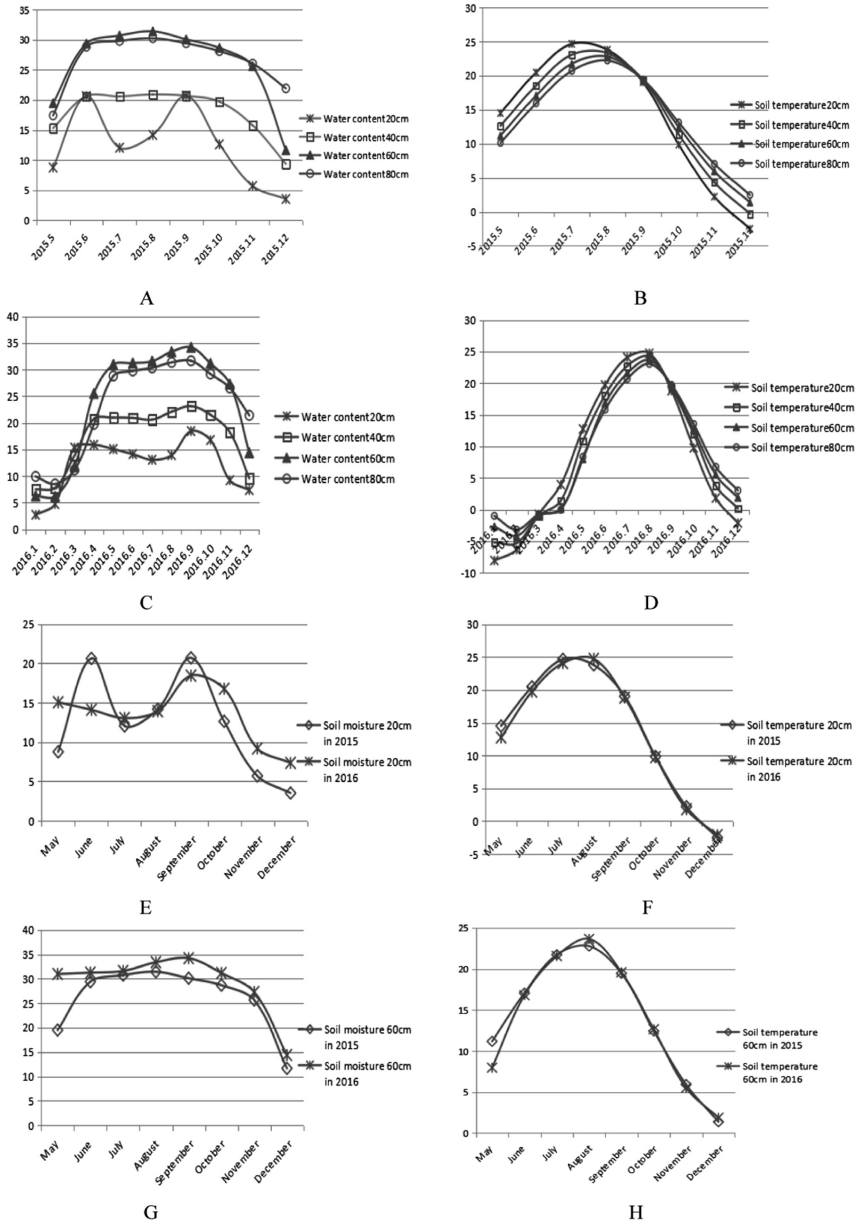


Fig. 6. Analysis of massive soil temperature and humidity data of intelligent agricultural monitoring network in Jilin province. A. Moisture trend of 0–80 cm soil in 2015; B. Temperature trend of 0–80 cm soil in 2015; C. Moisture trend of 0–80 cm soil in 2016; D. Temperature trend of 0–80 cm soil in 2016; E. Moisture trend comparison of 0–20 cm soil between 2015 and 2016; F. Temperature trend comparison of 0–20 cm soil between 2015 and 2016; G. Moisture trend comparison of 40–60 cm soil between 2015 and 2016; H. Temperature trend comparison of 40–60 cm soil between 2015 and 2016.

20 cm and 60 cm in 2015 was compared with that in 2016, affected by climate factors such as rainfall and light in different years, there were some differences, but the soil temperature did not change significantly in previous years. The analysis results show that the intelligent agriculture monitoring network based on Spark platform can deal with soil moisture data in real-time and effectively. It provides support for precision agricultural production such as timely sowing of crops and water-saving irrigation and so on.

4 Conclusion and Prospect

Through accessing the soil air temperature and humidity data from intelligent monitoring network of the National Spark Program “Integration and demonstration of corn precise operation technology based on Internet of things” demonstration area at Nong’an county in real time through the intelligent agricultural monitoring platform, research on Spark platform for big data processing of Intelligent Agriculture in Jilin province found that:

- (1) Spark and Hadoop platform efficiency comparison test results show that, the Spark platform has the advantage of reducing IO overhead with its memory computing, Hadoop is more suitable for dealing with real time big data of intelligent agriculture monitoring network in Jilin province.
- (2) The agricultural big data processing method of intelligent agriculture in Jilin Province based on Spark platform, using the machine learning algorithm characterized by dynamic and rapid expansion, combining the Spark streaming flow calculation framework, able to real-time analyze continuous and rapid changes in the massive data. Moreover, the calculation results are faster and more accurate. The implementation of precision agriculture and the wisdom of agricultural big data processing have a certain role in promoting.
- (3) For this study, the problem of the data quantity is small, but the monitoring network real-time data processing needs large, in the future, we will further adopt the Spark platform to combine the better clustering algorithm, make the sensor transmission data to be timely and effective treatment, utilize the advantages of large data processing, combine soil moisture content with big data information, constructing perfect intelligent monitoring system of agriculture.

Acknowledgments. This work was funded by the China Spark Program. 2015GA660004. “Integration and demonstration of corn precise operation technology based on Internet of things”.

References

1. Cheng, X., Jin, X., Wang, Y., Guo, J., Zhang, T., Li Guojie, J.: Large data system and analysis technology. *J. Softw.* (09), 1889–1908 (2014)
2. Reyes-Ortiz, J.L., Oneto, L., Anguita, D.: Big data analytics in the cloud: spark on Hadoop vs MPI/OpenMP on beowulf. *Procedia Comput. Sci.* **53**, 121–130 (2015)

3. Feng, Y., Huarui, W., Huaji, Z., Haihui, Z., Xiang, S.: Based on Hadoop's massive agricultural data resource management platform. *Comput. Eng.* **12**, 242–244 (2011)
4. Shyam, R., Bharathi Ganesh, H.B., Sachin Kumar, S., Poornachandran, P., Soman, K.P.: Apache spark a big data analytics platform for smart grid. *Procedia Technol.* **21**, 171–178 (2015)
5. Qi, R., Wang, Z., Huang, Y., Li S.: Based on Spark's parallel combination test case set generation method. *J. Comput. Sci.*, 1–18 (2017)
6. Jian, L., Guifen, C., Ying, M., Hang, C.: Research and system realization of farmland environment simulation monitoring based on 3D GIS. *Chin. J. Agric. Sci. Technol.* **3**, 50–55 (2017)
7. Czerwinski, D.: Digital filter implementation in Hadoop data mining system. *Comput. Netw.*, 410–420 (2015)
8. He, Q., Wang, H., Zhuang, F., Shang, T., Shi, Z.: Parallel sampling from big data with uncertainty distribution. *Fuzzy Sets Syst.*, 117–133 (2015)
9. Yang, Z., Zheng, Q., Wang, S., Yang, J., Zhou, L.: Adaptive task scheduling strategy under heterogeneous Spark cluster. *Comput. Eng.* **1**, 31–35 (2016)
10. Chen, G.F., Dong, W., Jiang, J., Wang, G.W.: Variable—rata fertilization decision—making system based on visualization toolkit and spatial fuzzy clustering. *Sens. Lett.* **01**, 230–235 (2012)
11. Fan, Z., Zhaokang, Y., Fanping, X., Kun, Y., Zhangye, W.: Visualization of large data heat map based on Spark. *J. Comput. Aided Des. Graph.* **11**, 1881–1886 (2016)
12. Chen, G., Yang, Y., Guo, H., Sun, X., Chen, H., Cai, L.: Analysis and research of k-means algorithm in soil fertility based on Hadoop platform. In: Li, D., Chen, Y. (eds.) CCTA 2014. IAICT, vol. 452, pp. 304–312. Springer, Cham (2015). https://doi.org/10.1007/978-3-319-19620-6_35
13. Cai, L.: Based on large data processing technology Hadoop platform maize precision fertilization intelligent decision system research. Jilin Agricultural University, Changchun (2015)
14. Xin, W., Kan, L., Rongguo, C.: Distributed spatial data analysis framework based on Shark/Spark. *Earth Inf. Sci.* **04**, 401–407 (2015)
15. Xiande, Z.: Based on the Spark platform real-time flow calculation recommendation system research and implementation. Jiangsu University, Jiangsu (2016)
16. Wen, Q., Wang, J., Zhu, H., Cao, Y., Long, M.: Distributed hash learning method for approximate nearest neighbor query. *J. Comput.* **01**, 192–206 (2017)
17. Li, W., Chen, Y., Guo, K., Guo, S., Liu, Z.: Parallel limit learning machine based on improved particle swarm optimization. *Pattern Recognit. Artif. Intell.* **09**, 840–849 (2016)
18. Ziyu, L.: Big Data Technology Principle and Application. People's Posts and Telecommunications Press, Beijing (2017)
19. Yang, T., Wang, J., Yang, T., Zhang, X.: A data processing mechanism for high-efficiency large-scale graphs in Spark. *Appl. Res. Comput.* **12**, 3730–3734 (2016)
20. Heng, C.: A Spark-based distributed semantic data distributed reasoning framework. *Comput. Sci.* **S2**, 93–96 (2016)
21. Zhang, X., Chen, H., Qian, J., Dong, Y.: HSSM: a method of maximizing hierarchical data for streaming data. *J. Comput. Res. Dev.* **08**, 1792–1805 (2016)
22. Sun, Z., Du, K., Zheng, F., Yin, S.: Research and application of large data in wisdom agriculture. *Chin. Agric. Sci. Technol. Rev.* **06**, 63–71 (2013)



Summary of Agricultural Drought Monitoring by Remote Sensing at Home and Abroad

Meng Wang, Tao Liu^(✉), Shouzhen Ling, Xueyan Sui, Huimin Yao, and Xuehui Hou

Key Laboratory of East China Urban Agriculture,
Shandong Institute of Agriculture Sustainable Development,
Ministry of Agriculture, Jinan 250100, China
s.a.s.l.t@163.com

Abstract. Drought is one of the major natural disasters which causes very severe impacts on economy and society, remote sensing is the efficient method which can dynamic monitor drought at a great range of scale, the research on agricultural drought monitoring has been an important issue. This paper introduces the principle of agricultural drought monitoring based on remote sensing technology, and reviews the current remote sensing approaches in drought monitoring. Combined with the current research hotspots, this paper offers the further research ideas by discussing the dominances and limitations of these methods.

Keywords: Agricultural drought · Remote sensing · Methods
Soil water

1 Introduction

Agriculture is the most fundamental and weakest link in our country's entire national economy. Crop production is directly related to the food security of our country and the increase of agricultural efficiency. Drought is a water shortage caused by the imbalance of water supply. Agricultural drought, the water deficit in crops, is mainly due to the imbalance between soil water supply and crop water demand, depending on the soil's water supply capacity and the physiological needs of crops. In recent years, agricultural disasters in China have occurred many times, agricultural drought because of its high frequency, long duration, large extent, to the agricultural economy caused serious influence, has become a major natural disasters in the world [1, 2].

The traditional drought monitoring method is based on the limited soil moisture monitoring site to determine the status of crops and plants being inhibited by insufficient water supply, and the description is qualitative. This method has limitations, it difficult to obtain accurate and timely agricultural drought and the development of time and space information. Remote sensing technology has the advantages of macro, rapid,

Fund project: Research and application of drought remote sensing monitoring and early-warning technology of winter wheat in Shandong province.

© IFIP International Federation for Information Processing 2019

Published by Springer Nature Switzerland AG 2019

D. Li and C. Zhao (Eds.): CCTA 2017, IFIP AICT 546, pp. 13–20, 2019.

https://doi.org/10.1007/978-3-030-06179-1_2

wide range and economy, which provides a new way for agricultural drought monitoring [3]. Remote sensing technology has become an important means of drought monitoring and has played an important role in agricultural drought monitoring [4].

2 The Background and Status of Drought Remote Sensing Monitoring Technology

Remote sensing technology is based on electromagnetic theory, application of various sensors on long-range target radiation and reflection of electromagnetic wave information, collection, processing, and finally, imaging, and on the ground all sorts of scenery detection and identification of a comprehensive technical [5].

Since the invention of the first airplane, aerial remote sensing was first applied militarily, and has been widely used in geology, engineering construction, map mapping, agricultural resources investigation and so on. Since the launch of the first satellite, remote sensing technology has been widely developed and widely used. With the continuous development of sensor technology, aerospace technology and communication technology, modern remote sensing technology has entered a new stage of multi-platform, multiphase and high resolution. Remote sensing technology and space science, electronic science, earth science, computer science and other edge discipline cross infiltration and mutual confluence, has gradually developed into a new type of earth space information science. According to different energy sources of detection targets, remote sensing is divided into active remote sensing technology and passive remote sensing technology. According to the representation of recorded information, remote sensing can be divided into image and non-image modes. Remote sensing can be divided into space, aviation and ground remote sensing technology according to the platform of remote sensor. Remote sensing technology has been widely used in land resources, land resources, vegetation resources, geology, cities, surveying and mapping, archaeology, environmental investigation monitoring and planning and management.

There are many classifications about drought [6–8], which can be divided into four categories: meteorological drought, hydrological drought, agricultural drought, and economic and social drought. Agricultural drought refers to the phenomenon of crop failure due to insufficient rainfall and inadequate irrigation in the process of crop growth. The key factor to reflect the drought is the soil moisture content [10]. Therefore, the direct target of using remote sensing for drought monitoring is soil moisture content. Remote sensing based on the theory of electromagnetic wave, drought, crops before and after the biochemical components in canopy structure has changed, the sensor receives electromagnetic wave changes, compare before and after the drought disaster information of electromagnetic analysis can obtain the scale of the crop. Research work about the drought remote sensing monitoring at home and abroad have been carried out for a long time, almost all the crops on agricultural drought disaster, the influence of using remote sensing data and other support, obtain accurate soil moisture content, set up the drought monitoring and evaluation methods have a lot of work to do. Scholars at home and abroad often using the thermal inertia method, vegetation index method of water supply, green index method, anomaly vegetation

index method, microwave spectroscopy, thermal infrared remote sensing, remote sensing soil moisture for a study of spectral reflection characteristic of soil moisture content, such as the relatively mature method of thermal inertia method, vegetation index method of water supply, the green index method, anomaly vegetation index method and microwave remote sensing.

3 Thermal Inertia Method

The thermal inertia is a measure of the thermal reaction of matter to temperature, reflecting the energy exchange of matter and the surrounding environment. The thermal inertia method is a more mature method for monitoring soil moisture. The thermal inertia reflects a thermal characteristic of soil. Its principle is that the soil with high water content has a large thermal inertia according to the heat capacity and heat conductivity of the water. Soil thermal inertia and there is a correlation between soil moisture content, soil heat capacity, thermal conductivity increases with the increase of soil moisture, soil thermal inertia also increases with the increase of soil water content.

The daily contrast of soil surface temperature is determined by the factors of soil internal and external factors. The internal factors mainly reflect the thermal conductivity of soil heat transfer capacity and heat capacity reflecting the soil heat storage capacity; External factors refer to the surface thermal equilibrium caused by solar radiation, air temperature, relative humidity, wind, cloud, water vapor, etc. Therefore, when using remote sensing information inversion of soil thermal inertia, needs the support of a large number of ground data, not only need to consider the solar radiation, atmospheric absorption and radiation, soil thermal radiation and heat conduction effect, also should take into account the evaporation, condensation and enrage effect on heat exchange, or parameters, calculation is more complicated.

In 1971, Price [11] first applied a model based on thermal inertia. In 1975, Kahle [12], Ju [13], according to the heat balance and heat conduction theory, improved the soil thermal inertia model, which combined the heat flux (H), latent heat flux (E) and surface heat flux (G) to the surface radiation energy. Price [12] proposes the Apparent Thermal Inertia (Apparent Thermal Inertia, ATI) concept, namely, ignore the latitude, the sun Angle, sunshine time, and the influence of the distance, only consider the soil reflectance and surface temperature changes. The apparent thermal inertia of soil can be obtained indirectly through remote sensing inversion of soil reflectivity and surface temperature. In practice, we usually use the apparent thermal inertia to approximate replace real thermal inertia, according to the surface of the heat balance equation and heat conduction equation to establish apparent thermal inertia (ATI) and soil moisture content between remote sensing information inversion model [14]. The surface temperature difference is small, the apparent thermal inertia is large, the soil water content is high; the surface temperature difference is large, the apparent thermal inertia is small, and the soil moisture content is low. In China since the early 1990s in the thermal inertia model theory and experimental research has made great progress, Ji [15], such as using MODIS data, through the establishment of apparent thermal inertia and soil moisture between the linear experience model, in Shaanxi province early February to March, 2005 occurred in late spring drought process monitoring tests have been carried

out. The thermal inertia of the surface temperature was calculated by using the modified surface temperature, and the soil moisture was obtained, and the drought conditions in Liaoning were monitored for years. By using NOAA/AVHRR satellite data, Guo *et al.* [17] and other methods used the apparent thermal inertia method to invert the shallow soil moisture. The thermal inertia method of soil moisture content requires strict registration of two remote sensing images in the research area, and the temperature difference is obtained by the light temperature. Since remote sensing image is affected by the cloud, it is difficult to get the image of cloud in the same research area day and night, so it is difficult to guarantee the accuracy of the diurnal temperature difference. When the soil vegetation coverage is high, the accuracy of the soil moisture content will be greatly reduced due to the influence of vegetation transpiration and soil moisture exchange.

4 Vegetation Water Supply Index Method

The vegetation water supply index is a comprehensive monitoring drought method based on surface temperature and vegetation index. The principle is that when the plant water supply is insufficient to cause the crop to die due to lack of water, the normalized vegetation index will drop sharply and the surface temperature of the leaf will rise rapidly. Definition [18] of Vegetation Supply Water Index (VSWI):

$$VSWI = NDVI/T_S$$

VSWI is the vegetation water supply index; T_S is the canopy temperature of vegetation; NDVI is the normalized vegetation index.

The physical meaning of vegetation water supply index method can be described as: when the vegetation water supply is normal, the vegetation index reflected by remote sensing information is stable during certain growth period. In case of suffering from drought, vegetation growth under water stress, to reduce moisture loss, plant stomata part will close, resulting in increased leaf temperature, vegetation canopy temperature, vegetation water supply is insufficient growth affected at the same time, vegetation remote sensing information is a reflection of the index will be reduced. The use of NOAA/AVHRR data to use the vegetation water supply index method was used to monitor the continuous drought disaster in the winter and spring in Fujian province from 2001 to 2002. Chen [20] and other use vegetation water supply index to monitor Guangdong province in October 2004 drought conditions. Vegetation water supply index when applied to the MODIS data, as a result of the MODIS data to get NDVI easier than NOAA/AVHRR data get NDVI to saturation, so the VSWI is applied to the high density vegetation biomass, its monitoring precision will decline. Ji [15] on the VSWI is improved, the model of NDVI to switch to the enhanced vegetation index (EVI), to improve the sensitivity of biomass area, and early April to May, 2005 in Shaanxi province in late spring drought monitoring.

5 Distance Vegetation Index Method

The distance vegetation index defines [21]:

$$ATNDVI = TNDVI - \overline{TNDVI}$$

$$TNDVI = \text{MAX}(NDVI(t))$$

ATNDVI is the distance vegetation index; TNDVI was the highest value of NDVI in the same period. T is the number of days; the evaluate the annual normalized vegetation index (NDVI).

In general, the light and temperature conditions in certain areas are not very different, and the vegetation growth condition is mainly related to water, and the water supply is the key factor for vegetation growth. The distance vegetation index method is from the perspective of vegetation growth. When the soil water supply is abundant, the vegetation grows well. Conversely, vegetation growth is inhibited. This method needs to be accumulated many years of remote sensing data to calculate the perennial ten-day average vegetation index, then the same period when the observation period of vegetation index compared with perennial average, judge condition of crop growth, and then to evaluate crop drought degree. Using the distance vegetation index method, the NOAA/AVHRR data were used to monitor the extreme drought in Heilongjiang province in the summer of 2000 [22]. According to the distance vegetation index, the drought was divided into severe drought, drought and normal 3 grades. In this paper, the relative distance map of vegetation index is supervised and classified, and the pseudo-color map of drought monitoring is generated, and the affected area of crops is calculated. The drought condition of grassland in Qinghai province was monitored by the vertical vegetation index [23]. Tansey [24], respectively, using 1982–1998 (1999) precipitation and temperature meteorological data, as well as the AVHRR NDVI remote sensing data are calculated by the Yellow River basin climate drought index, and analyzed the NDVI, the Yellow River basin are analyzed from the aspects of climate and vegetation features 18a to drought condition changes.

6 Microwave Remote Sensing

Microwave remote sensing is one of the most important methods for soil moisture monitoring. Microwave remote sensing has the characteristics of all-weather, multi-polarization and a certain transmission capability to the soil layer. The method of microwave remote sensing monitoring of agricultural drought is mainly passive microwave method and active microwave method. Generally passive microwave remote sensing cost is low, the time resolution is high, but the spatial resolution is low; The active microwave remote sensing cost is high, the spatial resolution is high, but the time resolution is low. Regardless of passive microwave remote sensing or active microwave remote sensing, the inversion results are affected by surface roughness and vegetation. How to reduce or eliminate the influence of surface roughness and vegetation is an important research direction of microwave remote sensing. Tansey

Moeremans and [25, 26] research shows that in bare land and sparse vegetation areas, after the near surface soil moisture and to a high degree of correlation between scattering coefficient, and that the surface roughness has a great influence on soil moisture monitoring. Li zhen and other [27] comprehensive active and passive microwave data and optical data monitoring soil moisture change, reduce the influence of vegetation, and improve the accuracy of soil moisture change monitoring. Liu wei, etc. [28] try polarization decomposition technique to overcome the influence of surface roughness and vegetation, the better estimation of vegetation covered surface soil moisture change, but this method requires high temporal resolution, must be full polarization data at the same time, the current spaceborne microwave sensor is difficult to meet the requirements; Rajat Bindlish [29] takes advantage of the improved IEM model to obtain the inverse results of 0.95 correlation with actual soil moisture. Microwave remote sensing is not affected by the interference of cloud, which can be used throughout the day, although greatly influenced by the surface parameters, but its for soil moisture estimation accuracy is high, is the method of monitoring soil moisture potential. However, the current microwave remote sensing usually can only reverse the moisture of soil surface, and the root system of crops is usually under 10 cm–20 cm, so the application of agricultural drought monitoring has certain limitations.

7 Conclusion

In recent years, agricultural drought in China has been frequent and serious, and accurate drought monitoring is of great significance. Agricultural drought involves many subjects such as agriculture, meteorology, hydrology and plant physiology. It is a complex phenomenon, and accurate crop drought monitoring is more difficult. Remote sensing data contains abundant surface comprehensive information and remote sensing technology has great potential in drought monitoring. At present, the domestic and foreign scholars in the field of agricultural drought remote sensing monitoring technology research a series of achievements, and explore some feasible methods and approaches, among the more mature method of thermal inertia method, vegetation water supply index method, anomaly vegetation index method and microwave remote sensing method, etc. Various monitoring technologies have their own advantages and disadvantages, and their applicability and accuracy are subject to further improvement and improvement.

- (1) The advantage of thermal inertia is that the method is simple and easy to obtain, suitable for use in the bare ground/low vegetation coverage area, and the disadvantage is that the scope of application is narrow;
- (2) The advantages of the vegetation water supply index method are that the parameters are clear and the accuracy is higher, which is suitable for the high and high vegetation coverage area, and the disadvantage is that the vegetation canopy temperature is difficult to obtain.
- (3) The advantage of the distance vegetation index method is clear, suitable for the medium and high vegetation coverage area. The disadvantage is that the remote sensing data and the monitoring results are in lag.

- (4) The advantages of microwave remote sensing method are all-weather and high precision, suitable for use in bare ground/vegetation coverage area, and the disadvantage is that monitoring soil is effective and shallow and cost is high.

In view of the advantages and disadvantages of the existing agricultural drought remote sensing monitoring technology, further agricultural drought monitoring research should strengthen the combination of crop physiology, morphological indexes and soil moisture content indexes. There are many available remote sensing data sources available, and the application of new remote sensing data sources in agricultural drought monitoring is actively carried out, such as the application of remote sensing data of GF-1. Further considering the use of multiple satellite sensors simultaneously to monitor the agricultural drought situation, the integrated radar data and the advantages of visible data make the monitoring results more comprehensive, accurate and timely. Using the advantages of remote sensing methods and solving the problem of technical practical application, the development and construction of a nationwide system of remote sensing monitoring of drought remote sensing will be a very challenging research work.

References

1. Zhiguo, H., et al.: China's Climate Resources. Science and Technology Press, Beijing (1993)
2. Li, M., Li, S., Li, Y.: Analysis of Drought Disaster in China in nearly 50 years. *Chin. Agric. Meteorol.* **24**(1), 8–11 (2003)
3. Hong, X., Wu, J., Liu, Y., et al.: Research on drought monitoring in china using remote sensing methods. *Remote Sens. Inf.* **24**(1), 55–58 (2005)
4. Weiguo, L.: Method and Application of Crop Remote Sensing Monitoring and Application. China Agricultural Science and Technology Press, Beijing (2013)
5. Mei, A., Peng, L., Qiming, Q.: Introduction to Remote Sensing. Higher Education Press, Beijing (2001)
6. American Meteorological Society. Meteorological drought: policy statement. American Meteorological Society (1997)
7. Keli, L.: Research on Drought Disaster in China and Countermeasures. Henan Science and Technology Press, Zhengzhou (1999)
8. Wilhite, D.A.: Preparing for drought: a methodology. In: Wilhite, D.A. (ed.) *Drought: A Global Assessment, Hazards and Disaster Series*, vol. II, pp. 89–104. Routledge, New York (2002)
9. Bowers, S.A., Hunks, R.J.: Reflection of radiant energy from soils. *Soil Sci.* **100**(2), 135–138 (1965)
10. Watson, K., Rowen, L.C., Offield, T.W.: Application of thermal modeling in the geologic interpretation of IR images. *Remote Sens. Environ.* **24**(3), 2017–2041 (1971)
11. Price, J.C.: Thermal inertia mapping: a new view of the earth. *J. Geophys. Res.* **82**(18), 25–31 (1977)
12. Kahle, A.B.: A simple thermal model of the earth's surface for geologic mapping by remote sensing. *J. Geophys. Res.* **82**(11), 1673 (1977)
13. Ju, W., Sun, H., Tang, Z.: The application of meteorological satellite remote sensing in drought monitoring. *Disaster Sci.* **12**(4), 25–29 (1996)

14. Zhang, S., Du, J., Jing, Y.: Research on the operational methods of remote sensing drought monitoring based on MODIS data. *Agric. Res. Arid Reg.* **24**(3), 1–6 (2006)
15. Ji, R., Xiu, B., Rui, F., et al.: Application of NOAA/HAVRR data to monitor soil moisture and drought area. *J. Disaster Prev. Mitig. Eng.* **25**(2), 157–161 (2005)
16. Guo, Q., Li, G.: Discussion on soil moisture content using thermal inertia method. *Chin. Agric. Meteorol.* **26**(4), 215–219 (2005)
17. Liping, Y., Xiaohua, Y., Cunhou, Z.: Application of vegetation water supply index method in drought monitoring in inner mongolia. *Inner Mongolia Agric. Sci. Technol.* **20**(1), 58–62 (2008)
18. Zhang, C., Li, W.: Research on remote sensing monitoring of drought disasters in Fjian province. *Meteorology* **30**(3), 22–25 (2004)
19. Deng, Y., Xiao, Q., Hang, J., et al.: Application of remote sensing monitoring of drought in Guangdong province in 2004. *J. Trop. Meteorol.* **22**(3), 237–240 (2006)
20. Wiyang, C., Qanguang, X., Yngwei, S.: The application of the remote vegetation index in the severe drought monitoring in 1992. *J. Remote Sens.* **24**(2), 106–112 (1994)
21. Xu, Y., Wu, M., Li, X., et al.: NOAA/AVHRR data in drought monitoring in heilongjiang. *J. Harbin Inst. Technol.* **10**(2), 51–53 (2005)
22. Yongmei, Z.: Application of NOAA/AVHRR data in grassland drought monitoring in pastoral areas of Qinghai province. *J. Appl. Meteorol.* **9**(4), 496–500 (1998)
23. Shengtian, Y., Changming, L., Rui, S.: Analysis of climate and vegetation characteristics of drought conditions in the yellow river basin. *J. Nat. Resour.* **18**(2), 136–141 (2003)
24. Tansey, K.J., Millington, A.C., Battikhi, A.M., et al.: Monitoring soil moisture dynamics using satellite imaging radar in northeastern Jordan. *Appl. Geograph.* **19**(4), 325–344 (1999)
25. Moeremans, B., Dautrebande, S.: Soil moisture evaluation by means of multitemporal ERS SAR PRI images and interferometric coherence. *J. Hydrol.* **234**(3–4), 162–169 (2000)
26. Li, Z., Guo, D.: Comprehensive active and passive microwave data monitoring soil moisture change. *J. Remote Sens.* **6**(6), 481–485 (2002)
27. Wei, L., Jianming, W.: Application of polarization decomposition technology in estimating soil moisture change in vegetation cover area. *Remote Sens. Inf.* **5**(4), 3–6 (2005)
28. Blindish, R., Jackson, T.J., Gasiewski, A.J., et al.: Soil moisture mapping and AMSR-E validation using the PSR in SM EX02. *Remote Sens. Environ.* **103**(2), 127–139 (2006)



Research and Application of 3D Visualization Plug-in Integration with ArcGIS

Yinglun Li, Guifen Chen^(✉), and Dongxue Wang

Jilin Agricultural University, Changchun 130118, China
617990443@qq.com, guifchen@163.com

Abstract. With the development of agricultural production data, more and more three-dimensional visualization of monitoring data has become the focus of agricultural information technology research. The application of ArcGIS visualization technology, 3D visualization of auxiliary plug-in, and the national Spark Program demonstration area of farmland monitoring data obtained in Jilin province Nong'an County Helong town of application. In this study, the use of C++ language, the introduction of three-dimensional visualization library SDK, compiled auxiliary plug-in ArcGIS software, optimize the joint jiulongzhen farmland monitoring data 3D visualization. The experimental results show that the preparation of the postprocessing plug-ins integrated into ArcGIS software can optimize the 3D visualization of monitoring data, the two-dimensional spatial variability of thematic map than the traditional representation of 3D data more natural, more clear, more intuitive, is of great significance for promoting the development of modern agriculture.

Keywords: ArcGIS · 3D visualization · Auxiliary plug ins · Farmland monitoring

1 Introduction

3D GIS is one of the new trends in the field of GIS. The 3D GIS is more realistic and visual than the two-dimensional GIS in expressing the objective world. It does not need the space entity for abstract symbols, but the geographical objects using stereo technology show to the user, and to provide humane and 3D simulation world interactive tools for users, users easier access to spatial information [1].

With the help of data visualization is the main graphical means to communicate clearly and effectively communicate with the information in order to effectively convey the concept, aesthetic form and function need to go hand in hand, by visually convey and key characteristics, in order to achieve in-depth insight into the rather sparse and complicated data set. Data visualization is closely related to information graphics, information visualization, scientific visualization and statistical graphics [2]. At present, data visualization is a very active and critical aspect in the field of research, teaching and development. The term “data visualization” enables the integration of mature scientific visualization with the field of younger information visualization.

In order to continue to promote the optimization of the agricultural economy, and realize the sustainable development of the industry and the optimization of regional

industrial structure, to further promote the wisdom of agricultural development, need comprehensive and timely grasp the dynamic development of agriculture, which requires the analysis of processing technology on the basis of the agricultural data and related data, characteristics of agricultural data meet the five characteristics of big data, a is a large amount of data, the two is fast processing speed, three types of data, the four is of high value, high accuracy is five [3]. The 3D visualization technology can use characteristics of agricultural data, continuous inspection data, identify the authenticity of data, more intuitive to find and put forward useful anomalies, analysis, understanding and duplicate data provides a useful tool for multidisciplinary collaboration to the bridge role.

2 Visual Data Types and Preprocessing

2.1 Visual Data Type

According to the attributes of the data source, types, dimensions, representations and other features, the visual data can be divided into one-dimensional data, two-dimensional data, multi-dimensional data, text and hypertext, graphics, image data, etc. And to visualize data, we first have to extract feature information from the data:

1. visual data is discrete data. In order to improve accuracy, difference method is needed.
2. visual data can be regular or irregular. Regular data can save storage space, and irregular data can give us greater freedom of expression.
3. the visual data must have an extension dimension, that is, the 5 data types mentioned earlier.

After identifying the issues related to data attributes, you need to prepare for dealing with large amounts of data. Data is produced at a much faster rate than it is managed and analyzed. The cardinality of the columns that need to be visualized is also a factor that should be taken into account. The high cardinality means that the column has a large number of different values, while the lower cardinality indicates that the column has a large number of duplicate values, such as [4].

2.2 Data Preprocessing

The visual module inputs analog data and experimental/measurement data from the computer, and includes data calls in the database. The objects of visual processing include symbols, structures, images, and signals". The generation and acquisition of primitive symbols, structures, images and signals are the tasks of scientists or engineers engaged in scientific and engineering calculations and experiments. How to transform these data into visual graphics (images) is the task of scientists and engineers engaged in scientific computing visualization applications. They combine with scientists engaged in basic research or engineering research, and use visual tools to implement

and complete the process of converting invisible objects into visible images. Usually, the processing of these raw data should include the following two aspects:

Raw data preprocessing and storage are usually used to visualize raw data, and the preprocessing section involves the following operations:

- (1) data format and standardization;
- (2) data transformation technology;
- (3) data compression and decompression.

The data processed through the above may have larger data capacity. It is usually stored in a standardized data interchange format. The NASA and other units of the National Supercomputing Center study the format and structure of scientific data storage and exchange, such as HDF, CDF, and NetCDF. These data formats are typically self describing, easy to store and read, and are widely used in large-scale numerical computations. Through the sensor Nong'an County Joint jiulongzhen soil moisture real-time data as shown in Fig. 1.

吉林农业大学
农安试验站
Hiljindsyz
注册

请先选择 土壤墒情 数据展示 数据查询与导出 技术支持

查询条件
开始时间 2017-07-01 结束时间 2017-07-20 查询 导出

数据展示

时间	水分10cm(%)	水分20cm(%)	水分30cm(%)	水分40cm(%)	水分50cm(%)	水分60cm(%)	水分70cm(%)	水分80cm(%)	土壤
2017-07-20 23	0.0	26.1	0.0	25.9	0.0	38.1	0.0	34.2	
2017-07-20 22	0.0	26.2	0.0	25.9	0.0	38.1	0.0	34.2	
2017-07-20 21	0.0	26.2	0.0	26.0	0.0	38.1	0.0	34.2	
2017-07-20 20	0.0	26.1	0.0	26.0	0.0	38.1	0.0	34.3	
2017-07-20 19	0.0	25.9	0.0	26.0	0.0	38.1	0.0	34.3	
2017-07-20 18	0.0	25.9	0.0	26.0	0.0	38.1	0.0	34.3	
2017-07-20 17	0.0	26.0	0.0	26.0	0.0	38.1	0.0	34.3	
2017-07-20 16	0.0	26.0	0.0	26.0	0.0	38.1	0.0	34.2	
2017-07-20 15	0.0	26.0	0.0	26.0	0.0	38.1	0.0	34.2	
2017-07-20 14	0.0	25.9	0.0	26.0	0.0	38.1	0.0	34.2	
2017-07-20 13	0.0	22.0	0.0	24.6	0.0	36.1	0.0	32.3	
2017-07-20 12	0.0	21.6	0.0	24.4	0.0	35.7	0.0	32.1	
2017-07-20 11	0.0	21.3	0.0	24.2	0.0	35.7	0.0	32.2	
2017-07-20 10	0.0	21.1	0.0	24.3	0.0	35.8	0.0	32.4	
2017-07-20 09	0.0	21.1	0.0	24.4	0.0	36.0	0.0	32.7	
2017-07-20 08	0.0	21.2	0.0	24.5	0.0	36.3	0.0	33.0	
2017-07-20 07	0.0	21.2	0.0	24.6	0.0	36.7	0.0	33.3	
2017-07-20 06	0.0	21.4	0.0	24.8	0.0	37.0	0.0	34.0	
2017-07-20 05	0.0	21.6	0.0	25.0	0.0	38.1	0.0	34.1	
2017-07-20 04	0.0	22.1	0.0	25.7	0.0	38.4	0.0	34.1	
2017-07-20 03	0.0	23.6	0.0	26.0	0.0	38.5	0.0	34.2	
2017-07-20 02	0.0	26.0	0.0	26.1	0.0	38.6	0.0	34.2	
2017-07-20 01	0.0	26.1	0.0	26.1	0.0	38.6	0.0	34.2	
2017-07-20 00	0.0	26.2	0.0	26.1	0.0	38.6	0.0	34.1	

« 上一页 第1页, 共20页 下一页 » 共480条记录

Fig. 1. Moisture Nong'an County Helong town farmland real time data

3 Construction of Plots Model

At present, there are two main ways to construct geological models: irregular triangular mesh (TIN) and regular grid method (Grid).

TIN is a continuous blanket of topographic surfaces consisting of many adjacent but not overlapping triangles. Different types of TIN have different generation methods. According to the geometric structure of the spatial distribution, there can be a general triangulation and Delaunay triangulation.

In contrast to TIN, Grid is a composite surface composed of several consecutive squares of the same shape in space. The data structure of Grid is very regular and simple. It is possible to construct continuous, smooth and smooth surfaces through these data, and the structure of the mathematical model is simple. Thus, Grid has the advantage of constructing a visual representation of good ground models [5].

Many scholars at home and abroad have made extensive research in the geological level generation methods, some scholars have used Grid triangulation into triangular data to generate geological level [6]. The triangulation is the simplest for Grid, which splits into the triangular mesh structure and gets the raw data in a regular and systematic way. From the rules of the generation of TIN is mainly in the grid decomposition can be combined in the triangle, regular grid case, with one or two days to form diagonal grid decomposition of a series of rules of the triangle. After data processing, the interpolation of geological space is carried out, and the purpose is to grid the data [7]. Based on the grid data obtained, geological layers are plotted by using VC++ and OpenGL.

The main idea of the establishment of this method based on TIN multilayer geological body is, according to the geological layers with the elevation information to establish the TIN into a boundary between two layers of TIN, using the boundary and TIN were built erected under two TIN layer, the vertical TIN to simulate the geological body solid part.

(1) data arrangement

The main tasks of data collation are drilling data extraction and data slicing. The borehole coordinate results table.Xls table data and coal quality testing results table.Xls table finishing, let it become a format for the “number, X, Y, Z for the superposition of the formation of documents. Converts to text files for subsequent program processing.

(2) data format conversion

Using the development program of AutoCAD2000 software, we can draw the above hierarchical data files, eliminate the error points and save the .Dwg format.

(3) loading elevation point data

Open Arcsence and add the “point” layer of the saved .Dwg data to the layer. Since the elevation of each stratum is different, the multilayer data is stacked up and down after loading the multi layer data point layer.

(4) establishing TIN

Using create, Analyst, create/modify, TIN, TIN, from, and features under 3D, choose to load the point layer to build the TIN and build the TIN (Elevation) to build the TIN. As shown in Fig. 2.

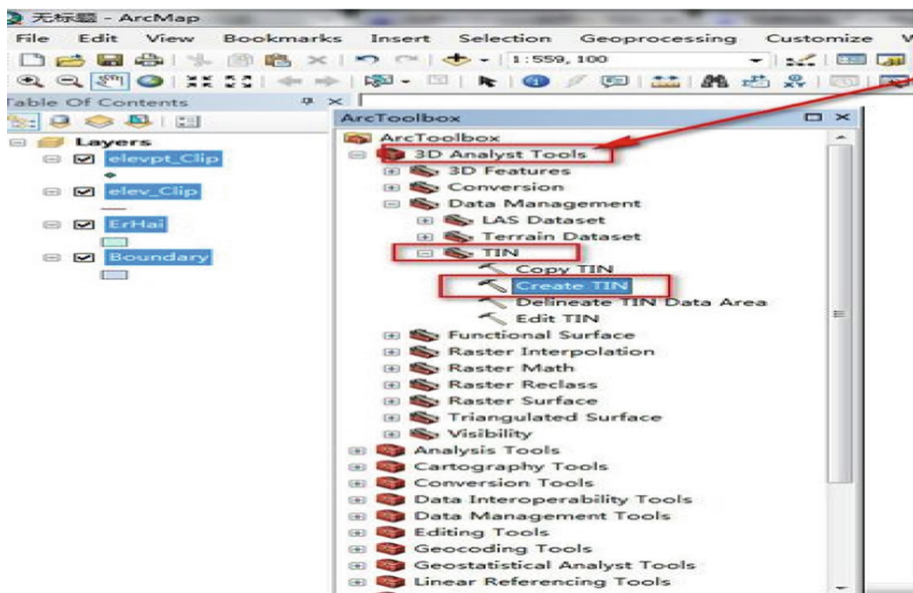


Fig. 2. The establishment of Nong'an County Helong town experimental field plots TIN model

(5) draw the boundaries of TIN

In AutoCAD2000, a closed boundary (i.e., a range of Tin) is plotted along the boundary of the geological point so that the upper and lower points are coupled into a geological body. After many experiments, it is proved that the geological boundary can be achieved by drawing the inner boundary near the boundary of the geological point. It is worth noting that, when drawing the inner boundary, the connection of the polygon side can reduce the unnecessary connection on the side of the geological body. The inner boundary is chosen, and its elevation is assigned in its characteristics. This value should be in the middle of the elevation of the upper and lower two points. As shown in Fig. 3.

(6) build DEM stretch layer

When you open the ArcScene and load the inner boundary, you can see that it is at the height of the two layer point, adjusted properly until the inner edge of the interface is in the middle of the two layer. Again, open the create TIN from Elevation create/modify Analyst under 3D TIN features, load the geological points and the inner edge interface, select a layer, set the Height source to the other attribute in the default format. Then select its corresponding inner edge interface, set its Triangulate attribute to hard erase, and the other two items to None. Select the saved path and click OK to build an upright TIN. Thus, the TIN formed by the geological point is the surface, and the geological body with the thickness of the TIN as the lateral body is formed.

In support of the national Spark Program, the experiment and research in the field of monitoring data obtained in Nong'an County, Jilin Province town of Helong. The

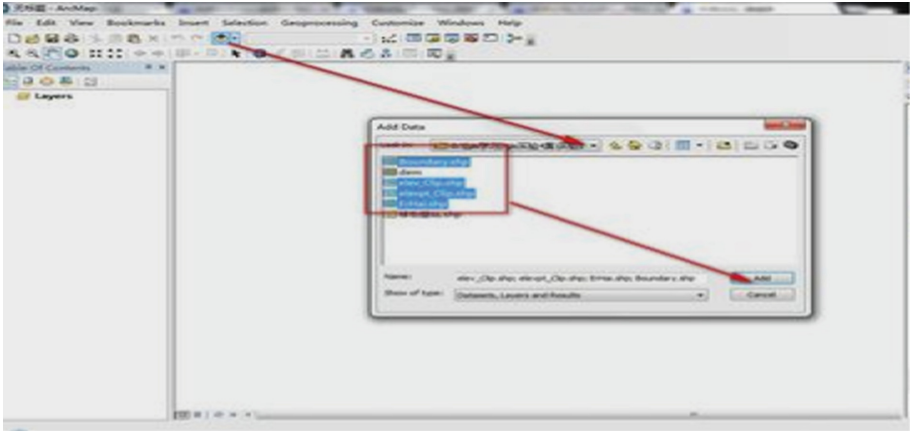


Fig. 3. Markers in Nong'an County Helong town experimental field plots TIN boundary

total area of the experimental plot is about 375 μ , and the grid size is set up [8]. There are several sampling points in the plot. We chose the moisture data for comprehensive analysis. After finishing, we drew a simple 3D block rendering by drawing the plots and the marked TIN points in ArcScene. As shown in Fig. 4.

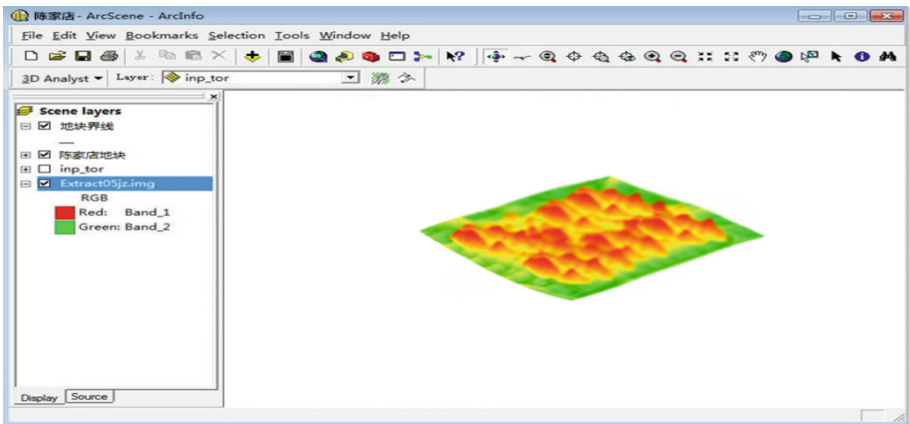


Fig. 4. Visual expression of soil moisture in farmland of Nong'an County Helong town

4 Development of 3D Visualization Plug-in Based on ArcGIS

ArcGIS 3D visualization plug-in development, we need to apply to the ArcGIS SDK software, and in the Visual Studio platform to write source code. Visual Studio is the most popular integrated development environment for Windows platform applications.

Visual Studio as an integrated solution, applicable to both individual and all sizes of development teams, seamless collaboration, improved production efficiency and concentration.

All of the ArcGIS plug-in source code has a single entry point, `main ()`, which is repeated with the action indicated by the selector. For the `main ()` prototype, this is the case:

```
PF_Err main (PF_Cmd cmd,
             PF_InData *in_data,
             PF_OutData *out_data,
             PF_ParamList params,
             PF_LayerDef *output,
             void *extra);
```

The first parameter is a selector whose value indicates the execution phase the plug-in is about to enter.

The second parameter is a callback function that points to the large data structure that contains the host application status information and hooks, which is a primary parameter.

The third parameter is a pointer to a structure that communicates its needs to the host as a plug-in. For example, error messages can be sent to the host via mail.

The structure of `pf_layerdef` output parameter point, which contains the output image information (including a pointer to the data): its size, its rowbytes value, and `extent_hint`, which is directly to the border area, really need to render [9].

Finally, the extra pointer is a special use parameter that is largely unused to the program. It points to different data structures at different times. If you decide to implement a custom user interface element, or a complex custom data type, you will only process this parameter [10].

4.1 ArcGIS Camera Plug-in Function

In the general case (without opening the 3 dimension layer attributes) camera has no effect, open the layer 3D attribute or some 3D effects can play a role, it can be simulated in 3D scene picture (picture Z attribute axis), allowing multiple layers to produce perspective, and also to support the light and material, projection/shadow. In software, the camera is virtual and will not have a track or a three stand for you to use. However, by simulating real-life camera movements, we can migrate our understanding to virtual cameras, so that we can better understand and apply it. In practice, we will find that the simple on camera animation, it is very difficult to achieve the desired effect, not our understanding is not enough, but the software itself is designed so that we need to find some way to simulate the camera in real life, to achieve our purpose.

4.2 ArcGIS Camera Plug-in Preparation

First, define the camera interface;

```
#define kAEGPCameraSuite          "AEGP Camera Suite"
#define kAEGPCameraSuiteVersion2  2 /* frozen in AE 5.5 */

typedef struct AEGP_CameraSuite2 {

    SPAPI A_Err    (*AEGP_GetCamera) (
        PR_RenderContextH    render_contextH,    /* >> */
        const A_Time         *comp_timeP,        /* >> */
        AEGP_LayerH          *camera_layerPH); /* << */
```

Then define the camera type;

```
SPAPI A_Err    (*AEGP_GetCameraType) (
    AEGP_LayerH    camera_layerH,        /* >> */
    AEGP_CameraType *camera_typeP);    /* << */
```

Define camera view;

```
SPAPI A_Err (*AEGP_GetDefaultCameraDistanceToImagePlane) (
    AEGP_CompH    compH,        /* >> */
    A_FpLong      *dist_to_planePF); /* << */

    // If a camera is created using aegp, then you must set the film
size units.
    // No default is provided.
```

Define camera size and size;

```
SPAPI A_Err    (*AEGP_GetCameraFilmSize) (
    AEGP_LayerH    camera_layerH,        /* >> */
    AEGP_FilmSizeUnits *film_size_unitsP, /* << */
    A_FpLong      *film_sizePF0);        /* << in pixels */
SPAPI A_Err    (*AEGP_SetCameraFilmSize) (
    AEGP_LayerH    camera_layerH,        /* >> */
    AEGP_FilmSizeUnits film_size_units,  /* >> */
    A_FpLong      *film_sizePF0);        /* >> in pixels */

} AEGP_CameraSuite2;
```


At this point, our plug-in program is complete, the plug-in code generation plug-in format files, import into the ArcGIS software database, open the software can be invoked. Figure 5 is the effect of observing the block data in the software after calling the camera plug-in.

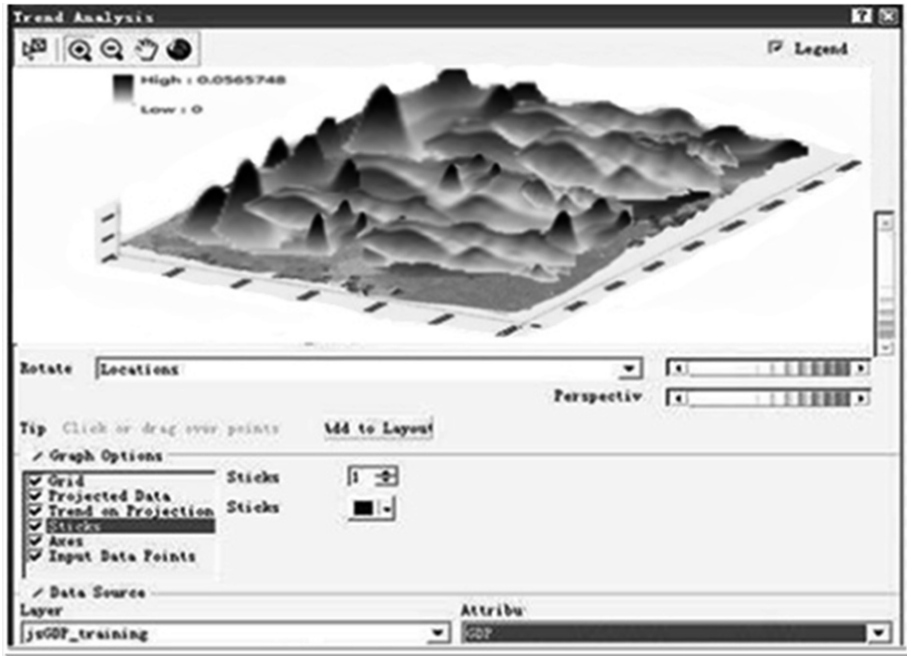


Fig. 5. Integrated camera plug-in after the soil moisture data observation effect diagram

5 Conclusion

With the help of data visualization is the main graphical means to communicate clearly and effectively communicate with the information in order to effectively convey the concept, through the convey and key characteristics, in order to achieve in-depth insight into the rather sparse and complex data sets. Research and experimental results show that

- (1) based on the ArcGIS software SDK source code to write the auxiliary plug-in and ArcGIS software integration, to make up for the ArcGIS software auxiliary function is not perfect, and optimize the visualization effect of agricultural monitoring data is feasible.
- (2) integrated plug-in ArcGIS software in the field monitoring data, obvious optimization effect of 3D visualization of monitoring data, the two-dimensional spatial variability of thematic map than the traditional representation of 3D data more natural, more clear, more intuitive. The results of the study are of great significance to the development of modern agriculture.

Acknowledgments. This work was funded by the China Spark Program.2015GA660004. “Integration and demonstration of corn precise operation technology based on Internet of things”.

References

1. Mei, X.: GIS: urban planning in the information age. Heilongjiang Transp. Sci. Technol. (2007)
2. Xue, H., Shang, M.: Rational analysis of GIS in urban planning and design. Urban surveying (2004)
3. Xu, W., Zhao, W., et al.: Application of RS and GIS in the planning of agricultural green space system. People Yangtze River (2008)
4. Xie, B., Li, L., et al.: Research on 3D graphic planning system of GIS and VR technology. Microcomputer information (2004)
5. Xie, Z.: A summary of three dimensional GIS aided agricultural planning. Appl. Sci. (2008)
6. Penggen, T., Liu, S., Chen, H.: Research and application of 3D geological model construction method. J. Jilin Univ. Earth Sci. Ed. **4**(2), 309–313 (2004)
7. Chen, Y., Zhong, E.: Three dimensional visualization management system of mine geological exploration and Research on the modeling technology Tian. Res. Dev. Min. Ind. **24**(1), 37–40 (2004)
8. Chen, Y.: Bell ear research mine geological exploration and visualization management system modeling. Min. Res. Dev. **24**(1), 37–40 (2004)
9. Wang, M.: Three-dimensional geological modeling of clouds present situation and development trend geotextile base **20**(4), 68–70 (2006)
10. Zhang, K., Wu, W., Bai, Y., et al.: Three-dimensional geological ArcGIS-based visualization Liaoning Technical University **26**(3), 345–347(2007)



Growth and Spectral Characteristics of Grassland in Response to Different Soil Textures

Xiaochun Zhong^{1,2}, Junchan Wang³, Liu Tao⁴, Chengming Sun⁴,
Zhemín Li^{1,2}, and Shengping Liu^{1,2}✉

¹ Institute of Agriculture Information,
Chinese Academy of Agriculture Sciences, Beijing, China
{zhongxiaochun, lizhemín, liushengping}@caas.cn

² Key Laboratory of Agro-information Services Technology,
Ministry of Agriculture, Beijing, China

³ Lixiahe Regional Institute of Agricultural Sciences,
Yangzhou, Jiangsu Province, China
wjc@wheat.org.cn

⁴ Jiangsu Key Laboratory of Crop Genetics and Physiology,
Co-innovation Center for Modern Production Technology of Grain Crops,
Yangzhou University, Yangzhou, China
{tliu, cmsun}@yzu.edu.cn

Abstract. Biomass and the chlorophyll content are important indicators to measure the growth and development of grasslands. Modeling using hyperspectral data is an important means to monitor grassland growth and development. In this paper, we studied Mexican maize grass, hybrid Pennisetum and hybrid Sudan grass under different soil texture treatments and determined the correlation between the canopy reflectance spectrum and plant growth status in different soil textures based on hyperspectral data. Our results showed that, under different soil texture treatments, the emergence rate of Mexican maize grass and hybrid Pennisetum did not differ significantly, whereas that of hybrid Sudan grass indicated a significant difference. Under different soil texture treatments, the trend of plant height variation was consistent. In terms of different types of grassland, it is generally feasible to establish a grassland yield spectral model based on the vegetation indexes NDVI and RVI, and the leaf SPAD values of the three types of grassland best fit the spectral parameter red edge area.

Keywords: Grassland · Biomass · SPAD value · Soil textures
Hyperspectral remote sensing

1 Introduction

Biomass is an important component of the ecosystem carbon pool, which is the main input source to the soil organic carbon pool [1]. Biomass is an important index to measure the growth and development of grassland and to guide production management [2]. Chlorophyll is an important pigment involved in grassland photosynthesis [3] and is

closely related to protein, nitrogen, moisture and other parameters [4]. It is a good indicator of photosynthetic efficiency and the development status of grasslands and also enables crop to exchange matter and energy with their surroundings. Therefore, the estimation of grassland biomass and the chlorophyll content has become an important method to evaluate grassland growth and development [5].

There are many grassland biomass and chlorophyll content acquisition methods; the traditional method has shortcomings such as being time and effort intensive, there are difficulties in scaling up, and vegetation is damaged [6]. Therefore, the traditional method cannot easily be used for the rapid acquisition of grassland biomass and chlorophyll content or the accurate monitoring of grassland growth and development. In recent years, with the application and development of hyperspectral remote sensing technology, hyperspectral data can be obtained by means of a hyperspectral imager, and quantitative analysis of weak spectral differences is carried out directly on the ground objects. The spectral diagnosis of plant leaf components is based on the spectral characteristics of plants. A large number of studies have shown a good correlation between the plant water, carbohydrate and chlorophyll contents and the spectral reflectance in specific bands [7]. Therefore, a relationship between the leaf components and the spectral reflectance can be established, and monitoring and diagnosis models of various plant biochemical parameters based on the reflectance spectrum can be developed; consequently, hyperspectral data have a strong advantage in grassland growth monitoring research [8].

Many domestic scholars have extensively studied the spectral characteristics of grasslands; the results show that grassland biomass and remote sensing vegetation indexes have a good correlation, but there are some differences in their correlation degrees [9]. In terms of a grassland biomass monitoring model, Clever et al. [10] studied a method to estimate grassland biomass based on a support vector machine that uses remote sensing data to extract grassland biomass and obtained the band with the best prediction ability. Chen et al. [11] studied the relationship between the grassland reflectance spectral characteristics of aboveground biomass, extracted a vegetation index from the spectral data, and established a dynamic monitoring model. In addition, the Dutch scholars Darvishzadeh et al. [12] used hyperspectral measurements of the grassland chlorophyll content. However, the grassland spectral characteristics may be limited by the environmental background, canopy structure, leaf moisture and soil texture.

In this paper, we studied the correlation between canopy reflectance characteristics and plant growth status under different soil texture treatments. We analyzed the sensitive bands and vegetation indexes that were closely related to plant biomass and nutrient status and established a plant biomass and SPAD value estimation model to promote the application of hyperspectral remote sensing technology in grassland growth and development monitoring and to provide a theoretical basis for large-scale, non-destructive and real-time monitoring of grassland growth using spectral technology.

2 Materials and Methods

2.1 Test Materials and Varieties

The experimental method is an indoor potting method. The experiment was conducted in 2016 at the Yangzhou University Agricultural College experimental farm. The tested varieties included three types of grasses: Mexican maize grass (A1), hybrid Pennisetum (A2), and South African hybrid Sudan grass (A3). Test pots: the plastic pot was 28 cm in diameter and 20 cm in height, and the bottom diameter was 18.5 cm. The surface area of the soil column was approximately 0.045 m². Soil properties: test farm loam, of which the hydrolysable nitrogen was 149.2 mg·kg⁻¹, the available phosphorus was 34.5 mg·kg⁻¹, the available potassium was 84.6 mg·kg⁻¹, and the soil organic matter content was 1.74%.

2.2 Experimental Design

According to the different soil textures, based on a quality ratio, three treatments, i.e., loam, loam:sand = 3:1, and loam:sand = 1:1, recorded as B1, B2 and B3, respectively, were established; each treatment consisted of 8 replicates. During the experimental period, the nutrient dosage was designed as N 120 kg/hm² (0.54 g/pot), P₂O₅ 100 kg/hm² (0.45 g/pot), K₂O 100 kg/hm² (0.45 g/pot), applied once as basal fertilizer; the fertilizer and soil were well mixed and added to the pot.

Seed sowing: Mexican maize grass (A1) seeds: 10 seeds/pot; hybrid Pennisetum (A2) seeds: 100 seeds/pot; South African hybrid Sudan grass (A3) seeds: 60 seeds/pot. When sowing, some of the soil was removed from the pot; the remaining soil was compacted in the pot; the grass seeds were evenly spread on the soil surface; the removed soil was returned to the pot, compacted; and finally, spray irrigation was applied at low a low amount but quite frequently to ensure the top 3 cm of the soil surface remained moist during the seedling stage.

2.3 Measurements

2.3.1 Spectral Determination

After emergence, we sampled approximately once per month. At every sampling, two pots of each grass species per treatment were examined. When measuring the canopy spectrum, measurements need to be collected under sunny (not cloudy) conditions with good light. In addition, a single vegetation type with nearly 100% coverage should be selected to avoid interference from other vegetation and soil. Further, atmospheric water vapor absorption also affects the canopy spectral data, especially around 1400 nm and 1900 nm, where there is considerable noise. Therefore, the visible and near infrared bands are used to study the canopy characteristics of different herbs.

We used the United States ASD FieldSpec 3 Hi-Res field portable terrestrial spectrometer for spectral measurements. When measuring, the sensor probe was pointed down in a vertical direction, about 60 cm from the top of the canopy. Each replicate of each treatment was measured 9 times (i.e., measured 3 times right above the top of the test pot, then rotated about 120° and measured 3 times, and then rotated

about 120° and measured 3 times); the average value was taken as the spectral reflectance of that replicate, and finally the average value of 3 replicates was recorded as the spectral reflectance value of the treatment. Calibration of a standard blank was needed; therefore, calibration was performed after each treatment was measured.

2.3.2 Determination of the SPAD Value

We used a portable SPAD-502 chlorophyll meter in the test: 5 newly fully developed leaves per pot were selected, and we measured the SPAD value in the upper, middle and lower parts of each leaf and calculated the average.

2.3.3 Determination of Aboveground Biomass

We selected representative grass plants, cut the aboveground part at the roots, and determined the fresh weight of collected samples in the laboratory. Then, the samples were subjected to 105 °C for half an hour, followed by oven drying at 65 °C to a constant weight, after which the dry weight was determined as the aboveground biomass.

2.3.4 Determination of Soil Dry Density and Water Content

We measured the soil dry density and soil water content during the last two periods: we selected soil samples where the roots were concentrated in a pot; a ring knife was used to collect potted soil 5–10 cm from the surface; and the fresh weight was determined. Then, in the laboratory, the soil samples were dried in an oven at 80 °C to a constant weight; the dry weight was determined; and the soil dry density and water content were calculated.

2.4 Data Processing and Mapping

ASD viewspec-pro software was used to read the measured source spectral data, and the raw data were preprocessed and averaged as the spectral value of the process. Excel 2010 and SPSS16.0 were used for data processing and statistical analysis.

3 Results and Analysis

3.1 The Emergence Rate of Grass Species in Different Soil Textures

The seedling emergence rate is the proportion of emerged seedlings relative to the total seedlings that should emergence (%). As can be seen from Table 1, there was no significant difference in the emergence rate of Mexican maize grass (A1) and hybrid Pennisetum (A2) under different soil texture treatments. The emergence rate of hybrid Sudan grass (A3) under the B1 treatment was significantly higher than that under the B2 and B3 treatments.

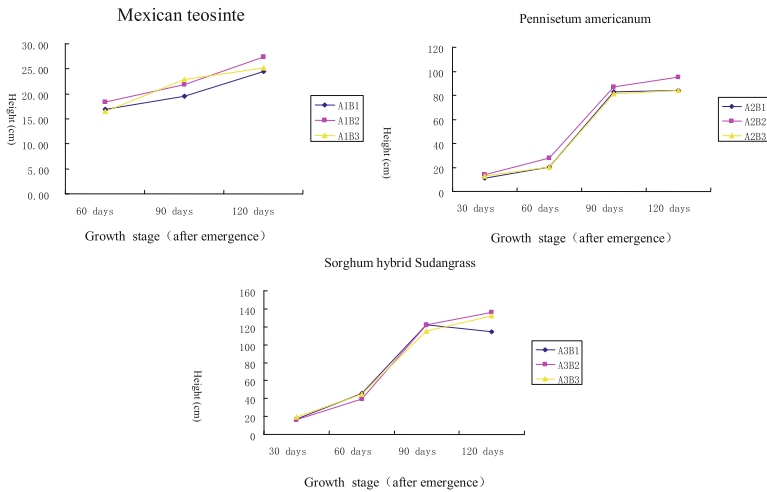
Table 1. The emergence rate of grass seed under different soil textures

Soil texture	Mexican teosinte A1	Pennisetum americanum A2	Sorghum hybrid sudangrass A3
B1	0.50a	0.41a	0.36a
B2	0.56a	0.49a	0.53b
B3	0.61a	0.51a	0.52b

The seedling emergence time was similar between hybrid Sudan grass and hybrid Pennisetum, whereas the emergence time of Mexican maize grass was later than that of the other two. However, the seedling emergence time was not significantly different between treatments for each species.

3.2 Plant Heights of the Grasses in Different Soil Textures and Periods

It can be seen from Fig. 1 that after emergence, the Mexican maize grass growth was relatively rapid, but then gradually slowed down. Hybrid Pennisetum was the fastest growing during the period from 60 to 90 days after emergence, and hybrid Sudan grass was the fastest growing during the period from 60 to 90 days after emergence.

**Fig. 1.** The plant height of grass under different soil textures and growth stages

3.3 Soil Dry Density and Water Content of the Grasses in Different Soil Textures and Periods

The soil dry density and water content of the test pots were measured by sampling test conducted 90 days and 120 days after emergence. The data in Tables 2 and 3 show a negative correlation between soil dry density and soil water content. This is because

across the three types of soil treatments, the sand content increased, soil dry density increased, and there was more sand and less clay; therefore, the soil permeability and ventilation capacity were good, but the water storage capacity was poor.

Table 2. The soil dry density (g/cm^3) of grass under different soil textures and growth stages

Soil texture	90 days after emergence			120 days after emergence		
	Mexican teosinte A1	Pennisetum americanum A2	Sorghum hybrid sudangrass A3	Mexican teosinte A1	Pennisetum americanum A2	Sorghum hybrid sudangrass A3
B1	1.07	1.08	1.21	1.11	1.06	1.08
B2	1.26	1.10	1.27	1.22	1.10	1.18
B3	1.42	1.36	1.35	1.30	1.31	1.21

Table 3. The soil moisture content (%) of grass under different soil textures and growth stages

Soil texture	90 days after emergence			120 days after emergence		
	Mexican teosinte A1	Pennisetum americanum A2	Sorghum hybrid sudangrass A3	Mexican teosinte A1	Pennisetum americanum A2	Sorghum hybrid sudangrass A3
B1	18.15	14.72	17.51	18.29	20.09	17.56
B2	14.33	8.53	13.49	13.88	11.96	13.33
B3	10.16	4.54	9.34	9.17	6.73	6.68

3.4 Dry Weight of Grasses in Different Soil Textures and Periods

It can be seen from Table 4 that the growth condition of Mexican maize grass under the B2 treatment was the best, but in the later stage of growth, the best growth occurred under the B3 treatment. The soil moisture content under the B3 treatment was more suitable for the late growth of Mexican maize grass.

Table 4. The dry weight (g/pot) under different soil textures and growth stages of Mexican teosinte

Soil texture	60 days after emergence	90 days after emergence	120 days after emergence
B1	18.70	38.05	50.85
B2	26.60	57.05	77.40
B3	19.70	49.10	86.80

It can be seen from Table 5 that there was no significant difference in the dry weight of hybrid Pennisetum in different soil textures, and the soil texture and water content had little effect on the growth of hybrid Pennisetum.

It can be seen from Table 6 that the growth condition of hybrid Sudan grass was the best in the middle and late growth stages under the B2 treatment, and the emergence rate was the highest under the B2 treatment. Thus, the soil with the B2 treatment was most conducive to the growth of hybrid Sudan grass.

Table 5. The dry weight (g/pot) under different soil textures and growth stages of *Pennisetum americanum*

Soil texture	30 days after emergence	60 days after emergence	90 days after emergence	120 days after emergence
B1	12.40	62.90	120.25	151.30
B2	16.80	68.40	124.80	147.10
B3	14.80	65.15	122.10	122.55

Table 6. The dry weight (g/pot) under different soil textures and growth stages of *Sorghum hybrid sudangrass*

Soil texture	30 days after emergence	60 days after emergence	90 days after emergence	120 days after emergence
B1	9.95	34.70	87.95	139.20
B2	7.85	45.75	104.50	153.85
B3	10.05	35.35	85.90	109.65

3.5 Relationship Between Dry Weight and Vegetation Index of Different Types of Grasses

We carried out correlation analysis of the dry weight and vegetation index of the grassland to test the degree of closeness between the two and to determine whether the sample can be used to determine the overall situation. The correlation coefficient is an important indicator to reflect this degree of closeness.

The correlation coefficients between four commonly used vegetation indexes, calculated using SPSS software, and the dry weights of different grasses are shown in Table 7.

Table 7. The correlation coefficient between vegetation index and dry weight of the three types of grass

Types		Vegetation index			
		NDVI	RVI	DVI	RDVI
Mexican teosinte	60 days after emergence	0.885*	0.937**	0.739	0.819*
	90 days after emergence	0.897*	0.894*	0.472	0.604
	120 days after emergence	0.921**	0.911*	0.36	0.529
<i>Pennisetum americanum</i>	30 days after emergence	0.910*	0.925**	0.459	0.683
	60 days after emergence	0.882*	0.910*	0.29	0.441
	90 days after emergence	0.941**	0.956**	0.209	0.48
	120 days after emergence	0.932**	0.904*	0.751	0.842*
<i>Sorghum hybrid Sudangrass</i>	30 days after emergence	0.877*	0.907*	0.746	0.816*
	60 days after emergence	0.943**	0.961**	0.56	0.692
	90 days after emergence	0.878*	0.912*	0.909*	0.916*
	120 days after emergence	0.893*	0.924**	0.14	0.592

It can be seen from Table 7 that there was a certain correlation between the normalized vegetation index (NDVI) and the ratio vegetation index (RVI) and grassland grass yield; therefore, it is feasible to establish a grass yield spectral model based on the two vegetation indexes. There were also some differences in the correlation between grass yield and different vegetation indexes, but there was no significant difference between the two vegetation indexes described above. Therefore, combined with the correlation between vegetation index and grass yield, different grassland types and fertility periods can be used in a practical and effective manner to establish a corresponding yield estimation model. Understanding the correlation between grass yield and vegetation indexes can help to further analyze the data, so as to achieve the purpose of determining the internal association within the data. After comparing various models, we found it best to use the power exponential model for estimation of grassland yield. Figures 2, 3 and 4 are analysis models of various types of grassland biomass and related vegetation indexes.

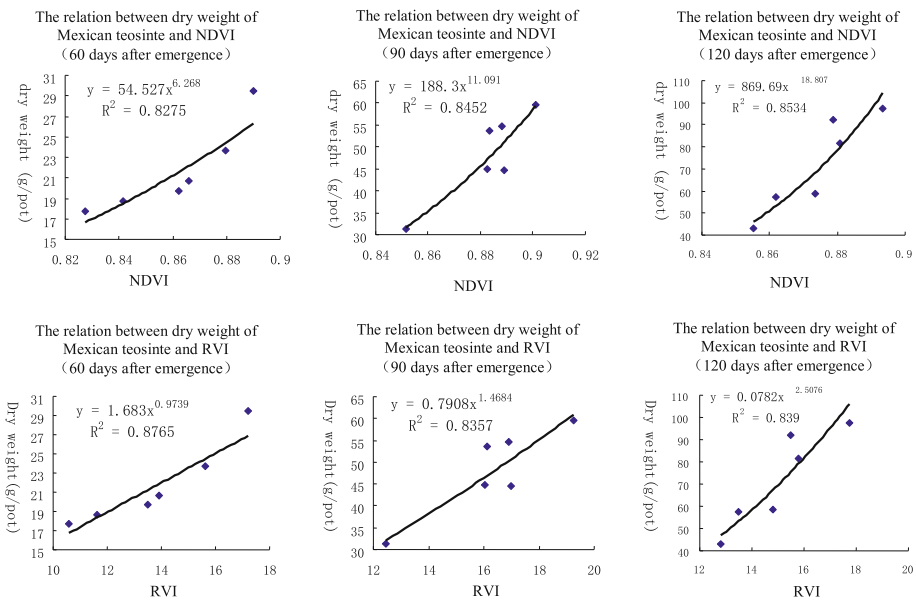


Fig. 2. The correlation between vegetation index (NDVI, RVI) and dry weight of Mexican teosinte under different growth

The corresponding yield estimation model and fitting effect of three types of grassland were different; the fitting effect is reflected by the R value: the greater the R value, the better the fit. The vegetation index was closely related to the dry weight of the grass, but the relationship between dry weights of the same type of grass and the two vegetation indexes (NDVI and RVI) was slightly different. There was also a difference between the vegetation index and the power exponential model of the dry weights of a particular grass at different growth stages.

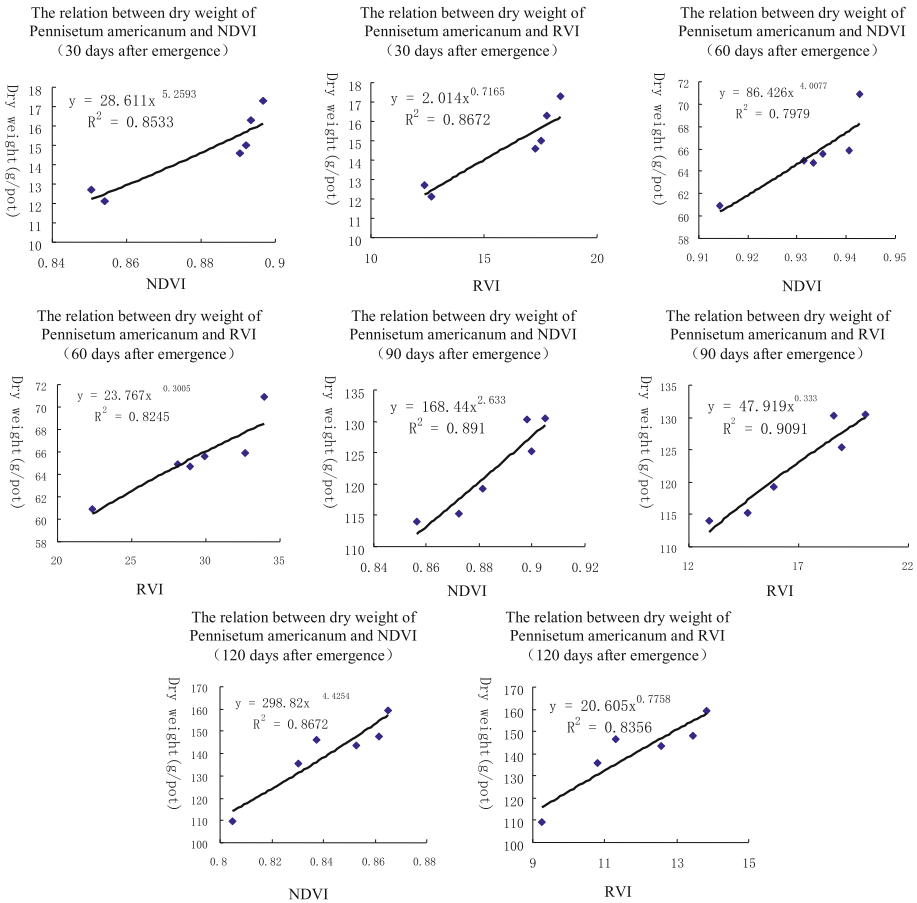


Fig. 3. The correlation between vegetation index (NDVI, RVI) and dry weight of *Pennisetum americanum* under different growth stages

Therefore, the grass yield model can be expressed as $y = ax^b$, where a and b are constants.

3.6 Relationship Between Dry Weight and Vegetation Index of Different Types of Grasses

Changes in the chlorophyll content will cause changes in plant leaf color. Under normal circumstances, the chlorophyll content can reflect the photosynthetic physiological state of plants to a certain extent. With an increase in the chlorophyll content, plant photosynthesis increases and is conducive to improving plant yield and quality [3]. Chlorophyll can describe crop canopy characteristics, reflecting leaf photosynthetic capacity and being used in the estimation of yield using the main parameters.

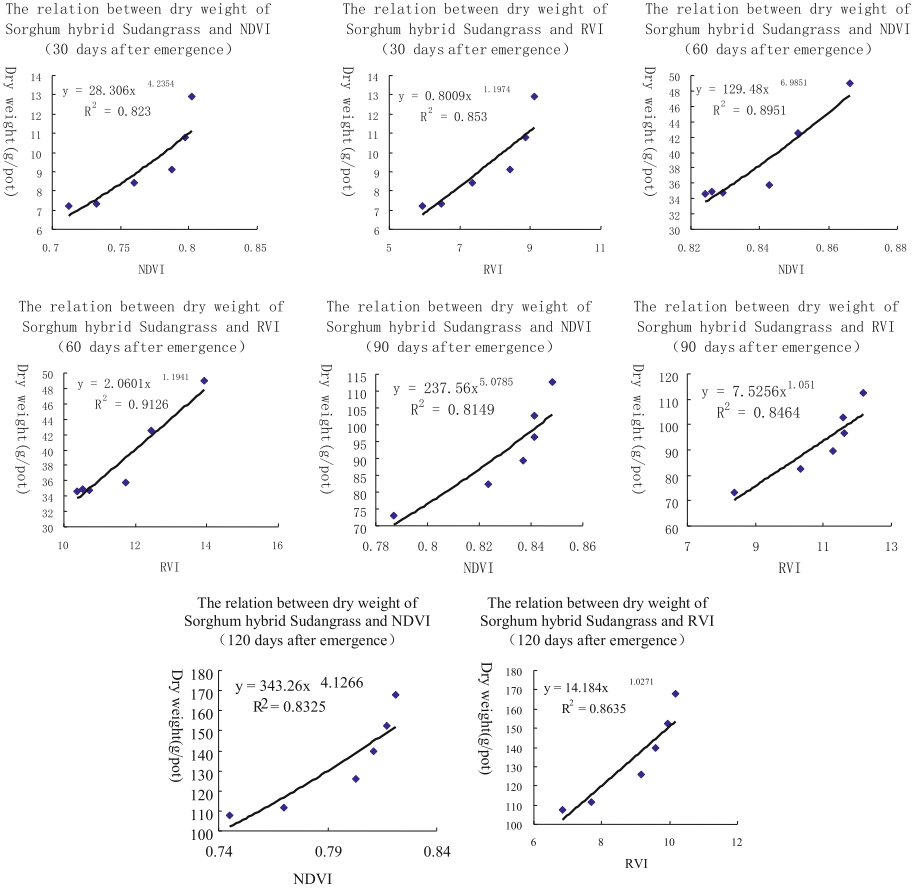


Fig. 4. The correlation between vegetation index (NDVI, RVI) and dry weight of Sorghum hybrid sudangrass under different growth stages

The information that chlorophyll conveys not only contains single leaf information but also part of the crop canopy information.

The phenomenon caused by the strong reflection formed by the absorption of vegetation chlorophyll in the red light band and the scattering of the near infrared band inside the leaf is called the red edge [4]. Previous studies have found close relationships between chlorophyll and red edge parameters.

The red edge parameters describing vegetation spectrum red edge characteristics in this paper mainly include [5, 6]:

- (1) Red edge position (λ_{red}): in the range of 680–750 nm; the corresponding wavelength of the reflection spectrum when the first order differential value reaches the maximum.
- (2) Red edge peak area: the area surrounded by the spectral first order differential value between 680–750 nm.

- (3) Minimum amplitude ($d\lambda_{\min}$): the corresponding minimum first order differential value between 680–750 nm.
- (4) Red edge amplitude ($d\lambda_{\text{red}}$): the first order differential value when the wavelength is the red edge.
- (5) Ratio of red edge amplitude to the minimum amplitude $d\lambda_{\text{red}}/d\lambda_{\min}$.

SPSS software was used to calculate the correlation coefficient between the SPAD value and the red edge parameter of entire growth period of different grasslands, as shown in Table 8.

Table 8. The correlation coefficient between the parameters of red edge and the SPAD value of the three types of grass

Types	Parameters of red edge				
	Red edge position λ_{red}	Red edge swing breadth $d\lambda_{\text{red}}$	Minimum swing breadth $d\lambda_{\min}$	Ratio $d\lambda_{\text{red}}/d\lambda_{\min}$	Peak area of red edge
Mexican teosinte	0.261	0.778**	0.654**	0.516*	0.747**
Pennisetum americanum	0.17	0.534**	-0.113	0.529**	0.603**
Sorghum hybrid sudangrass	0.454*	0.679**	0.524**	0.319	0.687**

It can be seen from Table 8 that the red edge area and red edge amplitude of the three grasses were significantly positively correlated with the SPAD values, and the red edge area was more strongly correlated with the SPAD values. We took the red edge area with the most relevant trait as the selected parameter and combined and established five estimation models based on the SPAD value of the red edge area: (1) Linear function model $y = a + bx$, (2) Logarithmic function model $y = a + b \times \ln(x)$, (3) Power function model $y = ax^b$, (4) Exponential function model $y = a \times e^{bx}$, and (5) Quadratic polynomial function model $y = ax^2 + bx + c$, to achieve the goal of a more accurate assessment of the SPAD value of grassland. The selection principle of the model is determined by the coefficient R^2 ; the larger the R^2 value, the better the model evaluation. According to the test results, among three grassland SPAD value estimation models, the quadratic polynomial model had the best estimation results.

Figure 5 results show that the SPAD value of the grassland was estimated practically and effectively by using the red edge area of the red edge parameter, and the SPAD value of hybrid Sudan grassland was the best among the three grassland types.

The reliability of the model was tested using the root mean square (RMSE), relative error (RE%) and determination coefficient (R^2). The results were plotted as a 1:1 correlation map to verify the optimal evaluation model of the grassland SPAD value.

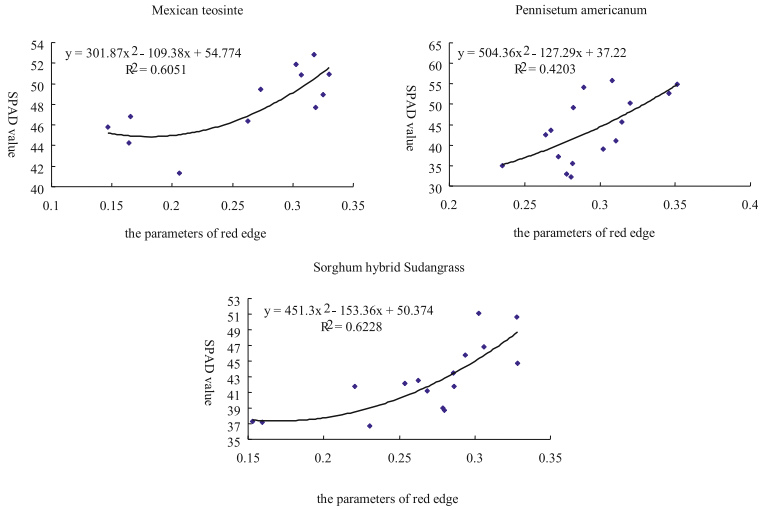


Fig. 5. The prediction models of SPAD value of the three types of grass

As shown in Fig. 6, the RMSE of the Mexican maize grass corresponding test model was 2.3218, the relative error RE was 3.53%, the determination coefficient R^2 was 0.7994, and the test accuracy was 96.47%.

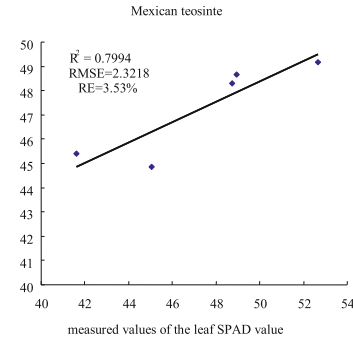


Fig. 6. The correlation between measured and simulated values of the leaf SPAD value of Mexican teosinte

As shown in Fig. 7, the RMSE of the hybrid Pennisetum corresponding model was 3.3678, the relative error RE was 6.99%, the determination coefficient R^2 was 0.655, and the test accuracy was 93.01%.

As shown in Fig. 8, the RMSE of the South African hybrid Sudan grass corresponding test model was 2.2721, the relative error RE was 4.50%, the determination coefficient R^2 was 0.8841, and the test accuracy was 95.50%.

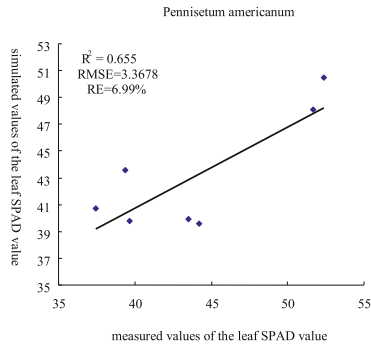


Fig. 7. The correlation between measured and simulated values of the leaf SPAD value of *Pennisetum americanum*

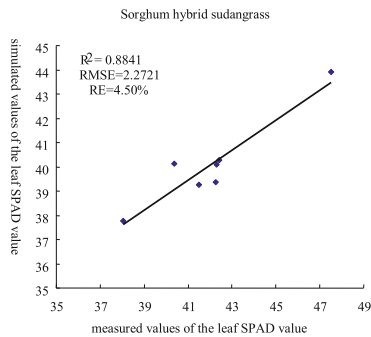


Fig. 8. The correlation between measured and simulated values of the leaf SPAD value of *Sorghum hybrid sudangrass*

4 Conclusion and Discussion

- (1) There was no significant difference in the emergence rate of hybrid *Pennisetum* and Mexican maize grass under different soil texture treatments. The hybrid Sudan grass had a higher emergence rate under the B2 and B3 treatments than the B1 treatment, and there was a significant difference.
- (2) There was no significant difference in plant height variation under different soil texture treatments. After emergence, the Mexican maize grass grew rapidly, and then the growth gradually slowed. The hybrid Sudan grass and hybrid *Pennisetum* grew the fastest during the period from 60 to 90 days after emergence.
- (3) The Mexican maize grass under the B2 treatment had the best growth condition in the early stage, but in the late growth stage, the soil water content under the B3 treatment was the most suitable. There was no significant difference in the dry weights of hybrid *Pennisetum* under different soil texture treatments during the entire growth period. It was observed that the soil texture and water content had little effect on the growth of hybrid *Pennisetum*. The hybrid Sudan grass under the B2 treatment had the best growth in the middle and late growth stage and the

highest rate of emergence; therefore, the soil texture in the B2 treatment was the most favorable for the growth of hybrid Sudan grass.

- (4) It is generally feasible to establish a yield estimation spectral model of different grasslands by using the vegetation indexes RVI and NDVI. The yield estimation model of grassland can be expressed as $y = ax^b$; a and b are constants.
- (5) We used the red edge peak area as the selected parameter, combined with the red edge peak area of the hyperspectral red edge parameter, and established a corresponding SPAD value estimation model; the quadratic polynomial model had the best estimation results. Among the three grassland types, the SPAD value estimation equation of Mexican maize grass was $y = 301.87x^2 - 109.38x + 54.774$; that of hybrid Sudan grass was $y = 451.3x^2 - 153.36x + 50.374$; and that of hybrid Pennisetum was $y = 504.36x^2 - 127.29x + 37.22$.

Acknowledgment. This research was supported by Technology Innovation Project Fund of Chinese Academy of Agricultural Sciences (2017).

References

1. Cao, M.K., Woodward, F.I.: Net primary and ecosystem production and carbon stocks of terrestrial ecosystems and their responses to climate change. *Glob. Change Biol.* **4**(2), 185–198 (1998)
2. Jmo, S., Johnson, K., Olson, R.J.: Estimating net primary productivity from grassland biomass dynamics measurements. *Glob. Change Biol.* **8**(8), 736–753 (2002)
3. Niinemets, U., Tenhunen, J.D.: A model separating leaf structural and physiological effects on carbon gain along light gradients for the shade-tolerant species *Acer saccharum*. *Plant Cell Environ.* **20**(7), 845–866 (1997)
4. Gáborčík, N.: Relationship between contents of chlorophyll (a + b) (SPAD values) and nitrogen of some temperate grasses. *Photosynthetica* **41**(2), 285–287 (2003)
5. Sun, J., Cao, H., Huang, Y.: Research advances of spectral technology in monitoring the growth and nutrition information of crop. *J. Agric. Sci. Technol.* **10**, 18–24 (2008)
6. Zhou, L., Xin, X., Li, G., et al.: Application progress on hyperspectral remote sensing in grassland monitoring. *Pratacultural Sci.* **26**(4), 20–27 (2009)
7. Qiao, X.: *The Primary Investigation in Diagnosing Nutrition Information of Crop Based on Hyperspectral Remote Sensing Technology*. Jilin University (2005)
8. Fan, Y., Wu, H., Jin, G.: Hyper spectral properties analysis of grassland types in Xinjiang. *Pratacultural Sci.* **23**(6), 15–18 (2006)
9. Zhichun, N., Shaoxiang, N.: Study on models for monitoring of grassland biomass around Qinghai lake assisted by remote sensing. *Acta Geogr. Sin.* **58**(5), 695–702 (2003)
10. Clevers, J.G.P.W., van der Heijden, G.W.A.M., Verzakov, S., et al.: Estimating grassland biomass using SVM band shaving of hyperspectral data. *Photogramm. Eng. Remote Sens.* **73**(10), 1141–1148 (2007)
11. Chen, J., Gu, S., Shen, M.G., et al.: Estimating aboveground biomass of grassland having a high canopy cover: an exploratory analysis of in situ hyperspectral data. *Int. J. Remote Sens.* **30**(24), 6497–6517 (2009)
12. Darvishzadeh, R., Skidmore, A., Schlerf, M., et al.: LAI and chlorophyll estimation for a heterogeneous grassland using hyperspectral measurements. *ISPRS J. Photogramm. Remote Sens.* **63**(4), 409–426 (2008)



Soil Moisture Estimation by Combining L-Band Brightness Temperature and Vegetation Related Information

Yuanyuan Fu^{1,2,3}, Chunjiang Zhao^{1,2,3(✉)}, Guijun Yang^{1,2,3},
and Haikuan Feng^{1,2,3}

¹ Key Laboratory of Quantitative Remote Sensing in Agriculture of Ministry of Agriculture P. R. China, Beijing Research Center for Information Technology in Agriculture, Beijing 100097, China

² National Engineering Research Center

for Information Technology in Agriculture, Beijing 100097, China
{fuyy, zhaocj, yanggj, fenghk}@nercita.org.cn

³ Beijing Engineering Research Center for Agriculture Internet of Things, Beijing 100097, China

Abstract. Passive radiometry at L-band has been widely accepted as one of the most promising techniques for monitoring soil moisture content (SMC). However, with vegetation cover, the scatter and attenuation of microwave signals by vegetation make the discrimination of SMC related signal complicated. To improve SMC estimate, this study proposed the combined use of L-band brightness temperature (T_B) and optical remote sensing data to take into account the effect of vegetation. The normalized difference infrared index (NDII) and enhanced vegetation index (EVI) were used as proxy for including the effect of vegetation water content and structure. Considering viewing angle effects, T_B data were normalized to three different angles (7° , 21.5° , and 38.5°). The model based on the combination of NDII and horizontally polarized T_B normalized to 7° produced the best result ($R^2 = 0.678$, $RMSE = 0.026 \text{ m}^3/\text{m}^3$). It suggests that involving NDII into the model could significantly improve pasture covered SMC estimation accuracy.

Keywords: Soil moisture · L-band brightness temperature
Vegetation water content · Normalized difference infrared index
Leaf area index · Enhanced vegetation index

1 Introduction

Soil moisture is a critical factor in many land applications such as hydrology [1], flood forecasting [2], and precision agriculture [3]. Therefore, it is important to get reliable information on the spatio-temporal variations of near-surface soil moisture. Soil moisture estimates are traditionally based on contact-based methods that measure the electrical resistivity, or on gravimetric methods that measure the volume of water. But these point measurements are time-consuming and often not applicable to large areas [4]. Microwave remote sensing methods including passive microwave radiometer and

active microwave (radar) deployed on either airborne or spaceborne platforms offer an effective way for retrieving spatial soil moisture estimates at different scales. In the past decades, passive microwave radiometer data have shown their increasing potential for quantifying and monitoring soil moisture [5–8]. Particularly, L-band brightness temperature (T_B) has been widely accepted as one of the most promising techniques for quantifying soil moisture. A number of field experiments have demonstrated that L-band T_B has high sensitivity to moisture status and has a nearly linear relationship with near-surface soil moisture, providing that vegetation conditions or soil characters are uniform [9–12]. In addition, L-band has been utilized and dedicated to Soil Moisture and Ocean Salinity (SMOS) mission [13], and NASA’s Soil Moisture Active/Passive (SMAP) mission [14].

Although passive microwave radiation at L-band can penetrate vegetation canopies to a certain extent, the difficulty in estimating soil moisture significantly increases in the presence of vegetation. The main reason is that vegetation canopies can scatter and attenuate microwave radiation from soil surface, and also emit their own energy, so the signal received is modified such that the discriminate component of the signal due to soil moisture becomes complex [15, 16]. Therefore, the effects of vegetation must be taken into account when retrieving soil moisture with vegetation cover. Wigneron et al. [15] pointed out that the effects of vegetation can be well approximated by a simple radiative transfer model based on the optical depth, which could be derived from vegetation indices. The study of Wang et al. [16] showed that deseasonalized time series of root-zone soil moisture and normalized difference vegetation index (NDVI) have a nearly linear relationship. Pause et al. [4] reported that soil moisture estimation was improved by combining airborne L-band T_B observations with leaf area index (LAI) retrieved from hyperspectral image data. Cho et al. [17] found that the relationship between enhanced vegetation index (EVI) and soil moisture is nearly linear as a function of the fraction of vegetation cover. The aforementioned studies all demonstrated that vegetation related information has a considerable correlation to soil moisture. However the combination of L-band T_B with vegetation related information, such as vegetation structure and vegetation water content (VWC), have not been quantitatively investigated for soil moisture retrieval. Thus, the objectives of this study are to (1) determine whether a multivariate linear model based on a combination of L-band T_B and vegetation structure related vegetation index could increase estimation accuracy; and (2) demonstrate if soil moisture estimation accuracy could be improved by combining L-band T_B with vegetation water content. We tested the use of normalized difference infrared index (NDII) and EVI, which were calculated from Landsat 5 Thematic Mapper (TM) images, to represent VWC and vegetation structure, respectively.

2 Data Sources

2.1 Ground Sampling Data from SMAPEX-3

The study site and data sets of the third Soil Moisture Active Passive Experiment (SMAPEX-3) [18] were used in this study. The SMAPEX-3 was undertaken in the

Yanco area (145°50' to 146°21' E, 34°40' to 35°0' S) located in the western plains of the Murrumbidgee Catchment, Australia. The topography of the study area is flat with altitude no more than 150 m. This region is characterized by semi-arid agricultural and grazing area. The analyses in this study were mainly based on sampling data from three grazing areas. The three-week long campaign was conducted from September 5th to September 23rd, 2011.

The near surface (0–5 cm) soil moisture measurements were acquired along 250 m spaced regular grids using the Hydra-probe Data Acquisition System (HDAS) [19] for each flight day. To improve the accuracy and efficiency of ground sampling, a measurement grid was uploaded on the HDAS screen. Three replicate measurements were taken at each predefined sampling location and then averaged to account for small-scale soil moisture variation. Because the spatial resolution of L-band T_B data was 1 km, the average value of about 16 soil moisture measurements was used to represent soil moisture of a 1 km \times 1 km grid. Thus, a total of 32 soil moisture measurements were obtained. Coincident with soil moisture sampling activities, the vegetation samples for LAI and VWC were also collected in the corresponding area. LAI observations were obtained by an LAI-2000 Plant Canopy Analyzer. At each location, an approximate 0.25 m² area of vegetation within the area was clipped at ground level and then sent to laboratory for VWC measurements. The detailed sampling protocol was further described in Panciera et al. [18].

2.2 L-Band T_B Data

L-band T_B was measured at two polarizations using the Polarimetric L-band Multi-beam Radiometer (PLMR) deployed on a light aircraft. The PLMR observes at both horizontal and vertical polarization using a polarization switch, with viewing angles of $\pm 7^\circ$, $\pm 21.5^\circ$ and $\pm 38.5^\circ$. A footprint size of nearly 1 km was achieved with a flying altitude of 3 km. The details of before and after flight calibrations, radiometric calibration and final geo-rectification can be found in Monerris et al. [20]. The output data were time sequential datasets of six beam position T_B values with geo-reference for each flight line. The T_B data collected on September 5th, September 18th, September 19th and September 21th, 2011 were used in the study for analyses.

To effectively use T_B data for retrieving soil moisture, the varying viewing angles should be taken into account through a normalization procedure [21]. For this study, the data were normalized to 7° , 21.5° and 38.5° , respectively, to evaluate the influence of viewing angle on soil moisture retrieval. Taking the normalized horizontal polarization T_B to 7° , for example, a correction factor was first computed for each beam position (BP) by deducting its mean from the average value of BP 3 and BP 4, and then this factor was added to all data point for that BP. The processed and geo-referenced T_B values were mapped at a resolution of 1 km. Figure 1 presents the maps of L-band T_B normalized to 7° in horizontal and vertical polarization acquired on September 5th, 2011.

Due to the relatively low flying height, atmospheric contribution on L-band T_B could be neglected. Consequently, the T_B data were normalized and divided by the ground measured soil temperature (T_s) to remove difference in observed T_B due to seasonal T_s changes.

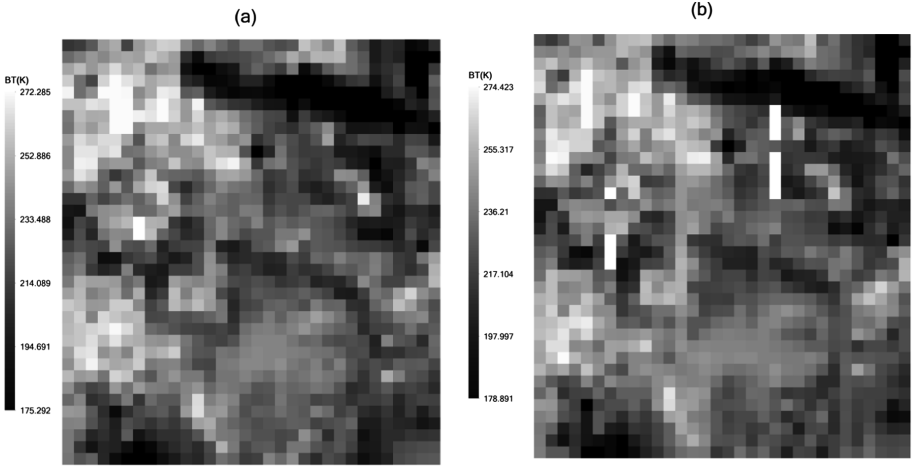


Fig. 1. Example of L-band T_B normalized to 7° in horizontal (a) and vertical (b) polarization acquired on September 5th, 2011.

2.3 Landsat 5 Thematic Mapper Data

Two images of clear sky Landsat 5 TM, acquired on September 2nd and September 18th, 2011, were used in this study. These two images provided concurrent measurements during the SMAPEX-3 campaign. Because the changes in vegetation (biomass, VWC and vegetation structure) are negligible within a week, a time shift of two or three days to the L-band T_B data acquisition could be acceptable. TM surface reflectance values were obtained by applying the atmospheric correction algorithm in ENVI FLAASH.

3 Methods

3.1 Using Enhanced Vegetation Index as an Indicator of Vegetation Structure

LAI is an important vegetation structure parameter and is commonly estimated by vegetation indices. According to the existing research, EVI has widely accepted as one of optimal vegetation indices for LAI retrieval due to its capability in reducing atmospheric and soil interference [22, 23]. Through the statistical analysis of pasture LAI, most of the LAI values from SMAPEX-3 fell into the interval of [0, 3]. Because the relationship between LAI and EVI is nearly linear when LAI is less than three [24, 25], EVI is used as a proxy of LAI in this study and can be computed according to Eq. (1).

$$EVI = 2.5 \frac{R_{NIR} - R_R}{R_{NIR} + 6R_R - 7.5R_B + 1} \quad (1)$$

where R_{NIR} , R_R and R_B represent the reflectance of near-infrared channel (780–900 nm), red channel (630–690 nm) and blue channel (450–520 nm), respectively.

3.2 Using Normalized Difference Infrared Index as an Indicator of VWC

Many studies [26–28] have explored the utility of Landsat TM images in retrieving VWC. It has been found that NDII is the most appropriate index for VWC retrieval using Landsat TM images. Therefore, NDII is utilized as a proxy of VWC in this study since the relationship between NDII and VWC is approximately linear [29, 30]. The NDII could be calculated according to Eq. (2).

$$NDII = \frac{R_{NIR} - R_{SWIR}}{R_{NIR} + R_{SWIR}} \quad (2)$$

where R_{NIR} and R_{SWIR} represent the reflectance of near-infrared channel (780–900 nm) and shortwave infrared channel (1550–1750 nm), respectively.

3.3 Image Registration

To determine whether involving TM vegetation data can reduce the effect of vegetation on microwave signal and improve soil estimation accuracy, horizontal polarization and vertical polarization L-band T_B data normalized to three different viewing angles were respectively combined with NDII and EVI in turn for soil moisture estimation. Because T_B data and vegetation data derived from Landsat 5 TM imageries have different spatial resolution, it is necessary to resample the EVI and NDII maps of $30 \text{ m} \times 30 \text{ m}$ to $1 \text{ km} \times 1 \text{ km}$ pixel. EVI and NDII maps were down-sampled using the nearest neighbor interpolation algorithm in this study.

3.4 Multivariate Linear Regression Modelling

The previous studies demonstrated that the relationship between L-band T_B and soil moisture is nearly linear [9, 18], and the relationship between vegetation related data and soil moisture is also approximately linear [16, 17]. Therefore, a multivariate linear regression model was adopted in this study to estimate soil moisture as a weighted sum of L-band T_B data and a vegetation related measurement. The model is trained as

$$Y = X\beta + \varepsilon \quad (3)$$

where the dependent variable Y is an $n \times 1$ vector for the soil moisture content with n being the number of training samples; the independent variable X is an $n \times 2$ matrix of the two observed values for each training sample. One observed value is the T_B of a given viewing angle under a given polarization, and the other is the vegetation information (NDII or EVI). The β is a 2×1 vector of regression coefficients and ε is an $n \times 1$ vector of residuals. The regression coefficients were obtained by minimizing a least square cost function of Eq. (3). Three viewing angles under two polarizations

were tested by applying the multivariate regression model with T_B and NDII, or with T_B and EVI.

3.5 Validation

Due to the limited number of samples in this study, leave-one-out cross validation (LOOCV) was utilized to assess the overall performance of different models. This meant that 32 individual calibration models were developed for each method. The average coefficient of determination (R_{avg}^2) and average root mean square error (RMSE_{avg}) of 32 calibration models were used to evaluate the calibration accuracy. The coefficient of determination for LOOCV (R_{cv}^2) and root mean square error for LOOCV (RMSE_{cv}) were selected to further compare the performances of various models. The proposed models $T_B + EVI$ and $T_B + NDII$ were compared with the case of using T_B only for three viewing angles of two polarizations.

4 Results

4.1 Multivariate Linear Regression Using the Combination of T_B and EVI

Table 1 gives the comparison results on the performance of the multivariate linear regression models. It shows that $T_B + EVI$ produced little better (or similar) results than those with the T_B only for both calibration and LOOCV analyses. In the multivariate linear regression analyses, models involving horizontal (H) polarization T_B performed considerably better than those involving vertical (V) polarization T_B . Of them, the model based on the combination of EVI and horizontal polarization T_B normalized to 7° yielded the best results for both calibration ($R_{avg}^2 = 0.686$, $RMSE_{avg} = 0.026 \text{ m}^3/\text{m}^3$) and validation ($R_{cv}^2 = 0.572$, $RMSE_{cv} = 0.029 \text{ m}^3/\text{m}^3$). The followed were models involving horizontal polarization T_B normalized to 38.5° . The models involving horizontal polarization T_B normalized to 21.5° performed the worst.

Table 1. Performance of the multivariate linear regression models based on the combination of L-band T_B and EVI for predicting soil moisture.

	Calibration		Validation	
	R_{avg}^2	RMSE _{avg} (m^3/m^3)	R_{cv}^2	RMSE _{cv} (m^3/m^3)
7°				
$T_B(\text{H})$	0.641	0.028	0.579	0.030
$T_B(\text{H}) + \text{EVI}$	0.686	0.026	0.572	0.029
$T_B(\text{V})$	0.594	0.030	0.516	0.032
$T_B(\text{V}) + \text{EVI}$	0.623	0.028	0.502	0.032

(continued)

Table 1. (continued)

	Calibration		Validation	
	R_{avg}^2	RMSE _{avg} (m ³ /m ³)	R_{cv}^2	RMSE _{cv} (m ³ /m ³)
21.5°				
T _B (H)	0.607	0.029	0.545	0.031
T _B (H) + EVI	0.640	0.028	0.541	0.031
T _B (V)	0.542	0.032	0.451	0.034
T _B (V) + EVI	0.583	0.030	0.453	0.033
38.5°				
T _B (H)	0.624	0.029	0.559	0.031
T _B (H) + EVI	0.674	0.026	0.559	0.030
T _B (V)	0.423	0.035	0.310	0.038
T _B (V) + EVI	0.500	0.032	0.356	0.036

4.2 Multivariate Linear Regression Using the Combination of T_B and NDII

Table 2 gives comparison results on the performance of the multivariate linear regression models based on the combination of L-band T_B and NDII for predicting soil moisture. This model produced generally better results than those with the T_B only, for both calibration and LOOCV analyses. In the multivariate linear regression analyses, models involving horizontal polarization T_B values performed considerably better than those involving vertical polarization T_B values. Among these models, the performances of models involving horizontal polarization T_B normalized to 7° were the best. Especially, the model based on the combination of horizontal polarization T_B and NDII resulted in the highest estimation accuracy with $R_{\text{cv}}^2 = 0.678$, $\text{RMSE}_{\text{cv}} = 0.026 \text{ m}^3/\text{m}^3$. The models involving horizontal polarization T_B normalized to 38.5° produced almost similar estimation accuracy to those involving horizontal polarization T_B normalized to 7°. The followed were models involving horizontal polarization T_B normalized to 21.5°.

Table 2. Performance of the multivariate linear regression models based on the combination of L-band T_B and NDII for predicting soil moisture.

	Calibration		Validation	
	R_{avg}^2	RMSE _{avg} (m ³ /m ³)	R_{cv}^2	RMSE _{cv} (m ³ /m ³)
7°				
T _B (H)	0.641	0.028	0.579	0.030
T _B (H) + NDII	0.746	0.023	0.678	0.026
T _B (V)	0.594	0.030	0.516	0.032
T _B (V) + NDII	0.692	0.025	0.614	0.028

(continued)

Table 2. (continued)

	Calibration		Validation	
	R_{avg}^2	RMSE _{avg} (m ³ /m ³)	R_{cv}^2	RMSE _{cv} (m ³ /m ³)
21.5°				
T _B (H)	0.607	0.029	0.545	0.031
T _B (H) + NDII	0.711	0.025	0.641	0.027
T _B (V)	0.542	0.032	0.451	0.034
T _B (V) + NDII	0.658	0.027	0.568	0.030
38.5°				
T _B (H)	0.624	0.029	0.559	0.031
T _B (H) + NDII	0.742	0.023	0.673	0.026
T _B (V)	0.423	0.035	0.310	0.038
T _B (V) + NDII	0.598	0.029	0.491	0.032

Figure 2(a) shows the relationship between the modeled results and the ground truth, when only T_B (H) 7° was used. Figure 2(b) shows the performance after NDII was added. In the comparison of Fig. 2(a) and (b), it can be observed that linear relationship between the measured soil moisture and the predicted soil moisture was significantly improved. This model increased R_{cv}^2 value by 0.099, and decreased the RMSE_{cv} value by 0.004 m³/m³ in the cross-validation after involving NDII.

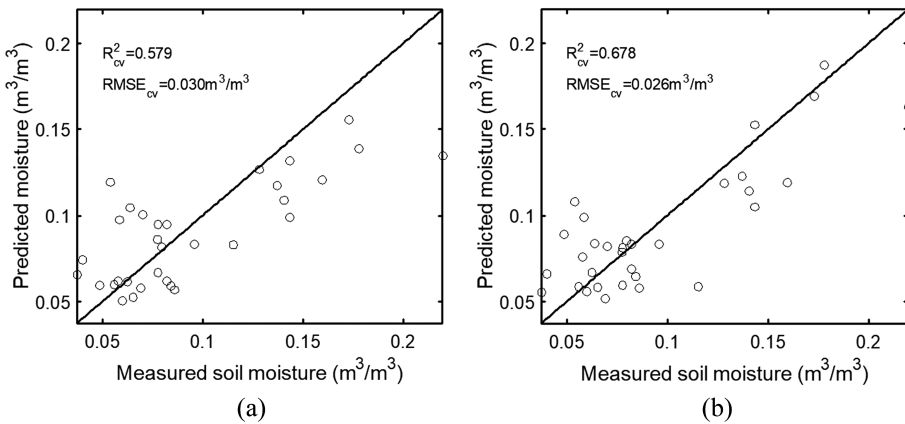


Fig. 2. LOOCV results before (a) and after (b) involving NDII for predicting soil moisture using horizontal polarization L-band T_B normalized to 7°. Note: The solid line is a one-to-one line.

5 Discussion and Conclusions

The SMAPEx-3 led to reliable passive radiometry data at L-band and corresponding ground sampling data including soil moisture and vegetation data. It allowed an assessment of the utility of passive radiometry data at L-band for use in estimating soil

moisture below pasture. It also made it possible to explore whether soil moisture estimation could be enhanced by involving vegetation related information.

The performance of multivariate linear regression models involving vegetation structure related information (LAI) was little better than those with only T_B under three viewing angles (Table 1). These results are not consistent with that observed in Pause et al. [4] who found that soil moisture estimation accuracy was significantly improved after combining L-band T_B and LAI. This study retrieved winter barley covered and winter rye covered soil moisture using horizontal polarization T_B data with 50 m spatial resolution and LAI estimated from hyperspectral data with 1.5 m spatial resolution. The primary reason is that hyperspectral data are more powerful than multispectral data for LAI estimation due to its approximately contiguous spectrum [31]. Furthermore, the best pasture LAI estimation accuracy got by EVI was relatively low ($R_{cv}^2 = 0.385$, $RMSE_{cv} = 0.75 \text{ m}^2/\text{m}^2$) based on Landsat 5 TM data in the study (the detailed comparison was not presented in this paper). It demonstrated that LAI estimation accuracy based on remote sensed data should be checked before involving LAI into soil moisture estimation. If LAI estimation is not accurate, it will not work to involve it during soil moisture estimation.

The models involving horizontal polarization T_B values performed better than those involving vertical polarization T_B values (Tables 1 and 2). It indicated that horizontal polarization T_B was more sensitive to soil moisture than vertical polarization T_B . Many researchers [4, 18] have given the same conclusion about this. The performances of multivariate linear regression models involving NDII were much better than those with only T_B at both polarizations under three different viewing angles. This is mainly due to the fact that involving NDII takes VWC into account and relieves the effect of vegetation on microwave signal. Among the three viewing angles, models based on T_B normalized to 7° or 38.5° resulted in better estimation accuracy than those based on T_B normalized to 21.5° with and without NDII. It confirmed that effects of vegetation and soil moisture estimation based on microwave signal are dependent on incidence angle.

In summary, this study demonstrated the potential application of involving vegetation related information into soil moisture estimation. The experimental results indicated that multivariate linear regression models using horizontal polarization T_B and NDII could significantly improve pasture covered soil moisture estimation accuracy. It is also worth mentioning that this newly developed method based on empirical models might be site-specific and thus needs recalibrating or testing the models with a certain amount of samples collected from an application area before applying the method to the area. It is necessary to do further study to verify the efficacy of the proposed method in different vegetation types and under different ecological areas.

Acknowledgements. This study was supported by the National Key Research and Development Program (2016YFD0300602), Natural Science Foundation of China (61661136003, 41601346, 41471285, 41471351, 41371349), China Postdoctoral Science Foundation Funded Project (2017M620675), the Special Funds for Technology innovation capacity building sponsored by the Beijing Academy of Agriculture and Forestry Sciences (KJCX20170423) and Beijing Postdoctoral Research Foundation. The authors wish to thank Xiuping Jia at University of New South Wales at Canberra, Jeffrey P. Walker and Xiaoling Wu at Monash University for providing comments and experimental data.

References

1. Crow, W.T., Chen, F., Reichle, R.H., et al.: L-band microwave remote sensing and land data assimilation improve the representation of pre-storm soil moisture conditions for hydrologic forecasting. *Geophys. Res. Lett.* **44**(11), 5495–5503 (2017)
2. Meng, S., Xie, X., Liang, S.: Assimilation of soil moisture and streamflow observations to improve flood forecasting with considering runoff routing lags. *J. Hydrol.* **550**, 568–579 (2017)
3. Tian, L., Yuan, S., Quiring, S.M.: Evaluation of six indices for monitoring agricultural drought in the south-central United States. *Agric. For. Meteorol.* **249**, 107–119 (2018)
4. Pause, M., Schulz, K., Zacharias, S., et al.: Near-surface soil moisture estimation by combining airborne L-band brightness temperature observations and imaging hyperspectral data at the field scale. *J. Appl. Remote Sens.* **6** (2012). <https://doi.org/10.1117/1.jrs.6.063516>
5. Wigneron, J.P., Jackson, T.J., O’neill, P., et al.: Modelling the passive microwave signature from land surfaces: a review of recent results and application to the L-band SMOS SMAP soil moisture retrieval algorithms. *Remote Sens. Environ.* **192**, 238–262 (2017)
6. Kolassa, J., Reichle, R.H., Draper, C.S.: Merging active and passive microwave observations in soil moisture data assimilation. *Remote Sens. Environ.* **191**, 117–130 (2017)
7. Chan, S.K., Bindlish, R., O’Neill, P.E., et al.: Assessment of the SMAP passive soil moisture product. *IEEE Trans. Geosci. Remote Sens.* **54**(8), 4994–5007 (2016)
8. Santi, E., Paloscia, S., Pettinato, S., et al.: Application of artificial neural networks for the soil moisture retrieval from active and passive microwave spaceborne sensors. *Int. J. Appl. Earth Obs. Geoinf.* **48**, 61–73 (2016)
9. Merlin, O., Walker, J.P., Kalma, J.D., et al.: The NAFE’06 data set: towards soil moisture retrieval at intermediate resolution. *Adv. Water Resour.* **31**, 1444–1455 (2008)
10. Colliander, A., Jackson, T., McNairn, H., et al.: Comparison of airborne passive and active L-band system (PALS) brightness temperature measurements to SMOS observations during the SMAP validation experiment 2012 (SMAPVEX12). *IEEE Geosci. Remote Sens. Lett.* **12** (4), 801–805 (2015)
11. Fernandez-Moran, R., Wigneron, J.P., Lopez-Baeza, E., et al.: Roughness and vegetation parameterizations at L-band for soil moisture retrievals over a vineyard field. *Remote Sens. Environ.* **170**, 269–279 (2015)
12. Chen, X., Su, Y., Liao, J., et al.: Detecting significant decreasing trends of land surface soil moisture in eastern China during the past three decades (1979–2010). *J. Geophys. Res. Atmos.* **121**(10), 5177–5192 (2016)
13. Kerr, Y.H., Waldteufel, P., Wigneron, J.P., et al.: Soil moisture retrieval from space: the soil moisture and ocean salinity (SMOS) mission. *IEEE Trans. Geosci. Remote Sens.* **39**, 1729–1735 (2001)
14. Entekhabi, D., Njoku, E.G., O’Neill, P.E., et al.: The soil moisture active passive (SMAP) mission. *Proc. IEEE* **98**(5), 704–716 (2010)
15. Wigneron, J.P., Kerr, Y., Waldteufel, P., et al.: L-band microwave emission of the biosphere (L-MEB) model: description and calibration against experimental data sets over crop fields. *Remote Sens. Environ.* **107**(4), 639–655 (2007)
16. Wang, X., Xie, H., Guan, H., et al.: Different responses of MODIS-derived NDVI to root-zone soil moisture in semi-arid and humid regions. *J. Hydrol.* **340**, 12–24 (2007)
17. Cho, J., Lee, Y.W., Han, K.S.: The effect of fractional vegetation cover on the relationship between EVI and soil moisture in non-forest regions. *Remote Sens. Lett.* **5**, 37–45 (2014)

18. Panciera, R., Walker, J.P., Jackson, T.J., et al.: The soil moisture active passive experiments (SMAPEX): toward soil moisture retrieval from the SMAP mission. *IEEE Trans. Geosci. Remote Sens.* **52**, 490–507 (2014)
19. Merlin, O., Walker, J., Panciera, R., Young, R., Kalma, J., Kim, E.: Soil moisture measurement in heterogeneous terrain. In: *Proceedings of International Congress on MODSIM*, pp. 2604–2610 (2007)
20. Monerris, A., Walker, J. P., Panciera, R., et al.: The third soil moisture active passive experiment. In: *The 19th International Congress on Modeling and Simulation (MODSIM2011)*. Modelling and Simulation Society of Australia and New Zealand, pp. 1980–1986 (2011)
21. Jackson, T.J., Le Vine, D.M., Swift, C.T., et al.: Large area mapping of soil moisture using the ESTAR passive microwave radiometer in Washita'92. *Remote Sens. Environ.* **54**, 27–37 (1995)
22. Jiang, Z., Huete, A.R., Didan, K., et al.: Development of a two-band enhanced vegetation index without a blue band. *Remote Sens. Environ.* **112**(10), 3833–3845 (2008)
23. Thenkabail, P.S., Lyon, J.G. (eds.): *Hyperspectral Remote Sensing of Vegetation*. CRC Press, New York (2016)
24. Fu, Y., Yang, G., Wang, J., et al.: A comparative analysis of spectral vegetation indices to estimate crop leaf area index. *Intell. Autom. Soft Comput.* **19**(3), 315–326 (2013)
25. Wu, M., Wu, C., Huang, W., et al.: High-resolution leaf area index estimation from synthetic Landsat data generated by a spatial and temporal data fusion model. *Comput. Electron. Agric.* **115**, 1–11 (2015)
26. Trombetti, M., Riaño, D., Rubio, M.A., et al.: Multi-temporal vegetation canopy water content retrieval and interpretation using artificial neural networks for the continental USA. *Remote Sens. Environ.* **112**(1), 203–215 (2008)
27. Adam, E., Mutanga, O., Rugege, D.: Multispectral and hyperspectral remote sensing for identification and mapping of wetland vegetation: a review. *Wetlands Ecol. Manag.* **18**(3), 281–296 (2010)
28. Gao, Y., Walker, J.P., Allahmoradi, M., et al.: Optical sensing of vegetation water content: a synthesis study. *IEEE J. Sel. Top. Appl. Earth Obs. Remote Sens.* **8**(4), 1456–1464 (2015)
29. Cosh, M.H., Tao, J., Jackson, T.J., et al.: Vegetation water content mapping in a diverse agricultural landscape: national airborne field experiment 2006. *J. Appl. Remote Sens.* **4**, 043532 (2010)
30. Xiao, Y., Zhao, W., Zhou, D., et al.: Sensitivity analysis of vegetation reflectance to biochemical and biophysical variables at leaf, canopy, and regional scales. *IEEE Trans. Geosci. Remote Sens.* **52**(7), 4014–4024 (2014)
31. Xing, J., Symons, S., Shahin, M., et al.: Detection of sprout damage in Canada Western Red Spring wheat with multiple wavebands using visible/near-infrared hyperspectral imaging. *Biosys. Eng.* **106**, 188–194 (2010)



Study on Precision Fertilization Model Based on Fusion Algorithm of Cluster and RBF Neural Network

Shan Zhao, Guifen Chen^(✉), Siwei Fu, and Enze Xiao

College of Information and Technology Science, Jilin Agricultural University,
Changchun 130118, Jilin, China
guifchen@163.com

Abstract. Precision fertilization is the core content of precision agriculture technology. There was a complex non-linear relationship between crop optimal fertilization and soil fertility. The single model is difficult to accurately describe its complex relationship and change law, making the crop accurate fertilizer is difficult to determine; Neural network technology to solve this problem provides a new way of thinking. But a single radial basis function network (RBF) neural network fertilization model is too dependent on the selection of the hidden layer data center. Therefore, this paper proposes a decision-making technique based on fuzzy C-means (FCM) clustering and RBF neural network fusion algorithm. The fusion algorithm first uses the FCM algorithm to select multiple RBF networks in the training samples. Based on this, the least squares (OLS) training network is used to optimize the data center. Finally, an improved RBF neural network model is established. In this paper, the model is applied to the maize precision operation demonstration base, soil nutrient and maize yield as the input of neural network, using the precision fertilization amount of maize as output. The model of precision fertilization of maize was established. And the model was used to make the precision fertilization decision of maize. Experimental results show: The improved RBF neural network is compared with the traditional BP network to reduce the error by 0.47. Compared with the model, the error of the RBF neural network method is reduced by 0.045. Significantly improve the prediction accuracy, reduce the calculation time. Can effectively guide the precise fertilization.

Keywords: Fusion optimization algorithm · FCM · OLS · RBF
Precision fertilization model

1 Introduction

Maize production in Jilin Province, agricultural production occupies an extremely important position, is the largest planting area in Jilin Province, food crops, production accounted for 12.5% of the country, to 27.88 million t. corn production of Jilin Province is essential to China's food security. Reasonable application of chemical fertilizers is one of the important guarantees of high and stable yield of maize. According to the soil type, soil fertility and maize fertilizer characteristics to fertilize scientifically and reasonably is particularly important. Variable fertilization technology is an important part of precision

agriculture, It is based on the actual needs of crops, based on scientific fertilization methods, Identify variables inputs on crop To a certain extent, increased corn production. In the case of reasonable control of the amount of fertilizer, you can achieve both the purpose of reducing investment and increase production. Because of the high nonlinearity between yield and soil nutrient and fertilization, neural network is considered to be a powerful tool to solve nonlinear problems, Therefore, a number of different forms of neural networks are used for precise fertilization decisions. In 2001, Pokrajac et al. Presented a neural network-based decision support system to provide precise fertilization recommendations; In 2002, Teng Qingfang and others tried to use the neural network to establish the soil fertilization model; In 2004, Ma Weilin et al. Proposed a method of variable fertilization decision-making based on data envelopment analysis and artificial neural network. In 2007, Lan Weijuan et al. Applied radial basis function network to variable fertilization decision. The use of RBF network to study the variable fertilization decision has the advantages of simple structure, rapid training process and good promotion ability. It is superior to the BP network in terms of approaching ability and learning speed, and can simplify the structure and learning rules of the network. Therefore, this paper uses FCM algorithm and OLS fusion algorithm to optimize RBF neural network, and constructs a RBF neural network prediction model based on fusion algorithm, To adapt the content of soil nutrients, fertilizer and food production randomness, complexity and nonlinear variation, Through the different soil types and yield prediction fertilization, to explore the realization of high yield of corn nitrogen, phosphorus, potassium fertilizer the best amount of application, For the rational use of fertilizer on the production, improve fertilizer utilization to provide a reference. To guide the variable fertilization in production of maize in central Jilin Province, in order to improve food productivity, to achieve sustainable development of productivity.

2 Technology and Methods

Techniques employed herein route is divided into three parts: first, Normalizing treatment the Data samples, and using the FCM algorithm select primary data center; the second usage OLS to train RBF neural network to generate a regression matrix, preferably the data center; Thirdly, using the RBF neural network to construct the precision fertilization model. The specific description shown in Fig. 1:

2.1 RBF Neural Network Prediction Algorithm

The RBF (Radial Basis Function) neural network model was proposed by Moody and Darken in 1988, it is a three-layer feedforward neural network, the first layer is the input layer, composed of the source node; the second layer for the hidden layer, the activation function using radial basis function (this article is Gaussian function), and Usually defined as any data sample to a data center Euclidean distance between the monotonic function; The third layer is the output layer, the hidden layer to the output layer using linear activation function. In this paper, four factors affecting the amount of maize fertilizer were obtained, so the input vector $n = 4$, h hidden layer, m output vector is the amount of soil fertilization of Alkaline N (N) Available phosphorus (P) Available potassium (K), so $m = 3$ (Fig. 2).

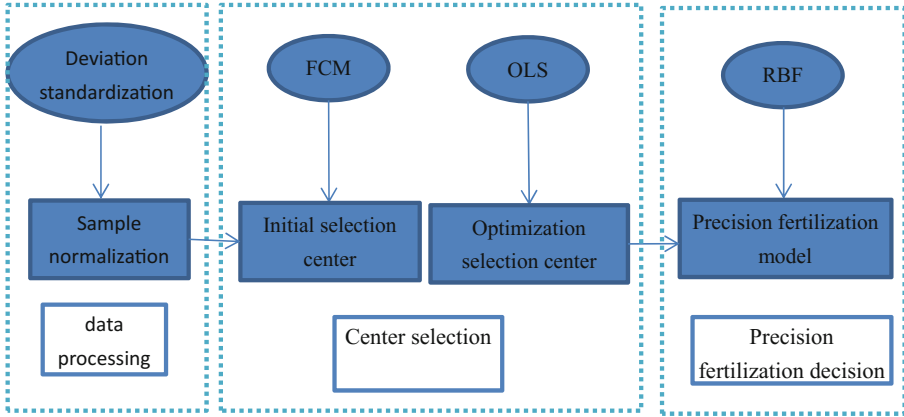


Fig. 1. The technical roadmap for this article

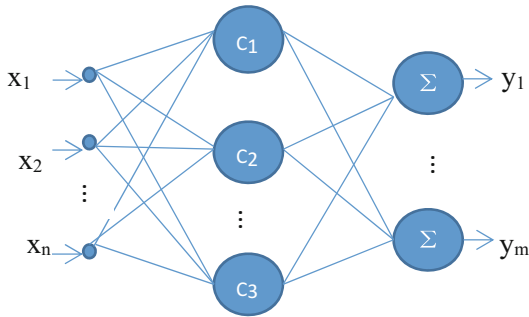


Fig. 2. RBF network structure

By RBFNN learning process and its network mapping relationship, RBF performance depends on the strong choice of the center number, the center value and its location. Therefore, if all the input as a candidate space, it will bring a very large amount of calculation, reducing network performance. In order to overcome this deficiency, FCM algorithm can be used to narrow the candidate space and reduce the network size to improve the computational efficiency.

2.2 FCM Clustering Algorithm Primary Network Center

Fuzzy C-means (FCM) is proposed by Bezdek et al. FCM compared with the traditional clustering analysis algorithm, It introduced the fuzzy mathematics theory, which is an unsupervised clustering algorithm based on objective function. Corn soil nutrient, yield and fertilizer data samples usually have serious non-linear characteristics, Single model is difficult to describe, so it is necessary to divide the data sample set into different subclasses. The in order to reduce the number of RBFNN centers, FCM

clustering is used to initialize the sample training set. And can improve the speed of network computing efficiency, so that the forecast is more accurate.

The basic idea of FCM is to divide all data samples into c fuzzy groups, The cluster center of each fuzzy group is determined by minimizing the objective function value. And the degree of membership in the $[0, 1]$ is used to determine the degree to which each given data belongs to each fuzzy group. Its membership matrix U must satisfy Eq. (1):

$$\sum_{i=1}^c u_{ij} = 1, \forall j = 1, \dots, n \tag{1}$$

The objective function of FCM algorithm is generally as follows (2):

$$J(U, c_1, \dots, c_c) = \sum_{i=1}^c J_i = \sum_{i=1}^c \sum_j^n u_{ij}^k d_{ij}^2 \tag{2}$$

In the formula, u_{ij} is the degree of membership; $d_{ij} = \|c_i - x_j\|$ represents the Euclidean distance between the i -th cluster center and the j -th data point; c_i is the clustering center of each fuzzy group; $k \in [1, \infty)$ is a weighted power exponent. In order to achieve the minimum target function, We introduce the Lagrangian multiplier $\lambda_j (j = [1, n])$. The constructor is shown in Eq. 3:

$$J(U, c_i, \dots, c_c, \lambda_n) = J(U, c_1, \dots, c_c) + \sum_{j=1}^n \lambda_j \left(\sum_{i=1}^c u_{ij} - 1 \right) = \sum_{i=1}^c \sum_j^n u_{ij}^k d_{ij}^2 + \sum_{i=1}^n \lambda_j \left(\sum_{i=1}^c u_{ij} - 1 \right) \tag{3}$$

Derivating the parameters for each parameter, the requirement of Making Formula 3 Minimal is

$$c_i = \frac{\sum_{j=1}^n u_{ij}^k x_j}{\sum_{i=1}^n u_{ij}^k} \tag{4}$$

And

$$u_{ij} = \frac{1}{\sum_{k=1}^c \left(\frac{d_{ij}}{d_{kj}} \right)^{2/(k-1)}} \tag{5}$$

The specific FCM algorithm steps are as follows:

- Step 1: Given the clustering category $c, 2 \leq c \leq N, N$ is the number of initial data samples, Initial membership matrix is $U(0)$, And set the threshold ε ;
- Step 2: initialize the cluster center $c_i(t), i = 1, 2, \dots, n$;

Step 3: calculate the membership degree $u_{ij}(t)$ with the formula (5), $i = 1, 2, \dots, c$; $j = 1, 2, \dots, n$;

Step 4: Use the obtained membership degree to correct the cluster center $c_i(t + 1)$, $i = 1, 2, \dots, c$ according to (4);

Step 5: Calculate the error $e = \sum_{i=1}^c \|c_i(t + 1) - c_i(t)\|^2$. If $e < E_{\max}$ the operation is over, otherwise let $t + 1 = t$, return to the third step.

2.3 Orthogonal Least Squares Optimization Center

RBF network center selection orthogonal least squares (orthogonal least squares algorithm OLS) algorithm, Which solves the key problems in the construction of radial basis function network. OLS algorithm uses the orthogonalization method to independently calculate the contribution of the regression operator to the output, so the center selection step is simple and effective. OLS algorithm is the basic idea: The center of the radial basis function is chosen as a subset of the training pattern, Choose one sample at a time, Through the orthogonal regression matrix, the regression operator with large error compression ratio is selected, And the number of regression operators is determined by the selected tolerance, And then find the network weight. The RBF neural network is trained with OLS, and the matrix representation of the expected output response is:

$$Y = \hat{Y} + E = \phi W + E \quad (6)$$

Where $Y \in R^{n \times 3}$ is the desired output matrix; $\hat{Y} \in R^{n \times 3}$ is the output matrix of the neural network model; $\Phi \in R^{n \times h}$ is the regression matrix; $E \in R^{n \times 3}$ is the output error matrix. In this paper, Schmidt orthogonalization method to reduce the output error. OLS algorithm can save storage space and improve operation efficiency, and is very suitable for training RBF network. The RBF neural network trained by OLS can obtain a more optimized data center, improve the accuracy of the network, greatly reduce the computational complexity of the network and improve the training speed.

3 Application of RBF Neural Network Fusion Algorithm in Precision Fertilization Decision of Maize

3.1 Experimental Data

Experimental data from the “National Spark Program” in Jilin Province, Nong’an County, Helong Town, Chen Jiadian Village and Kai’an town experimental field. In order to achieve accurate fertilization, the grid was divided into grid, the grid size is 40 m × 40 m. Figure 3 is Chenjiadian village and Kai’an town experimental field grid.

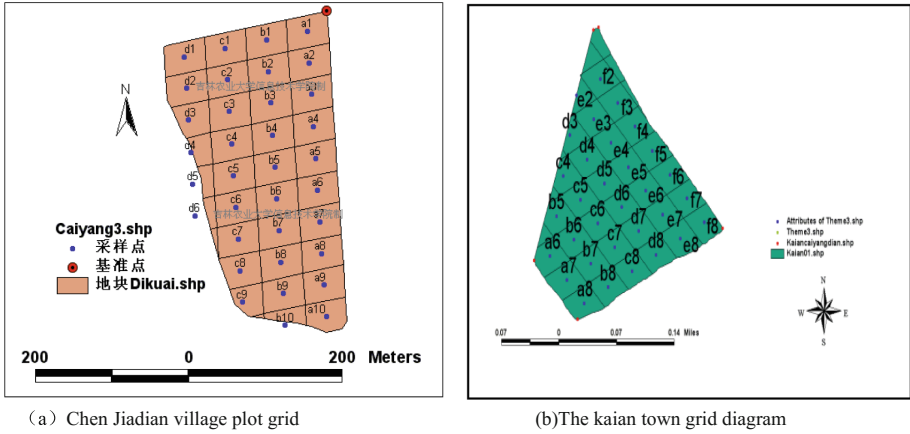


Fig. 3. Experimental area grid

In the year of 2015, the experimental field was tested, fertilized and tested, and finally 64 samples were obtained. Each sample consisted of seven attributes: soil N, P, K content, actual yield, N, P, K fertilizer. The amount of application, part of the experimental data shown in Tables 1 and 2:

Table 1. Chenjiadian village experimental field

Plots	N content mg/kg	P content mg/kg	K content mg/kg	N amount kg/hm	P amount kg/hm	K amount kg/hm	Measured yield kg/hm
a1	115	14.8	159	75.6	32.3	64.8	8303
a2	115	14.8	159	75.6	32.3	66.1	8470
a3	136	17.55	159	76.9	31.4	66.8	8556
a4	136	17.55	159	76.9	31.4	66.1	8461
a5	133	14.6	182	76.7	32.4	66.3	8684
a6	133	14.6	182	76.7	32.4	56.2	7367
a7	129	17.55	182	76.5	31.4	61.1	8002
a8	129	17.55	182	76.5	31.4	65.4	8564
a9	118	16.3	165	75.3	32.3	60.1	7745
a10	125	15.8	179	77.1	32.3	62.7	8192

Table 2. Kai'an town experimental field

Plots	N content mg/kg	P content mg/kg	K content mg/kg	N amount kg/hm	P amount kg/hm	K amount kg/hm	Measured yield kg/hm
a6	133	26.7	240	76.7	28.80	70.0	7696.5
a7	108.5	38.6	270	75.2	26.20	61.6	7592.25
a8	161	30.3	180	78.7	27.96	72.2	8180.25
b5	108.5	35.8	230	75.2	26.76	65.7	7805.25
b6	101.5	35.2	230	74.8	26.89	66.0	8817
b7	140	30.7	160	77.2	27.87	73.4	7587.75

(continued)

Table 2. (continued)

Plots	N content mg/kg	P content mg/kg	K content mg/kg	N amount kg/hm	P amount kg/hm	K amount kg/hm	Measured yield kg/hm
b8	175	36.2	200	79.8	26.68	67.5	7221.75
c4	98	21.4	220	74.6	30.22	74.9	6804
c5	112	32.45	280	75.4	27.46	63.9	7360.5
c6	168	33.2	240	79.2	27.31	66.3	7576.5

3.2 Pretreatment of Training Samples

In the process of network model training will appear a larger input variable to suppress the phenomenon of smaller input variables, resulting in increased network training time, and even the network can not converge. If the data dimension is inconsistent, it is easy to cause the sickness of the model. In order to remove the data in the dimension and the order of magnitude to establish the impact of network accuracy, After obtaining the sample vector, this paper takes the normalization of the data samples to deal with, namely:

$$x'_{pi} = \frac{x_{pi} - \min\{x_i\}}{\max\{x_i\} - \min\{x_i\}} \tag{7}$$

In the formula: X_{pi} is the raw data of the i -th variable of the p th sample, X'_{pi} is the normalized processing data for the i -th variable of the p th sample. The preprocessed sample data range is (0, 1).

3.3 Construction of Fertilization Model

In order to achieve the target yield of corn, this paper establishes a RBF neural network model based on fusion algorithm, Study the best fertilization model of maize to achieve high yield of maize. Taking the soil nutrient content of Chenjiadian experiment field and the input as the neural network, the amount of fertilizer applied as the output of the neural network, In this paper, based on the RBF neural network fertilization model shown in Fig. 4:

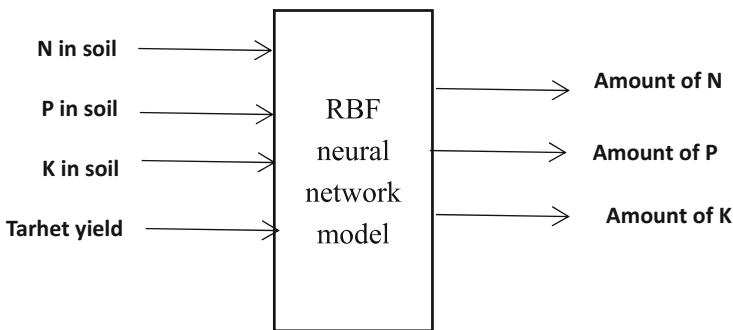


Fig. 4. RBF neural network fertilization model

(1) Different algorithms to predict performance comparison

In the training RBF network, the FCM algorithm, take $c = 20$, in all the samples, through clustering, the first selected cluster center number 20 data centers; use OLS training RBF, take the error threshold of 0.01 to get regression Matrix information, On the basis of the initial selection of 20 centers, and then enter the choice, and finally get 10 effective data center. Using BP network, single RBF network and post-training RBF neural network (FCM-OLS-RBF) to test the sample, Test results are shown in Table 3:

Table 3. Comparison of different algorithms for prediction performance

	BP	RBF	FCM-OLS-RBF
TIME (s)	2.008	2.234	1.158
MSE	0.67115	0.243501	0.2

It can be seen from Table 3 that from the prediction accuracy, the FCM-OLS-RBF model constructed in this paper has a prediction error of 0.2, which is obviously better than RBF network and BP network. From the processing speed, FCM-OLS-RBF network is 1.93,1.73 times faster than single RBF network and BP neural network in predicting 10 samples. Thus, the RBF network after the improved algorithm has higher accuracy and faster speed than the single RBF network and the traditional BP network, and the practicability is stronger.

(2) FCM-OLS-RBF fusion algorithm simulation experiment

In this experiment, 64 samples of soil nutrient content, yield and actual fertilization amount in Chenjiadian and Kai'an were divided into three parts, Of which 44 samples were used as training set, 10 samples were used as validation sets, and the remaining 10 samples were used as test sets. Before training RBF network, we first use FCM algorithm to select 20 centers in all training samples, then train the network with OLS, and finally select 10 centers. Finally, the trained RBF neural network was used to predict the soil fertilization amount of maize in the field of maize, Simulation results are shown in Fig. 5:

It can be seen from Fig. 5 that the predictive curve of FCM-OLS-RBF network is in good agreement with the measured curve, especially the predicted value and measured value of N and P, and the deviation is very small, Showing its higher prediction accuracy.

It can be seen from Fig. 6 that the relative error of nitrogen, phosphorus and potassium fertilizers is about 0.1%, and the maximum error is below 0.25%, which can meet the requirements of actual production.

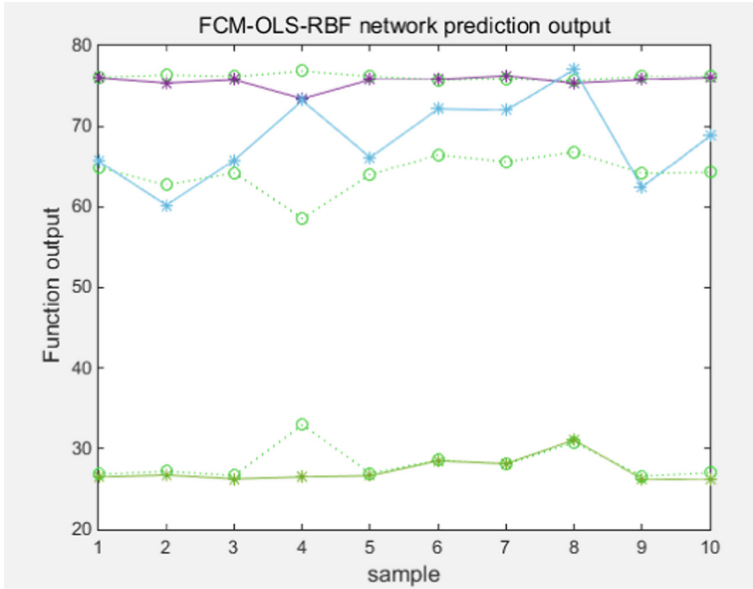


Fig. 5. FCM-OLS-RBF network simulation results

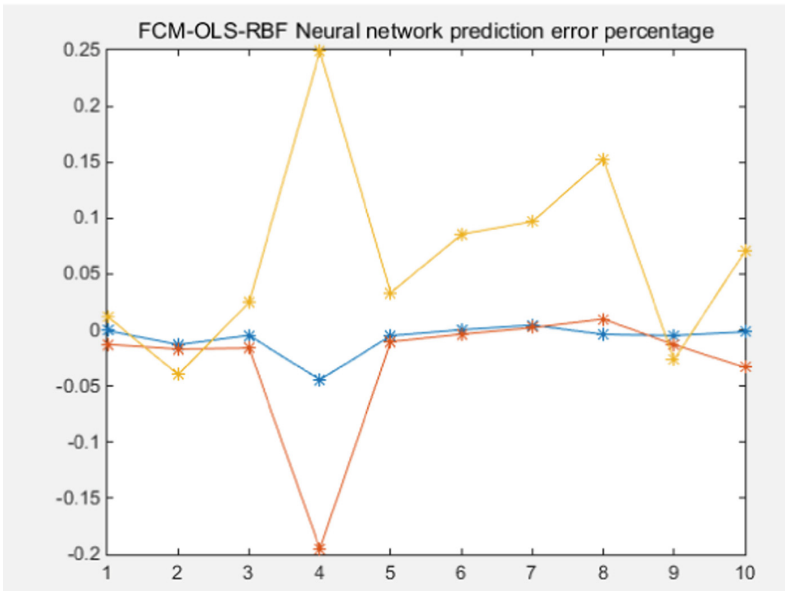


Fig. 6. FCM-OLS-RBF network prediction error

4 Conclusion

This paper focuses on the RBF neural network algorithm based on FCM clustering and OLS, and compares it with the traditional RBF and BP neural network. Finally, the method is applied to the precision fertilization problem. According to the experimental test, the following conclusions are drawn:

- (1) FCM-OLS-RBF fertilization prediction model training speed, good convergence, In the case of large quantities of non-linear and accurate fertilization applications, Compared with the traditional RBF and BP network prediction results, it also shows its better evaluation accuracy. Both to ensure the accuracy of the network while simplifying the algorithm and network structure;
- (2) The fertilization model based on FCM-OLS-RBF neural network can simulate the nonlinear relationship between soil test and fertilization, which is superior to the traditional fertilization model and can be used as a quantitative model to guide the accurate fertilization;
- (3) A large number of training samples are needed to predict with a neural network, or the accuracy of prediction can not be accurately fitted due to the high degree of non-linear relationship between the factors and fertilization.

And because the factors affecting the amount of corn fertilization varied and intricate, the factors that affect the yield is not only the amount of fertilizer problems. In the future, with the deepening of the practice of variable fertilization, the accumulation of data is rich, can provide a broader basis for improving production.

Acknowledgments. This work was funded by National Spark Program “Based on the Internet of Things precise operation of corn technology integration and demonstration” (2015GA660004) 2015–2017.

References

1. Yang, J., Liu, X.-X., Fan, H.-M.: Study on nitrogen fertilizer effect of different types of soils in Jilin Province. *Mod. Agric. Sci. Technol.* **18**, 9–10+13 (2015)
2. Xie, J.-G., Wang, L.-C., Yin, C.-X., Hou, Y.-P., Zhang, G.-H., Yu, L.: Study on fertilization effect of different types of soils in Jilin Province. *Corn Sci.* **04**, 167–171 (2008)
3. Yu, H., Liu, J., Jin, D., Yang, Y., Liu, D.: A new neural network ensemble method and its application in precision fertilization. *Comput. Res. Dev.* **09**, 1530–1538 (2010)
4. Lan, W., Mao, P., Du, D., Wang, J.: Study on variable fertilization decision based on radial basis function network. *Anhui Agric. Sci.* **21**, 6505–6507 (2007)
5. Zhang, C., et al.: Effects of N, P, K and potassium on maize in different soil types in the central Jilin Province. *Northeast Agric. Sci.* **04**, 58–62 (2016)
6. Li, Z., Chen, Z.: Slope stability evaluation method based on RBF-FCM-OLS. *Surv. Sci. Technol.* **06**, 1–4+17 (2016)
7. Cui, G., et al.: Study on prediction of blast furnace temperature by distributed RBF network model based on FCM. *Ind. Control Comput.* **07**, 1–2+5 (2013)
8. Lei, S., Liu, H., He, J., He, X., Xue, Q.: Application of dynamic K-means clustering algorithm in RBF neural network center selection. *Inf. Syst. Eng.* **06**, 83–85 (2011)

9. Hu, J., Li, D., Chen, G., et al.: Image segmentation method for crop nutrient deficiency based on fuzzy C-Means clustering algorithm. *Intell. Autom. Soft Comput.* **18**(8), 1145–1155 (2012)
10. Si, X., Peng, Z., Yuan, H., et al.: Research on cucumber downy mildew images classification based on fuzzy pattern recognition. *Sens. Lett.* **10**(1–2), 643–648 (2012)
11. Su, T., Ye, S., Sun, W.: Thermal machine error compensation modeling based on FCM clustering and RBF neural network. *Comb. Mach. Tools Autom. Process. Technol.* **10**, 1–4 +9 (2011)
12. Guan, S., Gao, J., Zhang, B., Liu, X.: Traffic flow prediction based on K-means clustering algorithm RBF neural network traffic flow prediction. *J. Qingdao Univ. (Eng. Technol. Edition)* **02**, 20–23 (2014)
13. Chen, Q., Zhang, J., Wang, F., Zheng, Z.: Optimal flight time prediction based on OLS-RBF neural network. *Aeronaut. Comput. Technol.* **04**, 42–45 (2015)
14. Liu, J.: Design and implementation of RBF network based on OLS algorithm. *Comput. Age* **07**, 21–22 + 25 (2010)
15. Chen, F.X., Cheng, J., Hu, Y., Zhou, Y., Zhao, Y.: Ants good pure spatial prediction of soil chromium content based on RBF neural network. *Geography* **01**, 69–74 (2013)
16. Linbo, W.: Study on tide level prediction of tidal reach based on improved OLS-RBF model. *Water Conserv. Plan. Des.* **06**, 51–54 (2017)
17. Lin, F.: Application of gray neural network in grain yield prediction. *Comput. Simul.* **04**, 225–228 + 267 (2012)
18. Zhao, X., Chen, G., Wan, B., Gao, J.: Based on the improved BP neural network integrated crop fertilization model. *J. Agric. Eng.* **12**, 193–198 (2010)
19. Jin, S., Liu, G., Yan, X., Shi, H., Cheng, L.: The necessity and application prospect of precision agriculture in China. *J. Zhejiang Agric. Sci.* **02**, 414–416 (2010)
20. Zhang, Y., Song, B., Wang, D., Yang, Q., Dong, Z.: Effects of variable fertilization on maize yield traits. *Mod. Agric.* **11**, 14–15 (2010)
21. Chen, H., Cao, L.Y., Chen, G.: Research on the evaluation and forecast of spatio-temporal variability of soil fertility in black soil area of Songliao Plain. *Sens. Lett.* **12**(3–4), 743–748 (2014)



Study on Three-Dimensional Data Acquisition of Crop Grains

Zetao Yu^{1,2}, Weiliang Wen^{1,2}, Xinyu Guo^{1,2}(✉), and Xianju Lu^{1,2}

¹ Beijing Research Center for Information Technology in Agriculture, Beijing, China

{yuzt, wenwl, guoxy, luxj}@nercita.org.cn

² Beijing Key Laboratory of Digital Plant, Beijing, China

Abstract. The rapid, efficient and non-destructive 3D morphological data acquisition of plants are great significance to the study of digital plant, functional structural plant model and crop phenotype. This paper discusses 3D data acquisition methods for smaller plant organs, which take maize grain as an example. Smartscan and Micro-CT scanning can be used to obtain the morphological data of the grains. The efficiency, accuracy, processing of data in two scanning ways are compared and analyzed. The results shows that the Micro-CT is more suitable for obtaining information of internal structure of maize grain. While grain morphology in SmartScan can get better visualization than Micro-CT, and the former one can also obtain image texture information. These two kinds of methods for volume measurement have good consistency except for Denghai 605. The study will provide theoretical basis for obtaining 3D data of plant organs at smaller scales.

Keywords: Maize grain · Three dimensional scanning · SmartScan
Micro-CT

1 Introduction

With the popularity of three-dimensional (3D) data acquisition technology and equipment, the measurement, analysis and 3D reconstruction of plant morphology based on 3D data have become a hotspot in plant science [1]. 3D plant modeling is the basis of digital plants [2, 3] and functional structural plant models (FSPMs) [4], and also an important part of crop phenotype studies [5]. Nowadays, the 3D morphological modeling of plant leaves, stems, ears and other organs have been studied [6–9]. However, there are few researches on small-scale plant organs such as grains. Grains, the most direct factors of yield, will indirectly affect the morphological structure of the plants.

Compared with the traditional data acquisition method, Smartscan and Micro-CT can all be used to obtain non-contact and high precision 3D data measurement. With scanning speed, high precision, all digital and detailed features can be obtained [10, 11]. Smartscan (white light stripes projection scanning) is a micro-projection technology (MPT). Thought high-precision optical measurement technology, scanners could measure the entire surface of the object. The accuracy of acquired point cloud

achieve sub-millimeter range, and the operation resolution are excellent [12]. At present the main application areas of MPT are quality control, reverse engineering and 3D modeling, especially works of art and archaeological research and digital archiving [13, 14]. Micro-CT (micro-computer tomography) is a non-contact 3D imaging technique that can clearly acquire the external configuration and internal micro structures of the sample without destroying itself. It has a great application value for micro-scale plant organs or plant tissue [15, 16].

To provide data and technical support for micro-scale plant visualization, choosing maize grain as an example, and compare two kinds of 3D morphological acquisition methods. The main results are include data acquisition efficiency, scanning precision, scanning effect, scanning scope, and scanning condition requirement.

2 Material and Method

2.1 3D Data Acquisition Devices

SmartScan^{3D}-5.0 color 3D scanner (AICON three-dimensional Systems GmbH, Braunschweig, Germany) is used as white light stripe projection 3D scanning, which mainly composed of host computer (high-end professional workstation), sensor (white-blue LED light source; two professional high resolution CCD digital camera in left and right) and a turntable which can be rotated by 180°, as shown in Fig. 1(a). For the small-scale plant organs, S-30 digital lens is selected for grains point cloud acquisition. Its measuring range is between 30–1500 mm and the accuracy is $\pm 7 \mu\text{m}$. The maize grains are scanned from six sides, as shown in Fig. 2. The data acquisition time is basically 0.5–1 h.

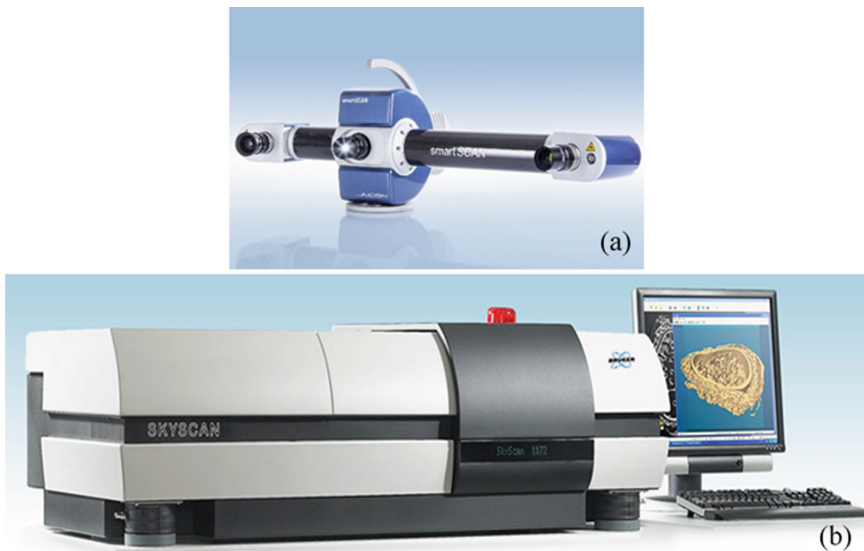


Fig. 1. Two kinds of 3D data acquisition devices

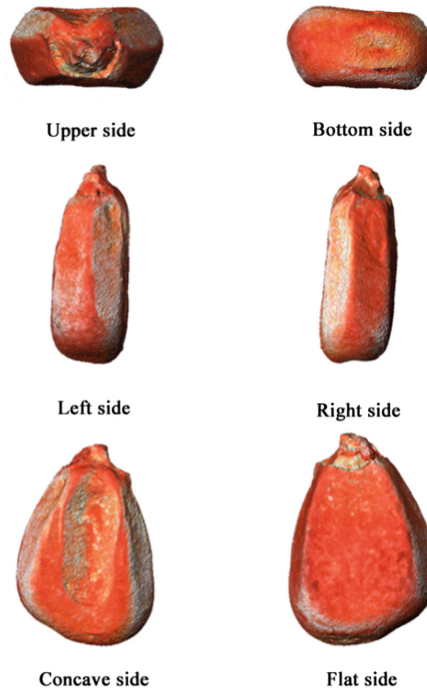


Fig. 2. Six point cloud side of grains in white scanner (Jingke665 as an example)

We select Bruker Micro-CT (SkyScan 1172) to acquire the 3D morphological data, which provide 40 kV/250 mA X-ray source and 1.3 megapixel CCD camera. The measuring range is between 27–50 mm, as shown in Fig. 1(b). When using Micro-CT to scan maize grains, the sample is placed in the equipment. It is necessary to adjust the pixel size and exposure time of the sample and X-ray source, in order to ensure the sample is in the middle of view field, so that the scanned 3D image is more accuracy. 3D structure of the splicing and volume calculation needs the support of the software CT Vox and CTAn.

2.2 Material

Dent grain (Yedan13, Liangyu99 and Denghai605) and semi-dent grain (Nongda108, Jingdan38 and Jingke665) are selected as different grain samples, as shown in Fig. 3. These selected maize cultivars are commonly used varieties with high stable yield and good quality. By using the two 3D data acquisition equipment, the 3D structural data of grains are obtained, and the advantages and disadvantages of the two methods will be compared.

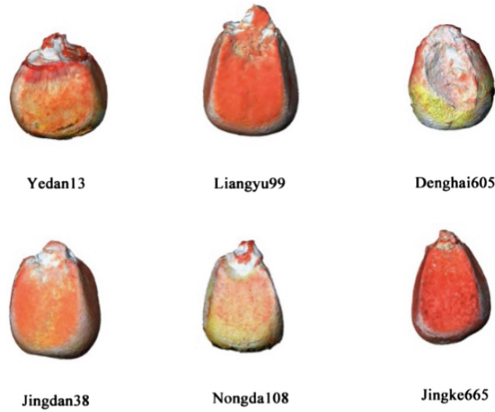


Fig. 3. Grains configuration of six maize varieties

3 Result and Discussion

The high quality 3D model is important for the measurement, simplification, and parameterization of control points and key trait of the sample. SmartScan and Micro-CT have their own adaptation scenarios and ranges. Therefore, these two 3D data acquisition equipment with respect to data acquisition efficiency, accuracy, scanning range, and post-processing are compared and analyzed.

3.1 Evaluation of Data Acquisition Efficiency, Accuracy, and Post-processing

Two kinds of 3D data acquisition methods have differences in data acquisition efficiency, scanning accuracy, scanning range and post-processing.

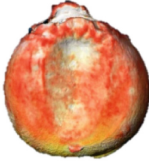



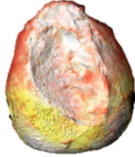



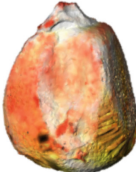



Data Acquisition Efficiency. SmartScan scanning process is longer than Micro-CT. The former need to scan every six sides of the surface, and search for same cloud points which between two adjacent scanning position. When using Micro-CT, it only need to put the grain into the device and set the relevant parameters, then the 3D structure of the grain can be directly output.

Scanning Accuracy. The comparison can be seen in Table 1, SmartScan for the external structure can achieve a better level and its accuracy is μm level. Micro-CT can detect the structure of the internal contents of the grain, the accuracy is higher than the SmartScan, which can also reach the μm level.

Scanning Range. SmartScan and Micro-CT are best suited for indoor environments, and the former one is more portable than the latter.

Post-processing. Unlike Smartscan, Micro-CT does not require multi-station scanning and splicing. The geometric model can directly generate. While Micro-CT also need to scan out the gray-scale and binarized 3D model can calculate the morphological parameters.

Table 1. Visualization result of grains scanned by Smartscan and Micro-CT

Grains type	Variety	Scan result	
		SmartScan	Micro-CT
Dent grains (<i>Zea mays L. indentata Sturt</i>)	Yedan13		
	Liangyu99		
	Denghai605		
Half-dent grains (<i>Zea mays L. semindentata Kulesh</i>)	Jingdan38		
	Nongda108		
	Jingke665		

3.2 Volume Measurement

For maize grains, the volume is one of the most important representations of external structure. The data obtained by two kinds of 3D data acquisition equipment need to further processing. The point cloud model constructed by SmartScan need use corresponding software (3D Reshaper or Geomagic Studio) to produce corresponding volume of closed geometric model. Micro-CT output grayscale 3D models need binarized, and Bruker's CTAn is used to calculate the volume and other parameters. Comparing the differences between two kinds of acquisition methods, and combining with the 3D visualization of the grid data (Table 1), it can more intuitively contrast the grains structural differences.

From the 3D data in Table 1 and Fig. 4, it can be seen that the two kinds of 3D data acquisition methods have no obvious difference in other varieties except for Denghai605, which show the application of two devices in grain structures. Denghai605 in the two methods has big difference may built on the 3D model of SmartScan which cannot fill a small hole, so that the geometric model is not closed, which makes the volume calculation becomes larger.

In summary, two methods can be used to obtain the external volume data, SmartScan effect is better than Micro-CT, the latter one can obtain internal embryo and endosperm and other related parameters, which is better than the acquisition of external volume data.

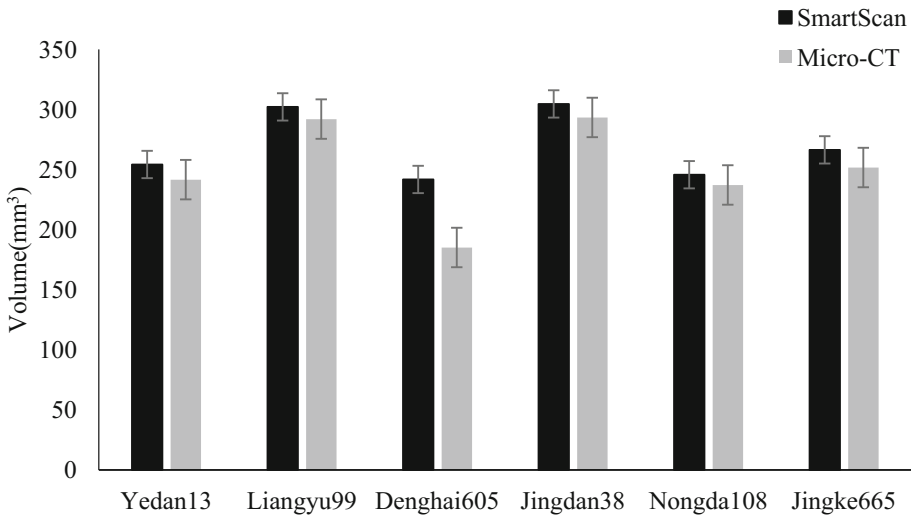


Fig. 4. Different grains volume comparisons

4 Conclusions

Through the above analysis and comparison, it is feasible to obtain 3D point cloud data of maize grains by using SmartScan and Micro-CT instruments. On the basis of the acquired morphological data, the evaluation of data acquisition efficiency, precision and post-processing have the following conclusions:

- (1) As SmartScan need scan different sides to find same cloud points for splicing, Micro-CT's advantage is more obvious than Smartscan.
- (2) Both SmartScan and Micro-CT can reach μm level with high accuracy and cloud promise the morphological details of grains. However, Micro-CT has no surface color texture.
- (3) With respect to scanning range, both can be used indoors, Micro-CT is as less portable as SmartScan.
- (4) For post-processing of scanning, SmartScan need to remove the background impurities and the merger of the simplified processing, but Micro-CT only need to remove the contents.
- (5) The two methods are less difference of volume calculation, but SmartScan have better effect than Micro-CT.

To summarize, two scanning way can be used for maize grains 3D morphological data acquisition. Micro-CT is better for analyzing the interior morphometrics of the grain and SmartScan is more suitable to acquire the 3D appearance of grains.

Acknowledgements. This work was supported by the National Natural Science Foundation of China (31601215), the Natural Science Foundation of Beijing Municipality (4162028), the Beijing Academy of Agricultural and Forestry Sciences Youth Research Fund (QNJJ201625), the Scientific and Technological Innovation Team of Beijing Academy of Agricultural and Forestry Sciences (JNKYT201604) and the National Technology Research and Development Program of China (2013AA102404-02).

References

1. Jonathon, A.G., Michael, P., Andrew, P.F., et al.: Approaches to three-dimensional reconstruction of plant shoot topology and geometry. *Funct. Plant Biol.* **44**(1), 62–75 (2017)
2. Zhao, C., Lu, S., Guo, X., et al.: Advances in digital plant research: three-dimensional digitization of plant morphology. *China Agric. Sci.* **48**(17), 3415–3428 (2015)
3. Zhao, C., Lu, S., Guo, X., et al.: Digital plant and its technical system. *China Agric. Sci.* **43**(10), 2023–2030 (2010)
4. Vos, J., Evers, J.B., Buck-Sorlin, G.H., et al.: Functional–structural plant modelling: a new versatile tool in crop science. *J. Exp. Bot.* **61**(8), 2101–2115 (2010)
5. Robert, T.F., Mark, T.: Phenomics–technologies to relieve the phenotyping bottleneck. *Trends Plant Sci.* **16**(12), 635–644 (2011)
6. Fang, H., Hu, L., He, R., et al.: Study on three-dimensional information collection method of plant. *Chin. J. Agric. Eng.* **28**(3), 142–147 (2012)
7. Xiao, B., Guo, X., Wang, J., et al.: Study on morphological modeling and mesh simplification of maize leaves. *J. Agric. Sci.* **40**(4), 693–697 (2007)

8. Wen, W., Guo, X., Lu, X., et al.: Construction of three-dimensional template resource library for maize. *J. Agric. Mech.* **47**(8), 266–272 (2016)
9. Fang, W., Feng, H., Yang, W., et al.: High-throughput volumetric reconstruction for three dimensional wheat plant architecture studies. *J. Innov. Opt. Health Sci.* **9**(05), 137–165 (2016)
10. Zhang, J., Li, Z., Zhang, N., et al.: Study on three-dimensional information acquisition and reconstruction of crops based on measured data. *J. Huazhong Agric. Univ.* **32**(4), 126–134 (2013)
11. Wei, X., Xiao, B., Guo, X., et al.: Application of three-dimensional laser scanning technology in plant scanning. *Chin. Agric. Sci. Bull.* **26**(20), 373–377 (2010)
12. Mara, H., Breuckmann, B., Lang-Auinger, C.: Multi-spectral high-resolution three-dimensional-acquisition for rapid archaeological documentation and analysis. In: 2009 17th European IEEE Signal Processing Conference, pp. 1205–1209 (2009)
13. Akca, D., Gruen, A., Breuckmann, B., et al.: High definition three-dimensional-scanning of arts objects and paintings. **2**, 50–58 (2007)
14. Bretzke, K., Conard, N.J.: Evaluating morphological variability in lithic assemblages using three-dimensional models of stone artifacts. *J. Archaeol. Sci.* **39**(12), 3741–3749 (2012)
15. Yang, W., Xu, X., Bi, K., et al.: Adaptive region of interest method for analytical micro-CT reconstruction. *J. X-ray Sci. Technol.* **19**(1), 23–33 (2011)
16. Du, J., Zhang, Y., Guo, X., et al.: Micron-scale phenotyping quantification and three-dimensional microstructure reconstruction of vascular bundles within maize stalks based on micro-CT scanning. *Funct. Plant Biol.* **44**(1), 10–22 (2017)



An Agricultural Habitat Information Acquisition and Remote Intelligent Decision System Based on the Internet of Things

Ze Lin Hu¹, Yi Gao^{2(✉)}, Miao Li¹, Hua Long Li¹, Xuan Jiang Yang¹,
and Zhi Run Ma¹

¹ Institute of Intelligent Machines, Chinese Academy of Sciences,
Hefei 230031, Anhui, China
zluhu@iim.ac.cn

² Yunnan Minority Language Working Committee,
Kunming 650499, Yunnan, China
498898209@qq.com

Abstract. On the basis of the information perception technology and mobile interconnection technology, through the technology of Agriculture Internet of Things, the multi-sensor system integration is realized, and the collaborative sensing of habitat information come true in crop production. This paper designs architecture of hardware and software for the system. By wireless multi-hop and seamless connection technologies of “triple net integration”, common interfaces and scanning technologies of multi-sensor standard signal transform are used to achieve the multi-parameter information acquisition of crop during its growth. Wireless monitoring nodes of the Agriculture Internet of Things are distributed in each measurement point of the farmland, and they are responsible for information collection, pretreatment, and wireless transmission of eight parameters data, including the environment temperature, environment temperature, Light intensity, Carbon dioxide content, soil temperature, soil humidity, soil pH, soil salt. The data processing and service system execute remote data storage and on-line information release. The intelligent decision support system achieve real-time warning of abnormal parameters. Experiments show that the architecture of the system is reasonable, and the system has good accuracy, stability and reliability, in line with the practical application of grassroots agricultural field.

Keywords: The Internet of Things · Intelligent decision
Agriculture habitat information · Information acquisition · ZigBee
ARM

Y. Gao—Funded projects: National Natural Science Foundation (No. 31371533), Anhui Science and Technology Research Program (No. 1604a0702017), National key research and development plan (No. 2017YFD0701603).

© IFIP International Federation for Information Processing 2019

Published by Springer Nature Switzerland AG 2019

D. Li and C. Zhao (Eds.): CCTA 2017, IFIP AICT 546, pp. 75–85, 2019.

https://doi.org/10.1007/978-3-030-06179-1_8

1 Introduction

In recent years, Chinese scholars have launched a broad and in-depth study for farmland environment monitoring. These studies mainly rely on 3S (GIS, RS, GPS) technology in a large range, and take the way of artificial ground survey in a small range. Surely these studies have made a lot of valuable research results. However, from the practical application, the farmland environmental information monitoring system that based on 3S technology has some questions of data imprecise, poor real-time and poor efficiency [1]. At present the network technology and wireless communication technology have been rapid development. Especially the development and maturity of ZigBee and GPRS/CDMA technology made up for the lack of abovementioned research, and to provide an effective way for improving China’s agricultural information monitoring system. Currently the data transmission technology which based on ZigBee and GPRS/CDMA has a number of typical applications in some related areas. However through integrating long-distance data collection with agricultural expert system for field data collection, processing data and sending messages to provide timely service to farmers, the related researches still needs to strengthen [2]. This paper

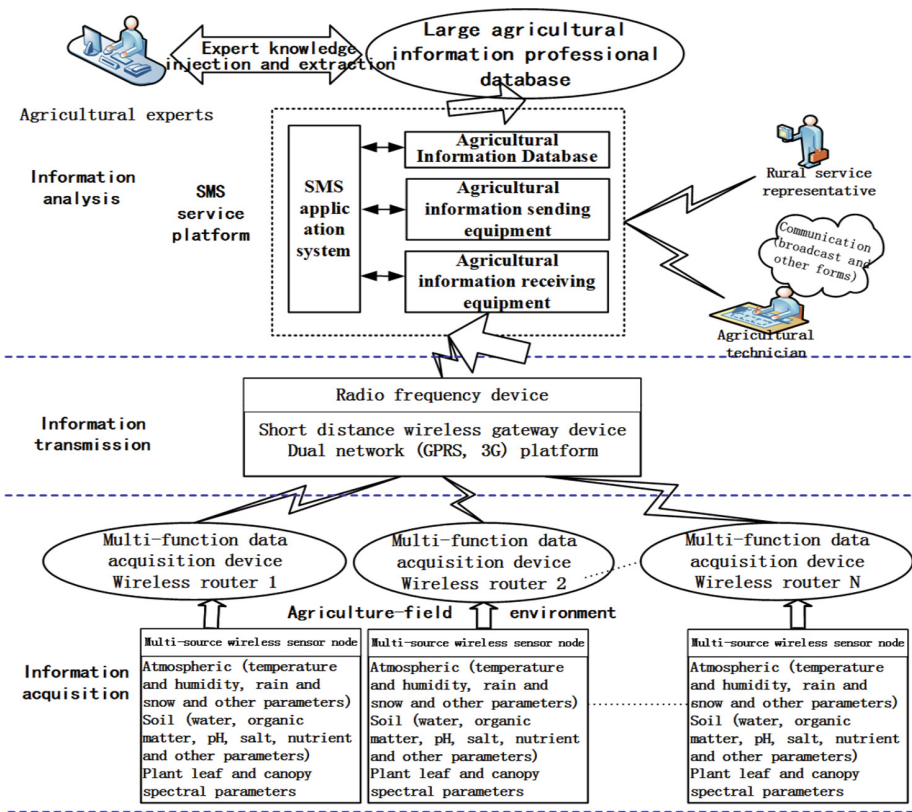


Fig. 1. The system architecture

has developed a wireless information monitoring field and timely service system which based on ZigBee and 4G technology, which can uniformly monitor and manage the environmental parameters (including environmental temperature and humidity, soil temperature and humidity, light, rainfall, soil pH) that distributed in farmland through the ZigBee wireless network, while can use the SMS to release production guidance information to the farmers at any time [3].

2 Design of Architecture of the System

The entire monitoring and service system consists of a monitoring host, a ZigBee network and an expert system. The ZigBee network consists of a ZigBee gateway node and a number of ZigBee sub-nodes that connect multiple external sensors. They form a wireless monitoring network. The ZigBee network sub-nodes collect the environmental parameters in the agricultural area through various sensors [4]. The collected data of environmental parameters are sent to the gateway node according to the ZigBee protocol through the wireless communication module of the terminal node. The gateway node will real-timely send the received information back to the server knowledge base system through the serial port, and give timely guidance according to the expert knowledge [5]. The whole system architecture is shown in Fig. 1.

3 Design and Implementation of System Function

3.1 Design of Hardware Structure of Sub-node

The sub-node hardware structure of Lower position machine is designed for multiple modular, and its structure is shown in Fig. 2. It mainly consists of the sensor module, data processing module, ZigBee communication module and power supply module [6].

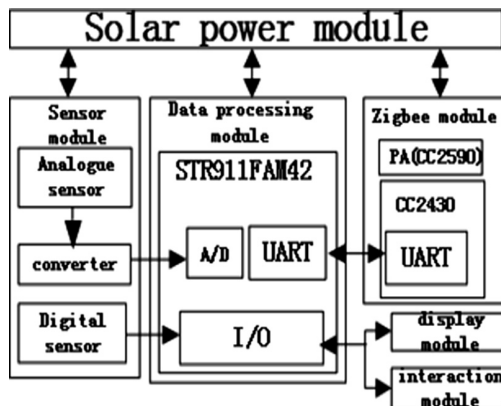


Fig. 2. Hardware structure of a sub-node

The data processing module is mainly composed of integrated A/D converter and the microprocessor that has a certain storage capacity. It is responsible for node network transaction management, data conversion and control of power supply of the external equipment. It combined the display module with keyboard module to achieve on-site data display and parameters setting [3]. The data acquisition module is composed of various sensors (environmental temperature and humidity, soil temperature and humidity, rainfall, light, soil pH and soil salinity). It is responsible for the quick and accurate collection of environmental information in the field. The wireless communication module is responsible for the data transmission and instruction transceiver among gateway nodes. The power management module is responsible for providing all of sub-nodes with the power in the entire network [7].

This paper selected a 32-bit low-power ARM11 microprocessor STR911FAM42 that the ST company developed as the core of data processing module. For other common low-end microcontrollers, it has richer resources and low power consumption, and can provide some processing capacity for future system function expansion [8]. In addition to the normal operating mode, it has also different levels of low-power operation mode, and is very suitable for low-energy farmland information monitoring applications in the field [9].

3.2 Design of Software Structure of Sub-node

The sub-node of lower position machine mainly realized the functions of sensor information acquisition, field data display and working parameter setting and ZigBee network communication. The AT commands are used to realize the communication between the data processing module and the ZigBee wireless communication module, which simplifies the communication process and ensures the versatility of the ZigBee wireless module. In order to reduce power consumption, here the following measures are taken: (1) When the sub-node is idle, the microprocessor is in sleep mode, when the RTC alarm and external interrupt come, it is in wake mode; (2) when the microprocessor acquires sensor data, through the I/O port The mouth control electronics relay is closed to supply power to the sensor, and the electronic relay is disconnected at other times [10]. The program flow of sub-node is shown in Fig. 3.

Compared with the assembly language, the C language is easy to develop, readable, good maintenance and other good characteristics, so the software program of sub-node is written in C language. In order to ensure the accuracy of the sensor data, using 4 Bytes to represent the data, in line with IEEE 754 floating point definition. The sub-node sends the data to the gateway node in the following format, where the leading byte includes the packet sequence number, the node ID, etc. The extended byte is used to extend the additional sensor data and the frame check bit [11] (Table 1).

Table 1. The sub-node sends the data to the gateway node.

Leading byte	Sensor 1#	...	Sensor 10#	Extended bytes
4 Bytes	4 Bytes	...	4 Bytes	4 Bytes

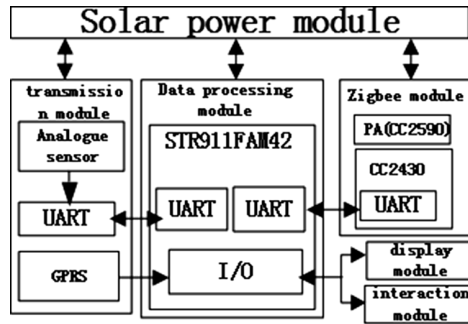


Fig. 3. Hardware structure of a gateway node

In the mountain farmland environment, due to changes in terrain, the wireless signal is easy to be interfered, resulting in data packet loss and error. Therefore, the sub-node software can reduce the data packet loss and bit error rate by increasing the number of data transmission and frame checking. At the same time, the software filtering technology is adopted to improve the accuracy of data acquisition [12].

3.3 Design of Hardware Structure of Gateway Node

The hardware structure of gateway node of the lower position machine realized modular design, the structure is shown in Fig. 3, mainly consisting of remote data transmission module, data processing module, ZigBee communication module and power supply module [13].

The data processing module is still using STR911FAM42 as the core unit, and responsible for the node network transaction management, data processing and control of external equipment such as power supply, and combined with the display module and keyboard module to achieve node information display and work parameter settings. The remote transmission terminal is responsible for the remote information Transmission, and collecting farmland environmental information quickly and accurately [14]. The ZigBee communication module is responsible for data transmission and instructions transceiver among sub-nodes. The power management module is responsible for providing energy to the entire gateway node [15].

3.4 Design of Gateway Node Software Structure

The software design of gateway node of the lower position machine mainly includes the network communication program that based on ZigBee protocol, the node information display, the information storage and forwarding program. The flow of main program is: the gateway node stores and integrates the data received from the sub-nodes, and encapsulates the data into the data frame according to the corresponding working parameters and the agreed code. Then they are sent to the industrial host through serial port 0, and keeps inquiring serial status until all the data is finished sending [16]. And then it is ready to receive the next packet. The gateway node main program flow is shown in Fig. 4.

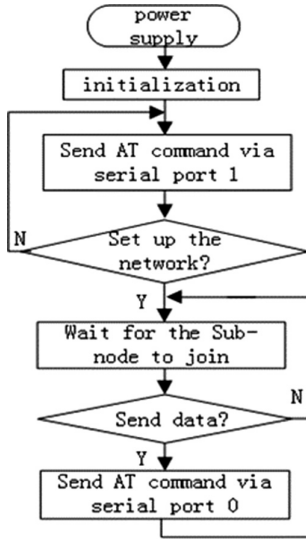


Fig. 4. Gateway node flow

4 Intelligent Decision Support Application System

Taking intelligent information processing as the core technology, the expert knowledge is integrated into the network service center to build a knowledge base. Through the technologies of multi-point automatic acquisition of the field farmland environmental data, wireless transmission based on public band, virtual online expert analysis and decision-making, and integration of remote real-time sensing data, the rapid diagnosis of farmland information and remote monitoring is realized. It actively push early warning and forecasting information. The real-time data collected by the system terminal are carried out data fusion and mining through the intelligent information processing module. Further the knowledge base system is integrated into the relevant pest forecast and fertilization decision-making module [17]. The decision-making results are submitted to the SMS service platform, and the real-time information is sent to the users. Through the GSM Modem (CM310) module and RS-485 computer communication interface, these are submitted to the WEB service system for network publishing [18]. At the same time, we use the methods of model calculation, knowledge reasoning and qualitative and quantitative ways to realize the comprehensive reasoning and decision based on production rules. Finally the real-time early warning information and intelligent decision-making of crops is achieved according to real-time data and processed data and rule base [19]. As shown in Figs. 5 and 6 below.

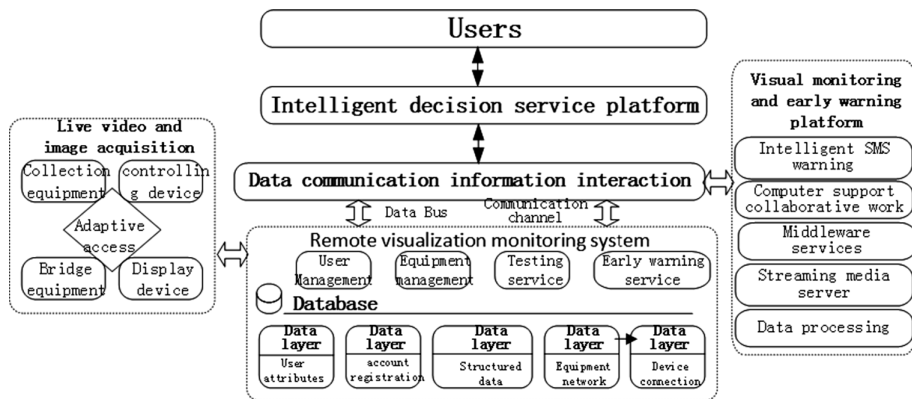


Fig. 5. Intelligent decision support service system structure

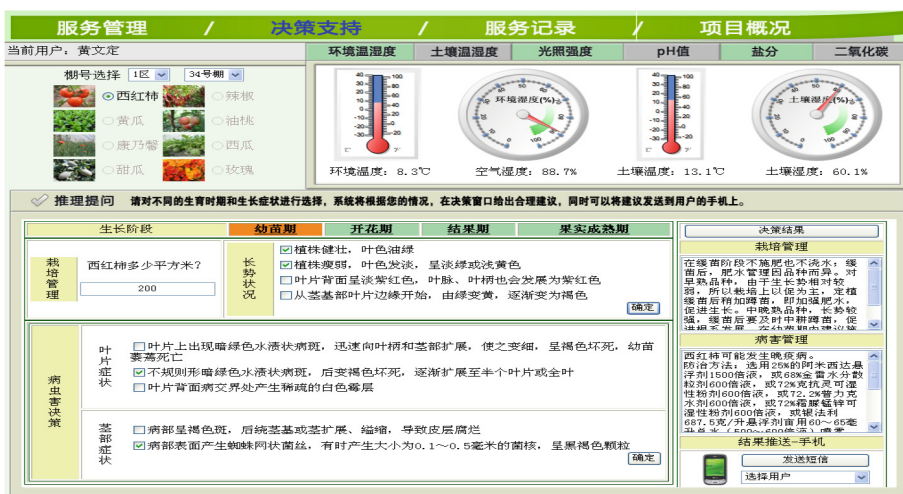


Fig. 6. Display interface of intelligent decision support service system

5 System Experiment and Analysis

In order to test the stability and reliability of the system, the environment temperature and humidity sensor, soil temperature and humidity sensor, light sensor and other sensors are connected with the terminal ZigBee node that installed in the field farmland monitoring point. the terminal nodes collect these sensing data, after the data are each finished to send, it will automatically enter the sleep mode, and recovery wake mode after receiving the acquisition command, and fulfill re-acquisition of data, continuous monitoring for a month. The gateway node displays the received data and uploads the received data, then transmitted to industrial control host through the serial port. The system display interface is shown in Fig. 7 below. The data curve is drawn as shown in Fig. 8.



Fig. 7. Display interface of the entire system

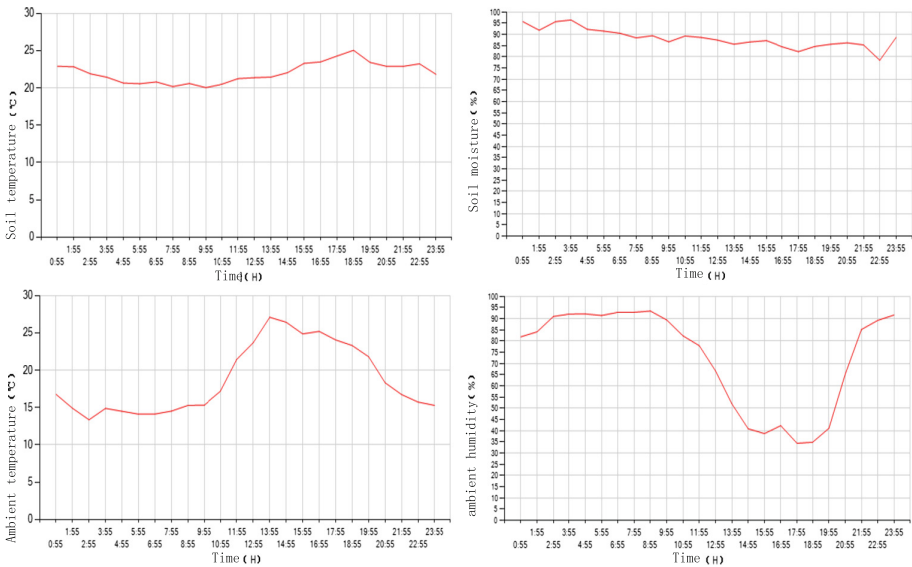


Fig. 8. Analysis of trends of crop habitat information

The experimental data show the terminal nodes have send the 24 groups data of the environmental temperature and humidity, soil temperature and humidity, light intensity and other sensors in a month of monitoring, and the gateway node has received all of sensing data in real time. The loss rate of data packet is zero, and the collected data are accurate and reliable. At the same time in application demonstration of the system, this paper also carried out testing wireless transmission distance of the data, the current system can achieve barrier-free network transmission distance of 800 m, point-to-point communication distance of about 2.5 km. Relatively the transmission distance of a common ZigBee transceiver module is 200 m. So the communication distance of our designed system is increased by about 10 times. So our system has achieved the desired effect.

The above experimental results show that the wireless sensor network based on ZigBee and ARM11 technology has good stability and reliability, and can provide real-time reliable and accurate on-line monitoring services for habitat parameters acquisition and precision agricultural production.

6 Conclusion

This paper briefly introduced the basic principle of the farmland information monitoring system based on ZigBee and ARM11 technology, as well as the development process of the system's hardware and software. The stability and reliability of the system is verified. The ZigBee and ARM11 technologies are applied to field farmland information transmission, and has greatly improved the reliability and real-time of the system [20]. The expansion and maintenance of the node is also very easy. It help improve the economic management of precision agricultural production [21].

Although the system needs to further improve in anti-interference, anti-fading, energy saving and network topology, the system's integration of a variety of wireless communication technologies is very good learning for the existing 3S-based economic farmland information monitoring system. With the growth of demand for economic farmland products, China's agricultural production needs to be further developed on the existing basis [22]. Future agricultural production requirements will strengthen integrated of a variety of information technologies. The advantages of integrated multi-system are played for the efficient management farmland production and providing accurate scientific basis [23].

References

1. Shi, K., Tang, M., Wang, Z.: Research of Heterogeneous Network Protocol Data Fusion in Smart Home Control System Based on Spatial Outlier. In: IEEE Conference Publications, vol. 179, pp. 851–856 (2014)
2. Liu, D., Cao, X., Huang, C.: Intelligent agriculture greenhouse environment monitoring system based on IOT technology. In: Unan University, Research, Institute New Energy & Energy Saving & Emiss Reduction, Changsha University of Science & Technology, Communication, Research Institute. LNCS, vol. 4128, pp. 487–4908 (2015)

3. Yu, G., Wang, W., Xie, J.: Information acquisition and expert decision system. in litchi orchard based on internet of things. *Trans. Chin. Soc. Agric. Eng.* **32**, 144–152 (2016)
4. Qi, J., Liu, G.-P.: Design and implementation of a new wireless sensor network node. In: *IEEE Conference Publications*, vol. 50, pp. 144–152 (2017)
5. Song, X., Gao, J., Ma, J., Niu, S., He, H.: HTME: a data streams processing strategy based on Hoeffding tree in MapReduce environment. In: *IEEE Conference Publications*, vol. 66, pp. 1042–1045 (2016)
6. Xu, Z.: HTME: Design and implementation of intelligent gateway for smart home. In: *IEEE Conference Publications*, vol. 36, pp. 4713–4718 (2016)
7. Sung, T.-W., Lin, F.-T.: A 2-phase scheme for decreasing orphan devices in ZigBee networks. In: *IEEE Conference Publications*, vol. 12, pp. 1–2 (2016)
8. Jiang, J., Gao, Z., Shen, H., Wang, C.: Research on the fire warning program of cotton warehousing based on IoT technology. In: *IEEE Conference Publications*, vol. 96, pp. 1–4 (2015)
9. Wang, W., Xie, J., Lu, H., Lin, J., Mo, H.: Information acquisition and expert decision system in litchi orchard based on internet of things. *Nongye Gongcheng Xuebao/Trans. Chin. Soc. Agric. Eng.* **32**(20), 144–152 (2016)
10. Yu, J., Zhang, W.: Study on agricultural condition monitoring and diagnosing of integrated platform based on the internet of things. In: Li, D., Chen, Y. (eds.) *CCTA 2012. IAICT*, vol. 392, pp. 244–250. Springer, Heidelberg (2013). https://doi.org/10.1007/978-3-642-36124-1_30
11. Yuan, Z., Gu, C., Yang, F.: Research on intelligent agricultural machinery control platform based on multi-discipline technology integration. *Nongye Gongcheng Xuebao/Trans. Chin. Soc. Agric. Eng.* **33**, 1–11 (2017)
12. Tian, Y., Zheng, B., Li, Z.: Agricultural greenhouse environment monitoring system based on Internet of Things. In: *2017 3rd IEEE International Conference on Computer and Communications (ICCC)*, pp. 2981–2985 (2017)
13. Deb, S., Paul, S., Das, S., Saha, S., Das, C., Das, P.: Physical remote agent with integrated data acquisition elements (PRIDE)-An IOT based secluded machine interaction. In: *2017 International Conference on Computing, Communication and Automation (ICCCA)*, pp. 1301–1305 (2017)
14. Zou, C.-J.: Research and implementation of agricultural environment monitoring based on Internet of Things. In: *2014 Fifth International Conference on Intelligent Systems Design and Engineering Applications*, pp. 748–752 (2017)
15. Du, J., Guo, J., Xu, D., Huang, Q.: A remote monitoring system of temperature and humidity based on OneNet cloud service platform. In: *2017 IEEE Electrical Design of Advanced Packaging and Systems Symposium (EDAPS)*, pp. 1–3 (2017)
16. Abraham, S., Shahbazian, A., Dao, K., Tran, H., Thompson, P.: An Internet of Things (IoT)-based aquaponics facility. In: *2017 IEEE Global Humanitarian Technology Conference (GHTC)*, pp. 1–2 (2017)
17. Wu, Q., Liang, Y., Li, Y., Liang, Y.: Research on intelligent acquisition of smart agricultural big data. In: *2017 25th International Conference on Geoinformatics*, pp. 1–7 (2017)
18. Maiti, P., Sahoo, B., Turuk, A.K., Satpathy, S.: Sensors data collection architecture in the Internet of Mobile Things as a service (IoMTaaS) platform. In: *2017 International Conference on I-SMAC (IoT in Social, Mobile, Analytics and Cloud) (I-SMAC)*, pp. 1–2 (2017)
19. Suakanto, S., Engel, V.J.L., Hutagalung, M., Angela, D.: Sensor networks data acquisition and task management for decision support of smart farming. In: *2016 International Conference on Information Technology Systems and Innovation (ICITSI)*, pp. 1–5 (2016)

20. Rajeswari, S., Suthendran, K., Rajakumar, K.: A smart agricultural model by integrating IoT, mobile and cloud-based big data analytics. In: 2017 International Conference on Intelligent Computing and Control (I2C2), pp. 1–5 (2017)
21. Mekala, M.S., Viswanathan, P.: A novel technology for smart agriculture based on IoT with cloud computing. In: 2017 International Conference on I-SMAC (IoT in Social, Mobile, Analytics and Cloud) (I-SMAC), pp. 75–82 (2017)
22. Patil, K.A., Kale, N.R.: A model for smart agriculture using IoT. In: 2016 International Conference on Global Trends in Signal Processing, Information Computing and Communication (ICGTSPICC), pp. 543–545 (2016)
23. Ping, L.: Agricultural Drought Data Acquisition and Transmission System Based on Internet of Things. In: 2014 Fifth International Conference on Intelligent Systems Design and Engineering Applications, pp. 128–132 (2016)



Comprehensive Evaluation of Soil Fertility in Yanzhou District Based on Principal Component Analysis

Qiuting Zhang^{1,2} and Xia Geng^{1,2} (✉)

¹ College of Information Science and Engineering,
Shandong Agricultural University, Tai'an, Shandong, China
Zhang_qiuting@163.com, gx@sda.u.edu.cn

² National Engineering Research Center for Information Technology
in Agriculture, Beijing, China

Abstract. Soil fertility is the basis of sustainable agricultural development. Scientific and rational evaluation of soil fertility can better promote the development of agricultural informatization and modernization. Based on the data of 166 soil samples in Yanzhou District in 2014, the effects of pH, OM, AN, AP and AK were chosen as evaluation indexes, SPSS was used to analyze the soil fertility status. The results showed that the overall level of soil fertility was below the medium: Among the 166 samples, there were 149 in the medium and low fertility, accounting for 89.76%. The content of soil OM and AN was in medium and slightly lower level. In view of the above results, organic fertilizer, humic acid and nitrogen fertilizer should be added. Soil AP and AK content was in the middle and above the level, so the fertilizer could be maintained in order to achieve balanced fertilization.

Keywords: Principal component analysis · Yanzhou district
Comprehensive evaluation · Soil fertility

1 Introduction

Comprehensive evaluation of soil fertility, can not only balance the fertilization but also improve the utilization efficiency of water and fertilizer of cultivated land. It can also improve the field management and provide a theoretical basis for the precise management of soil nutrients and rational use of soil resources. Moreover, it can minimize harm to the environment so it is of great significance for the protection of agricultural ecological environment and for the sustainable development of agriculture [1–3]. In recent years, more and more scholars have applied mathematical statistics to the quantitative study of soil fertility: Cluster analysis [4–6], factor analysis [7–9], and principal component analysis [10–12] have been widely used in soil fertility evaluation. There are many indexes affecting soil fertility, and they have certain correlation that may lead to overlap of information in the index. However, the principal component analysis method can overcome the correlation and overlap and use fewer indexes to replace the original more indexes. Meanwhile, the method can give an objective weighting based on the relative importance among the indicators, so as to avoid the

subjective influence of the comprehensive evaluator. Now, the principal component analysis method has been widely used more and more. Therefore, this paper carried a comprehensive evaluation of soil fertility in Yanzhou district by principal component analysis based on the previous studies and selected three categories indexes that can be measurable, such as soil nutrition index, soil biology index and soil environment index, specifically selected available nitrogen (AN), available phosphorus (AP), available potassium (AK), organic matter (OM) and pH to realize the comprehensive and quantitative evaluation of soil fertility.

2 General Situation of Study Region

Yanzhou District is located in the northeastern part of Jining City, Shandong Province, and located between northern latitude $35^{\circ}23'31''$ and $35^{\circ}43'17''$ and between east longitude $116^{\circ}35'21''$ and $116^{\circ}53'36''$ east in longitude. The total land area is 534.82 km^2 and the basic farmland area is 2.8110 million hectares. The cultivated land area is 3.1769 million hectares, accounting for 59.40% of the total land area of the district. Yanzhou administers 4 subdistricts and 6 towns. The climate is warm temperate East Asian continental monsoon climate. The annual average temperature is 14.1°C , the average annual precipitation is 681 mm and the annual total sunshine are 2635.0 h. There are 177 days in a year without frost. It is located in piedmont plain where belongs to the middle mountainous region of Taiyi mountain's southwest of Shandong Province. Plain area is 64670 hectares, accounting for 99.7% of the total area. Soil types are divided into cinnamon soil, fluvo-aquic soil, lime concretion black soil 3 categories, 5 sub-categories, 7 soil genus, 30 soil species. Among them, fluvo aquic soil is the main soil type, accounting for 76.24% of the total cultivated land area, 18.69% of sandy black soil and 5.07% of fluvo aquic soil.

3 Research Method

3.1 Determination of Study Scope

Xinyan town ranked first for the comprehensive economic strength among all towns of Jining City, Xiaomeng town is an important grain production base, and has the reputation of "Northwest granary" in Yanzhou, Caohe town is located in the northernmost of Yanzhou District and Da'an town is a national ecological town and is a national key town. These four towns are all located around the urban district of Yanzhou and they are concentrated in population and agricultural activities, so the four towns are used as sampling areas.

3.2 Sample Analysis

The data comes from the results of the plowed layers soil sampling in 2014. There are 166 sampling sites in Yanzhou District. According to the land use type and applicable conditions, the surface soil samples of 0–20 cm depth were collected around the survey

sites by GPS positioning technology, and the soil samples which were equivalent to more than 3 kg of dry soil were retained. The collected soil samples were brought back to the laboratory and dried, ground and sieved in a cool ventilated place and then keep it for later use. Analysis method is based on the Agricultural Technology Extension Service Center of the Ministry of agriculture compiled “The investigation and quality evaluation of cultivated land productivity”. Soil pH was measured by potentiometry, OM was measured by potassium dichromate oxidation-external heating method, AN was measured by alkaline hydrolysis diffusion method, AP was measured by sodium bicarbonate extraction Mo-Sb colorimetry and AK was measured by ammonium acetate flame photometric method.

4 Data Processing and Analysis

4.1 Data Processing

Traditional (General) Statistical Analysis. The soil nutrient contents of 166 soil samples were statistically analyzed by SPSS.

Principal Component Analysis. Standardize the raw data, establish the correlation coefficient matrix of the index, find the characteristic roots and eigenvectors of the correlation coefficient matrix, determine the number of principal components by the cumulative variance contribution rate, find the principal component.

4.2 Traditional Statistical Analysis of Soil Fertility

166 soil sample data which collected from Yanzhou District, Jining City, Shandong province were analyzed by using the SPSS statistical analysis software. (shown in Table 1). The soil pH content was 6.800–7.200, the average was 7. The OM content of 6.142–24.759 g/kg, the average was 14.980 g/kg. AP and AK value were 9.850–92.025 mg/kg and 37.466–270.908 mg/kg, the average was 30.044 mg/kg and 118.584 mg/kg respectively. The content of AN was 35–238 mg/kg, and the mean value was 84.467 mg/kg.

Table 1. Traditional statistical data of soil nutrients in YanZhou district

Indexes	Maximum	Minimum	Average	Standard deviation	Coefficient of variation	Skewness	Peak value	Median
OM g/kg	24.759	6.142	14.980	2.983	19.916	0.114	0.928	15.081
pH	7.200	6.800	7.007	0.141	2.019	-0.106	-1.344	7.000
AN mg/kg	238.000	35.000	84.467	27.303	32.324	1.753	6.801	84.000
AP mg/kg	92.025	9.850	30.044	16.659	55.450	1.391	2.033	26.563
AK mg/kg	270.908	37.466	118.584	37.441	31.573	1.205	3.201	118.162

The description of the 166 soil nutrients (Table 1) showed that the spatial distribution of soil nutrients in the sample area is not uniform. The distribution of AK in all indicators had tremendous difference, the maximum value was 7.03 times of the minimum value. The distribution of the remaining nutrients was as follows: AN > AP > OM > pH, AN: 203.000 mg/kg, AP 82.175 mg/kg, OM 18.616 g/kg, pH 0.400. The dispersion degree of soil spatial variability is usually expressed as the standard deviation or relative standard deviation (coefficient of variation) of a series of measurements. It is often considered that when the coefficient of variation less than or equal to 10% is weak variability, when the coefficient of variation more than 10% and less than 100% is moderate variability, when the coefficient of variation more than or equal to 100% is strong variability. Results showed that the spatial variability of soil nutrients follows the order of AP AN AK OM pH. Except for the weak variation of pH in soil nutrients, all of them were between 10% and 100%, which were moderately variable. The coefficient of variation showed biggest variations of soil nutrients was AP. The maximum value of AP was 9.3 times of the minimum value. And the variation degree of pH was the smallest in totally five indicators. Therefore, the spatial distribution of soil nutrients in Yanzhou district was uneven.

Based on the grading standards of the second national soil survey grading standards (national soil survey office, 1992), the contents of OM and AN in Yanzhou district were below the medium level (up to level four), the content of AP was rich (more than 20 mg/kg, up to level two), high potassium content (more than 100 mg/kg, up to level three). Soil organic matter, an important source of soil elements, especially nitrogen and phosphorus, has the capacity of improving soil retention of water and fertilizer and raising soil buffer capacity. Generally speaking, the amount of soil organic matter is an important indicator of soil fertility. On the basis of the analysis of the data, it can be seen that the content of soil organic matter in Yanzhou district is medium and slightly lower. Therefore, organic fertilizer and humic acid should be added. Nitrogen fertilizer should be applied in nitrogen deficient soil to promoting growth and development of crop. The content of available phosphorus and available potassium in the soil was in the middle and above level, so the fertilization amount can be maintained to achieve the balanced fertilization.

4.3 Principal Component Analysis

Principal component analysis should first standardize the original data, and then establish the correlation coefficient matrix of variables. The correlation coefficient matrix was shown in Table 2.

Table 2. Correlation coefficient matrix

Indexes	Correlation	pH	OM	AN	AP	AK
pH	Pearson	1.000	0.132	0.088	0.082	0.089
OM	Pearson		1.000	0.064	0.105	0.386**
AN	Pearson			1.000	0.007	0.128
AP	Pearson				1.000	0.051
AK	Pearson					1.000

** correlation is significant at the 0.01 level (2-tailed)

Initial factor load matrix showed that (Table 3), organic matter and available potassium had a greater positive load on the first principal component, indicating that organic matter and available potassium content were the most important factors affecting soil fertility. Available phosphorus has a greater positive load on the second principal component, indicating that available phosphorus is also an important factor affecting soil fertility.

Table 3. Initial factor load matrix and eigenvector

Indexes	Principal component		Eigenvector	
	1	2	A1	A2
pH	0.42	0.29	0.34	0.29
OM	0.76	-0.03	0.62	-0.03
AN	0.35	-0.44	0.28	-0.44
AP	0.30	0.82	0.24	0.81
AK	0.75	-0.25	0.60	-0.25

4.3.1 Extract Principal Component

The standardized data were analyzed by principal component analysis. According to the principle that the eigenvalue is greater than 1, two principal components are selected. The contribution of first principal component to soil fertility was 30.5%. The cumulative variance contribution rate of the first 2 components reached 50.6%. Due to it reflected the original 5 fertility elements of the majority of the information, it is reliable to use principal component analysis to study the soil fertility in Yanzhou district (Table 4).

Table 4. Eigenvalue and variance contribution rate table

Total variance explained						
Component	Initial eigenvalues			Extraction sums of squared loadings		
	Total	% of variance	Cumulative %	Total	% of variance	Cumulative%
1	1.523	30.462	30.462	1.523	30.462	30.462
2	1.005	20.107	50.569	1.005	20.107	50.569
3	0.984	19.678	70.247			
4	0.885	17.704	87.951			
5	0.602	12.049	100.000			

4.3.2 Principal Component Score and Comprehensive Score

Finally, factor scores were calculated. The variance contribution rate of each factor accounted for the proportion of the total variance contribution rate of two factors were used as weights to obtain a composite score.

$$F_1 = 0.34 * X_1 + 0.62 * X_2 + 0.28 * X_3 + 0.24 * X_4 + 0.60 * X_5 \quad (1)$$

$$F_2 = 0.29 * X_1 - 0.03 * X_2 - 0.44 * X_3 + 0.81 * X_4 - 0.25 * X_5 \quad (2)$$

$$F = 0.305 * F_1 + 0.201 * F_2 \quad (3)$$

Among them, X_1 represents pH, X_2 represents OM, X_3 represents AN, X_4 represents AP and X_5 represents AK.

The results showed that the comprehensive scoring range was between -1.99 and 3.64 . According to the range of comprehensive score, the soil fertility was divided into the following 3 grades (Table 5): high fertility type ($F \geq 1$), medium fertility type ($0 < F < 1$), low fertility type ($F \leq 0$). Among the 166 valid data, the number of samples in high fertility group was 17, accounting for only 10.24%. The number of samples in low fertility group was 84, accounting for 50.60%. The sample of medium fertility group was 65, and the proportion was 39.16% by principal component analysis. Xinyan Town, Da'an Town and Xiaomeng Town's low fertility type accounted

Table 5. Sample number and proportion of fertility level

Fertility level	Town's name	Sample number	Sample size	Proportion %
Low fertility type ($F \leq 0$)	Xinyan town	16 17 21 22 23 25 26 27 31 32 34 35 36 37 40 41 44 46 47 48 50 51 56 57 58 59 60 63 64 66 67 68	32	19.28
	Da'an town	1 3 5 7 69 70 72 73 74 75 76 79 80 81 83 85 87 89 91 92 95	21	12.65
	Caohe town	10 11 12 101 103 104 108 113 114 123 114 125	12	7.23
	Xiaomeng town	14 128 129 130 133 134 135 136 137 138 140 141 142 143 151 152 153 163 164	19	11.45
Medium fertility type ($0 < F < 1$)	Xinyan town	18 19 20 24 28 29 30 33 38 42 43 45 49 52 53 55 61 62 65	19	11.45
	Da'an town	2 4 6 8 71 77 78 84 88 90 93 94 96 97	14	8.43
	Caohe town	9 99 100 102 106 107 109 110 111 112 115 116 118 119 120 121 126 127	18	10.84
	Xiaomeng town	13 15 131 144 147 149 155 156 158 159 160 162 166	14	8.43
High fertility type ($F \geq 1$)	Xinyan town	39 54	2	1.20
	Da'an town	82 86 98	3	1.81
	Caohe town	105 117 122	3	1.81
	Xiaomeng town	132 145 146 148 150 154 157 161 165	9	5.42

for the highest proportion. There were 32 low fertility types in 53 samples of Xinyan Town, accounting for 60.38%. There were 21 low fertility types in 38 samples of Daan Town, accounting for 55.26%. There were 19 low fertility types in 42 samples, accounting for 45.24%. This showed that the three towns had lower soil fertility. The highest proportion of Caohe town was the middle fertility type. There were 18 medium fertility types in 33 samples, accounting for 55.26%, more than half, so the soil fertility of Caohe town belonged to medium level.

5 Conclusion and Discussion

The spatial distribution of soil nutrient in Yanzhou district was uneven. Results showed that the spatial variability of soil nutrients follow the order of AK AN AK OM pH. According to the variation degree of soil nutrient, OM accounted for 19.916%, AN accounted for 32.324%, AP accounted for 55.450%, AK accounted for 31.573%. Therefore OM and AN and AP and AK belonged to moderate variability. While pH accounted for 2.019%, belonged to weak variability.

The soil OM and AN of cultivated land in Yanzhou district was medium and slightly lower. Therefore, the organic fertilizer, humic acid and nitrogen fertilizer should be added. The contents of AP and AK in soil were in the middle or higher level, and the amount of fertilizer remained unchanged, so as to achieve balanced fertilization.

The soil fertility level in Yanzhou district was lower than the medium. According to the principal component analysis, the sample number of medium fertility type was 149, accounting for 89.76% in total 166 samples. Meanwhile the soil samples with high fertility level were 17 and only accounting for 10.24%.

In the three types, the proportion of low fertility type was highest in Xinyan town, Da'an town and Xiaomeng town, which was 60.38%, 55.26%, 45.24% respectively, showing that the soil fertility of these towns were relatively low; in Caohe town town, medium fertility type accounted for the greatest proportion, the number of which was 18 samples, accounting for 55.26% in total 33 samples, therefore the soil fertility of Caohe town belonged to the middle level.

Acknowledgment. This work was supported by the open research project of the National Engineering Research Center for Information Technology in Agriculture (KF2014W51-059).

References

1. Luo, D.Q., Bai, J., Xie, D.T.: Research on evaluation norm and method of soil fertility. *J. Soil Environ. Sci.* **11**(2), 202–205 (2002)
2. Wang, Z.L.: Study on comprehensive evaluation and spatial variability of soil fertility on Sanjiang plain. Northeast Agricultural University (2008)
3. Huang, A., Yang, L.A., Du, T., Wang, L.A., Zhang, B., Yuan, G.: Comprehensive assessment of soil nutrients based on PCA. *J. Arid Zone Res.* **31**(5), 819–825 (2014)
4. Wen, Y.C., et al.: Comprehensive assessment methodology of characteristics of soil fertility under different fertilization regimes in North China. *J. Trans. Chin. Soc. Agric. Eng.* **31**(7), 91–99 (2015)

5. Zhu, Y.L.: Studies on temporal and spatial variability of the major soil fertility in Hebei Province. Agricultural University of Hebei (2014)
6. Chen, L.M., et al.: Evaluation on soil fertility quality of newly cultivated light sierozem under different fertilization with methods of principal component and cluster analyses. *J. Soils* **40**(6), 971–975 (2008)
7. Duan, B.T., et al.: Integrated evaluation of soil fertility based on factor analysis. *J. Modern Agric. Sci. Technol.* **7**, 228–230 (2016)
8. Tan, X.M., Geng, Y.H., Jiang, X.B., Zhou, Y.Q.: Evaluation of soil fertility of different vegetation types in Ruxi River valley based on factor analysis. *J. Acta Agric. Jiangxi* **26**(5), 14–18 (2014)
9. Cao, W.P., Wu, F.Q., Lei, J.Y., Zhao, L.S., Yu, X.L.: Evaluation of soil fertility quality in different tillage treatments based on factor analysis—a case of the southern edge of the Mu Su desert. *J. Northwest A F Univ. (Nat. Sci. Ed.)* **39**(1), 159–165 (2011)
10. Zhang, Y.G., Shi, Y.J., Wu, Z.B.: Assessment on soil fertility status of jujube orchards based on principal component analysis. *J. Southwest China J. Agric. Sci.* **29**(5), 1156–1160 (2016)
11. Zhang, L.: Soil Fertility Evaluation & Improvement Measures of Walnut Orchards in Wushi County. Xinjiang Agriculture University, Xinjiang (2015)
12. Li, P., Wang, P., Dai, W., Wang, D., Deng, Z.F., Zhao, C.: Evaluation of soil fertility in subtropical forests. *J. Beijing For. Univ.* **32**(3), 52–58 (2010)



Advances in Monitoring Soil Nutrients by Near Infrared Spectroscopy

Yan Wang^{1(✉)}, Bei Cui², Yanhua Zhou¹, and Xiudong Sun¹

¹ Shanghai Vocational College of Agriculture and Forestry, Shanghai, China
14432@shafc.edu.cn

² Institute of Remote Sensing and Digital Earth, Chinese Academy of Sciences,
Sanya, China
cuibei@radi.ac.cn

Abstract. Soil nutrients play an important role in crop growth, and traditional monitoring methods are still the first choice for high precision measurement. However, it is necessary to have a quicker and simpler way to improve the efficiency of soil nutrient monitoring because of its long monitoring time, pollution and high labor cost. Near infrared spectroscopy has become the focus of its research because of its rapid and pollution-free advantages. At present, using near infrared spectroscopy to distinguish soil types, soil heavy metal pollution technology has become increasingly mature, but the soil nutrients, such as monitoring of soil organic matter, available phosphorus, available potassium, available nitrogen is still in the research stage. This paper reviews the recent research results of soil nutrients in near infrared spectrum monitoring technology based on collation, summary and key technology of common data processing method, and analysis the advantages and disadvantages of different detection methods for soil nutrient direction of near infrared spectroscopy technology put forward suggestions to further research.

Keywords: Near infrared spectroscopy · Soil nutrients

1 Introduction

Soil nutrients mainly refer to the contents of organic matter, available phosphorus, available potassium and available nitrogen in soil. Soil nutrients can provide nutrients needed for crop growth, but also constitute an important component of soil structure and determine soil physical and chemical properties. It is important for crop growth. Soil nutrient content directly influences crop yield, and it is also an important index to guide fertilization decision-making.

Traditional soil nutrient determination was completed in the laboratory by chemical reagents. Poor timeliness, high labor costs, easy to cause pollution. How to rapidly and efficiently determine soil nutrients is an urgent problem to be solved in the development of precision agriculture (precision agriculture, PA). Near infrared spectroscopy (Near Infrared Spectrometry, NIR) is an important component of remote sensing technology, and its advantages of nondestructive and rapid detection have become the focus of research. Different soil texture, water storage capacity and soil particle size make it

possible to detect soil nutrient content by near infrared spectroscopy. At present, the technology of near infrared spectroscopy to distinguish soil types and soil heavy metals pollution is becoming more and more mature. But the application of some soil nutrients content is not yet mature. In this paper, the application of near infrared spectroscopy in soil nutrient testing was analyzed, in order to promote the application of NIR in soil nutrient testing and improve the speed and efficiency of PA development.

2 Recent Research Status of in Monitoring Soil Nutrients by Near Infrared Spectroscopy

Soil indicators closely related to crop growth include organic matter, available phosphorus, available potassium and available nitrogen. The detection of soil nutrient indexes will help to understand the overall situation of soil, guide the rational allocation of land resources in the field, and make fertilization decisions and predict the quality and output of agricultural products. The research of rapid and efficient soil nutrient detection technology is the focus of recent research. NIR has become the research focus of soil nutrient detection technology because of its nondestructive, rapid and other advantages.

Soil organic matter refers to organic matter containing carbon in soil, including residues of various animals and plants, microorganisms and organic matter (Dou 2010), which are decomposed and synthesized. Soil organic matter plays an important role in soil formation and soil fertility. The contents of available phosphorus, available potassium and available nitrogen in soil reflect the storage and supply ability of nutrients in soil to a certain extent.

The study of soil organic matter content by NIR began in the middle of the 1980s. In recent years, there are many achievements, and the soil organic matter sensitive bands, detection methods and models are also gradually deepened. The research of near infrared spectroscopy in China started late. In recent years, many scholars have made great efforts to explore the methods of detecting soil nutrients by near infrared spectroscopy.

Gao and Lu (2011) using FOSSXDS Near Infrared Spectroscopy Analyzer in 85 soil samples collected from northeast spectra, the correlation coefficient spectrum and successive projection algorithm for near infrared spectral analysis of the soil, and excellent characteristics of wavelength of total nitrogen and organic matter were selected. A high signal-to-noise ratio near infrared spectroscopy system based on the characteristic wavelength was developed, and the near infrared spectra and measurement results of soil samples were analyzed. The system can effectively measure total nitrogen and organic matter content in soil nutrients.

Zhang et al. (2012) the 5 main types of soil in the research China in central and eastern regions as the research object, various pretreatment methods combined treatment, combined with partial least squares (PLS) calibration model for each spectral region. The results show that the near infrared spectrum can be used to estimate soil total nitrogen, and a better prediction result can be obtained by using the frequency band ($4000\text{--}5500\text{ cm}^{-1}$) as the modeling area.

Li et al. (2012) in 72 soil samples collected from the Beijing suburb of an experimental field as test materials, the application of Fu Liye transform near infrared spectroscopy analysis of total nitrogen, soil total potassium, organic matter, nutrient content and pH value. By using partial least squares (PLS) on the measured data of soil nutrient and spectral values using regression analysis to establish prediction model, the results show that the established method of partial least squares regression model can accurately predict the nutrient in Beijing cinnamon soil total nitrogen and organic matter, total potassium and pH value of 4 was predicted based on nutrient.

Song et al. (2012) by orthogonal signal correction (OSC) method can be correlated with the concentration profiles of the advantage of picture information, the corrected information mapping and partial least squares (PLS) method combined by near infrared spectroscopy of different soil texture, soil, clay loam sand: discriminant analysis.

Liu and Zhang (2013) using visible/short wave near infrared spectroscopy (Vis/SW-NIR) analysis to measure soil available nitrogen (N) and available potassium (K). The application of genetic algorithm in soil nutrient analysis is discussed. The correction model is established by least squares support vector machine (LS-SVM) according to the optimization results. The results show that the visible/short wave near infrared spectrum based on the genetic algorithm can be used as a method for the determination of soil physical and chemical properties by using LS-SVM modeling.

Wang et al. (2013) in the middle and lower reaches of Yangtze River main grain producing area of paddy soil as the research object, collecting 17 kinds of different treatments of 136 soil samples in 350–2500 nm near infrared spectroscopy, using partial least squares regression analysis the quantitative analysis model of total carbon, total nitrogen, carbon and nitrogen combined with cross validation method of near infrared diffuse a method of analysis of reflectance spectra measured with the traditional chemical ratio, available potassium, available phosphorus, soil conductivity, soil pH index. The results show that the total carbon, total nitrogen, carbon to nitrogen ratio and pH model are very good. The predicted results of the available K model are good, while the results of the available P and conductivity models are very unsatisfactory.

Wu et al. (2014) to study the paddy soil in Yuxi tobacco science and technology demonstration park in Yunnan Province, 6 nitrogen levels, 144 soil samples, the spectral modeling method of the content of soil available nitrogen, phosphorus and potassium in the fast estimation, by far scatter correction and first derivative spectral preprocessing, through spectral correlation analysis of feature selection and application of local bands, nonlinear regression analysis modeling method, results show that using the local BP neural local modeling method to establish the soil available nitrogen, phosphorus and potassium content of the quantitative analysis model, which can realize the rapid diagnosis of soil nutrients.

Fang et al. (2015) based on near infrared spectroscopy combined with continuous projection algorithm and regression coefficient analysis, the total nitrogen content of soil was studied. The near infrared spectrum data of farmland soil samples were collected, and the total number of soil samples was 394. Partial least squares regression (PLS), multiple linear regression (MLR) and least squares support vector machine (LS-SVM) modeling were adopted to establish the prediction model of total nitrogen. The results show that the characteristic wavelength based on the continuous projection algorithm and the regression coefficient analysis can be applied to the detection of total nitrogen in

soil by near infrared spectroscopy. At the same time, the method used in this study can simplify the model and be suitable for developing portable soil nutrient detector.

Zeng et al. (2015) were studied in purple soil of Sichuan Chongqing area, analysis of soil moisture influence on prediction accuracy of soil organic matter content in purple, and the conversion of near infrared spectral absorbance of certain water content under dry soil conditions was then to establish the prediction model of near infrared spectroscopy of organic matter content by PLS method. Compared with original model prediction accuracy has improved significantly.

He et al. (2012) acquisition experiment field of Northwest Agriculture and Forestry University and the surrounding farmland soil total 160, synchronous acquisition of soil available phosphorus content and the corresponding near infrared spectral data, respectively, using four kinds of modeling methods, finally found modeling method of least squares support vector machine method can effectively predict the content of soil available phosphorus.

Wu et al. (2016) to explore the method of near infrared spectroscopy in field rapid determination of soil total nitrogen and available nitrogen content, soil spectral signal acquisition, combined with partial least squares method and principal component analysis method, respectively. The calibration model for determination of nitrogen content of soil total nitrogen and alkali solution is established.

Table 1 shows the spectral data after wavelet de-noising based on near infrared spectroscopy combined with PLS method to establish the model of soil total nitrogen and available nitrogen content, the correlation coefficient of the calibration set and validation set were higher than that of near infrared spectra by the multiple scattering correction, RMES is on the contrary, show that wavelet transform the de-noising effect is better than the multiple scattering correction de-noising effect.

Table 1. Evaluation indices of the calibration models of soil TN and AN by two pretreatment methods combined with PLS modeling approach

Modeling object	Model	Spectral preprocessing method	R2	RMSE
TN	Calibration set	Multivariate scattering correction	0.7549	0.1829
		Wavelet de-noising	0.8385	0.1521
	Validation set	Multivariate scattering correction	0.7339	0.1895
		Wavelet de-noising	0.7549	0.1842
AN	Calibration set	Multivariate scattering correction	0.7879	0.2018
		Wavelet de-noising	0.8665	0.0077
	Validation set	Multivariate scattering correction	0.7113	0.2308
		Wavelet de-noising	0.7961	0.0094

Relationships between predicted and measured values of soil total nitrogen and available nitrogen are shown in Figs. 1 and 2. Comprehensive analysis results show that the application of near infrared spectroscopic techniques on soil total nitrogen and available nitrogen content of quantitative prediction is feasible, and the application of wavelet transform to preprocess spectral redundancy, and partial least squares method can effectively improve the accuracy of the model is significantly improved.

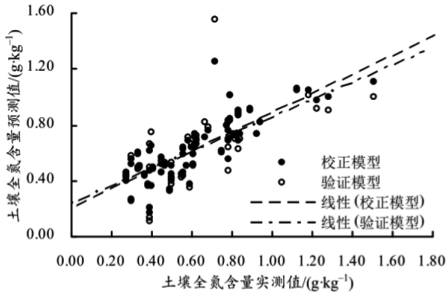


Fig. 1. Relationship between predicted and measured values of soil total nitrogen

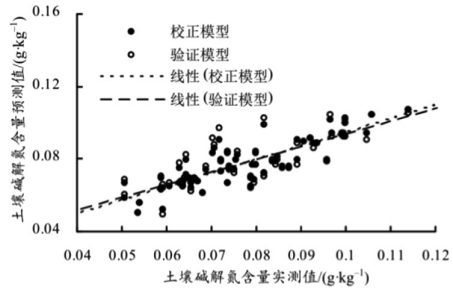


Fig. 2. Relationship between predicted and measured values of soil available nitrogen

3 Conclusion

3.1 The Methods of Data Analysis in Different Regions Still Need to Be Explored

The research on soil nutrients detection by NIR mainly focuses on the data analysis method. Data analysis mainly refers to the pretreatment mode and modeling method of near infrared spectrum data, and the purpose of modeling is to explore the stable conventional model for predicting soil nutrient content. Most of the existing researches are based on specific regions, and data analysis methods suitable for monitoring soil nutrients in various regions are still being explored. Future research on universal data analysis method is still the key direction for research and development of soil nutrient detection.

3.2 The Gap Processing of Spectral Data Between Different Years Still Needs to Be Explored

The pretreatment of spectral data is mainly aimed at eliminating the influence of water, particle size and soil type on soil nutrient detection, and improving the universality and stability of the model. At present, the research results show that the spectral data preprocessing way absorbance, mean normalization, 5 point mean filter smoothing processing can effectively increase the prediction accuracy of the model. But the spectral data are mostly data at the same time, and there are significant differences in the measured spectral data in different years. In the future, narrowing the gap between spectral data years is still a direction of research.

3.3 The General Modeling Method Between Different Years Still Needs to Be Explored

The modeling method has been greatly improved. From the early linear regression analysis to the current partial least squares, local neural network analysis and least squares support vector machine, the prediction accuracy of the model has been

significantly improved. But because of the soil type and the time of soil testing, the prediction effect of the model in different years is decreasing year by year. In order to develop a rapid detection instrument for Soil Nutrients Based on near infrared spectroscopy, the stability and universality of the model are still an important direction of the research.

References

- Dou, S.: Soil Organic Matter. Science Press, Beijing (2010). (in Chinese)
- Gao, H., Lu, Q.: Near infrared spectroscopy analysis and measuring system for primary nutrient of soil. *Spectrosc. Spectr. Anal.* **31**(5), 1245–1249 (2011). (in Chinese with English abstract)
- Zhang, J., Tian, Y., Yao, X., et al.: Estimating model of soil total nitrogen content based on near-infrared spectroscopy analysis. *Trans. Chin. Soc. Agric. Eng. (Trans. CSAE)* **28**(12), 183–188 (2012). (in Chinese with English abstract)
- He, D., Yang, C., Yang, Q., et al.: Research progress of real-time measurement of soil attributes for precision agriculture. *Trans. Chin. Soc. Agric. Eng. (Trans. CSAE)* **28**(7), 78–85 (2012). (in Chinese with English abstract)
- Song, H., Qin, G., Han, X., et al.: Soil classification based on near infrared reflectance spectroscopy and orthogonal signal correction-partial least square. *Trans. Chin. Soc. Agric. Eng. (Trans. CSAE)* **28**(7), 168–171 (2012). (in Chinese with English abstract)
- Li, J., Zhang, X., Yuan, Y., et al.: Analysis of soil nutrient content based on near infrared reflectance spectroscopy in Beijing region. *Trans. CSAE* **28**(2), 176–179 (2012). (in Chinese with English abstract)
- Liu, X., Zhang, H.L.: Study on soil nutrients by using near-infrared spectroscopy based on the GA method. *J. Irrig. Drain.* **32**(2), 138–141 (2013). (in Chinese with English abstract)
- Wang, C., Huang, C., Yu, G., et al.: Rapid evaluation of soil quality through a near infrared-partial least squares (NIR-PLS) method. *Acta Pedol. Sin.* **50**(5), 881–890 (2013). (in Chinese with English abstract)
- Wu, Q., Yang, Y., Xu, Z., et al.: Applying local neural networks and visible/near infrared spectroscopy to estimating available nitrogen, phosphorus and potassium in soil. *Spectrosc. Spectr. Anal.* **34**(8), 2102–2105 (2014). (in Chinese with English abstract)
- Zeng, J., Li, G., Zhou, S.: A research of the effects of soil moisture on NIR spectroscopic detection of organic matter content in purple soil. *J. Southwest Univ. (Nat. Sci. Ed.)* **37**(10), 167–173 (2015). (in Chinese with English abstract)
- Fang, X., Huang, L., et al.: Spectroscopy and spectral detection measurement of soil total nitrogen using near infrared spectroscopy combined with RCA and SPA. *Spectrosc. Spectr. Anal.* **35**(5), 1248–1252 (2015). (in Chinese with English abstract)
- Wu, J., Kong, L., Li, Y., et al.: Prediction models of total and available soil nitrogen based on near infrared spectroscopy. *J. Hunan Agric. Univ. (Nat. Sci.)* **42**(1), 91–96 (2016). (in Chinese with English abstract)



Microwave Mixing Technique for Nondestructive Measurement of Moisture Content of Particulate Agricultural Products

Chenxiao Li¹, Yanlei Xu¹, He Gong¹, Yuanyuan Liu¹,
and Qian Song²(✉)

¹ College of Information, Jilin Agriculture University, Changchun, Jilin, China
lichenxiao2000@163.com, yanleixu@163.com,
29878671@qq.com, 24973770@qq.com

² College of Physics, Jilin University, Changchun, Jilin, China
songqian0323@163.com

Abstract. A new method for nondestructive measurement of moisture content of particulate agricultural products is developed using microwave mixing technique. A double horn system with a relative vertical distance of one-fourth wavelengths is designed to measure the reflected microwave signals. The particulate materials are interacted with microwave at a frequency of 10.5 GHz, and the reflected microwave signal is mixed with the launch signal. Corns with different moisture contents are chosen as samples. Calibration models for moisture content are proposed in accordance with the measurement of the differential attenuation of the microwave mixing signal. A moisture content from 6.8% to 30.1% is obtained with a coefficient of determination of 0.98 and a standard error of calibration value of 1.12%.

Keywords: Moisture content · Microwaves · Mixing technique
Nondestructive measuring

1 Introduction

Water is an important component of industrial and agricultural production. Moisture content directly affects the quality of storage and processing conditions of agricultural products. The measurement of moisture content has important scientific significance and application value in agriculture product processing applications.

To achieve automatic processing and production, the moisture measurement process of agricultural products needs to be completed accurately and quickly, and the tested samples are not damaged. The drying weighing method is often used as a calibration method. Each measurement requires very few samples [1, 2]. The process is destructive and time and energy consuming. Resistance method needs to measure the impedance of samples between probes, with low accuracy and destructive measurement. RF capacitance method is a non-destructive measurement, in which samples are added between capacitor plates and water content is retrieved by measuring capacitance changes [3, 4]. However, the method results in bulk density of sample, thereby causing

a large number of measurement errors. It is an urgent research topic to realize on-line non-destructive and high-precision detection of moisture content in agricultural products.

In recent decades, microwave measurements have been used in many industrial applications. Microwave moisture content sensing measures the relative insensitivity to ionic conductivity, during which the electromagnetic energy is mainly absorbed by water. This selective absorption is due to the polar characteristic of the water molecules and their high permittivity compared with that of dry matter [5, 6]. Water molecules have very strong polarity, and microwave has a high frequency, so the interaction between the two will lead to energy storage and loss. The dielectric constant critically depends on the moisture content of water-containing materials at constant frequency and temperature [7]. There are many reports on dielectric constant measurement, including resonant cavity method and transmission line method [8, 9]. The dielectric constant of the sample is calculated by measuring the stationed Bobbi and field strength of the microwave. During the measurement, the sample is strictly confined to the waveguide cavity or coaxial line, which limits the application of on-line measurement [10].

Free-space technology presents great flexibility and does not bound microwaves to specific regions. After the interaction between microwave and sample, the transmission energy and phase will change. The moisture content and bulk density of sample can be measured by measuring the transmission parameters of microwave [11]. The microwave transmitting and receiving antennas are fixed on both sides of the measured sample. The thickness of the sample should be kept constant during the measurement to determine the relative attenuation of microwave energy. Therefore, the dual probe method cannot be applied to the situation where the thickness of the sample changes continuously during the flow. In our previous studies, a free-space microwave reflection measurement system with a single sensor is designed for the nondestructive determination of moisture content and bulk density [12]. The amplitude and phase parameters of traveling-standing wave are measured through the microwave horn antenna of continuous motion. However, for large particles of material, the single probe measurement sensitivity decreases as microwave scattering increases.

In the present study, a double probe microwave reflection measurement system is designed. The reflected microwave signal is mixed with the launch signal. Two radar probes are fixed separately on the position of signal maxima and minima. Measuring sensitivity is increased by differential output. This method is fast, continuous, and nondestructive. The measuring sensor does not directly contact with the grain materials, thereby facilitating its use in the real-time monitoring and controlling processes of moisture content of industrial and agricultural products.

2 Materials and Methods

The microwave moisture measurement system described here is based on a free-space reflection method and possesses the advantages of being nondestructive and not requiring sample preparation and physical contact with the material. Moisture content is determined from the measurement of attenuation and phase shift after the incident

wave reflection from the material surface. A transmit and reflection wave mixing method is designed to determine the parameters of attenuation and phase shift.

2.1 Principle of Microwave Mixing Moisture Measurement

The schematic view of this microwaves mixing moisture measurement is shown in Fig. 1. The materials are interacted with microwave, and the reflected microwave signal is mixed with the launch signal in the mixing diode. $U_L(t)$ is the incident wave signal with the frequency ω_L , and $U_S(t)$ is the reflected microwave signal with the frequency ω_S . D_1 is a Schottky mixing diode. The DC offset voltage E_0 is used to make sure the diode working well. Finally, the signals are processed by an amplifier and a low pass filter.

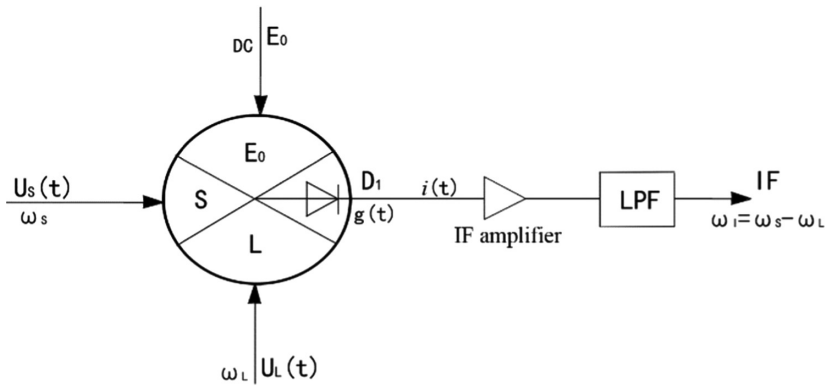


Fig. 1. The schematic view of microwave mixing process

The mixing principle is described as follows. The incident wave signal $U_L(t)$ and the reflected microwave signal $U_S(t)$ can be described as

$$U_L(t) = U_L \cos \omega_L t, \tag{1}$$

$$U_S(t) = U_S \cos(\omega_S t + \varphi). \tag{2}$$

The incident and reflected waves have different amplitudes and phases. After contact with the material, the reflected microwave $U_S(t)$ is a small variation compared with the incident wave. So the current $i(t)$ flowing through the Schottky diode mixer D_1 can be expanded as Taylor series

$$\begin{aligned} i(t) &= f(E_0 + U_L(t) + U_S(t)) \\ &= f(E_0 + U_L \cos \omega_L t) + f'(E_0 + U_L \cos \omega_L t)U_S \cos(\omega_S t + \varphi) \\ &\quad + \frac{1}{2!}f''(E_0 + U_L \cos \omega_L t)(U_S \cos(\omega_S t + \varphi))^2 + \dots \end{aligned} \tag{3}$$

The first expansion is a large signal, which contains the DC and local microwave fundamental signals. Other items are small signals. For the second item of Eq. (3)

$$\begin{aligned}
 i(t) &= f'(E_0 + U_L \cos \omega_L t) U_S \cos(\omega_S t + \varphi) \\
 &= g_0 U_S \cos(\omega_S t + \varphi) + \sum_{n=1}^{\infty} g_n U_S \cos((n\omega_L + \omega_S)t + \varphi) \\
 &\quad + \sum_{n=1}^{\infty} g_n U_S \cos((n\omega_L - \omega_S)t + \varphi).
 \end{aligned}
 \tag{4}$$

In (4), g_n is the conductance of the diode mixer and it is a constant for the given diode. After the mixing signals passing through the low-pass filter, the differential frequency signal, at the point $n = 1$, can be expressed as follows

$$i(t) = g_1 U_S \cos((\omega_L - \omega_S)t + \varphi).
 \tag{5}$$

In actual measurement, the relative distance between the microwave probe and the material remains constant. So the frequency of the incident wave is equivalent to the reflected microwave. Then we can get the following equation

$$I_0 = g_1 U_S \cos \varphi.
 \tag{6}$$

In (6), g_1 is the o conductance constant of the diode. U_S is the amplitude of reflected microwave, which is proportional to the moisture content of tested materials. φ is the relative phase value of the reflection microwave. The value $\cos \varphi$ varies periodically from 1 to -1 with the different relative position of the antenna probe and the material. The mixing signal has the best sensitivity when the microwave antenna is fixed in one of the two phase extreme points ($\cos \varphi = 1$ or -1).

In this study, two microwave antennas are mounted on the maximum and minimum phase positions respectively. In experimental measurement, two mixing signals are opposite to each other. The moisture content of the material is obtained by difference operation of the two signals. Microwave mixing technique has greatly facilitated the high-frequency signal processing and extraction in moisture measurement.

2.2 Microwave Measurement System

The measurement system consists of microwave cavity oscillator, double horn antenna, mixer, sample holder, differential amplifier, and data processing unit. The construction of microwave measurement system is illustrated in Fig. 2. Two microwave horn antennas, which transmit and receive signals independently, are mounted on the same side of the sample holder. The sample container is made of acrylic material, rectangular and filled with the tested sample. The vertical distance of microwave transceiver probes 1 and 2 is $\lambda/4$, which relates to microwave wavelengths. Prior to the actual measurement, the distance L between probe 2 and the sample surface needs to be adjusted to ensure that the mixing signal is at the limit value. When L is finalized, the phase

difference φ between mixing signals A and B is π . Therefore, the mixing current presents opposite changes between signals A and B, as shown in Eq. (6).

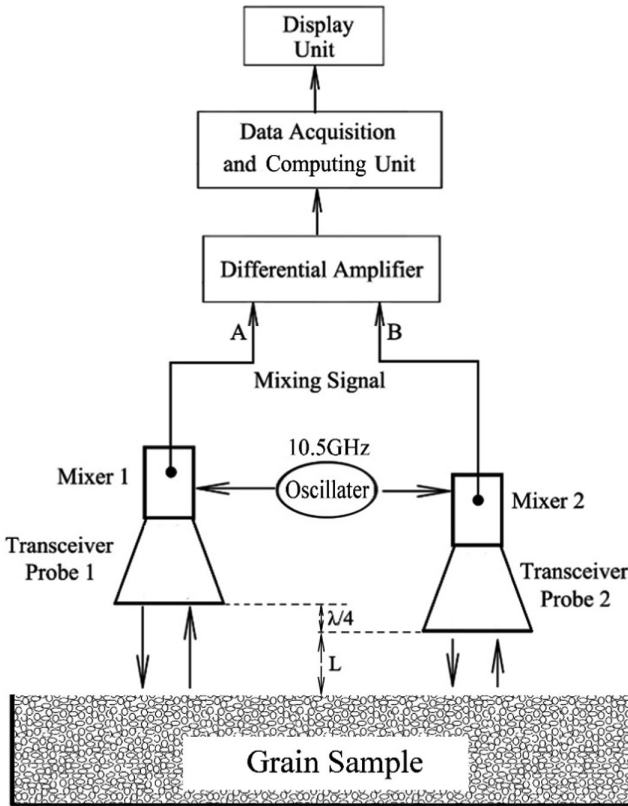


Fig. 2. Schematic diagram of double horn antenna microwave measurement system

The microwave sensors are designed as follows. The continuous microwave signal with a frequency of 10.5 GHz and a power of 20 mW is generated by a Gunn diode. The waveguide cavity is wr90, and the oscillating diode is mounted in the waveguide cavity. The microwave cavity oscillator is connected with the horn antenna. The aperture of the microwave horn antenna is $8.4 \text{ cm} \times 6 \text{ cm}$ and the output gain at the frequency of 10.5 GHz is 17.2 dBi. The incident and reflected waves are detected by a Schottky mixer diode. Finally, mixing signals A and B are measured by using the differential amplifier.

The output voltage of the differential amplifier is linearly related to the moisture content of the tested materials. In accordance with the fitting equation, a data acquisition and adjustment unit is designed with different modes to realize the display and control of moisture content.

2.3 Sample Preparation

Corns are used as the experimental sample in this study. Each sample consists of approximately 10 kg of material and is dried by natural drying prior to the experiments. The moisture content of the sample is determined by drying and weighing. A certain amount of the sample is placed in the drying equipment at a temperature of 130 °C until the weight is constant. Moisture content is calculated as follows:

$$M(\%) = m_w / (m_w + m_d), \quad (7)$$

where M is the moisture content of corn, m_w is the mass of water, and m_d is the mass of dry matter.

The initial moisture content of corn sample is 6.8%. The water content of the sample was increased by adding water and stirring evenly. The samples were prepared with the distance of 3% water content. A total of 8 samples with moisture contents from 6.8% to 30.1% for corn are prepared. Samples are placed in a sealed plastic bag for at least 24 h at 4 °C to equilibrate. Before the measurement, the samples were transferred to room temperature for at least 24 h to achieve a temperature balance.

2.4 Measurement Procedure

The sample container is filled with corn samples and placed on the side of the microwave antenna. The surface of the sample is perpendicular to the direction of microwave radiation. The size of the sample container should be larger than the microwave antenna to reduce the edge scattering interference of the microwave.

The microwave horn antenna is fixed on the sliding orbit, and the position of the antenna can be adjusted freely. The distance between antenna probe 2 and sample surface is L_1 . In measurement, the electric field of space microwave varies periodically with the change of L_1 . The voltage signal B detected by the digital voltmeter changes with the increase in horn antenna distance. The variations in voltage signal B with the antenna distance L for corn with an initial moisture content of 6.8% are illustrated in Fig. 3.

Two extreme points, V_{min} and V_{max} , appear with the increase in horn antenna distance. The corresponding antenna distances are 2.4 and 9.8 mm. During the experiment, two microwave antenna probes are fixed in the two positions. Extreme position distance is 7.4 mm, which is in good agreement with the theoretical calculations of $\lambda/4$ at 10.5 GHz.

For each corn sample with specific moisture content, measurements are repeated and performed three times. Mixing voltage signals A and B are recorded by using the digital voltmeter, and the differential values are calculated for data fitting.

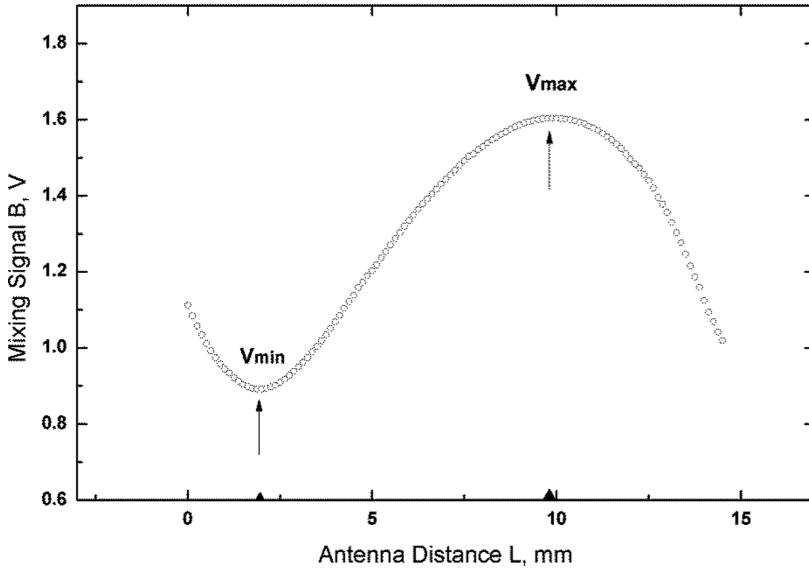


Fig. 3. Variation of voltage signal B with antenna distance L at the moisture content of 6.8%

3 Experimental Results

The relationship between moisture contents and mixing voltage signals of corn samples is shown in Fig. 4. The sample is measured at room temperature (24 °C) with eight different moisture contents in increments of approximately 3%. The moisture contents

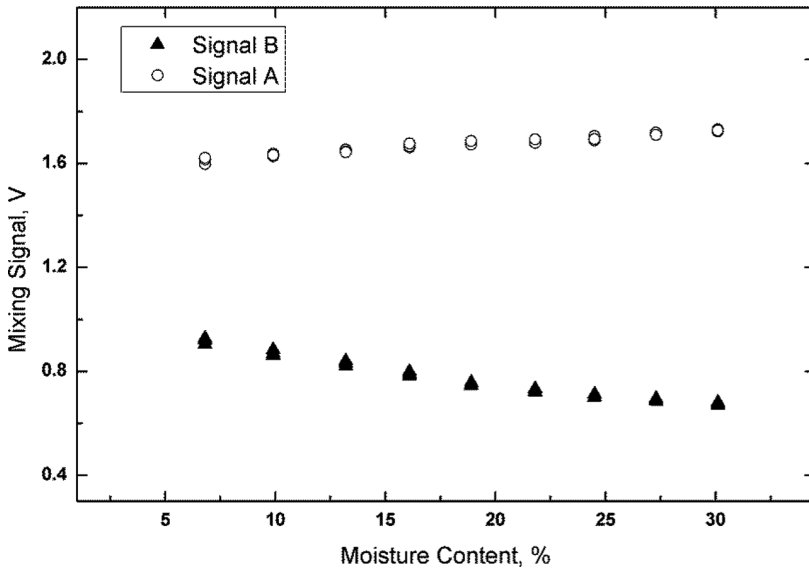


Fig. 4. The variations in the mixing signal with moisture content. The round and triangle data are output of probe 1 and probe 2 respectively.

vary from 6.8% to 30.1%. Each of the samples is repeated for three times, and 48 sets of data are recorded.

Curves A and B represent the output of the two microwave probes. The trends of A and B variation with moisture content are opposite to each other because the phase difference between the mixing signals is π . Curve B presents a greater slope than curve A because of the close measuring distance.

The variations in the differential mixing signals with moisture content are illustrated in Fig. 5. The sensitivity of the differential signal is obviously improved compared with that of a single mixing output probe 1 or probe 2. The differential output is generally linear. Therefore, calibration equation is assumed as follows:

$$M_C(\%) = a_0 U_d + b_0, \tag{8}$$

where a_0 and b_0 are the coefficients, U_d is the differential signal voltage, and M_C is the moisture content of corn. The calibration equation is obtained by statistically analyzing all experimental data to determine the coefficients. The results show that, the coefficients a_0 and b_0 are 63.86 and 38.79, respectively. The moisture content is determined with an R^2 of 0.98, and the standard error of calibration (SEC) is 1.12%.

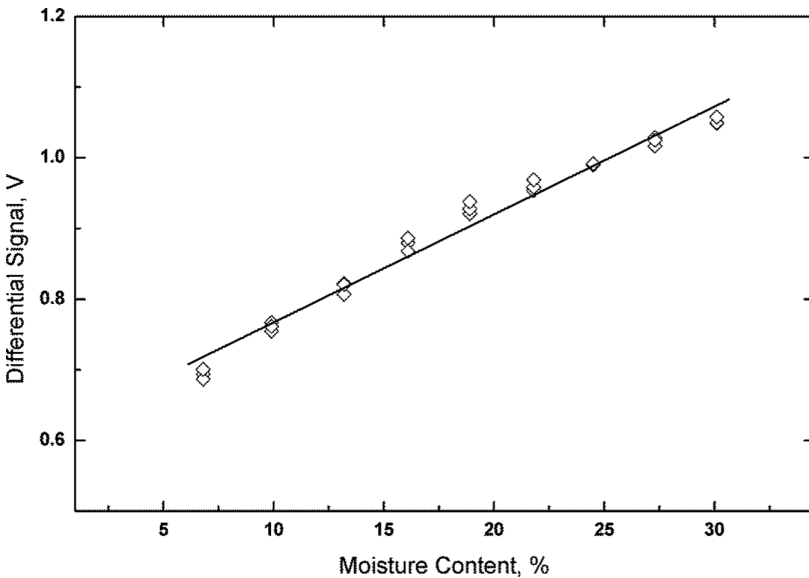


Fig. 5. Differential mixing signal versus the moisture content of corn

Particulate material microwave scattering is a major error factor. The main source of microwave scattering is the inhomogeneity of sample distribution, which is affected by the size, shape and water content of the particles. Temperature and bulk density also affect the measurement results. In the experiment, the particle of materials should be stacked compactly and orderly to reduce the irregular scattering of microwaves.

4 Conclusion

A microwave mixing system is designed for the rapid and nondestructive determination of moisture content of grain materials. The measurement system consists of microwave cavity oscillator, double horn antenna, mixer, sample holder, differential amplifier, and data processing unit. The reflected microwave signal is mixed with the launch signal. Measuring sensitivity is increased by using the double probe microwave reflection measurement system. In accordance with the fitting calibration equation, the moisture content of corn is determined with a coefficient of determination (R^2) of 0.98 and a standard SEC of 1.12%. The proposed measuring method is suitable for the independent moisture measurement of monomers and on-line moisture measurement, and also meets the real-time monitoring needs of agricultural products moisture change in industry.

Acknowledgment. This work was supported by Jilin Scientific and Technological Development Program (No. 20180520016JH) and the Scientific Research Foundation of Jilin Agricultural University (No. 201719).

References

1. Martínez-López, E., Lira-Cortés, L.: Measurement of moisture content of some hydrated ionic materials by oven drying. *MAPAN* **30**(4), 239–247 (2015)
2. Walker, J.P., Willgoose, G.R., Kalma, J.D.: In situ measurement of soil moisture: a comparison of techniques. *J. Hydrol.* **293**(1–4), 85–99 (2004). NOVA. The University of Newcastle's Digital Repository
3. Wu, K.: Measurement of soil moisture change in spatially heterogeneous weathered soils using a capacitance probe. *Hydrol. Process.* **12**(1), 135–146 (2015)
4. Kim, K.B., Kim, J.H., Lee, S.S., et al.: Measurement of grain moisture content using microwave attenuation at 10.5 GHz and moisture density. *IEEE Trans. Instrum. Meas.* **51**(1), 72–77 (2000)
5. Nelson, S.O., Trabelsi, S.: Factors influencing the dielectric properties of agricultural and food products. *J. Microw. Power Electromagn. Energy: A Publ. Int. Microw. Power Inst.* **46**(2), 93–107 (2012)
6. Trabelsi, S., Nelson, S.O.: Nondestructive sensing of physical properties of granular materials by microwave permittivity measurement. *IEEE Trans. Instrum. Meas.* **55**(3), 953–963 (2006)
7. Trabelsi, S., Lewis, M.A., Nelson, S.O.: Microwave moisture meter for in-shell peanut kernels. *Food Control* **66**, 283–290 (2016)
8. Krupka, J.: REVIEW ARTICLE: frequency domain complex permittivity measurements at microwave frequencies. *Meas. Sci. Technol.* **17**(6), 55–70 (2006)
9. Hashemi, A., Rashidi, M., Kurtis, K.E., et al.: Microwave dielectric properties measurements of sodium and potassium water glasses. *Mater. Lett.* **169**, 10–12 (2016)
10. Nigmatullin, R., Nelson, S.O.: New quantitative “reading” of dielectric spectra of complex biological systems. *IEEE Trans. Dielectr. Electr. Insul.* **13**(6), 1325–1334 (2006)
11. Trabelsi, S., Paz, A.M., Nelson, S.O.: Microwave dielectric method for the rapid, non-destructive determination of bulk density and moisture content of peanut hull pellets. *Biosys. Eng.* **115**(3), 332–338 (2013)
12. Li, C., Han, B., Zhang, T.: Free-space reflection method for measuring moisture content and bulk density of particulate materials at microwave frequency. *Rev. Sci. Instrum.* **86**(3), 227–237 (2015)



China's Wine Import Industry: An Economic Analysis of Influencing Trade Factors

Yu Hu^{1,2}, Wei Ma^{1,2(✉)}, Ruimei Wang^{1,2}, Huan Song^{1,2},
Weisong Mu^{1,2}, Dong Tian^{1,2}, and Jianying Feng^{1,2}

¹ College of Economic and Management, China Agricultural University,
Beijing, China

{bs20163110665, wangruimei, songhuan3}@cau.edu.cn,
mawei1963@163.com

² College of Information and Electrical Engineering,
China Agricultural University, Beijing, China

1030665381@qq.com, 1042025956@qq.com, 41935068@qq.com

Abstract. In recent years, China is undergoing a huge economic transformation since joining in World Trade Organization (WTO) and it has showed an increasing demand for wine. As China's wine consumption market is increasingly larger, the European market is becoming increasingly saturated, more and more wine foreign trade and foreign capital have chosen to enter China. Since 1996, China's wine imports have gradually increased and the trade deficit has significantly expanded. Thus, the objective of this study is to analyze the China's competitiveness of wine in the international market. We mainly focus on the factors that most influenced the performance of imported wines from 1995 to 2014. The aim is to testify if the wine imports affect the China's own wine industry and examine which factors influence the Chinese wine industry most. This study uses Constant Market Share (CMS) econometric model to analyze the influencing factors of China's grain import fluctuation. The deep introduction on wine trade has important practical significance for the development of international trade and the improvement of industrial policies. The procured result of empirical model demonstrates that competitiveness is not always a predominant factor throughout the period, especially in wine industry.

Keywords: CMS model · Import · Wine · Competitiveness

1 Introduction

Over the past two decades, with the improvement of people's living standards, the rate of China's economic growth has an amazing pace. Although China has a long-term traditional to consume grain alcohol production in holidays, with the improvement of living standards and the influence of Western culture, more and more people especially educated young professionals and government campaigns led a trend to drink wine and an increase in wine consumption. (Sun 2009), Undoubtedly, under the background of global economic integration, the continuous increase in wine imports has largely guaranteed domestic demand, making China a very promising exporting market (Mitry et al. 2009). Furthermore, the reduction of import duties after participating in the WTO

in 2001, the import volume of wine has presented a strong momentum. Today, compared with other countries, China's wine industry is still largely undeveloped and has great potential for development. Since joining WTO and the implementation of the wine import tariffs reduced policy, the wine industry has been greatly impacted by imported wine, China has urgently needs to promote the development of the domestic wine industry and improve the international competitiveness of its own wine industry.

However, the income growth and cost effectiveness of imported wine has changed the consumption situation remarkably. Because the low price and better taste of imported wine, more and more people prefer imported wine especially the traditional European products. In order to deal with this situation, China has expanded its area of vineyards and rising from 15th in 2001 to fifth largest wine producer in the world, according to OIV report in 2015.

Consequently, the tremendous consumption market has made China became a much more attractive destination for foreign vintners. The import volume of wine has grown strongly during the last decades. According to United Nation's Commodity Trade Statistics Database, in the case of a general expansion of import demand in the world, China's wine yield hovered from 25 million liters to 112 million liters. Furthermore, the average wine consumption per person rises from 0.20 L in 1990 to 1.24 L in 2015. However, compared with the world average, China's wine consumption only accounts for 36.7%. With the influx of a large number of imported wines, there are still technical barriers in wine industry such as wine production, transportation and preservation. Because of these problems, there is still a big gap between Mainland China and other old wine production countries like France. Infrastructure, consumption, and market competition have made a big gap in the wine industry.

In regards to the massive trade deficit, is it for China to decrease wine import and to develop its own wine industry? At present, the domestic research on wine trade is mostly descriptive. This paper intends to empirically analyze the fluctuation of China's wine import trade and its causes through the CMS model. We also discussed what measures the Chinese government and wine producers should take to reduce the impact of imported wine on domestic wines. In addition, how to use its rich geographic resources and low import tariffs to benefit from its wine industry is a basic contribution of this paper. These questions should be deep thinking in this process.

In this paper, we first analyze the status of China's wine import and export to see why China's wine trade deficit is surging. Then we use the Constant Market Share (CMS) model to verify the fluctuation of wine import trade in China. We analyze the impact of structure, competitiveness, and secondary structure and competitiveness from three perspectives to determine the main factors affecting our wine industry. Through the empirical research, we could provide a strong policy support and reference for import and export trade of related product.

2 Literature Review

Many previous researches had a deep research on the wine development in China. But there are few domestic researchers focus on the fluctuation of import trade of wine contrast by the export trade of agricultural products as a whole at present and they also have done a great deal of research on it from theory to practice. There is not much research on wine imports. Most research methods only focus on the statistical analysis of economic indicators. The research objects are wines, and there are few researches on the factors and causes of the fluctuations of the wine import trade at home and abroad.

As mentioned above, many foreign researchers have made intensive studies on the Chinese wine industry. Muhammad et al. (2014) examined Chinese wine imports from wine consumption patterns perspective. He thinks that one-off structural changes may not reflect the changes in demand over the past decade. When China joins WTO successfully in 2001, researchers have found that some of the WTO's rules on tariff reduction help the development of the wine industry and demonstrate that open deals are feasible. More importantly, the evidence had shown that China's market share in wine industry was not affected by the financial crisis (Guo and Feng 2013). Other researchers analyze the effect of the globalization in Chinese wine industry. They proposed that China had considerable potential in wine consumption, while there may be huge potential for export as well. Besides, another group of researchers analyze export competitiveness. They discuss the positive and negative aspects of free trade from both theoretical and empirical levels.

Although quantitative analysis has been limited, most of researches on wine import trade mainly focus on measuring the economic benefits of different tariffs or quota policies, rarely analyzing the influencing factors and causes of the fluctuation of wine prices at home and abroad. They use theoretical methods to analyze the different type of wine products' patterns.

These studies have important implications for the analysis of the factors affecting the import development of China and wine industry. What is the reason for the growth of wine imports in China? Is it because of the increase of competitiveness of foreign wines or the expansion of domestic demand? Although these researchers have made significant contributions in this field, we should make a new industry synthesis analysis to better understand the Chinese wine industry because of the rapid growth of wine imports.

3 An over Overview of Chinese Wine Market

Chinese people are used to drink alcohol at special occasion like social banquets and business meetings, besides when going to friends' home they usually bring it as gift (Liu and Murphy 2007). With the continuous growth of the national consumption demand and the improvement of the living standard, Chinese wine market continues to grow, and the wine import scale expands rapidly (Huang and Rozelle 1998).

Due to the accession to the World Economic and Trade Organization and increasing demand for wine in China in recent years, the openness of the market has gradually increased and the imports of wine has increased significantly which makes

China risen form 9th to 5th in the world. Figure 1 shows a time series plot of Chinese wine import over the post 2002–2016. As the figure shows import of wine has shown dramatically increase since 2008. From 2002 to 2016, wine yield in China has risen by a tremendous 1987%, exceeding the world average of 20%. At the same time, China’s average purchase price for wine from 2002 was 1.67 CNY/g in 2012 at 3.29 CNY/g, with a compound annual growth rate of 7% which was related to the demand for wine. This may be due not only to the increase in the share of domestic wines but also to the increasing cost rising cost of production. China has imported a lot of a lot of wine in bulk to reduce the cost of wine production.

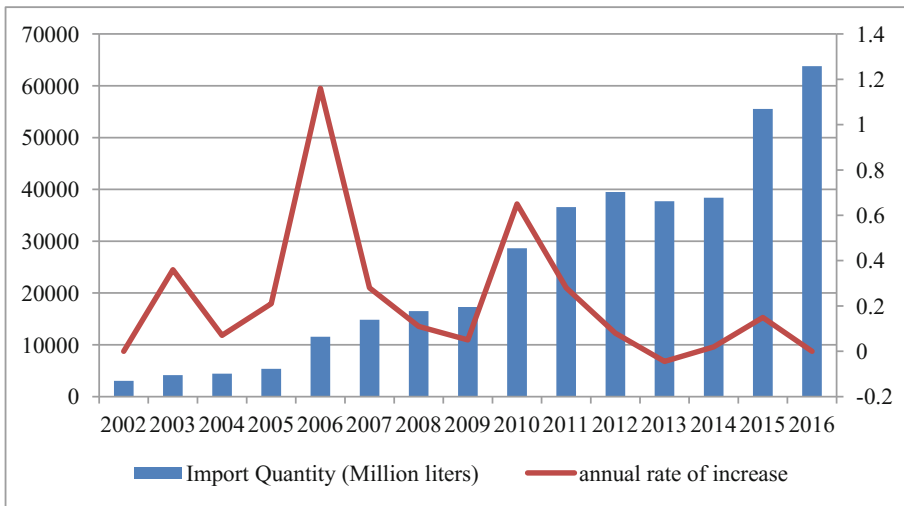


Fig. 1. Chinese wine import quantity and annual rate of increase in China in 2002–2016

At present, there are about 500 wineries in China. Many of them are very small, geographically dispersed and have insufficient capacity. With good natural conditions and low labor costs, there is great potential for domestic wines development. The extent to which Chinese wine consumption and production are developed is a problem that many foreign wine manufacturers are very concerned about. Because of the current global economic climate, wine import and consumption have slowed down. This long-term trend will reverse as income increases (Chaney 2008). Due to the competitions of foreign suppliers, the domestic market share of domestic wines gradually declined. To a certain extent, brand loyalty is still one of the important factors affecting consumers’ purchase of wine which is also a benefit to Chinese wine manufacturers. The domestic wine industry, which is at a comparative disadvantage, is facing increasingly fierce international competition.

4 Methods

Based on the consideration of many internal and external influences, we use the CMS model to explore the fluctuations in China's import trade since 1995 and its causes, providing a basis for the adjustment and formulation of wine industry policies. Hence, to infer China's wine imports, this research explores and discusses these questions by using the Constant Market Share (CMS) model. The CMS (Constant Market Share) model is a constant market share model. It was initially proposed by Tyszynski (1951) and has been revised and refined by Stern and other scholars. It has become the main method for studying export competitiveness and market trade growth at present. For decades, foreign scholars have generally used this model to study the national export competitiveness and trade fluctuations and have been widely used by domestic scholars in recent years. In terms of export competitiveness, more scholars use the CMS model to study the dynamic changes in export competitiveness. This modeling approach is based on market share as a constant amount as a research hypothesis. Now let's briefly introduce this model.

First, consider the market share in exporter's market may be defined as follow, where S represents the focus country's share of the market, q is the focus country's exports and Q is the exports of the standard.

$$S = q/Q \tag{1}$$

The standard's exports of commodity i to market j is defined as Q_{ij} . Differentiating with respect to time yields, the change in the share of market share between an initial year (time 0) and year t is

$$\Delta q = \sum_i \sum_j S_{ij}^0 \Delta Q_{ij} + \sum_i \sum_j Q_{ij}^0 \Delta S_{ij} + \sum_i \sum_j \Delta S_{ij} \Delta Q_{ij} \tag{2}$$

strucrual effece competitive effect second-order effect

This equation can be rewritten as following:

$$\begin{aligned} \Delta q = & S^0 \Delta Q + \left[\sum_i \sum_j S_{ij}^0 \Delta Q_{ij} - \sum_i S_i^0 \Delta Q_i \right] + \left[\sum_i \sum_j S_{ij}^0 \Delta Q_{ij} - \sum_i S_j^0 \Delta Q_j \right] \\ & \text{growth effece} \qquad \text{market effect} \qquad \text{commodity effect} \\ & + \left\{ \left[\sum_i S_i^0 \Delta Q_i - S^0 \Delta Q \right] - \left[\sum_i \sum_j S_{ij}^0 \Delta Q_{ij} - \sum_i S_j^0 \Delta Q_j \right] \right\} + \Delta S Q^0 \\ & \qquad \text{stuctural interaction effect} \qquad \text{general competitive effect} \tag{3} \\ & + \left[\sum_i \sum_j \Delta S_{ij} Q_{ij}^0 - \Delta S Q^0 \right] + (Q^1/Q^0 - 1) \sum_i \sum_j \Delta S_{ij} Q_{ij}^0 \\ & \text{specific competitive effect} \qquad \text{pure second-order effect} \\ & + \left[\sum_i \sum_j \Delta S_{ij} \Delta Q_{ij} - (Q^1/Q^0 - 1) \sum_i \sum_j \Delta S_{ij} Q_{ij}^0 \right] \\ & \qquad \text{dynamic strucrual residual} \end{aligned}$$

Where

$$\sum_i \sum_j S_{ij}^0 \Delta Q_{ij} = S^0 \Delta Q + [\sum_i \sum_j S_{ij}^0 \Delta Q_{ij} - \sum_i S_i^0 \Delta Q_i] + [\sum_i \sum_j S_{ij}^0 \Delta Q_{ij} - \sum_i S_j^0 \Delta Q_j] + \left\{ [\sum_i S_i^0 \Delta Q_i - S^0 \Delta Q] - [\sum_i \sum_j S_{ij}^0 \Delta Q_{ij} - \sum_i S_j^0 \Delta Q_j] \right\} \tag{4}$$

$$\sum_i \sum_j Q_{ij}^0 \Delta S_{ij} = \Delta S Q^0 + [\sum_i \sum_j \Delta S_{ij} Q_{ij}^0 - \Delta S Q^0] \tag{5}$$

$$\sum_i \sum_j \Delta S_{ij} \Delta Q_{ij} = (Q^1 / Q^0 - 1) \sum_i \sum_j \Delta S_{ij} Q_{ij}^0 + [\sum_i \sum_j \Delta S_{ij} \Delta Q_{ij} - (Q^1 / Q^0 - 1) \sum_i \sum_j \Delta S_{ij} Q_{ij}^0] \tag{6}$$

Equation (4) is the structural effect which means changes in China’s wine imports are caused by changes in the overall import demand for wine in the world. Then, it could be divided into growth effect, market effect, commodity effect and structural interaction effect. Equation (5) is competitive effect which measures the influence of changes in China’s wine imports caused by changes in the gravity of China’s wine imports. Competitiveness refers to the import competitive attraction of China’s wine consumer market to other countries. As for Eq. (6) is the second-order effect. It measures the changes in import value caused by changes in the competitiveness of China’s wine imports and changes in the world’s wine import demand. This model has made empirical analysis of factors affecting the growth of Chinese imported wine and analyzed the degree to which the importer gains market share without changing the pattern of world exports and destinations

5 The CMS Decomposition Results

The CMS model decomposition was based on years, and the end of each stage is the beginning of the next stage. The result of the selected cycle is then represented by the average of the annual decomposition results. Using this method, it does not affect the final results when selecting the year as the start of the entire period. We utilize CMS model to make empirical research in the view of wine and classification to analyze the impact on China’s wine industry from 1995 to 2014, such as China’s wine industry, influence import factors, market structure and market. Then reveal the extent of the impact. We divided the year into 6 periods.

The data used in this model is product data according to HS classification. This data mainly derived from the COMTRADE database created by the UN Statistical Office, World Trade Organization reports and other data about China’s wine imports from. Since the implementation of the HS code in 1988, there has been a fourth revised edition of the HS2007 commodity classification method which is used in parallel with

the HS2002 commodity classification method and the sample period is 1995–2014. Furthermore, we divide it into 6 periods.

Table 1 presents the two levels of decomposition results in each one period by using CMS model. According to the table, China increased its wine imports during that period and China's wine import fluctuations are the result of structural effects, competition effects, and second-order effects. However, there are significant differences in the direction and degree of action of the three forces at different stages on wine imports. In the first level CMS decomposition, the results show that the growth of imported wine trade from 1995 to 2014 was mainly due to competitive effects. In terms of percentage, the proportion of China's wine imports in the world's total imports rose from 0.023% to 4.21%, nearly 183 times in 20 years. The contribution of the competitive effects to the increase in imports ranged from -66.00% (period II) to 135.81% (period VI). The second level CMS decomposition results further indicate that the fluctuation of China's wine import trade can actually be attributed to domestic macroeconomic factors, world economic factors, market structure factors, commodity structure factors, import gravitational factors, and the effects of the interaction of these factors. Furthermore, the result of second-order effect means there is a connection between the imports value and structural effects, competitive effects.

Table 1. Constant market share model for wine imports of China

Items	1995–1998		1998–2001		2001–2006		2006–2009		2009–2012		2012–2014	
	Average	%	Average	%	Average	%	Average	%	Average	%	Average	%
Δq	26.75	100	-11.63	-100	111.85	100	262.10	100	1078.51	100	-62.82	-100
Structural effect	0.85	3.19	-0.50	-4.29	16.94	15.14	-13.01	-4.96	97.98	9.08	125.33	199.52
Growth effect	0.96	3.57	0.44	-3.78	16.11	14.41	17.01	6.49	114.50	10.62	83.20	132.45
Market effect	0.07	0.28	4.43	38.10	-39.80	-35.58	-39.80	-15.18	-25.11	-2.33	46.93	74.72
Commodity effect	0.28	1.06	-1.99	-17.08	2.97	2.65	14.41	5.50	-16.51	-1.53	132.69	211.24
Interaction effect	-0.46	-1.72	-3.38	-29.08	37.65	33.66	-4.64	-1.77	25.09	2.33	-137.49	-218.88
Competitive effect	25.89	96.77	-7.68	-66.00	56.36	50.39	272.97	104.15	912.03	84.56	85.31	135.81
General competitive effect	23.10	86.35	-12.41	-106.67	58.70	52.48	269.10	102.67	808.08	74.93	-158.41	-252.18
Specific competitive effect	2.79	10.42	4.73	40.67	-2.34	-2.09	3.87	1.48	103.95	9.64	243.72	388.00
Second-order effect	0.01	0.04	-3.46	-29.71	38.55	34.47	2.14	0.82	125.33	6.35	-273.46	-435.34
Pure second-order effect	10.76	40.21	-0.09	-0.81	38.09	34.06	33.58	12.81	228.25	21.16	4.98	7.94
Dynamic structural residual	-10.75	-40.17	-3.36	-28.91	0.46	0.41	-31.43	-11.99	-159.75	-14.81	-278.44	-443.27

5.1 Structural Effect

The structural effect reflects the impact of the change in the wine imports on its import performance. Among the six periods, China has a positive growth effect which implies that the increase of Chinese wine imports is consistent with the world market demand

growth trend for wine. All the whole years, Chinese wine import value increased from 85 million to 1.25 billion US dollars. In the past 20 years, the import demand of the world market has increased by 25.796 billion U.S. dollars, an increase of 256.83%.

Especially in recent years, the domestic macroeconomic development has been gradually optimistic. The increase in GDP has been maintained at more than 7% and consumption in the commodity market has become increasingly active. In 2014, the total retail sales of consumer goods in China reached 26.2 trillion CNY, a year-on-year increase of 12.0%, and a real increase of 10.9% after deducting price factors. The income of residents increased substantially, an increase of 9.0% over the previous year. Due to the recovery of China's economy and the implementation of policies to expand domestic demand, import barriers have also gradually declined. In addition, the reduction in import tariffs on wine and the improvement in the living standards of residents have also stimulated the import of Chinese wine. With China's accession to WTO in 2001, the economy is getting better. Especially in the period 6, the contribution rate of growth effect is 132.45%, compared with the first initial stage of rise 37 times.

With the rapid growth of the world economy, the structural effects have become more and more influential. The optimization of the import structure compensates for the lack of competitive growth. China's wine import trade has grown steadily under the interaction of structure and competitiveness. The reduction of tariffs has greatly reduced the cost of imports, and favorable domestic macroeconomic factors will push China's wine import trade to the next high point. The effect of world economic development to China's wine imports is increasingly important, especially after accession to WTO and financial crisis. From the results, we can also infer that about one-third of the growth of China's wine imports is brought by the overall growth of world economy.

5.2 Competitive Effect

According to the Table 1, in the 20 years from 1995 to 2014, the competitiveness effects were the main factors affecting the growth of China's wine imports. Competitiveness effect can reflect the impact of China's wine import gravity on import trade which can be further divided into general competitive effect and specific competitive effect. From period 1 to period 6, the general competitive effect has changed from 86.35% to -252.18%. Based on the above analysis, we can see that the huge demand for wine has been the main reason for the rapid growth of Chinese wine imports throughout the year. And competitive effects are easily affected by the external economic environment like Asia financial crisis.

5.3 Second-Order Effect

From the years of 1995 to 2014, the pure second-order effect has always been positive which indicates that China's import of wine is consistent with the changes of world wine demand. From period 1 to period 6, the dynamic structural residual changes from 40.17% to -443.27%. It also reveals that China's imports of wine is irrational

distribution. By the way, China's share of imports growth in France, Spain and other major countries is slow which indicates that trade with less developed country is one of the main factors resulting in the reduction of Chinese wine imports.

6 Conclusions

Based on the empirical study of wine import trade in China, the results show that:

First, the increase in China's wine imports from 1995 to 2014 was mainly due to competitive effects. In the last decades, wine consumption and production in China has achieved tremendous advancements in development. Even though the global financial crisis broke out in 2008, China's wine imports have not been affected and the competitive effect has remained high. The improvement of the commodity structure and the growing demand for wine by the people has given China a strong attraction to wine imports. At the same time, the competitiveness of China's wine imports fluctuates with the fluctuations of the world economy. The direction of change in import competitiveness is consistent with the change in the overall world wine import demand. The development of import trade has enabled China's wine industry to coexist with risks and interests. In 2014, Chinese per capita consumption of wine was 1.17 L but only one third of foreigner.

Secondly, from a data point of view, there are certain problems in the structure of China's wine import market, and the market structure has no obvious advantage. From the view of dynamic structural residual, imported wines have a relatively slow increase in their import share in the category of goods with rapid growth in export demand, and there is a certain gap with the world export level. The exporting countries for wine are mainly Chile, Australia, France and the United States.

Finally, this paper highlight an analysis of the factors affecting China's imported wine. The result shows that in order to withstand risks and develop domestic and foreign markets, we should rationally adjust the import structure, actively coordinate and stabilize regional economic development, guide industrial integration, and take the road of industrialized management. Moreover, creating a good external environment, establishing industry legislation and strengthening industrial supervision are also effective measures. Effective competition and learning, timely exchange of international experience and technology; continue to explore comparative advantages, pay attention to the cultivation of competitiveness; market demand as a guide to promote the coordinated development of domestic import trade and domestic industries.

Acknowledgements. The financial support was from the China Agricultural Research System (CARS-30).

References

- Huang, J., Rozelle, S.: Market development and food demand in rural China. *China Econ. Rev.* **9**, 25–45 (1998)
- Mitry, D., Smith, D.E., Jenster, P.V.: China's role in global competition in the wine industry: a new contestant and future trends. *Int. J. Wine Res.* **1**, 19–25 (2009)
- Muhammad, A., Leister, A.M., Mcphail, L., Chen, W.: The evolution of foreign wine demand in china. *Aust. J. Agric. Resour. Econ.* **58**(3), 392–408 (2014)
- Chaney, J.: China could become the wine industry's next Chile. *Int. Herald Tribune* **1**, 21–25 (2008)
- Guo, Z., Feng, Y.: Modeling of the impact of the financial crisis and china's accession to WTO on china's exports to Germany. *Econ. Model.* **31**, 474–483 (2013)
- Liu, F., Murphy, J.: A qualitative study of Chinese wine consumption and purchasing implications for Australia wines. *Int. J. Wine Bus. Res.* **19**, 98–113 (2007)
- Sun, B.B.: National Wine Market People's Republic of China. U.S. Department of Agriculture, Foreign Agricultural Service. Gain Report Number CH9808 (2009)
- Tyszynski, H.: World trade in manufactured commodities, 1899–1955. *Manchester Sch.* **19**(3), 272–304 (1951)



Three - Dimensional Visualization of Soil Nutrient Evolution in Maize Precision Operation Area Based on ArcGIS

Enze Xiao, Guifen Chen^(✉), Shan Zhao, and Siwei Fu

College of Information and Technology Science, Jilin Agricultural University,
Changchun 130118, Jilin, China
350101994@qq.com, guifchen@163.com

Abstract. With the development of 3D GIS technology, the application of 3D GIS in agriculture has become a hotspot in agricultural information technology research. A total of 109 soil samples were collected from the soil of Jilin Province Yushu City Gongpeng Town No. 13 Village No. 7 test area. Three - dimensional visualization of soil nutrient evolution in maize precise operation area was carried out by using ArcGIS technology. Firstly, the Kriging optimal interpolation method was used to calculate the sampling points of soil nutrient space in the field of maize test field. Then three-dimensional spatial map of soil available phosphorus, available potassium available nitrogen and other nutrient contents during the period from 2005 to 2009 were established by using the spatial analysis technique of 3D GIS. By comparing its three-dimensional thematic map, analyze trends in the evolution of its soil fertility characteristics. The results showed that the difference of soil fertility was gentle after four years of variable fertilization, and the effect of precision fertilization was verified.

Keywords: Soil nutrient · 3D GIS · Variable fertilization
Kriging interpolation method

1 Introduction

With the development of computer science and 3D simulation technology, the development and application of 3D GIS are becoming more and more mature. 3D GIS can truly perceive the objective world, present the spatial geography phenomenon to the user, and carry on the three-dimensional spatial analysis operation to the space object. However, the current three-dimensional GIS in the field of agricultural applications less [1]. Therefore, this study in the national “863” project demonstration base in Yushu City Gongpeng Town No. 13 Village No. 7 test area by 40 m * 40 m grid sampling. The soil nutrient content was measured and the characteristics of soil nutrient evolution were discussed by using the three-dimensional GIS spatial analysis technique. The spatial variation of soil nutrient after precision fertilization was analyzed and analyzed, which provided a reliable basis for the division of farmland precision management area and Implementation of Precise Operation of Corn [2].

2 Materials and Methods

2.1 Overview of the Study Area

The study area is the experimental field of the NO. 13th village of Gongpeng Town, Yushu City, Jilin Province. It is located in the eastern part of Jilin Province and is a semi-humid temperate continental monsoon climate. It is characterized by four distinct seasons, winter long summer short, annual precipitation in the 500–600 mm, the vast majority of concentrated in the warm season, accounting for about 90% of annual precipitation, the annual average temperature of 4.6–5.6 °C. Soil type is a typical black soil, the main crop is corn and soybeans, etc. It is an important commodity grain base in Jilin Province [3, 4].

In the national “863” project “Research and Application of Corn Precision Operation System” and the national Spark plan “Integration and Demonstration of Precision Training Technology of Corn Based on Internet of Things and demonstration of” the strong support of the project in Yushu City Gongpeng Town No.13 Village continuous four years of variable fertilization operations, the accumulation of a large number of soil nutrient space data. Therefore, this article selected the Yushu City Gongpeng Town No.13 Village No. 7 plots were experimented and research. The total area of the test field is about 375 mu, and the grid size is set to A1~L11 as the sampling point [5]. We selected the three kinds of nutrient data of available phosphorus, available nitrogen and available potassium respectively, and the application of the algorithm for four years of continuous variable fertilization from 2005 (before variable fertilization) to 2009 on the Yushu City Gongpeng Town No. 13 Village No. 7 plots.

2.2 Data Collection

Application of GPS (Global Satellite Differential Positioning System) device for precise positioning, the use of ArcGIS software to produce the soil grid sampling map, sample distribution shown in Fig. 1.

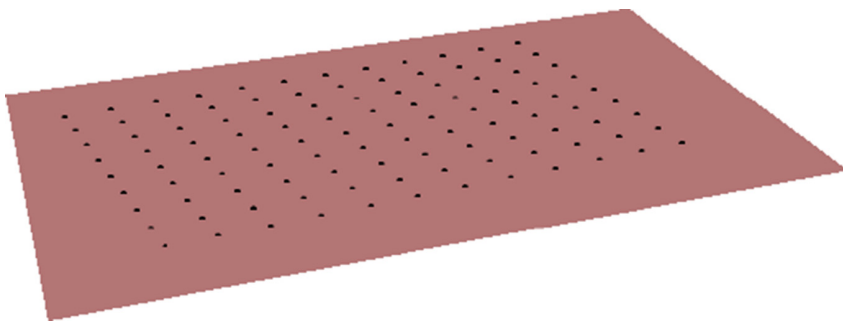


Fig. 1. Sampling grid diagram

2.3 Research Methods

In this paper, the Kriging optimal interpolation method was used to calculate the sampling points of soil nutrient space in the field of maize experiment field. On this basis, the three-dimensional visualization of soil nutrient multidimensional spatial data was realized by regular body element model. Through the three-dimensional Kriging interpolation algorithm, the original data contained in the spatial distribution of features without significant loss of the situation first passed to the estimated grid points other than the unknown data, so that the structure of the three-dimensional space model more realistic real soil environment. The three-dimensional Kriging interpolation method is essentially an improved score for the inverse distance weighting method, but it is still a linear interpolation method [6]. The principle of Kriging interpolation is that the attribute $Z(x)$ at the point $X_i \in A$ ($i = 1, 2, \dots, n$) is $Z(X_i)$, the interpolated point $X_0 \in A(X_0)$, the Kriging interpolation result $Z^*(X_0)$ is the weighted sum of the known sampling point attribute values $Z(X_i)$ ($i = 1, 2, \dots, n$).

$$Z^*(X_0) = \sum \lambda_i Z(X_i) \tag{1}$$

(1) where λ_i is the weight coefficient of the attribute value to be determined. There is a certain correlation between $Z(X_i)$, which is related to the distance, but also to its relative direction change. Thus, the three-dimensional Kriging method refers to the object of study as a regionally controllable amount of change. We obtain the matrix of coefficient coefficients of the attribute value Kriging by using the spherical model, and then determine the augmented matrix for the spatial position of each unknown point. We obtain the weight coefficient value by solving the Kriging equation group, and then we can get each. The estimated value of the attribute value and the estimated variance of the attribute value.

2.4 3D GIS Spatial Analysis Technique

2.4.1 Information Acquisition

The spatial data of sampling points in 2005, 2007 and 2009 were obtained by GPS respectively and the data of the soil samples of the sampling points were obtained as shown in Table 1 (Tables 2 and 3).

Table 1. Data about YuShu city and GongPeng town in the year of 2005

Soil number	N	P2O5	K	X	Y
7-A1	186.82	16.44	138.00	126.316244	45.0033416
7-A2	166.66	10.07	130.00	126.316128	45.0036914
7-A3	182.11	11.77	120.00	126.316013	45.0040413
7-B1	137.76	20.68	130.00	126.316738	45.0034264
7-B2	135.07	12.40	120.00	126.316622	45.0037763
7-B3	145.82	17.71	114.00	126.316506	45.0041262
7-C1	114.91	6.04	123.00	126.317232	45.0035113
7-C2	174.05	8.80	108.00	126.317116	45.0038612
7-C3	137.76	11.56	108.00	126.317566	45.0042115
7-D1	180.77	9.22	113.00	126.317726	45.0035962
7-D2	151.20	10.07	102.00	126.31761	45.0039461
7-D3	134.40	7.73	122.00	126.317494	45.0042959

Table 2. Data about YuShu city and GongPeng town in the year of 2007

Soil number	N	P2O5	K	X	Y
7-A1	124.85	8.04	64	126.316244	45.0033416
7-A2	137.34	9.99	80	126.316128	45.0036914
7-A3	131.09	10.23	75	126.316013	45.0040413
7-B1	115.49	13.16	100	126.316738	45.0034264
7-B2	106.12	10.72	90	126.316622	45.0037763
7-B3	115.49	14.86	80	126.316506	45.0041262
7-C1	121.73	9.50	62	126.317232	45.0035113
7-C2	109.25	11.70	64	126.317116	45.0038612
7-C3	127.97	8.28	99	126.317	45.004211
7-D1	152.94	26.32	72	126.317726	45.0035962
7-D2	127.97	9.50	80	126.31761	45.0039461
7-D3	118.61	30.95	70	126.317494	45.0042959

Table 3. Data about YuShu city and GongPeng town in the year of 2009

Soil number	N	P2O5	K	X	Y
7-A1	139.55	9.93	110	126.316244	45.0033416
7-A2	137.06	14.54	101	126.316128	45.0036914
7-A3	127.72	18.71	110	126.316013	45.0040413
7-B1	138.31	14.76	130	126.316738	45.0034264
7-B2	139.31	17.48	134	126.316622	45.0037763
7-B3	133.95	34.31	130	126.316506	45.0041262
7-C1	152.64	41.12	101	126.317232	45.0035113
7-C2	132.08	38.26	125	126.317116	45.0038612
7-C3	149.52	41.12	110	126.317	45.004211
7-D1	137.06	21.57	132	126.317726	45.0035962
7-D2	130.21	11.90	148	126.31761	45.0039461
7-D3	133.95	20.47	150	126.317494	45.0042959

2.4.2 ArcScene Three-Dimensional Model of the Establishment

Firstly, the attribute information of available phosphorus, available nitrogen and available potassium in the soil of Gongpeng Town in Yushu City of Jilin Province in 2005, 2007 and 2009 were transformed into spatial information. Then, the Kriging interpolation method is used to calculate the element values of the points in the three-dimensional space in the region. On the basis of this, the 3D visualization of soil element data is realized by ArcScene.

- (1) First open the ArcScene module, the ArcMap in the two-dimensional data (Fig. 2) into the ArcScene, while loading DEM data (Fig. 3).

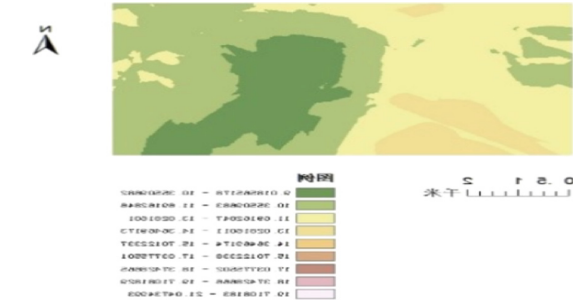


Fig. 2. 2D spatial variation of available phosphorus in 2005

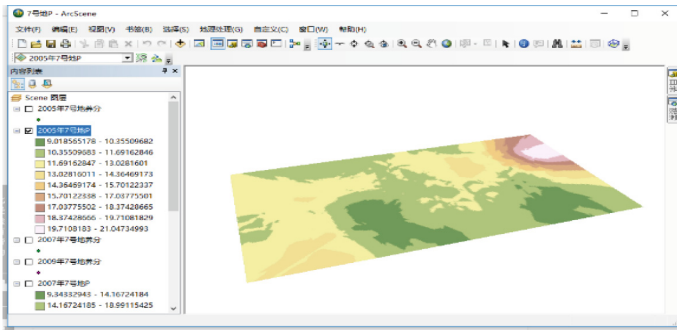


Fig. 3. Two-dimensional model after registration in ArcMap

- (2) Now, the DEM or two-dimensional. Then find the left side of the layer file, right click to open a drop down menu. Click “Properties”, a pop-up “Layer Properties” dialog box, as shown in Fig. 4.

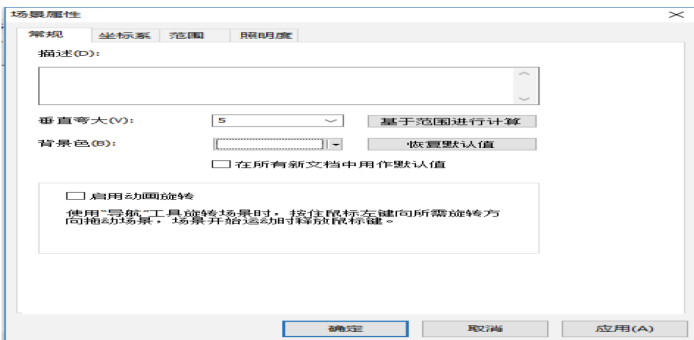


Fig. 4. Layer Properties

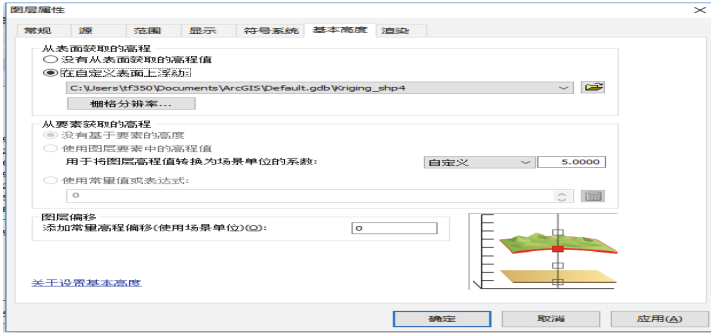


Fig. 5. Scene property

- (3) In the “Elevation from Surface”, select “Float on a custom surface” (the surface here is itself). You can find click “OK”, DEM did some changes, but this is not very obvious.
- (4) Then click on the “Scene layer”, select the “scene properties” option (Fig. 5), opened a “scene properties” menu. Here you can adjust the value of “vertical exaggerated” and set it to 5. Now you can see, the DEM’s three-dimensional sense has been very strong.

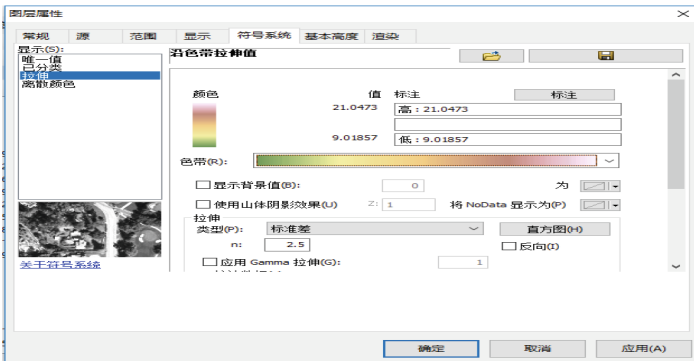


Fig. 6. Stretch

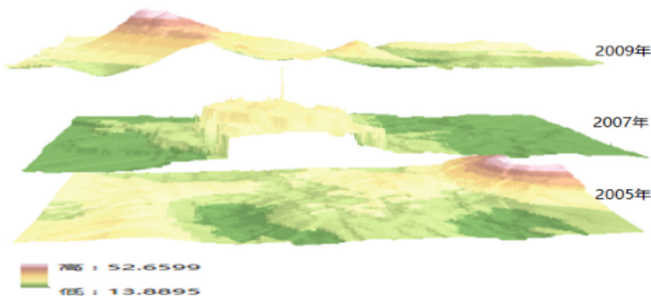


Fig. 7. Spatial variability of available phosphorus in 2005–2009

- (5) Change the color of the model, and then in step 2 to open the “layer properties”, the color is set to eye-catching color (Fig. 6). So that the completion of the three-dimensional model [7].

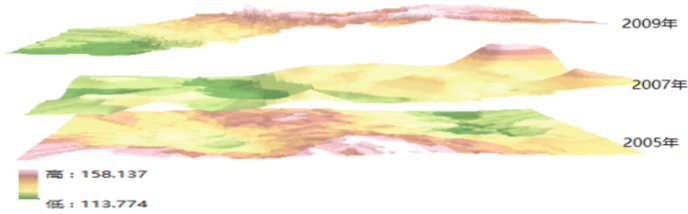


Fig. 8. Spatial variability of available Potassium in 2005–2009

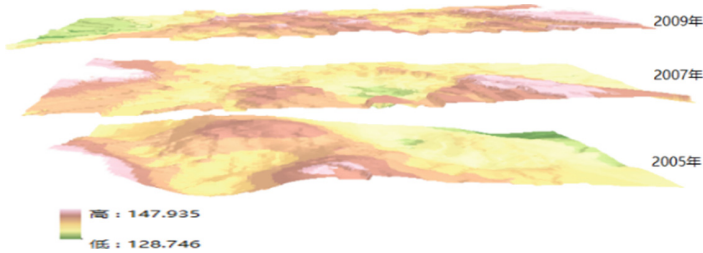


Fig. 9. Spatial variability of available nitrogen in 2005–2009

From Figs. 7, 8 and 9, it is the three-dimensional spatial distribution of available nitrogen, available phosphorus and available potassium in soil nutrients of groundwater No. 7 and the historical evolution of soil nutrient content can be analyzed according to these historical data [8].

3 The Results and Analysis

It can be seen from Figs. 7, 8 and 9 that the nutrient content of soil is gradually increased with the implementation of variable fertilization [9, 10]. The available nitrogen content increased from 121.15 mg/kg in 2005 to 139.31 mg/kg in 2009, and the available phosphorus content increased from 12.20 mg/kg in 2005 to 21.07 mg/kg in 2009, and the available potassium content increased from 113.95 mg/kg in 2005 to 137.89 mg/kg in 2009. As the amount of fertilizer to phosphate-based, so in the individual years of available nitrogen and available potassium content is not much change. At the same time, with the implementation of variable fertilization techniques, the difference of soil available nutrient content in different years was gradually reduced, which was probably due to the slow release of soil available phosphorus and available potassium in soil. The results show that the implementation of variable fertilization technology, while improving the soil fertility, but also promote the soil fertility balance, is conducive to the correct evaluation of soil fertility changes.

4 Conclusion

- (1) 3D GIS (Figs. 7, 8 and 9) can show more information than the two-dimensional spatial variation map (Fig. 2), and the spatial variation of soil available nutrient is more clear, Intuitive and true.
- (2) The high degree of data change in the three-dimensional spatial variation map can fully prove the significant effect of variable fertilization in 2005 and 2009, which is beneficial to the correct evaluation of soil fertility change.
- (3) Three-dimensional visualization technology can not only be applied to the three-dimensional distribution of soil nutrient spatial distribution, which can let users experience the spatial distribution characteristics of real soil nutrient, which is beneficial to soil fertility analysis and evaluation, but also the soil nutrient three-dimensional spatial variation map for any mobile, rotation, split and extraction operations. The process and results of variable fertilization are tested and forecasted, which provides an objective, image and reliable auxiliary decision tool.

Acknowledgments. This work was funded by the China Spark Program. 2015GA66004. “Integration and demonstration of corn precise operation technology based on Internet of things”.

Project Funding. The national spark program project: Precise operation technology integration and demonstration of corn (No. 2015GA660004).

References

1. Wang, X., Wu, D., Wang, Z.: Study on dynamic monitoring of basic farmland based on GPS and GIS technology. *J. Urban Surv.* **05**, 13–15 (2013)
2. Wang, H., Li, D., Hou, Z., Lu, X.: Spatial and temporal variability of soil nutrients in farmland based on GIS. *Xinjiang Agric. Sci.* **10**, 1872–1878 (2013)
3. Zhao, Y., Chen, G., Wang, Y.: Study on spatial variability of soil nutrients based on GIS. *Northwest Agric. Sci.* **6**, 195–198 (2005)
4. Jiang, J.: Based on the spatial fuzzy clustering of visual variable fertilization decision-making system. Jilin Agricultural University (2011)
5. Zhao, Y., Wang, Y., Han, H., Chen, G.: Spatial variation of soil nutrients in typical black soil region of Jilin province. *China Agric. Mechanization* **2**, 72–75 (2012)
6. Jiang, J., Chen, G.: Study and realization of three-dimensional visualization of soil nutrients based on VTK. *Agric. Netw. Inf.* **03**, 10–13 (2011)
7. Qin, L.P.: ArcScene campus three-dimensional scene of the establishment. *Chin. Names* **06**, 78–79 (2014)
8. Lu, X., Ma, W., Wei, X.: Spatial variability of soil fertility in agricultural science and technology demonstration park supported by GIS technology. *J. Zhejiang Agric. Sci.* **03**, 3–6 (2004)
9. Chen, H., Cao, L., Chen, G.: Study and application of temporal and spatial variability of soil fertility. *J. Chin. Soc. Agric. Mechanization* **04**, 268–273 (2014)
10. Hu, S., Li, K.: Three-dimensional GIS key technology research. *Geospat. Inf.* **03**, 9–12 (2008)



Characteristics of the Warming Trend During Winter Wheat Growing Seasons in Jiangsu Province of China

Xiangying Xu^{1,2}, Xinkai Zhu¹, Wenshan Guo^{1(✉)}, Chunyan Li¹,
and Jinfeng Ding¹

¹ Jiangsu Provincial Key Lab of Crop Genetics and Physiology/Wheat Research Institute, Yangzhou University, Yangzhou 225009, China
{xuxy, xkzhu, guows, licy, jfdin}@yzu.edu.cn

² Information and Engineering College, Yangzhou University, Yangzhou, China

Abstract. Global warming has great influences on crop yields. However, several researchers have concluded that global warming has taken a “hiatus” in recent years. Here, we hope to identify the temperature trends of the winter wheat growing seasons and quantitatively estimate the effects of temperature variations on wheat yields. We carry out trend analysis on daily maximum (Tmax) and minimum temperatures (Tmin) from 1980 to 2014 in Jiangsu Province of China. The results indicate there are increasing trends for both Tmax and Tmin during 35 years, but no significant trends in the years after 2000. In addition, the increasing rates of the Tmin are larger than those of Tmax over the 35 years within all stations and all growing stages, which suggests that winter wheat is exposed to asymmetrical warming. The results of correlation analysis and regression analysis reveal that increases in Tmin have significant adverse effects on wheat yields.

Keywords: Winter wheat · Yield · Asymmetric warming

1 Introduction

Global warming has received much attention in public and scientific fields. Researchers have found increases in average temperatures of the land surface, and that the minimum (mostly nighttime) temperatures, Tmin, and the maximum (mostly daytime) temperatures, Tmax, have increased asymmetrically during the past decades [1, 2]. Asymmetric warming, which means the rate at which Tmin increases is larger than the rate at which Tmax increases, has been confirmed in most parts of the world [3–5]. The reason for this may involve a variety of factors, such as changes in cloud cover and urban growth. However, as described in IPCC (the Intergovernmental Panel on Climate Change) Fifth Assessment Report, there has been a slowdown in the increasing trend of global temperatures since the end of the last century, which was termed as a “hiatus” [6]. Several recent modeling studies have shown that the reason for this anomaly may be related to a La Niña-like cooling, volcanic eruptions, or the strengthening Pacific trade winds over the past twenty years [7–10]. Nevertheless, some other studies do not agree

with the point that a “hiatus” was appeared in the global warming trend [11, 12]. They believe that short-term variations do not change the ongoing global warming.

Despite the different opinions about the global warming trend, most scholars generally share similar views about the threat of increasing temperatures to crop production. Many studies have been carried out to reveal the impacts of global warming on crop production, especially the yield and quality formation, with simulated crop models and field experiments [13–17]. Scholars found that the global long-term warming trend had changed crop production, including shortened growing periods and shifting planting boundaries. However, most of the simulation models used in recent studies are less accurate at higher temperatures than normal ones [18]. Further, the field experiments with artificial heating have limitations in observing the long-term temperature trends and have difficulties detecting long-term crop responses to temperature. Therefore, in this study, we resorted to statistical methods and used observation data to investigate the effects of temperature on crop yields.

Jiangsu is a major province of agriculture in China, and it has a dense population. Winter wheat is a staple crop in Jiangsu. Wheat production has an important effect on the livelihood of the people and the provincial economy. However, the province is situated in a transition zone between warm temperate zones to subtropical zones. Extreme climatic events, including extreme temperatures, take place with high frequency in Jiangsu Province. Although the authors of several studies have shown that Jiangsu became warming obviously in the past decades [16, 25, 29], few of them reveal the warming trend of winter wheat growing seasons as well as the quantitative estimation of wheat yields variations in the warming circumstance. Therefore, in this study, the objectives are to analyze the temperature evolution of wheat growing seasons during the past 35 years in Jiangsu and quantify the wheat yield responses to temperatures to help farmers cope with future climatic changes and ensure there is a reliable food supply in this area.

2 Materials and Methods

2.1 Data

Daily temperature data from 1979 to 2014 of four meteorological stations in Jiangsu Province was obtained from the China Meteorological Administration [19]. To analyze the temperature evolution of winter wheat growing seasons, we divided the whole growing season into four stages according to the periods mentioned in the main crop growth period database of the National Agricultural Scientific Data Sharing Center [20]. The four stages are: seedling stage (S1), overwintering stage (S2), reviving to anthesis stage (S3), post-anthesis stage (S4). The locations and wheat growing seasons of the four stations are shown in Table 1. The yearly yields per hectare of the four stations during 1980–2014 were obtained from the local statistical yearbooks.

Table 1. Locations and growing seasons of four meteorological stations in Jiangsu Province

Stations	Latitude	Longitude	S1	S2	S3	S4
Ganyu	34° 30'N	119° 04'E	15 th Oct. ~ 25 th Dec.	26 th Dec. ~ 25 th Feb.	26 th Feb. ~ 25 th Apr.	26 th Apr. ~ 2 nd Jun.
Xuzhou	34° 10'N	117° 05'E				
Dongtai	32° 31'N	120° 11'E	25 th Oct. ~ 5 th Jan.	6 th Jan. ~ 20 th Feb.	21 th Feb. ~ 20 th Apr.	21 th Apr. ~ 28 th May
Nanjing	32° 00'N	118° 29'E				

2.2 Mann-Kendall Test for Temperature Trend Analysis

The nonparametric Mann-Kendall test was used in this study for the trend analysis of temperatures during winter wheat growing seasons. It is a rank-based testing method recommended by WMO (the World Meteorological Organization) and is widely used in meteorology, hydrology, and other fields [21]. Because temperature data does not always follow normal distribution, like most meteorological data, it is better to choose a nonparametric test method than a parameter test to avoid using the parameters of population distributions. The merit of this method is that the data need not to obey the normal distribution and it can eliminate the interference of a few outliers [22]. The calculation of Mann-Kendall test is as follows:

Suppose X is a time series $(x_1, x_2, x_3 \dots x_n)$. The original hypothesis (H_0) is that X has no significant changing trend, while the alternative hypothesis (H_1) assumes it has. Firstly, the S value is calculated thusly:

$$S = \sum_{k=1}^{n-1} \sum_{j=k+1}^n \text{sgn}(x_j - x_k) \tag{1}$$

where x_j, x_k are the values in time series X ($j > k$). The sgn is a sign function, which is calculated as follows:

$$\text{sgn}(x_j - x_k) = \begin{cases} +1, & x_j - x_k > 0 \\ 0, & x_j - x_k = 0 \\ -1, & x_j - x_k < 0 \end{cases} \tag{2}$$

When the sample length (n) is larger than 10, the statistical variable S is supposed to be approximately normal and the expectation of S is 0. The variance is calculated as follows:

$$\text{VAR}(S) = \frac{1}{18} \left[n(n-1)(2n+5) - \sum_i e_i(e_i-1)(2e_i+5) \right] \tag{3}$$

where e_i is the number of repeated variables. Then transform S to Z , which follows the standardized normal distribution.

$$Z = \begin{cases} \frac{S-1}{\sqrt{\text{VAR}(S)}}, & S > 0 \\ 0, & S = 0 \\ \frac{S+1}{\sqrt{\text{VAR}(S)}}, & S < 0 \end{cases} \quad (4)$$

When $|Z| \geq Z_{\alpha/2}$, the alternative hypothesis is accepted at the α significant level. A positive Z value indicates that sequence X has an increasing trend, while a negative one indicates that X has a decreasing trend. We use Sen’s slope to compute the value of the trends following the method described in the paper of Santos et al. [23]. The formulation of the slope is as follows:

$$\text{Slope} = \text{median}((x_j - x_k)/(j - k)) \quad (5)$$

where the notations of x_j and x_k are the same as Eq. (1). Function median is used to calculate the median.

2.3 Yield De-trending

To evaluate the yield responses to the variability of temperature, we collected data about annual wheat yields for 35 years. Benefiting from the improvements in cultivation techniques and the optimization of government policies, the yields of the four sites consistently increased in past decades. To eliminate bias caused by technological improvements, the linear trend was removed from the original yield series, and the residuals of the yields were obtained as meteorological yields [24]. The statistical analysis of wheat yield responses to temperatures was performed using the de-trended yields of four stations. The distribution of the de-trended yields was fitted with the normal distribution and passed the Kolmogorov-Smirnov (K-S) test which was used to compute a distance between the empirical and cumulative distribution function of the de-trended yield sequences [24]. The null hypothesis is that the yield residuals sequence accord with the theory distribution of normal, and the result indicates that it cannot be rejected. The frequency histogram of yield residuals is shown in Fig. 1.

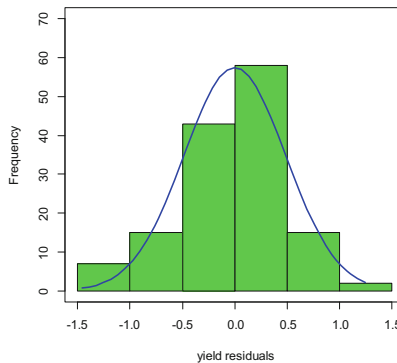


Fig. 1. Frequency histogram of yield residuals of four stations

2.4 Correlation Analysis and Regression Analysis

The Pearson coefficient was applied in this study to determine the correlation between wheat yields and growing season temperatures. The calculation was performed in R software, and the coefficient of the linear association is between -1 and $+1$.

Multivariate regression was used to estimate the impacts of changes in Tmax and Tmin on wheat yields. The formula is as follows:

$$Y = \text{const} + \alpha * \text{Tmax} + \beta * \text{Tmin} \tag{6}$$

where Y is the yield residuals. α and β are the coefficients of Tmax and Tmin.

3 Results

3.1 Temperature Trend

Temperature Trend of the Winter Wheat Growing Season. The air temperature data about the growing seasons at the four stations were computed. Trend analysis was used to detect the temperature trends from 1980 to 2014 compared to the trends in the years before and after 2000. Table 2 shows the annual changes in the Tmax, Tmin, and Tav_g (average daily temperatures) values of the four stations during wheat growing seasons by Mann-Kendall test and Sen’s slope method.

Table 2. Changes of annual average temperatures during wheat growing seasons

Periods	Stations	Trend slope (°C/year)		
		Tavg	Tmax	Tmin
1980–2014	Ganyu	0.044**	0.032*	0.057**
	Xuzhou	0.046**	0.029*	0.061**
	Dongtai	0.046**	0.044**	0.048**
	Nanjing	0.056**	0.050**	0.071**
1980–1999	Ganyu	0.075 **	0.074**	0.116**
	Xuzhou	0.048*	0.042	0.068**
	Dongtai	0.077**	0.076**	0.090**
	Nanjing	0.077**	0.077**	0.096**
2000–2014	Ganyu	-0.075	-0.022	-0.141*
	Xuzhou	-0.003	-0.003	-0.014
	Dongtai	-0.038	-0.027	-0.049
	Nanjing	-0.010	0.004	-0.017

Note: Tav_g, Tmax, and Tmin represent the average, maximum, and minimum temperatures of the day, respectively. **, * indicate trend significance at $P < 0.01, 0.05$.

The result indicates that from 1980 to 2014, the average, maximum, and minimum daily temperatures in wheat growing seasons significantly increased. Compared to the other three stations, the southern station, Nanjing, has the largest slope. However, the T_{min} increased faster than the T_{max} at all four stations. This result is similar to the conclusion drawn by Peng et al. [26] in their study of rice yields at latitude $14^{\circ} 11' N$, longitude $121^{\circ} 15' E$. When we divide the period of 35 years into two stages (the last 20 years and the first 15 years of the 20th and 21st century), entirely different trends are revealed. In the years before 2000, the temperature significantly increased at most of the stations, and the T_{min} increased faster than T_{avg} and T_{max} . On the contrary, in the years after 2000, the variations of the temperatures are not significant in most stations and the signs of the slope are negative, indicating that the temperatures have downward trends. These anomalies in the winter wheat growing seasons are similar to the temperature anomalies mentioned as the “hiatus” in the global warming of this century in other studies. Nevertheless, whether the changes in the trends are short-term fluctuations is still unknown.

Temperature Trends of Four Growing Stages. Because temperature variations in different growing stages may lead to different effects on wheat yields, we analyzed the temperature trends in four stages. The results are shown in Table 3. Because the average temperature is between the maximum and minimum temperatures and it evolved similarly as them, it was not taken into consideration.

Different trends were observed in the three study periods and four growing stages. From 1980 to 2014, the temperatures in the reviving and jointing stages (S3) and post-anthesis stages (S4) significantly increased. Similarly, T_{min} increased faster than T_{max} in most cases, except at Dongtai and Nanjing during S3. Nevertheless, during the 20 years before 2000, temperatures of overwintering stages (S2) increased more pronouncedly than in other stages. Furthermore, during the 15 years after 2000, there are hardly any obvious trends in the four stages at all stations, except Ganyu in S3.

Figure 2 illustrates the temperature trends over 35 years. It shows that during S3 and S4, T_{max} and T_{min} were generally higher in this century than in the last century, except for several low points in the trends, among which the most obvious one is the anomaly around 2010. In contrast, the peak values of the trends do not show obvious decreases compared to the temperatures in the years before 2000. This may confirm the hypothesis that global warming in the 21st century is expected to resume once the anomalous hiatus ends [7].

3.2 Correlation Between Yield and Temperature

The correlation between winter wheat yield and temperature was analyzed by using the Pearson correlation coefficient and regression analysis. We used yield and temperature residuals to calculate the Pearson coefficients for all 35 years. The result indicates that average temperature of the whole growing season has a significantly negative influence on wheat yields ($r = -0.24$). T_{min} has a very significant ($P < 0.01$) influence on wheat yields ($r = -0.30$) while T_{max} has a less pronounced correlation with wheat yields. In addition, the correlations between yield and T_{max} and T_{min} during the four

Table 3. Changes in the maximum and minimum temperatures during the four growing stages

Periods	Stations		Trend slope (°C/year)				
			S1	S2	S3	S4	
1980–2014	Ganyu	Tmax	0.014	0.024	0.055*	0.046	
		Tmin	0.049*	0.048	0.063**	0.056**	
	Xuzhou	Tmax	0.010	0.029	0.055*	0.025	
		Tmin	0.047**	0.057**	0.077**	0.066**	
	Dongtai	Tmax	0.018	0.033	0.096**	0.055*	
		Tmin	0.039*	0.037	0.060**	0.052**	
	Nanjing	Tmax	0.017	0.026	0.116 **	0.054*	
		Tmin	0.082**	0.066**	0.083**	0.068**	
	1980–1999	Ganyu	Tmax	0.058	0.126**	0.022	0.028
			Tmin	0.116*	0.153**	0.110**	0.077*
		Xuzhou	Tmax	0.046	0.114*	-0.003	-0.044
			Tmin	0.057	0.124**	0.084*	0.031
Dongtai		Tmax	0.068	0.072**	0.085*	0.040	
		Tmin	0.092*	0.093*	0.086*	0.093*	
Nanjing		Tmax	0.057	0.090*	0.075	0.015	
		Tmin	0.089*	0.095*	0.087	0.081**	
2000–2014		Ganyu	Tmax	-0.003	-0.019	-0.107	0.088
			Tmin	-0.126	-0.153	-0.176*	-0.037
		Xuzhou	Tmax	0.053	-0.032	-0.102	0.041
			Tmin	-0.019	-0.012	-0.049	0.043
	Dongtai	Tmax	0.022	0.001	-0.037	0.060	
		Tmin	-0.086	-0.060	-0.060	0.034	
	Nanjing	Tmax	0.024	-0.004	-0.036	0.058	
		Tmin	0.010	-0.028	-0.020	0.016	

Note: S1, S2, S3, and S4 represent seedling stage, overwintering stage, reviving and jointing stage, and post-anthesis stage, respectively. **, * indicate a significant trends at $P < 0.01$, 0.05 , respectively.

growing stages have been computed (see Table 4). Besides S4, the Tmin values of the other three stages have significant negative relationships with wheat yields from the four stations.

3.3 Yield Responses to Temperature

The regression model (Formula 7) shows that yield residuals are significantly affected by Tmin ($P < 0.001$) but not significantly affected by Tmax. This result indicates that the increasing minimum temperatures of the wheat growing season have more adverse effects on the yield. A 0.1°C increase in minimum temperature will cause wheat yield losses of 28.5 kg/ha.

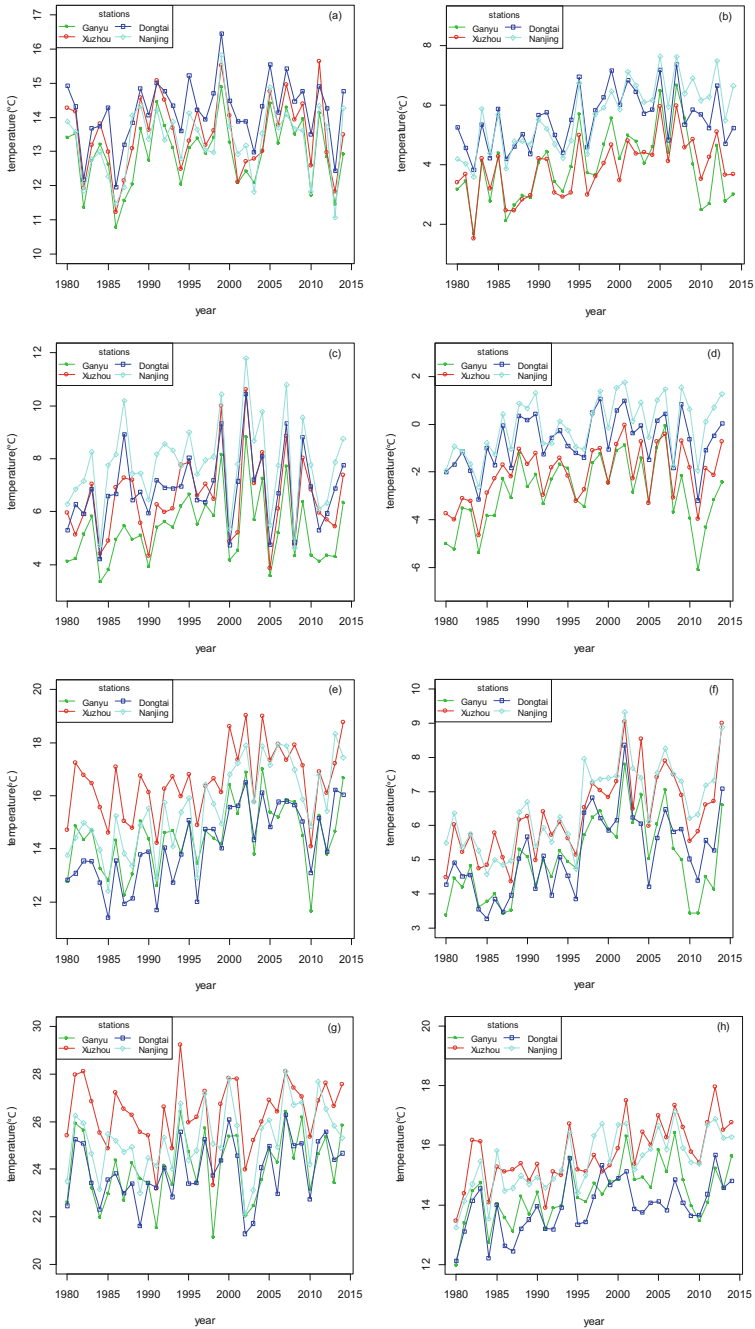


Fig. 2. The maximum and minimum temperatures in seedling stage (S1), overwintering stage (S2), reviving and jointing stage (S3), and post-anthesis stage (S4). Note: (a), (c), (e), and (g) are the maximum temperatures of the four stations during S1, S2, S3, and S4, respectively. (b), (d), (f), and (h) are the minimum temperatures of the four stations during S1, S2, S3, and S4, respectively.

Table 4. The Pearson correlation coefficients of wheat yields and temperatures over 35 years

Stage	Tmax	Tmin
Whole growing season	-0.12	-0.30***
S1	-0.12	-0.20*
S2	-0.13	-0.28**
S3	-0.18	-0.27**
S4	0.21*	-0.09

Note: S1, S2, S3, and S4 represent seedling stage, overwintering stage, reviving and jointing stage, and post-anthesis stage, respectively. ***, ** and * indicate correlation significance of $P < 0.001$, 0.01, and 0.05, respectively.

$$Y = 0.091 * Tmax - 0.285 * Tmin \tag{7}$$

Table 5 reveals the quantitative yield responses to temperature of the four growing stages. We can conclude that the Tmin of each growing stage is significantly related to wheat yields and Tmin increases would lead to yield losses. Moreover, the Tmin in S4 has the biggest influence according to the coefficients. This may be due to the fact that the late growth stage of winter wheat is more important in yield formation. Interestingly, only in S4 was Tmax found to have a significant positive correlation with wheat yields. This implies that the effects of temperatures on wheat yields are unbalanced for day and night. Zhang et al. [27] report that low night temperatures can significantly prolong the relative steady phase (RSP) of chlorophyll content and photosynthetic active duration (PAD) and, thereby, increase the leaf source capacity and wheat yields [27]. Zhang et al. [28] also report that nocturnal warming significantly reduces soil microbial biomass carbon and nitrogen content and microbial respiration rate. Therefore, it affects soil nutrient supply and winter wheat growth [28]. For these reasons, the minimum temperatures, which have obviously increased in recent decades, deserve much attention due to their adverse effects. The Tmax of the post-anthesis stage, which does not increase as significantly as Tmin, has positive effects on wheat yield improvement because it promotes photosynthesis, increasing the enzyme activity of the crop and enlarging the diurnal temperature range (DTR) [16, 29]. The results of the regression analysis suggest that the Tmax and Tmin of each growing stage account for only 2.8% to 9.3% of the yield variations. It appears that the asymmetric warming during the past 35 years did not seriously affect the wheat yields in Jiangsu Province. A similar conclusion was obtained by Hou et al. [30] in the study of the North China Plain (NCP) [30].

Table 5. The regression analysis of wheat yield residuals

Stage		Tmax	Tmin	R ²
W	Coef.	0.091	-0.285***	0.080
	p-value	0.310	0.0006	0.001
S1	Coef.	-0.017	-0.105*	0.028
	p-value	0.715	0.047	0.051
S2	Coef.	0.031	-0.147**	0.070
	p-value	0.399	0.002	0.003
S3	Coef.	0.004	-0.144*	0.061
	p-value	0.935	0.014	0.005
S4	Coef.	0.140***	-0.196**	0.093
	p-value	0.0002	0.003	0.0004

Note: W, S1, S2, S3, and S4 represent the whole growing season, seedling stage, overwintering stage, reviving and jointing stage, and post-anthesis stage, respectively. Coef. represents coefficient. *, ** and *** indicate statistical significance of $P < 0.05$, 0.01, and 0.001.

4 Discussion and Conclusions

Besides the impacts of temperature, winter wheat yields are influenced by many other meteorological factors, such as precipitation, solar radiation, and wind speed. However, a comparison of these other meteorological factors shows that temperature has the most obvious changing trend in Jiangsu, which may change precipitation frequency and intensity according to the results of studies on other areas in Asia [31]. Therefore, temperature variations have considerable influences on wheat production.

In this study, the Tmax and Tmin changes in the winter wheat growing seasons display a significantly asymmetrical warming trend in Jiangsu Province. The increasing rate of Tmin is obviously larger than that of Tmax over the 35 years examined in this study. We cannot confirm the existences of a global warming “hiatus” because there are no significant increasing or decreasing trends for both Tmax and Tmin during all growing stages of 2000–2014. The temperatures of the four growing stages display similar asymmetrical trends in Tmax and Tmin. Moreover, the Tmin values of the pre-anthesis stages have negative influences on wheat yields, while the Tmax values of the post-anthesis stages have positive influences on wheat yields. The regression model indicates that Tmin has had more adverse influences on wheat yields than Tmax, regardless of growth stage, during the past 35 years. Generally, according to our study, the impacts of temperature increase on wheat yields over the past three decades are not serious. This result partly reflects the adaptability of crop production in Jiangsu Province.

The present research is conducted on four stations. The next step of our research is to collect observations from a dense grid of stations in Jiangsu and obtain accurate results that cover the whole province.

Acknowledgments. This work was supported by the National Key Research and Development Program of China (2016YFD0300107) and the Specialized Research Fund for the Doctoral Program of Higher Education (doctoral supervisor) (NO: 20133250110001). It was also supported by the National Natural Science Foundation of China (NO: 31401317).

References

1. Karl, T.R., Kuk, G., et al.: Global warming: evidence for asymmetric diurnal temperature change. *Geophys. Res. Lett.* **18**(12), 2253–2256 (1991)
2. Karl, T.R., Jones, P.D., Knight, R.W., et al.: A new perspective on recent global warming: Asymmetric trends of daily maximum and minimum temperature. *Bull. Am. Meteor. Soc.* **74** (6), 1007–1023 (1993)
3. Easterling, D.R., Horton, B., Jones, P.D., et al.: Maximum and minimum temperature trends for the globe. *Science* **277**(18), 364–367 (1997)
4. Peng, S., Piao, S., et al.: Asymmetric effects of daytime and night-time warming on Northern Hemisphere vegetation. *Nature* **501**, 88–95 (2013)
5. Siddik, M.A.Z., Rahman, M.: Trend analysis of maximum, minimum, and average temperatures in Bangladesh: 1961–2008. *Theor. Appl. Climatol* **116**(3–4), 721–730 (2014)
6. Stocker, T.F., Qin, D., Plattner, G.-K., Tignor, M., Allen, S.K., et al.: IPCC, Climate Change 2013: The Physical Science Basis. Contribution of Working Group I to the Fifth Assessment Report of the Intergovernmental Panel on Climate Change. Cambridge University Press, Cambridge (2013)
7. England, M.H., McGregor, S., et al.: Recent intensification of wind-driven circulation in the Pacific and the ongoing warming hiatus. *Nat. Clim. Chang.* **4**(3), 222–227 (2014)
8. Kosaka, Y., Xie, S.-P.: Recent global-warming hiatus tied to equatorial Pacific surface cooling. *Nature* **501**, 403–407 (2013). <https://doi.org/10.1038/nature12534>
9. Santer, B.D., et al.: Volcanic contribution to decadal changes in tropospheric temperature. *Nat. Geosci.* **7**, 185–189 (2014). <https://doi.org/10.1038/ngeo2098>
10. Easterling, D.R., Wehner, M.F.: Is the climate warming or cooling? *Geophys. Res. Lett.* **36** (8), 262–275 (2009)
11. Cahill, N., Rahmstorf, S., Parnell, A.C.: Change points of global temperature. *Environ. Res. Lett.* **10**(8), S309 (2015). <https://doi.org/10.1088/1748-9326/10/8/084002>
12. Karl, T.R., Arguez, A., Huang, B., et al.: Possible artifacts of data biases in the recent global surface warming hiatus. *Science* **348**(6242), 1469 (2015)
13. Gourджи, S.M., Sibley, A.M., Lobell, D.B.: Global crop exposure to critical high temperatures in the reproductive period: historical trends and future projections. *Environ. Res. Lett.* **8**(2), 024041 (2013). <https://doi.org/10.1088/1748-9326/8/2/024041>
14. Deryng, D., Conway, D., et al.: Global crop yield response to extreme heat stress under multiple climate change futures. *Environ. Res. Lett.* **9**(3), 2033–2053 (2014)
15. Lobell, D.B., Tebaldi, C.: Getting caught with our plants down: the risks of a global crop yield slowdown from climate trends in the next two decades. *Environ. Res. Lett.* **9**(7), 74003–74010 (2014)
16. Zhao, H.: Physiological effects of post-anthesis high temperature and water stress on wheat quality formation. Nanjng Agricultural University (2006)

17. Li, K., Yang, X., et al.: The possible effects of global warming on cropping systems in china VIII—the effects of climate change on planting boundaries of different winter-spring varieties of winter wheat in China. *Sci. Agric. Sin.* **46**(8), 1583–1594 (2013). <https://doi.org/10.3864/j.issn.0578-1752.2013.08.007>
18. Asseng, S., et al.: Rising temperatures reduce global wheat production. *Nat. Clim. Chang.* **5**, 143–147 (2014). <https://doi.org/10.1038/nclimate2470>
19. National Meteorological Information Center of China Meteorological Administration. <http://data.cma.cn/site/index.html>
20. Main crop growth period database of the National Agricultural Scientific Data Sharing Center. http://old.agridata.cn/module_db/index_new.asp?Rid=A070413
21. Cao, J., et al.: Mann-Kendall examination and application in the analysis of precipitation trend. *Agric. Sci. Technol. Equip.* **179**(5) (2008). <https://doi.org/10.16313/j.cnki.nykjyzb.2008.05.008>
22. Hamed, K.H., et al.: Trend detection in hydrologic data: the Mann-Kendall trend test under the scaling hypothesis. *J. Hydrol.* **349**(3–4), 350–363 (2008)
23. Santos, M., Fragoso, M.: Precipitation variability in Northern Portugal: data homogeneity assessment and trends in extreme precipitation indices. *Atmos. Res.* **131**(5), 34–45 (2013)
24. Potopová, V., Štěpánek, P., Možný, M., Türkott, L., Soukup, J.: Performance of the standardized precipitation evapotranspiration index at various lags for agricultural drought risk assessment in the Czech Republic. *Agric. For. Meteorol.* **202**(202), 26–38 (2015)
25. Zhou, X., Gao, Q., et al.: Long term temperature trends and spatial patterns of the interdecadal variations in Jiangsu. *J. Nanjing Inst. Meteorol.* **29**(2), 196–202 (2006)
26. Peng, S., Huang, J., et al.: Rice yields decline with higher night temperature from global warming. *Proc. Natl. Acad. Sci. U.S.A.* **101**(27), 9971 (2004)
27. Zhang, R., Fang, Z.: Influence of different nighttime temperatures on the photosynthesis of the flag leaf and yield in wheat. *Acta Agron. Sin.* **20**(6), 710–715 (1994). (in Chinese)
28. Zhang, M., Han, Z., et al.: Impact of nighttime warming on soil microbial biomass carbon/nitrogen and activity in main winter wheat cropping areas in China. *Chin. J. Eco-Agric.* **20**(11), 1464–1470 (2012). (in Chinese)
29. Fan, Y.: Effects of winter and spring night warming on grain yield formation in wheat and its physiological mechanism. Nanjign Agricultural University (2015)
30. Hou, R., Zhu, O., et al.: Is the change of winter wheat yield under warming caused by shortened reproductive period? *Ecol. Evol.* **2**(12), 2999–3008 (2012)
31. Poudel, S., Shaw, R.: The relationships between climate variability and crop yield in a mountainous environment: a case study in Lamjung district. *Nepal. Climate* **4**(1), 13 (2016). <https://doi.org/10.3390/cli4010013>



Estimation of Leaf Nitrogen Concentration of Winter Wheat Using UAV-Based RGB Imagery

Qinglin Niu^{1,2}, Haikuan Feng^{2,3}, Changchun Li¹, Guijun Yang^{2,3(✉)},
Yuanyuan Fu^{2,3}, Zhenhai Li^{2,3}, and Haojie Pei^{1,2}

¹ School of Surveying and Land Information Engineering,
Henan Polytechnic University, Jiaozuo 454000, China
niuql2011@126.com, lichangchun610@126.com,
xmljphj@163.com

² Key Laboratory of Quantitative Remote Sensing in Agriculture P.R. China,
Beijing Research Center for Information Technology in Agriculture,
Beijing 100097, China
fenghaikuan123@163.com, fyy0201@163.com,
lizh323@126.com

³ National Engineering Research Center for Information Technology
in Agriculture, Beijing 100097, China
yanggj@nercita.org.cn

Abstract. Leaf nitrogen concentration (LNC) of winter wheat can reflect its nitrogen (N) status. Rapid, non-destructive and accurate monitoring of LNC of winter wheat has important practical applications in monitoring N nutrition and fertilizing management. The experimental site of winter wheat was located at Xiaotangshan National Demonstration Base of Precision Agricultural Research located in Changping District, Beijing, China. High spatial resolution digital images of the winter wheat were acquired using a low-cost unmanned aerial vehicle (UAV) with digital camera system at three key growth stages of booting, flowering and filling during April to June in 2015. Firstly, the acquired UAV digital images were mosaicked to generate a Digital Orthophoto Map (DOM) of the entire experimental site and 15 digital image variables were constructed. Then, based on the ground measured data onto LNC and digital image variables derived from the DOM for 48 sampling plots of winter wheat, linear and stepwise regression models were constructed for estimating LNC. Finally, the optimum model for estimating LNC was screened out by comprehensively considering the coefficient of determination (R^2), the root mean square error ($RMSE$), the normalized root mean square error ($nRMSE$) and the simplicity of model calibrating and validating. The experimental results showed that the linear regression model of r/b that was one of the digital image variables for estimating LNC had the best accuracy with the model's calibration and validation of R^2 , $RMSE$ and $nRMSE$ were 0.76, 0.40, 11.97% and 0.69, 0.43, 13.02%, respectively. The results suggest that it is feasible to estimate LNC of winter wheat based on the DOM acquired by UAV remote sensing platform carrying a low-cost, high-resolution digital camera, which can rapidly and non-destructively obtains the LNC of winter wheat experiment site and provide a quick and low-cost method for monitoring N nutrition and fertilizing management.

Keywords: Winter wheat · Leaf nitrogen concentration (LNC)
Remote sensing · Unmanned aerial vehicle (UAV) · Digital imagery
High-resolution

1 Introduction

Nitrogen (N) is one of the essential nutrient elements for crop growth and is closely related to the growth status, photosynthesis and yield of crops [1, 2]. It is difficult to timely and appropriately compute the amount of fertilizer that crops need and to avoid excess fertilization according to the demand for crop growth. In addition, it has become an important issue to minimize the pollution of fertilizer to the environment while maintaining the high crop yield at the same time to achieve sustainable development [3]. Leaf nitrogen concentration (LNC) is an important indicator of the crop N nutrition. It is an important guiding significance of crop N nutrition monitoring and fertilizer management to rapidly, non-destructively, accurately and low-costly estimate crop LNC using remote sensing technology [4–6].

Agriculture is one of the most important and widely used fields of remote sensing technology. Remote sensing technology has the characteristics of rapid, non-destructive and high-throughput acquisition of ground feature information and is developing towards the direction of quantification and high precision [7]. Satellite, aviation, and proximal remote sensing are limited in the application of precision agriculture because of their limitations [4, 8, 9]. Unmanned aerial vehicle (UAV) remote sensing has the advantages of easy platform construction, low operation and maintenance cost, flexible mobility, controllable flight height and short operation cycle [5, 10–12].

Multispectral, hyperspectral or light detection and ranging (LIDAR) sensors are relatively heavy, which greatly reduces the flight time of UAV when mounted on, and these sensors are more expensive than digital cameras, and the subsequent processing of data is complex, which seriously hinders their extensive applications in precision agriculture [10, 13–16]. With the rapid development of UAV and sensor technology, UAV platforms and digital cameras are developed toward the mass consumption levels. They have the characteristics of low-price, miniaturization, light, and intelligence, and the spatial resolution of digital cameras is becoming higher and higher. The above reasons make it possible for a UAV to be mounted with digital cameras as a low-cost remote sensing data acquisition platform, which has become a hot spot of practical research in precision agriculture [5, 10, 17–20].

At present, UAV remote sensing platform is equipped with low-cost and high-resolution digital cameras, which is used to estimate crop phenotypic parameters. The parameters are mainly about the morphological structure parameters. However, the crop physiological and biochemical parameters are few. In this study, high-resolution digital camera images were acquired and used to generate a DOM of the research area and corresponding LNC values of 48 sampling plots were measured synchronously. Linear and stepwise regression analysis models are constructed to estimate LNC of winter wheat using digital image variables from the DOM and measured LNC. In the end, the optimum model for estimating LNC was screened out by comprehensively

considering the coefficient of determination (R^2), root mean square error ($RMSE$), normalized root mean square error ($nRMSE$) and the simplicity of model calibrating and validating. This study proves that digital camera mounted on UAV remote sensing system can be applied to winter wheat to rapidly, non-destructively monitor and evaluate N nutrition and yield potential, which provides a rapid, low-cost and high efficient technical mean for N management and growth monitoring of winter wheat.

2 Materials and Methods

2.1 Experiment Design

The experiment was carried out from September 2014 to June 2015 at Xiaotangshan National Demonstration Base of Precision Agricultural Research (40°10'N, 116°26'E) in Changping District, Beijing, China. It has a flat terrain with an altitude of 30 m above sea level and features a typical semi-humid continental monsoon climate. The soil type is fluvio-aquatic soil and the previous crop was maize. The winter wheat varieties were “zhongmai175 (ZM175)” and “jing 9843 (J9843)”.

The size of winter wheat field was 85 m × 32 m. There were 48 sampling plots, 16 treatments, three replicates and orthogonal test. The area of each plot was 48 m² (6 m × 8 m), and the planting spacing was 15 cm. There were four different N level treatments, namely, 0 kg urea/mu (N1), 13 kg urea/mu (N2), 26 kg urea/mu (N3) and 39 kg urea/mu (N4). Each of the 16 plots was treated with N at four different N levels (Fig. 1).

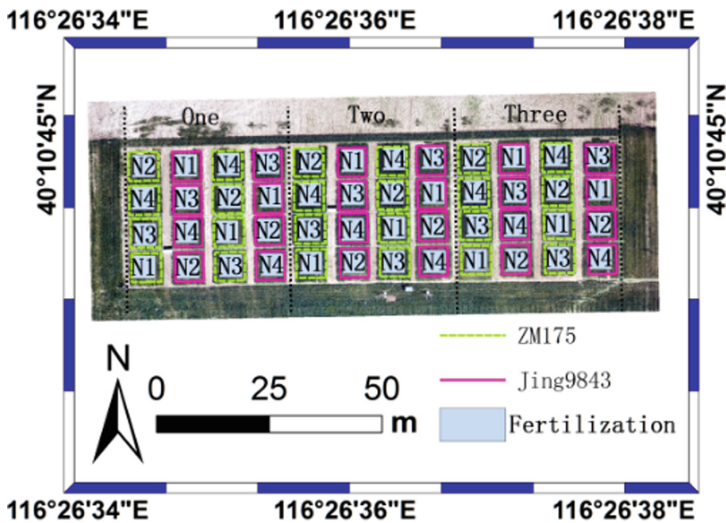


Fig. 1. Experiment design of variable rate fertilization of winter wheat

2.2 Acquisition and Preprocessing of UAV Digital Images and LNC

The winter wheat data of LNC and UAV high-resolution digital images were obtained at the booting stage (April 26, 2015), flowering stage (May 13, 2015) and filling stage (May 22, 2015). A fixed quadrat ($2 \times 0.15 \text{ m} \times 1 \text{ m}$) with group representation was selected as the sampling area for LNC measurements of every plot. In the fixed quadrat, the 20 winter wheat plants of representative were selected, and the leaves were placed in paper bags after organ separation. The picked leaves were then put into an oven with $105 \text{ }^\circ\text{C}$ for a half-hour to inactivate enzymes in plants rapidly. Next, the oven will be set at $80 \text{ }^\circ\text{C}$ for more than 48 h until the weight remained unchanged. LNC (LNC, %) was measured on crushed leaves using Kjeldahl apparatus (Buchi B-339, Sweden, FOSS). A total of 144 winter wheat samples were obtained at three key growth stages (The maximum value of LNC was 4.45%, the minimum value of LNC was 1.16%, the average value of LNC was 3.34%, the standard deviation of LNC was 0.80 and the coefficient of variation of LNC was 0.24).

The UAV remote sensing data was obtained by data acquisition platform of an eight rotors electric UAV (single arm length: 386 mm, airframe net quality: 4.2 kg, mass load: 6 kg, endurance time: 15–20 min) equipped with a high-resolution digital camera and position and orientation (POS) which aimed at acquiring the position and orientation information of digital camera. The high-resolution digital camera model was SONY Cyber-shot DSC-Q100 with the weight and size were 179 g and $62.5 \text{ mm} \times 62.5 \text{ mm} \times 55.5 \text{ mm}$; it had a 20 million pixel CMOS sensor and had a fixed focal length at 10 mm (fixed focus shooting). The high-resolution true color digital images of a spatial resolution of 0.013 m were obtained using the UAV system, which flew at the height of 50 m during 12:00–13:00 in synchronously with the ground data acquisition when the weather was clear and the solar radiation intensity was stable. The three UAV remote sensing experiments used the same design of flying routes.

The mosaic of UAV high-resolution digital images was performed with the aid of Agisoft PhotoScan software. The digital images were matched with the corresponding POS data and after photos alignment and dense cloud points building in PhotoScan. The optimized camera location parameters were estimated and sparse and dense cloud points of the experimental area were generated. A 3D polygon mesh model of experimental area was reconstructed based on the generated dense cloud points, which represented the surface geometry of winter wheat canopies. Finally, the canopy orthoimage of the winter wheat experimental area was generated and exported as TIFF format.

2.3 Digital Image Variable Selection

The average digital number (DN) values of canopies red (R), green (G) and blue (B) channels of each measured plot were extracted from canopy orthoimage of the winter wheat experimental area. The normalized red (r), green (g) and blue (b) digital image variables were calculated based on the DN values from the canopy orthoimage. The normalized formulas were as follows [21–23]:

$$r = \frac{R}{R + G + B} \quad (1)$$

$$g = \frac{G}{R + G + B} \quad (2)$$

$$b = \frac{B}{R + G + B} \quad (3)$$

Where R , G , and B were the DN values extracted from canopy orthoimage, respectively. According to the existing research results and the relationship between LNC and visible vegetation index, 12 vegetation indices within the range of visible light spectrum were selected. In this study, 15 digital image variables were selected to estimate LNC of winter wheat (Table 1).

Table 1. Digital image variables associated with LNC

Image variable	Formula	Reference	Variable encoding
r	$r = r$	✓	VI1
g	$g = g$	✓	VI2
b	$b = b$	✓	VI3
MGRVI	$MGRVI = (g^2 - r^2)/(g^2 + r^2)$	[19]	VI4
RGBVI	$RGBVI = (g^2 - b * r)/(g^2 + b * r)$	[19]	VI5
GRVI	$GRVI = (g - r)/(g + r)$	[24]	VI6
GLA	$GLA = (2 * g - r - b)/(2 * g + r + b)$	[25]	VI7
ExR	$ExR = 1.4 * r - g$	[26]	VI8
ExG	$ExG = 2 * g - r - b$	[27]	VI9
ExGR	$ExGR = ExG - 1.4 * r - g$	[26]	VI10
CIVE	$CIVE = 0.441 * r - 0.881 * g + 0.385 * b + 18.78745$	[28]	VI11
VARI	$VARI = (g - r)/(g + r - b)$	[29]	VI12
g/r	$g/r = g/r$	✓	VI13
g/b	$g/b = g/b$	✓	VI14
r/b	$r/b = r/b$	✓	VI15

Note: “✓” indicates the experience of visible vegetation parameters and r , g , and b represent normalized DN values of R , G and B channels from orthoimage.

2.4 Methods and Statistical Analysis

Firstly, the DN values of R , G and B channels were extracted based on the high-resolution digital orthoimage of winter wheat and the digital image variables were calculated. 70% of the total sample data were randomly selected as the modeling data set and the correlation between digital image variables and LNC was analyzed. Secondly, based on the result of above correlation analysis, the LNC estimation models

were constructed by methods of the linear and stepwise regression analysis. The predictive ability of the LNC estimation models was evaluated by using remaining 30% sample data (as the validation dataset) that were not involved in model calibrating.

Linear regression analysis was based on the correlation analysis between digital image variables and LNC. The estimation model of LNC was constructed according to the absolute value of correlation coefficients from large to a small order for LNC. In stepwise regression analysis, the estimation model added or removed a variable at a time when the model was built.

At the same time, variables were reevaluated, including the degree of significance of the regression coefficients and whether to delete variables based on its importance. Predictor variables might be added or deleted several times until the best model was obtained. The Akaike information criterion (AIC) took into account the statistical fitting of the model and the number of variables fitted. A model with smaller AIC values needs to be selected firstly, which shows that the model obtains sufficient fit with fewer variables.

The coefficient of determination (R^2), the root mean square error ($RMSE$) and the normalized root mean square error ($nRMSE$) were chosen as the indices to evaluate the accuracy of estimation and verification model. The larger R^2 of calibration and verification model and the smaller the corresponding $RMSE$ and $nRMSE$, the better of the predictive ability of models. The computational formulas are as follows:

$$R^2 = \frac{\sum_{i=1}^n (X_i - \bar{X})^2 (Y_i - \bar{Y})^2}{n \sum_{i=1}^n (X_i - \bar{X})^2 \sum_{i=1}^n (Y_i - \bar{Y})^2} \quad (4)$$

$$RMSE = \sqrt{\frac{\sum_{i=1}^n (Y_i - X_i)^2}{n}} \quad (5)$$

$$nRMSE = \frac{RMSE}{\bar{X}} \quad (6)$$

In the formula, X_i , \bar{X} , Y_i and \bar{Y} represent the measured values, the mean value of measured value, the estimated value and the mean value of estimated value; n represents the sample size of the model.

3 Results and Analysis

3.1 Correlation Analysis Between LNC of Winter Wheat and Digital Image Variables

70% of the sample data, which contains a total of 101 items, were randomly selected as the modeling data set. The digital image variables were constructed based on the modeling data set and the correlation between digital image variables and LNC were

calculated. The results of the correlation analysis were shown in Fig. 2. The significance test of variables was carried out by referring to the table of critical values of correlation coefficients. When the degree of freedom of variable was 99, the absolute value of the correlation coefficient was great than 0.26, reaching 0.01 of the significant level. The degree of freedom of the correlation analysis was 99 in this study and the significance of the variable reached 0.01 significant level when the absolute value of the correlation coefficient of the variable was greater than 0.26. The absolute value of the correlation coefficient between digital image variable, r/b , b , r , ExR, VARI, GRVI and g/r and MGRVI, ExGR, g/b , CIVE, g and GLA and ExG, RGBVI and LNC were 0.87, 0.84, 0.82, 0.75, 0.74, 0.73, 0.69, 0.61, 0.45, 0.41, 0.31, greater than 0.26 in Fig. 2. The results of correlation analysis showed that the correlation between the selected digital image variables and LNC was 0.01 significant.

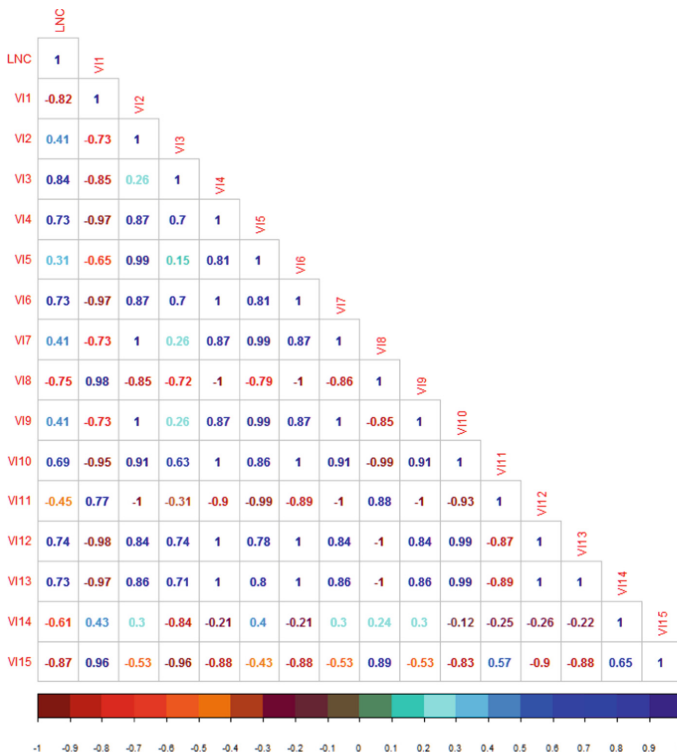


Fig. 2. Result of Pearson correlation analysis between digital image variables and LNC

3.2 Establishment of Linear Regression Analysis Model

Based on the results of correlation analysis between digital image variables and LNC, the variables were sorted by correlativity. Then, a linear regression model of each

digital image variable for estimating LNC was constructed. The results of linear regression analysis were shown in Table 2. The AIC value, R^2 , $RMSE$, and $nRMSE$ of the linear regression model were considered comprehensively. The optimal linear estimation model of LNC was chosen, whose variable was r/b . The AIC value, R^2 , $RMSE$ and $nRMSE$ of the optimal model were 108.66, 0.76, 0.40, 11.97%, respectively.

Table 2. Result of linear regression analysis of digital image variables and LNC

Digital image variable	Regression equation	AIC value	R^2	$RMSE$	$nRMSE/\%$
r/b	$y = -5.06 * x + 9.67$	108.86	0.76	0.40	11.97
b	$y = 46.58 * x - 9.43$	126.66	0.71	0.44	13.07
r	$y = -31.95 * x + 14.24$	140.14	0.67	0.47	13.97
ExR	$y = -15.81 * x + 4.82$	170.64	0.55	0.55	16.25
VARI	$y = 8.58 * x + 2.49$	171.50	0.55	0.55	16.32
GRVI	$y = 14.01 * x + 2.50$	176.39	0.53	0.56	16.72
g/r	$y = 6.34 * x - 3.83$	176.88	0.53	0.56	16.76
MGRVI	$y = 7.08 * x + 2.50$	176.36	0.53	0.56	16.72
ExGR	$y = 11.50 * x + 11.50$	188.35	0.47	0.60	17.74
g/b	$y = -6.30 * x + 12.22$	205.56	0.37	0.65	19.32
CIVE	$y = -23.69 * x + 446.51$	229.98	0.20	0.73	21.80
g	$y = 29.02 * x - 7.80$	234.12	0.17	0.75	22.25
GLA	$y = 13.89 * x + 1.82$	233.89	0.17	0.75	22.22
ExG	$y = 9.67 * x + 1.87$	234.12	0.17	0.75	22.25
RGBVI	$y = 5.91 * x + 2.03$	241.96	0.10	0.78	23.13

3.3 Establishment of Stepwise Regression Analysis Model

The 15 digital image variables selected were analyzed by stepwise regression and the estimation models of LNC of winter wheat were constructed. The AIC value, R^2 , $RMSE$, and $nRMSE$ of the stepwise regression model were calculated and the degree of significance of the coefficients of the regression model was judged. The results of stepwise regression analysis were shown in Table 3. Evaluation indices of the stepwise regression analysis model were comprehensively considered. The optimal stepwise regression model for LNC of winter wheat was selected, consisting of 3 variables, r , g/b and r/b . The regression equation of the optimal stepwise regression model was $LNC = 142.56 * r + 12.18 * g/b - 29.98 * r/b - 24.91$, and the model's R^2 , $RMSE$ and $nRMSE$ were 0.79, 0.8, 11.34%, respectively.

Table 3. Result of stepwise regression analysis of digital image variables and LNC

Number of independent variables	AIC value	Significance of regression coefficient	R^2	RMSE	nRMSE/%
15	103.36	Neither of the 16 was significant	0.81	0.36	10.65
6	96.65	3 were 0.05 significant, 4 were not significant	0.81	0.36	10.72
5	97.47	5 were 0.05 significant, 1 was not significant	0.80	0.37	10.87
4	100.16	1 was 0.001 significant, 2 were 0.05 significant, 2 were not significant	0.79	0.37	11.13
3	100.15	2 were 0.001 significant, 1 was 0.01 significant, 1 was 0.05 significant	0.79	0.38	11.24
2	108.11	2 were 0.001 significant, 1 was not significant	0.77	0.40	11.81

Note: degree of significance, “***”:0.001, “**”:0.01, “*”:0.05.

3.4 Optimal LNC Estimation Model Selection

The predictive ability of the linear and stepwise regression analysis model was evaluated using 101 sample data involved in modeling and 43 sample data not involved in modeling. The optimal estimation model was screened taking R^2 , $RMSE$ and $nRMSE$ as evaluation indices and the results were shown in Table 4 and Fig. 3.

Table 4. Comparison of LNC of winter wheat estimation models

Regression model	R^2	$RMSE$	$nRMSE/\%$
<i>Modeling indicators (101 samples)</i>			
Linear	0.76	0.40	11.97
Stepwise	0.79	0.38	11.24
<i>Validating indicators (43 samples)</i>			
Linear	0.69	0.43	13.02
Stepwise	0.39	0.43	13.16

The evaluation indices of model calibration and verification of LNC of winter wheat and the degree of simplicity of model application were considered comprehensively. The R^2 , $RMSE$, and $nRMSE$ of linear regression model were compared with the stepwise regression model. The R^2 of linear regression was 0.76, smaller than 0.79 from the stepwise regression model. The $RMSE$ of linear regression model was 0.40, 0.02 larger than that of the stepwise regression model. The $nRMSE$ of linear regression was 11.97%, 0.73% larger than that of the stepwise regression model. Therefore, the calibrating accuracies of linear and stepwise regression were approximate. However, model validation capabilities were evaluated using samples not involved in modeling. The R^2 , $RMSE$, and $nRMSE$ of linear regression model validation were 0.69, 0.43 and

13.02%, respectively. Compared with the stepwise regression model, R^2 and $RMSE$ were equal and $nRMSE$ was 0.14% smaller. The results showed that the linear regression model used only one variable and the stepwise regression model had three variables. The linear regression modeling variables were less than two and its predictive ability was a little better compared with the stepwise regression model. Comprehensively considering the accuracy and simplicity of the model, the linear regression model $LNC = -5.06 * r/b + 9.67$, which constructed by the digital image variable of r/b , was used to estimate LNC of winter wheat in this study.

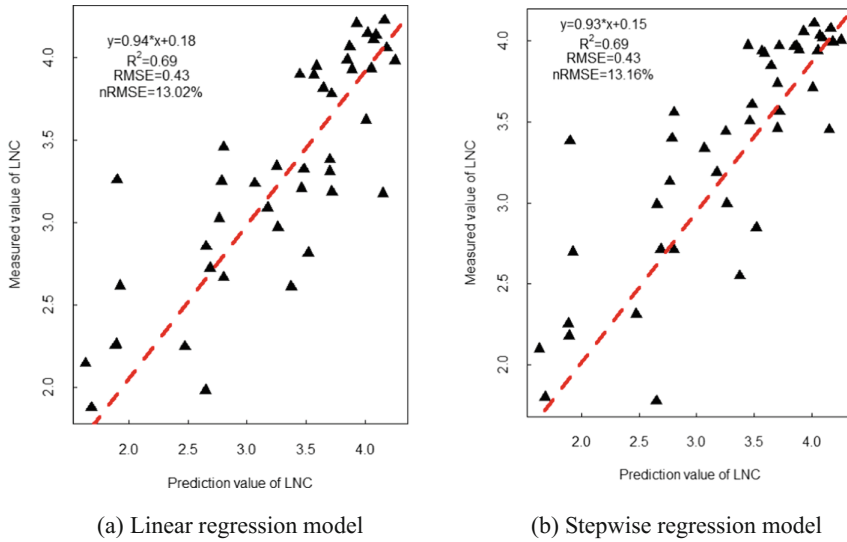
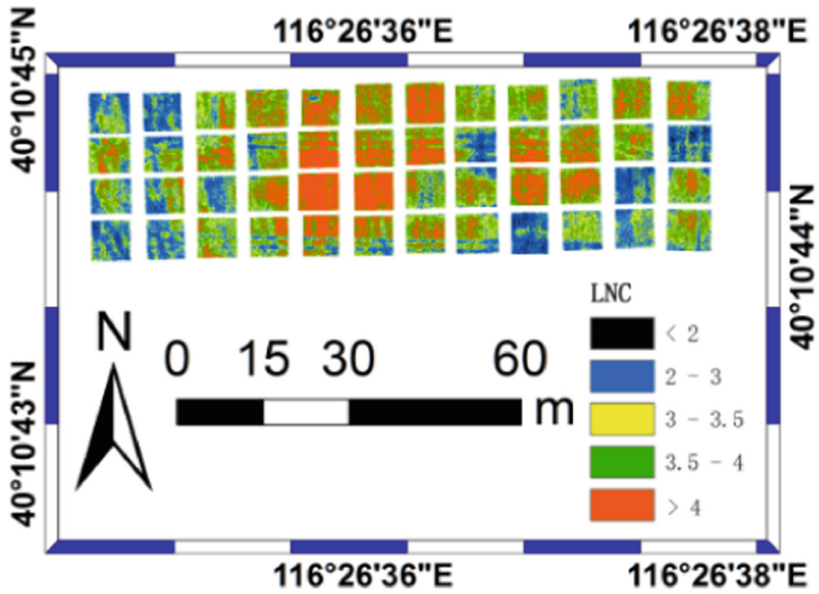
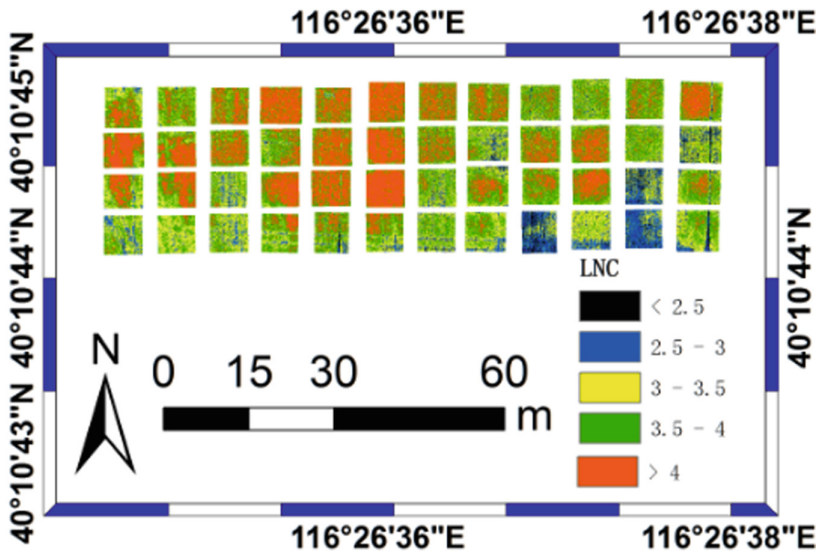


Fig. 3. Relationship of LNC of winter wheat between measured and model estimated values

The spatial distribution of LNC of the winter wheat experimental area was estimated based on the optimal regression equation. The results of the LNC spatial distribution map were shown in Fig. 4. The LNC in booting stage, flowering stage, and filling stage of winter wheat was significantly affected by N treatment. With the increase of N application rate, the corresponding LNC of winter wheat increased in turn. However, with the growth period advancing, LNC of winter wheat showed a downward trend and it was consistent with the physiological process of winter wheat N from the leaves to the grain. At booting stage of LNC, on the whole, LNC treated with N1 was between 2–3, LNC treated with N2 was between 3.5–4, LNC treated with N3 and N4 were more than 4 and LNC treated with N4 was much higher than that of N3. LNC in the flowering stage was lower than booting stage on the whole. However, LNC treated with N1 and N2 increased and still lower than that of N3 and N4. At the filling stage, LNC decreased as a whole, mainly due to the rapid transfer of N from leaves to grain.

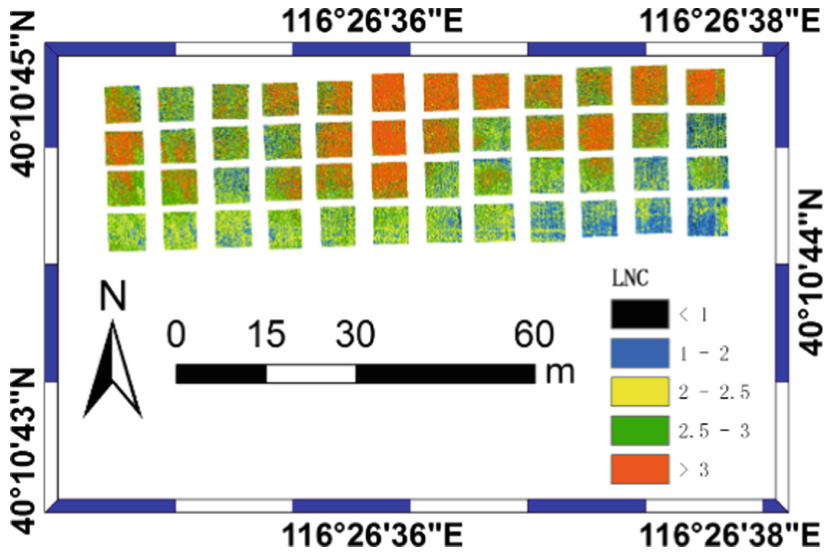


(a) Booting stage



(b) Flowering stage

Fig. 4. Spatial distribution of LNC estimation of winter wheat



(c) Filling stage

Fig. 4. (continued)

4 Discussion

At present, rapid prediction of morphological structure and physiological and biochemical parameters of crops based on UAV remote sensing technology has become a hot spot of remote sensing research in precision agriculture. Yang [10] summed up the status of precision agricultural applications using UAV as the remote sensing platform, equipped with a variety of light remote sensing sensors. Jin [5] used UAV to carry low-cost and high-resolution digital camera flying at the height of 3 to 7 m and at the speed of 1 m/s and obtained the high-resolution digital images of the experimental area. Then, the planting density of winter wheat was estimated with high precision. The above cases show that remote sensing platforms couple high-resolution digital cameras with UAVs have become one of the focuses of research because of their traits of low-cost, simple operation, convenient to use and high spatial resolution. However, relatively few studies on LNC of winter wheat are carried out based on UAV remote sensing platforms equipped with low-cost and high-resolution digital camera. In this study, the high-resolution digital orthoimages of UAV and measured LNC values were acquired at booting, flowering and filling stages of winter wheat. The linear regression model of r/b was used to establish the estimation model of LNC based on the random selection of 101 sample data. By using the remaining 43 sample data which were not involved in modeling, the estimation model was validated. The analysis showed that the linear regression model of r/b had higher accuracy when estimating LNC and the stability of the model was better, which is consistent with the results of [17–19, 23], using the digital images of UAV to estimate yield, LNC and biomass of maize, biomass

of barley, leaf area index and yield of winter wheat. In the field of crop LNC estimation studies, the result of this study and the reference[17] using the visible vegetation indices based on orthoimage of UAV to estimate LNC of maize had the similar conclusion.

In this study, the LNC of winter wheat was estimated based on UAV high-resolution digital orthoimage. The linear regression estimation model of LNC constructed by digital image variable r/b , whether it can be well applied to LNC of winter wheat monitoring in other areas, needs further verification. As well as, whether similar problems such as the saturation effect of vegetation index will interfere with the predictive power of the LNC estimation model, which will serve as a follow-up research focus.

5 Conclusion

The high-resolution digital images were acquired for three winter wheat growth stages (booting, flowering, filling) using a UAV remote sensing platform with low-cost and high-resolution digital camera. Digital image variables were extracted based on the digital orthoimages. The correlation analyses of digital image variables and LNC were carried out and linear and stepwise regression models were constructed. The R^2 , $RMSE$, and $nRMSE$ of model calibration and validation and the simplicity of model were evaluated comprehensively. Finally, the linear regression model constructed by r/b was used to estimate the LNC of winter wheat. Conclusions were drawn as follows:

1. The selected 15 digital image variables were significantly related to LNC at the 0.01 significance level. Among them, r/b got the strongest correlation with LNC (-0.87) and RGBVI got the weakest correlation with LNC (0.31).
2. The LNC estimation models were established by selecting 70% of sample data at random (a total of 101 samples). The remaining 30% sample data (a total of 43 samples) which were not involved in calibrating, were used to validate the estimation model. Among them, the r/b linear regression estimation model was the best. The calibration and validation accuracy of this model $R^2 = 0.76$, $RMSE = 0.40$, $nRMSE = 11.97\%$ and $R^2 = 0.69$, $RMSE = 0.43$, $nRMSE = 13.02\%$.
3. UAV remote sensing platform equipped with low-cost and high-resolution digital camera can quickly, non-destructively and accurately estimate LNC of winter wheat from orthoimage, which provides a rapid and low-cost technique for N monitoring and N management in winter wheat.

References

1. Scheromm, P., Martin, G., Bergoin, A., et al.: Influence of nitrogen fertilization on the potential bread-baking quality of two wheat cultivars differing in their responses to increasing nitrogen supplies. *Cereal Chem.* **69**, 664–670 (1993)
2. Guo, S.L., Dang, T.H., Hao, M.D.: Effects of fertilization on wheat yield, NO_3-N accumulation and soil water content in semi-arid area of China. *Scientia Agricultura Sinica* **4** (4), 745–751 (2005)

3. Pjir, P., Hatfield, J.L., Schepers, J.S., et al.: Remote sensing for crop management. *Photogram. Eng. Remote Sens.* **69**(6), 647–664 (2003)
4. Xu, X.G., Zhao, C.J., Wang, J.H., et al.: Using optimal combination method and in situ hyperspectral measurements to estimate leaf nitrogen concentration in barley. *Precision Agric.* **15**(2), 227–240 (2014)
5. Jin, X., Liu, S., Baret, F., et al.: Estimates of plant density of wheat crops at emergence from very low altitude UAV imagery. *Remote Sens. Environ.* **198**, 105–114 (2017)
6. Moharana, S., Dutta, S.: Spatial variability of chlorophyll and nitrogen content of rice from hyperspectral imagery. *ISPRS J. Photogram. Remote Sens.* **122**, 17–29 (2016)
7. Zhao, C.J.: Advances of research and application in remote sensing for agriculture. *Trans. Chin. Soc. Agric. Mach.* **45**(12), 277–293 (2014)
8. Zhou, W.T., Wu, B.F., Zhang, M., et al.: Comprehensive monitoring of crop growth – take India as an example. *J. Remote Sens.* **19**(4), 539–549 (2015)
9. Tang, J.M., Liao, Q.H., Liu, Y.Q., et al.: Estimating leaf area index of crops based on hyperspectral compact airborne spectrographic imager (CASI) data. *Spectrosc. Spectral Anal.* **35**(5), 1351–1356 (2015)
10. Yang, G., Liu, J., Zhao, C., et al.: Unmanned aerial vehicle remote sensing for field-based crop phenotyping: current status and perspectives. *Front. Plant Sci.* **8**, 1111 (2017)
11. Zhang, C., Kovacs, J.M.: The application of small unmanned aerial systems for precision agriculture: a review. *Precision Agric.* **13**(6), 693–712 (2012)
12. Shao, S., Wei, X., et al.: Framework of SAGI agriculture remote sensing and its perspectives in supporting national food security. *J. Integr. Agric.* **13**(7), 1443–1450 (2014)
13. Candiago, S., Remondino, F., De Giglio, M., et al.: Evaluating multispectral images and vegetation indices for precision farming applications from UAV images. *Remote Sens.* **7**(4), 4026–4047 (2015)
14. Suomalainen, J., Anders, N., Iqbal, S., et al.: A lightweight hyperspectral mapping system and photogrammetric processing chain for unmanned aerial vehicles. *Remote Sens.* **6**(11), 11013–11030 (2014)
15. Zhao, X.Q., Yang, G.J., Liu, J.G., et al.: Estimation of soybean breeding yield based on optimization of spatial scale of UAV hyperspectral image. *Trans. CSAE* **33**(1), 110–116 (2017)
16. Nie, S., Wang, C., Dong, P., et al.: Estimating leaf area index of maize using airborne discrete-return LiDAR Data. *Remote Sens. Lett.* **9**(7), 3259–3266 (2016)
17. Vergaradiaz, O., Zamanallah, M.A., Masuka, B., et al.: A novel remote sensing approach for prediction of maize yield under different conditions of nitrogen fertilization. *Front. Plant Sci.* **7**, 666 (2016)
18. Li, W., Niu, Z., Chen, H., et al.: Remote estimation of canopy height and aboveground biomass of maize using high-resolution stereo images from a low-cost unmanned aerial vehicle system. *Ecol. Ind.* **67**, 637–648 (2016)
19. Bendig, J., Yu, K., Aasen, H., et al.: Combining UAV-based plant height from crop surface models, visible, and near-infrared vegetation indices for biomass monitoring in barley. *Int. J. Appl. Earth Obs. Geoinf.* **39**, 79–87 (2015)
20. Schirrmann, M., Giebel, A., Gleiniger, F., et al.: Monitoring agronomic parameters of winter wheat crops with low-cost UAV imagery. *Remote Sens.* **8**(9), 706 (2016)
21. Saberioon, M.M., Amin, M.S.M., Anuar, A.R., et al.: Assessment of rice leaf chlorophyll content using visible bands at different growth stages at both the leaf and canopy scale. *Int. J. Appl. Earth Obs. Geoinf.* **32**(10), 35–45 (2014)
22. Torres-Sánchez, J., López-Granados, F., Peña, J.M.: An automatic object-based method for optimal thresholding in UAV images: application for vegetation detection in herbaceous crops. *Comput. Electron. Agric.* **114**(C), 43–52 (2015)

23. Zhou, X., Zheng, H.B., Xu, X.Q., et al.: Predicting grain yield in rice using multi-temporal vegetation indices from UAV-based multispectral and digital imagery. *ISPRS J. Photogram. Remote Sens.* **130**, 246–255 (2017)
24. Tucker, C.J.: Red and photographic infrared linear combinations for monitoring vegetation. *Remote Sens. Environ.* **8**(2), 127–150 (1979)
25. Louhaichi, M., Borman, M.M., Johnson, D.E.: Spatially located platform and aerial photography for documentation of grazing impacts on wheat. *Geocarto Int.* **16**(1), 65–70 (2001)
26. Meyer, G.E., Neto, J.C.: Verification of color vegetation indices for automated crop imaging applications. *Comput. Electron. Agric.* **63**(2), 282–293 (2008)
27. Woebbecke, D.M., Meyer, G.E., Von Bargaen, K., et al.: Color indices for weed identification under various soil, residue, and lighting conditions. *Trans. ASAE* **38**(1), 259–269 (1995)
28. Kataoka, T., Kaneko, T., Okamoto, H., et al.: Crop growth estimation system using machine vision. In: *Proceedings of 2003 IEEE/ASME International Conference on Advanced Intelligent Mechatronics, AIM 2003*, vol. 2, pp. b1079–b1083. IEEE (2003)
29. Gitelson, A.A., Viña, A., Arkebauer, T.J., et al.: Remote estimation of leaf area index and green leaf biomass in maize canopies. *Geophys. Res. Lett.* **30**(5) (2003)



New NNI Model in Winter Wheat Based on Hyperspectral Index

Wang Jianwen^{1,2,3,4,5}, Li Zhenhai^{2,3,4,5(✉)}, Xu Xingang^{2,3,4,5},
Zhu Hongchun¹, Feng Haikuan^{2,3,4,5}, Liu Chang^{2,3,4,5},
Gan Ping^{1,2,3,4,5}, and Xu Xiaobin^{1,2,3,4,5}

¹ College of Geomatics, Shandong University of Science and Technology,
Qingdao, Shandong 266590, China

wangjw@163.com, sdny_xa@163.com, ganpingzd@163.com,
xuxb17@outlook.com

² Key Laboratory of Quantitative Remote Sensing in Agriculture
of Ministry of Agriculture P. R. China,

Beijing Research Center for Information Technology in Agriculture,
Beijing 100097, China

lizh323@126.com, fenghaikuan123@163.com,

liuchang_123@outlook.com

³ National Engineering Research Center for Information Technology in
Agriculture, Beijing 100097, China

xuxg@nercita.org.cn

⁴ Key Laboratory for Information Technologies in Agriculture,
The Ministry of Agriculture, Beijing 100097, China

⁵ Beijing Engineering Research Center of Agricultural Internet of Things,
Beijing 100097, China

Abstract. Nitrogen nutrition index (NNI) can monitor winter wheat nitrogen status precisely. Current studies by remote sensing data are to construct the above-ground biomass (AGB) and plant nitrogen concentration (PNC) with spectral indices, respectively, and then substitute them into established NNI equation. This leads to an accumulation of unavoidable error. Therefore, the objective in the study was to construct a direct NNI equation with remote sensing data to reduce this error. Field measurements data including AGB, PNC and canopy hyperspectral at different winter wheat growth stages during 2012/2013, 2013/2014, 2014/2015, 2015/2016 growing seasons in Beijing, China were collected. This study was endeavored to establish a vegetation index critical N dilution curve (N_{vic}) with two different spectral indices, RTVI (Red edge Triangular Vegetation Index) and NDVI/PPR (the ratio of the normalized difference vegetation index to the plant pigment ratio), which are sensitive to AGB and PNC, respectively. The vegetation index NNI (NNI_{vi}) was calculated from the ratio between the NDVI/PPR and N_{vic} . Results showed that (1) N_{vic} can be described by an equation, $N_{vic} = 1106.4(VIRTVI)^{-1.512}$, where RTVI ranged from 2.39 to 22.14; the determination coefficient (R^2) was 0.57; (2) The NNI based on the above N_{vic} dilution curve was in good accordance with the classical NNI, with the root mean square error (RMSE), normalized RMSE (nRMSE) and normalized average error (NAE) of 0.194, 22%, and 11%, respectively. The critical nitrogen dilution model constructed in this study was available for winter

wheat nitrogen status monitoring. Thus, this study offers a new method which was suitable and convenient for estimating the NNI of the winter wheat and it can reduce quadratic error for constructing NNI through indices directly instead of inverting AGB and PNC.

Keywords: Winter wheat · NNI · Spectral indices
The critical N dilution curve

1 Introduction

Nitrogen (N) is an indispensable chemical element for plant growing and an acquired agricultural input to increase yield [1, 2]. In the process of canopy growth in cereal crop, it needed a great deal of N [3]. Farmers applied more N fertilizer in fields than basic need during last few decades to ensure productivity [4]. However, excessive use of N did increase the economic burden of peasants, and even worth, it gives rise to environmental pollutions, such as soil acidification, eutrophication, emissions of greenhouse gas [5] and the contamination of surface and ground-water [6]. Improving N use efficiency has become growing importance concerning economic costs and environmental problems [2, 3].

Precise fertilization was proposed to reduce environmental problems caused by too much N fertilizer applied to the fields in modern agriculture [2]. Critical N concentration (N_c) means maximum growth could be achieved by applying the least but necessary nitrogen. Nitrogen nutrition index (NNI), as the ratio of plant nitrogen concentration (PNC) and corresponding N_c , is a suitable and reliable indicator of diagnosing of N in crops [7–9, 22]. N nutrition was considered perfect when NNI equals one; if NNI was great than one, N nutrition was considered luxurious; and N nutrition was insufficient if NNI was less than one [8].

A real-time and non-destructive monitoring technology need to be proposed to uphold the accurate detection of N in precision agriculture. Remote sensing methods were put forward by Lemaire et al. for the advantage of non-destructive and real-time during plant growth, and with this technology the NNI can be monitored rapidly in a large region [10].

Applying optical sensors to diagnose NNI has been an important research topic in recent years [11–13, 19–21]. Some scholars tried to estimate the PNC and above-ground biomass (AGB) with N and dry biomass related vegetation indices, respectively, and then the estimated PNC and AGB were used to calculate the NNI [11, 12]. Cilia et al. Calculated the parameters (e.g., leaf actual N content and biomass) for the production of the NNI with MCARI/MTVI2 (a chlorophyll concentration index referred to as the Modified Chlorophyll Absorption Ratio Index/Modified Triangular Vegetation Index 2) and MTVI2 related to LAI, respectively. And then the method was applied on the airborne hyperspectral image to diagnose the crop N deficiency zone [12]. Xia et al. found that GreenSeeker sensor-based indices (VIs) can explain the variability of AGB and PNC, respectively, and then used to calculate spring maize NNI in Northeast China [7]. However, most of them contributed to inverse the N

concentration and AGB first, and then get the NNI. In this process, Error will be accumulated and lead to a poor result. Little has been reported to construct NNI directly using spectral indices.

Therefore, the purposes of this study are as follows: (i) to construct a vegetation index critical nitrogen dilution model (N_{vic}) directly based on spectral indices for winter wheat in Beijing and then get the NNI; (ii) to compare the performance of the above NNI based N_{vic} with the traditional NNI.

2 Materials and Methods

2.1 Study Area and Experimental Design

Four years' experiments were carried out in the same region, Xiaotangshan town (40° 10'30"– 40°11'20"N, 116°26'01" – 116°27'10"E), Changping District, Beijing, PR China and different growing seasons. 2012/2013, 2013/2014, 2014/2015, 2015/2016 were used to inverse the NNI. The climate in this study zone is A semi-humid continental monsoon climate. Field treatments include fertilizer rates at each growing season. Half nitrogen fertilizer was employed on the ground before seeding and the other half at the jointing stage (Table 1).

2.2 Data Acquisition

2.2.1 Biomass and N Concentration Data

Biochemical data was observed at jointing, booting and anthesis stages, during four growing season data in 2012/2013, 2013/2014, 2014/2015, 2015/2016. The AGB data was obtained at the same places where the hyperspectral data were measured through collecting 30–50 representative samples from each plot. All fresh winter wheat were divided into different parts, leaves, stems and spikes. Then all parts were sent to the oven and heated to 105 °C for almost one hour and then over dried down to 80 °C until the weight never changed, and their final dry weights were recorded using a delicate scale. Weights of stem and leaf were added up to calculate the AGB. The plant N concentration was measured with the micro-Kjeldahl way (Bremner and Mulvaney) [14].

2.2.2 Hyperspectral Data

Canopy reflectance data was collected by an ASD FieldSpec Pro FR spectroradiometer (Analytical Spectral Devices, Boulder, USA). A 1.4 nm sampling interval was set up between 350 nm and 1050 nm, and the sampling interval was set up between 1050 nm and 2500 nm was a 2 nm. In order to avoid the impact of change in the intensity of sunlight, spectral data were measured between 10a.m and 2p.m at a sunny day without cloud. The reflectance was acquired from the spectral radiance by using a 40 cm by 40 cm white BaSO₄ reference panel, finally. In the same zone, ten spectral curves were observed at the same plot, and then the final spectral data were obtained by averaging the ten curves.

2.3 Spectral Indices

In this study, we endeavored to establish a vegetation index critical N dilution curve (N_{vic}) with two different spectral indices Red-edge Triangular Vegetation Index (RTVI) [15] and ratio of the normalized difference vegetation index to the plant pigment ratio (NDVI/PPR) [16] which are sensitive to AGB and PNC, respectively. The formulas of RTVI and NDVI/PPR are as follows:

$$RTVI = (100(R_{750} - R_{730}) - 10(R_{750} - R_{550})) \text{sqrt}(R_{700}/R_{670}) \quad (1)$$

$$Ndv/ppr = (r_{550} + r_{450}) (r_{800} - r_{670}) / [(r_{550} - r_{450}) (r_{800} + r_{670})] \quad (2)$$

Where R_i means the reflectance at band i .

2.4 Data Analysis

Calculating N_{vic} dilution curve needs to determine the N_c points where N neither limits nor enhances plant growth. As listed in Table 1, four years' data, AGB and PNC under different N levels, were analyzed with the least significant difference (LSD 0.05) by the IBM SPSS version 19 (IBM Corporation, USA). N limited points were defined as points that the AGB would significantly increase if any additional N fertilizer were applied. Whilst, a N unlimited data points were defined as points that PNC would increase significantly but AGB would not change obviously with any additional N fertilizer applied. The construction process of traditional N_c dilution curve in this study were referred to Zhao et al. [17]. In the study, we attempt to construct N_{vic} curve directly from hyperspectral data, and the detailed N_{vic} construction based on the RTVI and NDVI/PPR are as follows: (1) all data points under each N treatment were taken by RTVI and NDVI/PPR; (2) the N-limited treatments points were used to fit a simple straight line; (3) the N unlimited data points were averaged as the maximum RTVI value and then with the maximum RTVI value as a vertical line; (4) N_{vic} points were obtained as the intersection points; and (5) a power regression equation were fitted with these N_{vic} points, that is N_{vic} curve.

The measured NNI model was as follows:

$$NNI = N_a / N_c \quad (3)$$

The vegetation index was calculated according to the equation:

$$NNI_{vi} = (NDVI/PPR) / N_{vic} \quad (4)$$

In Eqs. 3 and 4, N_a represents the actual PNC, and N_c represents the winter wheat critical nitrogen content, N_{vic} is the vegetation index critical N.

Finally, the determination coefficient (R^2), root mean square error (RMSE), normalized RMSE (nRMSE) and normalized average error (NAE) were employed to judge of the accuracy of the estimated model.

3 Results and Analysis

3.1 Plant N Concentration and Above Ground Biomass Under Different N Level

AGB were varied under different N application level at the vegetative growth period. As the amount of nitrogen application increased, AGB gradually increased. The AGB of the winter wheat develop from 1.863 to 10.632 t ha⁻¹ at different growing periods, and seasons (Table 1). The AGB were significantly different under N0 to N2 applications, it indicated that N fertilizer had obviously influence on the crops growth. But it showed a different result under N2 and N3 fertilizer level in 2013/2016. During four growing seasons, AGB under different N treatments can be described by the following formula 5 at the 5% probability level.

$$AGB_0 < AGB_1 < AGB_2 = AGB_3 \quad (5)$$

where AGB_i represented AGB at N_i application, respectively, i = 0, 1, 2, 3.

Table 1. AGB (t ha⁻¹) in winter wheat under varied nitrogen levels conducted during 2013–2016 growing seasons.

Year	N treatment (kg.hm ⁻²)	Growth period		
		Jointing	Booting	Anthesis
2012–2013	N0 (0)		3.009 ^c	3.901 ^c
	N1 (90)		4.805 ^b	7.397 ^b
	N2 (180)		5.443 ^{ab}	9.371 ^a
	N3 (360)		5.884 ^a	1.063 ^a
2013–2014	N0 (0)	2.419 ^c	3.752 ^c	7.514 ^c
	N1 (90)	2.541 ^{bc}	4.316 ^{bc}	8.133 ^{bc}
	N2 (180)	2.877 ^{bc}	4.733 ^{ab}	8.502 ^{ab}
	N3 (360)	3.138 ^{ab}	5.098 ^a	9.313 ^a
2014–2015	N0 (0)	2.261 ^c	3.933 ^c	6.214 ^c
	N1 (90)	2.383 ^{bc}	4.897 ^{bc}	7.817 ^{bc}
	N2 (180)	2.789 ^{ab}	5.692 ^{ab}	8.588 ^{ab}
	N3 (360)	2.841 ^{ab}	5.931 ^{ab}	8.538 ^{ab}
2015–2016	N0 (0)	1.863 ^c	5.016 ^c	7.728 ^c
	N1 (90)	2.460 ^{bc}	5.359 ^{bc}	9.118 ^b
	N2 (180)	2.730 ^{ab}	6.034 ^{ab}	9.455 ^{ab}
	N3 (360)	2.721 ^{ab}	5.554 ^{ab}	9.592 ^{ab}

Different small letters exhibit the significant differences between the treatments at 0.05 level

3.2 N_c in Winter Wheat

Calculating of the critical data points were conducted at the vegetative growth period in winter wheat in this study. For each sampling date, N_c and N_{vic} points would be acquired by two lines' interception, the vertical and oblique lines. With increase of AGB and RTVI, the critical points value decreases; the trend lines of traditional critical dilution curve and the vegetation index critical N dilution curve could be described as the following equation (Fig. 1):

$$N_c = 5.28 \cdot AGB^{-0.4} \tag{6}$$

$$N_{vic} = 1106.4 \cdot VI_{RTVI}^{-1.512} \tag{7}$$

Where AGB is the above-ground biomass, VIRTVI is the vegetation index value of RTVI.

The N_c dilution model established by Justes et al. [18], $N_c = 5.35 \cdot AGB^{-0.44}$, has been widely adopted as a classical model for wheat. The AGB-based N_c model (R² = 0.792) in this study was similar to the model constructed by Justes et al. [18]. It can be used to validate the new NNI model. The trend of the N_{vic} dilution curve, NDVI/PPR value decreases with the increasing of RTVI, are same to the N_c. However the coefficient *a* and *b* values of 1106.4 and 1.512, respectively for the VI-based are far greater than the coefficient (5.28, 0.457) for the AGB-based N_c curve. Coefficient *b* characterized the decline tendency of the PNC and NDVI/PPR value with plant growth, and therefore the N_{vic} is more sensitive to the N concentration. Results indicated that the increase of RTVI and AGB had similar influence on N dilution at vegetative stages.

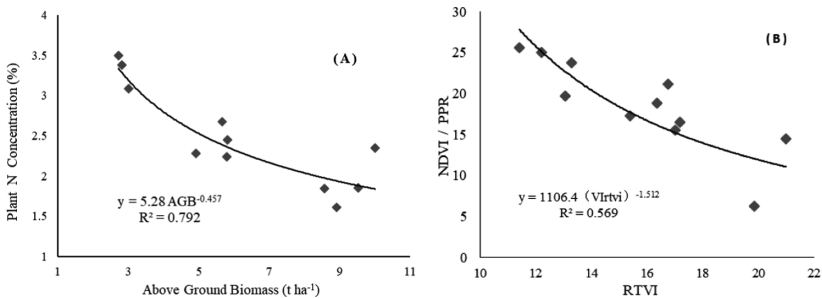


Fig. 1. Critical dilution curve. A: traditional critical dilution curve, B: the vegetation index based critical N dilution model

3.3 Performance of the Vegetation Index NNI_{vi} Based on N_{vic}

NNI_{vi} were calculated with the procedure proposed in Sect. 2.4 was compared with the measured NNI are shown in Fig. 2. The N_{vic}-based NNI prediction models showed a good simulation result between measured NNI and the vegetation index NNI. The

performance of the model was estimated with a RMSE value of 0.194, nRMSE value to be 22% and NAE were 11%. The results showed that studied method offered a new and useful tool for estimating the NNI.

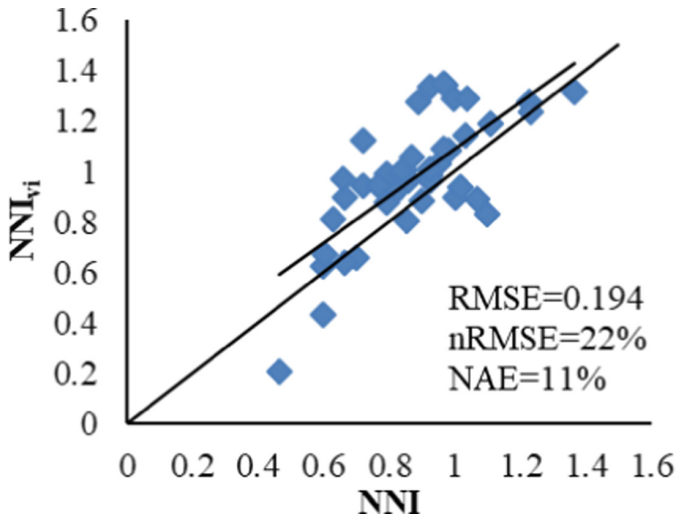


Fig. 2. Comparison of NNI_{vi} and NNI

4 Conclusions

This study proved that the developed critical N dilution model can be used for the diagnosis of nitrogen status in winter wheat in the study region. The good agreement between the traditional NNI and NNI_{vi} supports the use of two vegetation index to substitute the AGB and PNC to inverse NNI. The method in this study offers a new and potential method which was suitable and convenient for estimating the NNI in winter wheat. Furthermore, it can reduce quadric error by constructing NNI through indices directly instead of inverting AGB and PNC.

Acknowledgments. This research was funded by the National Natural Science Foundation of China (Grant no. 61661136003, 41471285,41601346) and National Key Technologies of Research and Development Program (2017YFD0201501, 2016YFD0300603-5).

References

1. Chen, P.: A comparison of two approaches for estimating the wheat nitrogen nutrition index using remote sensing. *Remote Sens.* **7**(4), 4527–4548 (2015)
2. Zhao, B., Yao, X., Tian, Y.C.: New critical nitrogen curve based on leaf area index for winter wheat. *Agron. J.* **106**(2), 379 (2014)

3. Yao, X., Ata-Ul-Karim, S.T., Zhu, Y., et al.: Development of critical nitrogen dilution curve in rice based on leaf dry matter. *Eur. J. Agron.* **55**(2), 20–28 (2014)
4. Schröder, J.J., Neeteson, J.J., Oenema, O., Struik, P.C.: Does the crop or the soil indicate how to save nitrogen in maize production? Reviewing the state of the art. *Field Crop Res.* **66**, 151–164 (2000)
5. He, Z., Qiu, X., Ataulkarim, S.T., et al.: Development of a critical nitrogen dilution curve of double cropping rice in South China. *Front. Plant Sci.* **8**, 638 (2017)
6. López-Bellido, L., López-Bellido, R.J., Redondo, R.: Nitrogen efficiency in wheat under rainfed Mediterranean conditions as affected by split nitrogen application. *Field Crop Res.* **94**, 86–97 (2005)
7. Xia, T., Miao, Y., Wu, D., et al.: Active optical sensing of spring maize for in-season diagnosis of nitrogen status based on nitrogen nutrition index. *Remote Sens.* **8**(7), 605 (2016)
8. Padilla, F.M., Peña-Fleitas, M.T., Gallardo, M., et al.: Determination of sufficiency values of canopy reflectance vegetation indices for maximum growth and yield of cucumber. *Eur. J. Agron.* **84**, 1–15 (2017)
9. Ata-Ul-Karim, S.T., Liu, X., Lu, Z., et al.: In-season estimation of rice grain yield using critical nitrogen dilution curve. *Field Crops Res.* **195**, 1–8 (2016)
10. Lemaire, G., Marie-Hélène, J., François, G.: Diagnosis tool for plant and crop N status in vegetative stage theory and practices for crop N management. *Eur. J. Agron.* **28**, 614–624 (2008)
11. Chen, P.F., Haboudane, D., Tremblay, N., et al.: New spectral indicator assessing the efficiency of crop nitrogen treatment in corn and wheat. *Remote Sens. Environ.* **114**(9), 1987–1997 (2010)
12. Cilia, C., Panigada, C., Rossini, M., et al.: Nitrogen status assessment for variable rate fertilization in maize through hyperspectral imagery. *Remote Sens.* **6**(7), 6549–6565 (2014)
13. Huang, S., Miao, Y., Zhao, G., et al.: Satellite remote sensing-based in-season diagnosis of rice nitrogen status in Northeast China. *Remote Sens.* **7**(8), 10646–10667 (2015)
14. Bremner, J.M., Mulvaney, C.S.: Nitrogen-total. In: Page, A.L. (ed.) *Methods of Soil Analysis, Part II*, pp. 595–624. American Society of Agronomy, Madison (1982)
15. Chen, P.F., Nicolas, T., Wang, J.H., et al.: New index for crop canopy fresh biomass estimation. *Spectrosc. Spectral Anal.* **30**(2), 512 (2010)
16. Jin, X., Li, Z., Feng, H., et al.: Newly combined spectral indices to improve estimation of total leaf chlorophyll content in cotton. *IEEE J. Sel. Top. Appl. Earth Obs. Remote Sens.* **7** (11), 4589–4600 (2014)
17. Zhao, B., Tahir, A.U.K.S., Yao, X., et al.: A new curve of critical nitrogen concentration based on spike dry matter for winter wheat in Eastern China. *PLoS ONE* **11**(10), e0164545 (2016)
18. Justes, E., Mary, B., Meynard, J.M., et al.: Determination of a critical nitrogen dilution curve for winter wheat crops. *Ann. Bot.* **74**(4), 397–407 (1994)
19. Haiying, L., Hongchun, Z.: Hyperspectral characteristic analysis for leaf nitrogen content in different growth stages of winter wheat. *Appl. Opt.* **55**(34), D151 (2016)
20. Cilia, C., Panigada, C., Rossini, M., et al.: Nitrogen status assessment for variable rate fertilization in maize through hyperspectral imagery. *Remote Sensing* **6**(7), 6549–6565 (2014)
21. Eitel, J.U.H., Magney, T.S., Vierling, L.A., et al.: LiDAR based biomass and crop nitrogen estimates for rapid, non-destructive assessment of wheat nitrogen status. *Field Crops Res.* **159**(159), 21–32 (2014)
22. Ata-Ul-Karim, S.T., Liu, X., Lu, Z., et al.: Estimation of nitrogen fertilizer requirement for rice crop using critical nitrogen dilution curve. *Field Crops Res.* **201**, 32–40 (2017)



Fruit Trees 3D Data Acquisition and Reconstruction Based on Multi-source

Sheng Wu^{1,2,3}, Boxiang Xiao^{1,2,3}, Weiliang Wen^{1,2,3},
Xinyu Guo^{1,2,3} (✉), and Long Liu^{1,2,3}

¹ National Engineering Research Center for Information
Technology in Agriculture, Beijing, China
guoxy@nercita.org.cn

² Beijing Research Center for Information Technology in Agriculture,
Beijing, China

³ Beijing Key Lab of Digital Plant, Beijing, China

Abstract. In order to realize three-dimensional reconstruction of canopy at different growth stages of fruit trees, 3D data acquisition methods and canopy reconstruction methods were studied. Based on the analysis of morphological and structural changes in fruit phenological phase, and integrating the advantages of different data acquisition techniques, the data acquisition method of fruit tree morphological structure based on multi-source is proposed. In the dormant period, the canopy skeleton is extracted based on point cloud data; in the leaf curtain stage, a new artificial coding method of canopy structure is constructed, and the data of new shoots and leaves is obtained efficiently; and organ template data is obtained synchronously, and the organ template library is constructed. Then, a multi-source data fusion modeling method is proposed to reconstruct the three-dimensional canopy of fruit trees at different growth stages. And the feasibility of the method is verified by 12 year old open central leader system apple trees, the results show that compared with the manual data acquisition method, the method improves the efficiency by more than 5 times, and the error rate is less than 6%. It provides a feasible scheme for the continuous data acquisition and canopy 3D reconstruction of fruit trees, so as to provide technical support for virtual modeling, scientific calculation and experimental simulations.

Keywords: Fruit tree · Canopy · Multi-source · Data acquisition
Reconstruction

1 Introduction

With the development of digital plant technology, 3D canopy data and 3D modeling technology are widely used in tree characterization, growth simulation, virtual management of orchard and so on [1–3]. At present, there are three main ways to acquire three-dimensional shape of fruit tree: image technology, 3D digital technology and 3D scanning technology. The domestic and foreign researchers have achieved good results in the field crop 3D reconstruction [4–6], however, 3D reconstruction of fruit tree is still the technical difficulties and research hotspots. Different from the field crops, the

morphological and structural characteristics of the fruit trees include: tall crowns, complex branches, excessive number of leaves and artificial pruning. Because of the occlusion between organs, data missing and data noise exist in all kinds of data seriously, the 3D model based on single source data acquisition technology is difficult to meet the requirements of experimental accuracy [7–11]. Integrating the advantages of different data acquisition technologies, this paper proposes a method to obtain morphological structure based on multi-source data fusion of fruit tree phenology, and the 3D modeling of the apple tree have constructed by this method. Taking the open central leader system apple trees as the experimental object, the experimental results show that the modeling efficiency is improved greatly by comparing with the artificial method, and has a realistic visualization effect. Therefore, this method provides a feasible scheme for the continuous data acquisition of fruit tree growth.

2 Fruit Tree Morphology and Structure Characteristics

Different from the common trees, the tree shape is affected by artificial pruning, and the tree structure changes greatly. The tree structure of fruit tree conforms to the model of axis structure, and has obvious phenology characteristics. During the phenology phase, the canopy structure of fruit trees changes obviously, and the leaf curtain formation has a strong gradual process through the growth process of long leaves, flowers, fruits and leaves.

2.1 Axial Structure

According to the axis reference model, the structure of the plant is composed of plant axis, and the axis reference model is faithful to the growth and development characteristics of plants [12]. Therefore, the tree structure and the topological relationship between branches can be described using the axial structure model and the directed tree structure method. As shown in Fig. 1, the tree structure is branched and layered according to the branch structure, each of which is a regular axis structure, and the last layer consists of leaves, fruits, or flowers.

2.2 Leaf Curtain

Leaf curtain is composed of all leaves on various branches, and the leaf curtain gradually forms with the growth of leaves. The canopy leaves of fruit trees are large in number, different in space, and seriously cross and block each other, therefore, the acquirement of leaf curtain data is a difficult point. Take the apple tree for example, leaf growth is usually characterized by two states: clustered and simple leaves, and the leaves alternate in a spiral form and rotate 144° between the two leaves [13], and most clustered leaves grow on shoots. Different branching structures form different leaf curtain structures, and when the long branch is more, the time of formation of leaf curtain is later [14]. Therefore, a data acquisition plan should be designed according to the tree structure.

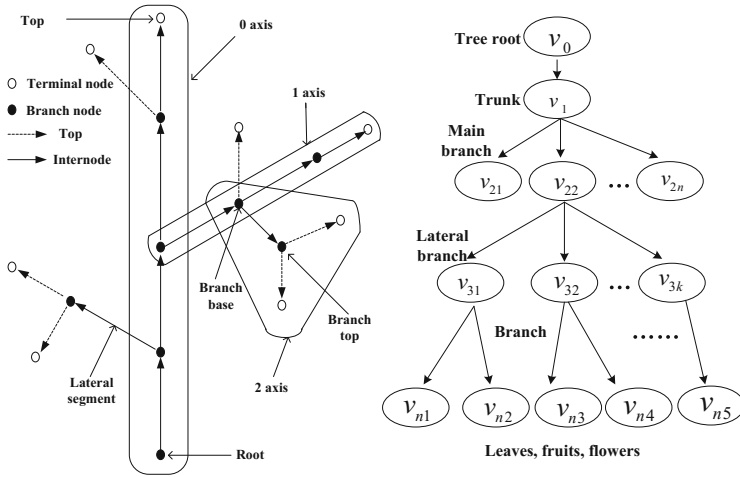


Fig. 1. Fruit axis structure (left) and directed tree structure model (right)

2.3 Phenological Phase

Fruit trees are perennial plants, with obvious annual growth cycle, and the annual growth cycle of fruit trees is also called phenology. In the phenological period of fruit trees, the crown changes through sprout, shoot growth, flowering, fruiting, maturation and other processes. Take the apple tree for example, in the general year, apple trees germinate in late march and begin to flower in early april, the spring shoots stop growing in mid-June, and leaves begin to fall in early November. The phenological phases are staggered and connected, and in addition, they are related to varieties [15], as shown in Fig. 2.

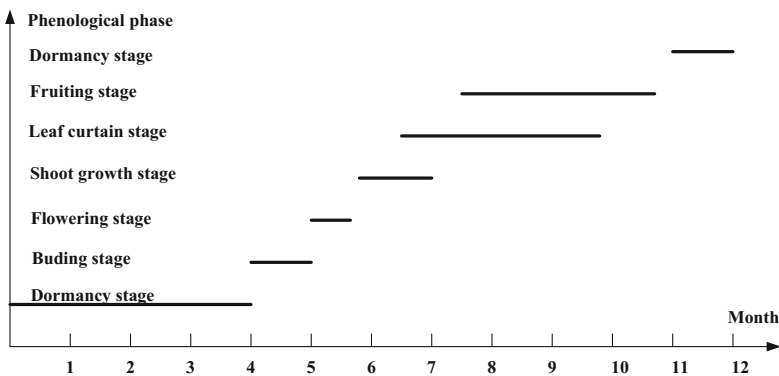


Fig. 2. The annual growth phenology of apple tree

3 Method

3.1 Data Acquisition Process

The phenological and structural characteristics of fruit tree provides the guidance on the time axis for obtaining canopy structure throughout the year. At present, the use of different equipment to obtain canopy data has its own limitations, mainly in: point cloud data obtained from a 3D scanner cause large loss due to occlusion, and the use of three-dimensional digitizer equipment can only obtain small range data and the workload is great. Therefore, we integrate a variety of data acquisition devices, and optimize the data acquisition process, and establish the data acquisition process of the tree canopy structure based on multi-source information fusion. Data acquisition is carried out at four critical periods, such as deciduous stage, flowering stage, leaf curtain formation stage and fruit ripening stage. The data acquisition flow diagram is shown in Fig. 3, and the specific steps are as follows:

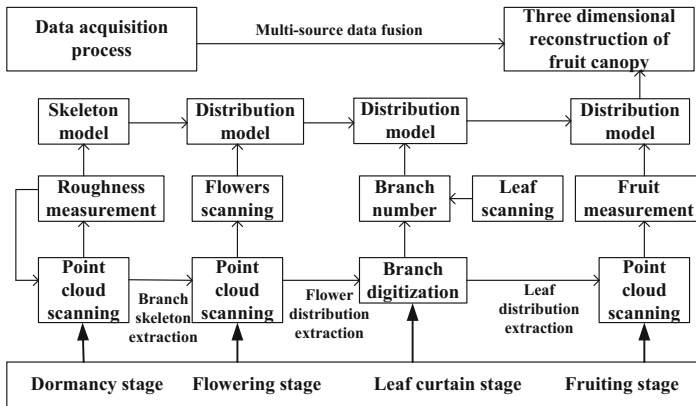


Fig. 3. Data acquisition process of fruit morphological structure based on multi-source

- (1) In the defoliation period, the canopy without leaves is scanned by the Focus3D three dimensional laser scanner [16] and the roughness of branches was measured manually to correct the tree roughness model. The scene and the tree point cloud data obtained by using the Faro scanner are shown in Fig. 4
- (2) In the flowering period, first of all, the canopy with flowers is scanned by the Focus3D three dimensional laser scanner to obtain the distribution of flowers, and some typical flowers are scanned using the Artec Eva scanner to set up branches template(see the Fig. 5).
- (3) In the canopy formation period, first of all, the different kinds of branch structures are obtained by using digital instruments(Polhemus FASTSCAN), the key points of the information including: starting point, end point, petiole point, leaf blade point, blade tip point, blade edge point, etc., and the collection rules are shown in Fig. 6. Then, some typical leaves are scanned using the Artec Eva scanner to set up



Fig. 4. The equipment and rule diagram of crown digitizer

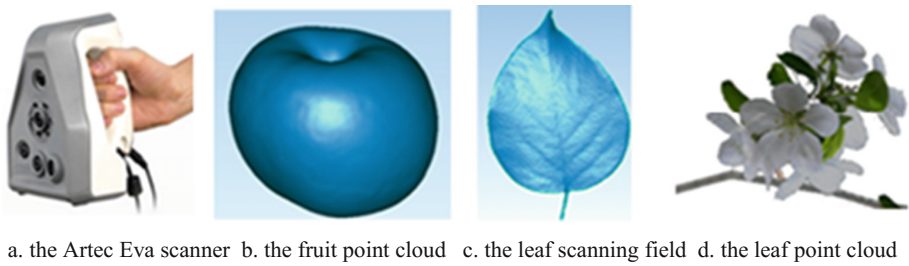


Fig. 5. Organ point cloud scan results

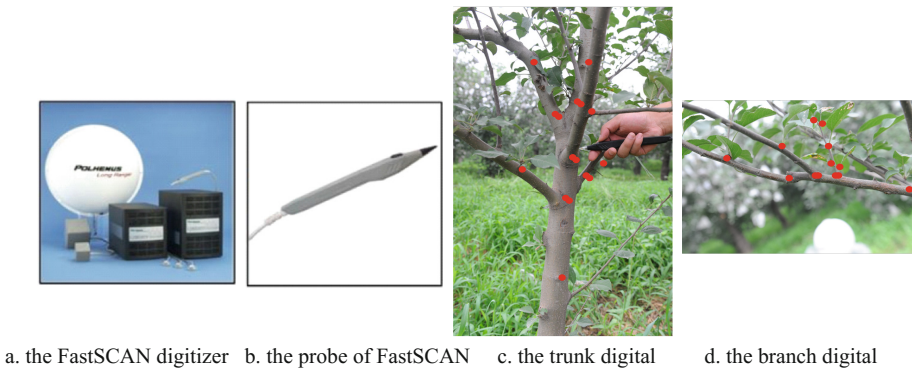


Fig. 6. The equipment and rule diagram of crown digitizer

leaf template. Finally, the number and length of different branches and the number of leaves on these branches are obtained by manual measurement and statistics.

- (4) In fruit ripening period, the canopy with fruits is scanned by the Faro Focus3D three dimensional laser scanner to obtain the distribution of fruits, and different types of fruit diameter are measured to validate the fruit 3D model.

3.2 Data Fusion and Modeling

3.2.1 Fruit Tree Skeleton Extraction Based on Point Cloud

The canopy skeleton can be extracted by processing the tree canopy cloud data without leaf, commonly used point cloud processing algorithms include: Laplacian operator contraction, K neighborhood map connection, geodesic map, level set algorithm and so on. Firstly, the Delaunay neighborhood of each point is computed based on the Laplacian operator of point cloud [17], and the Laplacian weighted matrix L is constructed according to the Delaunay neighborhood data, and the shrinkage matrix W_L and the shape matrix W_H are established as constraint factors, and the point cloud matrix P is iterated iteratively with energy minimization, and the iterative contraction equation is shown in Eqs. 1–2. After a finite iteration, the original dense point cloud will become very thin and approach the skeleton points. Secondly, the K neighborhood map, geodesic map and level set are used to fit skeleton for the shrinkage points [18]. Finally, the algorithm of point cloud circumcission [11] is used to solve the branch radius and patch the small branches. Thus, the canopy fruit tree is reconstructed exactly based on point cloud, and the solving process is shown in Fig. 7.

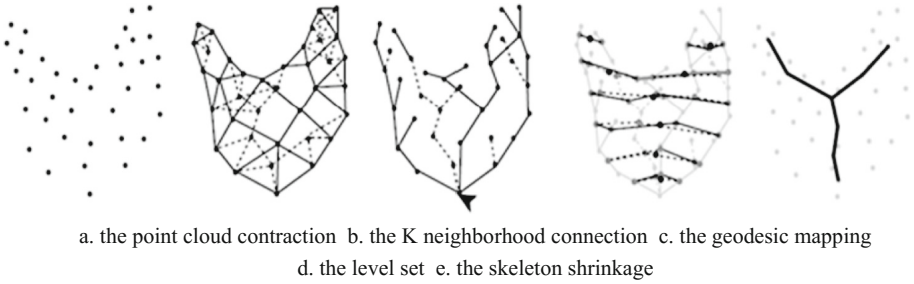


Fig. 7. The point cloud skeleton extraction algorithm process

$$\begin{bmatrix} W_L^t L^t \\ W_H^t \end{bmatrix} P^{t+1} = \begin{bmatrix} 0 \\ W_H^t P^t \end{bmatrix} \quad (1)$$

$$\|W_L L P'\|^2 + \sum_i W_{H,i}^2 \|p'_i - p_i\|^2 \quad (2)$$

3.2.2 Coding Representation of Canopy Topology

In order to facilitate the manual survey of canopy structure data, this paper proposes an efficient coding method for branch topological structure. The branch structure is recorded according to the branch level, and each branch records one row of data. The encoding is divided into two parts: the coding head and the coding body. The coding head information includes the number of branch (m), the number of parent branch (n), the length of branch (L) and the coarseness of branch (d). The coding body information includes all the organs on a branch and branch structure, and the types of organs on the

branches are composed of leaves, clustered leaves, branches, flowers, fruits and so on, they are encoded respectively by A, B, C, D and E; Typically, the leaves are continuous, and in order to simplify the recording representation, A_i is used to represent the successive single leaves on the present branch, and i represents the number of consecutive single leaves, similar to the method used for coding flowers and fruit organs; For leaf clusters, the number of leaves on a leaf cluster should be recorded, so B_j leaves are encoded, and j is the number of leaves on the leaf cluster; and D_h is used as branch encoding, where h is the row number of the branch. The sketch map of the coding representation is shown in Fig. 8. The encoding method can be used orderly and conveniently for data investigators to reduce the recording error of survey data, improve the efficiency of manual investigation and increase the amount of investigation information.

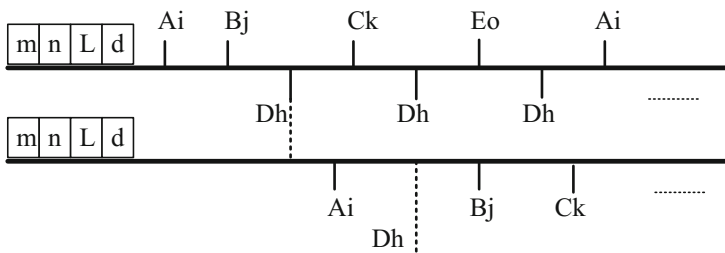


Fig. 8. The sketch map of the coding representation

3.2.3 The Linear Relationship Model of New Branches and Leaves

The branches with different growth directions were selected as the mother branches, and the number of new shoots and the number of leaves on the branches are recorded according to the order from bottom to top. The branch types are divided into four kinds according to the length of branches: long branch (>15 cm), middle branch (5–15 cm), short branch (<5 cm) and leafage branch. At the beginning of the shoot growth, the artificial survey experiments are carried out at intervals until leaf crown forming. Then, based on the artificial survey data, a new branch volume relation model is established, as shown in the Fig. 9. And the linear relationship model between branch length and leaf number is established based on the artificial survey data, as shown in the Fig. 9. Typically, the constructed model conforms to varietal characteristics, so the same tree type and the same breed do not need repeated investigations.

3.2.4 Multi-source Data Fusion Modeling

According to this method, the canopy morphological data of a growing year of fruit trees was systematically obtained, the data obtained in accordance with the classification of data source mainly includes: canopy cloud data of dormancy stage, flowering stage and fruit maturity stage; organs cloud data of leaves, flowers, fruits and other organs; the local branches of digital data, the topological structure of artificial crown

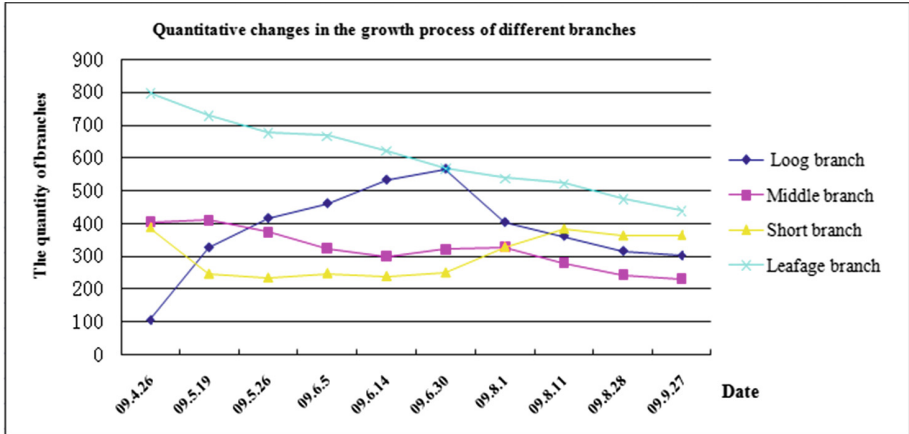


Fig. 9. Quantitative changes in the growth process of different branches

survey data, and so on 4 types data. In a growth year, the morphological structure of fruit trees vary with the new branches changes, the skeleton was reconstructed based on the dormant canopy cloud data, and the reconstructed skeleton was basically stable in one growing year, and it can be concluded that the later canopy data is based on the growth of the skeleton. Then the canopy distribution of flowers and fruits can be easily obtained by processing the point cloud data at flowering and ripening stages [19–21]. And through the gridding modeling of point cloud data of leaves, flowers and fruits, the template library of organs can be constructed, and the organ arrangement can be realized on the canopy skeleton. Finally, the statistical model of blade azimuth and inclination angle are constructed through the statistical analysis of local branches of digital data [22], and the branch and leaf distribution model is constructed by statistical analysis of the artificial data of the crown topology. Therefore, based on the statistical model and organ template, the new branches and leaves are planted on the basis of the canopy skeleton model, and the canopy structure of fruit tree is reconstructed for one year of growth.

4 Result

4.1 Visualization Effect

The feasibility of the method is verified by 12 year old open central leader system apple trees, and the data acquisition scene is shown in Fig. 11a. The skeleton key points of the canopy cloud are extracted at the defoliation stage, and the extracted skeleton key points are shown in Fig. 11b. Then the new branch canopy 3D model (Fig. 11c) and the leaf canopy 3D model (Fig. 11d) are generated based on the artificial survey data. And the 3D model of leaf canopy is rendered from different directions, and the visual effects are shown in Fig. 10f and 11e. According to the visualization results, the three-dimensional model of fruit canopy with different growth stages can be constructed based on the method, with higher accuracy and better visualization effect.

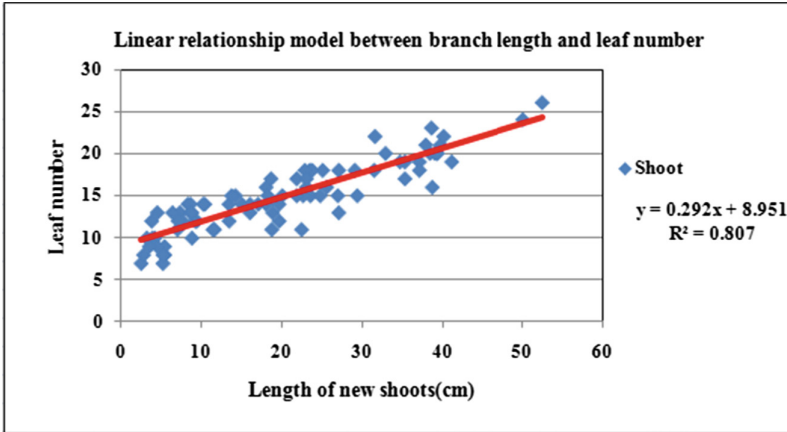


Fig. 10. The linear relationship model of new branches and leaves

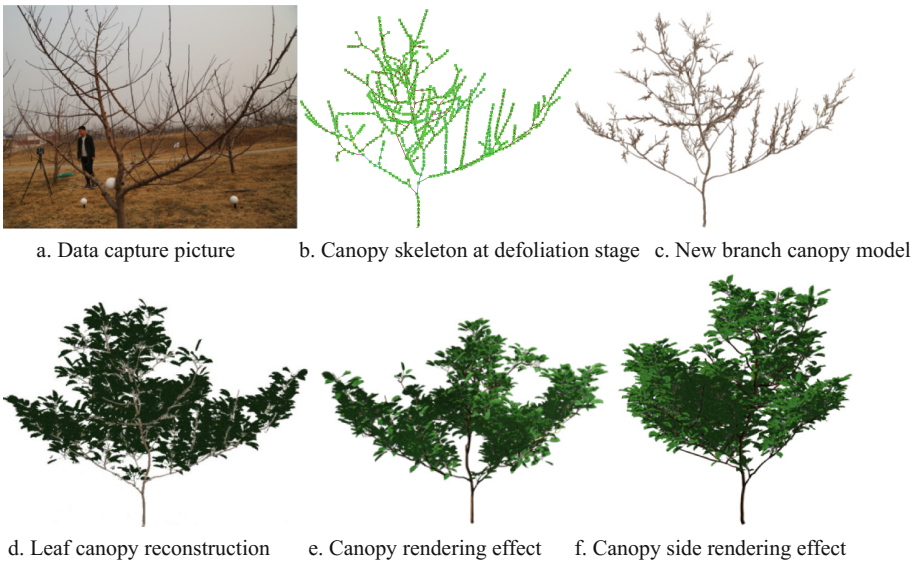


Fig. 11. Canopy reconstruction process and visualization effect

4.2 Accuracy and Efficiency

Compared with the measured data, the accuracy and efficiency of the proposed method are verified. The measured data is obtained by a wide range of three-dimensional digitizer, and the process of data acquisition requires two artificial participants. The leaf number, leaf area index are considered as the important indicator of canopy structure, therefore, on the basis of these two indexes, the accuracy of this paper method is compared and analyzed for three evacuation layered form apple trees, and the time

consuming ratio of the two methods is recorded. The contrast results are shown in Table 1, the results show that the error rate of blade number is less than 5%, and the error rate of leaf area index is less than 6% by this paper method, and in terms of time efficiency, for a single fruit, this method is more than 5 times digital methods, and for the orchard group modeling, this method is 10 times more than the digital method, and lower labor costs.

Table 1. Comparison of canopy reconstruction accuracy and efficiency

Fruit tree	Leaf number			Leaf area index			Time/h		
	Our method	3D digital	Error rate/%	Our method	3D digital	Error rate/%	Our method	3D digital	Efficiency ratio
No. 1	3146	3265	3.64	3.16	3.32	4.82	0.9	8	8.9:1
No. 2	3468	3639	4.70	3.49	3.67	4.90	0.9	8.6	9.5:1
No. 3	2841	2746	3.46	3.14	2.99	5.01	0.8	7.4	9.3:1

5 Conclusions

In this paper, we present an efficient method for obtaining and reconstructing morphological structure of fruit tree canopy based on multi-source. The experimental results show that the method can realize 3D continuous reconstruction of fruit canopy in a growing year. The reconstructed 3D canopy model has a realistic visualization effect, and compared with the manual method, this method improves the efficiency by more than 5 times, and the error rate is less than 6%. So this paper provides a feasible scheme for the continuous data acquisition and canopy 3D reconstruction of fruit trees, and provides technical support for virtual modeling, scientific calculation and experimental simulations. However, our method depends on the foliage growth model. In the future, we will further optimize the growth model through a large number of experimental data, so that it can be applied to different fruit tree shapes.

Acknowledgements. This work was supported by Beijing Postdoctoral Research Foundation, Beijing Municipal Natural Science Foundation (Grant NO. 4162028), and, Scientific and Technological Innovation Team of Beijing Academy of Agricultural and Forestry Sciences (JN KYT201604).

References

1. Zhao, C., Lu, S., Guo, X., et al.: Exploration of digital plant and its technology system. *Sci. Agricultura Sin.* **43**(10), 2023–2030 (2010)
2. Yan, W., Chonghui, F., Daowei, J., et al.: Comparison on fruit crown characteristics and quality of different tree canopy shapes. *Acta Agriculturae Boreali-Occidentalis Sin.* **20**(12), 93–97 (2011)

3. Gao, Z.Q., Zhao, C.X., Cheng, J.J., et al.: Tree structure and 3-D distribution of radiation in canopy of apple trees with different canopy structures in China. *Chin. J. Eco-Agric.* **20**(1), 63–68 (2012)
4. Yuan, X., Zhao, C., Wen, W., et al.: Detailed modeling of 3-D configuration of tomato plant. *Trans. Chin. Soc. Agric. Mach.* **43**(12), 204–210 (2012)
5. Wu, Y., Cao, W., Tang, L., et al.: OpenGL-based visual technology for wheat morphology. *Trans. CSAE.* **25**(1), 121–126 (2009)
6. Xinyu, G., Chunjiang, Z., Boxiang, X., et al.: Design and implementation of three-dimensional geometric morphological modeling and visualization system for maize. *Trans. CSAE.* **23**(4), 144–148 (2007)
7. Liu, J., Jiang, Z., Li, H., et al.: Easy modeling of realistic trees from freehand sketches. *Front. Comput. Sci.* **6**(6), 756–768 (2012)
8. Zhang, X., Li, H., Dai, M., et al.: Data-driven synthetic modeling of trees. *IEEE Trans. Vis. Comput. Graph.* **20**(9), 1214–1226 (2014)
9. Delagrangé, S., Jauvin, C., Rochon, P.: PypeTree: a tool for reconstructing tree perennial tissues from point clouds. *Sensors* **14**(3), 4271–4289 (2014)
10. Lu, S., Guo, X., Zhao, Z., et al.: Shape reconstruction of fruit tree from colored 3D point cloud. In: *The 7th International Conference on Function-Structural Plant Models*, Saariselk, Finland, pp. 55–57 (2013)
11. Wu, S., Xiao, B., Guo, X., Wen, W., Zhao, C.: An accurate fruit tree canopy reconstruction method based on dense point cloud. *ICIC Express Lett. Part B: Appl.* **8**(1), 159–165 (2017)
12. Shi, Y., Cheng, X., Zhang, H.: Three dimensional trees emulation based on parametric L-system. *J. Tongji Univ. (Nat. Sci.)* **39**(12), 1871–1876 (2011)
13. Shu, H., et al.: *Apple Science*. China Agriculture Press, Beijing (1995)
14. Xingwang, Z., et al.: *Cultivation Techniques of Apple in Yunnan*. Yunnan Science and Technology Press, Kunming (1995)
15. Xia, X., Qiu, Y., Li, Z., et al.: Response of key ecological factors of Apple phenology to typical topography of orchard. *Jiangsu Agric. Sci.* **40**(9), 175–181 (2016)
16. Johnson, M., Liscio, E.: Suspect height estimation using the Faro Focus3D laser scanner. *J. Forensic Sci.* **60**(6), 1582 (2015)
17. Cao, J., Tagliasacchi, A., Olson, M., et al.: Point cloud skeletons via Laplacian-based contraction. In: *Shape Modeling International Conference SMI*, Aix En Provence, pp. 187–197 (2010)
18. Verroust, A., Lazarus, F.: Extracting skeletal curves from 3D scattered data. *Vis. Comput.* **16**(1), 15–25 (2000)
19. Ma, X., Meng, Q., Zhang, L., et al.: Image mosaics reconstruction of canopy organ morphology of apple trees. *Trans. Chin. Soc. Agric. Eng.* **30**(12), 154–162 (2014)
20. Lu, S., Guo, X., Zhao, C., et al.: Shape reconstruction of fruit tree from colored 3D point cloud. In: *The 7th International Conference on Functional-Structural Plant Models*, Saariselkä, Finland, pp. 55–57 (2013)
21. Sun, Z., Lu, S., Guo, X., et al.: Surfaces reconstruction of plant leaves based on point cloud data. *Trans. Chin. Soc. Agric. Eng.* **28**(3), 184–190 (2012)
22. Dong, Q., Wang, Y., Yang, L., et al.: Parameter identification of tomato 3D architectural model and simulation. *Trans. CSAE.* **26**(Suppl. 2), 38–42 (2010)



Comparison of Remote Sensing Estimation Methods for Winter Wheat Leaf Nitrogen Content

Chunlan Zhang¹, Fuquan Tang², Heli Li³(✉), Guijun Yang³,
Haikuan Feng³, and Chang Liu³

¹ College of Architecture Engineering, Shandong Xiehe University,
Jinan 250107, Shandong, China

1964362790@qq.com

² College of Geomatics, Xi'an University of Science and Technology,
Xi'an 710054, Shanxi, China

fquantang@163.com

³ National Engineering Research Center for Information Technology
in Agriculture, Beijing 100097, China

1h1237666@126.com, yanggj@nercita.org.cn,

fenghaikuan123@163.com, 1224129134@qq.com

Abstract. Leaf nitrogen content (LNC) is a good indicator of the nutritional status of winter wheat, and remote sensing monitoring of nitrogen level in winter wheat growth period can not only grasp the crop nutrient and growth conditions, but also help to improve the yield and quality. In this study, field data of canopy reflectance and LNC of winter wheat of three critical growth stages were collected for different treatments during 2014/2015 and 2015/2016. The correlation between LNC of winter wheat and 16 spectral indices was compared and analyzed, and then 4 spectral indices of NDSI (R_{594} , R_{506}), RSI (R_{592} , R_{506}), mSR_{705} and $mNDVI_{705}$ were selected. On the basis of this, linear regression (LR) model, multiple stepwise regression (MSR) model and random forest regression (RFR) model were constructed and validated with independent data sets in 2014/2015. To further compare the accuracy, stability and applicability of three inversion models, the robustness tests were conducted based on the independent data sets under three different conditions in 2015/2016. The result showed that the RFR model had the best estimation accuracy among the three models, and the value of R^2 and RMSE in modeling set respectively were 0.962 and 0.276, and the value of R^2 and RMSE in validation set were 0.898 and 0.401. In addition, the RFR model had a higher R^2 and lower RMSE than the other two models under each condition. It indicated that the RFR model combined with multiple spectral indices and random forest algorithm had higher precision and applicability, so it can effectively and rapidly retrieve the LNC of winter wheat.

Keywords: Leaf nitrogen content (LNC) · Remote sensing · Winter wheat Comparison

1 Introduction

Nitrogen has the most significant effect on photosynthesis, growth and development, yield and quality formation, and is also a mineral element with high crop demand and application [1]. When the crop is lack of nitrogen, it will seriously affect the yield and quality of the crop, otherwise, it will cause certain pollution to the environment. Therefore, assessment of crop nitrogen content rapidly, nondestructively and accurately is important for monitoring crop growth, improving the nitrogen use efficiency and developing precision agriculture [2].

Winter wheat is one of the main grain crops in China, and its nitrogen nutrition assessment is beneficial to growth diagnosis and field technical management. The traditional method of crop nitrogen diagnosis was mainly through laboratory chemical analysis, which usually required destructive sampling, resulting in poor timeliness and strong subjectivity. Hyperspectral remote sensing technology has gained extensive attention in the field of crop nitrogen nutrition diagnosis because of its large amount of information, high spectral resolution and continuous wave band [3]. At present, many scholars have done a lot of researches on crop nitrogen content estimation. Nguyen et al. [4] have used partial least squares regression method to estimate the nitrogen content of rice, and concluded that it was feasible to estimate crop nitrogen content based on spectral reflectance. After that, the estimation accuracy of crop nitrogen content was improved by screening sensitive bands and constructing vegetation index [1, 5, 6]. Other researchers have used artificial neural network method to retrieve the nitrogen content of crop [7]. Although predecessors have done a great deal of work and achieved fruitful results in monitoring crop nitrogen content, different inversion methods had their own characteristics. Linear regression model has the advantages of simple, easy to construct and visualization, but it also has some shortcomings, such as too many parameters in the process of fitting, and high dimensional data can not get the optimal solution. Machine learning algorithm, as a new learning method developed on the basis of statistical learning theory, is a very powerful tool for data analysis and mining, and it can solve the defects of linear regression model very well.

In view of this, this study selects a variety of spectral indices, and establishes three LNC estimation models based on linear regression, multivariate stepwise regression and random forest algorithm. To further explore an accurate and robust model for remote sensing of winter wheat LNC, this study will elucidate the predictive ability and relative advantage of three inversion models from the aspects of predictive accuracy, stability, applicability with independent data sets.

2 Materials and Methods

2.1 Experimental Design

The winter wheat field experiments were carried out in 2014/2015 and 2015/2016 at the National Experimental Station for Precision Agriculture (116.44°E, 40.18°N) in northeast Beijing, China. This site is characterized by a semi-humid continental

monsoon climate, with mean annual temperature and average elevation of 13 °C and 36 m, respectively.

A winter wheat field experiment was carried out in 2014/2015 under different variety, nitrogen levels and water treatments. The winter wheat varieties were Jing 9843 and Zhongmai 175. Nitrogen levels were 0 kg/hm², 195 kg/hm², 390 kg/hm², 585 kg/hm², and the nitrogen fertilizer was urea. Water treatments were rain feed, normal irrigation amount (675 m³/hm²), 1.5 times the normal amount of irrigation. A total of 16 experimental treatments were designed and each treatment was repeated 3 times, therefore, there were 48 experimental plots, and the area of each plot was 48 m². Other field management shall be carried out according to local normal level.

A winter wheat field experiment was conducted in 2015/2016 and designed 3 treatments (i.e., different variety, different test areas and different nitrogen levels). The winter wheat varieties were Lunxuan 167 and Jingdong 18. The two test areas were north and south, in which north area nitrogen treatments were 39 kg/hm², 195 kg/hm², 390 kg/hm², 585 kg/hm²; southern nitrogen treatments were 39 kg/hm², 390 kg/hm² (base fertilizer), 195 kg/hm² (base fertilizer) + 195 kg/hm² (after manuring), 195 kg/hm² (base fertilizer) + 390 kg/hm² (after manuring), and the nitrogen fertilizer was urea. A total of 16 experimental treatments were designed and each treatment was repeated 3 times, therefore, there were 48 experimental plots, and the area of each plot was 135 m². Other field management shall be carried out according to local normal level.

2.2 Data Collection

In this study, field data of canopy reflectance and LNC of winter wheat of three critical growth stages (i.e., flag leaf period, flowering period and filling period) were collected for different treatments in 2015 and 2016, respectively.

2.2.1 Canopy Spectrometry Collection

The winter wheat canopy reflectance was obtained by the ASD FieldSpec FR2500 spectrometer. The wavelength range of American ASD FieldSpec FR2500 spectrometer is from 350 nm to 2500 nm, and the spectral re-sampling interval is 1 nm. The weather was clear during the measure and the time of Beijing was 10:00 to 14:00. During observation, the probe was always vertical downward, about 1.0 m from the ground, with 25° field angle. In each experimental plot, we collected 10 records and took the average reflectance as the canopy spectral reflectance of the plot, and the standard white plate correction was carried out immediately before and after each measurement.

2.2.2 LNC Determination

In each experimental plot, 20 representative winter wheat plants were selected as sample, and loaded them into sealed bags immediately and brought back to the laboratory. First of all, the separation of stems and leaves, leaves after the separation were purified at 105 °C about 30 min. Then, then dried to the constant weight under the condition of 75 °C. After grinding, the leaf nitrogen content of winter wheat was determined by the micro-Kjeldahl method.

2.3 Spectral Index Selection

Spectral index was a spectral parameter obtained by combining different spectral bands with a certain algebraic form [8], and it could reduce the background interference on canopy spectral characteristics, so the sensitivity was better than single band [9, 10]. According to the results of previous studies, 16 spectral indices related to LNC were selected (Table 1).

Table 1. Spectral indices related to LNC in this study.

Spectral index (abbreviation, reference)	Formula	Quotation
Normalized difference vegetation index (NDVI, [11])	$(R_{800} - R_{670}) / (R_{800} + R_{670})$	[12]
Simple ratio index (SR ₇₀₅ , [13])	R_{750} / R_{705}	[14]
GMI1 ([13])	R_{750} / R_{550}	[14]
GMI2 ([13])	R_{750} / R_{700}	[14]
Red edge normalized index (NDVI ₇₀₅ , [15])	$(R_{750} - R_{705}) / (R_{750} + R_{705})$	[16]
Modified red edge ratio index (mSR ₇₀₅ , [17])	$(R_{750} - R_{445}) / (R_{705} - R_{445})$	[18]
Modified red edge normalized vegetation index (mNDVI ₇₀₅ , [17])	$(R_{750} - R_{705}) / (R_{750} + R_{705} - 2 \times R_{445})$	[18]
Red edge index (VOG1, [19])	R_{740} / R_{720}	[20]
Modified ratio index (MSR, [21])	$(R_{800} / R_{670} - 1) / \sqrt{(R_{800} / R_{670} + 1)}$	[22]
CIrededge ([23])	$R_{750} / R_{720} - 1$	[24]
Green normalized difference vegetation index (GNDVI, [25])	$(R_{750} - R_{550}) / (R_{750} + R_{550})$	[26]
RI-half ([27])	R_{747} / R_{708}	[20]
RSI (D ₇₄₀ , D ₅₂₂)	D_{740} / D_{522}	[6]
RSI (R ₈₁₅ , R ₇₀₄)	R_{815} / R_{704}	[28]
Normalized difference spectral index NDSI (i, j)	$(R_i - R_j) / (R_i + R_j)$	[29]
Ratio spectral index RSI (i, j)	R_i / R_j	[29]

Note: R is spectral reflectance. i and j are any two bands in a certain wavelength range.

2.4 Data Analysis

In this study, three LNC inversion models (i.e., LR, MSR and RFR) were constructed with 70% samples using SPSS 19.0 and MATLAB software and validated with the remaining 30% in 2014/2015. Then the robustness of three regression models was further tested by using independent data sets of different varieties, different growth

stages and different test areas in 2015/2016. Among them, the random forest algorithm is a statistical machine learning algorithm proposed by Breiman [30] in 2001. It uses Bootstrap resampling method to extract multiple training samples from the original samples, and each training sample is grown into a single decision tree. Then many relatively independent decision trees are combined to build a decision forest. Finally, we determine the final forecast results by using voting methods. This study was based on MATLAB program code for random forest regression, in which the number of decision trees was 1000, and the segmentation variable was 3.

2.5 Accuracy Evaluation

Determination coefficient (R^2), root mean square error (RMSE) and relative prediction deviation (RPD) were regarded as indicators to evaluate the predictive performance of the models in this study. Generally speaking, the closer the R^2 is to 1, the smaller RMSE, and the better predictive performance of the estimated model, otherwise, the predictive performance is poor. For RPD, the model forecast ability is excellent when $RPD \geq 2$; it can be used for rough evaluation of samples when $1.4 < RPD < 2$; otherwise, the model fails to predict the samples [31].

3 Results and Analysis

3.1 Correlation Between Spectral Index and LNC

As can be seen from Table 2, there was the correlation coefficient between spectral index and LNC. As a whole, the spectral indices used in this study were strongly related to LNC, and $|r|$ was above 0.70, and all of them have reached a very significant level of 0.01. Among them, the correlation coefficient between mNDVI₇₀₅ and LNC was the highest ($r = 0.835$), and the correlation minimum was NDVI ($r = 0.736$). At the same time, this study analyzed the correlation between NDSI, RSI and the LNC of any two bands in the range of 400–1000 nm, as shown in Fig. 1. The result showed that the spectral indices made up of 594 nm, 592 nm and 506 nm bands were more sensitive to LNC. NDSI(R_{594} , R_{506}) and RSI(R_{592} , R_{506}) all had highly significant negative correlation with LNC, with correlation coefficient r of -0.907 and -0.911 , respectively.

According to statistics, it can be regarded as highly relevant where correlation coefficient $|r| \geq 0.8$; when correlation coefficient $0.5 \leq |r| < 0.8$, it can be regarded as a moderate correlation; otherwise, it can be regarded as a low correlation [32]. As can be seen from Table 2, there were 8 spectral indices that were highly related to LNC, namely NDVI₇₀₅, mSR₇₀₅, mNDVI₇₀₅, VOG1, CIrededge, GNDVI, NDSI(R_{594} , R_{506}), RSI(R_{592} , R_{506}), and there were 8 spectral indices that were moderately related to LNC, namely NDVI, SR₇₀₅, MSR, GMI1, GMI2, RI-half, RSI(D_{740} , D_{522}), RSI(R_{815} , R_{704}).

Table 2. Correlation coefficients between spectral index and LNC.

Spectral index	r	Spectral index	r
NDVI	0.736**	GNDVI	0.809**
SR ₇₀₅	0.791**	GMI1	0.778**
NDVI ₇₀₅	0.802**	GMI2	0.781**
mSR ₇₀₅	0.825**	RI-half	0.796**
mNDVI ₇₀₅	0.835**	RSI(D ₇₄₀ , D ₅₂₂)	0.797**
VOG1	0.806**	RSI(R ₈₁₅ , R ₇₀₄)	0.785**
MSR	0.759**	NDSI(R ₅₉₄ , R ₅₀₆)	-0.907**
Cirededge	0.801**	RSI(R ₅₉₂ , R ₅₀₆)	-0.911**

Note: **represents significant at the 0.01 level of probability.

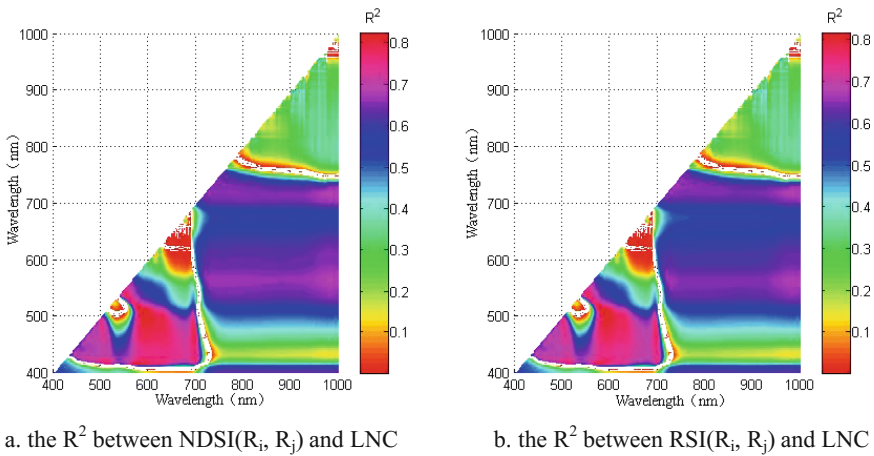


Fig. 1. The R² between spectral indices and LNC

3.2 Selective Preference of Spectral Index

On the basis of the study above, 8 highly correlated spectral indices were selected for further analysis according to the correlation between spectral indices and LNC. As shown in Table 3, the determination coefficients of the inversion models of winter wheat LNC based on 8 spectral indices were examined by extremely significant, and the coefficient of determination of RSI (R₅₉₂, R₅₀₆) was the largest, and the R² was 0.831. In this study, the R² and F were used as the criteria for selecting better spectral indices. The closer the R² is to 1, the higher the accuracy of the model, and the greater the F value, the more significant the regression relationship is. Therefore, 4 spectral indices were selected as the better spectral indices, and the 4 spectral indices were mNDVI₇₀₅, mSR₇₀₅, NDSI(R₅₉₄, R₅₀₆), RSI(R₅₉₂, R₅₀₆).

Table 3. Correlation analysis between spectral index and LNC.

Spectral index	R ²	F	Spectral index	R ²	F
NDVI ₇₀₅	0.643**	169.492	GNDVI	0.654**	177.757
mNDVI ₇₀₅	0.698**	216.879	VOG1	0.650**	174.620
mSR ₇₀₅	0.681**	200.808	NDSI(R ₅₉₄ , R ₅₀₆)	0.823**	436.126
CIrededge	0.641**	167.751	RSI(R ₅₉₂ , R ₅₀₆)	0.831**	460.604

Note: **represents significant at the 0.01 level of probability.

3.3 Construction and Verification of LNC Estimation Model for Winter Wheat

This study constructed the LNC estimation model according to the three methods. The three methods were as follows: (1) With LNC as dependent variable, RSI(R₅₉₂, R₅₀₆), the highest spectral index of R² and F, was chosen as independent variable, and a linear regression model (LR) was constructed. (2) 4 better spectral indices (i.e., mNDVI₇₀₅, mSR₇₀₅, NDSI(R₅₉₄, R₅₀₆), RSI(R₅₉₂, R₅₀₆)) were selected as independent variables, and the LNC remote sensing estimation model (MSR) was constructed by multiple stepwise regression method. (3) 4 better spectral indices (i.e., mNDVI₇₀₅, mSR₇₀₅, NDSI(R₅₉₄, R₅₀₆), RSI(R₅₉₂, R₅₀₆)) were selected as independent variables, and the LNC remote sensing estimation model (RFR) was constructed by the random forest algorithm.

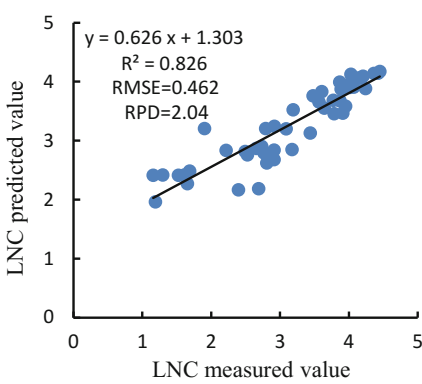
The LNC estimation models that were constructed based on three modeling methods using 2014/2015 data were shown in Table 4. The estimation accuracy of three models was more than 0.8, and the RMSE was between 0.276 and 0.288. These results showed that the three models can be used for rapid, nondestructive and accurate monitoring of LNC of winter wheat, and among them, the effect of RFR model was the best. But in comparison, the estimation accuracy of multivariate stepwise regression (MSR) model was slightly better than that of linear regression (LR) model, and the estimation accuracy of the random forest regression (RFR) model was the highest, with R² and RMSE of 0.962 and 0.276 respectively. It was possible that the information contained in a single spectral index had different degrees of saturation, and the error of crop nitrogen content estimation was greater. The multiple regression model could input more band information related to LNC, which could not only improve the estimation accuracy of the model, but also improved the stability. Random forest algorithm is a multivariate regression method based on statistics, and it has the advantages of strong noise tolerance, high efficiency in dealing with large data sets, and difficult to overfitting, so it is suitable for solving LNC inverse problem.

In order to compare the predictive ability of three estimation models, each model was used to predict 48 samples of the independent data-sets, and the results of three models were shown in Table 4 and Fig. 2. The result showed that the verification accuracy of three models was more than 0.8, and the RPD of the three models was greater than 2, indicating that the three models can predict the LNC better. However, the RFR had some advantages over the other two models in LNC estimation of winter wheat and the value of validation set of R² and RMSE were 0.898 and 0.401. The

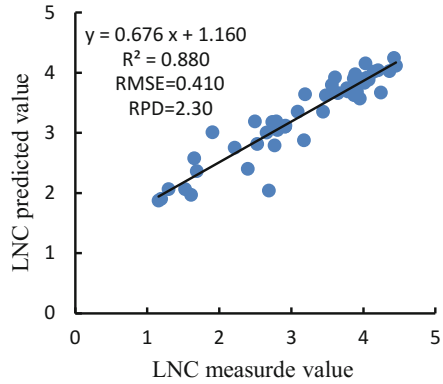
reason may be that the RFR model used Out of Bag data (OOB) to establish error unbiased estimation during the data calculation. In summary, the difference of estimation performance of three regression models was little, but the random forest

Table 4. Comparison of LNC estimation models constructed by three methods.

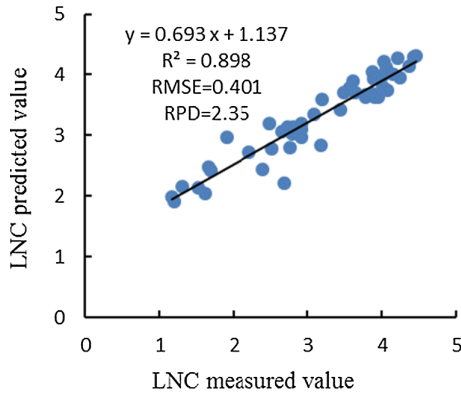
Estimation model	Model expression	Modeling		Verification	
		R ²	RMSE	R ²	RMSE
LR	$V_{LNC} = -3.49V_{RSI(R592, R506)} + 8.949$	0.831	0.288	0.826	0.462
MSR	$V_{LNC} = 7.257V_{RSI(R592, R506)} + 15.254V_{NDSI(R594, R506)} + 0.078V_{mSR705} - 0.114V_{mNDVI705} + 11.180$	0.842	0.280	0.880	0.410
RFR		0.962	0.276	0.898	0.401



a. Prediction result based on LR



b. Prediction result based on MSR



c. Prediction result based on RFR

Fig. 2. Relationship between measured value and predicted value based on 3 methods

regression model (RFR) performed slightly better. The robustness of three regression models was further tested by using independent data sets of different varieties, stages and test areas in 2015/2016, so as to select the LNC estimation model of winter wheat with high precision, good stability and strong applicability.

3.4 Robustness Test of LNC Estimation Model for Winter Wheat

For inversion results of winter wheat LNC about different varieties (Table 5), the estimation accuracy of three estimation models was that the loose variety Lunxuan 167 lower than compact variety Jingdong 18, while the inversion accuracy of RFR model for loose type and compact type were the highest. As can be seen from Table 6, the inversion results of the three models in different growth stages were different, but the RFR model had the best inversion accuracy relative to LR and MSR at three growth stages. The LNC inversion results (Table 7) of winter wheat from different experimental areas showed that the accuracy of three estimation models to the north was higher than the south area, and the accuracy of RFR model in two test areas was higher than that of the other two models. Based on the above analysis, RFR model was not only robust to the LNC estimation of winter wheat under different conditions in different years, but also the estimation accuracy was higher than that of LR model and MSR model. It showed that the RFR model constructed in this study had high precision and good applicability, and it was a preferred model for estimating winter wheat LNC.

Table 5. LNC estimation results of winter wheat for different cultivars.

Varieties	Estimation model	R ²	RMSE
Jingdong 18	LR	0.686	0.965
	MSR	0.704	0.870
	RFR	0.760	0.848
Lunxuan 167	LR	0.511	0.755
	MSR	0.547	0.720
	RFR	0.702	0.695

Table 6. LNC estimation results of winter wheat for different growth stages.

Growth stages	Estimation model	R ²	RMSE
Flag leaf period	LR	0.458	0.373
	MSR	0.539	0.393
	RFR	0.631	0.392
Flowering period	LR	0.416	0.793
	MSR	0.565	0.737
	RFR	0.699	0.179
Filling period	LR	0.323	0.978
	MSR	0.582	0.934
	RFR	0.748	0.158

Table 7. LNC estimation results of winter wheat for different test areas.

Test areas	Estimation model	R ²	RMSE
North area	LR	0.606	0.890
	MSR	0.667	0.827
	RFR	0.786	0.802
South area	LR	0.440	0.841
	MSR	0.534	0.768
	RFR	0.632	0.749

4 Conclusions

In this study, correlation analysis between spectral index and LNC was carried out based on canopy spectral data and LNC of winter wheat under different years (i.e., 2014/2015, 2015/2016), different treatments (i.e., varieties, fertilizer and water supply), different growth stages (i.e., jointing stage, flowering stage and filling stage). Then, the LNC estimation models of winter wheat were constructed by three methods of linear regression, stepwise regression and random forest regression, and the accuracy and stability of the LNC estimation model were verified. The results were as follows:

- (1) The correlation between the four spectral indices (i.e., NDSI(R₅₉₄, R₅₀₆), RSI(R₅₉₂, R₅₀₆), mSR₇₀₅, mNDVI₇₀₅) and LNC of winter wheat was preferable, and RSI(R₅₉₂, R₅₀₆) had the highest correlation with LNC ($r = -0.911$). The accuracy of three estimation models was above 0.8, indicating that the three estimation models can be used for rapid, nondestructive and accurate LNC monitoring of winter wheat. Among them, the RFR model had the best effect. In the modeling set, the value of R² and RMSE respectively were 0.962 and 0.276, and in the verification set, the value of R² and RMSE respectively were 0.898 and 0.401.
- (2) The applicability of the three models was further tested by using 2015/2016 data. It was found that the estimation accuracy of the RFR model was higher than the other two estimation models for each set of experimental samples, moreover, the LNC estimation of winter wheat was robust under different conditions in different years, so it can be regarded as the preferred model for the estimation of winter wheat LNC.

Acknowledgments. This work was supported in part by the National key research and development program (2016YFD0200600, 2016YFD02006030) and National Natural Science Foundation of China (No. 41671411; 41471351, 41601346).

References

1. Tian, Y.C., Zhu, Y., Yao, X., Liu, X.J., Cao, W.X.: Nondestructive monitoring of crop nitrogen nutrition based on spectral information. *Chin. J. Ecol.* (09), 1454–1463(2007)
2. Li, Y.M., Zhang, X.J., Zhang, L.G.: Hyperspectral nitrogen estimation model of remote sensing in rice. *Jiangsu Agric. Sci.* **44**(8), 435–439 (2014)

3. Wang, R.H., Song, X.Y., Li, Z.H.: Estimation of winter wheat nitrogen nutrition index using hyperspectral remote sensing. *Trans. Chin. Soc. Agric. Eng.* **30**(19), 191–198 (2014)
4. Nguyen, H.T., Kim, J.H., Nguyen, A.T.: Using canopy reflectance and partial least squares regression to calculate within-field statistical variation in crop growth and nitrogen status of rice. *Precis. Agric.* **7**(4), 249–264 (2006)
5. He, L., et al.: Improved remote sensing of leaf nitrogen concentration in winter wheat using multi-angular hyperspectral data. *Remote Sens. Environ.* **174**(174), 122–133 (2016)
6. Inoue, Y.S., Sakaiya, E.J., Zhu, Y., Takahashi, W.: Diagnostic mapping of canopy nitrogen content in rice based on hyperspectral measurements. *Remote Sens. Environ.* **126**, 210–221 (2012)
7. Zhang, C.H., Kovacs, J.M., Wachowiak, M.P.: Relationship between hyperspectral measurements and mangrove leaf nitrogen concentrations. *Remote Sens.* **5**(2), 891–908 (2013)
8. Tong, Q.X., Zhang, B., Zheng, L.F.: *Hyperspectral Remote Sensing*. Higher Education Press, Beijing (2006)
9. Jiang, H.L., Yang, H., Chen, X.P., Wang, S.D., Li, X.K., Liu, K.: Research on accuracy and stability of inverting vegetation chlorophyll content by spectral index method. *Spectrosc. Spectr. Anal.* **35**(04), 975–981 (2015)
10. Hunt, E.R., Doraiswamy, P.C., McMurtrey, J.E.: A visible band index for remote sensing leaf chlorophyll content at the canopy scale. *Int. J. Appl. Earth Obs. Geoinf.* **21**, 103–112 (2013)
11. Peñuelas, J., Isla, R., Filella, I.: Visible and near-infrared reflectance assessment of salinity effects on Barley. *Crop Sci.* **37**(1), 198–202 (1997)
12. Tanaka, S., Kawamura, K., Maki, M.: Spectral index for quantifying leaf area index of winter wheat by field hyperspectral measurements: a case study in Gifu prefecture, central Japan. *Remote Sens.* **7**(5), 5329–5346 (2015)
13. Gitelson, A.A., Merzlyak, M.N.: Quantitative estimation of chlorophyll-a using reflectance spectral: experiments with autumn chestnut and maple leaves. *J. Photochem. Photobiol. B-Biol.* **22**(3), 247–252 (1994)
14. Asner, G.P., Martin, R.E., Knapp, D.E.: Spectroscopy of canopy chemicals in humid tropical forests. *Remote Sens. Environ.* **115**(12), 3587–3598 (2011)
15. Gitelson, A.A., Merzlyak, M.N.: Spectral reflectance changes associated with autumn senescence of *Aesculus Hippocastanum* L. and *Acer Platanoides* L. leaves. Spectral features and relation to chlorophyll estimation. *J. Plant Physiol.* **143**(3), 286–292 (1994)
16. He, J., Liu, B.F., Li, J.: Monitoring model of leaf area index of winter wheat based on hyperspectral reflectance at different growth stages. *Trans. Chin. Soc. Agric. Eng.* **30**(24), 141–150 (2014)
17. Datt, B.: A new reflectance index for remote sensing of chlorophyll content in higher plants: tests using eucalyptus leaves. *J. Plant Physiol.* **154**(1), 30–36 (1999)
18. Sims, D.A., Gamon, J.A.: Relationships between leaf pigment content and spectral reflectance across a wide range of species, leaf structures and developmental stages. *Remote Sens. Environ.* **81**(2), 337–354 (2002)
19. Vogelmann, J.E., Rock, B.N., Moss, D.M.: Red edge spectral measurements from sugar maple leaves. *Int. J. Remote Sens.* **14**(8), 1563–1575 (1993)
20. Yin, X.J., Zhang, Q., Zhao, Q.Z.: Remote sensing inversion of nitrogen content based on SVM in processing tomato early blight leaves. *Trans. Chin. Soc. Agric. Mach.* **45**(11), 280–285+39 (2014)
21. Richardson, A.J., Weigand, C.: Distinguishing vegetation from soil background information. *Photogramm. Eng. Remote Sens.* **43**(12), 1541–1552 (1977)

22. Chen, J.M.: Evaluation of vegetation indices and a modified simple ratio for boreal applications. *Can. J. Remote Sens.* **22**(3), 229–242 (1996)
23. Gitelson, A.A., Vina, A., Ciganda, V.: Remote estimation of canopy chlorophyll content in crops. *Geophys. Res. Lett.* **32**(8), 1–4 (2005)
24. Dash, J., Curran, P.J.: Evaluation of the MERIS terrestrial chlorophyll index (MTCI). *Adv. Space Res.* **39**(1), 100–104 (2007)
25. Baret, F., Guyot, G.: Potentials and limits of vegetation indices for LAI and APAR assessment. *Remote Sens. Environ.* **35**(2), 161–173 (1991)
26. Lelong, C.C.D., Burger, P., Jubelin, G.: Assessment of unmanned aerial vehicles imagery for quantitative monitoring of wheat crop in small plots. *Sensors* **8**(5), 3557–3585 (2008)
27. Gupta, R.K., Vijayan, D., Prasad, T.S.: Comparative analysis of red-edge hyperspectral indices. *Adv. Space Res.* **32**(11), 2217–2222 (2003)
28. Inoue, Y., Guérif, M., Baret, F.: Simple and robust methods for remote sensing of canopy chlorophyll content: a comparative analysis of hyperspectral data for different types of vegetation. *Plant, Cell Environ.* **39**, 2609–2623 (2016)
29. Qin, Z.F., Chang, Q.R., Xie, B.N., Shen, J.: Rice leaf nitrogen content estimation based on hyperspectral imagery of UAV in yellow river diversion irrigation district. *Trans. Chin. Soc. Agric. Eng.* **32**(23), 77–85 (2016)
30. Breiman, L.: Random forests. *Mach. Learn.* **45**(1), 5–32 (2001)
31. Tian, Y.C., Gu, K.J., Xu, C.: Comparison of different hyperspectral vegetation indices for canopy leaf nitrogen concentration estimation in rice. *Plant Soil* **376**(1/2), 193–209 (2014)
32. Xia, T., Wu, W.B., Zhou, Q.B.: Comparison of two inversion methods for winter wheat leaf area index based on hyperspectral remote sensing. *Trans. Chin. Soc. Agric. Eng.* **29**(3), 139–147 (2013)



Design and Implementation of the Wheat Population Nutrition Detection System

Lei Shi¹, Qiguo Duan², Mingyang Xiong¹, Juanjuan Zhang¹,
Lihong Song¹, and Xinming Ma¹(✉)

¹ Collaborative Innovation Center of Henan Grain Crops,
College of Information and Management Science,
Henan Agricultural University, Zhengzhou 450002, China
sleicn@126.com, 2577341098@qq.com,
zhangjuan_2003@126.com, 1565406188@qq.com,
xinmingma@126.com

² Zhengzhou Commodity Exchange, Zhengzhou 450008, China
dqgc@126.com

Abstract. It will impact the overall yield and quality of wheat if the malnutrition in the wheat growing season is not timely found. Thus, it is necessary to carry out timely nutrition detection of the wheat population in the field. Based on the techniques of Java web development and image processing, this paper constructs the estimation model of the field wheat population condition, designs and implements the automatic nutrition detection and analysis system based on field wheat population images. By using the received images of crop growth group, the system detects the nutrition condition of wheat population cultivated in the field quickly, and gives assisted fertilization decision to farmers for reducing the effect of wheat malnutrition on the yield and quality of wheat.

Keywords: Image processing · Wheat population · Nutrition detection
Intelligent diagnosis

1 Introduction

Wheat is one of the most important food crops in the world, and it is also an important grain crop in China. It is very important to improve the yield and quality of wheat for ensuring the safety of grain production in China. Current research on wheat automatic monitoring in China mainly focused on environmental testing [1–3], the seedlings diagnosis [4, 5], anomaly detection [6–8] and etc. The nutritional status of wheat is an important factor, and timely detection of the nutritional status of wheat at each growth stage is very significant for food production. Previous nutritional status of different growth stages of wheat were carried out extensive analysis experiments, studies have shown that chemical analysis in the laboratory can accurately measure the nutritional status of wheat, but this method would cause damage to the wheat plants, and the experimental results tend to be a lagging indicator and in a low detection efficiency. SPAD chlorophyll meter is more accurate. However, the plant leaf area determined by

this method is limited, and it is difficult to apply in field conditions. The current identification mean is according to the experts in the field of the nutrition. This method is time-consuming and laborious, and is affected by personal experience. At present, it has been shown that the changes of crop leaf color can reflect the nutritional status of the plant leaves, and application of image processing technology in detecting nutrition status in the wheat growth has become a hot research topic [9, 10].

In recent years, computer image processing technology has been widely used in the fields of industry and agriculture. For example, Zhang et al. used the RGB and HSI color models to analyze the related characteristics of cucumber leaf nitrogen content, phosphorus ratio and water content, and realized the nutrient detection of greenhouse cucumber plants [11]. Jia et al. used the image processing software applications such as color depth rice canopy and the corresponding elongation stage in rice crop nutrition analysis, and rice nitrogen nutrition rapid diagnostic method was established [12]. Wang et al. applied image data processing exchange in the tobacco samples, established TMDHSV model to determine the maturity of tobacco [13]. Liu extracted image of rice plant morphological parameters and used image to achieve the detection of rice growing [14]. The above studies are based the test sample obtained from an individual sample and crop ideal results, however the research of nutrition detection system in wheat field environment is rarely reported.

In this study, available wheat nutritional surveillance model is researched based on image processing technology, JavaEE technology platform is used to design and implement the field wheat population image analysis system for nutrition detection. The system aims to solve the problem that the modern farmers can not accurately detect the nutritional status of the wheat population in the field environment, and provide technical support for the future farmland real-time monitoring system.

2 The Overall System Design Framework

Wheat nutrition detection system uses the images. The acquired images of wheat are analyzed and processed, and the model features are extracted. The nutritional status and the corresponding solutions are given to the users through the human interface.

2.1 The Three-Tier Architecture of the System

The system is mainly based on B/S (Browser/Server) structure. the three-tier structure, i.e., data layer, logic layer and presentation layer are used for the field wheat population image collection, storage and processing analysis, decision of the nutritional status of wheat populations [15]. The system structure is shown in Fig. 1.

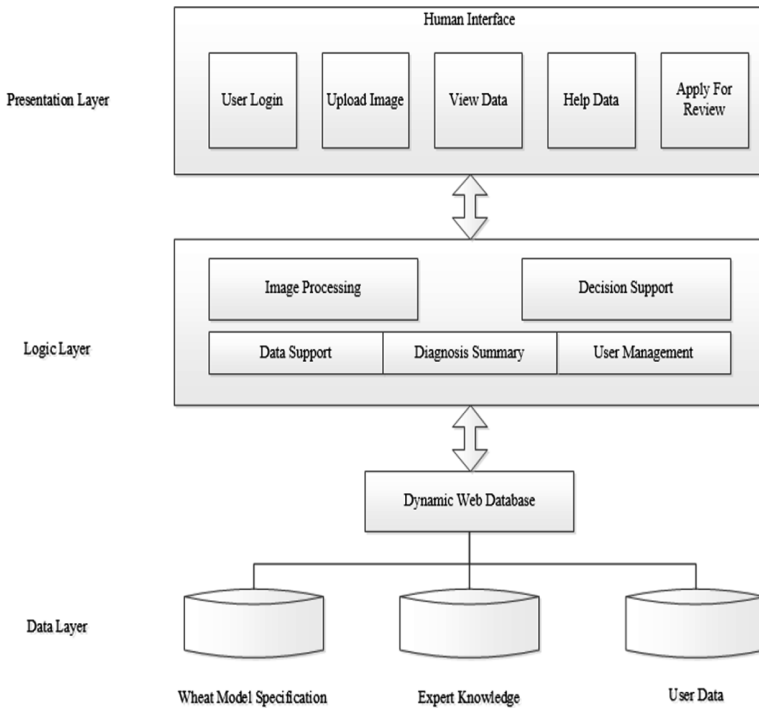


Fig. 1. System architecture diagram

(1) The data layer is located on the server and database side, which stores the core data of the system. It includes various user data, image feature model and the corresponding auxiliary fertilization program to provide image analysis support, decision-making knowledge warehouse. Thus, it plays the role to support the entire system.

(2) The logic layer is the main function and business logic of the core processing module. The main functions of the image processor and the decision support module are two key parts. The image processor receives image information from the interface. After the process of image normalization, image segmentation and image denoising, features are extracted based on model and the decisions are given.

(3) The presentation layer is the interface that the user interacts with the system. Wheat population nutrition diagnosis system is displayed to the user. The user can upload images in the presentation layer.

The system used the three-tier design to obtain good stability and scalability, so it is easy to maintenance the system.

2.2 The Main Process Design System

In the wheat population nutrition detection system, users upload images to a Web server and select wheat varieties. The images is applied in normalization, segmentation, de-noising process by the image processor module, and then the image color

characteristics of wheat colony is extracted. Then, the decision support module extracts the analysis results, these color features will be matched with the estimated model, and feature of those analysis are stored into the database. Finally, decision support system gives targeted fertilization views, and the user can access the system through the Web page to view the results of the analysis about the image and expert advice [16]. The specific processes are shown in Fig. 2.

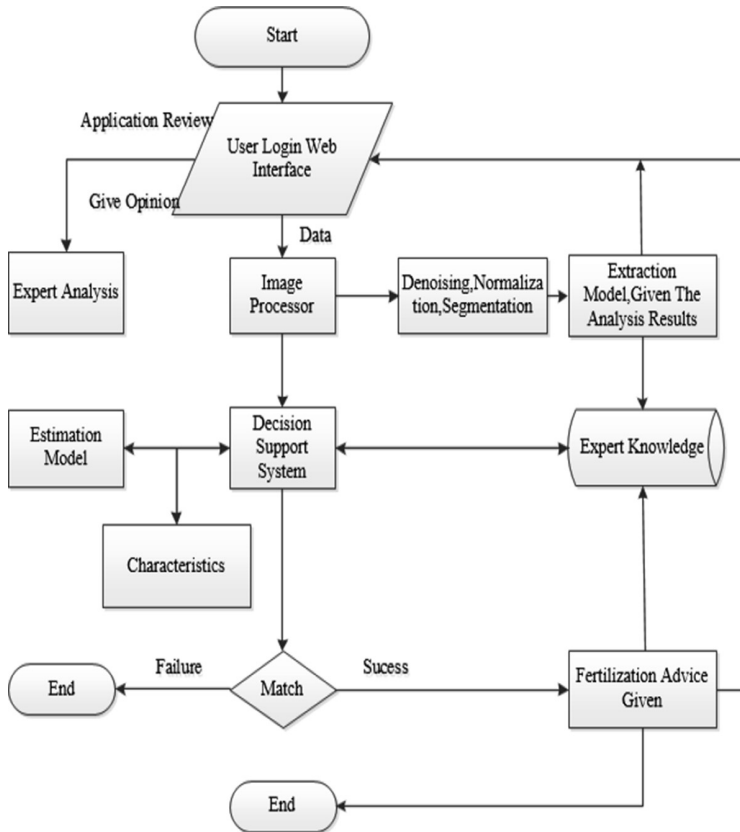


Fig. 2. Systems business flowchart

2.3 System Main Function Modules

The function module of the system includes five parts, i.e., professional knowledge integration, intelligent diagnostics, user management, system management, help module. The function module of the system is shown in Fig. 3.

Integration of Professional Knowledge. The content of professional knowledge integration includes image model specification and expert knowledge integration. This section uses a variety of image models and the corresponding nutritional status data to determine the nutritional status of the wheat group images.

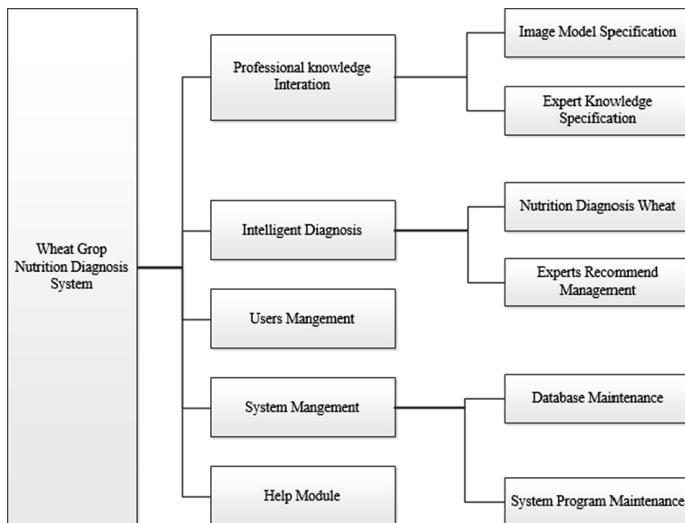


Fig. 3. System functional schematic

Intelligent Diagnosis. The intelligent diagnosis module is the core part of the system. This part combines the experts' experience and the research results of modern agriculture, and obtains the regularity between the wheat nutrition status and the group image parameters. The specific process is used to analyze the data and the appropriate expert advice is given.

User Management. The users of the system are divided into three kinds of authority: ordinary users, expert users and administrator users. The administrator user is responsible for assigning the rights of the expert user and the ordinary user. The expert user can add or modify the expert knowledge base. Ordinary users can only query and browse the results.

3 Implementation and Application of System

3.1 Developing and Operating Environment

The system is based on B/S (Browser/Server) mode, and follows the JavaEE (Java Platform Enterprise Edition). The three-tier Web architecture is designed, and SSH2 (Struts2+Spring+Hibernate) is used to develop the framework. The MySQL is used as database. The open source Apache Tomcat 6.0 Server is used as WEB application server, and Java language is used for program development. Color image segmentation, normalization and morphological denoising are used to complete the image processing.

3.2 System Implementation

3.2.1 Image Processing System Working Method

The role of the image processing system is to get the original image normalization, segmentation, denoising, and image model extraction [17]. This system mainly uses three image processing techniques to carry on the processing and to identify wheat population images.

(1) The image normalization. Wheat image processing system can be applied for images collected from the open field environment. In order to avoid the effects of light and shadow on the images, the images need to be normalized. Normalization methods are shown as Eqs. (1) and (2) [18].

$$\begin{cases} r = \frac{R}{R+G+B} \\ g = \frac{G}{R+G+B} \\ b = \frac{B}{R+G+B} \end{cases} \quad (1)$$

$$\begin{cases} r = \frac{R}{\sqrt{R^2+G^2+B^2}} \\ g = \frac{G}{\sqrt{R^2+G^2+B^2}} \\ b = \frac{B}{\sqrt{R^2+G^2+B^2}} \end{cases} \quad (2)$$

(2) Image segmentation. This system creates the image segmentation method based on pattern recognition technology. In order to build an unsupervised image segmentation model, this paper uses the RGB color model to create pattern recognition and classification rules by Mahalanobis distance [18]. Methods are shown as Eq. (3) [19].

$$D(z, a) = [(z - a)^T C^{-1} (z - a)]^{\frac{1}{2}} \quad (3)$$

(3) Morphological image Clean-up. After image segmentation of wheat population images, the result is a binary image. It contains a lot of noise formed by the image segmentation, the system uses the morphological image processing for the image denoising. The method is shown as Eqs. (4) and (5) [19].

$$A \circ B = (A \ominus B) \oplus B \quad (4)$$

$$A \cdot B = (A \oplus B) \ominus B \quad (5)$$

In this system, the image processing module is achieved in Matlab, and then is compiled and integrated into the system by Matlab Builder JA. The server deploys MCR (Matlab Compiler Runtime) to provide the runtime environment and dependencies.

3.2.2 Decision Support System

Decision support mechanism is associated with every component of the system. Decision support system contributes to provide users with the necessary data and information from the intelligent simulation expert, to help users identify the problems, to match the correct decision model, to query the information required by various users.

The man-machine interface returns information to the user, provides the necessary support for the right decisions.

3.2.3 System Database

The function of the system database is to organize the large amount of estimating model parameters and knowledge of agricultural experts in a certain pattern. It provides knowledge storage, maintenance and data retrieval [20, 21]. The system adopts the top-down strategy and distributed database design strategy [22, 23].

3.3 System Application

The system interface is shown in Fig. 4. The user can upload the collected images of wheat population. The results returned by the system is shown in Fig. 5.



Fig. 4. User interface of uploading images



Fig. 5. Interface of presenting system analysis results

After comparing with the conclusions from multiple sets of image systems and suggestions from experts, it shows that the detection results and treatment advices of the wheat nutrition status are basically consistent with the expert suggestions. The nutritional status of the system meets the basic application requirements. The system is designed and developed reasonably, so it has simple interface operation, and has good stability and practicality.

4 Conclusion

In this paper, wheat population nutrition detection system is designed and implemented by using Java web developing technology framework. The functions of the system have been tested and applied in the demonstration areas. The results show that the advantages of systems are accurate identification and rapid diagnosis in nutrition detection of field population wheat. In the future work, the improvement of the model and pattern recognition methods are important research direction.

Acknowledgement. This work is supported by the National Natural Science Foundation of the People's Republic of China (Grant No. 31501225), the Key Scientific Research Projects of Colleges and Universities of Henan Province (Grant No. 16A520055), the Modern Agriculture Industry Technology System in Henan Province (Grant No. S2010-01-G04), the National Key Research and Development Program of China (Grant No. 2016YFD0300609) and the China Scholarship Council (No. 201709160005).

References

1. Sun, Z.F., Cao, H.T., Li, H.L.: Based on GPRS and WEB achieve the greenhouse environment information collection system. *Agric. Eng.* **22**(6), 131–134 (2006)
2. Lv, Y.T., Du, K.M., Sun, Z.F.: Greenhouse remote monitoring and diagnosis. *Manag. Syst. Agric. Netw. Inf.* (9), 14–16 (2008)
3. Zhao, W., Sun, Z.F., Du, K.M.: GPRS and WEB-based greenhouse remote automatic control system design and implementation. *Microcomput. Inf.* **26**(11), 20–22 (2010)
4. Xia, Y., Sun, Z.H., Du, K.M.: Things wheat-based growth of the seedlings diagnosis and management system design and implementation. *Agric. Eng.* **29**(5), 117–124 (2013)
5. Zhang, Q., Huang, W.J., Xu, T.Y.: Wheat growth of the seedlings remote monitoring and diagnostic system. *Agric. Eng.* **27**(12), 115–119 (2011)
6. Wang, Z.L., Wang, B., Wang, Z.J.: Farmland soil moisture monitoring and predicting system design and implementation. *Agric. Eng.* **22**(2), 188–190 (2006)
7. Zhou, Y., Gao, P.: Design and implementation of integrated crop pest forecasting system. *Comput. Appl.* **34**, 141–144 (2014)
8. Zhu, X.F.: Weed Research in Support Vector Machine. Jiangsu University (2010)
9. Lin, K.Y., Xu, L.H., Wu, J.H.: Advances in computer vision technology in crop growth monitoring. *Agric. Eng.* **20**(2), 279–283 (2004)
10. Ma, X.M.: Introduction to Agricultural Information. China Agricultural Science and Technology Press (2009)
11. Zhang, Y.N., Li, M.Z., Zhang, X.J.: Greenhouse cucumber leaves nutrition information based on computer vision technology. *Agric. Eng.* **21**(8), 102–105 (2005)

12. Jia, L.L., Fan, M.S., Zhang, F.S.: Application of digital camera rice nitrogen nutrition diagnosis. *Spectrosc. Spectral Anal.* **29**(8), 2176–2179 (2009)
13. Wang, Q., Xi, L., Ren, Y.N.: Determination method based on leaf maturity computer vision technology. *Agric. Eng.* **28**(4), 175–179 (2012)
14. Liu, J.C.: Based on digital image processing technology to detect rice growing research. Nanjing Agricultural College (2007)
15. Wang, J.: Three-tier B/S mode. *Software GUIDE*, vol. 10, no. 3, pp. 30–31 (2011)
16. Pang, X.D.: Based on digital image processing technology wheat nutritional status of remote detection system and implementation of. Henan Agricultural University (2014)
17. Chen, B.Q., Guo, X.M., Li, X.H.: Wheat disease diagnostic image processing algorithms. *Based Agric. Mach.* **40**(12), 190–195 (2009)
18. Shi, L., Pang, X.D., Yu, Y.: Unsupervised segmentation of wheat color image based on Mahalanobis distance. *Henan Agric. Univ.* **48**(1), 87–90 (2014)
19. Gonzalez, W., Ruan, Q.Q.: *Digital Image Processing Technology*. Electronic Industry Press, Beijing (2011)
20. Guo, L., Wang, F., Zhang, Y.: Crop remote-sensing monitoring management system design and implementation. *Agric. Eng.* **29**(3), 132–138 (2013)
21. Xi, L., Zhang, H., Guo, W.: Distributed free agricultural digital authentication system construction and realization. *Agric. Eng.* **26**(8), 236–242 (2010)
22. Shao, P.Y.: *Distributed Database System and Its Application*, 2nd edn., pp. 39–65. Science Press, Beijing (2005)
23. Li, S.J., Yang, H.J., Huang, Y.H., Zhou, Q.: Geo-spatial Big Data storage based on NoSQL database. *Geomatics Inf. Sci. Wuhan Univ.* **42**(2), 163–169 (2017)



Hyperspectral Estimation Methods for Chlorophyll Content of Apple Based on Random Forest

Haojie Pei^{1,2,3,4,5}, Changchun Li^{5(✉)}, Haikuan Feng^{1,2,3,4(✉)},
Guijun Yang^{1,2,3,4}, Mingxing Liu^{1,2,3,4,5}, and Zhichao Wu^{1,2,3,4,5}

¹ Key Laboratory of Quantitative Remote Sensing in Agriculture
of Ministry of Agriculture People's Republic of China,
Beijing Research Center for Information Technology in Agriculture,
Beijing 100097, China

xmljphj@163.com, fenghaikuan123@163.com,
guijun.yang@163.com, WZC032018@163.com,
liumingxingreal@126.com

² National Engineering Research Center for Information Technology
in Agriculture, Beijing 100097, China

³ Key Laboratory for Information Technologies in Agriculture,
the Ministry of Agriculture, Beijing 100097, China

⁴ Beijing Engineering Research Center of Agricultural Internet of Things,
Beijing 100097, China

⁵ School of Surveying and Land Information Engineering,
Henan Polytechnic University, Jiaozuo 454000, China
lichangchun610@126.com

Abstract. Chlorophyll content is a good indicator of fruit tree nutrition stress, photosynthesis, and another physiological state. 10 vegetation indices were selected and used as input variables of RF model, the number of input variables was gradually increased from 1 to 10. The modeling accuracy of 10 RF models with vegetation indices was compared. Finally, the accuracy of 2 estimation models, the RF model with the original spectrum, and the RF optimal model with vegetation indices were established and compared. The result, For modeling accuracy of 2 models, the R^2 of four models are 0.527 and 0.609, and the $RMSE$ of 2 models are 8.728 and 7.930 $\mu\text{g}/\text{cm}^2$, respectively. For validation accuracy of 2 models, R^2 of 2models is 0.411 and 0.843, $RMSE$ is 14.455 and 11.034 $\mu\text{g}/\text{cm}^2$, respectively. The result showed, (1) the accuracy of RF model with vegetation indices is higher than the other model. (2) The RF model with vegetation indices can estimate the chlorophyll content of apple leaves more accurately and it had the potential for estimating chlorophyll content of apple leaf. And it provides a new method for the accurate estimation of chlorophyll of apple leaves.

Keywords: Apple leaf · Hyperspectral · Chlorophyll · RF

1 Introduction

Chlorophyll content is an important biochemical parameter in the growth process of fruit trees. It is instructive for the photosynthetic capacity, developmental stage and nutritional status of fruit trees. And it is the indicator that the fruit trees are affected by environmental stress and disease indicator [1, 2]. It is very important to use the hyperspectral extraction of leaf chlorophyll content information to monitor the growth status and nutritional diagnosis of fruit trees. In recent years, domestic and foreign fruit trees remote sensing monitoring has made some progress. The model of red edge spectrum and grape chlorophyll content was established, the RMSE (Root mean square error) $<30 \text{ mg m}^{-2}$. The original spectrum of apple leaf and the leaf spectrum of wavelet filter, the support vector machine, and partial least squares were used to establish the chlorophyll estimation model [3]. The correlation between original leaf spectrum and first-order differential spectrum of apple leaves and chlorophyll content of apple leaves was analyzed. The leaf chlorophyll regression model was established with the spectral position, vegetation index and spectral area as the variables, respectively. The results showed that the exponential model constructed by blue edge position had higher estimation accuracy [4]. The total nitrogen content of the leaves of pear was combined with the original spectral sensitive band and the first-order differential sensitive band, and the total nitrogen content of the leaves was established by stepwise regression analysis. Finally, the first order differential of the spectrum was determined to participate in the constructed model as the leaf total nitrogen content estimation model [5]. The original spectrum of apple leaf, the first order differential spectroscopy, the principal component analysis method and the stepwise regression analysis method were used to establish the chlorophyll content estimation model [6]. Researchers have made a number of attempts to estimate the chlorophyll content of leaves of fruit trees. In the case of remote sensing monitoring of fruit trees, the use of random forest (RF) methods has been rare, and RF has been used as a machine learning method in Agricultural remote sensing field. Construction of Vegetation Index, RF and Artificial Neural Network were used for inversion of winter wheat leaf area index with Environmental Satellite Data [7]. Based on the RF construction model, the vegetation index was used to estimate the soil and plant analyzer development (SAPD) of the winter wheat using the high score number one satellite data [8]. Establishment of SPAD Inversion Algorithm for Wheat Jointing Stage, Booting Stage and Flowering Stage by RF Regression Algorithm [9]. A hyperspectral model for the determination of leaf area index of apple trees using support vector machine and RF [10]. The potential of RF to estimate the biomass of winter wheat was confirmed by constructing the model by combining the correlation coefficient, gray correlation and bag data importance respectively [11].

Analysis of domestic and foreign research results found that most of the research focused on a single growth period of fruit trees for nutritional diagnosis, resulting in the results of the whole tree growth cycle for the nutritional status of the lack of evaluation criteria and guidance [3], this article is for 2 consecutive years estimation of chlorophyll content in leaves of apple during whole growth period. Most studies use only the chlorophyll-related sensitive bands or only use the vegetation index to model, and there is no comparison between the sensitive bands and the vegetation index.

In summary, based on the original spectral and vegetation indices, the 2 models were compared with the original spectral sensitivity and the vegetation indices respectively. The aim of this study was to apply the RF model to the estimation of chlorophyll content and to select the optimal model for estimating the chlorophyll content of apple leaves in order to provide a guide for the rapid estimation of chlorophyll content.

2 Materials and Methods

2.1 Overview of the Study Area

The experiment was carried out from 2012 to 2013 in the apple orchard of Xiazhai Village, Chaoquan Town, Feicheng City, Shandong Province. The line spacing was 5 m, the plant spacing was 3 m, the tree height was about 3 m, the tree trunk was about 0.5 m, and the tree is spindle-shaped (Fig. 1).

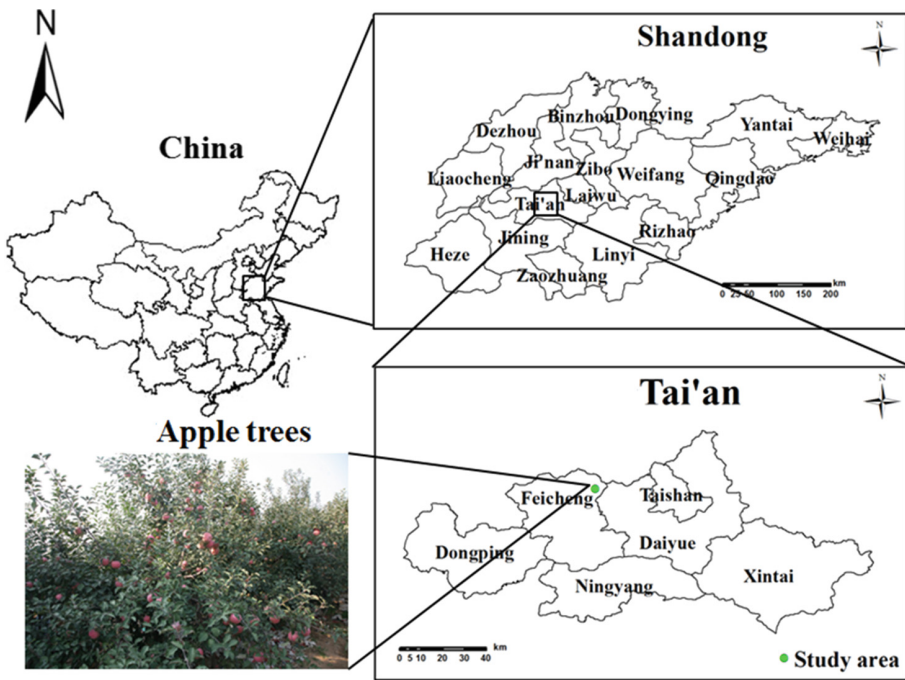


Fig. 1. Study area map

2.2 Leaf Sampling and Spectrophotometry

4 leaves were taken for each tree, each leaf in the north, south, east and west direction, respectively. Leaves were sampled and placed in self-styled bags, each tree as a sample

and quickly sent back to the laboratory for spectral measurement and chlorophyll sampling. 299 samples were obtained in 2012 including Fushi 220 and Gala 79, and 180 samples were sampled in 2013 including Fushi 135 and Gala 45.

The vein of the leaf should be avoided when the leaves spectrum were measured by ASD hyperspectral spectrometer. The spectral parameters are as follows: the spectral range of the spectrometer is 350–2 500 nm, and the interval is 1 nm. Each leaf was measured in four different positions (twice each side of the veins, and the veins were observed to cover the entire blade during the test), and the average of the four reflectances was taken as the reflectance of the leaf. Before measurement, the standard whiteboard with the blade holder was used to calibrate.

2.3 Determination of Chlorophyll Content in Apple Leaves

Leaf chlorophyll was sampled at the corresponding position of leaf spectral measurement. And leaf chlorophyll content was measured by chemical method. The four leaves of each tree were punched, and the veins of each leaf were avoided and play 8 holes, covering the entire blade, corresponding to the spectral measurement position. The sample mass is about 0.2 g. The sample was then put in 95% absolute ethanol solution and allowed to stand in a dark environment for 24 to 48 h until leaves become white. The chlorophyll content of the apple leaves was determined by ultraviolet spectrophotometer ($\mu\text{g}/\text{cm}^2$) [12]. The data collected in this study are shown in Table 1, and the statistical characteristics of the chlorophyll data obtained are shown in Table 2. The model was established using the data of chlorophyll content and leaf spectral reflectance ($n = 299$) of apple leaf in 2012, and the accuracy of RF model with sensitive bands and vegetation indices was verified by the data collected in 2013 ($n = 180$).

Table 1. List of data acquisition at each measured time

Date	Growth stage	Growth stage	Fushi samples	Gala samples	Chlorophyll content	Reflectance
2012-05-10	Fast-growing period of shoot	Fast-growing period of shoot	44	16	√	√
2012-07-03	Stop-growing period of shoot	Stop-growing period of shoot	44	15	√	√
2012-08-10	Fruit enlargement period	Fruit maturity period	44	16	√	√
2012-09-20	Fruit enlargement period	Leaf color period	44	16	√	√

(continued)

Table 1. (continued)

Date	Growth stage	Growth stage	Fushi samples	Gala samples	Chlorophyll content	Reflectance
2012-10-18	Fruit maturity	Leaf color period	44	16	√	√
2012 total			220	79	299	299
2013-04-20	Blooming period	Blooming period	27	9	√	√
2013-05-25	Fast-growing period of shoot	Fast-growing period of shoot	27	9	√	√
2013-07-18	Fast-growing period of autumn shoot	Fast-growing period of autumn shoot	27	9	√	√
2013-08-30	Fruit enlargement period	Fruit maturity period	27	9	√	√
2013-10-25	Fruit maturity period	Leaf color period	27	9	√	√
2013 total			135	45	180	180
Total			355	124	479	479

Note: √ represents the data was measured.

Table 2. The chlorophyll content statics of apple leaf

Samples	Sample quantity	Maximum value	Minimum value	Mean value	Standard deviation
Modeling set	299	112.562	51.291	76.529	12.707
Validation set	180	103.518	35.677	74.367	18.133
Total sample	479	112.562	35.677	75.717	14.996

2.4 Methods

2.4.1 Vegetation Index Selection

According to previous studies, 25 vegetation indices with good chlorophyll correlation were selected as variables for estimating chlorophyll content, as Table 3 shows.

Table 3. Summary of spectral indices related to chlorophyll content

Vegetation index	Formula	Reference
Normalized Pigment Chlorophyll Index, (NPCI)	$(R_{680} - R_{430}) / (R_{680} + R_{430})$	[13]
Simple Ratio Pigment Index, (SRPI)	R_{430} / R_{680}	[14]
Modified Chlorophyll Absorption Reflectance Index, (MCARI)	$[(R_{700} - R_{670}) - 0.2(R_{700} - R_{550})] (R_{700} / R_{670})$	[15]
Modified Chlorophyll Absorption Reflectance Index 2, (MCARI 2)	$1.2[2.5(R_{800} - R_{670}) - 1.3(R_{800} - R_{500})]$	[16]
Transformed Chlorophyll Absorption Ratio Index, (TCARI)	$3[(R_{700} - R_{670})] - 0.2(R_{700} - R_{550})(R_{700} / R_{670})$	[17]
MERIS Terrestrial Chlorophyll index, (MTCI)	$(R_{754} - R_{709}) / (R_{709} - R_{681})$	[18]
Modified Simple Ratio2, (MSR 2)	$(R_{750} - R_{445}) / (R_{705} - R_{445})$	[19]
Modified Normalized Difference Vegetation Index2, (MNDVI2)	$(R_{750} - R_{705}) / (R_{750} + R_{705} - 2R_{445})$	[19]
Normalized Difference Vegetation Index2, (NDVI2)	$(R_{750} - R_{705}) / (R_{750} + R_{705})$	[20]

(continued)

Table 3. (continued)

Vegetation index	Formula	Reference
Anthocyanin Reflectance Index, (ARI)	$(1/R_{550}) - (1/R_{700})$	[21]
Renormalized Difference Vegetation Index, (RDVI)	$RDVI = R_{800} - R_{670} / \sqrt{R_{800} + R_{670}}$	[22]
Improved Soil Adjusted Vegetation Index, (MSAVI)	$0.5 \left[2R_{800} + 1 - \sqrt{(2R_{800} + 1)^2 - 8(R_{800} - R_{670})} \right]$	[23]
Red-Edge Position, (REP)	$700 + 40 \frac{[(R_{670} + R_{780})/2] - R_{770}}{R_{740} - R_{700}}$	[24]
Spectral polygon vegetation index, (SPVI)	$0.4[3.7(R_{800} - R_{670}) - 1.2 R_{530} - R_{670}]$	[25]
Simple Ratio, (SR1)	R_{750}/R_{700}	[26]
Vogelmann Indices, (VOG)	R_{740}/R_{720}	[27]
Vogelmann Indices, (VOG2)	$(R_{734} - R_{747}) / (R_{715} + R_{726})$	[28]
Modified Chlorophyll Absorptions Integral, (MCAI)	$A - \int_{R_{552}}^{R_{752}} f$ A = area of the trapeze between R_{752} and R_{552} , f = reflectance curve	[29]
Derivative Index, (DI)	D_{730}/D_{706}	[30]
Chlorophyll Absorption Ratio Index, (CARI)	$CARI = \frac{ a \times R_{670} + R_{670} + b R_{700}}{\sqrt{a^2 + 1} \times R_{670}}$ $a = \frac{R_{700} - R_{550}}{150}, b = R_{550} \times a$	[31]
Double peak canopy nitrogen index (DCNI)	$(R_{720} - R_{700}) / (R_{700} - R_{670}) / (R_{720} - R_{670} + 0.03)$	[32]
Double peak canopy nitrogen index I (DCNI I)	$[(R_{750} - R_{670} + 0.09)(R_{750} - R_{700})] / (R_{700} - R_{670})$	[33]

(continued)

Table 3. (continued)

Vegetation index	Formula	Reference
Modified MERIS terrestrial chlorophyll index (MMTCI)	$[(R_{750} - R_{680} + 0.03)(R_{750} - R_{710})]/(R_{710} - R_{680})$	[33]
Combined indeIII	$[(R_{800} - R_{445})/(R_{800} - R_{680})]/(R_{800}/R_{670})$	[33]
Combined indexIV	$[(R_{550} - R_{450})/(R_{550} + R_{450})]/[(R_{800} - R_{670})/(R_{800} + R_{670})]$	[33]

2.4.2 Random Forest

RF is a machine learning algorithm published by American scientist Breiman [34] in 2001. RF based on bootstrap sampling method, extract multiple samples from original samples, use every decision tree to model each bootstrap sample, then combine multiple decision trees to predict, and finally decide the final prediction result by voting.

Bagging [35] is part of RF theory. Assuming that the sample size of the sample set is N , the number of Bootstrap samples taken per time is n , and this part of the sample that is not drawn is called the data outside the bag. These unselected out-of-pocket data can be used to estimate the classification strength of RF single tree, the greater the classification intensity, the smaller the generalization error of RF, the higher the accuracy of classification, and the more accurate prediction [36]. In this study, the importance of the existing vegetation index and the chlorophyll content was analyzed and sequenced using the out-of-pocket data estimation method in RF. The former vegetation index is modeled and estimated as a decision tree. Try to set the number of decision trees to 1000 for the best.

2.5 Statistical Analysis

In this paper, we estimate and verify the accuracy of the model selection coefficient (R^2), $RMSE$ as the evaluation criteria. In general, the smaller the $RMSE$, the greater the coefficient R^2 , indicating the higher the accuracy of the model.

3 Result and Analysis

3.1 Correlative Analysis of Chlorophyll Content and Spectrum in Leaves

The correlation between chlorophyll content and original spectrum of apple leaves in 2012 is shown in Fig. 2. There was a significant negative correlation between the leaf chlorophyll content and the original spectrum in the range of 525–581 nm and 693–735 nm; there was a significant positive correlation in the range of 745–1 350 nm. The

correlation coefficients were -0.46 , 0.66 and 0.61 , respectively, in the green, red and near-infrared bands, and 554 , 708 and 995 nm, respectively, in the bands with the best chlorophyll content. The reflectance of the three bands is used as the input variable for the RF model.

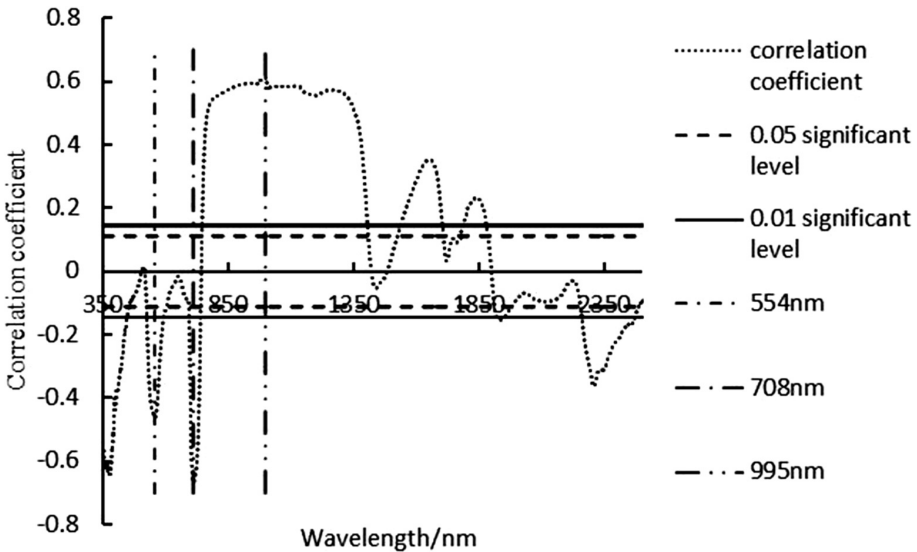


Fig. 2. Correlation between spectrum and chlorophyll content

3.2 RF Model Based on Original Spectrum

The RF spectra were constructed using the original spectral sensitivity bands 554 , 708 and 995 nm reflectance R_{554} , R_{708} , R_{995} , and the corresponding spectra and chlorophyll content in 2013 were verified. Modeling R^2 is 0.527 , RMSE is $8.728 \mu\text{g}/\text{cm}^2$, in Table 4.

Table 4. The accuracy of RF model with original spectrum

Model	Variable	RMSE ($\mu\text{g}/\text{cm}^2$)	R^2
RF	R_{554} , R_{708} , R_{995}	8.728	0.527

3.3 Screening of Vegetation Index

The correlation between chlorophyll content and vegetation index was calculated by using OOB importance estimation method. This paper only considers the top 10 vegetation indices after sorting, because of the operability and simplicity of the model, as shown in Table 5. The vegetation index is sorted by the OOB method.

Table 5. Sequence of relation between vegetation index and chlorophyll and OOB

Vegetation index	Importance of OOB	OOB ranking
NDVI2	6494.599	1
MMTCI	5612.955	2
MTCI	5191.305	3
VOG2	2805.643	4
ARI	2773.980	5
DCNI I	2277.633	6
VOG	2058.152	7
SR1	1611.043	8
MSR2	1587.592	9
MNDVI2	1562.748	10

3.4 Random Forest Optimal Model

According to the importance of OOB, the first 10 vegetation indices were selected, and the input number of vegetation index was increased to establish the chlorophyll content estimation model. The modeling results were shown in Table 6. As shown in Table 6, when the number of input vegetation indices increases from 1 to 5, the overall trend of R^2 increases and the RMSE decreases. When the number of vegetation indices is 5, R^2 reaches the maximum, 0.609, RMSE is the smallest, $7.930 \mu\text{g}/\text{cm}^2$. When the number of vegetation indices is 6–10, R^2 rises from 0.597 to 0.606, RMSE decreases from $8.067 \mu\text{g}/\text{cm}^2$ to $7.966 \mu\text{g}/\text{cm}^2$, but R^2 is less than 5 vegetation indices R^2 and RMSE are more than 5 vegetation Index of RMSE. Therefore, in the case of selecting the top 10 vegetation indices, the RF model constructed by the first five vegetation indices is the optimal model.

Table 6. Comparison of RF model accuracy with different vegetation indices

Number of vegetation index	RMSE ($\mu\text{g}/\text{cm}^2$)	R^2
1	10.305	0.380
2	9.199	0.483
3	8.752	0.527
4	8.765	0.525
5	7.930	0.609
6	8.067	0.597
7	8.046	0.599
8	8.031	0.600
9	8.008	0.602
10	7.966	0.606

3.5 Estimation and Verification of Chlorophyll Content

RF model verification accuracy was as shown in Fig. 3. For RF model based on the original spectrum, R^2 and $RMSE$ of validation were 0.411 and $14.455 \mu\text{g}/\text{cm}^2$, respectively. The validation accuracy of RF model with vegetation indices was R^2 0.843 and $RMSE$ $11.034 \mu\text{g}/\text{cm}^2$. The results indicate that the RF model based on vegetation index has high accuracy and good stability about the estimation of chlorophyll content. It is proved that the optimal model of vegetation based on vegetation index can be used to estimate the chlorophyll content of apple leaves.

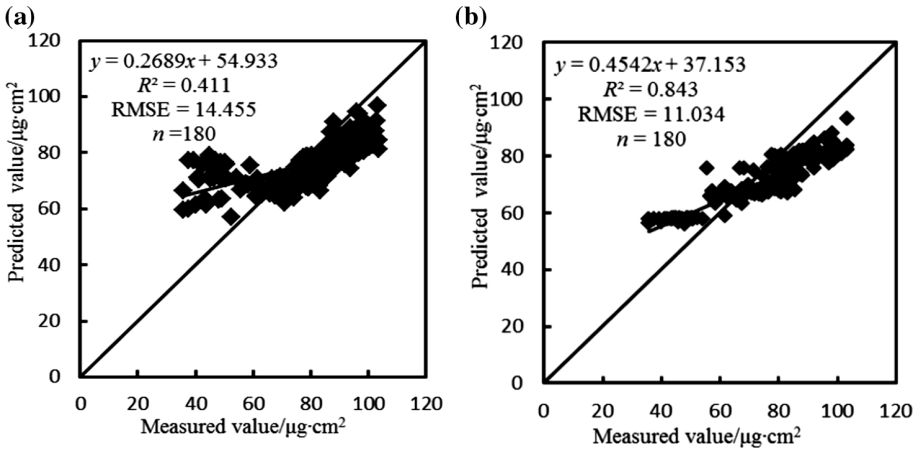


Fig. 3. (a) Validation of RF model with original spectrum. (b) Validation of RF model with vegetation indices

As the Fig. 3a shows, estimation ability of RF model with original spectrum was weak. When the measured value was $60 \mu\text{g}/\text{cm}^2$ below, the model estimates are overestimated, and when the measured values are greater than $75 \mu\text{g}/\text{cm}^2$, some of the estimates are underestimated, and the estimation value does not change with the increase of the measured value.

4 Conclusion

The RF model based on original spectrum and vegetation indices were established in this paper. The accuracy of RF model with vegetation indices is higher than the accuracy of RF model with original single bands. It can achieve an accurate estimation of apple chlorophyll content.

The accuracy of the RF model based on vegetation index is high. The main reason may be that the RF model based on the original spectrum is used for training data with only three sensitive bands of reflectivity, less model training data, RF models for larger data sets, and less significant for small-scale data.

There are still some shortcomings in this study. Due to climate reasons, the growth period in 2013 is not exactly the same as that in 2012. Because this research only used 2 years' experimental data, if we want to apply it to a large area, we still need more experimental data to improve the accuracy and stability of the model further. And the first collection of data in 2012 is the spring shoot, and the first collection of data in 2013 is the flowering period, while the chlorophyll content in the flowering period is low.

Based on the data collected in 2012 and 2013, the RF model based on the original spectrum and vegetation index was established, respectively and the conclusions as follows.

The sensitive single band 554 nm, 708 nm, 995 nm, were selected with good correlation between original spectrum and leaf chlorophyll content of the apple. The three bands were chosen as variables of RF model.

For modeling accuracy, the R^2 of RF model with sensitive bands and vegetation indices were 0.527 and 0.609, the $RMSE$ of that were 8.728 and 7.930 $\mu\text{g}/\text{cm}^2$, respectively. For validation accuracy, the R^2 of that were 0.411 and 0.843, and the $RMSE$ of that were 14.455 and 11.034 $\mu\text{g}/\text{cm}^2$.

The results showed that the estimation accuracy of chlorophyll content in RF model based on vegetation index is higher than that of RF based on the original spectrum, and the leaves chlorophyll content can be estimated more accurately. The RF model can be applied to the estimation of chlorophyll in apple leaves.

Acknowledgments. This work was supported in part by the National Natural Science Foundation of China (41601346, 41601369, 41471285, 41301475), Beijing Academy of agricultural and Forestry Sciences Innovation Capacity Construction Specific Projects (Grant no. KJCX20170423).

References

1. Jiang, J., Chen, Y., Huang, W.: Using hyperspectral remote sensing to estimate canopy chlorophyll density of wheat under yellow rust stress. *Spectrosc. Spectral Anal.* **30**(8), 2243–2247 (2010)
2. Xu, X., Zhao, C., Wang, J., Li, C., Liu, H.: Study on relationship between new characteristic parameters of spectral curve and chlorophyll content for rice. *Spectrosc. Spectral Anal.* **31**(1), 188–191 (2011)
3. Zhang, Y., Zheng, L., Li, M., Deng, X., Wang, S., Ji, R.: Construction of apple tree leaves nutrients prediction model based on spectral analysis. *Trans. Chin. Soc. Agric. Eng.* **29**(8), 171–178 (2013)
4. Li, M.: Correlation between apple leaf spectral reflectance and chlorophyll content and leaf total nitrogen. Northwest Agriculture and Forestry University (2009)
5. Li, P.: Study on modeling total and phosphorus content of Korla Fragrant Pear leaves based on Hyperspectrum by analysis. Xinjiang Agricultural University (2013)
6. Zhang, L.: Hyperspectral Estimation on Chlorophyll and Water Contents in Young Apple Leaves. Shandong Agricultural University (2013)

7. Wang, L., Zhou, X., Zhu, X., Guo, W.: Inverting wheat leaf area index based on HJ-CCD remote sensing data and random forest algorithm. *Trans. Chin. Soc. Agric. Eng.* **3**, 149–154 (2016)
8. Li, F., Wang, L., Liu, J., Chang, Q.: Remote sensing estimation of SPAD value for wheat leaf based on GF-1 data. *Trans. Chin. Soc. Agric. Mach.* **46**(9), 273–281 (2015)
9. Wang, L., Ma, C., Zhou, X., Zhu, X., Guo, W.: Estimation of wheat leaf SPAD value using RF algorithmic model and remote sensing data. *Trans. Chin. Soc. Agric. Mach.* **46**(1), 259–265 (2015)
10. Han, Z., et al.: Hyperspectral estimation of apple tree canopy LAI based on SVM and RF regression. *Spectros. Spectral Anal.* **36**(3), 800–805 (2016)
11. Yue, J., Yang, G., Feng, H.: Comparative of remote sensing estimation models of winter wheat biomass based on random forest algorithm. *Trans. Chin. Soc. Agric. Eng.* **18**, 175–182 (2016)
12. Lichtenthaler, H.K.: Chlorophylls and carotenoids: pigments of photosynthetic biomembranes. *Methods Enzymol.* **148**(34), 350–382 (1987)
13. Periuélas, J., Gamon, J.A., Fredeen, A.L., Merion, J., Field, C.B.: Reflectance indices associated with physiological changes in nitrogen- and water-limited sunflower leaves. *Rem. Sens. Environ.* **48**(2), 135–146 (1994)
14. Peñuelas, J., Filella, I., Lloret, P., Muñoz, F., Vilajeliu, M.: Reflectance assessment of mite effects on apple trees. *Int. J. Rem. Sens.* **16**(14), 2727–2733 (2010)
15. Daughtry, C.S.T., Walthall, C.L., Kim, M.S., Colstoun, E.B.D., Lii, M.M.: Estimating corn leaf chlorophyll concentration from leaf and canopy reflectance. *Rem. Sens. Environ.* **74**(2), 229–239 (2000)
16. Haboudane, D., Miller, J.R., Pattey, E., Zarco-Tejada, P.J., Strachan, I.B.: Hyperspectral vegetation indices and novel algorithms for predicting green LAI of crop canopies: modeling and validation in the context of precision agriculture. *Rem. Sens. Environ.* **90**(3), 337–352 (2004)
17. Haboudane, D., Miller, J.R., Tremblay, N., Zarco-Tejada, P.J., Dextraze, L.: Integrated narrow-band vegetation indices for prediction of crop chlorophyll content for application to precision agriculture. *Rem. Sens. Environ.* **81**(2), 416–426 (2002)
18. Dash, J., Curran, P.J.: The MERIS terrestrial chlorophyll index. *Int. J. Rem. Sens.* **25**(23), 5403–5413 (2004)
19. Sims, D.A., Gamon, J.A.: Relationships between leaf pigment content and spectral reflectance across a wide range of species, leaf structures and developmental stages. *Remote Sens. Environ.* **81**(2–3), 337–354 (2002)
20. Tucker, C.J.: Red and photographic infrared linear combinations for monitoring vegetation. *Rem. Sens. Environ.* **8**(2), 127–150 (1979)
21. Gitelson, A.A., Merzlyak, M.N., Chivkunova, O.B.: Optical properties and nondestructive estimation of anthocyanin content in plant leaves. *Photochem. Photobiol.* **74**(1), 38–45 (2001)
22. Roujean, J.L., Breon, F.M.: Estimating PAR absorbed by vegetation from bidirectional reflectance measurements. *Rem. Sens. Environ.* **51**(3), 375–384 (1995)
23. Qi, J., Chehbouni, A., Huete, A.R., Kerr, Y.H., Sorooshian, S.: A modified soil adjusted vegetation index. *Rem. Sens. Environ.* **48**(2), 119–126 (1994)
24. Guyot, G., Baret, F., Major, D.J.: High spectral resolution: determination of spectral shifts between the red and near infrared. *ISPRS Archives*, **XXVII** Part B7, 750–760 (1988)
25. Vincini, M., Frazzi, E., Alessio, P.D.: Angular dependence of maize and sugar beet VIs from directional CHRIS/Proba data (2006)
26. Gitelson, A.A., Merzlyak, M.N.: Remote estimation of chlorophyll content in higher plant leaves. *Int. J. Rem. Sens.* **18**(12), 2691–2697 (1997)

27. Vogelmann, J.E., Rock, B.N., Moss, D.M.: Red edge spectral measurements from sugar maple leaves. *Int. J. Rem. Sens.* **14**(8), 1563–1575 (1993)
28. Zarcotejada, P.J., Miller, J.R., Noland, T.L., Mohammed, G.H.: Scaling-up and model inversion methods with narrowband optical indices for chlorophyll content estimation in closed forest canopies with hyperspectral data. *IEEE Trans. Geosci. Rem. Sens.* **39**(7), 1491–1507 (2001)
29. Oppelt, N., Mauser, W.: The chlorophyll content of maize (*zea mays*) derived with the Airborne Imaging Spectrometer AVIS (2001)
30. Zarco-Tejada, P.J., Pushnik, J.C., Dobrowski, S., Ustin, S.L.: Steady-state chlorophyll a, fluorescence detection from canopy derivative reflectance and double-peak, red-edge effects. *Rem. Sens. Environ.* **84**(2), 283–294 (2003)
31. Kim, M.S., Daughtry, C.S.T., Chapelle, E.W.: The use of high spectral resolution bands for estimating absorbed photosynthetically active radiation (Apar.). In: *Proceedings of the Sixth Symposium on Physical Measurements and Signatures in Remote Sensing*, Val D' Isure, France, 17–21 January 1994, vol. 299 (1994)
32. Chen, P., Haboudane, D., Tremblay, N., Wang, J., Vigneault, P., Li, B.: New spectral indicator assessing the efficiency of crop nitrogen treatment in corn and wheat. *Rem. Sens. Environ.* **114**(9), 1987–1997 (2010)
33. Jin, X., Li, Z., Feng, H., Yang, G.: Newly combined spectral indices to improve estimation of total leaf chlorophyll content in cotton. *IEEE J. Sel. Top. Appl. Earth Observations Rem. Sens.* **1**(1), 4589–4600 (2014)
34. Breiman, L.: Random forests. *Mach. Learn.* **45**(1), 5–32 (2001)
35. Breiman, L.: Bagging predictors. *Mach. Learn.* **24**(2), 123–140 (1996)
36. Wolpert, D.H., Macready, W.G.: An efficient method to estimate bagging's generalization error, pp. 41–55. Santa Fe Institute (1999)



Improving Design of a PVDF Grain Loss Sensor for Combine Harvester

Liming Zhou, Yanwei Yuan^(✉), Junning Zhang, and Kang Niu

Chinese Academy of Agricultural Mechanization Sciences,
Beijing 100083, China

haiboll29@163.com, yyw215@163.com, zjn990210@163.com,
715675915@qq.com

Abstract. Online monitoring of grain loss is important to improve the efficiency of combine harvester. The traditional grain loss sensor needs to be frequently calibrated for different materials. In order to solve this problem, the grain loss sensor was developed based on PVDF (Polyvinylidene Fluoride) films. The band-pass filter based on LTC1068-200 was designed by frequency spectrum analysis of the wheat and rice grain impact response. And the dynamic voltage comparator with adaptive regulation of the threshold voltage according to the intensity of sensor signal was introduced here. Wheat and rice grain samples with different moisture content were prepared for the experiments and the results indicated the sensor had high measurement accuracy to the different samples.

Keywords: Combine harvester · Grain loss sensor · Band pass filter
Adaptive threshold voltage

1 Introduction

Grain loss is the key index for measuring the operating performance of the combine harvester. Traditional measurement method is to obtain the grain from material manually [1, 2]. With the development of sensors, electronics and information process technologies, the demand for precise and intelligent detection system for grain loss are rising. Online grain loss monitoring is important to improve harvest efficiency and quality operations.

At present, most of the grain loss monitoring system based on PZT, are to detect the number of passing grain kernels per unit time at the discharge end of the walker [3–7]. Liang proposed an impact type piezoelectric sensor for grain sieve loss monitoring, the signal conditioning circuits were developed to discriminate for full grains [8, 9]. But, it is very difficult to fit the different type of grains (such as rice and wheat) adaptively because of the fixed threshold voltage of the signal processing circuit. Since the kernel of grain is much harder than the straw, acoustic sensor had been used to detect the grain loss of harvester. The sound from the sensor was picked up by a microphone firstly, then the signal was processed by a computing device and displayed on a electric meter terminal. But the accuracy of this acoustic grain loss sensor is severely constrained by

working conditions, and the noise is a fatal factor for the acoustic sensor [10]. Microwave sensor was also used to detect the grain loss [11].

An array sensor made from PVDF film is designed to determine the grain loss [12]. In this paper, how to design the effective signal conditional circuit of the PVDF grain loss sensor was introduced to improve the resolution between the grain and stems.

The grain impact signals were analyzed for designing a high order band pass filter to discriminate grain online. In order to make the sensor fit rice or wheat grain automatically, the voltage compactor with adaptive threshold was used in this paper. Within the system, the grain loss for rice and wheat was determined and the precision of the method was tested.

2 Materials and Methods

2.1 Fabrication of the PVDF Sensor

The grain loss measuring system consists of the PVDF sensor array, signal conditioning circuit, communication interface and display meter. The array sensor was made from PVDF film, a new piezoelectric material, which was used broadly in the measuring sensor field recently. Compared with the piezoelectric ceramics, it had higher piezoelectric voltage coefficient and better responsive speed. The sensor array was made up of five cells, the size of every cell was $20 * 100 * 0.05$ mm, The PET film was affixed to the upper and lower surfaces to protect the sensor unit. In order to add the fuse, the foam rubber double-sided sealing tape was used to attach the sensor to the Aluminum support substrate. At the same time, the sealing tape can improve the deformation of the sensor and enhance the output signal. The frame is shown as Fig. 1.

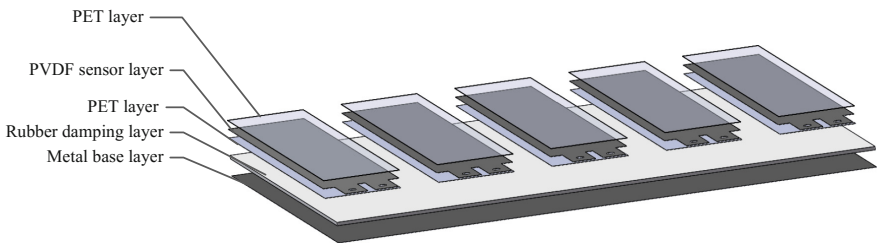


Fig. 1. PVDF sensor structure

2.2 Conditioning Circuit

The conditioning circuit was mainly used to deal with the weak charge signal generated by the PVDF sensor. The circuit was contained of charge conversion amplifier, voltage follower, high order band-pass filter, diode detection, adaptive voltage comparison module and counter. The structure is shown in Fig. 2.

Firstly, the charge conversion amplifier transforms the initial weak signal generated by the PVDF sensor into the voltage signal, and the amplitude of the voltage signal is

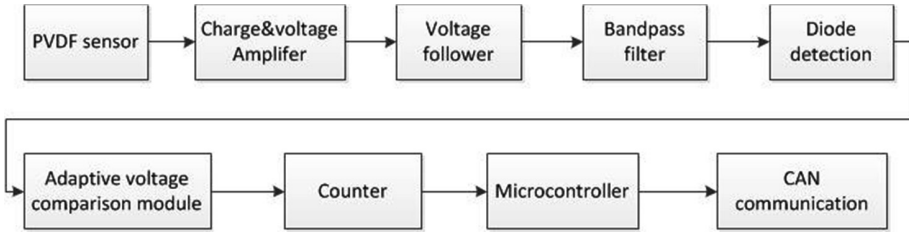


Fig. 2. Structure diagram of the signal conditioning circuit

between -4.5 V and 4.5 V. The signal is subjected to impedance conversion by a voltage follower to reduce the output impedance of the front stage circuit. Meanwhile, the pre-stage circuit is isolated from the post-stage circuit by means of the voltage follower. After band pass filtering, the material other than grain signals are weakened. The output signal through a diode detector which is a diode connected to a resistor and capacitor in parallel, and the envelope of the original signal was obtained. Schmitt trigger is used to transfer the envelope signal to rectangular digital pulse at the same frequency as the input. The trigger has a small amount of hysteresis that will help with noise rejection. The threshold of the trigger can adapt to input signal amplitude.

In this paper, the filter circuit and the voltage comparison circuit have been improved on the basis of the previous work. A band pass filter based on integrated chip was designed to improve the interference immunity of mechanical vibration and electricity. Meanwhile, the dynamic adjustment circuit of Schmitt Trigger threshold based on kernel signal was designed so that the threshold value of grain pulse could be adjusted automatically according to the signal envelop voltage.

2.3 Bandpass Filter Circuit

The amplified sensor signal often contains a variety of frequency band information. And the active filter circuit based on operational amplifier is usually used to discriminate the different frequency signal. In the previous experiment, it was found that the low order band pass filter was not well eliminated by the attenuation rate. If a high-order filter is designed based on an operational amplifier, the increased complexity of the circuit may adversely affect system reliability and stability. In addition, because of the influence of environmental factor, the filter performance may drift. Therefore, LTC-1068-200 can be applied to form eight-order Chebyshev band pass filter. The filter can emphasize seed signals in certain frequency ranges and reject signals in other frequency ranges. LTC1068-200 contains four high accuracy 2^{nd} order switched capacitor filter section.

In order to determine the reasonable parameters of the filter and ensure that the sensor has good application to wheat and rice grain, it is necessary to analyze the signals response of grain seed. Firstly, the sensor output signal was taken through a 200 amplifier, then to a Textronix TDS3000C oscilloscope, the scope's digitized signal was sent to a Matlab R2008b program for data collection and processing. The Fast Fourier

Transform were calculated using Matlab signal processing toolbox. The time and frequency response are shown in Figs. 3 and 4.

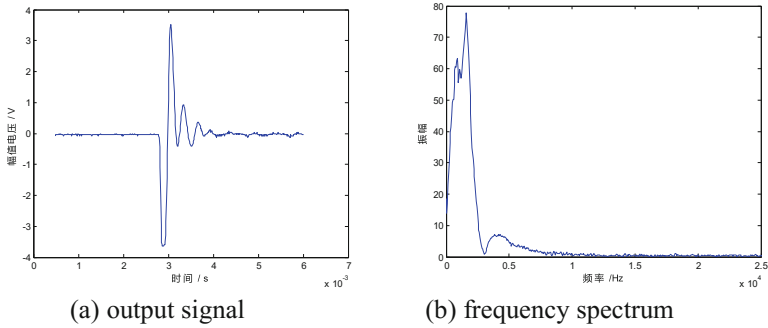


Fig. 3. Output voltage signal and its FFT transfer of wheat grain

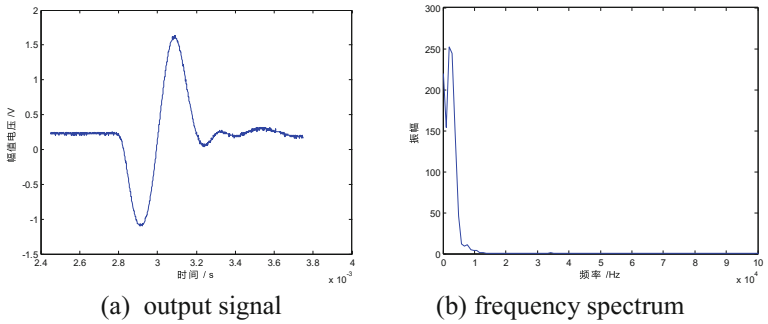


Fig. 4. Output voltage signal and its FFT transfer of rice grain

The curves in Figs. 3(a) and 4(a) are the response signal generated by the wheat and rice grain impact sensor. As can be seen from the curves, the voltage amplitude of wheat signal is about 3.5 V, and that of rice signal is about 1.7 V. In Figs. 3(b) and 4(b), we find that the center frequency of rice signal is 1.67 kHz and that of rice signal is 1.95 kHz. Obviously, the amplitude and characteristic of two kind signals are different.

According to the above analysis, it is determined that the center frequency of the designed eight order Chebyshev band pass filter is 1.81 kHz. The filter bandwidth is 800 Hz. Thus the range of frequencies passed by the filter is 1.41–2.21 kHz. The LTC1068-200 requires an external clock signal, which is usually obtained by crystal. This circuit is relatively complex, and also difficult to fine tune the frequency. The microcontroller STC11F02 was used as a signal generator to generate the desired pulse signal and was output by the CLKOUT pin, then the standard clock signal was sent to LTC1068. The eight order Chebyshev band pass filter was designed using Linear Technology's FilterCAD for Windows. Design of the filter is very easy with the help of

this program. Figure 5 shows the bandpass filter based on the LTC1068-200 with $\pm 5\text{ V}$ power supplies. In order to keep the impedance matching of the circuit, a voltage follower based on LT1355 was used here. The gain response curves of the band pass filter is shown in Fig. 6.

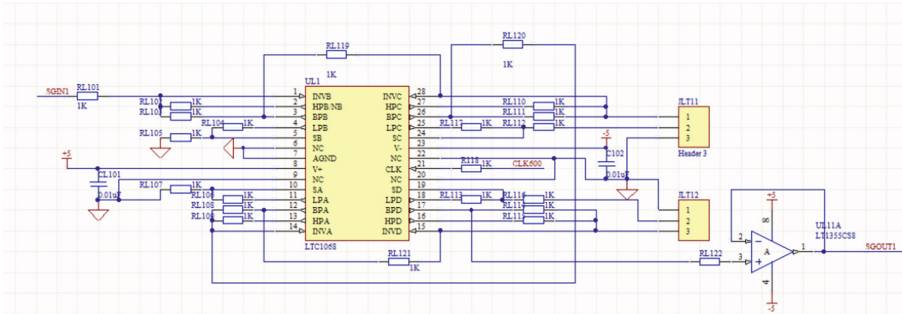


Fig. 5. Schematic of the Chebyshev filter

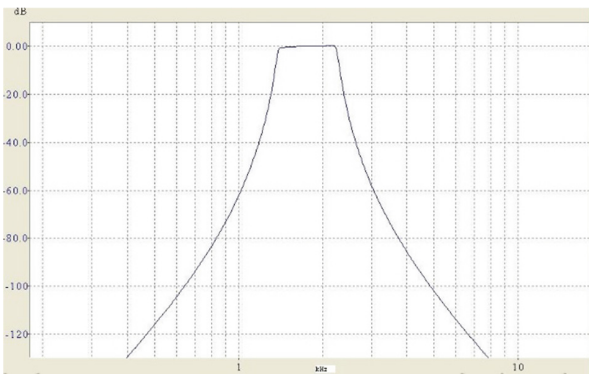


Fig. 6. Frequency response of the designed filter

It was observed that bandwidth of the designed filter in the -3db was not greater than 800 Hz in Fig. 6. It means that the filter can work very well. Meanwhile, the output signal of the filter was connected to the diode detector circuit in order to obtain the envelope of the grain signal.

2.4 Self-adaptive Voltage Compactor

After the envelope detecting, the pulse shaping circuit for active counting of grain signals was introduced here. The Schmitt trigger circuit was designed to obtain a standard square wave signal. Before the Schmitt trigger was used, the hysteresis and the threshold should be determined firstly. Due to the differences in the grain quality of

different breeds and moisture, the amplitude of the signal produced by the impact sensor was also different. Meanwhile the amplitude of signal was also affected by the angle and height of the grain drop. In this case the amplitude are variable, setting the thresholds to produce reliable triggering can be tricky [13]. Therefore, we proposed a signal shaping method based on the voltage comparator threshold, and designed a dynamic threshold adjustment circuit in this paper. With this circuit, the threshold voltage in the signal shaping can be adaptively adjusted to improve the signal shaping effect. The circuit schematic is shown in Fig. 7.

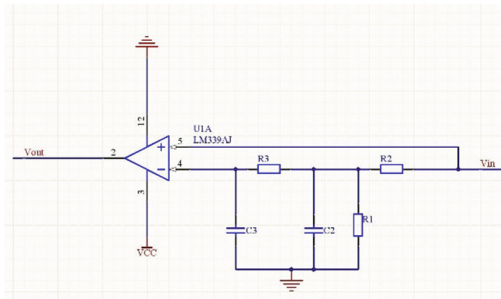


Fig. 7. Adaptive threshold voltage comparator

The enveloped module output was divided into two parts, one part was transferred into the positive input of Schmitt trigger, the other was connected to a second order low pass filter which was consisted of Resistor R2, R3 and Capacitor C2, C3. After the input signal V_{in} was filtered, the output DC signal associated with the input signal can be obtained. We can see that the resistor R1 and R2 form a voltage divider, thus the output voltage which is taken as the threshold of the trigger is a fraction of the input signal V_{in} . In other words, the threshold voltage of the compactor is matched to the input signal V_{in} adaptively. So, the accuracy of the comparator output was improved.

2.5 Counting and Communication

The electronic circuits design for the counting and communication was also applied here. The circuit board consisted of the CAN bus controller, Counter and Microcontroller unit (MCU). The standard pulse signal was connected to counter 82C54. The 82C54 is a high CMOS programmable interval timer, which has three independently programmable and functional 16-bit counters, each capable of handling clock input frequencies of up to 8 MHz. The interface using a bidirectional 8-bit ports on the microprocessor gives full control of the timer. Grain loss quantity is obtained by counting the number of pulse with use of counter of 82C54 for an operator set time period. The single chip STC12C5A60S2 was chosen as the monitor core of the system. The microcontroller provides a full duplex serial, SPI(Serial Peripheral Interface bus) and input/output module.

The MCP2515 was used in the grain loss monitoring sensor for data communication. It handles all of the transmitting and receiving of message packets that contain grain loss information via the CAN bus. The MCP2515 was configured and operated through a Serial Peripheral Interface (SPI) with a microcontroller. At the same time, the TJA1050 transceiver modules was also used as the interface between the MCP2515 CAN bus controller and the physical bus. The device provided differential transmit capability to the bus and differential receive capability to the CAN controller. In order to improve the performance of data communication, the optocoupler 6N137 was used to isolate the signals.

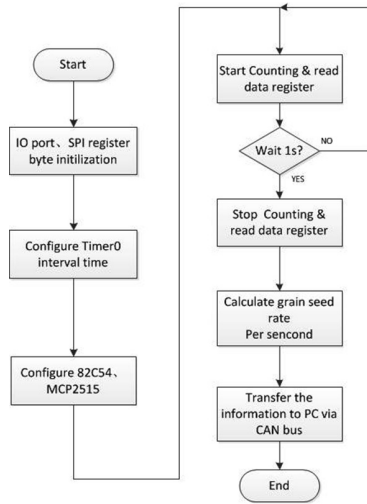


Fig. 8. Flowchart of the microcontroller

2.6 Software Design of the System

Keil C51 was used to develop the MCU program. Figure 8 shows the program flow for the monitoring system. The software of the sensor was composed of the initialization, counting and data communication. Initialization included initialization of the input/output ports, SPI, counter and CAN module control register setup and reset all related memory locations that were going to be used in the operation. The counter of microcontroller was used to measure the grain seed pulse rate per second. Data communication was used to transfer measured grain loss quality from the sensor to the upper machine.

3 Results and Discussion

3.1 Sensor Reliability Test

In order to determine the accuracy of grain loss sensor, two rice grain samples with moisture content of 18.3%, 23.2% and two wheat samples with moisture content of 19.1%, 25.3% were used in laboratory test. A total of 12 tests were conducted that included two type of grain and for two moisture contents. The fix angle and height of sensor in the experiments were same. The experiment instruments are shown in Fig. 9.

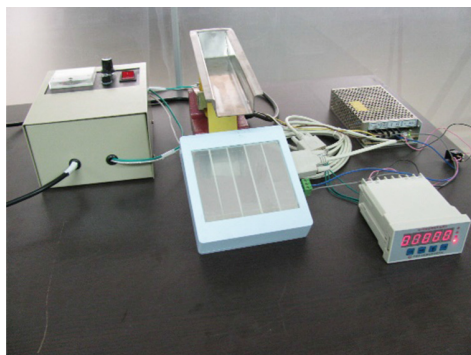


Fig. 9. Experiment instruments including PVDF sensor and vibration supplier

At the start of the experiment, the grains were put into electromagnetic vibration supplier, and the exciting current was regulated to keep the drop flow at 100 grain/s. Experiments were repeated three times for each sample.

Table 1 shows the relative error analysis of the results obtained by the developed sensor and manual under the same condition. From Table 1, it can be seen that the sensor can count the number of grain with the maximum measurement error of 4.8% for rice grain and that of 2.5% for wheat grain. The experiment results also show that the sensor has good measurement effect on wheat and rice grains under the same experimental conditions.

Table 1. Test results of grain loss obtained by sensor and manual

Test no.	Rice grain (MC = 18.3%)		Rice grain (MC = 23.2%)		Wheat grain (MC = 19.1%)		Wheat grain (MC = 25.3%)	
	Measured value	Relative error %	Measured value	Relative error %	Measured value	Relative error %	Measured value	Relative error %
1	989	1.1	961	3.9	983	1.7	979	2.1
2	952	4.8	959	4.1	975	2.5	1022	2.2
3	1039	3.9	982	1.8	990	1.0	1017	1.7

3.2 Discriminability of the Different Material

To verify the performance of the conditioning circuit, experiments were conducted with different materials. Three different materials (rice grain, hollow kernel and straw) were taken as experiment samples to test the effect of the sensor to distinguish seed from the materials. Thousand seeds mass of the grain mentioned here was 32.1 g. Firstly, the grain, hollow kernel and straw mentioned before were put into electromagnetic vibration supplier separately. Then the exciting current of supplier was regulated to keep the drop flow at a suitable value. The measured value and actual value were compared here.

Table 2 indicated that the sensor was sensitive to the grain and the misrecognition ratio was about 2.9%. It is insensitive to the hollow kernel and straw, the misrecognition ratio is in 4%. Thus the sensor can distinguish the grain from other material very well.

Table 2. Results of detecting grain and other materials

	Rice grain	Hollow kernel	Straw
Measured amount	971 grains	0.85 g	22 g
Actual amount	1000 grains	0.028 g	0.336 g
Misrecognition error	2.9%	3.29%	1.53%

4 Conclusions

In this study, the grain loss sensor based on PVDF film was present. The characteristic spectrum of rice and wheat grain was obtained based on the analysis of the frequency response of sensor. A signal conditioning circuit which included a Chebyshev bandpass filter with cutoff frequencies of 1.41–2.21 kHz and Schmitt voltage compactor with adaptive threshold was designed here to improve the detection accuracy and versatility. The test results show that the designed sensor still has a high detection accuracy after changing the material type without calibration. The maximum relative error of wheat and rice is 2.5% and 4.8%, and the grain can also be distinguished from the hollow kernel and straw effectively.

Acknowledgment. This research was funded by the National Key Research and Development Program of China (2016YFD0700305) and Science & Technology Nova Program of Beijing (Z1511000003150116) and Technology developing and achievement transformation project of XPCC(2015AC009).

References

1. Zhan, J., Liu, H., Hou, F.: Research advances and prospects of combine on precision agriculture in China. *Trans. Chin. Soc. Agric. Eng.* **21**(2), 179–182 (2005)
2. Zhan, Z., Li, Y., Chen, J., et al.: Grain separation loss monitoring system in combine harvester. *Comput. Electron. Agric.* **76**, 183–188 (2011)

3. Li, J., Jie, Z.: Analyses of combine harvester grain loss measurement. *Agric. Mech. Res.* **12**, 248–250 (2007)
4. Guy, H.J.O.: Offset grain loss sensor for combine harvesters. US patent 4540003 (1985)
5. Li, Y., Chen, Y., Zhao, Z.: Monitoring method and device for cleaning loss of combine harvester. *Trans. Chin. Soc. Agric. Mach.* **44**(S2), 7–11(2013)
6. Ni, J., Mao, H., Li, P.: Intelligent grain cleaning losses monitor based on array piezocrystals. *Trans. Chin. Soc. Agric. Mach.* **41**(8), 175–177 (2010)
7. Mao, H., Ni, J.: Finite element analysis measurement for array piezocrystals grain losses sensor. *Trans. Chin. Soc. Agric. Mach.* **39**(12), 123–126 (2008)
8. Liang, Z., Li, Y., Xu, L., et al.: Sensor for monitoring rice grain sieve losses in combine harvesters. *Biosyst. Eng.* **147**, 51–66 (2016)
9. Liang, Z., Li, Y., Xu, L., et al.: Optimum design of an array structure for the grain loss sensor to upgrade its resolution for harvesting rice in a combine harvester. *Biosyst. Eng.* **157**, 24–34 (2017)
10. Liu, C., Leonard, J.: Monitoring actual grain loss from an axial flow combine in real time. *Comput. Electron. Agric.* **9**(3), 231–242 (1993)
11. Kotyk, W.M., Kirk, T.G.: Unthreshed head grain loss monitor. US Patent, 4825146 (1989)
12. Zhou, L., Zhang, X., Liu, Y., et al.: Design of PVDF sensor for grain loss measuring. *Trans. Chin. Soc. Agric. Mach.* **41**(6), 167–171 (2010)
13. Yilmaz, D., Sagiroglu, H.C.: Development of measurement system for grain loss of some chickpea varieties. *Measurement* **66**, 73–79 (2015)



Maize Precision Farming Parallel Management Technology and Its Application in Northeast China

Xianju Lu^{1,2}, Xinyu Guo^{1,2(✉)}, Jiangchuan Fan^{1,2}, Sheng Luo³,
Yufa Song³, and Chunwei Li³

¹ Beijing Research Center for Information Technology in Agriculture,
Beijing, China

{luxj, guoxy, fanjc}@nercita.org.cn

² Beijing Key Lab of Digital Plant, Beijing, China

³ Yian County Agricultural Technology Promotion Center, Qiqihaer,
Heilongjiang, China

hytlsh@163.com, hljyaxsyf@163.com, hljyalcw@163.com

Abstract. Problems of extensive and low utilization of resources exist in the traditional maize cultivation. With the rapid development of computer technology and the internet of things, this paper proposed maize precision farming parallel management technology. This technology consists of three parts: management process, model system and digital support environment construction. The objective is to realize the quantitative decision-making of maize production target-control indicators-cultivation management scheme, and realize the analysis evaluation of production environment, production technology and farmers' operating management behavior. This technology was tested and applied preliminary in Yian County, Heilongjiang province. The application results showed that the maize precision farming parallel management technology can provide digital and scientific decision support and can achieve high production efficiency with lower fertilizer inputs and no-decreased yield.

Keywords: Precision farming · Parallel management · Maize
Northeast China

1 Introduction

Northeast China is comprised of Heilongjiang, Jilin, and Liaoning provinces, accounts for 30% of the total maize production in China and is important for ensuring China's food security. However, most of the farmers are doing the farming based on traditional knowledge. This plays a very big role in the crop production. This can't give full play to the potential of maize production, but also may cause serious waste of resources. The extensive application of information technology, especially the model and internet of things technology in the agriculture field, brings new opportunities for informatization and digitization of agricultural production management.

Over the years, agricultural researchers have done a lot of work in resolving the relationship between environment-technical measures and crop physiological and

ecological processes, and have established a series of agronomic mechanism models, knowledge models and knowledge rules [1–5]. Their works provide scientific theory, technical system and method means for describing the genetic characteristics of crop varieties, reflecting the interrelationship between crop and environment, as well as the purposeful, localized cultivation and management regulation, and then consequently laid good foundation for agricultural information research. Combining the crop cultivation management knowledge model with the crop growth model can achieve dynamic prediction and management decision of crop growth [6].

Internet of things is a technology that tends to connect various objects in the world to the internet [7, 8]. Applications are developed based on Internet of things enabled devices to monitor and control various domains based on applications [9]. Internet of things technology can be used to increase the crop production effectively to meet the growing needs of increasing population. Application of internet of things technology can helpful to increase the quality, quantity, sustainability and cost effectiveness of agricultural production [10].

Proper cultivation management is very important to improve the maize production. This paper introduces the control theory and method of artificial society, computational experiment and parallel execution to complex system, and puts forward the structure of precision farming parallel management system, providing a new assessment can be controlled precision agricultural management decision-making.

2 Technical Specifications for Parallel Management of Maize Precision Farming

2.1 Management Process

Maize precision farming parallel management process including four parts: planting plan and production target determination, cultivation scheme development before sowing, production warning and analysis and evaluation after harvest.

- ① The planting plan and production target determination. According to the geographical information of the production field, the cultivation plan and the management level of the production, the maize production potential of the field was calculated by using the maize precision farming parallel management scheme design model. Then the maize production target, mainly yield target was determined.
- ② Formulation of cultivation scheme before sowing. According to the yield target, the model of the parallel management plan of maize and the calculation method of the seed, fertilizer, water and pesticide were used to calculate and recommend the suitable varieties, sowing date, sowing density, and sowing depth, and then calculate the fertilization and irrigation schemes.
- ③ Warnings and regulations during maize growth stages. After sowing, real-time monitoring of maize growth and field environment is achieved by using Internet of Things technology and means, such as air temperature and humidity sensors, soil temperature and humidity sensors, multispectral

sensors, video surveillance systems. Using design model of maize precision farming parallel management scheme to analyze whether the crop growth deviates from the optimal growth indicators. If there is any deviation or disasters occur, the computational test algorithm is used to optimize the management of irrigation and fertilization, and form a regulation scheme.

- ④ Analysis and evaluation after maize harvest. After crop harvest, the database of crop production field archives is updated. Based on the data of the current year, re-evaluation of varieties, meteorology, soil, production level and cultivation scheme and model parameter adjustment are conducted using the design model of maize farming precision parallel management scheme. On this basis, the production target and cultivation scheme for the next year can be formulated.

2.2 Model System

Maize precision farming parallel management model system consists of maize knowledge model, growth model and structural-function model. Maize structural-function model mainly used to optimize analysis and visualization output.

The maize knowledge model is developed based on understanding, analysis, extraction and integration of experts' knowledge and experience, literature and experiment data for maize cultivation management, analyzation of the dynamic relationships of maize growth and management indices to variety types, ecological environments and production levels. The maize knowledge model is mainly designed to optimize the cultivation scheme, which includes yield target calculation, variety selection, sowing date, population density, fertilization strategy, irrigation management.

The maize growth model is based on the theory of crop-environment-atmosphere continuum. It can reflect the dynamic relationship between the maize growth and climatic conditions, management technology, soil physicochemical properties and genetic traits. The optimal cultivation management scheme based on the maize knowledge model is used as the input of maize growth model to carry out the process simulation analysis to achieve re-evaluation of varieties, meteorology, soil, productivity levels and cultivation scheme, as well as the adjustment of model parameters. Based on this, the production target and cultivation scheme of next year can be formulated.

The maize structure-function model is based on maize growth, morphology knowledge model and geometric model. It integrates the canopy radiation transfer model and three-dimensional visualization model, and realizes the canopy structure calculation, light interception, assimilation product distribution and organ growth simulation. The maize structure-function model is used to optimize the analysis and visualize the output.

2.3 Digital Support Environment Construction

Maize precision farming parallel management digital support environment includes the construction of the model database and the construction of the Internet of Thing system for real-time data acquisition.

The database construction includes geographic information, meteorological information, soil properties, variety information, agricultural materials information, farmers' management level and field management archival information, etc. The geographic information means the location of management plot. The meteorological information includes daily maximum/minimum temperature, air humidity, sunshine duration, radiation, precipitation, wind speed. The soil properties include soil type, bulk density, wilting point, field capacity, organic matter content, total nitrogen content, available phosphorus content, available potassium content and pH value. Farmers' management level is divided into three levels based on mechanization degree: high, medium and low. The field management archival information is the detail information of production process, including variety, sowing date, fertilizing/irrigate date and amount, etc.

The Internet of Things system for real-time data acquisition includes air temperature and humidity sensors, soil temperature and humidity sensors, multispectral sensors, video surveillance system and visible light, multispectral and infrared sensors based on unmanned aerial vehicle platform. It can provide real-time information such as crop growth, crop diseases, meteorological disasters, etc.

3 The Maize Precision Farming Parallel Management's Application in Heilongjiang Province

The maize precision farming parallel management technology was applied in Yian County, Heilongjiang Province. The demonstration base is located in Yian Provincial Agricultural Science and Technology Park. The maize cultivated land area is about 500 mu in the park. First, the digital support environment was constructed according to the maize precision farming technology of parallel management procedures (Fig. 1). The experiment field was 10 mu, the maize was planted based on two management scheme, one is according to the maize precision farming parallel management system and another is according to local farmers' traditional habits. The primary properties of the soil are presented in Tables 1 and 2.

According to the meteorological data and soil properties of the field plot, the maize precision farming parallel management system was used to make cultivation decision. In 2015, the yield target was made to 750 kg mu^{-1} , and the cultivation decision was made at rain-fed conditions. The two management scheme was showed in Table 3. Compared with the farmers' traditional scheme, the system scheme decreased the N input by 20 kg ha^{-1} , P_2O_5 input by 11 kg ha^{-1} , and increased K_2O input by 11 kg ha^{-1} .

The yield results of two schemes were showed in Table 4. Maize yield and yield components under system scheme were superior to that under traditional scheme. The results showed that the yield under system scheme was 8% higher than that under traditional scheme.



Fig. 1. Environmental data acquisition equipment installed at the experiment site

Table 1. Primary soil physical properties at the experimental site.

Depth	$\theta_{FC} \text{ cm}^3 \text{ cm}^{-3}$	$\theta_{WP} \text{ cm}^3 \text{ cm}^{-3}$	$K_s \text{ cm d}^{-1}$	Sand %	Silt %	Clay %
0–30 cm	0.301	0.125	1.1082	13.16	66.08	20.76
30–60 cm	0.295	0.127	0.9685	22.20	56.49	21.31
60–90 cm	0.361	0.182	0.5628	3.16	63.89	32.95

Table 2. Primary soil chemical properties of plough layer at the experimental site.

Layer	Total N g kg^{-1}	AP mg kg^{-1}	AK mg kg^{-1}	OM g kg^{-1}	CEC cmol kg^{-1}	pH
0–30 cm	1.94	36.0	239.2	29.7	28.1	5.8

Table 3. The two comparable management schemes

Scheme	Variety	Sowing date	Density plants ha^{-1}	Base fertilizer (kg ha^{-1})			Top dressing (kg ha^{-1})		
				N	P_2O_5	K_2O	N	P_2O_5	K_2O
System scheme	Jinongda501	May 3	75000	120	85	86	100	0	0
Traditional scheme	Jinongda501	April 28	82500	170	95	75	70	0	0

Table 4. Maize yield and yield components in two different schemes

Scheme	Ears length cm	Kernels per ear	Ears per ha	Bald length cm	100-kernel weight g	Harvest index	Yield kg ha ⁻¹
System scheme	20.22	584	77160	3.01	23.50	0.47	10590
Traditional scheme	18.87	531	80520	3.54	23.36	0.45	9840

4 Conclusions

The maize precision farming parallel management technology is established base on model system and Internet of Things. Its application in Northeast China proved that the maize precision farming parallel management technology is useful to improve maize production. The system scheme made from maize precision farming parallel management technology decreased cost input and increased farmers' profit compared with traditional scheme, and also alleviated the negative effect of chemical fertilizer on soil ecological environment. Therefore, the maize precision farming parallel management is a sustainable development technology that benefits to farmers and environment.

Acknowledgements. This work was supported by The National Key Research and development Program (2016YFD0300605-02), and the Scientific and Technological Innovation Team of Beijing Academy of Agricultural and Forestry Sciences (JNKYT201604).

References

1. Guo, X.Y., Zhao, C.J.: The development of maize growth simulation system based on process. *China Sci. Technol. Achievements* **90**(12), 53–55 (2004). (in Chinese)
2. Liang, H., Hu, K.L., Li, B.G., Liu, H.T.: Coupled simulation of soil water-heat-carbon-nitrogen process and crop growth at soil-plant-atmosphere continuum system. *Trans. Chin. Soc. Agric. Eng.* **30**(24), 54–66 (2014). (in Chinese)
3. Yang, H.S., Dobermann, A., Lindquist, J.L., Walters, D.T., Arkebauer, T.J., Cassman, K.G.: Hybrid-maize—a maize simulation model that combines two crop modeling approaches. *Field Crops Res.* **87**, 131–154 (2004)
4. Ahuja, L.R., Rojas, K.W., Hanson, J.D., et al.: *The Root Zone Water Quality Model*. Water Resources Publications LLC, Highlands Ranch, Ohios (2000)
5. Cao, W.X., Zhu, Y.: *Crop Management Knowledge Model*. China Agriculture Press, Beijing (2004)
6. Zhu, Y., Cao, W.X., Wang, Q.M., Tian, Y.C., Pan, J.: A knowledge model-and growth model-based decision support system for wheat management. *Scientia Agricultura Sinica.* **37** (6), 814–820 (2004). (in Chinese)
7. Fan, T.K.: Smart agriculture based on cloud computing and IOT. *J. Converg. Inf. Technol.* **8** (2), 210–216 (2013)

8. Hemlata, C., Sukhesh, K., Dipali, K.: Multidisciplinary model for smart agriculture using internet-of things (IOT), sensors, cloud-computing, mobile-computing & big-data analysis. *Int. J. Comput. Technol. Appl.* **6**(3), 374–382 (2015)
9. Duan, Y.: Design of intelligent agriculture management information system based on IOT. In: *International Conference on Intelligent Computation Technology and Automation*, vol. 1, pp. 1045–1049 (2011)
10. Sivabalan, M., Rajan, A., Balamuralidhar, P.: Towards a light weight internet of things platform architecture. *J. ICT Stand.* **1**, 241–252 (2013)



Research on Vegetation Ecologic Quality Index of Rocky Desertification in Karst Area of Guangxi Province Based on NPP and Fractional Vegetation Cover Since 2000

Xin Yang^{1,3}, Haihong Huang^{1,3(✉)}, Shuan Qian², and Hao Yan²

¹ Remote Sensing Application and Test Base of National Satellite Meteorology Centre, Nanning, China

huanghh63@163.com

² National Meteorological Center of CMA, Beijing, China

³ Institute of Meteorological Disaster Mitigation, Nanning 530022, People's Republic of China

Abstract. Karst rocky desertification is a kind of special and complicated surface form. Study established the Net primary productivity (NPP) estimation model based on the use of solar energy utilization of remote sensing data model in rocky desertification region of Guangxi province and the fractional vegetation cover (VFC) is obtained by the method of sub-pixel decomposition model. The comprehensive analysis method was used to establish vegetation ecologic quality index by using NPP and fractional vegetation cover to monitor the Rocky Desertification in the study area from 2000 to 2016, and mapping vegetation ecologic quality index grade classification. Results show that: (1) In 2016, vegetation ecologic quality index in rocky desertification region of Guangxi province is 87.6, the highest since 2000. Hechi city is the best in Guangxi Province. (2) From 2000 to 2016, vegetation ecologic quality index annual growth has a 1.04, the highest is 87.6 (in 2016) and the lowest is 63 (in 2004). The ecological restorations and environmental control projects have achieved remarkable results. (3) Great grade, Good grade and normal grade areas can account for 94.5%. And vegetation ecologic quality index decreased obviously in some relative development regions, such as Guilin city and Hezhou city.

Keywords: Karst rocky desertification · Vegetation ecologic quality index
NPP · Fractional vegetation cover

1 Introduction

Karst rocky desertification is a kind of special and complicated surface form, which is performance for the fragile ecological environment, and lead to the deterioration of regional ecological environment, so that drop the effective use of land resources, water resources have been destroyed, the survival of the foundation of the loss of biological resources. As an important index, NPP can reflect the changes of ecological environment; determine the ecosystem carbon source/sink effect. NPP is a key indicator of the

terrestrial carbon cycle. The different ecological models have been obtained by many ecologists or researchers such as Coughlan 1988, Running and Nemani et al. 1993, Gao and Liu 2008, BGC models. Currently, three BGC models are used. There are BIOME-BGC model, Terrestrial Ecosystem Model (TEM) and CENTURY model. Fractional vegetation cover is a key and land degradation. It is a very important parameter in developing climate and ecology model.

NPP and VFC are very important parameters in developing climate and ecology model. Study established the NPP estimation model based on the use of solar energy utilization of remote sensing data model in rocky desertification region of Guangxi province and the VFC is obtained by the method of sub-pixel decomposition model. The comprehensive analysis method was used to establish vegetation ecologic quality index by using NPP and VFC to monitor the Rocky Desertification in the study area, and mapping vegetation ecologic quality index grade classification.

2 Study Area and Data Used

2.1 Study Area

Study Karst rocky area is located in Guangxi Province between 104°26' E to 112°04' E and 20°54' N to 26°24' N. The study zones are blue areas (Fig. 1).

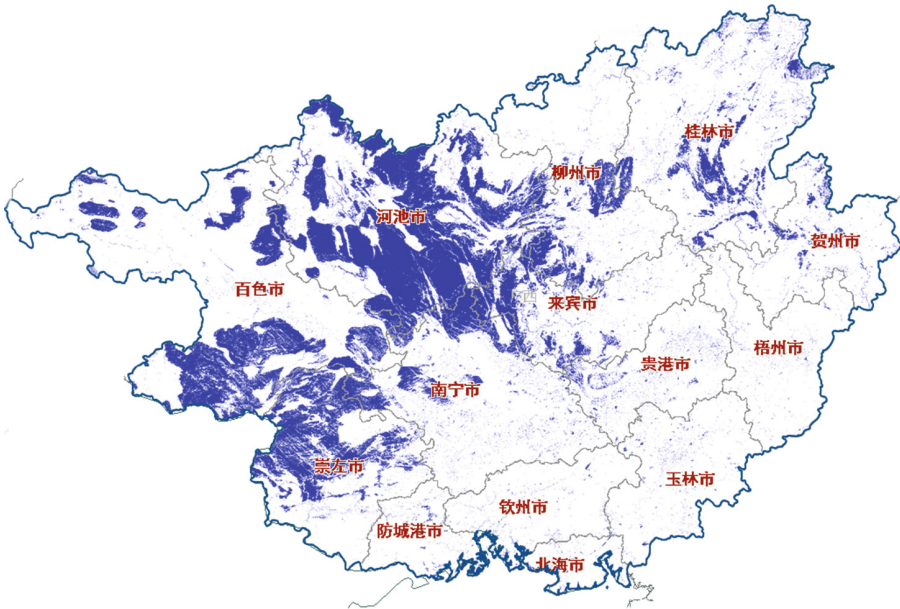


Fig. 1. Karst rocky areas of Guangxi Province (Color figure online)

2.2 Data List

See (Table 1).

Table 1. Data list of study.

Meteorological data	Remote sensing data	Environmental background data
Mean temperature	NDVI	Vegetation types
Sunshine duration	LST	Administrative divisions
Water-vapor pressure		
Dew-point temperature		

3 Methodology

NPP and VFC are very important parameters in developing climate and ecology model. The comprehensive analysis method was used to establish vegetation ecologic quality index by using NPP and fractional vegetation cover.

3.1 NPP Calculate

Our study was obtained by using seventeen-years historical data of NPP from NSMC (National Satellite Meteorological Centre) which obtained by using GloPEM model and extracted by using NOAA-AVHRR and MODIS data (2000–2016).

3.2 Fractional Vegetation Cover Calculate

Currently, field measurement method and remote sensing monitoring method are two methods of getting fractional vegetation cover. Field measurement method plays an important role in measure of fractional vegetation cover, which routinely widely used because of its high precision. However, this method is limited by bad weather, time and measure area condition. The method is also very expensive. With the development of remote sensing technique, remote sensing monitoring method in monitoring of fractional vegetation cover was provided. It possible to obtain fractional vegetation cover and its dynamic change in a large area, because remote sensing has the characteristics of periodic detection and large scale. The method has been widely used. In our study, pixel unmixing model was used to extract fractional vegetation cover because of its practical feature and simple. The VFC was modelled as:

$$VFC = (NDVI - NDVI_{soil}) / (NDVI_{veg} - NDVI_{soil}) \quad (1)$$

in which:

$$NDVI_{soil} = (VFC_{max} * NDVI_{min} - VFC_{min} * NDVI_{max}) / (VFC_{max} - VFC_{min})$$

$$NDVI_{veg} = ((1 - VFC_{min}) * NDVI_{max} - (1 - VFC_{max}) * NDVI_{min}) / (VFC_{max} - VFC_{min})$$

3.3 Vegetation Ecologic Quality Index Calculate

The vegetation ecologic quality index (VEQI) was generated by using 17-years records of annual NPP and VFC values of rocky desertification in Karst area of Guangxi Province. The pixel level estimated trend analysis was generated by using geostatistical method. The vegetation ecologic quality index trend of annual NPP was modelled as.

$$VEQI = NPP_t + VFC_t \tag{2}$$

4 Result and Discussion

By analyzing the Vegetation ecologic quality index (Figs. 2, 3 and 4) of rocky desertification in Karst area of Guangxi Province.

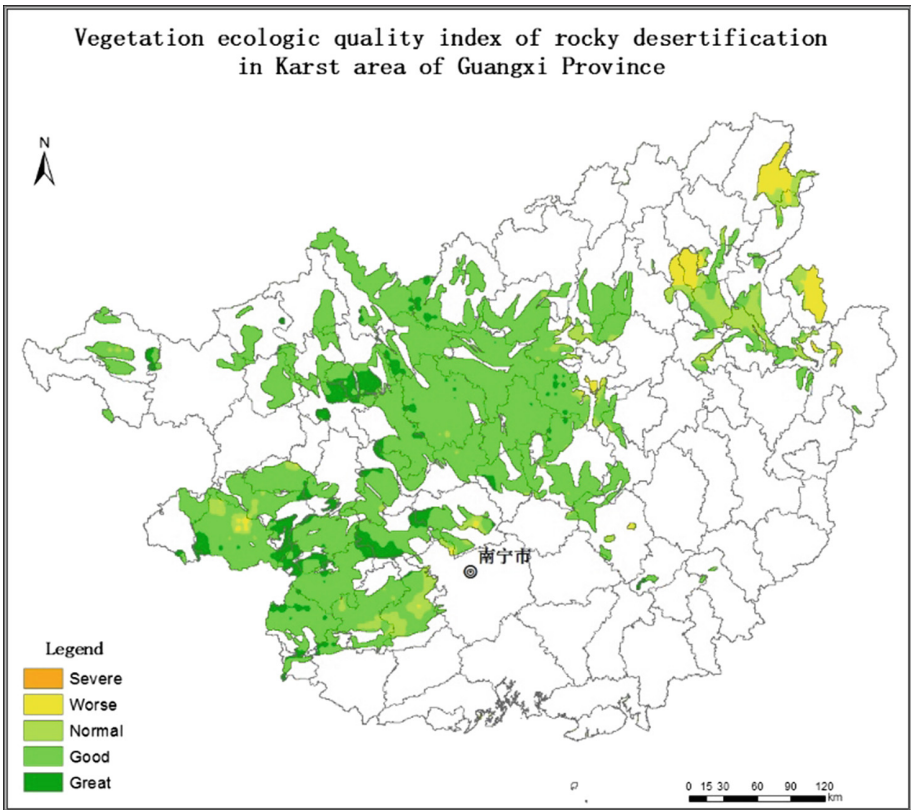


Fig. 2. Vegetation ecologic quality index of rocky desertification in Karst area in 2016



Fig. 3. Vegetation ecologic quality index of rocky desertification in Karst area of 14 cities in 2016



Fig. 4. Vegetation ecologic quality index of rocky desertification in Karst area from 2000 to 2016

- (1) In 2016, vegetation ecologic quality index in rocky desertification region of Guangxi province is 87.6, the highest since 2000. Hechi city is the best in Guangxi Province.
- (2) From 2000 to 2016, vegetation ecologic quality index annual growth has a 1.04, the highest is 87.6 (in 2016) and the lowest is 63 (in 2004). The ecological restorations and environmental control projects have achieved remarkable results.

- (3) Great grade, Good grade and normal grade areas can account for 94.5%. And vegetation ecologic quality index decreased obviously in some relative development regions, such as Guilin city and Hezhou city.

Acknowledgements. This research was supported by Special Fund for meteorological scientific Research in the Public Interest (GYHY201506017). Sincerely thanks are also due to Guangxi Climate center and National Satellite Meteorology Center for providing the data for this study.

References

- Bonan, G.B.: Forests and climate change: forcings, feedbacks, and the climate benefits of forests. *Science* **320**, 1444 (2008)
- Chhabra, A., Dadhwal, V.K.: Estimating terrestrial net primary productivity over India using satellite data. *Curr. Sci.* **86**(2), 269 (2004)
- Foster, I., Kesselman, C.: *The Grid: Blueprint for a New Computing Infrastructure*. Morgan Kaufmann, San Francisco (1999)
- Goetz, S.J., Prince, S.P., Smell, J., Gleason, A.C.: Inter annual variability of global terrestrial primary production: results of a model driven with global satellite observations. *J. Geophys. Res.* **105**(D15), 20077–20091 (2000)
- Fang, J., Piao, S., Tang, Z., Peng, C., Ji, W.: Inter annual variability in net primary production and precipitation. *Science* **293**, 1723 (2001)
- Knapp, K., Smith, M.D.: Variation among biomes in temporal dynamics of aboveground primary production. *Science* **291**, 481 (2001)
- Kumar, M., Monteith, J.L.: Remote sensing of crop growth. In: Smith, H. (ed.) *Plants and the Daylight Spectrum*, pp. 133–144. Academic Press, London (1981)
- Nemani, R.R., et al.: Climate-driven increases in global terrestrial net primary production from 1982 to 1999. *Science* **300**, 1560 (2003)
- Nemani, R., Running, S.W., Band, L.E., Peterson, D.L.: Regional hydroecological simulation system: an illustration of the integration of ecosystem models in a GIS. In: Goodchild, M.F., Parks, B.O., Steyaert, L.T. (eds.) *Environmental modeling with GIS*, pp. 296–304. Oxford University Press, New York (1993)
- Panigrahy, R.K., Panigrahy, S., Parihar, J.S.: Spatiotemporal pattern of agro ecosystem net primary productivity of India: a preliminary analysis using spot VGT data. In: *International Symposium on Geospatial Databases for Sustainable Development*, Goa, vol. 36, part 4, pp. 724–729 (2004)
- Prince, S.D.: A model of regional primary production to use with coarse resolution satellite data. *Int. J. Remote Sens.* **12**(6), 1313–1330 (1991)
- Running, S.W., Gower, S.T.: FOREST BGC, a general model of forest ecosystem processes for regional applications. II. Dynamic carbon allocation and nitrogen budgets. *Tree Physiol.* **9**, 147–160 (1991)
- Running, S.W., Coughlan, J.C.: A general model of forest ecosystem processes for regional applications I hydrological balance, canopy gas exchange and primary production processes. *Ecol. Model.* **42**, 125–154 (1988)
- Sabbe, H., Veroustraete, F.: Estimation of net primary and net ecosystem productivity of European terrestrial ecosystems by means of the C-Fix model and NOAA/AVHRR data. In: *VEGETATION 2000 Conference, 2 Years of Operation to Prepare the Future*, pp. 95–99. Space Application Institute, Joint Research Center, 21020 Ispra, Varese-Italy (2000)
- Gao, Z., Liu, J.: Simulation study of China's net primary production. *Chin. Sci. Bull.* **53**, 434–443 (2008)



Estimation of Leaf Nitrogen Content of Winter Wheat Based on Akaike's Information Criterion

Haojie Pei^{1,2,3,4}, Haikuan Feng^{1,2,3(✉)}, Fuqin Yang^{1,5}, Zhenhai Li^{1,2,3},
Guijun Yang^{1,2,3}, and Qinglin Niu^{1,2,3,4}

¹ Key Laboratory of Quantitative Remote Sensing in Agriculture of Ministry of Agriculture P. R. China, Beijing Research Center for Information Technology in Agriculture, Beijing 100097, China

xmljphj@163.com, fenghaikuan123@163.com,
yangfuqin0202@163.com, lizh323@126.com,
guijun.yang@163.com

² National Engineering Research Center for Information Technology in Agriculture, Beijing 100097, China

³ Beijing Engineering Research Center for Agriculture Internet of Things, Beijing 100097, China

⁴ School of Surveying and Land Information Engineering, Henan Polytechnic University, Jiaozuo 454000, China

⁵ College of Civil Engineering, Henan Institute of Engineering, Zhengzhou 451191, China

Abstract. Nitrogen is one of the important indices for evaluation of crop growth and output quality. At present, there are a lot of researches on the estimation of crop nitrogen content, but most of the studies do not consider whether the model established by vegetation index and crop nitrogen content is the best. The purpose of this study was to estimate the nitrogen content of wheat leaves and to establish a method and the optimal model for monitoring nitrogen content in wheat leaves. Spectral reflectance of leaves and concurrent leaf nitrogen content parameters of samples were acquired in during 2013 and 2014 wheat growth season, in Beijing Academy of Agriculture and Forestry Sciences. 17 vegetation indices related to nitrogen content were chosen, and the relationship between related vegetation indices and leaf nitrogen content were built for screening vegetation indices with variable importance projection (VIP). Choosing first 10 different vegetation indices after ranking with VIP value as the independent variable for estimating nitrogen content of leaf in wheat. And the number of vegetation indices was gradually increased from top 4 to 10. The leaf nitrogen content estimation model with different vegetation indices can be built using the integrated model of variable importance projection (VIP) - partial least squares (PLS). At the same time, Akaike's Information Criterion (AIC) value was calculated in different estimation model, and the AIC value of 7 different estimation model was compared. Then the optimal model with 5 vegetation indices was selected, which AIC value is the lowest. The optimal model was validated by leave one out cross-validation method. The result, (1) the comprehensive interpretation ability of the first 10 spectral indices on the nitrogen content of winter wheat leaves was PSSRc, GMI-2, SR705, RI-half, ZM, GMI-1, PSSRb, RI-3 dB,

VOGc and CIred edge. (2) The optimal model with 5 vegetation indices was selected from 7 models. (3) The decision coefficient (R^2) and root-mean-square error ($RMSE$) of the optimal model respectively were 0.73 and 0.33. The R^2 and $RMSE$ of wheat by validating were 0.73 and 0.33, respectively. The study showed: (1) The VIP-PLS model has higher ability to estimate the nitrogen content of leaf in wheat, which laying an important foundation for improving the precision of forecasting winter wheat leaf nitrogen content with remote sensing. (2) The AIC method can be used to select the optimal model, and the selected model has the higher predictive ability. And the optimal estimation model of wheat LNC can be obtained based on AIC.

Keywords: Leaf nitrogen content · Akaike's Information Criterion
Variable importance for projection · Partial least squares · Vegetation index

1 Introduction

Nitrogen is a “life element” in crop growth and development, rapid and accurate determination of nitrogen is conducive to the real-time management of nitrogen, providing a guarantee for high yield and quality of crops [1, 2]. The use of spectral reflectance and spectral index for crop nitrogen estimation has been an important content of agricultural remote sensing research, and domestic and foreign scholars have done a lot of research [3–5]. In the jointing stage of wheat, artificial neural network, support vector regression and random forest were used to establish the estimation model of nitrogen accumulation in wheat leaves [6]. The absorption characteristic spectrum (590–756 nm, 1096–1295 nm, 1295–1642 nm) were used to determine the characteristics of the depth and area of the leaves, and it can be a good total nitrogen content inversion [7]. A number of spectral indices were established using multi-spectral data of high score number satellite to estimate the nitrogen content of wheat leaves [8]. The new red edge bimodal parameters were constructed by using the ground spectrum, and the nitrogen content of wheat leaves was estimated by regression analysis [9]. The red edge index was used to estimate the nitrogen nutrition index [10]. The grey relational analysis was used to analyze the correlation of commonly used vegetation indices, and five indices of good vegetation indices were selected based on experience to participate in partial least squares regression (PLSR) [11, 12]. The Manhattan, Euclidean measures and a variety of neural networks were combined into an optimal model to predict the leaf nitrogen content. The results showed that the accuracy of the algorithm could predict leaf nitrogen content to 92.1% [13].

However, most researches do not consider whether the model established between crop nitrogen content and vegetation index is optimal. In this study, the variable importance projection (VIP) is used to sort the selected vegetation indices, and the number of different vegetation indices was selected as the input variables according to the importance of the vegetation index. The number of input variables was gradually increased. Based on the AIC, the optimum nitrogen content of winter wheat leaves estimation model was selected, and the optimal nitrogen content estimation model was selected to estimate the nitrogen content of winter wheat leaf. The purpose of this study

was to estimate the nitrogen content of wheat leaves, to establish a method and the optimal model for monitoring nitrogen content in wheat leaves.

2 Material and Method

2.1 Overview of the Study Area

The experiment was conducted at the wheat experiment base in Beijing Academy of Agriculture and Forestry in 2013–2014. The experiment base was located in Haidian District, Beijing, $39^{\circ} 56'N$, $116^{\circ} 16'E$, the specific location shown in Fig. 1. The district has four distinct seasons, cold and dry in winter, high temperature and rainy in summer, the average annual temperature of $12.5^{\circ}C$. Wheat was sown on September 29, 2013. And the soil was tested. The content of organic matter in the soil was 1.54–2.16 g/kg; the available potassium content was 77.54–216.27 mg/kg, the content of nitrate nitrogen was 6.99–21.40 mg/kg, the available phosphorus content was 29.92–136.44 mg/kg, the Total nitrogen content is 0.09–0.12 g/kg. The tested varieties were Jing 9428 and Nongda 211 respectively. Each plot size 1.2×1.5 m, planting 33.75 g, showing 6 lines, planting density of 6 million/hm². 40.5 g of urea per cell. 2 varieties, 5 water treatment, 4 repeat tests, water stress test from no water to water full saturation test, 0 m³/ha (W1), 225 m³/ha (W2), 450 m³/ha (W3), 675 m³/ha (W4), 900 m³/ha (W5), respectively. The test was conducted on April 20–21, 2014.

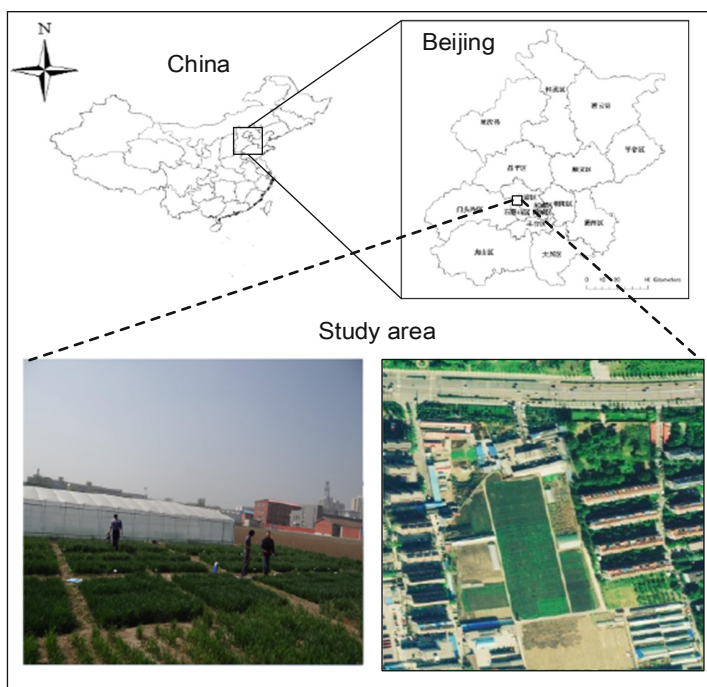


Fig. 1. Beijing academy of agriculture and forestry sciences

2.2 Leaf Spectrum Determination

Leaf spectrum measurements were carried out using an American FieldSpec® Pro FR spectrometer (ASD Inc. Boulder Colorado, USA) coupled with a hand-held leaf blade spectroscopy detector (ASD leaf clip). The wavelength range is 350–2500 nm, and the interval is 1 nm. Blade holder detector built-in quartz halogenated lamp, guaranteeing that the light source is stable. The blade detector can cover the whole leaf chamber of the leaf blade and has the same detection area. It can eliminate the background reflection, the spectral fluctuation caused by the curved surface of the blade, and the internal variation caused by the leaf blade. Before the measurement of the leaf spectrum, the dust on the surface of the blade was wiped off with a clean, damp cloth, and corrected with a standard whiteboard to reduce the error.

2.3 Leaf Nitrogen Content Determination

There are 40 wheat plots. Each plant is divided into 5 layers. 5 samples were taken per cell, and 5 layers of each plant were combined as samples of each layer, 199 samples in total. The samples were placed in a paper bag, placed in an oven at 105 °C for 30 min, and then each organ sample was dried at 80 °C for more than 48 h until constant mass. Finally, the dried crop leaves were crushed. The nitrogen content (N, %) of the crop leaves was measured using a Kjeldahl nitrogen apparatus (Buchi B-339, Switzerland).

2.4 Method

2.4.1 Selection of Vegetation Index

According to the previous research results and the significant relationship between vegetation index and leaf nitrogen content, 19 vegetation indices related to leaf nitrogen content were selected.

Table 1. Spectral indices for leaf nitrogen content

Spectral indices	Definitions	References
Pigment-specific simple ratio-b	$PSSR_b = R_{800}/R_{635}$	[14]
Pigment-specific simple ratio-c	$PSSR_c = R_{800}/R_{470}$	[14]
Gitelson and Merzlyak index-1	$GMI - 1 = R_{750}/R_{550}$	[15]
Gitelson and Merzlyak index-2	$GMI - 2 = R_{750}/R_{700}$	[15]
Simple ratio ₇₀₅	$SR_{705} = R_{750}/R_{705}$	[15]
Vogelman index a	$VOG_a = R_{740}/R_{720}$	[16]
Zarco and Miller	$ZM = R_{750}/R_{710}$	[17]
Ratio index-half	$RI - half = R_{747}/R_{708}$	[18]
Ratio index-1 dB	$RI - 1 \text{ dB} = R_{735}/R_{720}$	[18]
Ratio index-2 dB	$RI - 2 \text{ dB} = R_{738}/R_{720}$	[18]
Ratio index-3 dB	$RI - 3 \text{ dB} = R_{741}/R_{717}$	[18]

(continued)

Table 1. (continued)

Spectral indices	Definitions	References
Simple ratio _(533,565)	$SR(533, 565) = R_{533}/R_{565}$	[19]
Vogelman index c	$VOGc = \frac{(R_{734}-R_{747})}{(R_{715}+R_{720})}$	[17]
Normalized difference red edge	$NDRE = \frac{(R_{790}-R_{720})}{(R_{790}+R_{720})}$	[20]
Photochemical reflectance index	$PRI = \frac{(R_{570}-R_{531})}{(R_{570}+R_{531})}$	[21]
Red edge model	$CI_{rededge} = \frac{R_{750}}{R_{720}} - 1$	[22]
MCARI/MTVI2	MCARI/MTVI2	[23]
REP interpolation	$REP = \frac{700 + 40 \times [(R_{670} + R_{780})/2 - R_{700}]}{R_{740} - R_{700}}$	[24]
REPgauss	$R(\lambda) = R_s - (R_s - R_0) \exp\left[\frac{-(\lambda_0 - \lambda)^2}{2\sigma^2}\right]$	[25]

2.4.2 Variable Importance Projection

Variable projection importance (VIP) is a variable screening method based on partial least square (PLS), which describes the interpretation of the dependent variable to the dependent variable and ranks the independent variables according to their explanatory power [26, 27]. The formula is

$$V_{VIP_j} = \sqrt{\frac{k}{\sum_{h=1}^m r^2(y, c_h)} \sum_{h=1}^m r^2(y, c_h) w_{hj}^2} \tag{1}$$

k—the number of vegetation indices, m—The number of components extracted from the original vegetation index variables, c_h – Principal Component Analysis of Independent Variables of Correlated Vegetation Index, $r(y, c_h)$ – correlative coefficient of dependent variables and principal components of winter wheat, indicating that the ability of principal components to explain y(LAI of wheat), W_{hj} – Weight of Vegetation Index on Principal Components. The higher the VIP value, the stronger the vegetation index can explain the LAI and vice versa.

2.4.3 Akaike’s Information Criterion

The Akaike’s Information Criterion [28] is a measure of the goodness of fit of a statistical model that measures the complexity of the model and the goodness of fit of the model. AIC can be expressed as

$$AIC = n \ln S_p^2 + 2(k + 1) \tag{2}$$

n – the number of samples, S_p^2 – Residual Mean Square, k – Number of variables in the model.

2.4.4 Partial Least Squares

The partial least squares method is a multivariate statistical data analysis method, which mainly studies the multivariate regression model for single or multi-variables on the independent variables. The formula is

$$Y = a_0 + a_1X_1 + a_2X_2 + \dots + a_nX_n \tag{3}$$

a_0 – The intercept of the regression coefficient, a_i – regression coefficient, X_i – Independent variables 1–n.

2.5 Accuracy Verification

Leave one out cross-validation (LOOCV) each time to select a sample for verification, all other samples as a training sample. The model was validated, and the sample errors were calculated until all the samples were involved in the validation. LOOCV is the extreme case of K-cross-validation, and all values are modeled and validated. And it can avoid the problem of selection between modeling sample and verification sample in experimental design. This method can effectively evaluate the reliability and stability of the model.

The determination coefficient (R^2), root mean square error (RMSE) and relative error (RE) were selected as the indices to evaluate the modeling accuracy and validation accuracy. R^2 is indicating that the predictive value and the measured value of the degree of fit. R^2 is closer to 1, indicating that the higher the accuracy of the fitting curve. RMSE reflects the deviation between the predictive value and the measured value, the smaller the value, the higher the model accuracy. RE mainly reflects the credibility of the measurement. The smaller the relative error is, the more reliable the measured value. The calculation formula is shown below.

$$R^2 = \frac{(\sum xy - \frac{\sum x \sum y}{q})^2}{(\sum x^2 - \frac{(\sum x)^2}{q})(\sum y^2 - \frac{(\sum y)^2}{q})} \tag{4}$$

$$RMSE = \sqrt{\frac{\sum_{i=1}^q (y_i - \hat{y}_i)^2}{q}} \tag{5}$$

$$RE = \frac{|\sum_{i=1}^q \hat{y}_i - \sum_{i=1}^q y_i|}{\sum_{i=1}^q y_i} \times 100\% \tag{6}$$

x – vegetation index, y – crop LNC measured value, \hat{y} – the predicted value of the crop, q – the number of samples.

3 Results and Analysis

3.1 Analysis of VIP Between Vegetation Index and LNC of Winter Wheat

19 hyper-spectral indices (as shown in Table 1) were calculated based on hyper-spectral data of leaves in wheat. The relationship between the obtained hyper-spectral indices and the measured nitrogen content of wheat leaves were analyzed by VIP. The results about the ability of vegetation indices to explain nitrogen content in wheat leaves are shown in Table 2. At the flag stage of wheat, between the spectral index and the leaf nitrogen content of the wheat, the maximum VIP corresponding spectral index is PSSRc, and the VIP value is 1.1944. The smallest VIP corresponding spectral index is MCARI/MTVI, and the VIP value is 0.8815. The top 10 spectral indices ordered by the VIP values are, PSSRc, GMI-2, SR705, RI-half, ZM, GMI-1, PSSRb, RI-3 dB, VOGc and Clred edge, respectively.

Table 2. VIP and rank of evaluation index for LNC of winter wheat (n = 199)

Vegetation index	VIP	Ranking	Vegetation index	VIP	Ranking
PSSRc	1.1944	1	VOGa	1.1259	11
GMI-2	1.1897	2	RI-2 dB	1.1253	12
SR705	1.1843	3	RI-1 dB	1.1249	13
RI-half	1.1730	4	NDRE	1.1019	14
ZM	1.1659	5	REP	0.9680	15
GMI-1	1.1631	6	REPGAUSS	0.9643	16
PSSRb	1.1491	7	PRI	0.9565	17
RI-3 dB	1.1364	8	SR _(533,565)	0.9465	18
VOGc	1.1360	9	MCARI/MTVI	0.8815	19
Clred edge	1.1275	10			

3.2 Selection of Optimal LNC Estimation Model for Wheat

According to the VIP sequence shown in Table 2. The PLS models were constructed by using the different number of vegetation indices as the independent variables, calculating the AIC value of the model respectively. As shown in Table 3, when the number of independent variables was 5 vegetation indices, the AIC value was the smallest, and the AIC value was -427.878. The AIC principle of building model was using as few parameters as possible. According to the AIC principle, in the flag stage of wheat, 5 vegetation indices were selected as independent variables to build PLS model, and its equation was an optimal model. The model was $V_{LNC} = 4.9467 + 0.5186 V_{PSSRc} - 13.9993 V_{GMI-2} + 43.7809 V_{SR705} + 2.9433 V_{RI-half} - 36.7703 V_{ZM}$. The 5 vegetation indices were PSSRc, GMI-2, SR705, RI-half, and ZM. The R^2 , RMSE and RE of the model were 0.79, 0.33 and 0, respectively.

Table 3. Comparison of PLS regression equations built by wheat LNC different independent variables according to VIP (flag leaf stage)

The number of variables	Regression equation	R ²	RMSE	AIC
4	$V_{LNC} = 3.8885 + 0.4881V_{PSSRc} - 9.4837V_{GMI-2} + 41.3387V_{SR705} - 34.7129V_{RI-half}$	0.78	0.33	-424.580
5	$V_{LNC} = 4.9467 + 0.5186V_{PSSRc} - 13.9993V_{GMI-2} + 43.7809V_{SR705} + 2.9433V_{RI-half} - 36.7703V_{ZM}$	0.79	0.33	-427.878
6	$V_{LNC} = 5.0651 + 0.5004V_{PSSRc} - 14.1179V_{GMI-2} + 45.0444V_{SR705} + 0.0615V_{RI-half} - 35.3281V_{ZM} + 0.1789V_{GMI-1}$	0.79	0.33	-425.129
7	$V_{LNC} = 5.9001 + 0.4098V_{PSSRc} - 18.0207V_{GMI-2} + 55.1183V_{SR705} - 4.3869V_{RI-half} - 37.2390V_{ZM} - 0.1354V_{GMI-1} + 0.5298V_{PSSRb}$	0.79	0.33	-423.094
8	$V_{LNC} = 6.1881 + 0.4101V_{PSSRc} - 17.7359V_{GMI-2} + 53.4222V_{SR705} - 2.7516V_{RI-half} - 37.2390V_{ZM} - 0.1285V_{GMI-1} + 0.5186V_{PSSRb} - 1.0977V_{RI-3dB}$	0.79	0.33	-420.051
9	$V_{LNC} = 9.7976 + 0.4726V_{PSSRc} - 19.9056V_{GMI-2} + 69.2828V_{SR705} + 58.1725V_{RI-half} - 152.2723V_{ZM} - 0.1294V_{GMI-1} + 0.1085V_{PSSRb} + 36.2288V_{RI-3dB} - 121.1323V_{VOGc}$	0.79	0.32	-422.513
10	$V_{LNC} = 5.7079 + 0.5456V_{PSSRc} - 19.7727V_{GMI-2} + 76.3950V_{SR705} + 38.7431V_{RI-half} - 142.8775V_{ZM} + 2.6587V_{GMI-1} - 0.0605V_{PSSRb} + 43.8932V_{RI-3dB} - 88.1755V_{VOGc} - 3.2832V_{RSI(543.728)}$	0.79	0.32	-420.121

3.3 Verification of Optimal LNC Model for Winter Wheat

In order to verify the accuracy of VIP-PLS-AIC to predict the nitrogen status of wheat leaves, the data of wheat flag date of 2013–2014 were used respectively. For the nitrogen content of wheat leaves, the VIP-PLS-AIC model of 5 vegetation indices was validated. The results showed that R² and RMSE were 0.79 and 0.33 respectively. The predicted values and the measured values of the scatter plot have high consistency, indicating that the use of VIP-PLS-AIC for winter wheat leaf nitrogen status estimation with high accuracy and good reliability as shown in Fig. 2.

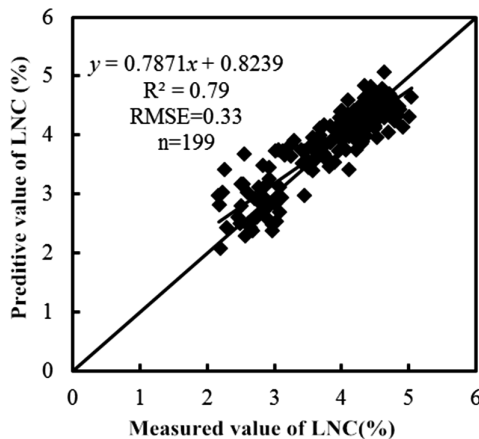


Fig. 2. Comparison of predicted and measured wheat LNC based on VIP-PLS-AIC

4 Conclusion

The relationship between vegetation index and LNC was evaluated by VIP. The vegetation index with the highest VIP value was PSSRc, and the vegetation index with the lowest VIP value was MCARI/MTVI.

The number of vegetation indices was increased as the input factors, PLS regression model was used to establish the regression model of seven wheat LNC. The optimal LNC model was selected by AIC criterion. The results show that the PLS model with 5 vegetation indices are the optimal model for estimating LNC.

In wheat LNC model, the R^2 of VIP-PLS-AIC model set and validation set are 0.79, and RMSE is 0.33. The results of modeling and validation show that the importance of ordination between vegetation index and wheat LNC was better by VIP. And the optimal estimation model of wheat LNC can be obtained based on AIC.

Acknowledgments. This work was supported in part by the National Key Research and Development Programs (2016YFD0300603-5), National Natural Science Foundation of China (No.41601346).

References

1. Wang, J.H., Zhao, C.J., Huang, W.J., et al.: Quantitative Remote Sensing of Agriculture. Science Press, Beijing (2008)
2. Pinter Jr., P.J., Hatfield, J.L., Schepers, J.S., et al.: Remote sensing for crop management. *Photogram. Eng. Remote Sens.* **69**(6), 647–664 (2003)
3. Hansen, P.M., Schjoerring, J.K.: Reflectance measurement of canopy biomass and nitrogen status in wheat crops using normalized difference vegetation indices and partial least squares regression. *Remote Sens. Environ.* **86**(4), 542–553 (2003)
4. Feng, W., Yao, X., Zhu, Y., et al.: Monitoring leaf nitrogen status with hyperspectral reflectance in wheat. *Eur. J. Agron.* **28**(3), 394–404 (2008)
5. Clevers, J., Kooistra, L.: Using hyperspectral remote sensing data for retrieving total canopy chlorophyll and nitrogen content. In: 2011 3rd Workshop on Hyperspectral Image and Signal Processing: Evolution in Remote Sensing, WHISPERS, pp. 1–4. IEEE (2011)
6. Cui, R., Liu, Y., Fu, J.: Estimation of winter leaf nitrogen accumulation using machine learning algorithm and visible spectral. *Spectrosc. Spectral Anal.* **36**(6), 1837–1842 (2016)
7. Zhang, X., Liu, L., Zhao, C., et al.: Estimating wheat nitrogen concentration with high spectral resolution image. *J. Remote Sens.* **7**(3), 176–181 (2003)
8. Li, F., Chang, Q., Shen, J., et al.: Remote sensing estimation of winter wheat leaf nitrogen content based on GF-1 satellite data. *Trans. Chin. Soc. Agric. Eng.* **32**(9), 157–164 (2016)
9. Fei, W., Zhu, Y., Yao, X., et al.: Monitoring nitrogen accumulation in wheat leaf with red edge characteristics parameters. *Trans. Chin. Soc. Agric. Eng.* **25**(11), 194–201 (2009)
10. Wang, R., Song, X., Li, Z., et al.: Estimation of winter wheat nitrogen nutrition index using hyperspectral remote sensing. *Trans. Chin. Soc. Agric. Eng.* **30**(19), 191–198 (2014)
11. Li, Z.H., Xu, X.G., Jin, X.L., et al.: Remote sensing prediction of winter wheat protein content based on nitrogen translocation and GRA-PLS method. *Sci. Agric. Sin.* **47**(19), 3780–3790 (2014)

12. Jin, X.L., Xu, X.G., Wang, J.H., et al.: Hyperspectral estimation of leaf water content for winter wheat based on relational analysis (GRA). *Spectrosc. Spectral Anal.* **32**(11), 3103–3106 (2012)
13. Gautam, R., Panigrahi, S., Franzen, D.: Neural network optimisation of remotely sensed maize leaf nitrogen with a genetic algorithm and linear programming using five performance parameters. *Biosys. Eng.* **95**(3), 359–370 (2006)
14. Blackburn, G.A.: Spectral indices for estimating photosynthetic pigment concentrations: a test using senescent tree leaves. *Int. J. Remote Sens.* **19**(4), 657–675 (1998)
15. Gitelson, A.A., Merzlyak, M.N.: Remote sensing of chlorophyll concentration in higher plant leaves. *Adv. Space Res.* **22**(5), 689–692 (1998)
16. Vogelmann, J.E., Rock, B.N., Moss, D.M.: Red edge spectral measurements from sugar maple leaves. *Remote Sens.* **14**(8), 1563–1575 (1993)
17. Zarco-Tejada, P.J., Miller, J.R., Noland, T.L., et al.: Scaling-up and model inversion methods with narrowband optical indices for chlorophyll content estimation in closed forest canopies with hyperspectral data. *IEEE Trans. Geosci. Remote Sens.* **39**(7), 1491–1507 (2001)
18. Gupta, R.K., Vijayan, D., Prasad, T.S.: Comparative analysis of red-edge hyperspectral indices. *Adv. Space Res.* **32**(11), 2217–2222 (2003)
19. Tian, Y.C., Yao, X., Yang, J., et al.: Assessing newly developed and published vegetation indices for estimating rice leaf nitrogen concentration with ground-and space-based hyperspectral reflectance. *Field Crops Res.* **120**(2), 299–310 (2011)
20. Rodriguez, D., Fitzgerald, G.J., Belford, R., et al.: Detection of nitrogen deficiency in wheat from spectral reflectance indices and basic crop eco-physiological concepts. *Crop Pasture Sci.* **57**(7), 781–789 (2006)
21. Penuelas, J., Baret, F., Filella, I.: Semi-empirical indices to assess carotenoids/chlorophyll a ratio from leaf spectral reflectance. *Photosynthetica* **31**, 221–230 (1995)
22. Dash, J., Curran, P.J.: Evaluation of the MERIS terrestrial chlorophyll index (MTCI). *Adv. Space Res.* **39**(1), 100–104 (2007)
23. Eitel, J.U.H., Long, D.S., Gessler, P.E., et al.: Using in-situ measurements to evaluate the new RapidEye™ satellite series for prediction of wheat nitrogen status. *Int. J. Remote Sens.* **28**(18), 4183–4190 (2007)
24. Guyot, G., Baret, F., Major, D.J.: High spectral resolution: determination of spectral shifts between the red and the near infrared. *Int. Arch. Photogram. Remote Sens.* **11**, 740–760 (1988)
25. Zhu, Y., Li, Y., Feng, W., et al.: Monitoring leaf nitrogen in wheat using canopy reflectance spectra. *Can. J. Plant Sci.* **86**(4), 1037–1046 (2006)
26. Zeng, T., Ju, C.Y., Cai, T.J., et al.: Selection of parameters for estimating canopy closure density using variable importance of projection criterion. *J. Beijing For. Univ.* **32**(6), 37–41 (2010)
27. Yang, F.Q., Feng, H.K., Li, Z.H., et al.: Estimation of leaf area index of winter wheat based on Akaike's information criterion. *Trans. Chin. Soc. Agric. Mach.* **46**(11), 112–120 (2015)
28. Akaike, H.: Information theory and an extension of the maximum likelihood principle[J]. In: Petrov, B.N., Csaki, F. (eds.) *2nd International Symposium of Information Theory*, pp. 267–281. Akademiai Kiado, Budapest (1973)



Monitoring of Winter Wheat Biomass Using UAV Hyperspectral Texture Features

Chang Liu^{1,2,3,4}, Guijun Yang^{2,3,4}, Zhenhai Li^{2,3,4} (✉), Fuquan Tang¹,
Haikuan Feng^{2,3,4}, Jianwen Wang^{2,3,4}, Chunlan Zhang^{1,2,3,4},
and Liyan Zhang^{2,3,4}

¹ College of Geomatics, Xi'an University of Science and Technology,
Xi'an, China

1224129134@qq.com, fuquantang@163.com,
1964362790@qq.com

² Key Laboratory of Quantitative Remote Sensing in Agriculture of Ministry
of Agriculture P. R. China, Beijing Research Center for Information Technology
in Agriculture, Beijing, China

guijun.yang@163.com, lizh323@126.com,
fenghaikuan123@163.com, 985764715@qq.com,
344014704@qq.com,

³ National Engineering Research Center for Information Technology
in Agriculture, Beijing, China

⁴ Beijing Engineering Research Center for Agriculture Internet of Things,
Beijing, China

Abstract. Biomass is an important indicator to evaluate vegetation life activities and hyperspectral imagery from unmanned aerial vehicle (UAV) supplied with abundant texture features shows a great potential to estimate crop biomass. In this paper, principal component analysis (PCA) was used to select the principal component bands from UAV hyperspectral image. Eight texture features from the principal component bands were extracted by Gray Level Co-occurrence Matrix method, and the sensitive texture features were finally selected to construct the biomass estimation model. The results show that: (1) Texture features mean, ent, sm, hom, con, dis of the first principal component (pca1) and the mean of the third principal component (pca3) were significantly correlated with the biomass. (2) The biomass model by multiple texture features ($R^2 = 0.654$, $RMSE = 0.808$ (10^3 kg/hm²)) demonstrated better fitting effect than that by single texture feature ($R^2 = 0.534$, $RMSE = 0.960$ (10^3 kg/hm²)). The biomass estimation model based on the texture features of multiple principal components had a good fitting effect. Therefore, texture features of the UAV platform can accurately predict the winter wheat biomass.

Keywords: Hyperspectral image · Texture feature · Biomass
Principal component

1 Introduction

Biomass is an important indicator to evaluate vegetation life activities and can be used as an important basis for growth monitoring and remote sensing estimation [1, 2]. The traditional method of biomass acquisition is not only destructive, consuming time and energy, but also difficult to achieve large area monitoring [3]. In recent years, hyperspectral remote sensing has been widely used in quantitative remote sensing of vegetation biomass with its advantages of timely, non-destructive, large monitoring area and high spectral resolution [3]. Many researchers have used satellite and the other remote sensing data to study the estimation of vegetation biomass. Chen et al. [4] using HJ-1C images, constructed a biomass estimation model based on the common vegetation index of NDVI, OSAVI, MSAVI, SAVI, MTVI2, finally, the result showed that the biomass model based on MTVI2 has the best performance to estimate grassland biomass. Fan et al. [5] constructed a linear regression biomass model, a multivariate linear regression biomass model and a partial least squares regression biomass model using spectral feature that extracted from hyperspectral data, which indicates that the three models have a good fitting effect to estimate biomass with the R^2 value of more than 0.9. The research of Gao et al. [6] showed that a multivariate regression biomass model constructed by TVI, MTVI2, GNDVI, NLI, MSR, RDVI and IPVI has a good inversion accuracy to shrubs. Satellite remote sensing technology can achieve large-scale remote sensing monitoring of agronomic parameter, however, the cycle time for acquiring data is long and the ground resolution of remote sensing image is not high enough, leading to a limited application in precision agriculture [7]. Meanwhile, the UAV platform for remote sensing technology, with the advantages of low maintenance costs, lightweight, flexible, can also obtain high spatial resolution and temporal resolution of remote sensing data, so it has become a hot topic in precision agriculture [8]. Yang [9] achieved biomass inversion of winter wheat based on the UAV platform laser radar technology. Zhang et al. [10] made use of UAV images to construct an estimation models between different vegetation index and grassland biomass, and the model constructed by NGRDI has a good fitting effect with the R^2 value of 0.856. Lu et al. [11] obtained hyperspectral data through the UAV platform, and establish a stagewise estimation model of soybean biomass by spectral characteristics and plant height, which indicates a good fitting effect. Although many scholars has used spectral information for biomass inversion, but there was still saturation phenomenon exist. It is difficult to solve the above problems according to the simple spectral information, while, remote sensing technology based on UAV platform can obtain abundant texture information and can provide support for the retrieval of biomass. Nichol et al. [12] found that the accuracy of biomass estimation model based on AVNIR-2 and SPOT-5 multispectral data can be improved in combination with texture features compared to single spectral features. The results of Xu et al. [13] show that there was a strong correlation between texture features and biomass using Landsat 8 OLI multispectral image data. Mu et al. [14] indicated that texture features of vegetation indices have higher ability to estimate biomass than vegetation indices. Therefore, in this study, we attempted to use principal component analysis to transform the original hyperspectral image acquired by UAV platform, and extract texture feature from the principal component bands containing most of the information, then estimating winter wheat

biomass by texture features. This research provided a way for hyperspectral remote sensing estimation of biomass based on the UAV platform.

2 Materials and Methods

2.1 Study Area

Field experiment was conducted in the 2014–2015 winter wheat growing season at Xiaotangshan National Experiment Station for Precision Agriculture, Changping District, Beijing, China. Changping district has a moderate climate and four distinctive seasons, which is located in $40^{\circ}00'–40^{\circ}21'N$, $116^{\circ}34'–117^{\circ}00'E$ with an altitude of 36 m. The previous crop is maize, and the type of soil is silt loam in the experiment field.

The experiment was designed with an orthogonal experiment of variety, nitrogen fertilization and irrigation (Fig. 1). Experiment area were divided into 48 plots and set to three replications. The two varieties of winter wheat were Jing9843 and Zhong-mai175. Nitrogen fertilizer application rates included four levels, 0 kg/hm^2 , 195 kg/hm^2 , 390 kg/hm^2 , 780 kg/hm^2 . The irrigation included three levels, rainfall, normal irrigation with 100 mm and excess irrigation with 200 mm.

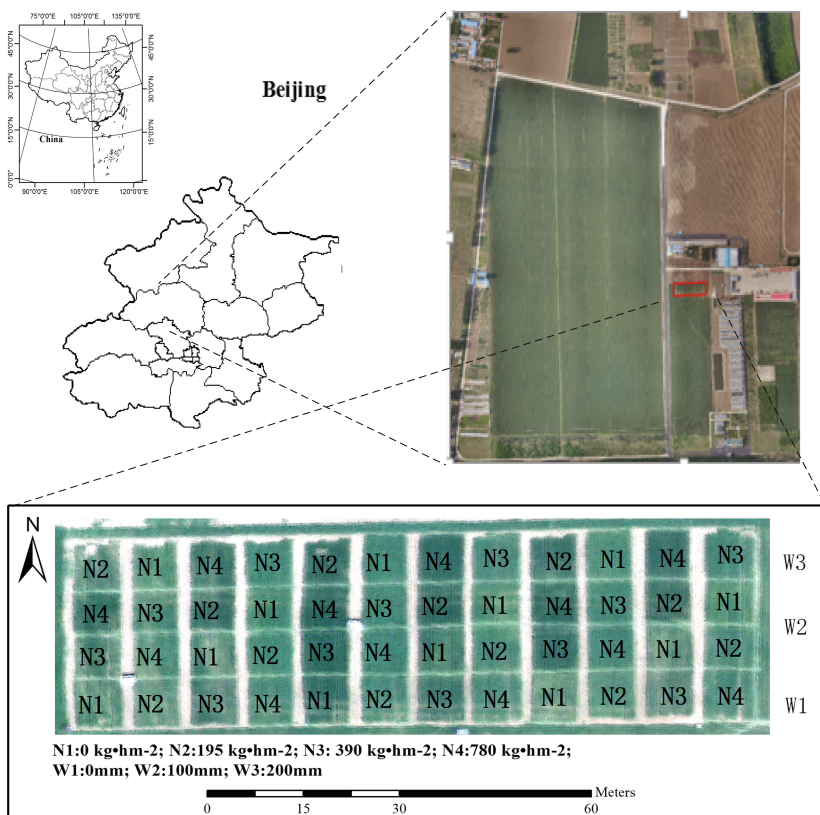


Fig. 1. Location of study area and experiment design

2.2 Field Measurements

Above ground biomass data was collected in the experiment at booting stage (26 April 2015) of winter wheat. A fixed area 0.3 m^2 was surveyed for the population density. 20 representative wheat tillers were selected from each plot. The samples were separated to stems and leaves, then stored in paper bags to be dried. Until the sub-organ samples became constant weight (about 24 h–48 h) in the oven, the dry weight of each sample can be obtained. Then biomass of winter wheat in per unit area was calculated by population density and dry weight of sample.

2.3 Hyperspectral Data and Pre-processing

Hyperspectral image at UAV platform (Fig. 2) was obtained at same time (April 26, 2015). The spectrometer was UHD 185, which is a new type of snapshot hyperspectral sensor and weighs 470 g. Its sensor can capture 450 nm–950 nm wavelengths with a sample interval of 4 nm. Finally, hyperspectral image and panchromatic image can be obtained both from the UHD 185.

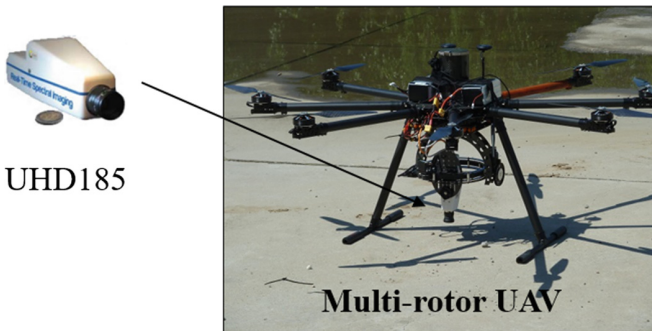


Fig. 2. UAV platform with UHD 185

According to the needs of this paper, we use Cubert-Pilot (Cubert, Germany) for image fusion of hyperspectral image and panchromatic images, and use Photoscan (Agisoft, Russia) for image stitching [15]. Then, the hyperspectral image was processed with ENVI software (Exelis Visual Information Solutions, USA) for radiation correction, atmospheric correction, and cutting [16].

2.4 Methods

The original hyperspectral image was transformed by principal component analysis, and the principal component bands containing much information were selected for texture analysis. Eight texture features, Mean, Variance, Homogeneity, Contrast, Dissimilarity, Entropy, Second Moment, and Correlation (Table 1) were extracted from the principal component bands at different window sizes (3×3 , 5×5 , 7×7 , 9×9 , 11×11 , 15×15 , 21×21) by Gray Level Co-occurrence Matrix method. The region

of interest from texture images of different bands were extracted by ArcGIS 10.3.1 (Esri, USA), then texture feature values of the extracted regions were obtained. The biomass estimation model was constructed by the sensitive texture features after analyzing the correlation between texture features and above ground biomass using Pearson correlation analysis in SPSS 22.0 (IBM, USA).

Table 1. Texture features and its formulas in this study

Texture feature	Formulas
Mean (<i>mean</i>)	$mean = \sum_{i,j=0}^{N-1} iP(i,j)$
Variance (<i>var</i>)	$var = \sum_{i,j=0}^{N-1} iP_{i,j}(i - mean)^2$
Homogeneity (<i>hom</i>)	$hom = \sum_{i,j=0}^{N-1} i \frac{P_{i,j}}{1 + (i-j)^2}$
Contrast (<i>con</i>)	$con = \sum_{i,j=0}^{N-1} iP_{i,j}(i - j)^2$
Dissimilarity (<i>dis</i>)	$dis = \sum_{i,j=0}^{N-1} iP_{i,j} i - j $
Entropy (<i>ent</i>)	$ent = \sum_{i,j=0}^{N-1} iP_{i,j}(-\ln P_{i,j})$
Second Moment (<i>sm</i>)	$sm = \sum_{i,j=0}^{N-1} iP_{i,j}^2$
Correlation (<i>corr</i>)	$corr = \sum_{i,j=0}^{N-1} iP_{i,j} \left[\frac{(i-mean)(j-mean)}{\sqrt{var_i var_j}} \right]$

Note: $P(i,j) = \frac{V_{i,j}}{\sum_{i,j=0}^{N-1} V_{i,j}}$, where $V_{i,j}$ represents the pixel brightness value of the (i,j) th element, and N represents the window size of the texture analysis.

3 Results

3.1 Selection of Texture Bands

As is shown in Fig. 3, the first three principal components explain more than 99% of the hyperspectral image (pca1, pca2, and pca3 contained 67%, 32% and 0.5% information of the hyperspectral image respectively), which can account for most of the variance of the original image. These principal components (pca1, pca2, pca3) were selected for texture features analysis.

3.2 Correlation Analysis Between Texture Features and Biomass

The relationship between principal components textures and biomass is shown in Table 2. Most of the texture features of pca1 were significantly correlated with biomass and the correlation coefficients(r) distributed between 0.5 and 0.7. Pca1_3_sm (representing texture feature 'sm' of pca1 band at the 3×3 window) was sensitive to biomass with r value of -0.673 . As the window size changed, r values between texture features mean, hom, con, dis and biomass changed slightly. Mean of pca3 was significantly correlated to biomass with r value of 0.726 , and other texture features of pca2, pca3 had a low correlation with biomass, which correlation coefficients were

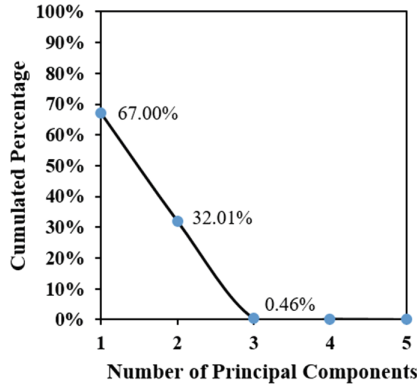


Fig. 3. Cumulated percentage variance in hyperspectral data of a number of PCs.

under 0.35. Therefore, *pcal_3_mean*, *pcal_3_hom*, *pcal_3_con*, *pcal_3_dis*, *pcal_3_ent*, *pcal_3_sm*, *pcal_3_var*, *pca3_3_mean* were selected as indexes of biomass estimation.

Table 2. Pearson’s correlation coefficients(*r*) between texture features and biomass

Principle component	Window	Texture feature							
		<i>mean</i>	<i>ent</i>	<i>sm</i>	<i>var</i>	<i>hom</i>	<i>con</i>	<i>dis</i>	<i>corr</i>
pca1	3 × 3	-0.588*	0.657*	-0.673*	0.584*	-0.638*	0.600*	0.626*	-0.171
	5 × 5	-0.588*	0.639*	-0.664*	0.561*	-0.638*	0.600*	0.626*	-0.077
	7 × 7	-0.588*	0.628*	-0.656*	0.548*	-0.638*	0.600*	0.626*	-0.149
	9 × 9	-0.587*	0.621*	-0.648*	0.544*	-0.638*	0.600*	0.626*	-0.182
	11 × 11	-0.587*	0.619*	-0.645*	0.551*	-0.638*	0.600*	0.626*	-0.187
	15 × 15	-0.587*	0.621*	-0.646*	0.562*	-0.638*	0.600*	0.626*	-0.179
21 × 21	-0.587*	0.631*	-0.655*	0.583*	-0.638*	0.600*	0.626*	-0.137	
pca2	3 × 3	-0.134	-0.064	0.092	-0.086	0.035	-0.033	-0.035	-0.083
	5 × 5	-0.134	-0.135	0.171	-0.194	0.035	-0.032	-0.034	-0.407*
	7 × 7	-0.134	-0.193	0.232	-0.267	0.035	-0.032	-0.035	-0.465*
	9 × 9	-0.134	-0.231	0.272	-0.301	0.035	-0.033	-0.035	-0.482*
	11 × 11	-0.134	-0.248	0.293	-0.309	0.035	-0.033	-0.035	-0.486*
	15 × 15	-0.134	-0.238	0.295	-0.278	0.035	-0.033	-0.035	-0.476*
21 × 21	-0.133	-0.218	0.284	-0.235	0.036	-0.033	-0.035	-0.443*	
pca3	3 × 3	-0.726*	-0.257	0.258	-0.224	0.251	-0.230	-0.248	0.470*
	5 × 5	-0.726*	-0.256	0.257	-0.214	0.252	-0.230	-0.249	0.235
	7 × 7	-0.726*	-0.247	0.247	-0.198	0.252	-0.231	-0.249	0.203
	9 × 9	-0.726*	-0.227	0.225	-0.159	0.253	-0.231	-0.250	0.311
	11 × 11	-0.726*	-0.195	0.193	-0.096	0.253	-0.232	-0.250	0.338
	15 × 15	-0.726*	-0.108	0.107	0.081	0.254	-0.232	-0.251	0.438*
21 × 21	-0.726*	-0.031	0.042	0.270	0.255	-0.233	-0.252	0.568*	

Note: * It means the correlation is significant at 0.01 level.

3.3 Biomass Estimation Model by Single Texture Feature

Linear, power, logarithmic and exponential function were used to construct biomass model based on the selected texture features, and the best models were selected to show in Table 3. As is shown in Table 3, determination coefficients (R^2) of biomass estimation model are maintained at 0.4. The logarithmic function model based on texture $pca3_3_mean$ has the best fitting effect with R^2 value of 0.534, RMSE value of 0.960 (10^3 kg/hm²). The exponential function model based on texture $pca1_3_sm$ has a R^2 value of 0.466, RMSE value of 0.806 (10^3 kg/hm²) ranking the second (Fig. 4).

Table 3. Biomass estimation model by single texture feature

Principal component	Texture feature	Modeling equation	R^2	RMSE (10^3 kg/hm ²)
pca1	<i>pca1_3_mean</i>	$y = 25.223e^{-0.094x}$	0.318	0.933
	<i>pca1_3_ent</i>	$y = 1.692x^{3.292}$	0.463	0.490
	<i>pca1_3_sm</i>	$y = 45.146e^{-7.366x}$	0.466	0.806
	<i>pca1_3_var</i>	$y = 12.801x^{1.163}$	0.396	0.889
	<i>pca1_3_hom</i>	$y = 1405.527e^{-7.839x}$	0.399	0.856
	<i>pca1_3_con</i>	$y = 7.356x^{1.258}$	0.409	0.875
	<i>pca1_3_dis</i>	$y = 14.062x^{1.948}$	0.428	0.849
pca3	<i>pca3_3_mean</i>	$y = 55.506 - 16.224\ln(x)$	0.534	0.960

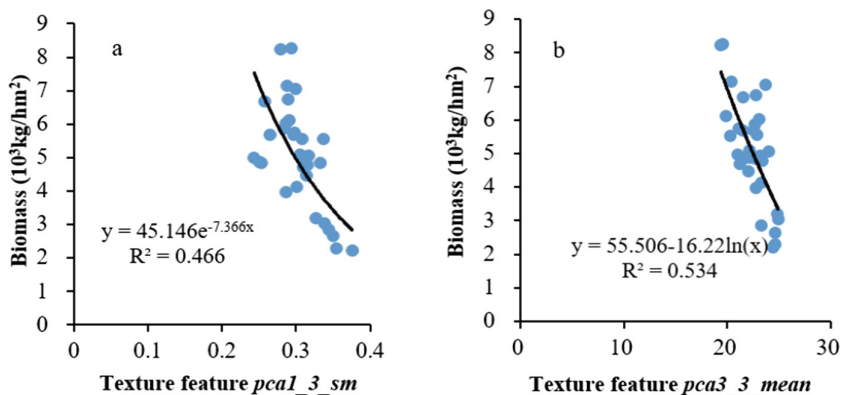


Fig. 4. Biomass estimation model by single texture feature; a. *pca1_3_sm*; b. *pca3_3_mean*;

3.4 Biomass Estimation Model by Multiple Texture Features

The biomass model based on the texture features of all principal components (Fig. 5) were built by multiple stepwise regression method. The R^2 and RMSE values between simulated and measured biomass were 0.654 and 0.808 (10^3 kg/hm²), respectively.

The results demonstrated that the fitting effect of biomass model based on multiple texture features is better than that by single texture feature. Texture information were

not completely taken into consideration when constructing the biomass model by single texture feature, while the biomass model based multiple texture features took advantage of several textures so that the estimation accuracy were improved. Using multiple texture features a potential prospect in estimating winter wheat biomass.

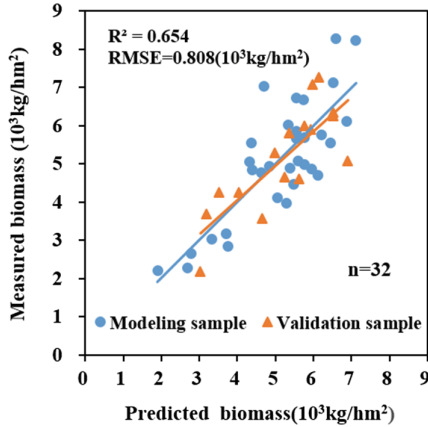


Fig. 5. Relationship between measured biomass and predicted biomass

3.5 Thematic Map of Winter Wheat Biomass

Thematic map of winter wheat biomass at booting stage was constructed by the biomass model based on the texture features of all principal components (Fig. 6). The map showed the winter wheat biomass of each plot in the experiment area. There were little biomass in the southwest and southeast, but much more biomass in the middle plots of the experiment area. The difference in biomass was resulted from different nitrogen fertilizer levels and irrigation levels. W3 treatment has higher biomass than W1 and W2 treatment, and W1 treatment has the lowest biomass. It is clear that sufficient irrigation

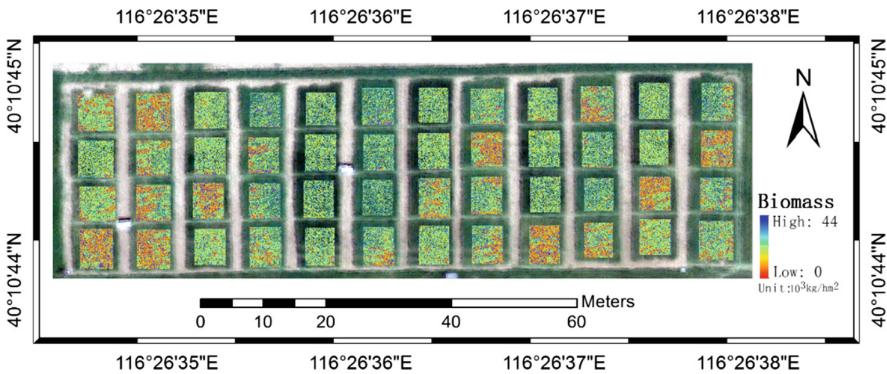


Fig. 6. Thematic map of winter wheat biomass at flagging stage

was beneficial for the growth of winter wheat biomass. N1 treatment had the lowest biomass. There was little difference between biomass of N2 and N3 treatment. When compared to N3 treatment, the biomass of N4 treatment increased slightly, sometimes it had no increase in biomass even decrease, which demonstrated that a suitable nitrogen fertilizer application rate can result in a faster grow in biomass of winter wheat.

4 Conclusions

In this study, the principal component bands were selected for texture feature analysis, and sensitive texture features that obtained from the principal component bands were used to construct the biomass estimation model. The results show that (1) *mean*, *ent*, *sm*, *hom*, *con*, *dis* of the first principal component (pca1) and the mean of the third principal component (pca3) were significantly correlated with the biomass at 0.01 level. (2) As the window size grows, the correlation coefficients between texture features *mean*, *hom*, *con*, *dis* and biomass changed slightly, which was almost stay in a steady state. (3) Biomass model by multiple texture features ($R^2 = 0.654$, RMSE = 0.808 (10^3 kg/hm²)) demonstrates better fitting effect than that by single texture feature ($R^2 = 0.534$, RMSE = 0.960 (10^3 kg/hm²)). The results suggest that the texture features of the UAV platform has a good application prospect in predicting winter wheat biomass, which can provide theoretical support and timely information for winter wheat growth monitoring and field production management.

Acknowledgments. This study was supported in part by the National Key Technologies of Research and Development Program (2016YFD0300602) and National Natural Science Foundation of China (Grant no. 61661136003, 41601346, 41471285, 441601346).

References

1. Du, X., Meng, J.H., Wu, B.F., et al.: Overview on monitoring crop biomass with remote sensing. *Spectrosc. Spectr. Anal.* **30**(11), 3098–3102 (2010)
2. Zhang, K., Wang, R.Y., Wang, X.P., et al.: Hyperspectral remote sensing estimation models for above ground fresh biomass of spring wheat on Loess Plateau. *J. Chin. J. Ecol.* **28**(6), 1155–1161 (2009)
3. Zhuang, D.Y., Li, W.G., Wu, L.Q.: Estimating winter wheat biomass based on satellite remote sensing. *J. Arid Land Resour. Environ.* **27**(10), 158–162 (2013)
4. Chen, P.F., Wang, J.L., Liao, X.Y., et al.: Using data of HI-1A/B Satellite for hulunbeier grassland aboveground biomass estimation. *J. Nat. Resour.* **25**(7), 1122–1131 (2010)
5. Fan, Y.B., Zhao, W.J., Gong, Z.N., et al.: Inversion methods for above-ground dry biomass of phragmites australis and typha angustifolia based on hyperspectral information. *Wetl. Sci.* **14**(5), 654–664 (2016)
6. Gao, M.L., Gong, Z.N., Zhao, W.J., et al.: The study of vitex negundo shrubs canopy biomass inversion in Beijing Jundu mountainous area based on vegetation indices. *Acta Ecol. Sin.* **34**(5), 1178–1188 (2014)

7. Gao, L., Yang, G.J., Wang, B.S., et al.: Soybean leaf area index retrieval with UAV (unmanned aerial vehicle) remote sensing imagery. *Chin. J. Eco-Agric.* **23**(7), 868–876 (2015)
8. Li, C.C., Niu, Q.L., Yang, G.J., et al.: Estimation of leaf area index of soybean breeding materials based on UAV digital images. *Trans. Chin. Soc. Agric. Mach.* **48**(8), 147–158 (2017)
9. Yang, F.: Estimation of winter wheat aboveground biomass with UAV LiDAR and hyperspectral data. Xi'an University of science and technology, Shaanxi (2017)
10. Zhang, Z.J., Li, A.N., Bian, J.H., et al.: Estimation aboveground biomass of grassland in zoige by visible vegetation index derived from unmaned aerial vehicle image. *Remote Sens. Technol. Appl.* **31**(1), 51–62 (2016)
11. Lu, G.Z., Yang, G.J., Zhao, X.Q., et al.: Inversion of soybean fresh biomass based on multi-payload unmanned aerial vehicles (UAVs). *Soybean Sci.* **36**(1), 41–50 (2017)
12. Sarker, L.R., Nichol, J.E.: Improved for set biomass estimates using ALOS AVNIR-2 Texture indices. *Remote Sens. Environ.* **115**(4), 968–977 (2011)
13. Xu, T.: Method and application of forest biomass estimation based on LiDAR and OLI multispectral data. Nanjing Agricultural University, Jiangsu (2015)
14. Mu, Q.E., Gao, Z.H., Bao, Y.H., et al.: Estimation of sparse vegetation biomass based on Grey-Level Co-occurrence Matrix of vegetation indices. *Remote Sens. Inf.* **31**(1), 58–63 (2016)
15. Yue, J.B., Yang, G.J., Li, C.C., et al.: Estimation of winter wheat above-ground biomass using unmanned aerial vehicle-based snapshot hyperspectral sensor and crop height improved models. *Remote Sens.* **9**(70), 801–819 (2017)
16. Deng, S.B.: ENVI Remote Sensing Image Processing Method. Science Publishing, Beijing (2010)



Reconstruction and Body Size Detection of 3D Sheep Body Model Based on Point Cloud Data

Yanqing Zhou, Heru Xue^(✉), Chunlan Wang, Xinhua Jiang,
Xiaojing Gao, and Jie Bai

College of Computer and Information Engineering,
Inner Mongolia Agricultural University, Hohhot, China
hellozhouyanqing@126.com, {xuehr, jiangxh, gaouxj4587,
Baijie2016}@imau.edu.cn, wangchunlan990@163.com

Abstract. Aiming at the high workload, low precision, strong stress of the traditional manual measurement to obtain the sheep growth parameters, a novel measurement technology was proposed. The specimen of the Sunite sheep about 2–3 years old were chosen for study. By reverse engineering technology, point cloud data of sheep was captured by the 3D laser scanner. Because of noise point cloud data, the improved algorithm of k-nearest neighbor was used to process the data. To improve the subsequent processing time and efficiency, octree coding was employed to reduce data, which can get evenly distribution of point cloud data and retain sheep features. Then, 3D surface model of sheep body was reconstructed using Delaunay triangulation. Some parameters were extracted, including sheep body length, body height, hip height, hip width and chest width. Compared actual parameters values with computing values of two ways, by Geomagic platform and the proposed algorithms on the Matlab, average relative errors of two ways were 1.23% and 1.01%, respectively. So results of the proposed algorithm were with small error range. Using the point clouds can reconstruct sheep surface for computing body size without stress.

Keywords: Sheep body parameters · Point clouds · Octree coding
Three-dimensional reconstruction · Data pretreatment

1 Introduction

In recent years, the conformation of animals has garnered close attention by the workers who are engaged in animal husbandry and breeding. It not only reflects production performance and genetic characteristics, but also indicates the shape and yield of different cuts of meat [1]. For example, the milk production and breeding of dairy cow are predicted employing linear appraisal of conformation [2]. Currently most judgements of animal conformation are executed by eye or hand, and largely depended on the subjective assessment of the stockman or purchaser [3, 4].

Body parameters can be estimated from shape measurements, indicating the animal growth development, such as weight body length, chest depth, rump height, body height. These parameters were directly measured by manual and contact operation. The calculation of the body measurements is very difficult especially when sheep is grazing

[5]. Traditional, the sheep is tied up or hung up on the scale to weight [6]. These operations are dangerous for the animal. Meanwhile, it has high workload, low precision and strong stress, leading to the reduction of production quality.

Image process and analysis technique have been successfully applied to estimate the animal body size indirectly from its dimensions. Some studies are listed in the following. Schofield estimated non-invasively the measurements from images [7]. A low-cost dual web-camera high-resolution system was developed to obtain three-dimensional position of homologous points in a scene, so as to estimate size and weight of live sheep [5]. Bewley et al. used digital images to determine body condition score for lactating dairy cows [8].

Recently, reverse engineering technology, adopting special measuring apparatus to get dimensional data, is used to reconstruct the surface model of animal and plants and measure their parameters with non-contact [9]. For example, Liu et al. used laser scanner to obtain point clouds, in order to reconstruct three dimension pig body [10]. Li et al. captured the point cloud data of a cattle hoof to build the three-dimensional geometrical modeling [11]. Zhang studied the papaya reconstruction to detect feature based on the point cloud data [12]. Obviously, the technology is widely used in agricultural applications with the advantage of accurately and fast obtaining 3D geometrical data.

Sunite sheep, one of the features of Inner Mongolia sheep, was selected as research object. Based on the reverse engineering technology, a large number of points on the sheep body surface were generated by the three-dimension laser scanner, and the pretreatment methods were discussed. 3D surface model of sheep body was reconstructed based on Delaunay triangulation. Subsequently, the parameters were extracted for sheep body size. This way meets the requirement of welfare production in sheep breeding.

The paper is organized as follow: Section 1 introduces the basic principle of laser scanner and collects the point cloud data of sheep. Section 2 predominantly focuses on pretreatment method, including data denoising and reduction, and reconstruction of sheep body. Section 3 describes parameters extraction and discusses results in detail. Section 4 highlights the conclusions.

2 Point Cloud Data Collection of Sheep Body

2.1 Composition and Principle of Three-Dimensional Laser Scanner

The captured methods of point cloud data can be divided into two kinds in accordance with sensing mode, which are contact measurement and non-contact measurement. Although the former is quite accuracy and reliable, it also has some deficiency, such as slow scanning speed and probe abrasion. The later can scan surface with high-speed and avoid of probe radius compensation, which has been widely used in reverse engineering [13]. The experiment device REVscan of point cloud acquisition belongs to non-contact measurement method, offered by Canada CreaForm Inc. with weighing only 980 g. The laser is safe for eye, the accuracy reaches 50 μ m. The devices mainly contain trigger, two CCD cameras, cross laser transmitter and LED lamp. The function

of four LED lamp around the CCD cameras is to shield the interference of light from the outside world. The working principle is the laser triangulation of distance. The laser launching points and CCD receiving points are in the ends of the baseline L , which constitute a triangle with the transmitted light and reflected light all together. The distance S between the baseline L and the measured object is determined by using the triangular geometry method, as shown in Fig. 1.

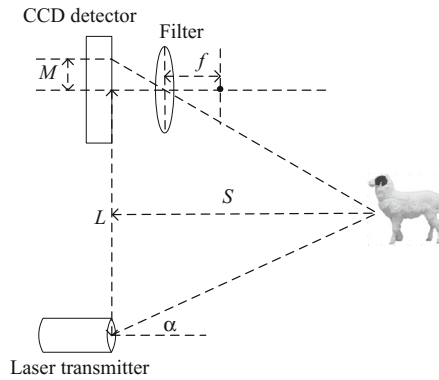


Fig. 1. The principle diagram of triangulation

Laser beam are transmitted toward the target according to certain angle. When the laser encounters the object, reflection will be happened, followed with detecting laser beam by CCD detector [14].

The reflected light through the filter appears the offset, whose value is M . Meanwhile, the laser scanning system measures the horizontal scanning angle α of every laser beam. Thus, the offset value M and the target distance S can be calculated by the formulas (1) and (2), respectively.

$$M = f \tan \alpha \tag{1}$$

$$S = \frac{L + M}{2 \tan \alpha} \tag{2}$$

The baseline L with high precision is generally short in three-dimensional laser scanner based on laser triangulation of distance, which determines the measurement range.

2.2 Composition and Principle of Three-Dimensional Laser Scanner

The experiment took place in the image processing and pattern recognition laboratory of our college in March 2017. The test object is Sunite sheep specimen about 2–3 years old. The point cloud data were collected by different two people. After calibrating the scanner and adjusting the scanner light supplement rate, the preparation work of the

scanner has done. When pressing trigger of REVscan scanner, the scanner starts to scan the surface from one point to another, namely by picking points through scanning the line. The scanning line is an intersection of the scanning plane and the sheep body [9]. The points are saved on the computer in the format of.vtx. When the data are operated on MATLAB platform, the data form will be transformed to.txt format.

3 Data Pretreatment and 3D Reconstruction of Sheep Body

The scan process is inevitably affected by external factor and instrument itself factor, leading to yielding the noise data among the collected point clouds. At the same time, the captured data are scatted disorderly. With the slow movement of scanner, the data quantity is more and more big, which influences the subsequent storage and processing. Therefore, it is necessary to preprocess the point cloud data. All of the experiments were executed on an Intel Core(TM) 2 Duo E7500 CPU @ 2.93 GHz and 3 GB RAM; the codes were written in MATLAB 2011b.

3.1 Point Cloud Data Denoising

The 3D point cloud data of sheep body by the different people acquisition are shown in the Fig. 2, containing 336352 points and 340972 points, respectively. It can be observed that the number of points are nearly equal with different people, but data differ from each other in details. The sophisticated people can obtain the clear sheep hooves.

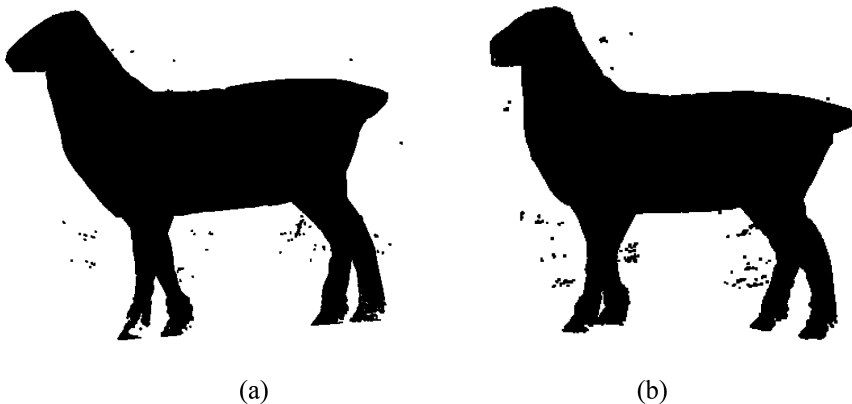


Fig. 2. The point cloud data of sheep body: (a) the first collection data, (b) the second collection data

In Fig. 2, there are a lots of noise data far away from the main body, unlike the normal point data, which are called the outliers [15, 16]. Since the traditional k-nearest neighbor search method has flaws in the aspect of computing speed and efficiency, the improved k-nearest neighbor method based on space block strategy is proposed, so as to eliminate the noise data. The three dimensional scattered point data are projected to

the plane, following by the rasterizing. The research field is reduced from the 27 adjacent grids to the 9 grids, significantly decreasing the computation and enhancing the search efficiency.

Denote n as the number of point clouds. Let $C \in \mathbb{R}^{n \times 3}$ be the matrix recording the 3D coordinates of the scattered point clouds of sheep body. The following specific steps are listed:

Step 1: Three-dimensional point clouds C of sheep body are projected on the two-dimensional planes from three directions, respectively.

Step 2: Scatted point cloud data sets on the every plane are divided into the plane mesh.

Step 3: k neighbors of each point $p_i = \{x_i, y_i, z_i\} (p_i \in \mathbb{R}^3, i = 1, 2, \dots, n)$ are searched in the any selected plane, then the average distance \bar{d} between point p_i and the k neighbors are calculated by Eq. (3). Where $K(p_i)$ is the set of local neighborhood of point p_i . When the point p_i has not enough neighbors in rectangular and its adjacent rectangular, the point is viewed as the isolated noise point, and it is deleted.

$$\bar{d} = \frac{1}{k} \sum_{j \in K(p_i)} \|p_i - p_j\| \tag{3}$$

Step 4: Let D be the threshold. The point p_i is regarded as the deleted candidate point if average distance $\bar{d} > D$.

Step 5: In the rest of two-dimensional plane, the steps (3) and (4) are executed, respectively. If the point p_i is also deemed to the delete candidate point, this point is removed, otherwise, keep it.

Using the proposed method, it is more efficient to recognize and remove the stray noise points. Finally, 325463 points and 339757 points sheep body on the two collection data are remained.

3.2 Point Cloud Data Reduction

The goal of data reduction is to employ as few data as possible to represent more information, making sure to improve the processing speed. The classical reduction methods, such as random, curvature, grid and unified, judge all point cloud data, resulting in a large amount of computation [17]. Whereas, octree coding is based on the region [18], which splits neighborhood space into many sub-cubes with the specified length, retaining the nearest points closing to the center of every sub-cube. Thereby the data reduction has done. The key steps are listed in the following.

- (a) Determining the number of octree layer according to the formula (4):

$$d_0 * 2^n \geq d_{max} \tag{4}$$

Where, d_{max} is the maximal length of bounding box of point clouds, d_0 is defined as the distance of points.

- (b) Dividing the point cloud data into the octree with n layers and calculating the octree coding of data points. Assuming the data point $P(x, y, z)$, where the spatial index of the sub-cube is (i, j, k) , then the index values i, j and k are converted to the binary form, respectively. According to the Eq. (7), the octree coding of data point $P(x, y, z)$ is obtained, where octree coding corresponding to the sub-cube is computed by the Eq. (8). The center point of sub-cube is calculated via the d_0 and the spatial index.

$$\begin{aligned} i &= \text{ceil}((x - x_{\min})/d_0) \\ j &= \text{ceil}((y - y_{\min})/d_0) \\ k &= \text{ceil}((z - z_{\min})/d_0) \end{aligned} \quad (5)$$

$$\begin{aligned} i &= i_0 2^0 + i_1 2^1 + \cdots + i_m 2^m + \cdots + i_{n-1} 2^{n-1} \\ j &= j_0 2^0 + j_1 2^1 + \cdots + j_m 2^m + \cdots + j_{n-1} 2^{n-1} \\ k &= k_0 2^0 + k_1 2^1 + \cdots + k_m 2^m + \cdots + k_{n-1} 2^{n-1} \end{aligned} \quad (6)$$

And, $i_m, j_m, k_m \in \{0, 1\}, m \in \{0, 1, \dots, n-1\}$.

$$q_m = i_m + j_m 2^1 + k_m 2^2 \quad (7)$$

$$Q = q_{n-1} \cdots q_m \cdots q_1 q_0 \quad (8)$$

- (c) Restoring the point cloud data according to the order of coding value, at the same time, the point with equal code values are stored in the same chain list.
- (d) Keeping the point with minimum distance between the center point and data if there are more than one data points on the chain list, so as to reduce the data points.

We compared octree coding with several generic methods, including curvature, grid and unified, as shown in Fig. 3 and Table 1. The reduction performance of different methods is evaluated by result pictures and the reduction rate. After many times of experiment, the parameter setting of four methods was specifically stated for getting a better result. The reduction proportion of curvature is set to 30%, the reduction distance of grid and uniform is respectively 6 mm and 5 mm, the number of octree coding layers is set to 7.

Four methods all presented a model of sheep in Fig. 3. Curvature method can decrease the number of point when local area was flat. It can be seen that the processing points based on other three methods were almost distributed uniformly on the surface of sheep body. The number of point clouds after octree coding were the least among the four algorithms, whose reduction rate was about 5.77%. Whereas, the number of point clouds after grid method were the largest. Comparatively, the streamline method of octree coding outperformed other methods and achieved the very low point cloud data with retaining sheep feature. When the same algorithm processes different data, the reduction rate remain unchanged. Thus, the reduction rate has nothing to do with data.

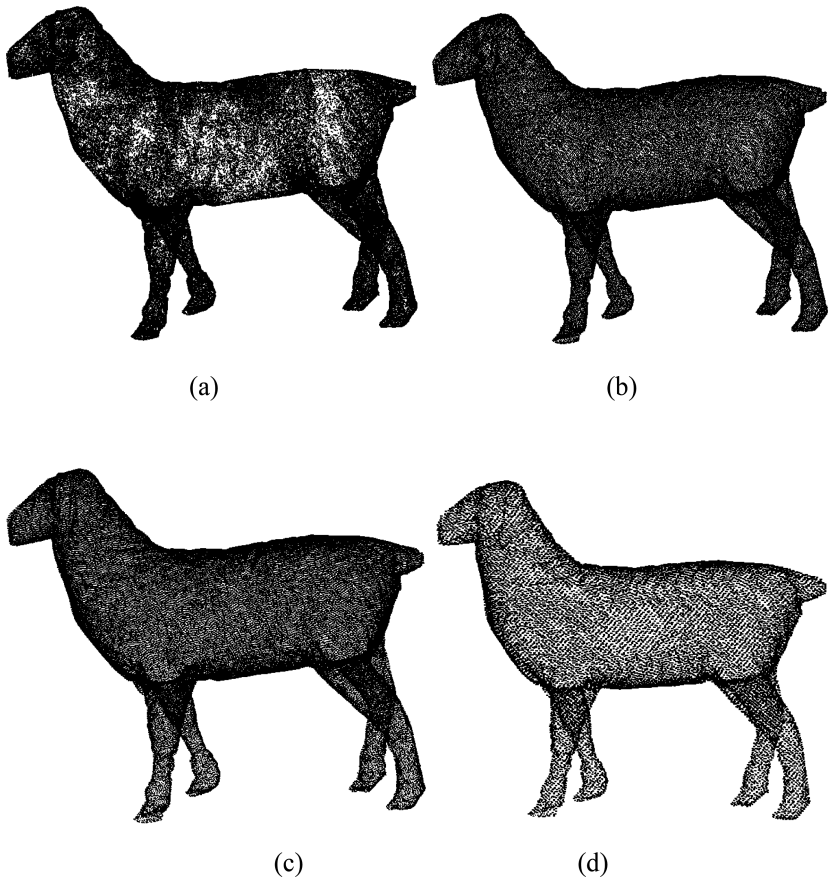


Fig. 3. Results of four reduction methods of data two: (a) Curvature; (b) Grid; (c) Uniform; (d) Octree coding

Table 1. Comparison of data points number and rate after reduction of different algorithms

Data	Algorithms	Data points no. after reduction	Reduction rate (%)
First collection data	Curvature	100639	30.00%
	Grid	56698	16.90%
	Uniform	44383	13.23%
	Octree coding	19323	5.76%
Second collection data	Curvature	101927	30.00%
	Grid	57504	16.93%
	Uniform	45215	13.31%
	Octree coding	19615	5.77%

3.3 Sheep Body Three-Dimensional Reconstruction

The three-dimensional reconstruction is to fulfill the process of sheep point clouds from points to surfaces. Using the sheep surface model, it is convenient to obtain and analyze the parameters of sheep. The definition of triangulation is to transform the scatted point into the triangle mesh [19]. The triangle is the simplest polygons, which can consist of the arbitrary polygons. The common way to construct the three-dimensional surface is to use the triangulation. In this study, the Delaunay triangulation was chosen to reconstruct the sheep body. After the data captured by different people employed the octree coding to eliminate, the results were view as the input data. The reconstruction results with 28518 and 39196 triangles were displayed in Fig. 4, on which the ear of sheep can be clearly seen. Whereas the edge of sheep hoof was slightly rough. This was because of the touching the ground to make the edge points difficult.

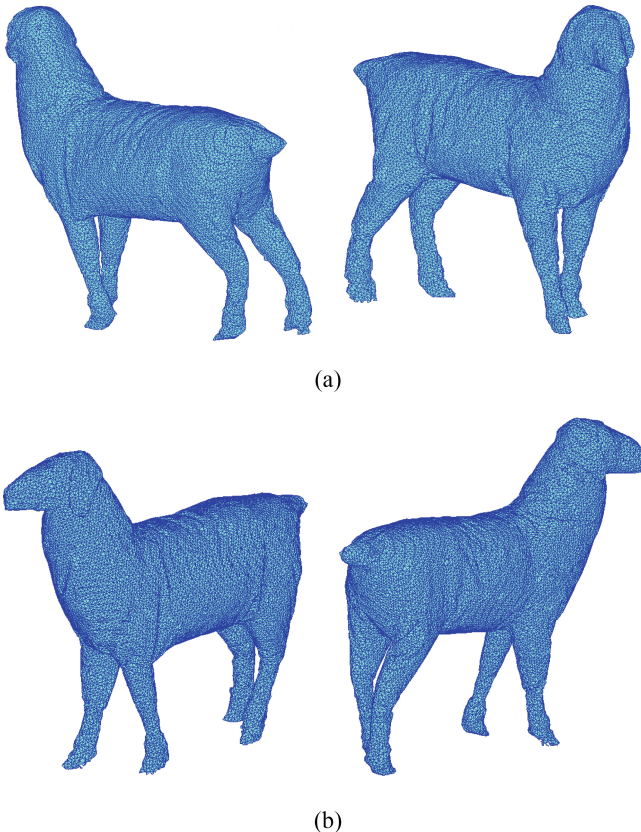


Fig. 4. Three dimensional reconstruction results based on octree coding: (a) first collection data, (b) second collection data

Particularly, the reconstruction time after of four reduction methods were compared in the Table 2. It can be found that the number of point after simplification were proportional to the reconstruction time with the almost same ratio about 3200. The top reconstruction time of about 34 s was obtained when the reduction results of curvature method was used as the input. The construction time based on octree coding was only 5.64 s and 6.09 s, respectively. Therefore, sparse data based on octree coding can yield a better effect.

Table 2. Font sizes of headings. Table captions should always be positioned *above* the tables.

Parameters	Manually measured values	Obtained values for first collection data		Obtained values for second collection data	
		Geomagic platform	Proposed algorithm	Geomagic platform	Proposed algorithm
Body length/cm	82.87	82.10 (0.93%)	82.13 (0.89%)	81.87 (1.21%)	82.41 (0.56%)
Height at withers/cm	73.43	72.32 (1.51%)	72.80 (0.86%)	74.25 (1.11%)	72.87 (0.76%)
Rump width/cm	28.07	27.11 (3.43%)	27.58 (1.75%)	27.26 (2.89%)	27.64 (1.52%)
Rump height/cm	74.7	74.62 (0.11%)	74.44 (0.34%)	74.68 (0.02%)	74.24 (0.62%)
Chest width/cm	27.4	27.34 (0.20%)	27.95 (2.01%)	27.16 (0.86%)	27.18 (0.81%)
Maximum error/%	–	3.43	2.01	2.89	1.52
Minimum error/%	–	0.11	0.34	0.02	0.56
Average relative error/%	–	1.24	1.17	1.22	0.85

4 Parameter Extraction and Analysis of Sheep Body

4.1 Method of Parameter Extraction

From the three-dimensional surface reconstruction, some body size measurements can be acquired. Traditional body measurements are carried out by the use of measuring tape calibrated in centimeters after restraining and holding the animals in an unforced position, including body length, height at wither, hip height, hip width and chest width. Height at withers is obtained as the highest point over the scapulae vertical to the ground. Rump height is obtained as the highest point over the sacrum vertical to the ground. Body length is obtained as the distance from the shoulder end to the distal end of the ischial tuberosity. Chest width refers to the back width just behind the foreleg. Rump width is determined as the back width over the sacrum [20, 21]. Measurement

locations were displayed in the Fig. 5, which are searched on the three dimensional model. The body length, rump width and chest width are achieved by the Euclidean distance employing the formula (9).

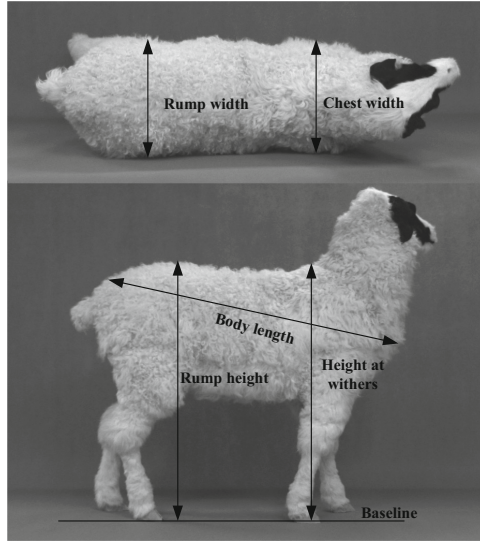


Fig. 5. Parameters of sheep body and their locations

$$L = \sqrt{(x_i - x_j)^2 + (y_i - y_j)^2 + (z_i - z_j)^2} \tag{9}$$

Where, (x_i, y_i, z_i) and (x_j, y_j, z_j) is the corresponding measured points coordinates of parameters, respectively.

Supposing the ground equation containing the baseline is denoted as $Ax + By + Cz + D = 0$, Height at wither and rump height are calculated in the following formula.

$$d = \frac{|Ax + By + Cz + D|}{\sqrt{A^2 + B^2 + C^2}} \tag{10}$$

Where, (x, y, z) is the measured point coordinate of the height at wither and rump height.

4.2 Results Analysis of Parameters

In this study, body length, height at wither, hip height, hip width and chest width values of sheep are both manually measured and obtained by reconstruction model according to the same point at the same time. Due to existing the error, the average values of several manually measurement were viewed as the finally value. To testify the

precision of the three dimension surface reconstruction of sheep, comparative studies were also conducted to between the manually measured values and the obtained measured values, with computation on the three dimensional model in two ways: one was to use Geomagic platform brought by scanner, the other was to apply the mentioned algorithm on MATLAB. Table 2 illustrated the sheep body size values using different data and different computation means, comparing the manually measured values. The relative error of measured values based on Geomagic platform and MATLAB were listed in the parentheses corresponding to the measured values.

It can be observed from Table 2, the obtained values slightly varied with the combination of runtime environment and captured data. The error of parameters based on Geomagic platform altered between -0.82 cm and 1.11 cm, whose rang was larger than that of the proposed algorithm, with the change of -0.55 cm to 0.74 cm. It proved that the proposed algorithm had an effect on the measurement performance. The measured values on Geomagic platform did not reveal a good stable performance with an average relative error of 1.23% , almost 1.01% higher than that of the algorithms in the paper on MATLAB. By comparing the relative error of different data, the measured results of the second collection data was superior to that of the data by first collection, with a little influence of the computation of sheep body size. Also, as can be seen, the measured values of rump width based three dimensional reconstructions exhibited the lowest measurement performance, which was mainly caused by the difficulty of the measured point search. Hence, three dimensional reconstruction of sheep body using proposed algorithm was an effective way to calculate the sheep body size, so as to improve the accuracy and stability.

5 Conclusions

In the study, we presented the three dimensional reconstruction system of sheep body based on point cloud data. The process comprises four steps: point clouds acquisition, preprocessing, three dimensional reconstruction and body size measurement. In the data preprocessing stage, the improved k-nearest neighbor was used for data denoising, and the octree coding was employed in the reduction data to enhance the research speed and decrease the number of the point clouds while preserving the intrinsic feature points, for it divided the data points into spatial neighbor. Three dimensional reconstruction of sheep body was built using the Delaunay triangulation. The novelty of the system of the algorithm was to calculate sheep body size based on point clouds. The measurement results made a comparison with the real values, which indicated that the proposed algorithm slightly outperformed Geomagic platform in the stability and accuracy. The paper provided a new method for the sheep body measurement, and three dimensional model can evaluate the sheep body shape, all of which are of significant importance to the sheep production and breeding. In addition, the new technology can be extended the other fields.

Acknowledgements. This work was supported by national and international scientific and technological cooperation special projects (No. 2015DFA00530), supported by national natural science foundation of China (No. 61461041).

References

1. Zhang, L., et al.: Advances in body size measurement and conformation appraisal for sheep. *Trans. Chin. Soc. Agric. Eng.* **32**, 190–197 (2016)
2. Zhen, Y., et al.: 3D synchronization imaging system for linear appraisal of dairy cow conformation. *Trans. Chin. Soc. Agric. Mach.* **40**(2), 175–179 (2009)
3. Wu, J.H., et al.: Extracting the three-dimensional shape of live pigs using stereo photogrammetry. *Comput. Electron. Agric.* **44**(3), 203–222 (2004)
4. Vieira, A., et al.: Development and validation of a visual body condition scoring system for dairy goats with picture-based training. *J. Dairy Sci.* **98**(9), 6597–6608 (2015)
5. Menesatti, P., et al.: A low-cost stereovision system to estimate size and weight of live sheep. *Comput. Electron. Agric.* **103**(2), 33–38 (2014)
6. Zhang, L., et al.: Design and experiment of non-stress measuring system for sheep's conformation parameters. *Trans. Chin. Soc. Agric. Mach.* **47**(11), 307–315 (2016)
7. Schofield, C.P., et al.: Monitoring pig growth using a prototype imaging system. *J. Agric. Eng. Res.* **72**(3), 205–210 (1999)
8. Bewley, J.M., et al.: Potential for estimation of body condition scores in dairy cattle from digital images. *J. Dairy Sci.* **91**(9), 3439–3453 (2008)
9. Yu, D.M., et al.: Application of reverse engineering technology in constructing prototype surface. *Appl. Mech. Mater.* **34**, 1154–1158 (2010)
10. Liu, T., et al.: Reconstruction and application of 3D pig body model based on point cloud data. *Nongye Jixie Xuebao/Trans. Chin. Soc. Agric. Mach.* **45**(6), 291–295 (2014)
11. Li, S., et al.: Three-dimensional geometrical modeling of the exterior configuration of a cattle hoof by reverse engineering technology. *Trans. Chin. Soc. Agric. Eng.* **20**(2), 156–160 (2004)
12. Zhang, B., et al.: Feature detection and three-dimensional reconstruction for papaya harvesting. *J. Agric. Mech. Res.* **12**, 212–216 (2016)
13. Yu, D.M., et al.: Reconstructing of prototype surface with reverse engineering and data process technology. *Key Eng. Mater.* **458**(458), 368–373 (2011)
14. Zhang, Q.F., Sun, X.S.: Measuring principle and developmental prospect of 3D laser scanner. *Beijing Surv. Mapp.* **1**, 39–42 (2011)
15. Fang, F., Cheng, X.: A fast data reduction method for massive scattered point clouds based on slicing. *Geomat. Inf. Sci. Wuhan Univ.* **38**(11), 1353–1357 (2013)
16. Wang Chunlan, X.H., Jiang, X., Zhou, Y.: The research of removing stray noise fast from point cloud data of three dimension. *J. Inner Mongolia Agric. Univ.* **38**(1), 93–97 (2017)
17. Lee, K.H., Woo, H., Suk, T.: Point data reduction using 3D grids. *Int. J. Adv. Manuf. Technol.* **18**(3), 201–210 (2001)
18. Wang, Y., et al.: Research on 3D modeling method based on hybrid octree structure. *Open Electr. Electron. Eng. J.* **8**(1), 323–329 (2014)
19. Romanoni, A., et al.: Automatic 3D reconstruction of manifold meshes via delaunay triangulation and mesh sweeping, pp. 1–8 (2016)
20. Sowande, O.S., Sobola, O.S.: Body measurements of west African dwarf sheep as parameters for estimation of live weight. *Trop. Anim. Health Prod.* **40**(6), 433–439 (2008)
21. Mahmud, M.A., et al.: Live body weight estimation using cannon bone length and other body linear measurements in Nigerian breeds of sheep. *J. Adv. Vet. Anim. Res.* **1**(4), 169–176 (2014)



Research on Irrigation System of Limited Water Supply for Soybean Crops in Shanxi Province

Lantao Ye^{1,2(✉)}, Yangren Wang^{1,2}, Qing Liu¹, and Sida Wang¹

¹ Department of Hydraulics Engineering, Tianjin Agricultural University, Tianjin 300384, China
yltao1982@126.com

² Tianjin Agricultural Water Conservancy Technology Engineering Center, Tianjin, China

Abstract. The limited water supply irrigation system for soybean crops in Shanxi Province was studied. The irrigation data of Limin experimental station in Linfen City, Shanxi Province had been selected. Frequency calculation of rainfall data of Limin was made, choosing 2010, 1993 and 1997 respectively as the sample year of plain water year (50%), water year dry year (75%) and special drought year (95%) of Limin. The Jensen model as the basis for calculation was selected, calculating the actual yield value of crop according to the actual crop water requirement, crop maximum water demand, sensitive index value and maximum crop yield at each stage. Through the selection of the number of days of irrigation, the optimization model of irrigation times was established. The limiting condition is the maximum actual yield. The quota irrigation system of soybean crops in different hydrological years was determined. According to calculation results, each target year was three times, with the highest amount of water.

Keywords: Irrigation system · Quota water supply · Shanxi Province Soybean crops

1 Introduction

With the continuous progress of human society, the level of scientific and technological production continues to develop, our demand for water is increasing and the range of use will become more and more extensive. Agricultural irrigation is no longer simple irrigation of crops, and how to carry out effective and reasonable scientific irrigation has become the consensus of people. Under the premise of the serious shortage of water resources, agricultural irrigation is difficult to make adequate supply of water needed for every stages of crops growthy, so the optimal utilization of irrigation water resources becomes more and more important. In the case of water shortages and insufficient water supply, the irrigation water is optimized at different stages of the crop to optimize the irrigation allocation, so as to obtain higher irrigation benefits and achieve the goal of increasing production in this way.

Linear programming, referred to as LP [1, 2], helps us to study linear constraints, as well as to understand some of the related objective functions. XiaoSujun et al. [3–5] started from the actual water sensitivity index and the water production function of a part of irrigation areas in the Yellow River. They pointed out the main irrigation time of all kinds of crops and Got the irrigation system under the condition of quota of water supply in irrigated area. Qiu Lin et al. [6–8] gave the irrigation system with a multi-level innovation model that contains the risk index of crop planting which not only reduces the risk of planting, but also reduces the amount of water used for irrigation. Based on the viewpoint of non sufficient irrigation, Wang Zhiliang et al. [9–11] provided a irrigation system suitable for single crop in irrigation area and a dynamic programming model. They set up models to analyze the combined use of various water resources, and in the model to reflect the first use of surface water facts. According to the advantages of the accelerated genetic algorithm (RAGA) and the multidimensional dynamic programming (DP) method, the genetic dynamic programming model (RAGA DP) was given by Fu Qiang et al. [12, 13], which is helpful to eliminate the premature precocity in the improvement of irrigation system, and to emphasize local optimization and not easy to get the most suitable. CuiYuanlai [14, 15] had analyzed the actual water production function of the crops and concluded that the net irrigation of crops during different growth periods was best suited to the deployment by means of SDP, getting an effective irrigation system for a single crop.

We should provide adequate water supply during the growth period where the crops need water for the most part. The specific time of yield increase is given when the irrigation critical water is obtained, and the crop yield under different irrigation levels is estimated in every target years of water. Determine how much water is used to determine yield, and then to optimize the irrigation system of crops. To promote the limited water resources to the maximum benefit in order to achieve the goal of water-saving irrigation. According to the different factors of different crops, we have made a suitable irrigation system, which has a remarkable effect on agricultural water saving. Therefore, it is significant to study the irrigation system of crop quota water supply.

2 Materials and Methods

2.1 Selection of Soybean Experiment

Through the experiment data of soybean in Shanxi province, the main experimental sites of soybean crops were distributed in the Hutuo River, Central Experimental Station, Wenyuhe, Licheng, Linfen, Huoquan and Limin. This study choosed the data of the Limin experimental station in the Linfen city of Shanxi Province to study the quota irrigation system.

2.2 Test Processing Design

According to the situation of rainfall and crop water requirement in the Limin test station in Shanxi Province, five treatments were designed according to the plan of the provincial hall. The area area was 34.8 m².

2.3 Field Operation Management

Using the local field cultivation and management measures, tested varieties was Fen bean 17, sowing rate was 10 kg/mu, it was fertilizers applied Yunnan phosphate fertilizer of 40 kg/mu. During intertill 3 times, the depth was 5 to 7 cm.

2.4 Meteorological Conditions of Soybean

The average temperature of soybean was 20.6° in growth period; the total rainfall was 216.4 mm, effective rainfall was 201.5 mm; belonging to plain water year, water surface evaporation (20 cm diameter) was 549 mm; sunshine hours was 500.1 h; the relative humidity was 76%; natural disasters did not occur.

2.5 Soil Moisture Determination

Soil moisture was determined by soil drilling and soil drying method. The soil depth was 140 cm, (0–20 cm, 20–40 cm, 40–60 cm, 60–80 cm, 80–100 cm, 100–120 cm, 120–140 cm), which was measured in seven layers. Soil moisture was measured every ten days during the growth period of soybean: on the 1st, 11th and 21st days of each month at the beginning of the growth stage and after precipitation.

2.6 Irrigation Situation

In the test, the water well irrigation, water meter measurement water quantity and the field irrigation water delivery system were adopted. The semi fixed plastic pipeline was used to transport water, and the water outlet pipe was connected with the hose for irrigation.

2.7 Field Observation Survey

At the growth stage of soybean, plant growth was observed, and yield structure were determined after harvest.

2.8 Basic Parameters

According to historical data, the soybean irrigation quota was 50 mm. In recent years, the maximum yield per mu of soybeans was 175 kg/mu. The soil basic parameters, soybean stages, crop coefficients and soybean growth period are shown in Tables 1 and 2.

Table 1. Soil basic parameters of test station

Area	Volume weight of soil (g/m ³)	Soil depth (m)	Field moisture capacity (percent by weight)	Wilting percentage (percent by weight)	Initial rate of water content
Limin	1.46	0.5	24.6	6	19.2

Table 2. Observation record of soybean growth period

Area	Year	Sow	Branch	Bloom	Pod	Seed-filling	Harvest
Limin	2008	5.19	7.2	7.12	7.22	8.12	9.12

3 Formulation of Soybean Quota Irrigation System

3.1 Frequency Calculation

Irrigation design reliability is that the probability of irrigation water consumption can be fully satisfied over the years in the irrigation area, generally expressed by the percentage of years which design irrigation water is fully satisfied in total computed years. Formula see form (1).

$$P = \frac{m}{n + 1} \times 100\% \tag{1}$$

Formula: P is the guarantee rate of irrigation design; m is to calculate the number of years when the water supply is greater than or equal to the irrigation water requirement; n is the total number of years for the calculation series, in large and medium-sized irrigation areas, the calendar year should not be less than 30 years.

Based on the analysis of precipitation frequency table in Linfen city of Shanxi Province, the meteorological data of three typical hydrological years in 2010 (50%), 1993 (75%) and 1997 (95%) were selected as the basis for the study of the quota irrigation system.

3.2 Calculation of Crop Water Requirement

In the study, the method of calculating the actual crop water requirement was adopted by reference to the water requirement.

Crop coefficient KcCrop coefficient can be divided into four stages: initial growth stage, rapid growth stage, middle fertility stage and mature stage. By referring to the crop coefficient recommended by FAO, the coefficient of soybean crop in Limin area is shown in Table 3.

Table 3. Coefficient of soybean fractional crop

Area	Growth stage	Initial growth stage	Rapid growth stage	Medium maturity stage	Full growth stage	Whole growth period
Limin	Crop coefficient	0.67	0.67–1.09	1.09	1.09–0.48	
	Days	20	30	40	27	117

Soil moisture correction coefficient. The model proposed by Lei Zhidong et al. (1988), see form (2).

$$K_s = \begin{cases} 1 & \theta \geq \theta_j \\ a + b\theta & \theta \leq \theta_j \\ 0 & \theta \leq \theta_{wp} \end{cases} \tag{2}$$

θ is the actual water content of soil root layer; θ_{wp} is permanent wilting point moisture content. θ_j is critical moisture content

Actual crop evapotranspiration. Meteorological factors, crop factors and soil factors should be taken into consideration in actual crop water requirements. Its formula is formula 3.

$$ET = K_s K_c ET_0 \tag{3}$$

In the formula, ET is the actual crop evapotranspiration; ET0 is the reference crop evapotranspiration; Kc is the crop coefficient; Ks is the soil water correction coefficient.

3.3 Determination of Crop Water Production Function

Crop water production function is a mathematical model which reflects the variation of crop yield and water content, and is the basic theoretical basis for irrigation planning, design and management of non sufficient irrigation. Jensen model is a static model of water production function, referred to as the multiplicative model, widely used in recent years. The expressions for the Jensen model are present in Eq. (4).

$$\frac{y}{y_m} = \prod_{i=1}^n \left(\frac{ET}{ET_{mi}} \right)^{\lambda_i} \tag{4}$$

In formula: n is the number of stages of crop fertility; i is the number of the crop stages; Y is the actual yield of crops (kg/hm²); Ym is the maximum yield (kg/hm²) for full irrigation. ETi is the actual evapotranspiration in i growth stage (mm); ETmi and Ym corresponding to the i evapotranspiration growth stage (mm); λ_i is a sensitive index in lambda i growth stage, reflecting the influence on output stage water shortage degree, and it is an important parameter in the model.

Selection of sensitivity index. According to the experimental data of Jensen model, the sensitive index of the growth stages of soybean crops was calculated, shown in Table 4.

Table 4. Sensitive index tables of different growth stages of soybean

Area	Year	Growth period	Sowing branching	Branches-flowering	Flowering-podding	Podding-Seed-filling	Seed-filling-mature
Limin	2009	Sensitivity index	0.0182	0.2527	0.1621	0.3292	0.2277
		Cumulative days	5	33	43	64	114

Calculation of water production function at each growth stage. Equation (3) shows that:

$$\frac{y}{y_m} = \left(\frac{ET}{ET_{m1}}\right)^{\lambda_1} \times \left(\frac{ET}{ET_{m2}}\right)^{\lambda_2} \times \dots \times \left(\frac{ET}{ET_{mn}}\right)^{\lambda_n}$$

$$y = \left(\frac{ET}{ET_{m1}}\right)^{\lambda_1} \times \left(\frac{ET}{ET_{m2}}\right)^{\lambda_2} \times \dots \times \left(\frac{ET}{ET_{mn}}\right)^{\lambda_n} \times y_m \tag{5}$$

Through the formula 5, the actual crop yield Y can be obtained according to the actual crop water requirement, crop maximum water demand, sensitive index value and maximum crop yield at each stage.

According to the sensitivity index, the actual water requirement, the maximum water requirement at each stage and the water production function value of the 5 growing stages was calculated.

3.4 Determination of Irrigation Time

According to the research of irrigation on soybean irrigation system, the irrigation times were determined up to 3 times. So the limited irrigation system has three kinds of circumstances, choosing once, twice and three times watering in each plain water year, as the limit conditions was the actual maximum yield.

The pattern search method is adopted in this research to derive the maximum yield of crops. In the process of probing derive, according to the coordinate direction, the values are searched at a certain step size, when exploration results failed, step length is shrinked and searched again, until the search step length is less than the given accuracy.

According to the above calculation process, the limited water supply irrigation system for soybean crops has been worked out in different hydrological years, as shown in Table 5.

Table 5. Soybean limited irrigation system

Hydrological year type	Irrigation frequency	Irrigation quota	Irrigation time	ET _m (mm)	ET ₀ (mm)	P (mm)	(kg/mu)
50% (2010)	1	50	36	372.11	416.12	246.3	114.41
	2		30/36				141.43
	3		10/30/36				161.55
75% (1993)	1		33	392.06	444.22	262.2	133.71
	2		16/33				159.05
	3		1/16/33				170.80
95% (1997)	1		31	494.26	552.82	167.5	107.11
	2		22/31				128.49
	3		22/31/52				141.95

4 Conclusion

This study selected the irrigation data of Limin experimental station in Linfen city of Shanxi province, the irrigation system of limited water supply for soybean crops were studied in Shanxi province. Rainfall data were calculated at choosing 2010, 1993 and 1997 respectively as the sample year of plain water year (50%), water year dry year (75%) and special drought year (95%) of Limin. The Jensen model were selected as the basis for calculation, calculating the actual yield value of crop according to the actual crop water requirement, crop maximum water demand, sensitive index value and maximum crop yield at each stage. Through the selection of the number of days of irrigation, the optimization model of irrigation times were established. Every kinds of target years of water was respectively chosen to fill the water once, two times, and three times. The limiting condition is the maximum actual yield. The quota irrigation system of soybean crops in different hydrological years in Limin area was determined. According to calculation results, each target year was three times, with the highest amount of water. In actual irrigation, water shortage is often encountered and irrigation is required according to the limited water supply system. Therefore, it is necessary to analyze the irrigation system with limited water supply. The calculation results can provide the basis for the establishment of irrigation system for local crops.

References

1. Wang, Y.: Irrigation and Drainage Engineering. China Water Conservancy and Hydropower Press, Beijing (2014)
2. De Louw, P.G.B., Eeman, S., Essink, G.H.P., Vermue, E., Post, V.E.A.: Rainwater lens dynamics and mixing between infiltrating rainwater and upward saline groundwater seepage beneath a tile-drained agricultural field. *J. Hydrol.* **501**, 133–145 (2013)
3. Cazarro, I., Hoekstra, A.Y., Choliz, J.S.: The water footprint of tourism in Spain. *Tour. Manag.* **40**, 90–101 (2014)
4. Yunfeng: Analysis of sprinkler irrigation system and economic benefit in eastern Inner Mongolia. *Econ. Technol. Mark.* 87–88 (2016)
5. Zhu, M., Sheina, Z.: Study on optimal irrigation system for water-saving tomato crops in Hetao irrigation area. *Rural. Water Conserv. Hydropower China*, 64–68+72 (2012)
6. Wang, Y., Wang, S., Zheng, Z., Zhao, B.: Study on economic irrigation system of drip-irrigation eggplant under film in greenhouse. *North Hortic.*, 46–50 (2016)
7. Heydari, M.M., Heydari, M.: Evaluation of pan coefficient equations for estimating reference crop evapotranspiration in the arid region. *Arch. Agron. Soil Sci.*, 715–731 (2014)
8. Tao, Hu, R., Lu, C.: Experimental study on the irrigation system of typical cash crops under the condition of Shannan spraying micro-irrigation. *Zhejiang Water Conserv. Sci. Technol.*, 18–20 (2014)
9. Xu, J., Guo, Y., Han-Zhuo: Study on optimization of water-saving irrigation system for summer maize in Luoyang. *People of the Yellow River*, 75–76 (2012)
10. Zheng, J.: Water-saving response mechanism and irrigation system optimization simulation of economic crops in inland arid region of northwest China. Chinese Agricultural University (2014)

11. Taraqqi, A.K.: 姬强, 王旭东. Impact of different tillage practices on soil organic carbon and water use efficiency under continuous wheat-maize binary cropping system. *Chin. J. Appl. Ecol.*, 1029–1035 (2014)
12. Garcia-Tejero, I.F., Arriaga, J., Duran-Zuazo, V.H., Muriel-Fernandez, J.L.: Predicting crop-water production functions for long-term effects of deficit irrigation on citrus productivity (SW Spain). *Arch. Agron. Soil Sci.* **59**(12), 1591–1606 (2013)
13. Song, T., Cai, H., Xu, J.: Water requirement and irrigation schedule of winter wheat and summer maize in Jinghuiqu Irrigation District. *J. Irrig. Drain.*, 52–56 (2017)
14. Azizian, A., Sepaskhah, A.R.: Maize response to different water, salinity and nitrogen levels: agronomic behavior. *Int. J. Plant Prod.* **8**(1), 107–130 (2014)
15. Cammalleri, C., Anderson, M.C., Gao, F., Hain, C.R., Kustas, W.P.: Mapping daily evapotranspiration at field scales over rainfed and irrigated agricultural areas using remote sensing data fusion. *Agric. For. Meteorol.* **186**, 1–11 (2014)
16. Hoff, H., Doll, P., Fader, M., Gerten, D., Hauser, S., Siebert, S.: Water footprints of cities-indicators for sustainable consumption and production. *Hydrol. Earth Syst. Sci.* **18**(1), 213–226 (2014)



Development and Application of Hyperspectral Remote Sensing

Huimin Xing^{1,2,3,4}, Haikuan Feng^{1,2,3,4}(✉), Jingying Fu^{1,2,3,4},
Xingang Xu^{1,2,3,4}, and Guijun Yang^{1,2,3,4}

¹ Key Laboratory of Quantitative Remote Sensing in Agriculture of Ministry of Agriculture P. R. China, Beijing Research Center for Information Technology in Agriculture, Beijing 100097, China

hmxing01@163.com, fenghaikua123@163.com

² National Engineering Research Center for Information Technology in Agriculture, Beijing 100097, China

³ Beijing Engineering Research Center of Agriculture Internet of Things, Beijing 100097, China

⁴ Institute of Geographic Sciences and Natural Resources Research, CAS, Beijing 100083, China

Abstract. Since the early 1960s, multispectral imagery has been served as the data source for earth observational remote sensing (RS) in the last thirty years; the advancement of sensor technology had made it accessible to collecting hundreds continues spectral bands-hyperspectral RS. Hyperspectral RS (HRS) is a new technique for observing the earth, which is different from the multi-spectral RS because of several hundreds of contiguous spectral bands. With a long history of development, HRS is widely used currently. This review details the development of HRS, data processing, characteristics, imaging mode of hyperspectral sensors and its applications, such as detecting and identifying the surface, monitoring agriculture and forest status, environmental studies, and military surveillance, etc.

Keywords: Hyperspectral remote sensing · Airborne · Space borne
Hyperspectral sensors · Plant ecology surveying

1 Introduction

The advancement and applications of remote sensing (RS) serve as a significant scientific technique in the 20 century. Hyperspectral remote sensing (HRS) is a new technique for observing the earth developed in the 1980's. Hyperspectral imagery is collected with instruments called "imaging spectrometers". The original definition of imaging spectrometry, proposed by Goetz et al. [1]. The definition shows that the hyperspectral imaging is different from the multispectral imaging. It needs the sensors to acquire images simultaneously in 100–200 or even more contiguous spectral bands. Each pixel of a hyperspectral image has a related radiance spectrum. Hyperspectral images, called as hypercube, include three dimensional blocks of data, two spatial and one spectral dimension, and integrate the major features of image and spectroscopy [2, 3].

Hyperspectral imaging has had a long history of development. The beginning of imaging spectrometry of the earth is rooted in the launching of Landsat-1 in the 1970's, and the field spectral measurements were taken to underpin the analysis of the Landsat-1 MSS (Multispectral Scanner) data. The field spectrometry, the airborne imaging spectrometer and the space borne imaging spectrometer are developing gradually with the development of the electronics, computing and software [4].

Airborne hyperspectral sensors have made somewhat successes in research and applications in a variety of fields, such as hydrological modeling and analysis platform (HyMap) and project for on-board autonomy (PROBA)-1 [5–12]. Useful and important as HRS is, the development, some techniques and applications related to it will be introduced.

2 The Development of the Hyperspectral Remote Sensing

2.1 Airborne Hyperspectral Remote Sensing

Airborne HRS has a long history of development dating back to 1983. Airborne Imaging Spectrometer (AIS)-1, the first generation imaging spectrometer was born in this year. The spectral range is from 0.99 μm to 2.4 μm , at 9.3 nm spectral resolution in 64 contiguous spectral bands. The second generation imaging spectrometer was AVIRIS, at the same time, it was the first imaging sensor. The AVIRIS can measure solar reflectance spectroscopy from 0.4 μm to 2.5 μm with 224 bands. It plays an important role in atmospheric correction, ecology and vegetation, snow and ice hydrology, inland and coastal waters, biomass burning, etc. [14, 15]. Subsequently, in 1989 ITRES Corporation, Alberta, Canada introduced a pushbroom imaging spectrograph, Compact Airborne Spectrographic Imager (CASI), which covers the region (0.43–0.86 μm) in 288 spectral bans. It primarily monitored and researched the aquatic and terrestrial applications [12, 16]. In 1994, the GER launched the Digital Airborne Imaging Spectrometer (DAIS) series, DAIS3715, DAIS7915, DAIS16115, and DAIS21115, HyMAP has also been developed in Australia in 1996 [17]. Following the CHRIS was launched on ESA'S PROBA platform in October 2000 [18, 19].

China began to develop hyperspectral imaging system in 1980's, the first Module Airborne Imaging Spectral (MAIS) ran in 1991. It is a sign that China has made a great breakthrough in technology and applications of airborne imaging spectral. And then, the Chinese Academy of Sciences successfully developed operational modular imaging spectrometer (OMIS) on the basis of MAIS, including OMIS-1 and OMIS-2, which belonged the Pushbroom Hyperspectral Imager (PHI), with 128 and 68 spectral bands from visible to TIR wavelength at the spectral region 0.46–12.5 μm they were primarily used in geology, agriculture, forest, ocean, etc. [20]. Chinese Moderate Resolution Imaging Spectrometer (CMODIS), as an ocean color satellite measure spectrometer, was launched on 25 March 2002 onboard the "Shenzhou-3" spaceship [21]. In addition, the interference imaging spectrometer, researched by Xi'an institute of optics and precision mechanics of Chinese Academy of Sciences (CAS), was lift off onboard Chang'E-1 in October 2007, the Environmental disaster reduction satellite (Env-DD) in September 2008, and the GF-5, will be taken in the near future. A variety

of imaging spectrometers in our country, OMIS and PHI represent the technical level of the imaging spectrometer in Asia, and also occupy an important position in the world.

2.2 Spaceborne Hyperspectral Remote Sensing

The history of spaceborne HRS is shorter than airborne HRS, the first HRS satellite launched in 1997 named LEWIS (Failure). The plans of high resolution imaging spectrometer (HIRIS) and Orbview-4 were also failed. However, it develops very well in recent 30 years, and its value has been put forward.

MODIS was launched successfully in December 1999, every 1 to 2 days, the MODIS pay a return visit the earth and acquires data, the spectral range of which is from 0.4 μm to 14 μm with 36 bands. These data can help us to well comprehend the global dynamics of earth.

ASTER is an imaging instrument flying on Terra. The goal of ASTER is to discover how the earth is changing by observing and modeling the earth system, and understand the importance of life on earth. MightySat-II was launched on 19 July 2000, which was the third generation imaging spectrometer, sun-synchronous orbit [22].

The space technology of China develops rapidly, the HJ-1A satellite was launched in September 2008. The hyperspectral imager provides earth imagery at 100 m spatial resolution and 5 nm spectral resolution, and its spectral range is from 0.45 μm to 0.95 μm . Tiangong-1(TG-1) spacecraft with the spaceborne hyperspectral Image of China was lunched from the Jiuquan spaceport boarded the Changzheng-2F rocket in September 29, 2011. The spaceborne hyperspectral image has the highest spectral and spatial resolution, and its spectral region is from VIS to SWIR. The hyperspectral images data are widely used in various fields, such as in land resources investigation, forestry, agriculture, exploration of oil and gas, mineral, marine, urban heat island effect, detection of atmospheric and environment, materials science and so on.

3 The Characteristics of Hyperspectral Remote Sensing Images

Different from the multispectral images, the HRS images have the following characteristics [24–26]. (1) Hypersectral images have a wide range of spectral response and high spatial resolution. The electromagnetic wavelength of imaging spectrometer is from VIS to NIR, and the spectral resolution reaches to nm level. (2) Combining the image and spectral. In the hyperspectral images data, the whole data of hyperspectral image is an image cube (Fig. 1), including spatial information and spectral information, and each pixel of image corresponds to a spectral curve (Fig. 2). (3) There are usually three kinds of models in hyperspectral images: image, spectrum and characteristic. (4) Due to huge quantity of data and high correlation between spectral bands, the information redundancy increases with bands, data and correlation between bands. (5) The signal-to-noise ratio (SNR) of hyperspectral image gets low. When the SNR of hyperspectral images data increases, the noise increases, simultaneously the difficulty of data processing increases.

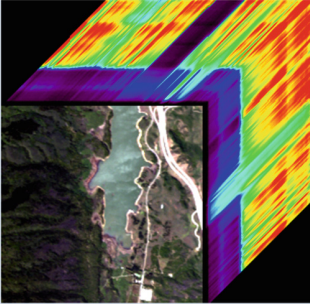


Fig. 1. 3D cube of hyperspectral images

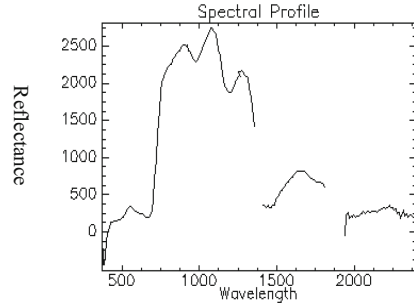


Fig. 2. Spectral curve of hyperspectral image

The HRS data, comparing with the wide-band panchromatic and multispectral rRS data, both spectral and spatial resolution, have been improved, significant advantages as following [27, 28]: (1) Hyperspectral images contain approximate contiguous spectral information of surface features, spectral reflectance curve of surface features can be obtained after rebuilding the spectral reflectance of hyperspectral image. The laboratory spectral analysis model can be applied in the RS with matching the measured values. (2) The identification ability of surface cover is greatly improved. The material with diagnostic spectral absorption characteristics can be detect, which can accurately distinguish the types of surface vegetation cover, material of road paved, etc. (3) In hyperspectral images, the terrain elements can be quantitatively or semi quantitatively classified, various parameters of surface cover can be estimated, and the accuracy and reliability of quantitative analysis can be improved. (4) Various algorithms are proposed for the classification of HIS. The traditional classification algorithms after dimensionality reduction, include Bayes classification method, decision tree (DT), neural network, support vector machine (SVM), kernel fisher discriminate (KFD), and so on.

4 The Imaging Mode of Hyperspectral Remote Sensing

In general, the imaging mode of HRS has five kinds as following: Linear scanning mode, Whiskbroom scanning mode, pushbroom scanning mode, Spectral and spatial crossed scanning mode, optical path difference scanning mode [24, 29, 30]:

- (1) Linear scanning mode. The spectrometer with this mode can obtain a whole scene image using a single detector.
- (2) The whiskbroom scanning mode. This mode belongs to opto-mechanical system, the spectrometer of this scanning mode uses line-array detectors, it gains parallel scanning line set by several detectors, arraying along the courses. Now, the whiskbroom scanning mode is used in full spectrum spectrometer, the wide of spectral form visible to infrared, such as Deadalus series, AVIRS, MAIS, OMIS, MSS, Thematic Mapper (TM) and FengYun (FY) meteorological satellite, etc.

- (3) The pushbroom scanning mode. This mode belongs to solid-state system. Now, the pushbroom spectrometer, including a two dimensional matrix detectors, one dimensional used as a spectrometer and another as a line array, has been widely used in spaceborne HRS. It generates a line image once a time without mobling components. At present, the pushbroom spectrometers are used in VIS/NIR bands, such as AIS-1, AIS-2, CASI, hyperspectral digital imaging collection (HYDICE) and PHI, etc.
- (4) Spectral and spatial crossed scanning mode. The imaging spectrometer with this scanning mode scans spectral dimension used the rotation of rotating filter plate or gradient filter. It is easy to achieve due to its simple design, but difficult to register the images owing to the spectral record respectively.
- (5) Optical path difference scanning mode (Fourier interferometric spectral scan). The imaging spectrometer with this scanning mode obtains spectral bands time-sharing and the Fourier spectrometer scans the spectral information. At present, this spectrometer is still in the experimental stage, such as the Fourier Transform Visible Hyperspectral Imager Spectrometer (FTVHIS) developed by U.S. Department of Defense, has 256 bands in 0.44–1.15 μm , with 0.6 nm spectral resolution and 0.6 mrad spatial resolution.

5 Processing and Analysis Technique of Hyperspectral Data

According the processing procedure, the processing of hyperspectral data is segmented into three stages: data preprocessing, analysis and application.

Data preprocessing, obtaining high accuracy spectral curve, reflects the spectral features of ground objects, is the main purpose. The major work of this stage is: radiometric calibration, atmospheric correction, geometric correction and image mosaic. Data analysis primary obtain feature information about applications. Hyperspectral data contains spatial information, spectral information and multi temporal information, etc. Data processing mainly includes: spectral feature extraction, feature parameter, etc. Data application, primary interprets the analysis results to meet the requirement of data application. At present, the studies focus on dimensionality reduction and classification.

5.1 Dimensionality Reduction of Hyperspectral Data

An important factor restricting the development of HRS is the huge quantity of data, high correlation between bands. This makes it difficult in data transmission, storage and management. In order to solve the problem of high dimensionality, feature extraction and selection are usually applied to reduce the dimension. Feature selection choose some effective bands from the original bands, without any change, and the feature extraction transform one or several original bands into new synthetic feature according specific function [31]. There are a number of methods in dimensionality reduction of hyperspectral data, including [25, 32] minimum noise fraction (MNF), spectral absorption feature parameter (SAFP), spectral encoding (SE), principal component

analysis (PCA), spectral derivative (SD), spectral absorption index (SAI), segmented principal components transform (SPCT), etc.

5.2 Classification of Hyperspectral Images

The classification algorithms of hyperspectral images are divided into supervised classification and unsupervised classification according to the training samples. The algorithms of unsupervised classification commonly include parallelepiped, clustering, splitting, dynamic clustering, K-means, etc. Training samples of supervised classification can be extracted from ROI or the spectral library. Supervised classification of a priori knowledge has higher classification accuracy than unsupervised. The algorithms of supervised includes correlation coefficient method, minimum distance classification (MDC), fisher linear Discriminant (FLD), spectral information divergence, and so on [33, 34]. In addition, some other methods are also used to classify, e.g. fuzzy classification, decision tree classification, least squares classification (LSC), maximum likelihood classification (MLC) [34], etc.

6 The Application of the Hyperspectral Remote Sensing

HRS has been extensively used in earth studies. With the development of HRS, there is a growing interest in the researches and applications in a variety of fields such as in coastal and inland water studies, disaster mitigation, geology, astronomy, urban studies, land cover, pharmaceuticals, medicine and military uses [2, 35–40]. This paper primarily introduces the applications in plant ecology surveying, atmospheric environmental assessment, geological prospecting, water quality monitoring, atmospheric environmental assessment and military application.

6.1 Plant Ecology Surveying

In agricultural study, it is significant to timely and precisely monitor crop growth status at large scale. Koppe et al. developed a model to forecast and reckon crop parameters based on multi- and hyperspectral satellite data [41]. The evaluation of chlorophyll content and the leaf area index (LAI) using RS technology can be estimated in precision agriculture [42]. Galvao et al., used the hyperspectral data to discriminate five important sugarcane varieties in Brazilian [6]. An Australian shows the results similarity with field observations who predicted the soil organic carbon (SOC) using Hyperion data. This technique will facilitate the implementation of digital soil mapping [43], and the similar result was found in mapping soil organic matter (SOM) using HRS images and multi-source data [44].

In addition, HRS is applied in vegetation [13], map post fire vegetation recovery [45], assess species diversity in homogeneous and heterogeneous forest and discriminate different forest tree species [46]. Jensen et al. investigated HRS technology to determine whether it can be used to accurately measure and the indicators of plant hazardous waste sites [47].

6.2 Atmospheric Environmental Assessment

The application of HRS, atmospheric environmental RS is one of the most important contents, it primarily monitor the O_3 , CO_2 , N_2O , CO , O_2 , CH_4 in the 400–2500 spectral range, aerosol. The studies showed that these could be detected in two atmospheric windows, in the visible range of 400–750 nm and the 0.85 nm, 1.06 nm, 1.22 nm, 1.60 nm, and 2.20 nm spectrum bands of NIR and MIR [48–51]. Bassani et al. presented a new physically-based method to obtain aerosol optical thick at 550 nm from hyperspectral image data, who only used the radiative information inherent in the VIR/NIR spectral domain [48]. Gao et al. computed the approximately values of NO_2 transmittances and reflectance near 400 nm over variety targets [49] and found that clouds could be detected and separated at the 1380 nm and 1500 nm by analyzing the spectral imaging data over arctic regions [52].

6.3 Geological Prospecting

HRS has been efficiently used in geological prospecting too, such as mineral exploration, hydrocarbon exploration, mineral resources exploration, mining environmental monitoring, mine ecological restoration and evaluation [53]. HRS technology can finely identify mineral by tens or hundreds of recorded bands in images and construct a complete reflectance spectrum of every pixel... Harris et al. used hyperspectral data to lithological map between VIS and NIR - SWIR range in southern Baffin Island, and successfully discriminated one major lithological group and three compositional units [8]. Merucci et al. demonstrate the efficacy of using the TIR image of the DASI hyperspectral datasets in lithological mapping [54]. Bishop et al. used the HRS technology to explore the porphyry-type deposits in various environmental [54].

6.4 Water Quality Monitoring

HRS images have been widely used to monitor the water quality of open water aquatic ecosystems. Those researches are mainly about the monitoring and estimating the organic matter content of water. Vos et al. used the hyperspectral data to obtain chlorophyll-a concentrations [55]. Koponen et al. used airborne hyperspectral spectrometer and simulated MERIS data for classification of Secchi depth, turbidity, chlorophyll and detected total phosphorus in three water quality [56]. Politi retrieved the chlorophyll-a concentrations and secchi discdepth (SDD) from eutrophic lakes using Terra and Aqua MODIS data [57]. Tilley et al. obtained the total ammonia concentrations using the narrow spectral bands hyperspectral reflectance of emergent macrophytes in wetland in south Texas, USA. Froidefond et al. observed high concentration mineral particles in surface water on the Mahury River by changing remote sensing reflectance [58]. Pulliainen et al. retrieved chlorophyll-a concentration using a semi-operative approach and showed the change of the spectrum shape characteristics and trophic of the lake water [59]. Since hyperion afforded sufficient sensitivity for detecting optical water quality, Vittorio and Arnold retrieved the chlorophyll concentrations, suspended matter and colored dissolved organic matter in Moreton Bay [60].

6.5 Military Applications

The hyperspectral data have been the main reconnaissance mean in military field and gradually replaced the multispectral RS. In the field of military reconnaissance, camouflage identification and battlefield environment reconnaissance are possible using the HRS, according to the different spectral characteristics of the targets, the composition and state of targets surface can be obtained. The real military targets (military vehicle or missile launching frame) of camouflage and stealth in the green vegetation and desert can be detected and identified from camouflage material and background, using the airborne and space reflection spectra data of AVIRIS, CASI or Hyperion [7, 15, 61–63], etc. Tiwari et al. extracted five targets (aircrafts) from synthetic images of the AVIRIS sensor generated and the single AVIRIS image [7]. Gu et al. detected three planes in each region of the AVIRIS images and OMIS images with the spatial resolution $3.5 * 3.5$ m [63]. White et al. analyzed various spectral wavelengths to coastal temperate forest characterization in Canada, that could help to identify the disguising artificial targets [63]. In addition, in military action, it is often overcome the influence of multiple targets moving for capturing and tracking in complex background. However, since the quickly changing of targets position, it is difficult to be tracked, and sometimes the tracked object is similar to the target tracking. In this case, the ordinary reconnaissance technology will do not play a role. The hyperspectral images can use the tracking method by capturing the contour of target, removing the noise signal and finally locking the tracked target [62].

7 Conclusion

Over the past 30 years, big advance has been made in the development and application of new RS technologies, that is being applied in agriculture, environment, vegetation, coastal and inland water studies, disaster mitigation, geology prospecting, astronomy, etc., pharmaceuticals, medicine and military uses. New materials and techniques should be used to improve the capabilities of the hyperspectral sensors, especially the spectral and spatial resolution. At the same time, the standard spectral library on the earth surface should be built. Thus the HRS will be applied more extensively.

Acknowledgements. This study was backed up by the National Natural Science Foundation of China (Grant no. 41601346, 41571416), Beijing Academy of agricultural and Forestry Sciences Innovation Capacity Construction Specific Projects (Grant no. KJCX20170423, KJCX20150409) and Beijing Natural Science Foundation of China (Grant no. 4152019).

References

1. Goetz, A.F.H., Vane, G., Solomon, J.E., Rock, B.N.: Imaging spectrometry for earth remote sensing. *Science* 7(228), 1147–1153 (1985)
2. Lu, R., Park, B.: Hyperspectral and multispectral imaging for food quality and safety. *Sens. Instrum. Food Qual. Saf.* 2(3), 131–132 (2008)

3. Gowen, A.A., O'donnell, C.P., Taghizadeh, M., et al.: Hyperspectral imaging for the investigation of quality deterioration in sliced mushrooms (*Agaricus Bisporus*) during storage. *Sens. Instrum. Food Qual. Saf.* **2**(3), 133–143 (2008)
4. Goetz, A.F.H.: Three decades of hyperspectral remote sensing of the earth: a personal view. *Remote Sens. Environ.* **113**, S5–S16 (2009)
5. Haboudane, D., Miller, J.R., Pattey, E., et al.: Hyperspectral vegetation indices and novel algorithms for predicting green LAI of crop canopies: modeling and validation in the context of precision agriculture. *Remote Sens. Environ.* **90**(3), 337–352 (2004)
6. Galvao, L., Formaggio, A., Tisot, D.: Discrimination of sugarcane varieties in Southeastern Brazil with EO-1 hyperion data. *Remote Sens. Environ.* **94**(4), 523–534 (2005)
7. Tiwari, K.C., Arora, M.K., Singh, D.: An assessment of independent component analysis for detection of military targets from hyperspectral images. *Int. J. Appl. Earth Obs. Geoinf.* **13** (5), 730–740 (2011)
8. Harris, J.R., Rogge, D., Hitchcock, R., et al.: Mapping lithology in Canada's Arctic: application of hyperspectral data using the minimum noise fraction transformation and matched filtering. *Can. J. Earth Sci.* **42**(12), 2173–2193 (2005)
9. Kokaly, R.F., Rockwell, B.W., Haire, S.L., et al.: Characterization of post-fire surface cover, soils, and burn severity at the Cerro Grande Fire, New Mexico, using hyperspectral and multispectral remote sensing. *Remote Sens. Environ.* **106**(3), 305–325 (2007)
10. Alakian, A., Marion, R., Briottet, X.: Radiative modeling and characterization of aerosol plumes in hyperspectral imagery, pp. 3219–3224 (2007)
11. Kneubuehler, M., Koetz, B., Huber, S., et al.: Monitoring vegetation growth using multitemporal CHRIS/PROBA data. In: 2006 IEEE International Geoscience and Remote Sensing Symposium, vol. 1–8, pp. 2677–2680 (2006)
12. Dekker, A.G., Malthus, T.J., Wijnen, M.M., et al.: The effect of spectral bandwidth and positioning on the spectral signature analysis of inland waters. *Remote Sens. Environ.* **41**(2–3), 211–225 (1992)
13. Pengra, B., Johnston, C., Loveland, T.: Mapping an invasive plant, phragmites australis, in coastal wetlands using the EO-1 hyperion hyperspectral sensor. *Remote Sens. Environ.* **108** (1), 74–81 (2007)
14. Green, R.O., Eastwood, M.L., Sarture, C.M., et al.: Imaging spectroscopy and the airborne visible infrared imaging spectrometer (AVIRIS). *Remote Sens. Environ.* **65**(3), 227–248 (1998)
15. Zagolski, F., Pinel, V., Romier, J., et al.: Forest canopy chemistry with high spectral resolution remote sensing. *Int. J. Remote Sens.* **17**(6), 1107–1128 (1996)
16. Babey, S.K., Anger, C.D.: Compact airborne spectrographic imager (CASI) - a progress review. In: *Imaging Spectrometry of the Terrestrial Environment*, pp. 152–163 (1993)
17. Cocks, T., Jenssen, R., Stewart, A., et al.: The HyMap (TM) airborne hyperspectral sensor: the system, calibration and performance. In: *1st Earsel Workshop on Imaging Spectroscopy*, pp. 37–42 (1998)
18. Cutter, M.A., Lobb, D.R., Williams, T.L., et al.: Integration and testing of the compact high-resolution imaging spectrometer (CHRIS). *Imaging Spectrom.* **3753**, 180–191 (1999)
19. Cutter, M., Lobb, D.: Design of the compact high-resolution imaging spectrometer (CHRIS), and future developments. In: *Proceedings of the 5th International Conference on Space Optics*, vol. 554, pp. 41–47 (2004)
20. Liu, Y.N., Xue, Y.Q., Wang, J.Y., et al.: Operational modular imaging spectrometer. *J. Infrared Millim. Waves* **21**(1), 9–13 (2002)
21. Mao, Z.H., Chen, J.Y., He, X.Q.: Evaluation of CMODIS-measured radiance by a hyperspectral model. *Int. J. Remote Sens.* **31**(19), 5179–5198 (2010)

22. Yarbrough, S., Caudill, T., Kouba, E., et al.: MightySat II.1 hyperspectral imager: summary of on-orbit performance. In: Descour, M.R., Shen, S.S. (eds.) *Imaging Spectrometry VII*, pp. 186–197 (2001)
23. Tong, Q., Zhang, B., Zheng, L.: *Hyperspectral Remote Sensing*. Higher Education Press, Beijing (2006)
24. Abdellaoui, B., Merzouk, A., Aberkan, M., et al.: hydrological balance and siltation of the saboun dam (Morocco). *Revue des Sciences de l'Eau*. **15**(4), 737–748 (2002)
25. Su, H., Du, P.: Study on feature selection and extraction of hyperspectral data. *Remote. Sens. Technol. Appl.* **21**(4), 288–293 (2006)
26. Zhang, L., Zhang, L.F.: *Hyperspectral Remote Sensing*. Wuhan University Press, Wuhan (2005)
27. Yang, G., Yu X., Feng, W., Liu, W., Chen, W., et al.: The development and application of hyperspectral RS Technology. *Bull. Surv. Mapp.* (10), 1–4 (2008)
28. Lu, W.: A research of feature extraction and classification techniques for target detection in hyperspectral image. Doctoral Dissertation (2005)
29. Tao, D.X., Jia, G.R., Yuan, Y., et al.: A digital sensor simulator of the pushbroom offner hyperspectral imaging spectrometer. *Sensor* **14**(12), 23822–23842 (2014)
30. Wang, J.N.: Performance analysis and development of airborne imaging spectrometer, new progress and development strategy of remote sensing. Science and Technology of China Press, Beijing (1996)
31. Liu, P., Lin, H., Sun, H., et al.: Dimensionality reduction method of hyperion EO-1 data. *J. Cent. South Univ. For. Technol.* **31**(11), 34–38 (2011)
32. Wang, X., Xiao, P., Guo, J.: Research on dimensionality reduction technology of hyperspectral data. *Bull. Soil Water Conserv.* **26**(6), 89–91 (2006)
33. Kruse, F.A., Lefkoff, A.B., Boardman, J.W., et al.: The spectral image-processing system (SIPS) - interactive visualization and analysis of imaging spectrometer data. *Remote Sens. Environ.* **44**(2–3), 145–163 (1993)
34. Ibraheem, I.: Comparative study of maximum likelihood and spectral angle mapper algorithms used for automated detection of melanoma. *Skin Res. Technol.* **21**(1), 84–89 (2015)
35. Tang, X., Pearlman, W.A.: Three-dimensional wavelet-based compression of hyperspectral images. In: Motta, G., Rizzo, F., Storer, J.A. (eds.) *Hyperspectral Data Compression*, pp. 273–308. Springer, Boston (2006). https://doi.org/10.1007/0-387-28600-4_10
36. Singh, C.B., Jayas, D.S., Paliwal, J., et al.: Identification of insect-damaged wheat kernels using short-wave near-infrared hyperspectral and digital colour imaging. *Comput. Electron. Agric.* **73**(2), 118–125 (2010)
37. Ye, X., Sakai, K., Manago, M., et al.: Prediction of citrus yield from airborne hyperspectral imagery. *Precis. Agric.* **8**(3), 111–125 (2007)
38. Strachan, I.B., Pattey, E., Boisvert, J.B., Cavalli, R.: Impact of nitrogen and environmental conditions on corn as detected by hyperspectral reflectance. *Remote Sens. Environ.* **80**, 213–224 (2002)
39. Flink, P., Lindell, L.T., Ostlund, C.: Statistical analysis of hyperspectral data from two swedish lakes. *Sci. Total. Environ.* **268**, 155–169 (2001)
40. Kunkel, B., Harms, J., Kummer, U., et al.: *Observing Land from Space: Science, Customers and Technology*, pp. 303–327. Kluwer Academic Publishers, Dordrecht (2000)
41. Koppe, W., Li, F., Gnyp, M.L., et al.: Evaluating multispectral and hyperspectral satellite remote sensing data for estimating winter wheat growth parameters at regional scale in the North China plain. *Photogramm. Fernerkund. Geoinf.* (3), 171–182 (2010)

42. Wu, C.Y., Han, X.Z., Niu, Z., et al.: An evaluation of EO-1 hyperspectral hyperion data for chlorophyll content and leaf area index estimation. *Int. J. Remote Sens.* **31**(4), 1079–1086 (2010)
43. Gomez, C., Viscarrarossel, R., Mcbratney, A.: Soil organic carbon prediction by hyperspectral remote sensing and field Vis-NIR spectroscopy: an australian case study. *Geoderma* **146**(3–4), 403–411 (2008)
44. Wang, J., Chen, Y.Q.: Mapping soil organic matter based on land degradation spectral response units using hyperion images. *Int. J. Appl. Earth ObservatiCon Geoinf.* **12**, S171–S180 (2010)
45. Mitri, G.H., Gitas, I.Z.: Mapping postfire vegetation recovery using EO-1 hyperion imagery. *IEEE Trans. Geosci. Remote Sens.* **48**(3), 1613–1618 (2010)
46. Ghiyamat, A., Shafri, H.Z.M.: A review on hyperspectral remote sensing for homogeneous and heterogeneous forest biodiversity assessment. *Int. J. Remote Sens.* **31**(7), 1837–1856 (2010)
47. Jensen, J.R., Gladden, J., Filippi, T., Pendergast, M.: Hyperspectral analysis of hazardous waste sites on the savannah river site, 55 (2003)
48. Bassani, C., Cavalli, R.M., Pignatti, S.: Aerosol optical retrieval and surface reflectance from airborne remote sensing data over land. *Sensors* **10**(7), 6421–6438 (2010)
49. Gao, B.-C., Montes, M.J., Davis, C.O., et al.: Atmospheric correction algorithms for hyperspectral remote sensing data of land and ocean. *Remote Sens. Environ.* **113**, S17–S24 (2009)
50. Vermote, E.F., Tanre, D., Deuze, J.L., et al.: Second simulation of the satellite signal in the solar spectrum, 6S: an overview. *IEEE Trans. Geosci. Remote Sens.* **35**(3), 675–686 (1997)
51. Gao, B.C., Montes, M.J., Ahmad, Z., et al.: Atmospheric correction algorithm for hyperspectral remote sensing of ocean color from space. *Appl. Opt.* **39**(6), 887–896 (2000)
52. Gao, B.C., Han, W., Tsay, S.C., et al.: Cloud detection over the arctic region using airborne imaging spectrometer data during the daytime. *J. Appl. Meteorol.* **37**(11), 1421–1429 (1998)
53. Merucci, L., Bogliolo, M.P., Buongiorno, M.F., et al.: Spectral emissivity and temperature maps of the solfatara crater from DAIS hyperspectral images. *Ann. Geophys.* **49**(1), 235–244 (2006)
54. Bishop, C.A., Liu, J.G., Mason, P.J.: Hyperspectral remote sensing for mineral exploration in Pulang, Yunnan Province, China. *Int. J. Remote. Sens.* **32**(9), 2409–2426 (2011)
55. Vos, R.J., Hakvoort, J.H.M., Jordans, R.W.J., et al.: Multiplatform optical monitoring of eutrophication in temporally and spatially variable lakes. *Sci. Total Environ.* **312**(1–3), 221–243 (2003)
56. Koponen, S., Pulliainen, J., Kallio, K., et al.: Lake water quality classification with airborne hyperspectral spectrometer and simulated MERIS data. *Remote Sens. Environ.* **79**, 51–59 (2002)
57. Politi, E., Cutler, M.E.J., Rowan, J.S.: Evaluating the spatial transferability and temporal repeatability of remote-sensing-based lake water quality retrieval algorithms at the european scale: a meta-analysis approach. *Int. J. Remote. Sens.* **36**(11), 2995–3023 (2015)
58. Tilley, D.R., Ahmed, M., Son, J.H., et al.: Hyperspectral reflectance of emergent macrophytes as an indicator of water column ammonia in an oligohaline, subtropical marsh. *Ecol. Eng.* **21**(2–3), 153–163 (2003)
59. Pulliainen, J., Kallio, K., Eloheimo, K., et al.: A semi-operative approach to lake water quality retrieval from remote sensing data. *Sci. Total Environ.* **268**(1–3), 79–93 (2001)
60. Bachmann, C.M., Donato, T.F., Lamela, G.M., et al.: Automatic classification of land cover on Smith Island, VA, using HyMAP imageryPCA. *IEEE Trans. Geosci. Remote Sens.* **40** (10), 2313–2330 (2002)

61. Luft, L., Neumann, C., Freude, M., et al.: Hyperspectral modeling of ecological indicators - a new approach for monitoring former military training areas. *Ecol. Ind.* **46**, 264–285 (2014)
62. Gu, Y.F., Wang, C., Wang, S.Z., et al.: Kernel-based regularized-angle spectral matching for target detection in hyperspectral imagery. *Pattern Recogn. Lett.* **32**(2), 114–119 (2011)
63. White, J.C., Gomez, C., Wulder, M.A., et al.: Characterizing temperate forest structural and spectral diversity with hyperion EO-1 data. *Remote Sens. Environ.* **114**(7), 1576–1589 (2010)
64. Zhang, C., Cheng, H., Chen, Z., et al.: The development of hyperspectral remote sensing and its threatening to military equipment. *Electro-optic Technol Appl.* **23**(1), 10–12 (2008)



Study on Spatial Distribution Characters of Rubber Yield and Soil Nutrients in Guangba Farm of Hainai Province

Bei Cui^{1,2(✉)}, Wenjiang Huang^{1,2}, Huichun Ye^{1,2}, and Qimin Cao³

¹ Institute of Remote Sensing and Digital Earth, Chinese Academy of Sciences, Beijing 100094, People's Republic of China

{cuiBei, huangwj, yehc}@radi.ac.cn

² Key Laboratory of Earth Observation, Sanya 572029, Hainan Province, People's Republic of China

³ Hainan State Farms Academy of Sciences, Haikou 570100, Hainan Province, People's Republic of China

271093491@qq.com

Abstract. Studying the spatial distribution characters of rubber yield and soil nutrients and the rule of spatial variability are important for suitable fertilization strategy in rubber plantation. This paper selected Hongquan Branch, Guangba Branch and Gongai Branch of Guangba Farm in Hainan province as study area and total of 327 samples were selected in the rubber plantation. The spatial distribution characters of rubber yield and five soil nutrients, including organic matter (OM), total nitrogen (TN), available phosphorus (AP), available potassium (AK), exchangeable calcium (Ca), were studied using traditional analysis method and geo-statistics analysis method. The results showed that: (1) The average value of rubber yield was 3.55 kg/hm² with moderate spatial variability and the average values of OM, N, P, K and Ca were 11.65 g/kg, 0.07%, 16.23 mg/kg, 49.65 mg/kg and 84.44 mg/kg, respectively. Soil OM, TN, AK and Ca had moderate spatial variability but AP had strong spatial variability. (2) Rubber yield and soil total nitrogen (N) nutrient had strong spatial dependence; soil OM, AP, AK and Ca had moderate spatial dependence. (3) Based on the previous reports of normal range of soil nutrients, soil OM and TN nutrient content were very low in the studied rubber plantation of Guangba Farm. Therefore, more nitrogen fertilizer should be applied in the rubber plantation in future.

Keywords: Spatial distribution characters · Rubber yield · Soil nutrients
Guangba Farm

1 Introduction

Rubber plantation soil is an important resource of nutrient for rubber tree, the fertility condition is closely related to rubber growth and production. However, due to the influence of complex terrain, different cultivation methods and many factors in the process of soil-forming, the spatial distribution pattern of soil nutrient in rubber plantation is not homogeneous but highly heterogeneous, which made the large spatial

variability of rubber yield. Therefore, studying the spatial distribution characters of rubber yield and soil nutrients and the rule of spatial variability are important to formulate a suitable fertilization strategy in rubber plantation.

Recently, many researches about the spatial variability of soil nutrients of rubber plantation could be found in the literatures. Yang *et al.* [1] pointed out that both soil total potassium and available potassium had moderate spatial dependence in rubber plantation of Danzhou city. Yang [2] showed that soil available potassium (AK) and total potassium (TK) had strong spatial dependence; soil available nitrogen (AN), total nitrogen (TN), available phosphorus (AP), total phosphorus (TP), pH and organic matter (OM) had moderate spatial dependence in Lanyang Town rubber plantation. Qin *et al.* [3] showed that both soil total phosphorus and available phosphorus at the depth of 0–20 cm and 20–40 cm had moderate spatial dependence in rubber plantation of Qiongzong County. Li *et al.* [4] found that OM, TN, available K (AK) and pH were at normal range but soil available P was below normal level in Dongfeng Farm of Yunnan province. In addition, all parameters of soil OM, TN, AK and pH had strong spatial dependence, indicting the spatial variability of these soil nutrients were mainly caused by structural factors, such as climate, terrain, agrotype and so on. Gao *et al.* [5] pointed out that soil available nitrogen, available phosphorus and available potassium had strong or moderate spatial dependence in rubber plantation of Ledong, Hainan. We can find from above researches that the spatial distribution characters of soil nutrients were different in different rubber plantations, even at the same site but at different time. So, the spatial distribution characters of soil nutrients should be studied for the specific research areas.

In addition, rubber yield is deeply affected by rubber plantation soil nutrients. Li *et al.* [6] pointed out the soil nutrients, such as nitrogen, potassium, phosphorus, can affect the rubber formation and latex flow through influencing the photosynthesis. So, the spatial heterogeneity of rubber plantation soil nutrients maybe lead to the spatial variability of rubber yield. Although many positive results of crop yield and soil nutrients have been reported in the literatures [7–10], there has rarely studies about the spatial variability characters of rubber yield and its relationship with soil nutrients so far.

In this study, rubber yield and five soil nutrients were studied in Hongquan Branch, Guangba Branch, Gongai Branch of Guangba Farm. The objectives of this study were: (i) to assess the condition of rubber yield and soil fertility in the rubber plantation of Guangba Farm; and (ii) to understand the spatial variability characters of rubber yield and soil nutrients using Geo-statistics method and the relationship between rubber yield and soil nutrients.

2 Materials and Methods

2.1 Study Area

The study area is Hongquan Branch, Guangba Branch, Gongai Branch of Guangba Farm, which is located in the Dongfang city of Hainan province. This site has a mean annual rainfall of 1600 mm and a mean annual temperature of 24.2 °C. The terrain slopes gently with slopes of about 10° and elevations of 120 m–160 m above the sea level. Rubber is one of the main economic forests planted in Guangba Farm with more

than 3333 hm² in area. We conducted field surveys of rubber plantations and obtained rubber yield and corresponding soil nutrient parameters data in about 327 rubber stands. The location of Guangba Farm and field survey samples are shown in Fig. 1.

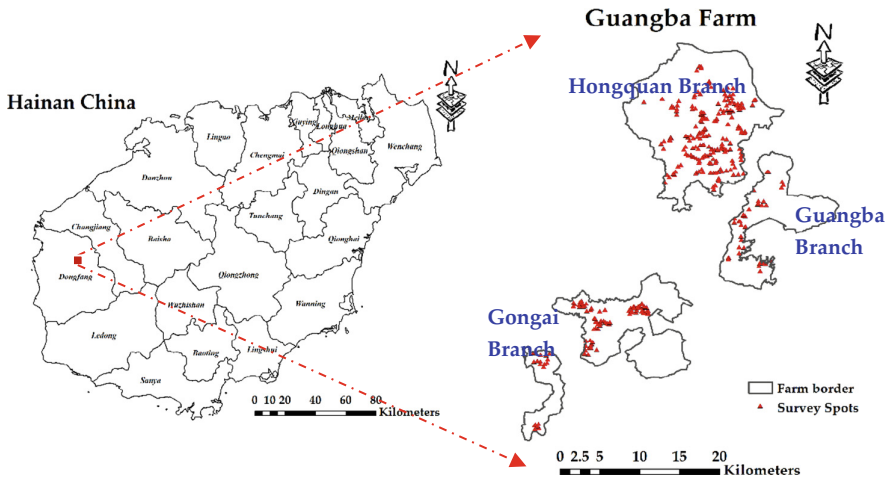


Fig. 1. The location of study area and field survey samples

2.2 Data Collection

In this study, a total of 327 rubber stands were randomly selected in the rubber plantation of Hongquan Branch, Guangba Branch, Gongai Branch of Guangba Farm in 2010. The detailed records of latex yield per time of each rubber stand were recorded, and the annual rubber yield at each rubber stand was calculated.

The corresponding 327 soil samples at the depth of 0–20 cm in the rubber plantation were collected in 2010. For each rubber stand, five representative soil-sampling sites were randomly selected within a 10 m radius near the center of site. Then they were mixed to form one composite sample representing this site. The location of each site was recorded by a DGPS receiver with accuracy of 0.2 m. Soil organic matter (OM) was calculated by using oil bath-K₂Cr₂O₇ titration method [11]. Soil total nitrogen (TN) was calculated by using semi-micro Kjeldahl method, soil available phosphorus (AP) was calculated by using Ammonium-hydrochloride method, soil available potassium (AK) was calculated by using NH₄OAc extraction- flame photometer method, and soil exchangeable calcium (Ca) was calculated by using 1 mol/L ammonium acetate exchange atomic absorption spectrophotometry [12].

2.3 Analyses Method and Software

The conventional statistics for raw experimental data was conducted using SPSS 22 software for Windows (SPSSInc., Chicago, IL, USA) with mean, maximum, minimum, standard deviation (SD), kurtosis, skewness and coefficient of variation (CV). Kurtosis

and skewness values were used to test whether the raw data follow normal distribution. If the raw data did not follow normal distribution, 3δ Method [13], logarithmic or power transformations should be applied to meet the hypothesis of geo-statistical analysis. Coefficient of variation (CV) was identified as a basic parameter for spatial variability. If $CV < 10\%$, it means weak spatial variability; if $10\% < CV < 100\%$, it means moderate spatial variability; if $CV > 100\%$, it means strong spatial variability.

The semi-variogram model was used to indicate spatial structure and the degree of spatial dependence of rubber yield and five soil nutrients. The semi-variogram model is described usually by five main parameters, i.e. nugget, partial sill, sill, range and Nugget/Sill [14]. Nugget means the spatial variation of variable was led by random factors and partial sill means the spatial variation was led by structure factors such as soil texture, crop variety and etc. Sill is the sum of nugget and partial sill, which means the total spatial variation of variable. The range means the max distance between two locations with spatial dependence. The last but the most important parameter is the value of Nugget/Sill ratio, which can directly indicate the degree of spatial dependence and the reason led to spatial variation by random or structure factors. If the value of Nugget/Sill ratio $< 25\%$, it means strong spatial dependence and structure factors as dominant variation reason; if $25\% < \text{Nugget/Sill ratio} < 75\%$, it means moderate spatial dependence; if Nugget/Sill ratio $> 75\%$, it means weak spatial dependence and random factors as dominant variation reason. The best fit theoretical semi-variogram model for different variables were simulated and the fitting accuracy were evaluated according to R^2 indicators. All above analysis were conducted using GS 10+ software (Fig. 2).

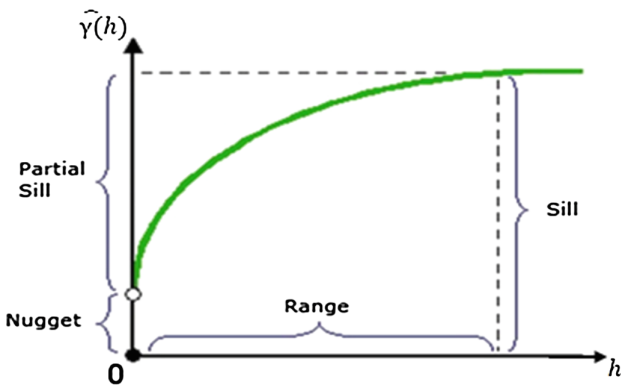


Fig. 2. Parameters of semi-variogram model [14]

3 Results

3.1 Analysis Rubber Yield and Soil Nutrients

The basic statistical information of rubber yield and five kinds of soil nutrients, including soil organic matter (OM), total nitrogen (N), available phosphorus (P), available potassium (K) and exchangeable calcium (Ca), were shown in Table 1. For

yield, OM, N, K and Ga, the coefficients of variation varied between 42.9% and 86.5%, which were greater than 10% and less than 100%, indicating all these parameters had moderate variability. However, the coefficient of variation for P reached up to 173.3%, which meant the variability of P was strong.

Furthermore, because Geo-statistics analysis require all data studied should be normally distributed, all outliers should firstly be checked before the testing of data normal distribution using the 3 δ Method. If the data are still non-normality distribution after correction outliers, data transform (log, square-root and etc.) should be used to ensure that the data obey the normal distribution. In this study, logarithm transition were used for the parameters of yield, P, K and Ga. Through the above-mentioned processing, the values of skewness and kurtosis of all data used in this study were very small as shown in Table 1, indicating that they were all normally distribution.

Table 1. The basic statistical information of rubber yield and five soil nutrients

	N	Min	Max	Mean	SD	CV (%)	Skewness	Kurtosis
Yield (kg/hm ²)	327	1.33	8.80	3.55	26.03	48.8%	0.34	-0.64
OM (g/kg)	327	0.50	29.10	11.65	5.72	49.1%	0.49	0.06
TN (%)	327	0.01	0.16	0.07	0.03	42.9%	0.81	0.46
AP (mg/kg)	327	1.10	165.70	16.23	28.12	173.3%	0.76	0.88
AK (mg/kg)	327	12.00	121.00	49.65	22.58	45.5%	-0.07	-0.14
Ga (mg/kg)	327	5.30	345.60	84.44	73.07	86.5%	-0.19	-0.45

Soil organic matter (OM); total nitrogen (TN); available phosphorus (AP); available potassium (AK); exchangeable calcium (Ga)

3.2 Analysis Spatial Distribution Characters of Rubber Yield and Soil Nutrients

To understand the spatial structure and distribution of rubber yield within the farm is very importance to understand the difference of production capacity among different rubber stands and to make specific fertilizer application strategies according to different levels of yield capacity regions.

In this study, the best fit theoretical semi-variogram model and parameters for rubber yield and five soil nutrients were given in Table 2 and Fig. 3. The Exponential model was found to be the best fit model for rubber yield, and the range for yield was 3.34 km. Nugget: sill ratio values for rubber yield was 15.30%, which was less than 25%, indicating strong spatial dependence mainly resulted from structural factors such as rubber cultivar, terrain, climate and so on. The best fit model for the five soil nutrients was Exponential model. The values of $C_0/(C_0 + C)$ for OM, AP, AK and Ga were in the range of 25%–75%, but for N was less than 25%, which indicated that soil OM, AP, AK and Ga had moderate spatial dependence and soil TN has strong spatial dependence. The R^2 for all parameters studied were in the range of 0.54–0.85, indicating that the selected models can preferably reflect the spatial distribution characters of these parameters.

Table 2. Best fit theoretical semi-variogram model and parameters for rubber yield and soil nutrients

	Model	Nugget	Sill	$C_0/(C_0 + C)$	Range (km)	R^2
Yield (kg/hm ²)	Exponential	0.03	0.17	15.30%	3.34	0.54
OM (g/kg)	Exponential	24.100	50.2100	48.0%	71.47	0.73
TN (%)	Exponential	0.0001	0.0008	14.2%	3.01	0.71
AP (mg/kg)	Exponential	0.5610	1.5020	37.4%	219.74	0.85
AK (mg/kg)	Exponential	0.1229	0.3658	33.6%	252.47	0.60
Ga (mg/kg)	Exponential	0.3100	0.9060	34.2%	12.36	0.74

Soil organic matter (OM); total nitrogen (TN); available phosphorus (AP); available potassium (AK); exchangeable calcium (Ga)

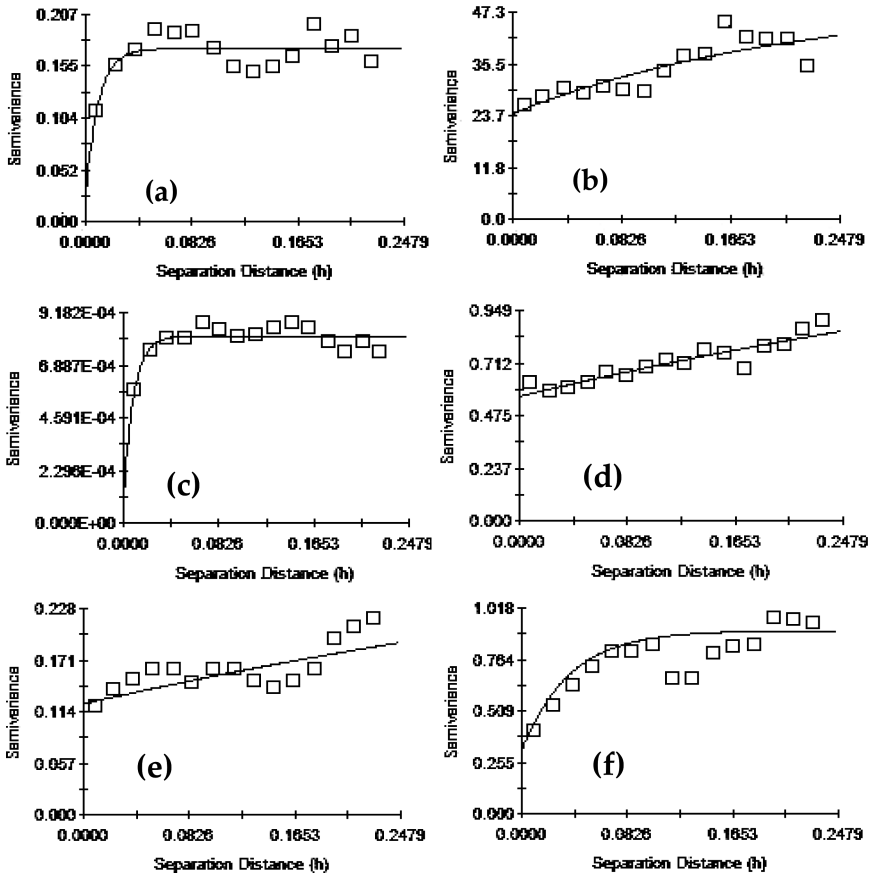


Fig. 3. The semi-variograms of rubber yield and soil nutrients in the rubber plantation (a): rubber yield; (b): soil organic matter (OM); (c): total nitrogen (TN); (d): available phosphorus (AP); (e): available potassium (AK); (f) exchangeable calcium (Ga)

3.3 Analysis the Potential Balance of Soil Nutrients in the Rubber Plantation

Studying the balance of different soil nutrients in rubber plantation is important for making rational fertilizer application strategy, improving the effectiveness of fertilization and maintaining a high and stable rubber production. Based on previous studies of rubber plantation soil fertility condition by He *et al.* [15] and Wu *et al.* [16], the normal range for soil OM, TN, AP and AK nutrient were 20 g/kg–25 g/kg, 0.08%–0.14%, 5 mg/kg–8 mg/kg, 40 mg/kg–60 mg/kg, respectively and the threshold value of Ga was 25 mg/kg. The classification of different soil properties in the study area were shown in Table 3. The results showed that the levels of soil organic matter (OM) and total nitrogen (TN) nutrient in the studied rubber plantation were very low. For available phosphorus (AP) and available potassium (AK), only 26.30% and 38.53% of samples, respectively, were among in the normal range; in other words, the soil available phosphorus and available potassium nutrient were too less or too much in most areas of rubber plantation. The soil in the studied area was rich in exchangeable calcium (Ga) with 81.96% samples greater than the threshold value (25 mg/kg).

Table 3. The classification of soil properties in rubber plantation of Guangba Farm

Soil properties		Low	Normal	High
Organic matter (OM)	Grading standard	<20 g/kg	20–25 g/kg	>25 g/kg
	Number	302	18	7
	Percentage (%)	92.35%	5.50%	2.14%
Total nitrogen (TN)	Grading standard	<0.08%	0.08–0.14%	>0.14%
	Number	223	97	7
	Percentage (%)	68.20%	29.66%	2.14%
Available phosphorus (AP)	Grading standard	<5 mg/kg	5–8 mg/kg	>8 mg/kg
	Number	90	86	151
	Percentage (%)	27.52%	26.30%	46.18%
Available potassium (AK)	Grading standard	<40 mg/kg	40–60 mg/kg	>60 mg/kg
	Number	122	126	79
	Percentage (%)	37.31%	38.53%	24.16%
Exchangeable calcium (Ga)	Grading standard	<25 mg/kg	≥ 25 mg/kg	/
	Number	59	268	/
	Percentage (%)	18.04%	81.96%	/

4 Discussion

In this study, rubber yield and soil nutrients shown obvious spatial dependence in the rubber plantation. The relationship between rubber yield and five soil nutrients were given in Table 4. Rubber yield were strongly related with soil available phosphorus (AP), available potassium (AK) and exchangeable calcium (Ga) at significance level of 0.01. But no relationships were found between yield and soil organic matter (OM), total

nitrogen (TN), which was contradictive with the previous study by An *et al.* [17], it could mainly because the serious lack of soil OM and N. Luo *et al.* [18] pointed out that the leaf nutrient content was directly related to the nutrient condition of rubber tree and the latex yield, although soil was the source of rubber tree nutrient. The immobilization capability of soil and the absorption capacity of rubber tree may lead to less OM and TN content in soil but more in rubber tree. Therefore, comprehensive consideration of the soil nutrient and leaf nutrient is essential to know the factors affecting rubber yield.

Table 4. The relationship between rubber yield and soil nutrients

	OM	TN	AP	AK	Ga	Yield
OM (g/kg)	1	0.763**	0.048	0.260**	0.223**	0.004
TN (%)	0.763**	1	0.042	0.205**	0.197**	0.001
AP (mg/kg)	0.048	0.042	1	0.130*	0.030	-0.154**
AK (mg/kg)	0.260**	0.205**	0.130*	1	0.543**	-0.176**
Ga (mg/kg)	0.223**	0.197**	0.030	0.543**	1	-0.185**
Yield (kg/hm ²)	-0.210	0.001	-0.154**	-0.176**	-0.185**	1

Note:* Significant at the 0.05 level; ** Significant at the 0.01 level.

Soil organic matter (OM); total nitrogen (TN); available phosphorus (AP); available potassium (AK); exchangeable calcium (Ga)

5 Conclusion

Studying the rule of spatial variability of rubber yield and soil nutrients and their spatial distribution characters are important to formulate a suitable fertilization strategy in rubber plantation. The spatial distribution characters of rubber yield and five soil nutrients, including OM, TN, AP, AK, Ga were studied by using traditional analysis method and geo-statistics analysis method in this paper.

The average value of rubber yield was 3.55 kg/hm² with moderate variability. For the five soil nutrients, the average values of OM, TN, AP, AK and Ga were 11.65 g/kg, 0.07%, 16.23 mg/kg, 49.65 mg/kg and 84.44 mg/kg, respectively. Soil OM, TN, AK and Ga had moderate variability but P had strong variability. Through the analysis of semi-variograms, rubber yield and soil TN nutrient had strong spatial dependence; rubber yield and soil OM, AP, AK and Ga had moderate spatial dependence. Based on the previous studies of standard range of soil nutrients, OM and TN nutrient were very low in the studied rubber plantation of Guangba Farm. Therefore, more nitrogen fertilizer should be applied in the rubber plantation in Guangba Farm in future.

Funding Information. This work was supported by National Natural Science Foundation of China (41801352), Natural Science Foundation of Hainan Province, China (20164179, 2016CXTD015), Youth Foundation of Director of Institute of Remote Sensing and Digital Earth, Chinese Academy of Sciences, China (ZZCEODE2015HT015), the Agricultural Science and Technology Innovation of Sanya (2015KJ04), the Technology Research, Development and Promotion Program of Hainan Province, China (ZDXM2015102), the Hainan Provincial Department of Science and Technology under Grant (ZDKJ2016021).

References

1. Yang, Z.J., Wei, J.S., He, P., Wu, B.S., Wu, M.: Spatial variance of potassium in rubber plantation soil in Danzhou city of Hainan province. *J. Northwest For. Univ.* **25**(5), 41–44 (2010)
2. Yang, Z.J.: Study on time-space variation characters of soil nutrients in different scales of rubber plantation. Hainan University, Haikou (2010)
3. Qin, H.D., et al.: Spatial variability and regionalized management of soil phosphorus nutrients in the rubber plantation in Qiongzong County. *Chin. J. Trop. Crops* **35**(2), 369–374 (2014)
4. Li, X.Q., Yu, L.X., Li, C.L., Lu, W.K.: Spatial distribution characteristic of soil nutrients in rubber plantation of Dongfeng Farm of Yunnan Province. *Southwest China J. Agric. Sci.* **28** (1), 292–298 (2015)
5. Gao, L., Wei, J.S., Wu, B.S., He, P., Wu, M.: Characteristics of spatial variability of soil nutrients in rubber plantation in Ledong Country, Hainan. *Chin. J. Trop. Crops* **35**(11), 2115–2120 (2014)
6. Li, G.Y., Wang, Q.B., Li, Y.Y., Zhou, S.X., Yu, H.Y.: A review of influencing factors on latex yield of *Hevea brasiliensis*. *Chin. J. Ecol.* **33**(2), 510–517 (2014)
7. Gao, X.Z., et al.: Spatial variability of soil nutrients and crop yield and site-specific fertilizer management. *Sci. Agric. Sinica* **35**(6), 660–666 (2002)
8. Yang, Y.L., Tian, C.Y., Sheng, J.D., Wen, Q.K.: A study on relationship between spatial variability of soil solute salt and the cotton growth. *Arid Land Geogr.* **4**, 329–335 (2002)
9. Yang, Y.L., Sheng, J.D., Tian, C.Y., Wen, Q.K.: A study on relationship between the spatial variability of saline anthropogenic alluvial soil available nitrogen, phosphorous, potassium and cotton growth. *Sci. Agric. Sinica* **36**(5), 542–547 (2003)
10. Cui, B.: The study of temporal and spatial variation of soil nutrient and winter wheat growth information on field scale. Shanxi Agricultural University, Shanxi (2013)
11. Nelson, D.W., Sommers, L.E.: A rapid and accurate method for estimating organic carbon in soil. *Proc. Indiana Acad. Sci.* **84**, 456–462 (1975)
12. Lu, R.K.: Methods of chemical analysis of agriculture soil. China Agricultural Science and Technology Press (2000)
13. Ding, X.D.: Comparisons among the methods of handling outliers. *Comput. Tech. Geophys. Geochem. Explor.* **18**(1), 71–77 (1996). (in Chinese with English Abstract)
14. Wang, Z.Q.: *Geostatistics and Application in Ecology*, 1st edn, pp. 35–149. Science Press, Beijing (1999). (in Chinese)
15. He, X.D., Lu, X.Z., Wu, X.P.: Study on soil fertility and utilization of soil fertility in Hainan island. *Trop. Agric. Sci.* **1**, 40–48 (1991)
16. Wu, M., He, P., Wei, J.S.: Integrated evaluation of soil fertility for rubber plantation in Hainan province. *Chin. Soil Fertil.* **2**, 1–5 (2009)
17. An, F., et al.: Nutrient conditions of rubber plantations and their relationship with latex yield under stimulated tapping system in Xishuangbanna. *Chin. J. Trop. Crops* **26**(3), 1–6 (2005)
18. Luo, W., Lin, Z.M., Cha, Z.Z.: The development course and trend of nutrition diagnosis of soil nutrition in rubber tree in China. In: *The First National Soil Testing and Fertilizer Technology seminar*, Hohhot, 9–10 July 2006



The Environment Intelligent Monitoring and Analysis for Enclosed Layer House with Four Overlap Tiers Cages in Winter

Hualong Li^{1,2}, Miao Li¹(✉), Junying Li³, Kai Zhan³,
and Xianwang Liu⁴

¹ Institute of Intelligent Machines, Chinese Academy of Sciences,
Hefei 230031, Anhui, China

lihualong2007@163.com, mli@iim.ac.cn

² University of Science and Technology of China, Hefei 230026, Anhui, China

³ Institute of Animal Husbandry and Veterinary,
Agricultural Academy of Anhui Province, Hefei 230031, Anhui, China

⁴ Anhui Agricultural University, Hefei 230026, Anhui, China

Abstract. This study aims at evaluating the environment quality scientifically and providing the corresponding optimization methods for facilities upgrade of enclosed henhouse with four overlap tiers cages. The intelligent environmental monitoring device for laying hens breeding was developed based on Internet of things to measure environmental parameters, including temperature, relative humidity, light intensity and CO₂ concentration, wind speed, dust concentration and other environmental parameters in winter, and to analyze their impact on the laying rate and egg quality. The results showed that the environmental parameters in henhouse different measuring points were different. The height of different hens cages have a certain effect with egg-laying rate and egg weight. It can be seen that the contradiction between ventilation and heat preservation should be coordinated in winter. On the premise of keeping suitable temperature, the ventilation should be increased to provide a good production environment for laying hens.

Keywords: Intelligent monitoring · Cascade cage · Environmental quality
Laying performance

1 Introduction

In recent years, there were accelerating transformation and upgrading of the laying hens industry towards standardization large system in China. Due to the influence of limited land resources, rising labor costs, livestock waste problems, the proportion of cascading caged layers gradually increased. Related survey shows that, as of 2013, there were about 10.25% hens breeding farms using cascade cage in China, which generally used 4–8 stacked cages breeding mode with automatic feeding, automatic collection of eggs, environmental control system and also with the transfer belt to clean up manure [1, 2]. And the small and medium-sized layers farms usually adopted four cascading cage feeding mode at present. Because of the increasing breeding density, the environment

control scientifically was the key point of the cascading cage layer facilities management [3, 4]. In this experiment, the important environment parameters were monitored in a renovated hen house with four stacked cages in winter, and analyzed the environmental quality and its impact on the laying rate and egg quality, in order to provide scientifically references for hen house environment quality control and the facility upgrade.

2 Materials and Methods

2.1 The Hen House Structure and Building Parameters

The experiment was carried out in a 4-tier automatic controlled laminated hen house owned by Anhui Jinan poultry Co. Ltd in Anqing city, with 87.4 m length, 10.4 m width, and 5.0 m height, which had three columns and four aisles with 1.45 m width each aisle. The hen house wall is 24 brick wall, and the roof was made of 15.0 cm color steel structure.

Wet curtains were installed in henhouse clean end and both two sides wall. Each wet curtain area was 81.90 m^2 and the thickness was 15 cm. Ten fans (fan power 1.10 KW and diameter 1.10 m) were located on the wall of the dirt end wall, which were divided into two layers and operated automatically by the environment controllers. There were total 30 plastic steel windows on the both two sides wall, with $1.90 \text{ m} \times 1.10 \text{ m}$ of each window area. There were 32 ventilation small windows with $1.00 \text{ m} \times 0.20 \text{ m}$ of each window area located on both two sides wall. The hen house adopted the longitudinal ventilation mode, with the plastic sheeting was used to seal the wet curtain in winter, and the fresh air entered the henhouse from the both two sides windows.

The four layers of stacked cages in henhouse were produced by Guangzhou Huanan Poultry Equipment Co. Ltd, with $600 \times 450 \text{ m} \times 400 \text{ mm}$ each single cage size, which could accommodate 6 laying hens. LED lights (220 V/5 W, color temperature 2400 k–2800 k) were located in the middle of the each aisle, according to the install way of alternating high and low. And the distance between each lamp was 2 m.

2.2 The Intelligent Environmental Monitoring Device

ARM 32-bit Cortex-M3 STM32F103VB as the core processor for the intelligent environmental monitoring device. The sensors of air temperature, relative humidity, CO_2 concentration, light intensity (CG-02, Hefei Henford Electronic Technology Co. Ltd. The measurement range of air temperature: $-40 \text{ }^\circ\text{C}$ – $+85 \text{ }^\circ\text{C}$, with the measurement accuracy: $\pm 0.3 \text{ }^\circ\text{C}$. The measurement range of relative humidity: 5%–95%, with measurement accuracy: $\pm 2\%$. The measurement range of light intensity: 0–100 lx, with measurement accuracy: $\pm 1 \text{ lx}$. The measurement range of CO_2 : 0–5000 mg/m^3 , with measurement accuracy: $\pm 50 \text{ mg}/\text{m}^3$, wind speed (HD403TS2, Italy DELTA Co. Ltd. The measurement range: 0.08–5.0 m/s, with measurement accuracy: $\pm 0.2 \text{ m/s}$) and dust concentration (DS-300, Shenzhen Blue Control Co. Ltd. The measurement range: 0–50 mg/m^3 , with measurement accuracy: $\pm 0.5 \text{ mg}/\text{m}^3$) were connected to the device by RS-485 bus. All sensors have been calibrated before leaving the factories.

The device was powered by the power management module included a DC12 V 48AH cell group with the corresponding power conversion circuit, and equipped with human-machine interface module included LCD and keyboard to realize the sample data real-time displaying and the configurable sampling period setting. The environment data could store in SD card combining with SD card data storage module and the real-time clock module, and also could send data to the remote server with GPRS wireless module (Xiamen Caimore Communication Technology Co. Ltd). The server monitoring software was developed based on SQL Server 2008, ASP. Net and visual studio 2010 web platform. It realized the real-time storage of environmental parameters information, user management, safety inspection, forms and statements establishment. The user could convenient query the henhouse environment parameters in real-time through the web page or intelligent mobile APP (Fig. 1). Other egg quality measuring instruments were also used in this experiment, such as egg quality multi-function tester EMT-5200, eggshell strength tester, vernier caliper, and so on [5].

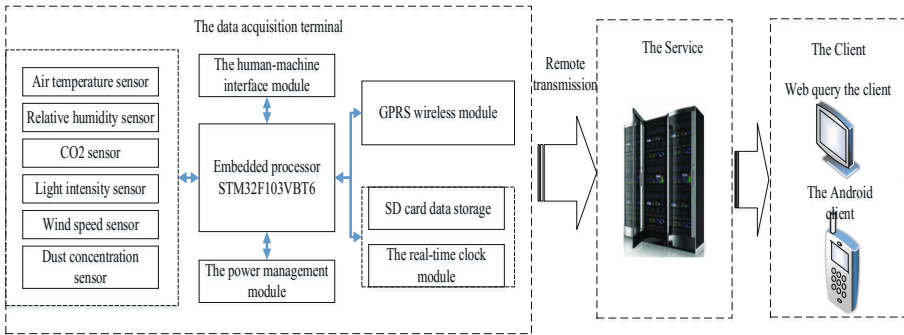


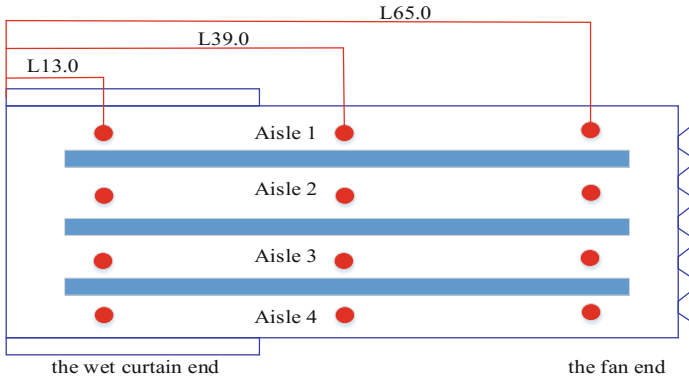
Fig. 1. The diagram of intelligent environmental monitoring device

2.3 The Design of Environmental Monitoring Experiment

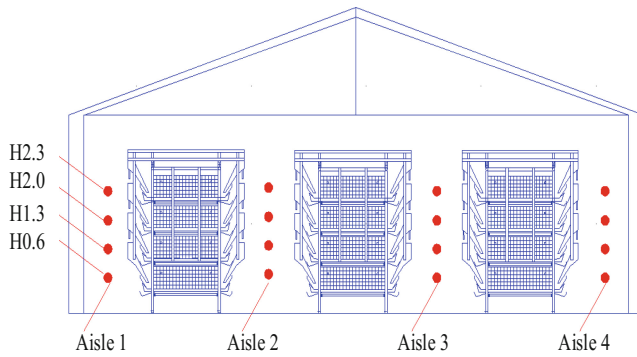
The experiment was conducted from January 1 to February 12, 2017. The temperature, relative humidity, CO₂ concentration, light intensity, wind speed and dust concentration of different points in the hen house were monitored. From the wet curtain end to the fan end, 3 points were measured which were 13.0 m, 39.0 m, 65.0 m (L13.0, L39.0, L65.0) of 4 aisles, respectively. Meanwhile, 4 points of 0.6 m, 1.3 m, 2.0 m and 2.6 m (H0.6, H1.3, H2.0 and H2.6) from the ground were measured each aisle (Fig. 2) [5, 6].

During the experiment, the number and the weight of eggs produced by 5 single cage laying hens in the measurement points were measured every day. The egg quality measured at the end of the experiment, which collected 2 eggs in single cage and 10 eggs for each measuring point. The egg quality measuring items included egg shell strength, egg shape index, haugh unit [7]. The measuring methods were carried out

according with the technical manual of livestock and poultry genetic resources formulated by the National Genetic Resources Commission [8].



(a) The diagram of longitudinal henhouse aisles sampling points



(b) The diagram of transverse henhouse aisle sampling points

Fig. 2. The diagram of henhouse aisle sampling points

2.4 Statistical Analysis

The experimental data were processed by the Microsoft office excel. The descriptive statistical parameters were calculated with by SPSS 20.0. The difference significance test was analyzed by single factor variance, and the LSD method was used in multiple comparisons. The data in the following tables mean average plus or minus standard deviation. When $P < 0.05$, there was a statistically significant difference in the confidence interval of 95%. When $P < 0.01$, there was a statistically significant difference in the 99% confidence interval [9].

3 Results and Discussion

3.1 Analysis of Environmental Quality and Laying Performance in Longitudinal Measuring Points

The environmental quality in longitudinal measuring points of hen house was shown in Table 1. It could be seen from table that the average temperature, relative humidity, wind speed, CO₂ concentration and dust concentration were 15.67 °C, 66.12%, 0.10 m/s, 2918.33 mg/m³ and 7.33 mg/m³ respectively. The average temperature and CO₂ concentration from the wet curtain end to the fan end of the hen house were gradually increasing [10]. The temperature and CO₂ concentration of determination point L13.0 m were significantly lower than that of the L 39.0 m and L 65.0 m (P < 0.05). The difference of wind speed among the longitudinal measuring points (L13.0 m, L39.0 m, and L 65.0 m) was not significant (P > 0.05). The relative humidity of L65.0 m was significantly lower than that of L13.0 m and L39.0 m (P < 0.05). The dust concentration of L13.0 m was significantly higher than that of L39.0 m and L65.0 m (P < 0.05).

Table 1. The environmental quality parameters change in longitudinal measuring points

Sampling points	Temperature (°C)	Relative humidity (%)	Wind speed (m/s)	CO ₂ concentration (mg/m ³)	Dust concentration (mg/m ³)
L _{13.0 m}	14.37 ± 2.92 ^a	65.67 ± 10.78 ^{ab}	0.10 ± 0.03 ^a	2570.17 ± 479.56 ^a	6.78 ± 3.56 ^a
L _{39.0 m}	15.65 ± 2.61 ^b	67.97 ± 10.60 ^a	0.09 ± 0.02 ^a	3013.56 ± 642.55 ^b	7.62 ± 3.07 ^a
L _{65.0 m}	16.99 ± 2.37 ^c	64.73 ± 9.97 ^b	0.11 ± 0.03 ^a	3172.58 ± 592.71 ^b	8.60 ± 3.56 ^a

Note: Different lowercase letters in the shoulder of the same column mean significantly different (P < 0.05). The same as the following tables.

The laying performance and egg quality of laying hens were shown in Table 2. Under the same feeding management conditions, the difference of the laying rate and average egg weight among the measuring points of L13.0 m, L39.0 m and L65.0 m were not significant (P > 0.05). The laying rate at the L39.0 m was higher than that of L13.0 m and L65.0 m (P > 0.05) and the average egg weight at L39.0 m was lower than that of L13.0 m and L65.0 m (P > 0.05). The difference of eggshell strength, egg shape index, haugh unit among the longitudinal points at L13.0 m, L39.0 m and L65.0 m were not significant (P > 0.05).

Table 2. The laying performance and egg quality in longitudinal measuring points

Sampling points	Laying rate (%)	Average egg weight (g)	Egg shape index	Shell strength (kg/cm ²)	Haugh unit
L _{13.0 m}	85.14 ± 16.06 ^a	59.04 ± 5.44 ^a	1.28 ± 0.04 ^a	4.67 ± 0.80 ^a	92.31 ± 3.63 ^a
L _{39.0 m}	86.20 ± 12.21 ^a	58.73 ± 2.29 ^a	1.28 ± 0.03 ^a	4.67 ± 0.76 ^a	91.85 ± 3.60 ^a
L _{65.0 m}	84.23 ± 12.69 ^a	58.94 ± 2.61 ^a	1.28 ± 0.04 ^a	4.60 ± 0.71 ^a	92.56 ± 3.40 ^a

3.2 Analysis of Environmental Quality and Laying Performance in Transverse Measuring Points

The environmental quality and laying performance in transverse measurement points were shown in Table 3. With the increase height of cage layers, the temperature and CO₂ concentration increasing gradually. The temperature in the measurement points at H0.6 m and H1.3 m were significantly lower than that of H2.0 m and H2.7 m ($P < 0.05$). The temperature in H0.6 m was the lowest, which was lower than the temperature of the measured point H2.7 m 3.14 °C. The relative humidity at H0.6 m and H1.3 m were significantly higher than that of H2.0 m and H2.7 m ($P < 0.05$).

The average light intensity was 52.25 lx and the light intensity at H0.6 m and H1.3 m were significantly higher than that of H2.0 m and H2.7 m ($P < 0.05$). Due to the experimental henhouse was reform from the old chicken coop and the plastic windows were installed on both sides wall, it led to the light intensity in the hen house was relatively too high to meet the requirement of national environmental quality standard of livestock and poultry farm (NY/T 388-1999) (30 lx) [11]. The CO₂ concentration in different measuring points were higher than 1500 mg/m³ of the requirement of national environmental quality standard of livestock and poultry farm. The CO₂ concentration at the highest measuring point on the cage H2.7 m was up to 3722.97 mg/m³, which was significantly higher than other measuring points ($P < 0.05$). The dust concentration at H2.7 m was significantly lower than that of other measurement points ($P < 0.05$) [12].

Table 3. The environmental quality parameters change in transverse measuring points

Sampling points	Temperature (°C)	Relative humidity (%)	Wind speed (m/s)	Light intensity (lx)	CO ₂ concentration (mg/m ³)
H _{0.6 m}	14.36 ± 2.47 ^a	67.29 ± 10.04 ^a	0.16 ± 0.19 ^a	57.65 ± 8.48 ^a	1991.65 ± 689.25 ^a
H _{1.3 m}	14.83 ± 2.26 ^a	69.18 ± 9.26 ^a	0.06 ± 0.11 ^b	64.25 ± 7.06 ^a	2476.45 ± 723.67 ^b
H _{2.0 m}	16.87 ± 2.87 ^b	62.67 ± 11.36 ^b	0.09 ± 0.09 ^b	45.57 ± 9.72 ^b	3190.49 ± 690.80 ^c
H _{2.7 m}	17.50 ± 2.63 ^c	63.72 ± 10.55 ^b	0.08 ± 0.15 ^b	43.67 ± 8.41 ^b	3722.97 ± 597.65 ^d

The laying performance and egg quality of laying hens were shown in Table 4. At the different height of the cages, the laying rate at H0.6 m was the highest, significantly higher than that of other cages ($P < 0.05$). The laying rate at H2.7 m was the lowest, significantly lower than that of other cages ($P < 0.05$). In the average egg weight, the egg weight at H0.6 m was significantly higher than the average egg weight at H2.7 m ($P < 0.05$). There was no significant difference of eggshell strength, egg shape index, haugh unit among at different cages height of H0.6 m, H1.3 m, H2.0 m and H2.7 m ($P > 0.05$) [13, 14].

Table 4. Analysis of laying performance and egg quality in transverse measuring points

Sampling points	Laying rate (%)	Average egg weight (g)	Egg shape index	Shell strength (kg/cm ²)	Haugh unit
H _{0.6 m}	90.69 ± 8.50 ^a	60.00 ± 3.25 ^a	1.28 ± 0.04 ^a	4.68 ± 0.74 ^a	92.57 ± 2.84 ^a
H _{1.3 m}	84.39 ± 12.31 ^b	59.43 ± 2.29 ^{ab}	1.28 ± 0.04 ^a	4.56 ± 0.80 ^a	91.84 ± 3.33 ^a
H _{2.0 m}	85.72 ± 9.78 ^b	58.74 ± 2.68 ^b	1.27 ± 0.04 ^a	4.65 ± 0.70 ^a	92.25 ± 4.21 ^a
H _{2.7 m}	77.74 ± 20.21 ^c	56.76 ± 5.53 ^c	1.28 ± 0.04 ^a	4.67 ± 0.82 ^a	92.15 ± 3.54 ^a

3.3 Correlation Analysis of Henhouse Environmental Quality

The analysis of henhouse environmental quality was shown in Table 5. It showed that in the enclosed henhouse with four overlap tiers cages, the temperature in the winter was significantly negatively correlated with the relative humidity ($P < 0.01$), which was positively correlated with CO₂ concentration ($P < 0.01$). The relative humidity was significantly negatively correlated with CO₂ concentration and wind speed ($P < 0.01$). The concentration of CO₂ was significantly negatively correlated with wind speed ($P < 0.01$) [15].

Table 5. The correlation analysis of laying house environment parameters in winter

	Temperature	Relative humidity	CO ₂ concentration	Wind speed	Dust concentration
Temperature					
Relative humidity	-0.473 ^{**}				
CO ₂ concentration	0.508 ^{**}	-0.202 ^{**}			
Wind speed	-0.056	-0.324 ^{**}	-0.195 ^{**}		
Dust concentration	0.128	-0.011	-0.019	-0.123	

Note: ** means extremely significantly different ($P < 0.01$).

4 Conclusions

In conclusion, the environment parameters such as temperature, relative humidity, light intensity, CO₂ concentration, wind speed, dust concentration at the different measuring points were different. The average temperature and CO₂ concentration from the wet curtain end to the fan end of the henhouse were gradually increasing. The result shows the consistency of environmental parameters in different positions of chicken coop is poor and the environment control system needs to be improved. Because the light intensity in the henhouse was relatively too high, the henhouse windows should be upgraded to reduce the light intensity to a reasonable range, which can meet the requirement of national environmental quality standard of livestock and poultry farm.

Additionally, according to the measurement experiment of egg quality in henhouse different positions, it can be seen that different environmental quality will affect the performance of laying hens. In order to provide a good environment for the laying hens, it is necessary to coordinate the contradiction between ventilation and heat preservation. And under the premise of keeping the temperature suitable, the ventilation rate should be increased.

Acknowledgments. The authors thank the financial support by National Key Research and Development Program (2016YFD0800901-03); National Key Technology Research and Development Program of the Ministry of Science and Technology of China (2014BAD08B11); Program 863 (SS2013AA102302). And thank Anhui Jinan poultry Co. Ltd for providing experimental conditions.

References

1. Kuang, W., Liu, H., Yao, Y., Xi, Z.: The monitoring and analysis of cascade cage laying house environmental quality and laying performance. *China Poult.* **39**(01), 64–65 (2017)
2. Shen, L., Niu, J., Liu, W., Yang, W., Li, H.: Study on distribution characteristics of environmental quality parameters in broiler house with three-overlap cages. *China Poult.* **38** (18), 37–41 (2016)
3. Troubleyn, E., Moerman, I., Demeester, P.: QoS challenges in wireless sensor networked robotic. *Wirel. Pers. Commun.* **70**(3), 1059–1075 (2013)
4. Sharma, V., Kumar, R.: A cooperative network framework for multi-UAV guided ground Ad Hoc networks. *J. Intell. Robot. Syst.* **77**(3/4), 629–652 (2015)
5. Li, H., et al.: Intelligent monitoring system for laminated henhouse based on Internet of Things. *Trans. Chin. Soc. Agric. Eng.* **31**(Supp. 2), 210–215 (2015)
6. Li, L., Huang, R., Huo, L., Li, J., Chen, H.: Design and experiment on monitoring device for layers individual production performance parameters. *Trans. Chin. Soc. Agric. Eng.* **28**(4), 160–164 (2012)
7. Mirzaee-Ghaleh, E., Omid, M., Keyhani, A., Dalvand, M.J.: Comparison of fuzzy and on/off controllers for winter season indoor climate management in a model poultry house. *Comput. Electron. Agric.* **110**, 18–195 (2015)
8. Chen, W.S.: *Technical Manual of Farm Animal Genetic Resource Survey*. China Agriculture Press, Beijing (2005)
9. Wu, J., Zhan, K., Li, J., Liu, W., Chen, G., Zhu, Y.: Effects of different cage temperature on performance, egg quality and serum indexes of laying hens in summer. *Anim. Husb. Vet. Med.* **44**(8), 34–37 (2012)
10. Lobeck, K.M., Endres, M.I., Janni, K.A., Fetrow, J.: Environmental characteristics and bacterial counts in bedding and milk bulk tank of low profile cross-ventilated, naturally ventilated, and compost bedded pack dairy barns. *Appl. Eng. Agric.* **28**(1), 117–128 (2012)
11. Quality Standards Office of Ministry of Agriculture of the People's Republic of China: NY/T388 -1999. National environmental quality standard of livestock and poultry farm. China Agriculture Press, Beijing (2008)
12. Wang, Y., Shi, H., Wang, Y., Li, B.: Effect of air inlets situation on microenvironment of layer house in winter. *China Poult.* **38**(16), 38–42 (2016)

13. Xin, H., Gates, R.S., Green, A.R., Mitloehner, F.M., Moore, P.A., Wathes, C.M.: Environmental impacts and sustainability of egg production systems. *Poult. Sci.* **90**(1), 263–277 (2011)
14. Xi, L., Wang, Y., Chang, J., Li, P.: Effect of housing range model with perches on production performance, egg quality and immune function of layer hens. *China Ani. Sci. Vet. Med.* **41**(115), 24–28 (2014)
15. Zhao, Y., Shepherd, T.A., Li, H., Xin, H.: Environmental assessment of three egg production systems—part i: monitoring system and indoor air quality. *Poult. Sci.* **94**(3), 518–533 (2015)



Research and Realization of Winter Wheat Yield Estimation Model Based on NDVI Index

Zhichao Wu^{1,2,3,4}, Changchun Li^{1(✉)}, Haikuan Feng^{2,3,4(✉)},
Bo Xu^{2,3,4}, Guijun Yang^{2,3,4}, Zhenhai Li^{2,3,4}, Haojie Pei^{1,2,3,4},
and Mingxing Liu^{1,2,3,4}

¹ School of Surveying and Land Information Engineering,
Henan Polytechnic University, Jiaozuo 454000, China
WZC032018@163.com, xmljphj@163.com,

lichangchun610@126.com, liumingxingreal@126.com

² National Engineering Research Center for Information Technology in
Agriculture, Beijing 100097, China
fenghaikuan123@163.com, guijun.yang@163.com,
lizh323@126.com

³ Key Laboratory for Information Technologies in Agriculture,
The Ministry of Agriculture, Beijing 100097, China

⁴ Beijing Engineering Research Center of Agricultural Internet of Things,
Beijing 100097, China

Abstract. The timely and accurate prediction of crop yield is of great significance to the formulation of national grain policy, the macro control of prices and the development of rural economy. In this paper, the NDVI values were calculated by using the measured spectral reflectance data of Winter Wheat during the whole growth period in 2014, combining with actual measured output, constructing a function model of NDVI index and measured output. The study concluded that the coefficient of determination (R^2) of the NDVI index and the measured yield model in the whole growth period was 0.78, the root mean square error is 40.795 (kg/mu), Standard root mean square error is 10.79%. The value of root mean square error of verification model is 49.297 (kg/mu), the value of standard root mean square error is 13.04%. Therefore, the estimation model obtained in this experiment has good reliability, It is feasible that the portable instrument for measuring the parameters of crop growth potential by using the estimation model.

Keywords: Total growth period · Winter wheat · Reflectance
NDVI · Measured yield

1 Introduction

Since the 1970s, remote sensing technology has been used in large area crop yield prediction. Precision agriculture has become an important modern agricultural production mode to improve the utilization rate of agricultural resources, reduce the cost of agricultural production and improve the agricultural ecological environment [1]. As an important grain crop in China, the safe production of wheat is an important guarantee

for the sustainable development of our country. Quickly and timely understanding of the distribution of wheat, generalization, growth status and yield dynamics, to facilitate government decision-makers and producers to take various regulatory measures to achieve the purpose of increasing production, income and efficiency [2]. Estimation of crop yield has gone through the sampling survey, statistical analysis, statistical model and meteorological satellite remote sensing data estimation stage [3]. China's yield estimation by remote sensing are summarized as follows: Spectral information - index - growth information - yield, spectrum - moisture and nitrogen - yield, spectral information - index - growth information - growth model - yield [4]. Many experts and scholars have studied the NDVI index based on the spectral reflectance of different crops, He et al. [5] research shows that the growth trend in the 3–5 month NDVI index, but the amplification of index was smaller, the production precision is highest in the May NDVI index; others believe that the current work of remote sensing is mainly by using single fertility period or some fertility period of spectral vegetation index and yield for regression analysis to estimate yield, such as NDVI index in China [6–9].

In this study, ASD spectroscopy was used to obtain reflectance data of crops during the whole growth period, calculate NDVI index and yield inversion. The reliability of the instrument is verified indirectly. At the same time, it lays a foundation for large-scale production forecasting.

2 Materials and Methods

2.1 Overview of the Study Area

The experimental area is located in Changping District, Beijing National Precision Agriculture Research and Demonstration Base, located at latitude $40^{\circ} 11'$, longitude $116^{\circ} 27'$, altitude 36 m, the base of fertile land, flat terrain, soil type for the soil base,

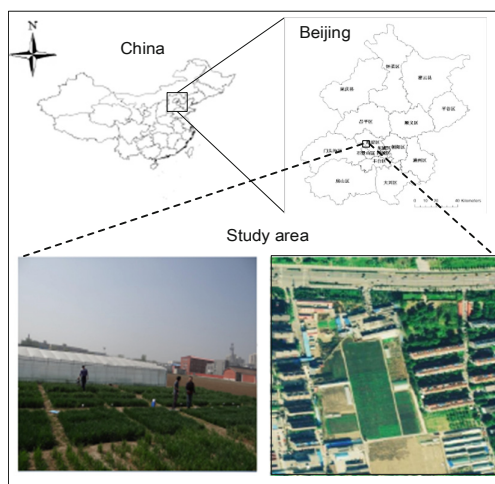


Fig. 1. National precision agriculture research and demonstration base

covers an area of about 2500 acres, climate type is a typical warm temperate semi-humid continental monsoon climate, the winter wheat crop is the base in late September early October planted (Fig. 1).

2.2 Research Design

There are two varieties of wheat used in this experiment, A and B, respectively, cross planting. There were 16 plots in the test field, and each plot was divided into three sub-districts for three replicates, each with an area of 48 m² (6 m × 8 m) and a line spacing of 15 cm. The experimental field also conducted nitrogen treatment (N1, N2, N3, N4) and water treatment (excessive, normal and rainfed). This experiment is to obtain the reflectance of crops, and the function of dealing with the corresponding NDVI index, the final function model using the measured output and the NDVI index to establish the estimation. Therefore, we should try to reduce the impact of irrelevant factors, so that the experiment from the normal water area selected experimental plots, such as the block 3, 6, 7, 10, 11, 15 six plots. Among them, using the data of the three plots 3, 6, 10 and 11 to establish the function model of different band length and reflectance. The experimental data of 12 cells were selected from 18 experimental communities to establish the functional model of the corresponding NDVI index in the measured area. The experimental data of the other six communities were used to validate the model (Fig. 2).

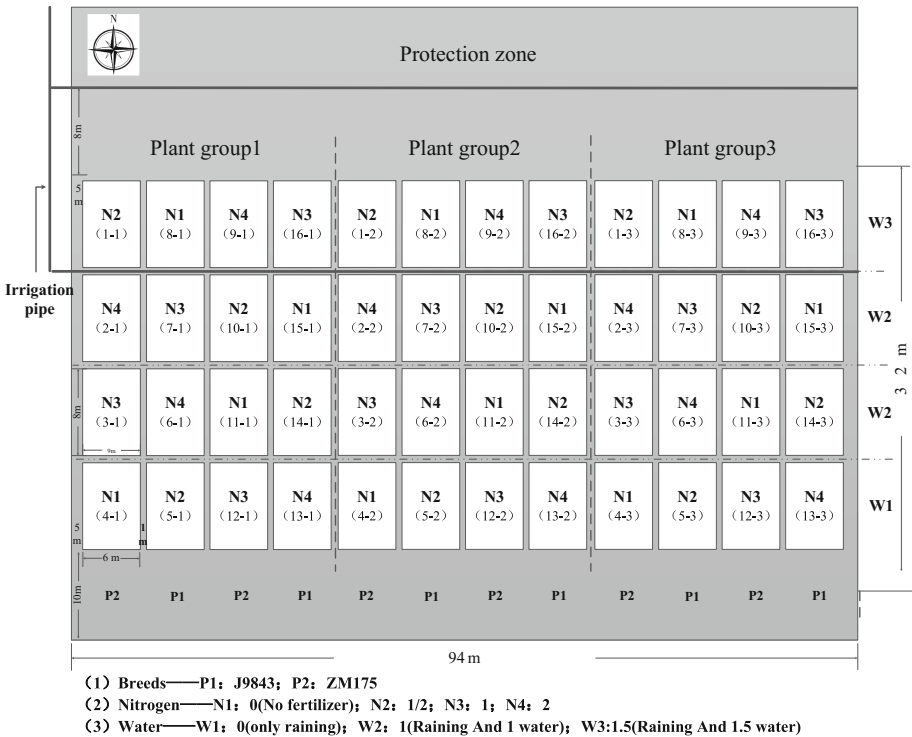


Fig. 2. Sketch map of experimental plots

2.3 Instrument Introduction

The following is a portable instrument for measuring crop growth parameters (Before using the instrument, the integrating sphere is used to perform spectral calibration on the instrument to ensure that the instrument can be used normally, and the basic parameters of the instrument are as follows). The instrument has two channels. By searching the relevant research status at home and abroad, the final choice is 650 nm and 810 nm as the channel wavelength of the instrument. The experiment date is from March 28 to May 17; the test time is 6:30 to 18:30, every half an hour to conduct a test. Before the experiment, the equipment should be set up and checked first, the instrument's sensor is facing the sun and level, and the sensor probe is 0.5 m from the canopy of the rice. Each collection area needs to collect 5 points of data, take the average as the spectral reflection of the sample point (Fig. 3, Table 1).



Fig. 3. Instrument for measuring crop growth parameters

Table 1. Hand-held portable crop growth parameters speedometer parameters

Parameter	Parameter value	Parameter	Parameter value
Operating wavelength RED	P = 650 nm ± 2 nm, FWHM 10 nm	Operating Wavelength NIR	p = 810 nm ± 2 nm, FWHM 10 nm
Relative indication error	8%	Non-linear error	1%
Up sensor	180°	Down sensor	36°

2.4 Determination Method

2.4.1 Spectral Data

The winter wheat canopy spectra were measured using a FieldSpec Pro FR2500 back-hanging field hyperspectral radiometer manufactured by American Analytical Spectral Device (ASD), the band value is 350–2500 nm. The canopy spectra were measured from 6 a.m. to 16 p.m., with clear weather, no wind or very small wind speed. When it was measured, the sensor probe is vertical downward, the vertical height is about 1 m from the top of the canopy, and 10 sampling spectra are recorded at each observation point, and the average value is taken as the reflection value of the observation point. In the process of measurement, the standard white board correction should be carried out before and after the observation of each group of targets (the standard white board reflectivity is 1, so the target spectrum is dimensionless relative reflectivity).

2.4.2 Normalized Difference Vegetation Index

NDVI: Refers to the increase in the near infrared range of green leaves scattering and red band range of chlorophyll absorption differences, generally used to detect vegetation growth status, vegetation coverage and eliminate partial radiation errors. In terms of the normalized difference vegetation index, the sensitivity will decrease when the LAI value is very high (LAI is the leaf area index), that is, when the vegetation is luxuriant. Calculation formula:

$$\text{NDVI} = \frac{\rho_{\text{NIR}} - \rho_{\text{RED}}}{\rho_{\text{NIR}} + \rho_{\text{RED}}} = \frac{\text{NIR} - R}{\text{NIR} + R} \quad (1)$$

The range of NDVI value is $-1 \sim 1$, a negative value indicates that the ground cover for cloud, water, snow, high reflection of visible light; 0 said that the rocks or bare soil, NIR and R are approximately equal; positive, said there is vegetation cover and increases with increasing coverage; $0.2 \sim 0.8$ is the general scope of green vegetation area [10].

2.4.3 Yield

This experiment was carried out on the basis of the experimental data (yield, asd) in 2014. The maximum measured output is 549.42 (kg/mu), the minimum is 223.03 (kg/mu), and the average value is 378.05 (kg/mu). Then, the NDVI index and the measured output are used to establish the model, and the NDVI index is tested to calculate the predicted output, and the corresponding RMSE and NRMSE are calculated.

2.5 Model Accuracy Evaluation

2.5.1 Validation Techniques

In this paper, we use 2/3 of the experimental data to establish the model, another third of the experimental data were validation for the model just created. In this paper, a total of 6 plots and 18 plots were selected for the experiment. The experimental data of 12 plots were randomly selected to establish the function model. The experimental data of 6 other plots were used to validate the model.

2.5.2 Coefficient of Determination

The coefficient of determination (coefficient of - determination, R) was used as the evaluation of the relationship between remote sensing estimation of biomass and biomass measurement standard. Calculation formula:

$$R^2 = \frac{(\sum xy - \frac{\sum x \sum y}{n})^2}{(\sum x^2 - \frac{(\sum x)^2}{n})(\sum y^2 - \frac{(\sum y)^2}{n})} \quad (2)$$

x, y stands for sample value, n stands for sample number; n stands for the number of samples. The higher the R^2 , the better the correlation between the variables involved in the evaluation, the higher the reference value; The smaller the R^2 , the lower the correlation, the smaller the reference value [11].

2.5.3 Root Mean Square Error

Root mean square error was used as a standard for evaluating the estimated biomass and measured biomass errors.

Calculation formula:

$$RMSE = \sqrt{\frac{\sum_{i=1}^n (y_i - \hat{y}_i)^2}{n}} \quad (3)$$

$$NRMSE = RMSE/X \quad (4)$$

y_i stands for measured value, \hat{y}_i stands for analog value, n stands for the number of samples, X stands for mean of the measured value. RMSE is very sensitive to larger errors. The smaller the RMSE, the higher the accuracy of the estimation results. RMSE has increased the penalty for single data (squared penalty), which makes the evaluation even more rigorous [12].

2.6 Statistical Analysis

In this study, determination coefficient (R^2) and root-mean-square error were regarded as indicators to interpret and quantify the relationship between NDVI and vegetation index. Generally speaking, the higher R^2 , the smaller RMSE, and the better ability of the estimated model between the NDVI and vegetation index, otherwise, the estimated ability is poor.

3 Results and Analysis

3.1 The Relationship Between the Length and Reflectivity of Different Plots of Winter Wheat in Different Bands

Refer to the literature at home and abroad indicated that the relationship between the length and reflectivity of Winter Wheat in different bands is linear regression model. From the measured data, the interception wavelength is between 640–660 nm and 800–820 nm. The function models of different band length and reflectivity of each block are obtained as follows (Tables 2, 3):

Table 2. The relationship between band and reflectivity in 640–660 nm

Block number	Relationship between long pulse and reflectance	Coefficient of determination (R^2)
3	$y = -0.0001x + 0.1246$	0.9851
6	$y = -0.0002x + 0.1473$	0.9886
10	$y = -0.0001x + 0.1182$	0.9846
11	$y = -0.0002x + 0.178$	0.9818

Table 3. The relationship between band and reflectivity in 800–810 nm

Block number	Relationship between long pulse and reflectance	Coefficient of determination (R^2)
3	$y = 0.0002x + 0.2049$	0.9262
6	$y = 0.0002x + 0.2316$	0.9454
10	$y = 0.0002x + 0.1878$	0.9622
11	$y = 0.0002x + 0.1214$	0.9799

3.2 A Functional Model for Measuring NDVI Index of Yield and Whole Growth Period Was Established

This study is based on the average reflectance of different bands of crops obtained in each plot obtained in 2014. The corresponding NDVI index is obtained by formula (1), following Table 4.

The measured output and NDVI data of 12 plots were obtained and analyzed statistically, obtained the function model of measuring yield and NDVI index, as follows. The relationship between measured yield and NDVI index is $y = 45.504e^{2.6504x}$, The R^2 is 0.78 by using formula (1–2), the RMSE is 40.795(kg/mu) by using formula (1–3), the NRMSE is 10.79%. The above data show that the model has certain reliability (Fig. 4).

3.3 Verification of Function Model

Using the NDVI index of the other six communities that did not participate in the model building are respectively used in the function model obtained in the previous section. Compared with measured output, calculated the RMSE is 49.297 (kg/mu) by using formula (1–3), the NRMSE is 13.04%. The above data show that the model has certain reliability.

Table 4. NDVI index of each experimental plot

Cell ID	NDVI index	Cell ID	NDVI index
p03-1	0.86	p10-1	0.83
p03-2	0.89	p10-2	0.85
p03-3	0.78	p10-3	0.82
p06-1	0.82	p11-1	0.54
p06-2	0.85	p11-2	0.74
p06-3	0.84	p11-3	0.56
p07-1	0.84	p15-1	0.85
p07-2	0.86	p15-2	0.68
p07-3	0.84	p15-3	0.73

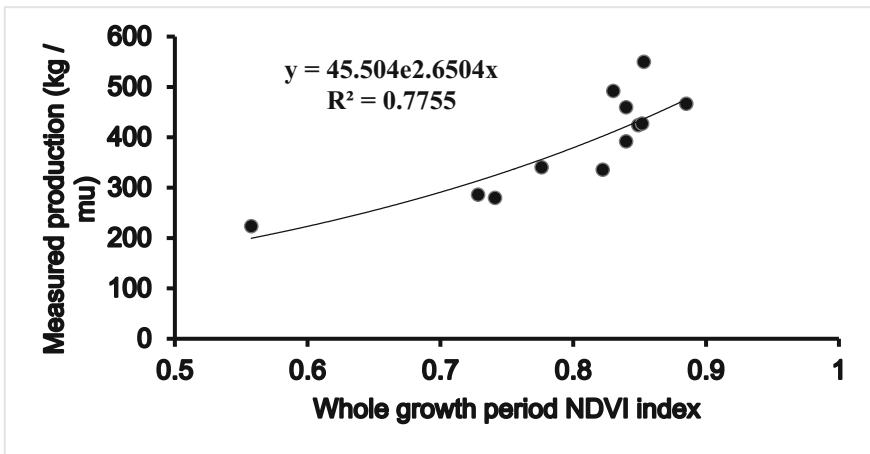


Fig. 4. NDVI index and measured yield model for full growth period

4 Conclusion

1. When the band length is 640–660 nm, the fitting model of band length and crop reflectivity is higher, and the influence of nitrogen treatment is smaller. When the band length is 800–810 nm, the fitting degree of normal nitrogen and nitrogen treatment is higher than that of semi nitrogen and nitrogen free treatment.

2. The estimation model established by using yield and NDVI index measured the decision coefficient R value is 0.78, the root mean square error of the value of RMSE is 40.795 (kg/mu), mean square error NRMSE value is 10.79%.
3. When model validation is performed, the root mean square error RMSE is 49.297 (kg/mu), and the standard root mean square error is 13.04%.

Acknowledgments. This work was supported in part by the National Natural Science Foundation of China (No. 41601346) and National Key Research and Development Programs (2016YFD0300603).

References

1. Wang, X.: Study on variable rate fertilization control of soybean in precision agriculture. Heilongjiang Bayi Agricultural University, Heilongjiang Province, Daqing City (2010)
2. Li, W.: Monitoring and forecasting of winter wheat yield classification based on TM remote sensing. In: China Remote Sensing Conference (2010)
3. Du, T.: Based on the MODIS-NDVI of Henan province winter wheat yield estimation model of. Chongqing University, Chongqing (2013)
4. Li, S., Li, M.: Yield estimation of winter wheat in early growth periods by vehicle-borne ground-based remotesensing system. *Trans. Chin. Soc. Agric. Eng.* **30**(3), 120–127 (2014)
5. He, Z., He, J.: NOAA-NDVI of Henan province winter wheat yield estimation by remote sensing. *Arid. Land Resour. Environ.* **27**(5), 46–52 (2013)
6. Maselli, F., Chiesi, M., Brilli, L., et al.: Simulation of olive fruit yield in Tuscany through the integration of remote sensing and ground data. *Ecol. Model.* **244**(1745), 1–12 (2012)
7. Dubovyk, O., Menz, G., Conrad, C., et al.: Spatio-temporal analyses of cropland degradation in the irrigated lowlands of Uzbekistan using remote-sensing and logistic regression modeling. *Environ. Monit. Assess.* **185**(6), 4775 (2013)
8. Huisman, I., Stiller, J., Fröhlich, J.: Application of remote sensors in mapping rice area and forecasting its production: a review. *Sensors* **15**(1), 769 (2015)
9. Bouvet, A., Toan, T.L.: Use of ENVISAT/ASAR wide-swath data for timely rice fields mapping in the Mekong river delta. *Remote Sens. Environ.* **115**(4), 1090–1101 (2011)
10. Deng, S., Chen, Q., Du, H., et al.: ENVI remote sensing image processing method. Higher Education Press, Beijing (2014)
11. Li, F.: Quantitative estimation of leaf nitrogen hyperspectral data and satellite image in winter wheat in Guanzhong area. Northwest Agriculture and Forestry University, Shaanxi City (2016)
12. Zhang, S., Zhang, M., Du, Y.: Study on the characteristic screening of proteomic mass spectrometry data by chemometrics. *Anal. Lab.* **31**(10), 106–109 (2012)



Study on Vegetation Classification Based on Spectral Knowledge Base

Peng Liu, Jingcheng Zhang^(✉), Bin Wang, Xuexue Zhang,
and Kaihua Wu

College of Life Information Science and Instrument Engineering,
Hangzhou Dianzi University, Hangzhou 310018, Zhejiang, China
zzwliupeng@163.com, zhangjc_rs@163.com,
wangb_rs@163.com, zhangxx_rs@163.com,
wukaihua@hdu.edu.cn

Abstract. A framework about spectral based vegetation classification was proposed, which serves as a core methodology of the vegetation spectral knowledge base. The hyperspectral reflectances of 13 types of plants were measured by an ASD FieldSpec 4 spectroradiometer. Two forms of spectral features were used for representing the key spectral characteristics of plants, including Vegetation index (VI) and spectral shape features. Based on these spectral features, a sensitivity analysis was performed to identify the most important features for establishing the classifier. The analysis of variance (ANOVA) and the cross-correlation analysis were applied to derive the sensitivity of features and remove features that have high correlations. Then, a classification method for differentiating plants was established by coupling some spectral similarity measures (e.g., ED) with some classification methods (e.g., BPANN and SVM). The results of discrimination analysis showed that a highest accuracy was produced by SVM with the OAA over 99% when using 7 sensitive VIs. The results suggested the framework about spectral based vegetation classification can form a basis for spectral knowledge base and application technology and further achieve a wide range of plant classification based on remote sensing.

Keywords: Vegetation classification · Hyperspectral · Feature extraction
Classification algorithm

1 Introduction

Recent advances in Hyperspectral provide opportunities to map plant species and vegetation at various scales and resolutions. Establish a spectral knowledge base is an effective management tool. Among them, the study of vegetation classification methods based on hyperspectral data is an important part of plant spectrum library. Over the last decade, vegetation canopy spectral reflectance has been successfully used in discriminating plant species (Schmidt and Skidmore 2003; Pu 2009; Allard et al. 2011; Peñuelas 1995a). Some detailed changes in spectral curves of hyperspectral data can be detected by spectral feature selection and extraction methods such as continuum

removal or derivative analysis. (Schmidt and Skidmore 2003; Abdel-Rahman et al. 2010). Gong et al. (1997) and Pu (2009) found that the first derivative of the tree spectrum can significantly improve the accuracy of the identification of the six species of common conifers in northern California and the 11 species of urban trees in Tampa, Florida. Prospero et al. (2014) used 47 spectral variables to classify 46 plant species in tropical wetland. A series of methods were used to select and extract features. Then a set of algorithms were used to build the classification model. Pu (2011) utilized a stepwise masking system to process the high-resolution IKONOS images and to identify and map urban forest tree species/groups. Bue et al. (2015) proposed a method of combining Multiple Endmember Spectral Mixture Analysis (MESMA) and Multi-class Discriminant Analysis (MDA) for classifying spectrally-similar species. In a case study for mapping urban trees, Pu and Landry (2012) found that the WV2 imagery produced a higher accuracy than the IKONOS imagery according to an independent validation. Zeng et al. (2017) chooses the wetland of Poyang Lake as the study area, and with the help of ASD FieldSpec4, it gets the reflecting curve of six advantage kinds of vegetation. Based on the pretreatment of original spectral data, this research uses a series of methods to analyze and compare the spectral curve, including derivative, Log (1/R), continuum removing and so on. Then, it uses the characteristic parameters of spectral to classify and extract the plant. Yu et al. (2017) used spectral derivative method and vegetation index method to construct spectral features. The artificial neural network method and factor analysis method were used to classify and extract typical vegetation.

The spectral based vegetation classification is one of the core technologies for establishing plant spectrum library. Based on hyperspectral measurements of a number of plant species, this paper focuses on the extraction and selection of spectral features for vegetation classification. Besides, combining with some pattern recognition algorithms, a framework for spectral based vegetation classification was established and evaluated.

2 Materials and Methods

2.1 Experimental Design and Data Acquisition

In this study, plant hyperspectral measurements were made in May 2017 in Hangzhou (Lon 120.34°, Lat 30.31°), where consisting a variety of plants. The plant canopy spectrometer was measured using an ASD Fieldspec FR2500 spectrometer with a sampling interval of 1.4 nm (350 to 1000 nm) and 2 nm (in the range of 1000 to 2500 nm). All spectral measurements are made in windless weather within 10:00 ~ 14:00. The sensor was placed at 60 cm above the plants' canopy. The spectral data is calibrated against a white reference panel to convert from the radiance signal to spectral reflectance. A total of 20 recordings were made and were then averaged to get one canopy spectrum. Per plant, 10-25 measurements were made in the field of view, and 13 species of plant hyperspectral data (n = 324) was Measured, including *Loropetalum chinense var. rubrum*, *Platyclusus orientalis (L.) Franco*, *Ilex crenata* Thunb., *Sedum sarmentosum* Bunge, *Rhododendron simsii* Planch., *Nelumbo nucifera* Gaertn.,

Pyracantha fortuneana (Maxim.) Li, *Buxus megistophylla*, *Ligustrum vicaryi*, *Paspalum thunbergii* Kunth ex Steud., *Mahonia fortune* (Lindl.) Fedde, *Photinia serrulata* Lindl. and *Buxus sinica* (Rehd. et Wils.) Cheng (Fig. 1).

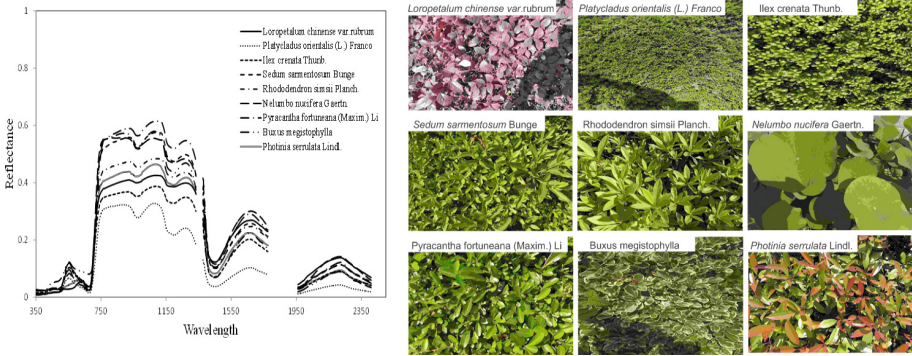


Fig. 1. Example of hyperspectral curves of different plants and their canopy pictures

2.2 Features Extraction

Vegetation Indices. In this paper, 13 classic vegetation indices (VIs) are purposely selected for plants classification (Table 1). Some of the VIs are sensitive to pigments variation, some of the VIs are sensitive to variation of leaf area or biomass, while some others are sensitive to the plants’ water contents. The different mechanisms of these VIs are important for indicating the spectral difference among plants. Besides, a sensitivity analysis by the analysis of variance (ANOVA) was performed to identify the most important VIs for establishing the classification model. In addition, a cross-correlation analysis were applied to eliminate features with relatively high information redundancy.

Table 1. The 13 vegetation indices extracted from hyperspectral data

Spectral index	Definition	Reference
EVI , Enhanced VI	$2.5(R_{NIR} - R_{red}) / (R_{NIR} + 6R_{red} - 7.5R_{blue} + 1)$	Huete et al. 2002
LAIDI , LAI Determining Index	R_{1250} / R_{1050}	Delalieux et al. 2008
NDVI , Normalized Difference Vegetation Index	$(R_{NIR} - R_{red}) / (R_{NIR} + R_{red})$	Rouse et al. 1973
NRI , Normalized Ratio Index	$(R_{874} - R_{1225}) / (R_{874} + R_{1225})$	Koppe et al. 2010
sLAIDI , Normalization or Standard of the LAIDI	$S(R_{1050} - R_{1250}) / (R_{1050} + R_{1250})$, where $S = 5$	Delalieux et al. 2008

(continued)

Table 1. (continued)

Spectral index	Definition	Reference
ACI , Anthocyanin Content Index	$R_{\text{green}}/R_{\text{NIR}}$	Van den Berg and Perkins2005
NPQI , Normalized Phaeophytinization Index	$(R_{415} - R_{435})/(R_{415} + R_{435})$	Barnes et al. 1992; Peñuelas et al. 1995b
PRI , Photochemical/Physiological Reflectance Index	$(R_{531} - R_{570})/(R_{531} + R_{570})$	Gamon et al. 1992
DSWI , Disease Water Stress Index	$(R_{802} + R_{547})/(R_{1657} + R_{682})$	Galvão et al. 2005
RVI_{hyp} , Hyperspectral Ratio VI	R_{1088}/R_{1148}	Schlerf et al. 2005
SIWSI , Shortwave Infrared Water Stress Index	$(R_{860} - R_{1640})/(R_{860} + R_{1640})$	Fensholt and Sandholt 2003
WI , Water Index	R_{900}/R_{970}	Peñuelas et al. 1997
RVSI , Red-Edge Vegetation Stress Index	$[(R_{712} + R_{752})/2] - R_{732}$	Merton and Huntington 1999

Spectral Shape Feature. Besides the VIs, some spectral shape feature including the first-order derivative features and continuum removal (CRM) features are also included. The derivative spectrum is the normalized spectral difference of two adjacent narrow-bands with their wavelength interval. Spectral derivative analysis can partially eliminate the effects of atmospheric effects, vegetation and environmental background (shadow, soil, etc.) which thus emphasize some essential characteristics of the plant (Demetriades-Shah et al. 1990; Tsai and Philpot 1998). The first derivative spectra can be calculated by:

$$\rho'(\lambda_i) \approx [\rho(\lambda_{i+1}) - \rho(\lambda_{i-1})]/\Delta\lambda \quad (1)$$

where, $\rho'(\lambda_i)$ is the first derivative.; $\rho(\lambda_i)$ is the reflectance at a wavelength (band) i ; $\Delta\lambda$ is the wavelength interval between λ_{i+1} and λ_{i-1} and equals twice bandwidth for this case. The continuum removal technique provided a quantitative measure of absorption features in plants' spectra (Fig. 2). Thereby, a total of 12 spectral shape features, including 9 first order differential features of red edge, blue edge and yellow edge, and the depth, width and area of CRM in bands range from 530 nm to 770 nm were extracted from the original spectra (Table 2).

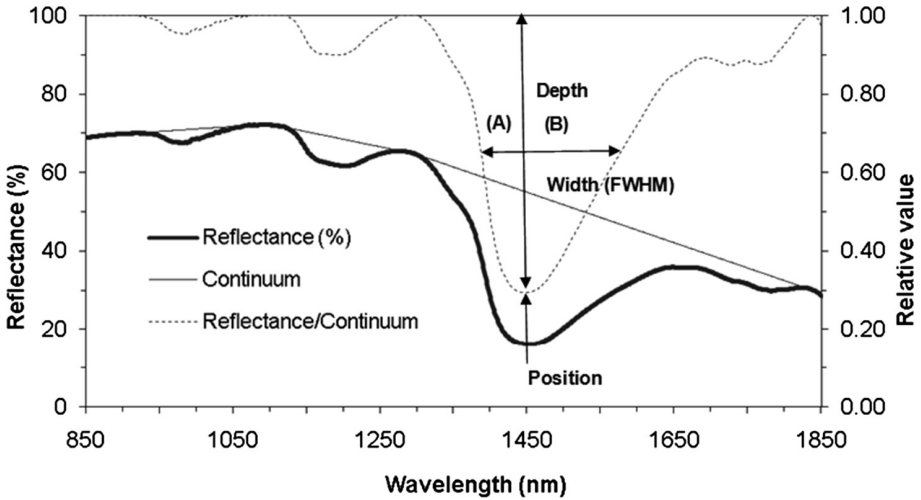


Fig. 2. Illustrated of CRM

Table 2. 12 spectral shape features

	Position	Band range (nm)	Features
First order differential features	Blue edge	490–540	Maximum differential value (BMV)
			Position of the maximum differential value (BPMV)
			Sum of differential values (BSV)
	Yellow edge	540–620	Maximum differential value (YMV)
			Position of the maximum differential value (YPMV)
			Sum of differential values (YSV)
	Red edge	660–780	Maximum differential value (RMV)
			Position of the maximum differential value (RPMV)
			Sum of differential values (RSV)
CRM features	NIR	530–770	Depth
			Width
			Area

2.3 Classification Algorithm

To achieve the spectral classification among different plants, three classification algorithms are tested, including Euclidian distance (ED), Support vector machines (SVM) and Artificial neural network (ANN). The Euclidian distance (ED) provides a measure of distance between two pixels or between a reference spectrum and a test spectrum in the L -dimensional feature space:

$$ED(\rho_t, \rho_r) = \left[\sum_{i=1}^L (\rho_{ti} - \rho_{ri})^2 \right]^{\frac{1}{2}} \tag{2}$$

Where, $\rho_r = [\rho_{r1}, \rho_{r2}, \dots, \rho_{rL}]^T$ and $\rho_t = [\rho_{t1}, \rho_{t2}, \dots, \rho_{tL}]^T$ are assumed as the reference spectrum (a laboratory or pixel spectrum known to characterize a target of interest) and the test spectrum, respectively. L represents the spectral dimensionality and equals to the number of bands of hyperspectral data (Kong et al. 2010). The SVM is a new type of classifiers that can efficiently overcome the Hughes phenomenon by directly seeking a separating surface (hyperplane) through an optimization procedure. The ANN has been proven that it works well even with small training sample size. The general principal of the ANN is demonstrated in Fig. 3.

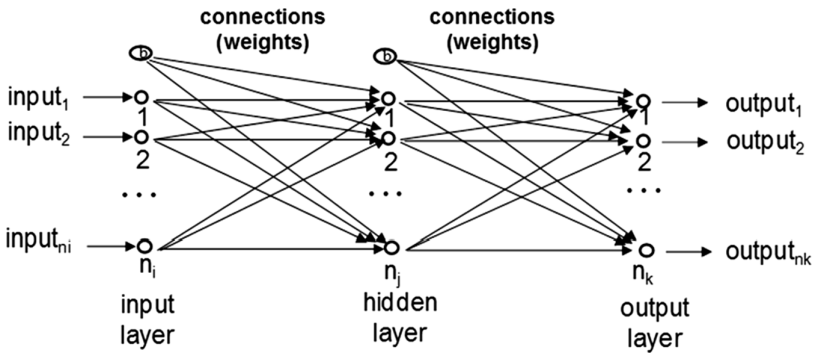


Fig. 3. Neural network structure

Based on the two types of spectral features, the plants classification models were established according to ED, SVM and ANN, respectively. The models were trained with 60% of the data ($n = 195$), whereas were validated against the left 40% of the data ($n = 129$). The accuracies of the classification are evaluated according to the overall accuracy (OAA) and kappa coefficient (Congalton and Mead 1983; Story and Congalton 1986). A flowchart of the entire analysis is demonstrated in Fig. 4.

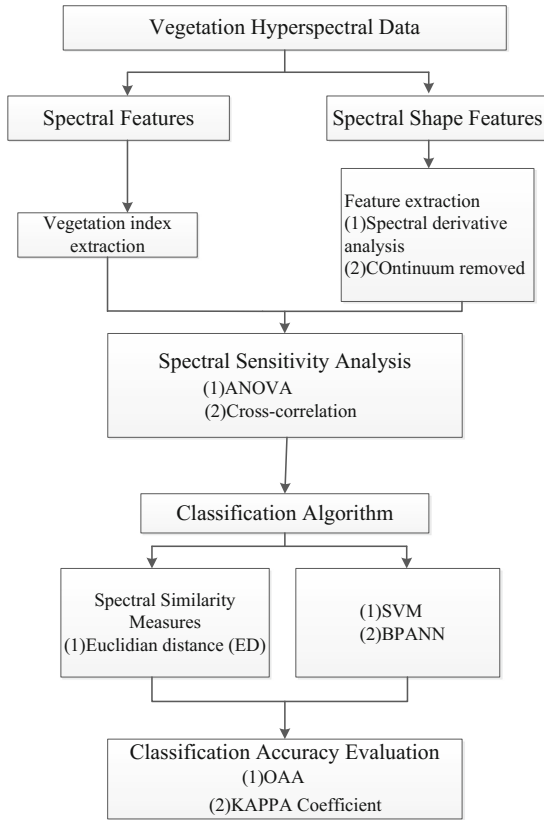


Fig. 4. Experimental flow graph

3 Results

3.1 Classification with VIs

According to the sensitivity analysis, a total of 13 VIs passed the ANOVA with p-value <0.01. Then, after the cross correlation check, 7 VIs were retained, including GI, NRI, ACI, RVSI, NDVI, NPQI, and TVI. The means of the 7 VIs were compared among all types of plants as shown in Fig. 5. The classification accuracies of ED, SVM and ANN were shown in Table 3.

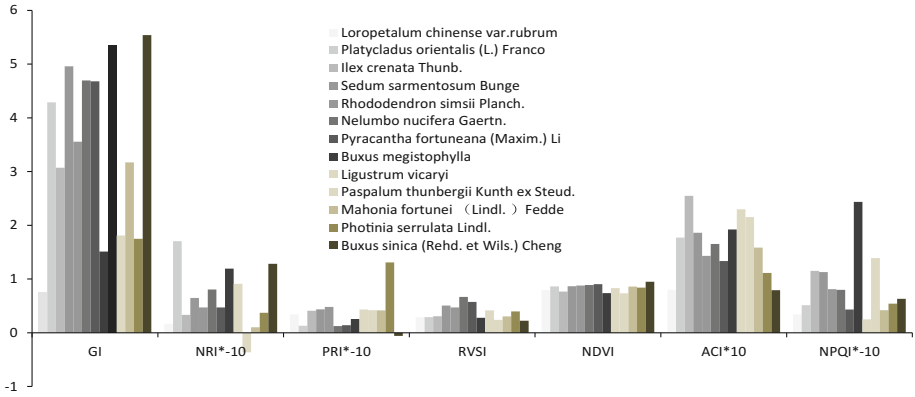


Fig. 5. Illustrates statistics of VIs

Table 3. Confusion matrix created using VIs

	OAA	KAPPA
ED	0.92	0.91
SVM	0.99	0.99
BPANN	0.84	0.82

3.2 Classification with Spectral Shape Features

According to the sensitivity analysis, a total of 12 spectral shape features passed the ANOVA with p-value <0.01. Then, after the cross correlation check, 7 spectral shape features were retained, including BMV, BPMV, YPMV, YPMV, RMV, Depth and Width. The means of the spectral shape features were compared among all types of plants as shown in Fig. 6. The classification accuracies of ED, SVM and ANN were shown in Table 4.

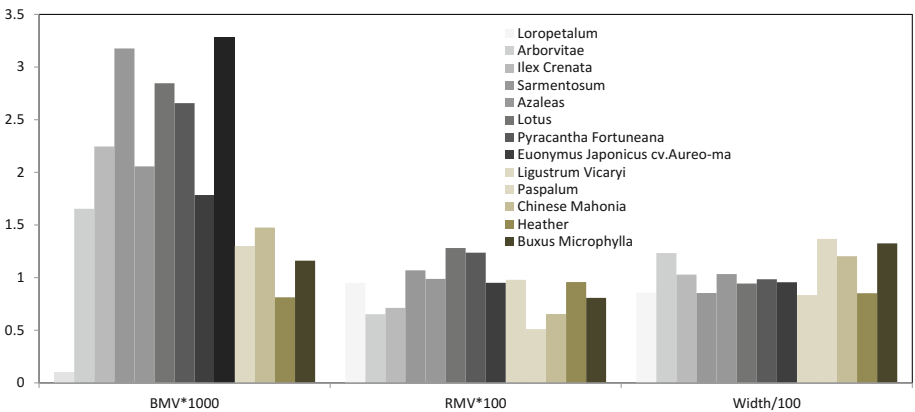


Fig. 6. Illustrates some statistics of spectral shape features

Table 4. Confusion matrix created using spectral shape features

	OAA	KAPPA
ED	0.54	0.50
SVM	0.50	0.46
BPANN	0.17	0.09

4 Discussions

In this comprehensive study by using hyperspectral data for classifying 13 plant species, it is encouraging that a satisfactory accuracy can be achieved by this spectral classification. Based on the sensitive VIs, the OAA that was produced by all three classification algorithms were over 84%. However, the OAA of the classification models that were based on spectral shape feature were all below 55%, which is not acceptable for application. Comparing with spectral shape features, the significant difference of VIs among plants may account for its higher classification accuracy (Figs. 5 and 6). Among the three classification algorithms, the highest accuracy was produced by SVM with the OAA over 99% whereas the lowest accuracy was produced by ANN. The classification ability based on spectral shape features is weak, and the selection and extraction of more sensitive features are to be further explored.

5 Concluding Remarks

In this study, hyperspectral data was used to classify plant species. (1) A total of 7 VIs and 7 spectral shape features were identified as most suitable for plants classification in our case. (2) Based on VIs and SVM algorithm, the highest classification accuracy can be achieved with OAA = 0.99. The results suggested the great potential of hyperspectral data in plants classification. The framework about spectral based vegetation classification can form a basis for spectral knowledge base and application technology and further achieve a wide range of plant classification based on remote sensing.

Acknowledgements. This work was supported by Zhejiang public welfare programme of agriculture technology (2016C32087), National Natural Science Foundation of China (41671415; 41601461) and Graduate Scientific Research Foundation of Hangzhou Dianzi University (CXJJ2017068).

References

- Schmidt, K.S., Skidmore, A.K.: Spectral discrimination of vegetation types in a coastal wetland. *Remote Sens. Environ.* **85**, 92–108 (2003)
- Pu, R.: Broadleaf species recognition with in situ hyperspectral data. *Int. J. Remote. Sensing.* **30** (11), 2759–2779 (2009)
- Allard, D., D'Or, D., Froidevaux, R.: An efficient maximum entropy approach for categorical variable prediction. *Eur. J. Soil Sci.* **62**, 381–393 (2011)

- Peñuelas, J., Baret, F., Filella, I.: Semi-empirical indices to assess carotenoids/chlorophyll, a ratio from leaf spectral reflectance. *Photosynthetica* **31**, 221–230 (1995a)
- Abdel-Rahman, E.M., Ahmed, F.B., Van den Berg, M.: Estimation of sugarcane leaf nitrogen concentration using in situ spectroscopy. *Int. J. Appl. Earth Obs. Geoinf.* **12**, S52–S57 (2010)
- Gong, P., Pu, R., Yu, B.: Conifer species recognition: An exploratory analysis of in situ hyperspectral data. *Remote Sens. Environ.* **62**, 189–200 (1997)
- Prospere, K., McLaren, K., Wilson, B.: Plant species discrimination in a tropical wetland using in situ hyperspectral data. *J. Remote Sens.* **6**(9), 8494–8523 (2014)
- Pu, R.: Mapping urban forest tree species using IKONOS imagery: preliminary results. *J. Environ. Monit. Assess.* **172**(1–4), 199–214 (2011)
- Bue, B.D., Thompson, D.R., Sellar, R.G., Podest, E.V., Eastwood, M.L., Helmlinger, M.C., et al.: Leveraging in-scene spectra for vegetation species discrimination with mesma-mda. *ISPRS J. Photogramm. Remote Sens.* **108**, 33–48 (2015)
- Pu, R., Landry, S.: A comparative analysis of high spatial resolution ikonos and worldview-2 imagery for mapping urban tree species. *Remote Sens. Environ.* **124**(9), 516–533 (2012)
- Zeng, S., Kuang, R., Xiao, Y., Zhao, Z.: Measured hyperspectral data classification of poyang lake wetland vegetation. *Remote Sens. Inf.* **32**(5), 75–81 (2017)
- Yu, J., Li, X., Zhang, Q., Shi, H., Xue, J., Chu, J.: Typical vegetation classification of Taihu lakeside based on measured hyperspectral data. *Jiangsu Agric. Sci.* **45**(5), 240–244 (2017)
- Huete, A., Didan, K., Miura, T., Rodriguez, E.P., Gao, X., Ferreira, L.G.: Overview of the radiometric and biophysical performance of the MODIS vegetation indices. *Remote Sens. Environ.* **83**, 195–213 (2002)
- Delalieux, S., Somers, B., Hereijgers, S., Verstraeten, W.W., Keulemans, W., Coppin, P.: A near-infrared narrow-waveband ratio to determine Leaf Area Index in orchards. *Remote Sens. Environ.* **112**, 3762–3772 (2008)
- Rouse, J.W., Haas, R.H., Schell, J.A., Deering, D.W.: Monitoring vegetation systems in the great plains with ERTS. In: *Proceedings Third ERTS Symposium*, vol. 1, 48–62 (1973)
- Koppe, W., Li, F., Gnyp, M.L., Miao, Y., Jia, L., Chen, X., et al.: Evaluating multispectral and hyperspectral satellite remote sensing data for estimating winter wheat growth parameters at regional scale in the north china plain. *Photogramm.-Fernerkund. – Geoinf.* **3**, 167–178 (2010)
- Berg, A.K.V.D., Perkins, T.D.: Non-destructive estimation of anthocyanin content in autumn sugar maple leaves. *Hortic. Sci.* **40**(3), 685–686 (2005)
- Barnes, J.D., Balaguer, L., Manrique, E., Elvira, S., Davison, A.W.: A reappraisal of the use of DMSO for the extraction and determination of chlorophylls a and b in lichens and higher plants. *Environ. Exp. Bot.* **32**, 85–100 (1992)
- Peñuelas, J., Filella, I., Lloret, P., Muñoz, F., Vilajeliu, M.: Reflectance assessment of mite effects on apple trees. *Int. J. Remote Sens.* **16**, 2727–2733 (1995b)
- Gamon, J.A., Penuelas, J., Field, C.B.: A narrow-waveband spectral index that tracks diurnal changes in photosynthetic efficiency. *Remote Sens. Environ.* **41**, 35–44 (1992)
- Galvão, L.S., Formaggio, A.R., Tisot, D.A.: Discrimination of sugarcane varieties in Southeastern Brazil with EO-1 hyperion data. *Remote Sens. Environ.* **94**, 523–534 (2005)
- Schlerf, M., Atzberger, C., Hill, J.: Remote sensing of forest biophysical variables using HyMap imaging spectrometer data. *Remote Sens. Environ.* **95**, 177–194 (2005)
- Fensholt, R., Sandholt, I.: Derivation of a shortwave infrared water stress index from MODIS near-and shortwave infrared data in a semiarid environment. *Remote Sens. Environ.* **87**(1), 111–121 (2003)
- Peñuelas, J., Piñol, J., Ogaya, R., Filella, I.: Estimation of plant water concentration by the reflectance water index WI (R900/R970). *Int. J. Remote Sens.* **18**, 2869–2875 (1997)

- Merton, R., Huntington, J.: Early simulation of the ARIES-1 satellite sensor for multi-temporal vegetation research derived from AVIRIS. In: Summaries of the Eight JPL Airborne Earth Science Workshop, 9–11 February, pp. 299–307. JPL Publication 99-17, Pasadena (1999)
- Demetriades-Shah, T.H., Steven, M.D., Clark, J.A.: High-resolution derivative spectra in remote-sensing. *Remote Sens. Environ.* **33**(1), 55–64 (1990)
- Tsai, F., Philpot, W.: Derivative analysis of hyperspectral data. *Remote Sens. Environ.* **66**(1), 41–51 (1998)
- Kong, X., Shu, N., Huang, W., Fu, J.: The research on effectiveness of spectral similarity measures for hyperspectral image. In: IEEE 2010 3rd International Congress on Image and Signal Processing (CISP2010), pp. 2269–2273 (2010)
- Congalton, R.G., Mead, R.A.: A quantitative method to test for consistency and correctness in photointerpretation. *Photogramm. Eng. Remote. Sens.* **49**(1), 69–74 (1983)
- Story, M., Congalton, R.G.: Accuracy assessment: A user's perspective. *Photogramm. Eng. Remote. Sens.* **52**(3), 397–399 (1986)



Hyperspectral Estimation of Nitrogen Content in Winter Wheat Leaves Based on Unmanned Aerial Vehicles

Liu Mingxing^{1,2,3,4}, Li Changchun^{1(✉)}, Feng Haikuan^{2,3,4(✉)},
Pei Haojie^{1,2,3,4}, Li Zhenhai^{2,3,4}, Yang Fuqin⁵, Yang Guijun^{2,3,4},
and Xu Shouzhi⁶

¹ School of Surveying and Land Information Engineering,
Henan Polytechnic University, Jiaozuo 454000, China
liumingxingreal@126.com, lichangchun610@126.com,
xmljphj@163.com

² National Engineering Research Center for Information Technology
in Agriculture, Beijing 100097, China
fenghaikuan123@163.com, lizh323@126.com,
guijun.yang@163.com

³ Key Laboratory for Information Technologies in Agriculture,
The Ministry of Agriculture, Beijing 100097, China

⁴ Beijing Engineering Research Center of Agricultural Internet of Things,
Beijing 100097, China

⁵ College of Civil Engineering, Henan Institute of Engineering,
Zhengzhou 451191, China
yangfuqin0202@163.com

⁶ National Calibration Center for Surveying Instruments, Beijing 100039, China
xsz2011@whu.edu.cn

Abstract. Leaf nitrogen content is an important index of crop growth and plays an important role in crop growth and development. In this paper, the hyperspectral data of winter wheat and the leaf nitrogen content is used to study winter wheat on flagging stage, flowering stage and grain filling stage. The estimation model of nitrogen content in winter wheat leaves at different growth stages is constructed by using partial least squares method and verified by using a cross-validation method. The results showed that R² and the RMSE of the three growth stages were 0.53, 0.68, 0.64 and 0.331%, 0.246% and 0.406% respectively, and R² and RMSE of model validation were 0.44, 0.71, 0.64 and 0.369%, 0.235% and 0.410%. Both the prediction model and the verification model had high reliability. Therefore, it is feasible for UAV to carry hyperspectral monitoring system for retrieving nitrogen content of winter wheat leaves.

Keywords: Unmanned aerial vehicles · Hyperspectral · Winter wheat
Leaf nitrogen content · Partial least squares method

1 Introduction

Nitrogen is the most important mineral nutrient element in crop life, which can promote the growth of vegetative organs such as roots, stems and leaves, expand the area of photosynthesis and enhance the accumulation of photosynthetic products [1, 2]. The nitrogen content directly affects crop growth and yield [3]. Inversion of crop nitrogen content by remote sensing system is one of the quantitative agricultural remote sensing hotspots. In order to establish the relationship between wheat nitrogen content and spectrum, domestic and foreign scholars have studied the changes of sensitive spectral bands in different growth stages of wheat [4, 5]. Zhang et al. [6] put forward the sensitivity study of retrieving leaf nitrogen content of Winter Wheat with different spectral vegetation index. The results showed that Using Hyperspectral Vegetation index can effectively achieve nitrogen content inversion of crop leaves. Zhu et al. [7] have put forward a preliminary study on the use of SPAD to predict chlorophyll and nitrogen content in wheat leaves. It turned out that the SPAD value of wheat leaves is positively correlated with total nitrogen content, and the total nitrogen content could be estimated by SPAD value for wheat nitrogen nutrition. Li et al. [8] have proposed a quantitative relationship between nitrogen content and canopy reflectance index in wheat leaves, and the results showed that the red edge position of canopy reflectance spectrum could indicate the leaf nitrogen content of wheat varieties with different protein types. Sun et al. [9] have raised the establishment and validation of GRNN hyperspectral remote sensing model for retrieving nitrogen content in winter wheat leaves based on GA. The results showed that the selected spectral parameters and the corresponding model could reflect the relationship between total nitrogen in wheat leaves, and the effect is better than the stepwise regression model. Zhang et al. [10] proposed rice leaf nitrogen Hyperspectral Estimation and inversion based on the model. Results showed that there is a good correlation between leaf nitrogen content and tillering stage normalized vegetation index. Wang et al. [11] have put forward to use wheat canopy reflectance spectra to retrieve the vertical distribution of nitrogen by PLS algorithm, and the results showed that it is feasible to use PLS algorithm to estimate the vertical distribution of total nitrogen in wheat leaves. Ju [12] has used land-air hyperspectral remote sensing to monitor the nitrogen status and growth characteristics of wheat. The results showed that the sensitive bands of leaf nitrogen are mainly in the visible and near-infrared bands, among which the red-edge region is the most significant. Zhai et al. [13] have raised hyperspectral differences and monitoring model construction of nitrogen content in wheat leaves based on different soil texture, and it turned out that using NDSI (FD710, FD690), DSI (R515, R460) and RSI (R535, R715) as independent variables, the estimation model can well predict the nitrogen content of wheat leaves in sandy, loamy and clay 3 germplasms. Li et al. [14] have proposed the estimation of nitrogen content in winter wheat leaves with wide band reflectance of the simulated multispectral satellite. The results showed that the spectral index based on the composite index (TCARI/OSAVI) and the transformed chlorophyll absorption

index (TCARI) has some advantages in monitoring the nitrogen content of wheat leaves during the whole growth period. Wang et al. [15] proposed to estimate the nitrogen nutrient index of Winter Wheat Based on hyperspectral. The results showed that the linear interpolation of the red edge position, the red edge correction single index, ratio index, simple ratio pigment index, index and spectral parameters in nitrogen have a good correlation, can be used for inversion of canopy nitrogen nutrition level. Yang et al. [16] have put forward the optimal regression model of plant nitrogen content at different growth stages based on the importance of variable projection - partial least squares - Akai information criterion integration model, and the results showed that the flag stage is the best period for monitoring the nitrogen nutrition of Winter Wheat by hyperspectral remote sensing. Liu et al. [17] have raised quantitative modeling for leaf nitrogen content of winter wheat using UAV-based hyperspectral data. The results showed that the predicted values are very good in jointing stage, flagging leaf stage, and flowering stage, while it is a little bit less in the filling stage.

This essay first analyzed the correlation between the original spectrum, the first derivative of the spectrum, the normalized spectral index (NDSI), the ratio spectral index (RSI) and the leaf nitrogen content, and then each growth period selects the spectra of the original spectral positive correlation maximum and negative correlation maximum, the spectra of first derivative positive correlation maximum and negative correlation maximum, a group of spectra with the greatest NDSI correlation value and a group of spectra with the greatest RSI correlation value, with a total of six parameters. Next, the estimation model of nitrogen content in winter wheat leaves is constructed by partial least squares method and verified by cross-validation method. So as to provide a new technical approach for hyperspectral remote sensing inversion of nitrogen content in winter wheat leaves.

2 Materials and Methods

2.1 Brief Introduction of Research Area

Field experiments were conducted at the National Precision Agriculture Research and demonstration base from 2014 to 2015. The base is located in the northeast of Beijing City, located at latitude $40^{\circ}00' - 40^{\circ}21'$, longitude $116^{\circ}34' - 117^{\circ}00'$. The Base covers an area of about 2500 acres, altitude 36 m, fertile land, flat terrain, and soil type is fluvo-aquic soil. The climate in the base area belongs to warm temperate semi-humid continental monsoon weather, four distinct seasons, cold and dry in winter, hot and rainy summer. The average temperature is 13°C , and the average annual precipitation is 510 mm. At the end of September, early winter wheat is planted here (Fig. 1).

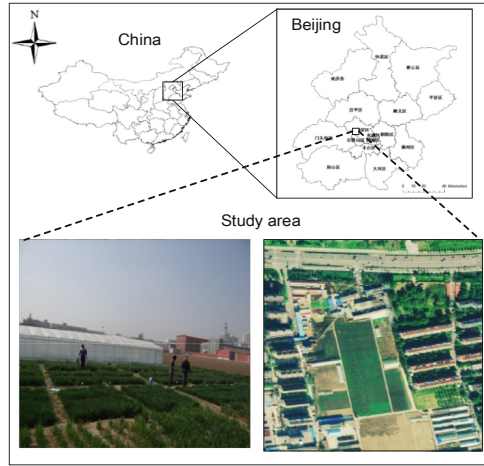


Fig. 1. National Precision Agriculture Research and demonstration base

2.2 Experimental Design

Using varieties, water, nitrogen fertilization orthogonal test; Wheat is divided into two varieties: Beijing 9843 (J9843), Zhongmai 175 (ZM175); There were 4 levels of fertilizer: 0 kg urea/acre (N1), 13 kg urea/acre (N2), 26 kg urea/acre (N3), 39 kg urea/acre (N4); Planting plots were processed 16 times and repeated 3 times. Field planting map (see below): From east to west, the total length is 84 m, and the total length is 32 m from south to North; The number of planting area is 48, and each area is 6 m * 8 m (Fig. 2).

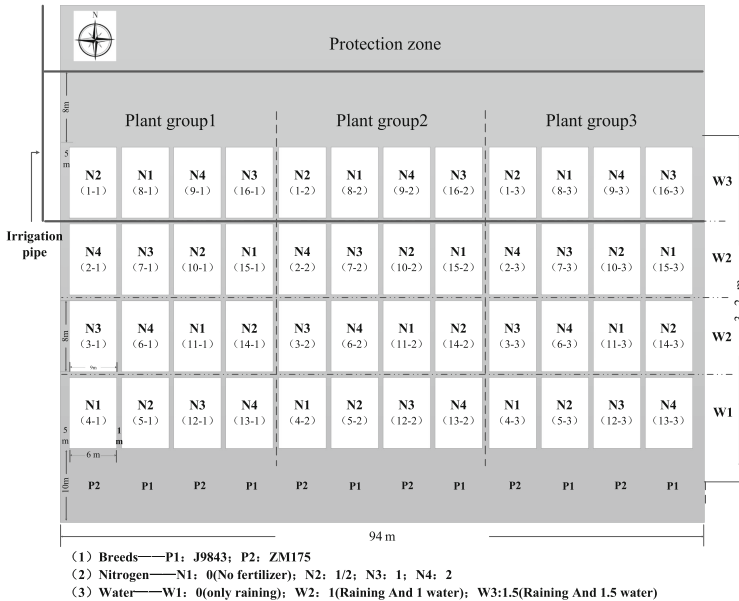


Fig. 2. Test plan

2.3 Data Acquisition and Processing

2.3.1 Leaf Nitrogen Content Data Acquisition

The nitrogen content of winter wheat leaves is collected at flagging stage (April 27, 2015), flowering stage (May 11, 2015) and grain filling stage (May 25, 2015). Twenty growing average winter wheat plants were selected as experimental samples for each plot. Firstly, The wheat samples were collected in paper bags and the leaves of wheat should be integral during collection. Next cut the wheat sample leaves separately in the test paper bag, and Put the paper bag in the 105 °C oven for half an hour. Then we reduced oven temperature immediately and maintained oven temperature of 80 °C for drying samples, drying for more than 24 h, until the quality of the sample remained unchanged. After drying, the sample blades were weighed and crushed, and the nitrogen content of the sample blades is measured by Kjeldahl apparatus. The nitrogen content of the sample leaves is the product of the nitrogen mass fraction and the sample biomass. Finally, the average nitrogen content of winter wheat leaves in each plot is taken as the value of nitrogen content in winter wheat leaves.

2.3.2 Hyperspectral Data Acquisition

The experiment used UAV equipped with a UHD-185 remote sensor to sample spectral of winter wheat from 10am to 2pm Beijing time in Changping districts when the weather is sunny and windless. The hyperspectral remote sensing images were collected at flagging stage (April 27, 2015), flowering stage (May 11, 2015) and grain filling stage (May 25, 2015), using the same flight route. The UHD-185 hyperspectral measures a range of 454 to 950 nm, a sampling interval of 4 nm, and a cubic resolution of one megapixel. The spectral range of the spectrometer is narrow, and the spectral resolution of the visible light to near-infrared band is nanometer order, and the number of spectral bands is large, and the band is continuous, which can meet the requirement of inversion of nitrogen content in winter wheat leaves. The UHD-185 hyperspectral sensor carried by the unmanned aerial vehicle (UAV) had been denoised and lens distortion correction before used.

The experiment used Agisoft photoscan software to splice UAV hyperspectral remote image. The pre-processed hyperspectral images were introduced into the ArcGIS software, and the rectangular region of interest is selected from the hyperspectral remote sensing image in combination with the 48 experimental plots. Finally, the average spectral reflectance of each experimental plot is extracted to obtain 125 spectral average reflectances at wavelengths 454 to 950 nm.

2.4 Method

2.4.1 Vegetation Index Selection

The normalized difference index NDSI [18] and the ratio spectral index RSI [19] were constructed by referring to the normalized vegetation index and the ratio vegetation index in the study of vegetation canopy spectra. These formulas are as follows:

$$\text{NDSI}(\lambda_1, \lambda_2) = \frac{R_{\lambda_2} - R_{\lambda_1}}{R_{\lambda_2} + R_{\lambda_1}} \quad (1)$$

$$\text{RSI}(\lambda_1, \lambda_2) = \frac{R_{\lambda_2}}{R_{\lambda_1}} \quad (2)$$

Where λ_1 is wavelength 1 and λ_2 is wavelength 2. R_{λ_1} represents spectral reflectance of winter wheat leaves at wavelength 1, and R_{λ_2} represents spectral reflectance of winter wheat leaves at wavelength 2.

2.4.2 Partial Least Squares Method

Partial least squares [20] is a multivariate statistical data analysis method that minimizes the square of the error and finds the best matching function model for a set of data. It is generally used to study the regression model of dependent variables for multiple independent variables. The simplest form is the linear relationship between the variable Y and the independent variable X, the expression is:

$$Y = a_0 + a_1X_1 + a_2X_2 + \cdots + a_nX_n \quad (3)$$

Where a_0 is the intercept of the regression coefficient; a_i is the regression coefficient; X_i is the independent variable 1–n.

2.5 Statistical Analysis

In this study, determination coefficient (R²) and root-mean-square error were regarded as indicators to interpret and quantify the relationship between LNC and vegetation index. Generally speaking, the higher R², the smaller RMSE, and the better ability of the estimated model between the LNC and vegetation index, otherwise, the estimated ability is poor.

3 Data Processing and Analysis

3.1 Analysis of Correlation Between Original Spectrum and Leaf Nitrogen Content

The correlation between the average reflectance of the arbitrary band spectrum and the nitrogen content of the corresponding wheat leaves is analyzed in the winter wheat flagging stage, flowering stage and grain filling stage, and the graphs of wavelength and correlation coefficient were obtained. Each growth period sorted the correlation coefficients and selected the spectra of the original spectral positive correlation maximum and negative correlation maximum.

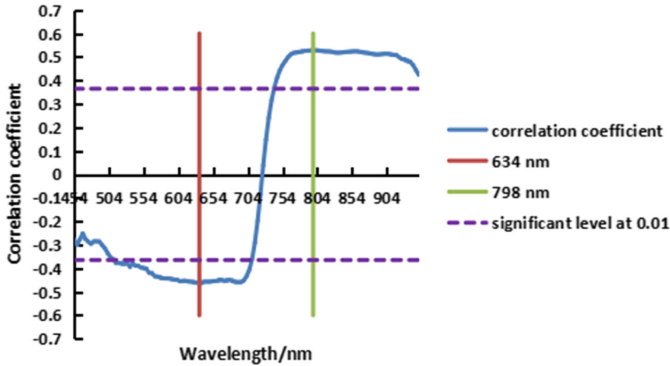


Fig. 3. Correlation between original spectrum and leaf nitrogen content at flagging stage

As shown in Fig. 3, In the range of 514 to 706 nm, the leaf nitrogen content is significantly negatively correlated with the original spectrum, and the correlation coefficient in the 634 nm band is the best, and the correlation coefficient is -0.46 . In the range of 742 to 950 nm, the leaf nitrogen content is significantly positively correlated with the original spectrum, and the correlation coefficient in the 798 nm band is the best, and the correlation coefficient is 0.53 . 634 nm band and 798 nm band are selected as the parameters for modeling the flagging stage of winter wheat.

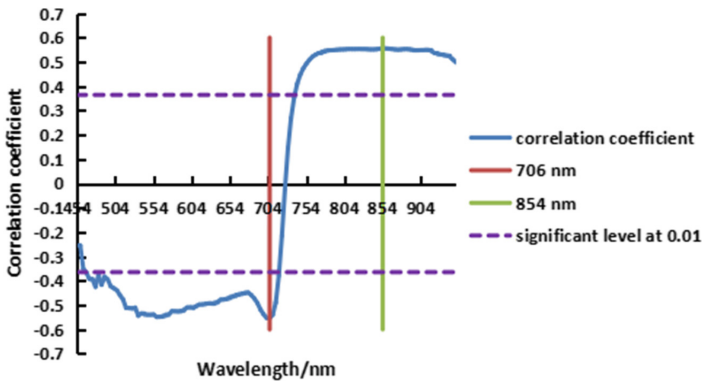


Fig. 4. Correlation between original spectrum and leaf nitrogen content at flowering stage

As shown in Fig. 4, In the range of 466 to 718 nm, the leaf nitrogen content is significantly negatively correlated with the original spectrum, and the correlation coefficient in the 706 nm band is the best, and the correlation coefficient is -0.55 . In the range of 742 to 950 nm, the leaf nitrogen content is significantly positively correlated with the original spectrum, and the correlation coefficient in the 854 nm band is the best, and the correlation coefficient is 0.56 . 706 nm band and 854 nm band are selected as the parameters for modeling the flowering stage of winter wheat.

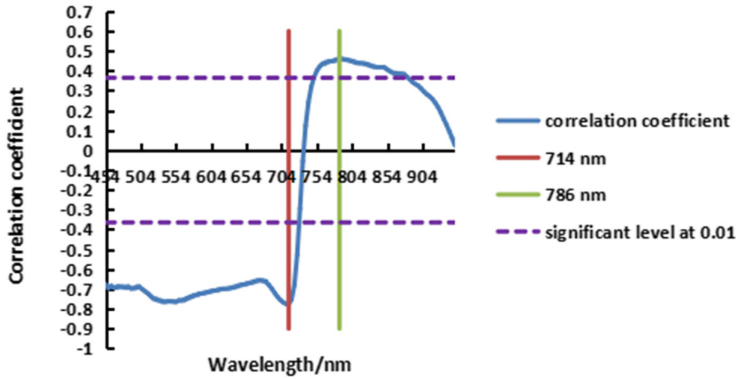


Fig. 5. Correlation between original spectrum and leaf nitrogen content at grain filling stage

As shown in Fig. 5, In the range of 454 to 726 nm, the leaf nitrogen content is significantly negatively correlated with the original spectrum, and the correlation coefficient in the 714 nm band is the best, and the correlation coefficient is -0.78 . In the range of 750 to 882 nm, the leaf nitrogen content is significantly positively correlated with the original spectrum, and the correlation coefficient in the 786 nm band is the best, and the correlation coefficient is 0.46 . 714 nm band and 786 nm band are selected as the parameters for modeling the grain filling of winter wheat.

3.2 Analysis of Correlation Between First Derivative of Spectrum and Leaf Nitrogen Content

The correlation between the first derivative of spectral average reflectance of the arbitrary band spectrum and the nitrogen content of the corresponding wheat leaves was analyzed in the winter wheat flagging stage, flowering stage and grain filling stage, and the graphs of wavelength and correlation coefficient were obtained. Each growth period Sorted the correlation coefficients and selected the spectra of first derivative positive correlation maximum and negative correlation maximum.

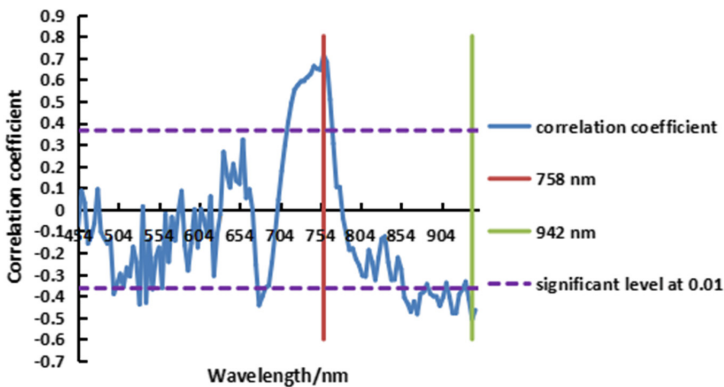


Fig. 6. Correlation between first derivative of spectrum and nitrogen content in leaves at flagging stage

As shown in Fig. 6, In the range of 714 to 766 nm, the leaf nitrogen content is significantly positively correlated with the first derivative of the spectrum, and the correlation coefficient in the 758 nm band is the best, and the correlation coefficient is 0.71. In the range of 858 to 882 nm, 890 to 906 nm, 914 to 930 nm, 938 to 930 nm and other sporadic spectrum, the leaf nitrogen content is significantly negatively correlated with the first derivative of the spectrum, and the correlation coefficient in the 942 nm band is the best, and the correlation coefficient is -0.51 . 758 nm band and 942 nm band are selected as the parameters for modeling the flagging stage of winter wheat.

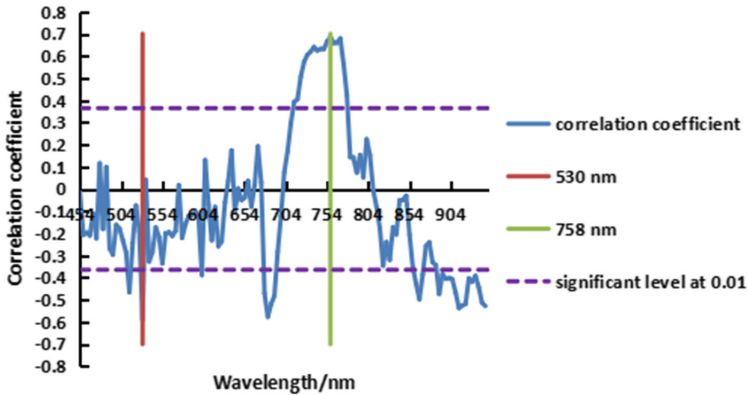


Fig. 7. Correlation between first derivative of spectrum and nitrogen content in leaves at flowering stage

As shown in Fig. 6, In the range of 714 to 778 nm, the leaf nitrogen content is significantly positively correlated with the first derivative of the spectrum, and the correlation coefficient in the 758 nm band is the best, and the correlation coefficient is 0.69. In the range of 530 nm, 678 to 690 nm, 862 to 870 nm, 890 to 946 nm and other sporadic spectrum, the leaf nitrogen content is significantly negatively correlated with the first derivative of the spectrum, and the correlation coefficient in the 530 nm band is the best, and the correlation coefficient is -0.59 . 530 nm band and 758 nm band are selected as the parameters for modeling the flowering stage of winter wheat (Fig. 8).

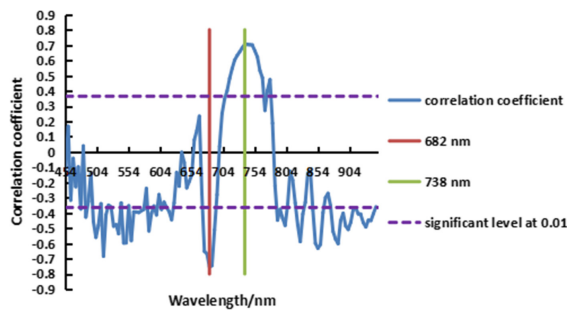


Fig. 8. Correlation between first derivative of spectrum and nitrogen content in leaves at grain filling stage

As shown in Fig. 7, In the range of 710 to 766 nm and 744 to 778 nm, the leaf nitrogen content is significantly positively correlated with the first derivative of the spectrum, and the correlation coefficient in the 738 nm band is the best, and the correlation coefficient is 0.71. In the range of 558 to 578 nm, 674 to 690 nm, 790 to 802 nm, 846 to 862 nm, 878 to 942 nm and other sporadic spectrum, the leaf nitrogen content is significantly negatively correlated with the first derivative of the spectrum, and the correlation coefficient in the 682 nm band is the best, and the correlation coefficient is -0.75 . 682 nm band and 730 nm band are selected as the parameters for modeling the grain filling stage of winter wheat.

3.3 Analysis of Correlation Between NDSI and Leaf Nitrogen Content

Using the MATLAB program, the NDSI of the spectral reflectance of any two bands in the winter wheat flagging stage, flowering stage and grain filling stage was calculated. Then the coefficient of determination between NDSI and leaf nitrogen content is calculated, and the contour map of each growth period was obtained, as shown in Figs. 9, 10 and 11.

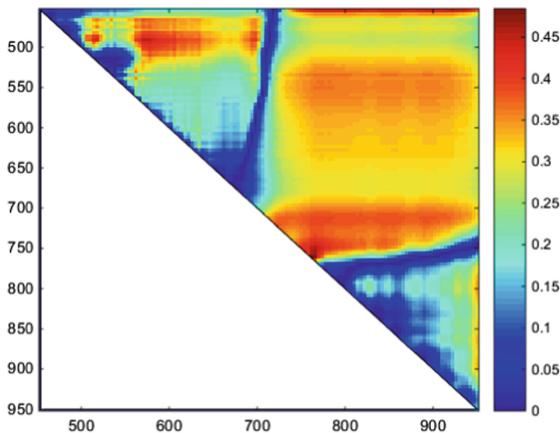


Fig. 9. Coefficient of determination between NDSI and leaf nitrogen content at flagging stage

As shown in Fig. 9, The leaf nitrogen content of winter wheat has a good correlation with NDSI in many bands during flagging stage. These bands are as follows: the range on the x-axis is 746 to 758 nm and the range on the y-axis is 762 to 766 nm. These regions show that the nitrogen content of leaf can be well estimated by using NDSI, and the coefficient of determination is above 0.45. NDSI[758, 762] has the best correlation, with a coefficient of determination of 0.48. NDSI[758, 762] is selected as the parameter for modeling at the flagging stage of winter wheat.

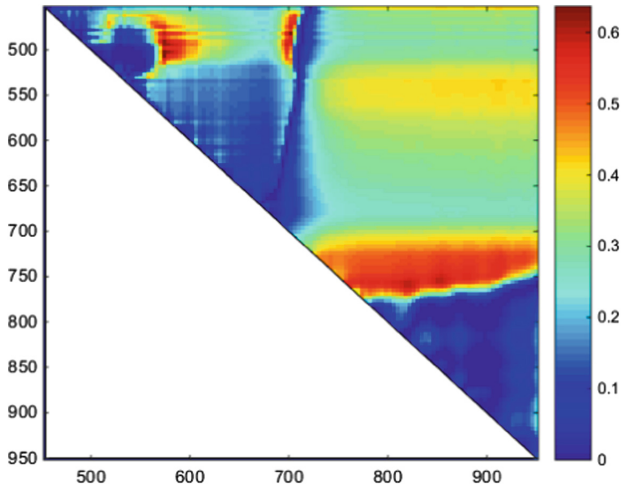


Fig. 10. Coefficient of determination between NDSI and leaf nitrogen content at flowering stage

As shown in Fig. 10, The leaf nitrogen content of winter wheat has a good correlation with NDSI in many bands during flowering stage. These bands are as follows: the range on the x-axis is 490 to 506 nm and the range on the y-axis is 574 to 578 nm. These regions show that the nitrogen content of leaf can be well estimated by using NDSI, and the coefficient of determination is above 0.6. NDSI[502, 574] has the best correlation, with a coefficient of determination of 0.64. NDSI[502, 574] is selected as the parameter for modeling at the flowering stage of winter wheat.

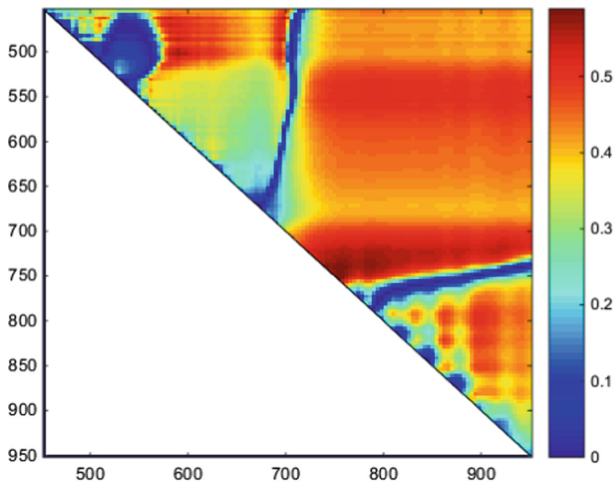


Fig. 11. Coefficient of determination between NDSI and leaf nitrogen content at grain filling stage

As shown in Fig. 11, The leaf nitrogen content of winter wheat has a good correlation with NDSI in many bands during grain filling stage. The band range is as follows: The range on the x-axis is 502 nm, and the range on the y-axis is 586 to 598 nm; the range on the x-axis is 718 to 726 nm, and the range on the y-axis is 750 to 850 nm; The range on the x-axis is 730 to 738 nm, and the range on the y-axis is 738 to 806 nm; the range on the x-axis is 742 to 750 nm, and the range on the y-axis is 754 to 766 nm. These regions show that the nitrogen content of leaf can be well estimated by using NDSI, and the coefficient of determination is above 0.55. NDSI[746, 754] has the best correlation, with a coefficient of determination of 0.59. NDSI[746, 754] is selected as the parameter for modeling at the flowering stage of winter wheat.

3.4 Analysis of Correlation Between RSI and Leaf Nitrogen Content

Using the MATLAB program, the RSI of the spectral reflectance of any two bands in the winter wheat flagging stage, flowering stage and grain filling stage was calculated. Then the coefficient of determination between RSI and leaf nitrogen content is calculated, and the contour map of each growth period was obtained, as shown in Figs. 12, 13 and 14.

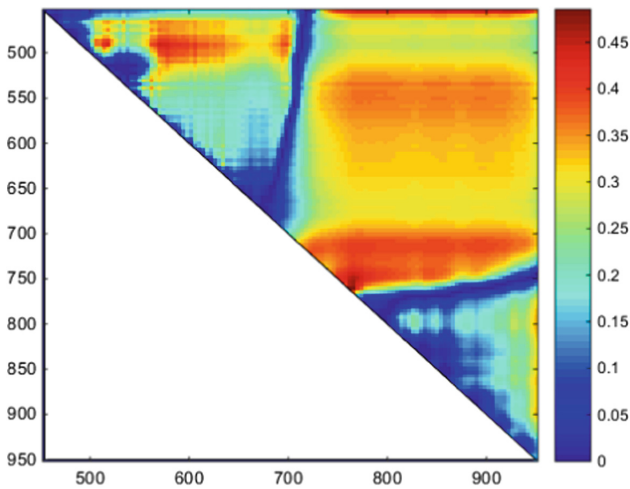


Fig. 12. Coefficient of determination between RSI and leaf nitrogen content at flagging stage

As shown in Fig. 12, The leaf nitrogen content of winter wheat has a good correlation with RSI in many bands during flagging stage. These bands are as follows: the range on the x-axis is 746 to 758 nm and the range on the y-axis is 762 to 766 nm. These regions show that the nitrogen content of leaf can be well estimated by using RSI, and the coefficient of determination is above 0.45. RSI[758, 762] has the best correlation, with a coefficient of determination of 0.49. RSI[758, 762] is selected as the parameter for modeling at the flagging stage of winter wheat.

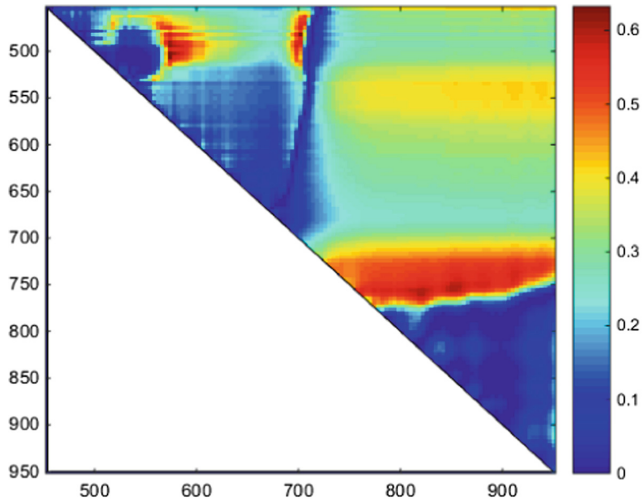


Fig. 13. Coefficient of determination between RSI and leaf nitrogen content at flowering stage

As shown in Fig. 13, The leaf nitrogen content of winter wheat has a good correlation with RSI in many bands during flowering stage. These bands are as follows: The range on the x-axis is 482 nm, and the range on the y-axis is 702 nm; the range on the x-axis is 490 nm, and the range on the y-axis is 574 nm; The range on the x-axis is 502 nm, and the range on the y-axis is 574 to 578 nm; the range on the x-axis is 508 nm, and the range on the y-axis is 574 nm. the range on the x-axis is 570 nm, and the range on the y-axis is 854 nm. These regions show that the nitrogen content of leaf can be well estimated by using RSI, and the coefficient of determination is above 0.6. RSI[502, 574] has the best correlation, with a coefficient of determination of 0.63. RSI[502, 574] is selected as the parameter for modeling at the flowering stage of winter wheat.

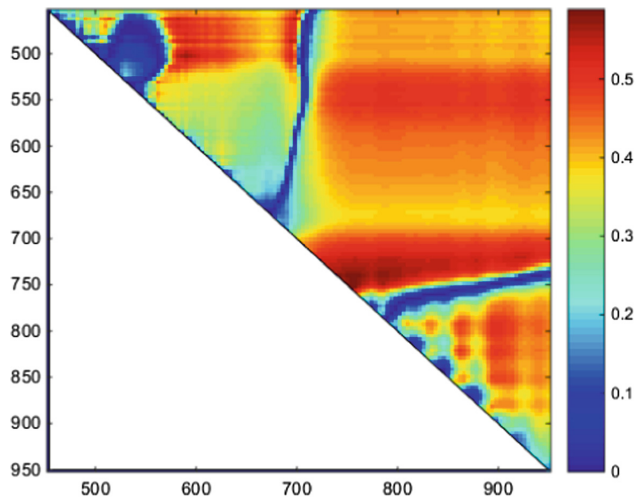


Fig. 14. Coefficient of determination between RSI and leaf nitrogen content at grain filling stage

As shown in Fig. 14, The leaf nitrogen content of winter wheat has a good correlation with RSI in many bands during flowering stage. These bands are as follows: The range on the x-axis is 502 nm, and the range on the y-axis is 586 to 594 nm; the range on the x-axis is 722 nm, and the range on the y-axis is 754 to 762 nm; The range on the x-axis is 722 nm, and the range on the y-axis is 782 to 802 nm; the range on the x-axis is 726 to 738 nm, and the range on the y-axis is 742 to 806 nm; the range on the x-axis is 726 to 734 nm, and the range on the y-axis is 810 to 818 nm. The range on the x-axis is 742 nm, and the range on the y-axis is 746 to 770 nm; the range on the x-axis is 742 nm, and the range on the y-axis is 778 to 798 nm; The range on the x-axis is 746 nm, and the range on the y-axis is 754 to 790 nm. These regions show that the nitrogen content of leaf can be well estimated by using RSI, and the coefficient of determination is above 0.55. RSI[502, 574] has the best correlation, with a coefficient of determination of 0.59. RSI[746, 754] is selected as the parameter for modeling at the grain filling stage of winter wheat.

4 Model Building and Accuracy Analysis

4.1 Model Building

At each stage of growth, we first selected the spectra of the original spectral positive correlation maximum and negative correlation maximum, the spectra of first derivative positive correlation maximum and negative correlation maximum, a group of spectra with the greatest NDSI correlation value and a group of spectra with the greatest RSI correlation value, with a total of six parameters. And then the partial least squares method was used to establish the estimation model of nitrogen content in leaves of winter wheat leaves at different growth stages. Finally, the relationship between the measured value and the predicted value was analyzed, as shown in Figs. 15, 16 and 17.

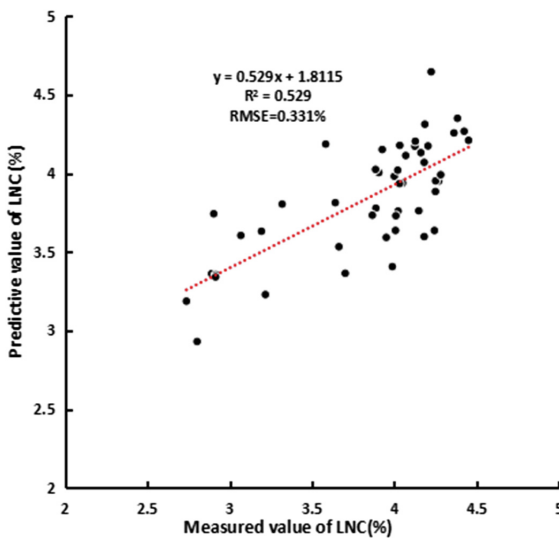


Fig. 15. Relationship between predicted LNC and measured LNC at flagging stage

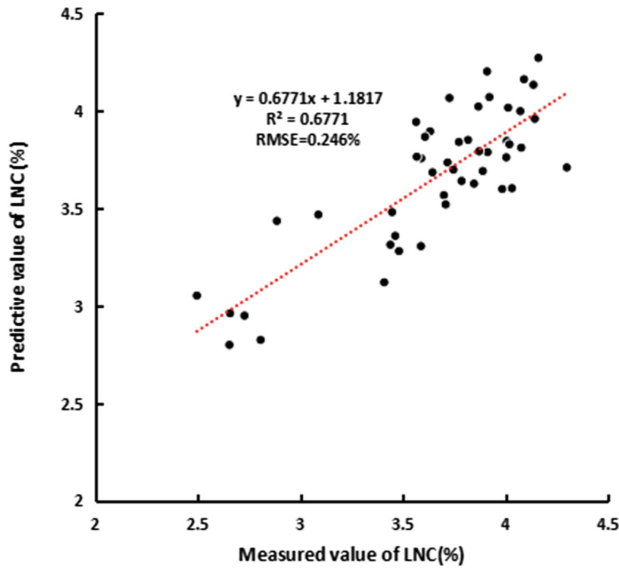


Fig. 16. Relationship between predicted LNC and measured LNC at flowering stage

After correlation analysis between spectral and leaf nitrogen content, the original spectral trough 634 nm and the peak 798 nm, spectral first derivative trough 942 nm and peak 758 nm, normalized spectral index maximum NDSI [758, 762] and ratio spectral index maximum RSI [758, 762] are chosen as modeling parameters at flagging stage. The equation between the predicted and measured values is $y = 0.529x + 1.8115$, and the value of R^2 and RMSE are 0.53 and 0.331% respectively.

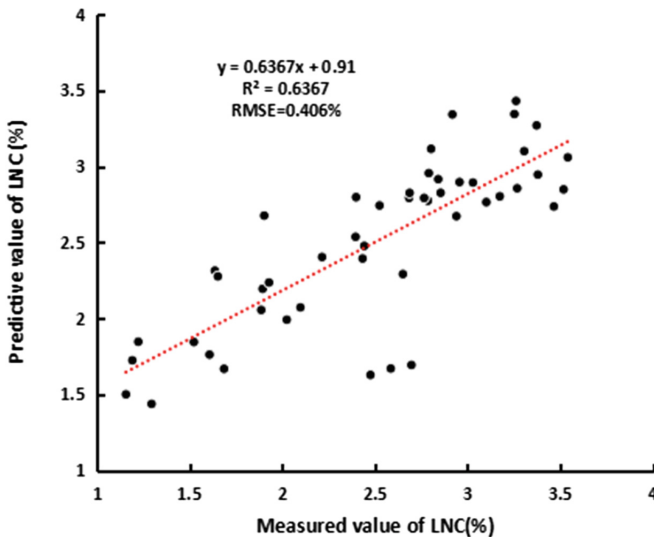


Fig. 17. Relationship between predicted LNC and measured LNC at grain filling stage

After correlation analysis between spectral and leaf nitrogen content, the original spectral trough 706 nm and the peak 854 nm, spectral first derivative trough 530 nm and peak 758 nm, normalized spectral index maximum NDSI[502, 574] and ratio spectral index maximum RSI [502, 574] are chosen as modeling parameters at flowering stage. The equation between the predicted and measured values is $y = 0.6671x + 1.1817$, and the value of R^2 and RMSE are 0.68 and 0.246% respectively.

After correlation analysis between spectral and leaf nitrogen content, the original spectral trough 714 nm and the peak 786 nm, spectral first derivative trough 682 nm and peak 738 nm, normalized spectral index maximum NDSI[746, 754] and ratio spectral index maximum RSI [746, 754] are chosen as modeling parameters at grain filling stage. The equation between the predicted and measured values is $y = 0.6367x + 0.91$, and the value of R^2 and RMSE are 0.64 and 0.406% respectively.

4.2 Model Validation

At each stage of growth, we first selected the spectra of the original spectral positive correlation maximum and negative correlation maximum, the spectra of first derivative positive correlation maximum and negative correlation maximum, a group of spectra with the greatest NDSI correlation value and a group of spectra with the greatest RSI correlation value, with a total of six parameters. And then the Leave a cross-validation method was used to validate the estimation model of nitrogen content in leaves of winter wheat leaves at different growth stages. The coefficient of determination (R^2) and the root mean square error (RMSE) were chosen as the indexes to evaluate the validation accuracy (Fig. 18).

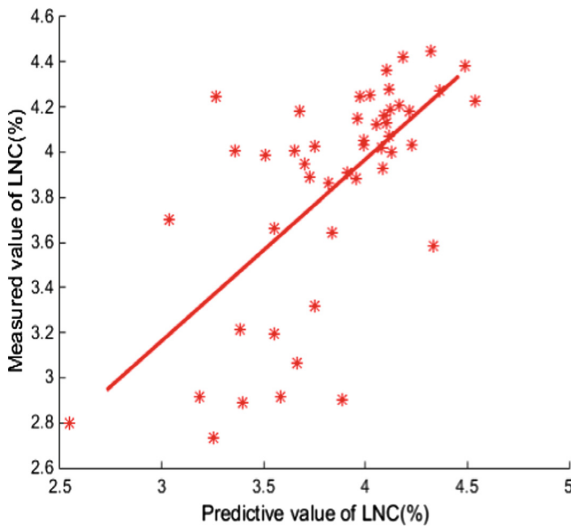


Fig. 18. Relationship between predicted LNC and measured LNC at flagging stage

At flagging stage, the original spectral trough 634 nm and the peak 798 nm, spectral first derivative trough 942 nm and peak 758 nm, normalized spectral index maximum NDSI[758, 762] and ratio spectral index maximum RSI [758, 762] are

chosen as model validation parameters. The value of R2 and RMSE are 0.4381 and 0.3695% respectively (Fig. 19).

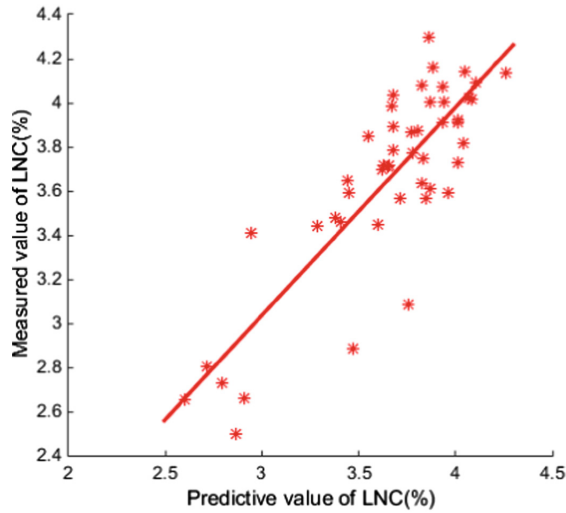


Fig. 19. Relationship between predicted LNC and measured LNC at flowering stage

At flowering stage, the original spectral trough 706 nm and the peak 854 nm, spectral first derivative trough 530 nm and peak 758 nm, normalized spectral index maximum NDSI[502, 574] and ratio spectral index maximum RSI [502, 574] are chosen as model validation parameters. The value of R2 and RMSE are 0.7085 and 0.2347% respectively (Fig. 20).

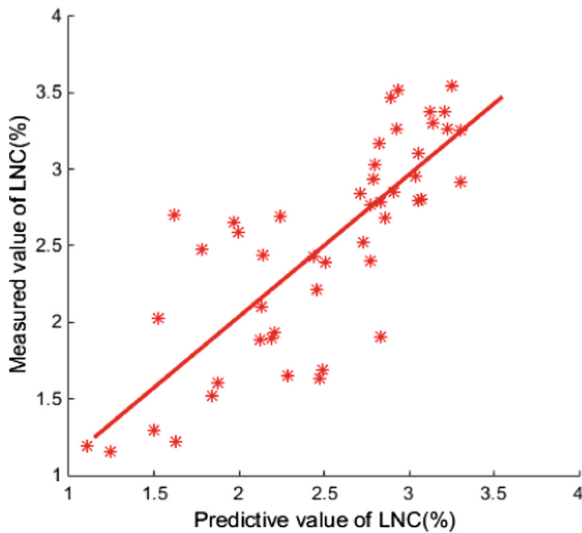


Fig. 20. Relationship between predicted LNC and measured LNC at grain filling stage

At grain filling stage, the original spectral trough 714 nm and the peak 786 nm, spectral first derivative trough 682 nm and peak 738 nm, normalized spectral index maximum NDSI[746, 754] and ratio spectral index maximum RSI [746, 754] are chosen as model validation parameters. The value of R^2 and RMSE are 0.6352 and 0.40869% respectively.

5 Conclusions

- (1) At different growth stages of winter wheat, we first analyze the correlation between the original spectrum, the first derivative of the spectrum, the normalized spectral index (NDSI), the ratio spectral index (RSI) and the leaf nitrogen content, and then screen out the best sensitive bands. these sensitive bands of the flagging stage are as follows: the original spectral 634 nm and 798 nm, spectral first derivative 942 nm and 758 nm, NDSI[758, 762] and RSI [758, 762]. these sensitive bands of the flowering stage are as follows: the original spectral 706 nm and 854 nm, spectral first derivative 530 nm and 758 nm, NDSI[502, 574] and RSI [502, 574]. these sensitive bands of the grain filling stage are as follows: the original spectral 714 nm and 786 nm, spectral first derivative 682 nm and 738 nm, NDSI[746, 754] and RSI [746, 754].
- (2) For these three growth stages of flagging stage, flowering stage and grain filling stage, the coefficient of determination (R^2) and the root mean square error (RMSE) of the model building were 0.53, 0.68, 0.64 and 0.331%, 0.246% and 0.406% respectively. The modeling coefficient of determination of the flowering stage is the biggest in these three growth stages, indicating that the flowering stage is the best growth stage for monitoring the nitrogen nutrition of winter wheat leaves by hyperspectral remote sensing.
- (3) For these three growth stages of flagging stage, flowering stage and grain filling stage, the coefficient of determination (R^2) and the root mean square error (RMSE) of model validation were 0.441, 0.71, 0.64 and 0.369%, 0.235% and 0.410% respectively. The results show that the estimation of the nitrogen content of winter wheat plant by using partial least squares method has high accuracy and good reliability. Therefore, it is feasible to monitor the nitrogen content of winter wheat by hyperspectral remote sensing image of UAV.

Acknowledgments. This work was supported in part by the National Key Research and Development Programs (2016YFD0300602), National Natural Science Foundation of China (No. 41601346), Surveying and mapping geographic information public industry scientific research projects (201512010).

References

1. Wang, J., Zhao, C., Huang, W., et al.: Quantitative agricultural remote sensing. Science Press, Beijing (2008)
2. Pinter Jr., P.J., Hatfield, J.L., Schepers, J.S., et al.: Remote sensing for crop management. *Potogrammetric Eng. Remote Sens.* **69**(6), 647–664 (2003)
3. Hansen, P.M., Schjoerring, J.K.: Reflectance measurement of canopy biomass and nitrogen status in wheat crops using normalized difference vegetation indices and partial least squares regression. *Remote Sens. Environ.* **86**(4), 542–553 (2003)
4. Feng, W., Yao, X., Zhu, Y., et al.: Monitoring leaf nitrogen status with hyperspectral reflectance in wheat. *Eur. J. Agron.* **28**(3), 394–404 (2008)
5. Clevers, J., Kooistra, L.: Using hyperspectral remote sensing data for retrieving total canopy chlorophyll and nitrogen content. In: 2011 3rd Workshop on Hyperspectral Image and Signal Processing: Evolution in Remote Sensing (WHISPERS), pp. 1–4. IEEE (2011)
6. Zhang, X., Zhang, L., Zhang, X., et al.: The sensitivity study of retrieving leaf nitrogen content of Winter Wheat with different spectral vegetation index. *Chin. Agric. Sci.* **50**(3), 474–485 (2017)
7. Zhu, X., Sheng, H., Gu, J., et al.: Preliminary study on predicting chlorophyll and nitrogen content in wheat leaves using SPAD value. *J. Wheat Crop.* **25**(2), 46–50 (2005)
8. Li, Y., Zhu, Y., Tian, Y., et al.: Quantitative relationship between leaf nitrogen content and canopy reflectance spectral index. *Proc. Crop* **26**(3), 3463–3469 (2006)
9. Sun, Y., Wang, J., Li, B., et al.: Establishment and validation of GRNN hyperspectral remote sensing model for retrieving winter wheat leaf nitrogen content based on GA. *Bull. Soils* **38**(3), 508–512 (2007)
10. Zhang, G., Xu, T., Yu, F., et al.: Rice leaf nitrogen Hyperspectral Estimation and inversion based on the model. *Zhejiang J. Agric. Sci.* **29**(5), 845–849 (2017)
11. Wang, J., Huang, W., Lao, C.L., et al.: Using wheat canopy reflectance spectra to retrieve the vertical distribution of nitrogen by PLS algorithm. *Spectrosc. Spectr. Anal.* **27**(7), 1319–1322 (2007)
12. Ju, C.: Monitoring nitrogen status and growth characteristics of wheat using ground air hyperspectral remote sensing. Nanjing Agricultural University (2008)
13. Zhai, Q., Zhang, J., Xiong, S., et al.: Hyperspectral differences and monitoring model construction of nitrogen content in wheat leaves based on different soil texture. *Agric. Sci. China* **46**(13), 2655–2667 (2013)
14. Li, F., Chang, Q., Shen, J., et al.: Estimation of nitrogen content in winter wheat leaves with wide band reflectance of simulated multispectral satellite. *Chin. J. Agric. Mach.* **47**(2), 302–308 (2016)
15. Wang, R., Song, X., Li, Z.: Estimation of nitrogen nutrition index of winter wheat based on hyperspectral analysis. *J. Agric. Eng.* **30**(19), 191–198 (2014)
16. Yang, F., Dai, H., Feng, H., et al.: Estimation of plant nitrogen content in winter wheat using hyperspectral based on akaike information criterion. *J. Agric. Eng.* **32**(23), 161–167 (2016)
17. Liu, H., Zhu, H., Wang, P., et al.: Quantitative modeling for leaf nitrogen content of winter wheat using UAV-based hyperspectral data. *Int. J. Remote Sens.* **38**(8–10), 2117–2134 (2017)
18. Li, B., Li, Z., Yu, T., et al.: Study on fractal dimension of vegetation cover in watershed based on normalized vegetation index. *J. Agric. Eng.* **30**(15), 239–247 (2014)
19. Tian, Y.C., Yao, X., Yang, J., et al.: Assessing newly developed and published vegetation indices for estimating rice leaf nitrogen concentration with ground-and space-based hyperspectral reflectance. *Field Crop. Res.* **120**(2), 299–310 (2011)
20. Luo, P., Guo, J., Li, Q., et al.: Discussion on modeling based on partial least squares regression. *J. Tianjin Univ. Nat. Sci. Eng. Technol.* **35**(6), 783–786 (2002)



Quantification of Root Anatomical Traits in *RGP* Transgenic Maize Plants Based on Micro-CT

Xiaodi Pan, Liming Ma, Ying Zhang, Jinglu Wang, Jianjun Du,
and Xinyu Guo (✉)

Beijing Key Lab of Digital Plant, Beijing Research Center
for Information Technology in Agriculture,
Beijing Academy of Agriculture and Forestry Sciences, Beijing, China
{panxd, ma1m, zhangying, wangjl, dujj,
guoxy}@nercita.org.cn

Abstract. The *RGP* transgenic plants show good resistance to drought especially reflected in corn yield. However, little is known about root traits which contribute to drought resistance. Here, we characterized root anatomy in the transgenic plants based on micro-CT scanning. Quantitative analysis of root anatomical traits showed that the drought-resistant *RGP* transgenic plants had larger root and stele cross-sectional areas in the fourth and the fifth whorls of nodal roots. The metaxylem vessel number and total area of metaxylem vessels was higher or larger in the fifth and the sixth whorls of nodal roots from *RGP* transgenic plants.

Keywords: Maize roots · Anatomical traits · Drought · Micro-CT

1 Introduction

Drought is an important environmental factor which affects the plant growth and productivity of field crops [1, 2]. The threat of drought stress on crop growth and food production is exacerbated by global climate change [3]. Roots are the primary sites of water uptake in plants. Roots are also an important part of plant fitness in drought and water-limited environments, as they adjust their growth and water absorption and transport properties to drought stress [4]. In the case of adaptive responses of crop root to drought stress, the focus of attention can be divided into two areas: root architecture and root anatomy. Root system architecture (RSA) phenotyping has attracted extensive attention such as the wide application of destructive and non-destructive techniques for phenotyping. For example, RSA could be determined in non-destructive manners by magnetic resonance imaging or X-ray computed tomography scanning when plants are growing in soils. Consequently, the three-dimensional modelling of RSA is receiving more and more attention. However, the researches on the anatomy of crop roots are less prevalent.

Root anatomical traits play important roles in root functions, such as water and nutrient absorption from soils, the resource transportation in plants, and the metabolic cost related with root growth [5–7]. Traits like the xylem vessel diameter could affect the axial water transport along the plant roots [8, 9], and the number and size of root cell layers and cell wall packing would affect the radial water flow [6].

A *RGP* (Root Growth Promoting) factor gene is specially expressed in the roots of maize plants, which was cloned from *Arabidopsis* and introduced to maize plants. The *RGP* transgenic maize plants show the advantage of drought resistance by reason of their stronger water absorption of roots. However, the root anatomical traits contributing to drought resistance is unclear. Phenotyping of root anatomy in *RGP* transgenic maize plants will contribute to revealing drought-resistant mechanisms of the *RGP* transgenic maize, and breeding maize varieties of improved drought resistance. In this work, images of root anatomical organization in the *RGP* transgenic and control maize plants were obtained by X-ray micro-computed tomography system. Anatomical traits such as the root/stele cross-sectional area, and number/size of metaxylem vessels were analyzed assisted by ImageJ software.

2 Materials and Methods

2.1 Plant Materials and Growth Conditions

Both the *RGP* transgenic maize line and the control line (inbred line Xu-178) were grown in a rainproof shelter located at Beijing Research Center for Information Technology in Agriculture. This experiment lasted from June to September in 2016. The plants were irrigated normally until 45 days after sowing, and then drought treatment began, that is, no further irrigation was applied. The plant roots of the two lines were sampled at the Silking stage (R1, eighty-six days after planting). About one centimeter root samples were obtained where were two centimeters from the root-shoot connections of the 1st to 6th whorl nodal roots, then fixed in the formalin-acetic acid-alcohol solution (70% ethanol:formaldehyde:acetic acid = 90:5:5, v/v) immediately, and then stored at 4 °C.

2.2 Image Acquisition and Analysis

The root sample preparation assay including sample drying and staining was performed according to the previous description [10]. These root samples were then placed into the micro-CT system for scanning (Type 1172, Bruker). The scanning voltage and current were set at 34 kV and 210 μ A. The sample-source distance was 51 mm and camera-source distance was 281 mm. Then X-ray projections of root samples were obtained which were digitized as 2000 \times 1332 pixel images. After that these projections could be further reconstructed to acquire a series of root transverse-sectional images with the NRecon software (Version:1.6.9.4, Bruker). These 8-bit BMP reconstructed images were analyzed for the extraction of root anatomical parameters assisted by ImageJ 1.50i software (<http://rsb.info.nih.gov/ij/>).

3 Results

3.1 Micro-CT Image Acquisition

Root samples from the 1st–6th whorl of nodal roots in the *RGP* transgenic and the control plants (CK) were scanned by micro-CT, and the reconstructed images of root

cross-sections. (2 cm from the base of nodal roots) with an image resolution of 3.4 μm per pixel were obtained (Fig. 1). The anatomical organization could be easily characterized from these micro-CT images (Fig. 1), because of the high contrast between anatomical structures including metaxylem vessels, cortex and epidermis (Fig. 1B).

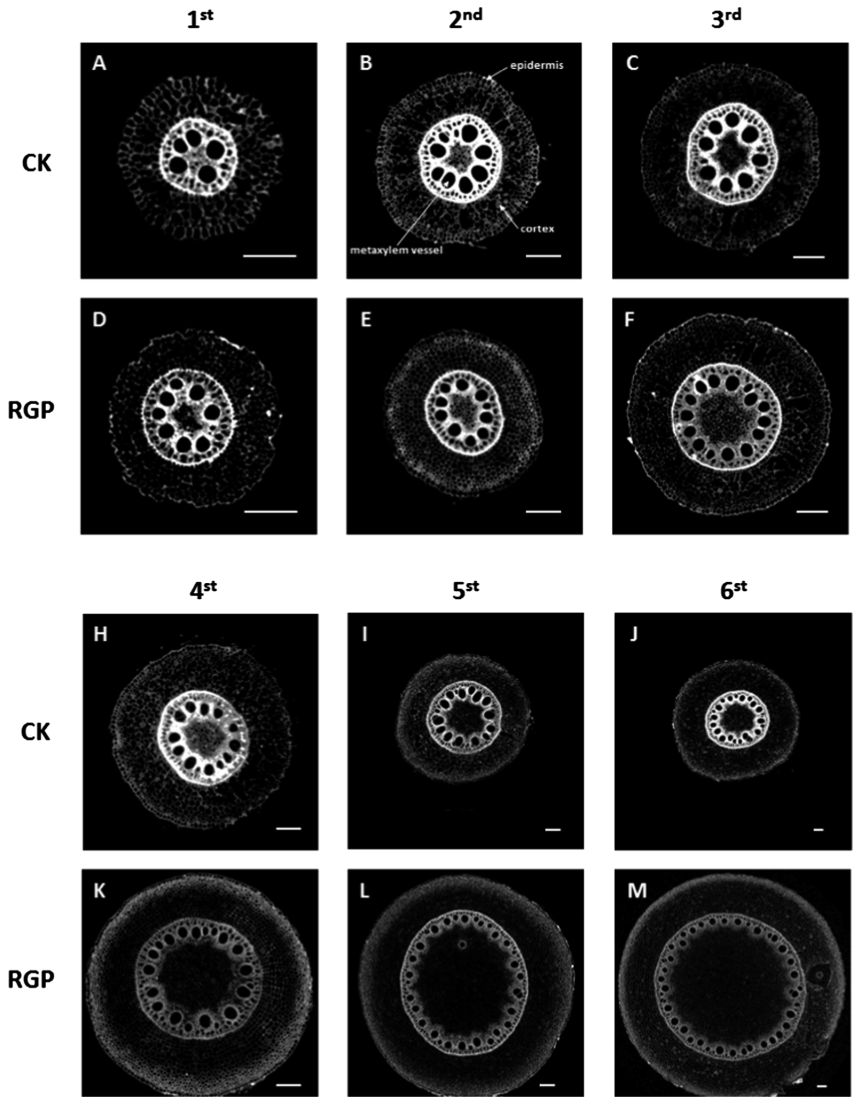


Fig. 1. Cross-section images of maize nodal roots by micro-CT scan showing anatomical organizations of the 1st–6th whorl of nodal roots from the control and *RGP* transgenic plants. The epidermis, cortex and metaxylem vessel are indicated in the picture B. Bars = 0.2 mm.

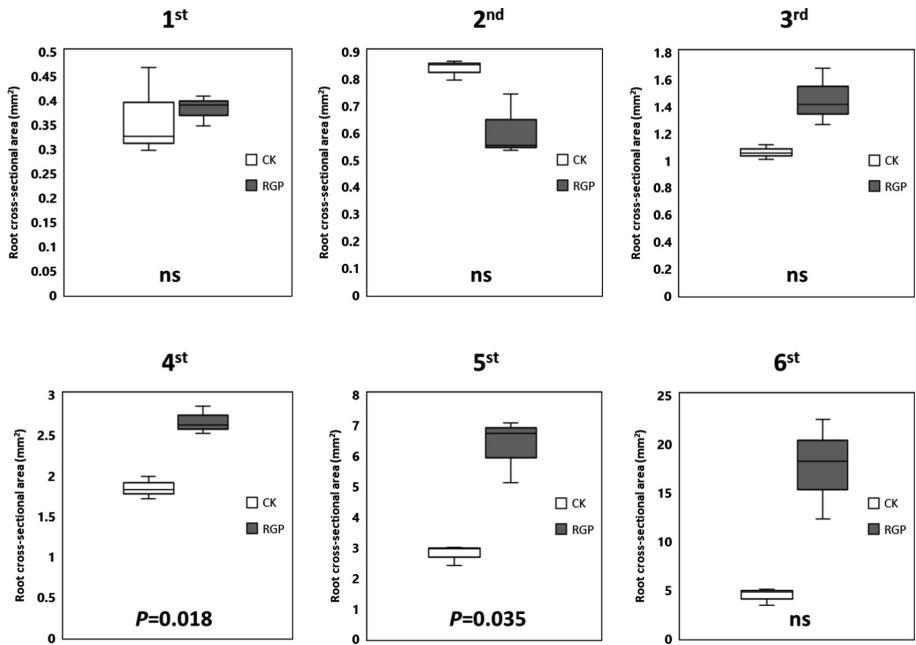


Fig. 2. Root cross-sectional area of the 1st–6th whorl of nodal roots from the *RGP* transgenic and control plants. The median value, lower and upper quartile are shown in the boxes. Error bars represent the highest and the lowest values. Student's *t*-test assay was used for *P* value calculation.

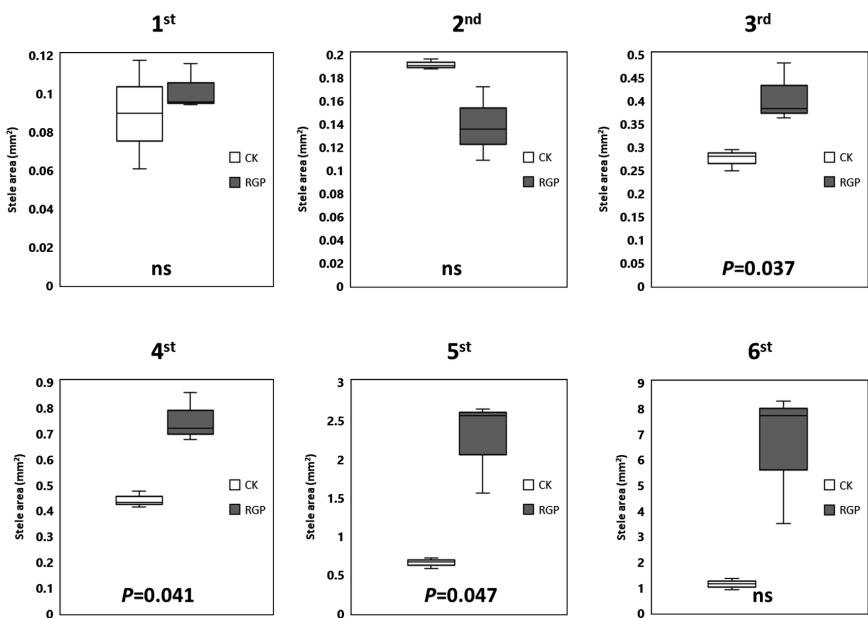


Fig. 3. Stele area of the 1st–6th whorl of nodal roots from the *RGP* transgenic line and the control line. The median value, the lower and upper quartile are shown in the boxes. Error bars represent the highest and the lowest values. Student's *t*-test assay was used for *P* value calculation.

3.2 Quantification of Root Anatomical Traits

Once the micro-CT cross-sectional images were obtained, quantitative information extraction could be performed assisted by the ImageJ software. Root and stele cross-sectional area of the 1st–6th whorl of nodal roots from the *RGP* transgenic and control (CK) plants were examined. The two parameters showed no significant difference in the 1st, 2nd and 6th whorls of nodal roots from the two genotypes (Figs. 2 and 3). However, the *RGP* transgenic line had significantly larger root cross-sectional area in the 4th and 5th whorls of nodal roots and larger stele area from the 3rd to 5th whorl of nodal roots (Figs. 2 and 3).

For the metaxylem vessels, both two maize lines show the increasing trend roughly in the number and the total area per root in the 1st–6th whorl of nodal roots (Fig. 4). The *RGP* transgenic plants had significantly more metaxylem vessels within the 1st–6th whorl of nodal roots compared to the control line with the exception of the 2nd whorl showing a non-significant difference (Fig. 4A). As to the total area of metaxylem vessels, the *RGP* transgenic plants also had a significant advantage in the 5th and 6th whorls of nodal roots compared to the control ones (Fig. 4B).

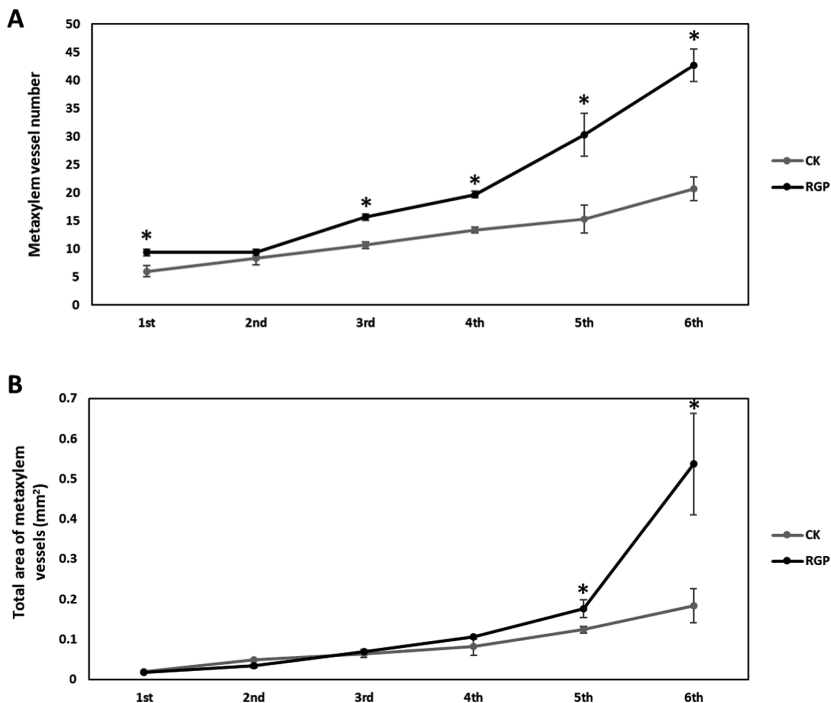


Fig. 4. Comparison of the metaxylem vessel number (A) and total area of metaxylem vessels (B) within the 1st–6th whorl of nodal roots between the *RGP* transgenic and control plants. Values are means \pm SD ($n = 3$) and asterisks mean statistically significant differences between the control and *RGP* transgenic lines. Student's *t*-test assay was used for *P* value calculation, $*P < 0.05$.

4 Discussion and Conclusions

In cereals such as maize, early work showed that roots lack secondary growth, so the metaxylem vessels play a key role in the axial water transport [6, 9]. As more water is expected to reach the metaxylem vessels in the basal part of nodal roots of adult maize plants, traits including the number and the size of metaxylem vessels in the basal region could be worthy of more attention compared to the distal region [11]. Consequently, the basal nodal root segments were examined in this work.

The X-ray micro-computed tomography is a non-destructive 3-D imaging technology which enables plant tissues to be examined in their natural state without serial-slicing procedures [12]. Micro-CT has an obvious advantage in the efficiency of image acquisition. It took only about 2 h for sample preparation (dehydration and drying), 20 min for image acquisition and reconstruction in this work. In the conventional histology, it is a time-consuming and laborious task to obtain a set of cross-sectional images. Moreover, plant tissues would be deformed or damaged during the inclusion, slicing into sections and staining processes despite cautious care using the conventional method. Recently, X-ray micro-CT has been applied to more and more plant organs, such as plant leaves [13] and crop seeds [14].

In summary, the drought-resistant *RGP* transgenic maize had obvious advantages in the root and stele cross-sectional area in the 4th and 5th whorls of nodal roots, and possessed more metaxylem vessels and larger total area of the metaxylem vessels within the 5th and 6th whorls of nodal roots in the water-limited environment. As the 4th–6th whorls of nodal roots would play significant roles at the reproductive growth stage of maize plants, these advantages could be in favor of axial water transport for further grain setting. Consequently, the distinct anatomical traits in the *RGP* transgenic maize plants could contribute to its drought resistance especially in the reproductive growth stage. In future, further researches will be carried out on the regulation mechanism of water acquisition in the *RGP* transgenic plants.

Acknowledgements. This work was supported by Beijing Natural Science Foundation (5174033), Beijing Postdoctoral Research Foundation (2016 ZZ-66), Postdoctoral Research Foundation of Beijing Academy of Agriculture and Forestry Sciences (Postdoctoral Number: 157939).

References

1. Heisey, P.W., Morris, M.L.: Economic impact of water-limited conditions on cereal grain production. In: Ribaut, J.M. (ed.) *Drought Adaptation in Cereals*. Haworth Press, New York (2006)
2. Lopes, M.S., Araus, J.L., van Heerden, P.D., Foyer, C.H.: Enhancing drought tolerance in C4 crops. *J. Exp. Bot.* **62**, 3135–3153 (2011)
3. van der Molen, M.K., et al.: Drought and ecosystem carbon cycling. *Agric. Forest. Meteorol.* **151**, 765–773 (2011)
4. Malamy, J.: Intrinsic and environmental response pathways that regulate root system architecture. *Plant, Cell Environ.* **28**(1), 67–77 (2005)

5. Burton, A.L., Williams, M., Lynch, J.P., Brown, K.M.: RootScan: software for high-throughput analysis of root anatomical traits. *Plant Soil* **357**, 189–203 (2012)
6. Lynch, J.P., Chimungu, J.G., Brown, K.M.: Root anatomical phenes associated with water acquisition from drying soil: targets for crop improvement. *J. Exp. Bot.* **65**, 6155–6166 (2014)
7. Tombesi, S., Johnson, R.S., Day, K.R., Dejong, T.M.: Relationships between xylem vessel characteristics, calculated axial hydraulic conductance and size-controlling capacity of peach rootstocks. *Ann. Bot.* **105**, 327–331 (2010)
8. Richards, R., Passioura, J.: Seminal root morphology and water use of wheat I. Environmental effects. *Crop Sci.* **21**, 249–252 (1981)
9. Passioura, J.: Roots and drought resistance. *Agric. Water Manag.* **7**, 265–280 (1983)
10. Pan, X., Ma, L., Zhang, Y., Wang, J., Du, J., Guo, X.: Three-dimensional reconstruction of maize roots and quantitative analysis of metaxylem vessels based on X-ray micro-computed tomography. *Can. J. Plant Sci.* **98**, 457–466 (2018)
11. Steinemann, S., Zeng, Z., McKay, A., Heuer, S., Langridge, P., Huang, C.Y.: Dynamic root responses to drought and rewatering in two wheat (*Triticum aestivum*) genotypes. *Plant Soil* **391**(1), 139–152 (2015)
12. Schoeman, L., Williams, P., du Plessis, A., Manley, M.: X-ray micro-computed CT tomography (μ CT) for non-destructive characterisation of food microstructure. *Trends Food Sci. Technol.* **47**, 10–24 (2016)
13. Dorca-Fornell, C., Pajor, R., Lehmeier, C., Pérez-Bueno, M., Bauch, M., Sloan, J., et al.: Increased leaf mesophyll porosity following transient retinoblastoma-related protein silencing is revealed by microcomputed tomography imaging and leads to a system-level physiological response to the altered cell division pattern. *Plant J.* **76**, 914–929 (2013)
14. Guelpa, A., Plessis, A.D., Kidd, M., Manley, M.: Non-destructive estimation of maize (*Zea mays* L.) kernel hardness by means of an X-ray micro-computed tomography (μ CT) density calibration. *Food Bioproc. Tech.* **8**, 1419–1429 (2015)



Effects of Exogenous Gamma-Aminobutyric Acid on Absorption and Regulation of Ion in Wheat Under Salinity Stress

Xiaodong Wang¹, Hongtu Dong¹, Peichen Hou², Hang Zhou¹,
Lulu He¹, and Cheng Wang²(✉)

¹ Department of Bio-Instruments, Beijing Research Center of Intelligent Equipment for Agriculture, Shugang Hua Yuan Middle Road No. 11, Haidian District, Beijing, China
wangxd@nercita.org.cn

² Beijing Research Center for Information Technology in Agriculture, Shugang Hua Yuan Middle Road No. 11, Haidian District, Beijing, China
wangc@nercita.org.cn

Abstract. Gamma-aminobutyric acid (GABA), a four-carbon non-protein amino acid, is a significant component of the free amino acid pool, there are numerous reports that rapid and large increases in GABA levels occur in plants, in response to a variety of biotic and abiotic stress. Based on its metabolism and putative roles in plants, GABA is considered a natural chemical to increase wheat salt-tolerance. So this study investigated the exogenous GABA on wheat seedling (*Triticum aestivum* L. cv. Changwu134 and zhouyuan9369) growth and absorption of salt ions under normal or salt-stressed conditions. The results demonstrated that salt stress inhibited growth of wheat seedlings, decreased dry weight and water content, altered ion balance within the stressed seedlings. Pretreatment with 50 mg/L GABA increased seedling biomass and K⁺ content in leaves, decreased Na⁺ content in leaves and roots under salt-stressed conditions by improving Na⁺ exclusion, K⁺ retention. These results indicated that exogenous 50 mg/L GABA improved seedling growth and alleviated the inhibition due to salt stress of wheat by altered ion balance. Exogenous GABA has the capability of restraining transportation of salt ions to leaves and sustaining normal function of leaves. And the effect of exogenous GABA is obvious in common variety (zhouyuan9369) than in salt-tolerance variety (changwu134).

Keywords: Gamma-aminobutyric acid (GABA) · Salinity stress
Wheat (*Triticum aestivum* L.) · Ion flux · Ion balance

1 Introduction

Salinity is one of the major environmental factors which limited plant growth and productivity, there is about 22% of the world's cultivated lands were influenced by salinity [1, 2]. Saline lands in China is approximately 4.88% of the total available lands, and 6.62% of the total agricultural lands have become salinization [3]. The saline soils are increasing with the development of industry and the irrigation in agriculture

[4]. Therefore, improve the salt resistance of crops and the cultivation measures are the most important methods for the use of saline soils in future [5].

There are lots of reports that several kinds of amino acids in plants under salt stress were increased, including proline, gamma-aminobutyric acid (GABA), and others. It has been proposed that free amino acids acted as osmolytes, which adjusted the osmosis [6]. Another view is that free amino acids through regulatory or osmosis protective functions, and then adjusted the osmosis in the plant [7]. Gamma-aminobutyric acid is one of the free amino acids in most organisms, which is a four-carbon non-protein amino acid and it plays very important role in organism [8]. There are numerous reports that rapid and large increases in GABA levels occur in plants, in response to a variety of biotic and abiotic stress, such as flooding, drought, cold, heat, hypoxia, UV radiation, pest, mechanical stimulation and damage [9–12]. GABA synthesis shows a relationship with plant defense and plant growth and development under stresses [8, 13]. The interaction between GABA and other stress-related phytohormones like abscisic acid and ethylene were also noted [14–16]. Recently roles for GABA as an intra-, inter-cellular and long-distance signaling molecule [17, 18], and an endogenous growth regulator [15, 19] in plants were suggested. Low concentration of GABA promotes growth but high level inhibits the growth of *Stellaria* [15].

There is some report on the effect of exogenous GABA on crop growth under abiotic stress conditions, which is essential to its possible agronomic application. Exogenous GABA application could promote the ROS metabolism and keep the stability of cell membrane, to enhance the tolerance of melon to salinity-alkalinity stress [20]. The resistance to root hypoxia short-term can be enhanced by the exogenous GABA on a sensitive genotype of *Prunus* [21]. Furthermore some reports show that exogenous Gamma-aminobutyric acid (GABA) ameliorated NaCl-induced K^+ efflux from barley roots rapidly [22, 23].

Based on its metabolism and putative roles in plants, GABA is considered a natural chemical to increase wheat thermo-tolerance. However, the effects of GABA on salt-resistance and ion transport under salt stress still need more experimental tests. We investigated the effects of GABA on seedling growth, accumulation of salt ions and the ion fluxes of Na^+ and K^+ on the response to salt stress in wheat, to explore the potential for its application to enhance the resistance of wheat to salt stress.

2 Materials and Methods

2.1 Plant Materials and Treatment

The experimental wheat materials were: Changwu134 (the salt tolerant one from Shanxi, china); Zhouyuan9369 (the high-yield one from Shandong Laizhou, china).

Seeds were surface disinfected with 5% NaClO for 6 min, then soaked in sterile water for 12 h. Each culture dishes put 50 seeds, lined with one layer of filter paper and wet with 20 ml treatment solutions: 1/2 Hoagland. Seeds were germinated in the dark with suitable germination temperature 25 °C, and changed the filter paper every 2 days. After 6 days, the young seedlings were about 6 cm height, then transferred these seedlings to plastic pots filled with 1/2 Hoagland solution, which grow on foam boards

(with same size holes). When the seedlings were 10 cm, the half of seedlings were treated with $50 \text{ mg}\cdot\text{L}^{-1}$ GABA solution (prepared with 1/2 Hoagland solution) and the control (1/2 Hoagland solution) for 24 h. After that, a half of the above seedlings were transfer to 150 mM NaCl solution. So the treatments in this experiment were CK, GABA, CK+NaCl, and GABA+NaCl. All the solutions were replaced every 2 days. Seedlings were grown in a growth chamber at day/night cycle of 14/10 h and normal temperature day/night was 25/20 °C. Flux measurement of Na^+ and K^+ were detected at 1 h and 24 h salt stress. After the salt stress, morphological characteristic, water content of plants were measured, leaves and roots were sampled from the each treatment plants of the six wheat materials and used for content analysis of Na^+ and K^+ .

2.2 Analysis of Na^+ and K^+

The extraction and measurement of Na^+ and K^+ in leaves and roots were tested according to Wang and Zhao with slight modifications [24]. Ten milliliters of dH_2O was added to the dried plant powder (each with 50 mg) and boiled for 2 h, then added dH_2O to make a final volume of 50 ml. After filtered, the Na^+ and K^+ content were assayed by the Atomic Absorption Spectrometry.

2.3 Measurements of Net K^+ and Na^+ Fluxes with SIET

K^+ and Na^+ net fluxes were non-invasively measured by using the scanning ion-selective electrode technique (SIET) (the SIET system is plants dynamic ion fluxes detection device, AI-IFDD-I; Beijing Research Center for Information Technology in Agriculture; Ma et al. [25]). The methods were slightly modified as described in Ma et al. [25]. In this experiment, we used the ion-selective microelectrode to measure the aim ions concentration gradients, which closed to the root and moved between two points in a stated distance of 30 μm . The time constant of the liquid ion exchange (LIX) electrodes and the mechanical distance of gradient are the main factors for stability of measurement. The SIET results can be as low as picomolar levels, the premise is each point need 1 to 2 s to measured, so every reciprocating process need about 3.3 s. The predefined sampling routine handled electrode move from one set to another, meanwhile moved by the three-dimensional micro stepper motor manipulator. The microelectrode ($\Phi 4.5 \pm 0.5 \mu\text{m}$, XY- CGQ-01; Xuyue (Beijing) Sci. and Tech. Co., Ltd., Beijing, China) was filled with a backfilling solution about 1 cm, the backfilling solution for Na^+ is 100 mM NaCl, K^+ is 100 mM KCl. Then the microelectrode front were filled with 15–20 μm of Na^+ (XY-SJ-Na; YoungerUSA) selective liquid ion-exchange cocktails (LIX) and 180–190 μm for K^+ (XY-SJ-K; YoungerUSA). Inserted the Ag/AgCl wire electrode holder (YG003-Y11; YoungerUSA) in the back of the electrode, and make sure the Ag/AgCl wire contact with the electrolyte solution in the electrode. For the accuracy of the experiment, using the calibrator verify the ion-selective electrodes by the calibration solution: (i) Na^+ : 0.5, 5 mM NaCl (Na^+ concentration in the measuring buffer was 0.9 mM); (ii) K^+ : 0.1, 1 mM KCl (K^+ concentration in the measuring buffer was 0.1 mM). The Nernst slopes of electrodes was $58 \pm 6 \text{ mV/decade}$ could be used in

our study, and the results were converted by Fick's law of diffusion into ion flux. The data and images acquisition, motion control were completed with the plants dynamic ion fluxes detection device's operational software.

3 Results

3.1 Effects of Exogenous GABA on Growth of Wheat Seedlings and Roots Under Salt Stress

24 h of salinity treatment affect the growth on shoot and root, with both stem and root length obviously reduced. However, the influence of salinity is different between wheat cultivars. For seedling height, compared with the control, the seedling length of Changwu134 was significantly lower after the salt treatment, and there was no difference between GABA treatment and CK after stress. For Zhouyuan9369, NaCl inhibited the growth of control, and there was no significant change under GABA treatment. For root length, GABA suppresses growth of Changwu134, under CK and salt stress conditions. In contrast, the application of GABA reduced the effect of salt stress for root (Fig. 1).

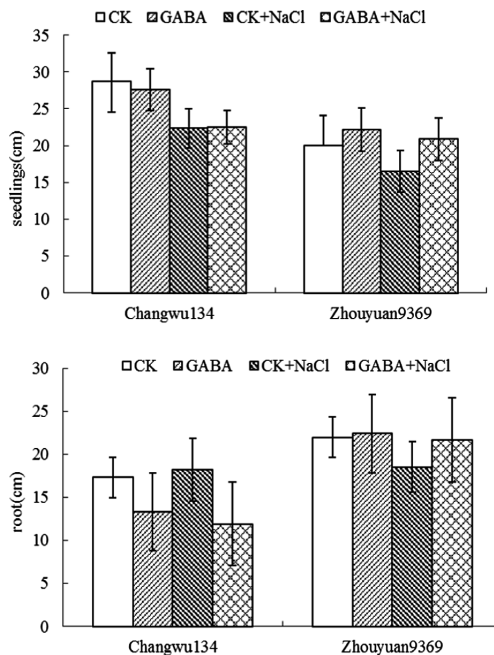


Fig. 1. Effect of GABA on seedling height and root length under normal conditions and salinity stress 2 days about two wheat cultivars: salt-tolerant (Changwu134) and high-yield (Zhouyuan9369)

3.2 Effects of GABA on Accumulation of Dry Matter in Wheat and Water Content in Leaves Under Normal Conditions and Salinity Stress

The growth of the two varieties of seedlings has been significantly inhibited by the treatment of 150 mM NaCl. Meanwhile, we identify the dry weight, water contain of the steam and the root have been reduced significantly.

The effects of GABA on the growth of wheat seedlings under salt stress were different due to cultivars. Pretreatment with 50 mg/L GABA increased stem dry weight, root dry weight and water content of stem for Zhouyuan9369. Changwu134, on the contrary, through GABA treatment, the water content of root become greater sensitivity under salt stress (Fig. 2).

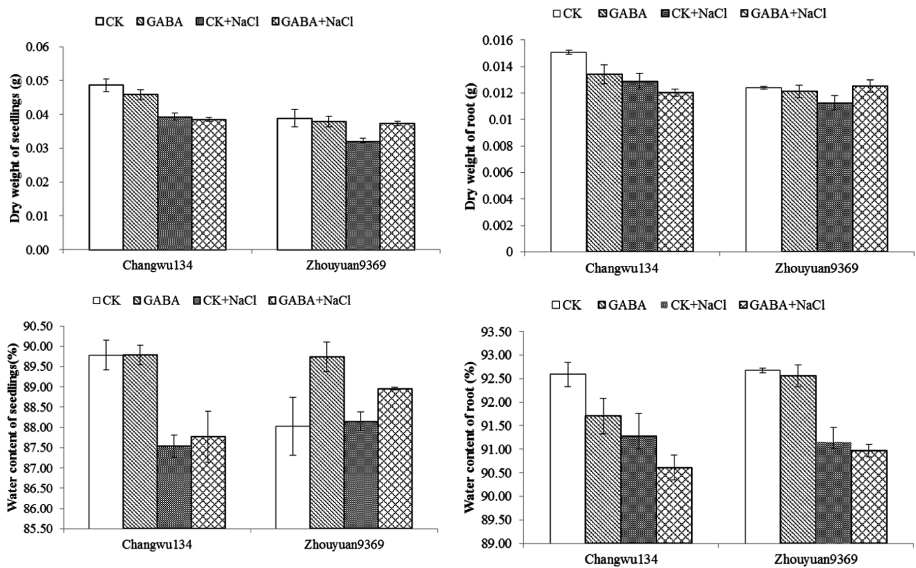


Fig. 2. Effect of GABA on dry weight and water contain under normal conditions and salinity stress 2 days about two wheat cultivars: salt-tolerant (Changwu134) and high-yield (Zhouyuan9369)

3.3 Exogenous GABA Changes in Content of K^+ and Na^+ in Roots and Leaves of Changwu134, Zhouyuan936 and Chinese-Spring Under Salinity Stress

In the 150 mM NaCl stress, K^+ concentrations were reduced in root of Changwu134, but there were no differences in stem K^+ content. Meanwhile the effect of salt stress on K^+ accumulation was significant fall off both in stem and root of Zhouyuan9369.

After pretreatment with 50 mg/L GABA, compared with NaCl treatment, NaCl+GABA treatment had no significant change the content of K^+ , except in leaves of Zhouyuan9369 were increased.

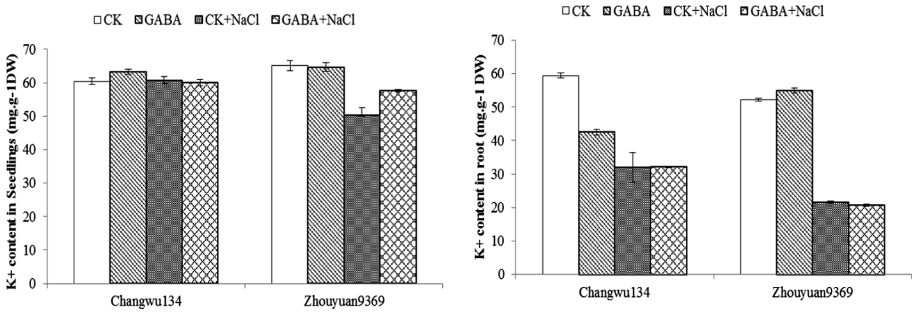


Fig. 3. The accumulation of K⁺ in the different organization of wheat under salt stress

Same as the most of research, salt stress caused dramatic increase in both stem and root Na⁺ content. After 150 mM NaCl treat 24 h, Changwu134 and Zhouyuan9369 were several fold increase in Na⁺ accumulation. It's worth noting that GABA greatly alleviated the effect of the accumulation of Na⁺ caused by NaCl stress on plants, especially on salt sensitive cultivar Zhouyuan9369, both in the shoot and root, however, in the root of Changwu134, have no evident changes.

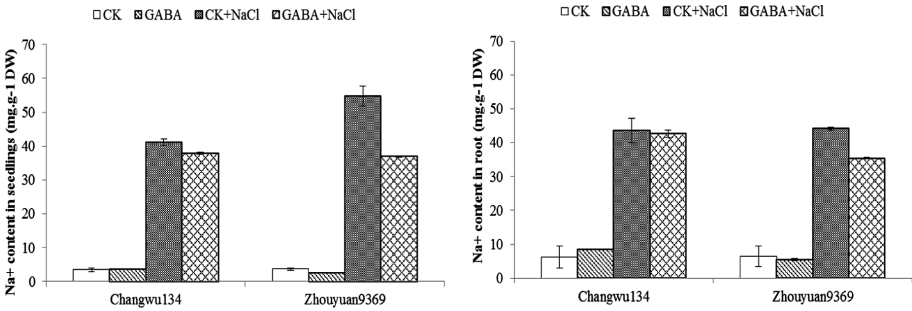


Fig. 4. The accumulation of Na⁺ in the different organization of wheat under salt stress

3.4 Effects of Exogenous GABA on K⁺ Fluxes in Roots of Changwu134, Zhouyuan9369 and Chinese-Spring Under Salinity Stress

To study the effect of GABA on K⁺ fluxes of Changwu134 and Zhouyuan9369 under the condition of salt stress. The non-invasive ion-selective microelectrode SIET technique was used to discover absorption of root K⁺ meiosis region in two kinds of wheat cultivars with the normal growth, 1 h-salt stress and 24 h-salt stress condition.

According to the detection results, it is found that K⁺ efflux of CK in salt-resistant variety Changwu134 was faster than that of wheat material processed by GABA under normal condition. With 1 h-salt stress, K⁺ efflux increases, while there is no obvious difference between K⁺ efflux of wheat material processed by GABA and CK. After 24 h salt stress, K⁺ efflux decreases and the distinction between them is still not

obvious. K^+ efflux of CK in salt-sensitive variety Zhouyuan9369 is a bit faster than that treated by GABA under normal condition. After 1 h of salt stress, CK and GABA treated efflux were both decreased, meanwhile, the treatment with GABA was become a little influx. After 24 h stress, K^+ efflux increased, and CK flux was significantly higher than GABA treated.

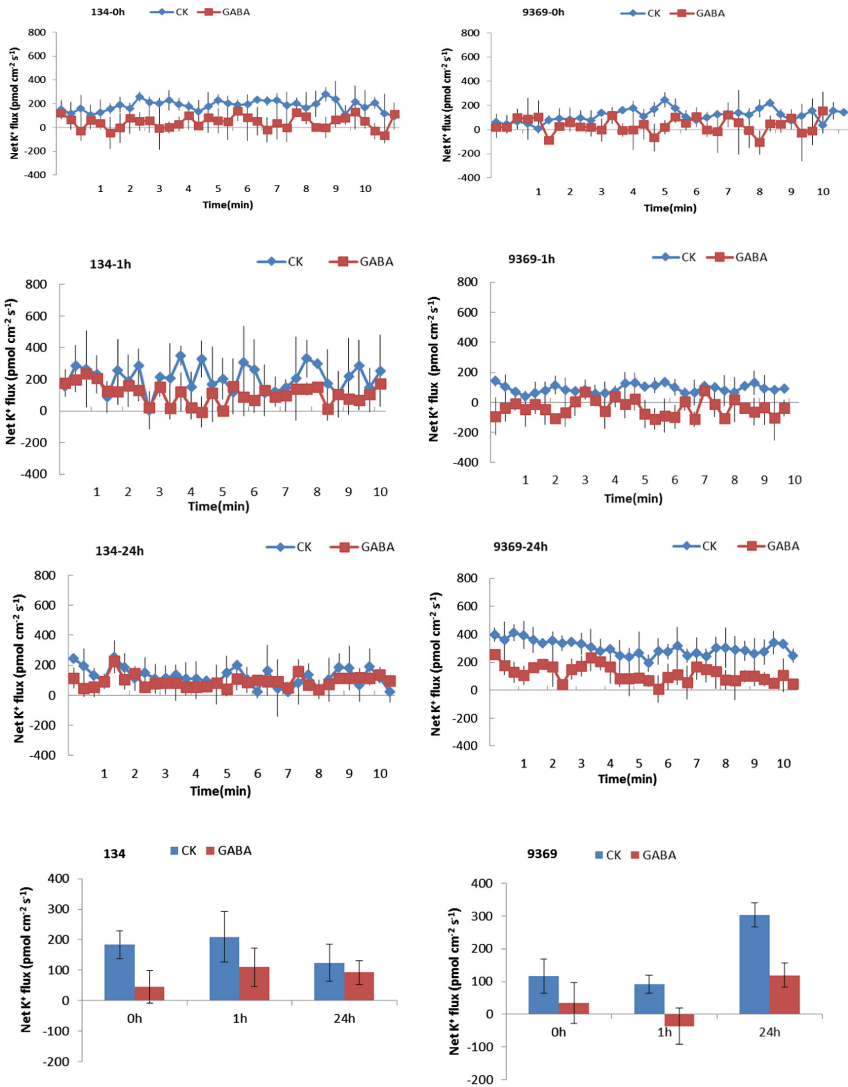


Fig. 5. K^+ fluxes measured from mature zone (10 mm from root tip) of two wheat cultivars in response to 150 mM NaCl treatments (0 h, 1 h, 24 h) (“+” response K^+ efflux; “-” response K^+ influx)

3.5 Effects of Exogenous GABA on Na⁺ Fluxes in Roots of Changwu134, Zhouyuan9369 and Chinese-Spring Under Salinity Stress

Ion fluxes data revealed that the Na⁺ flux at the root changed obviously after 1 h NaCl stress. There was a little influx of Na⁺ into the control seedlings, while the GABA pretreatment one had a higher efflux for Zhouyuan9369. For Changwu134, there was no significant difference in Na⁺ efflux between CK and GABA treatment compare with the control under non-stressed conditions.

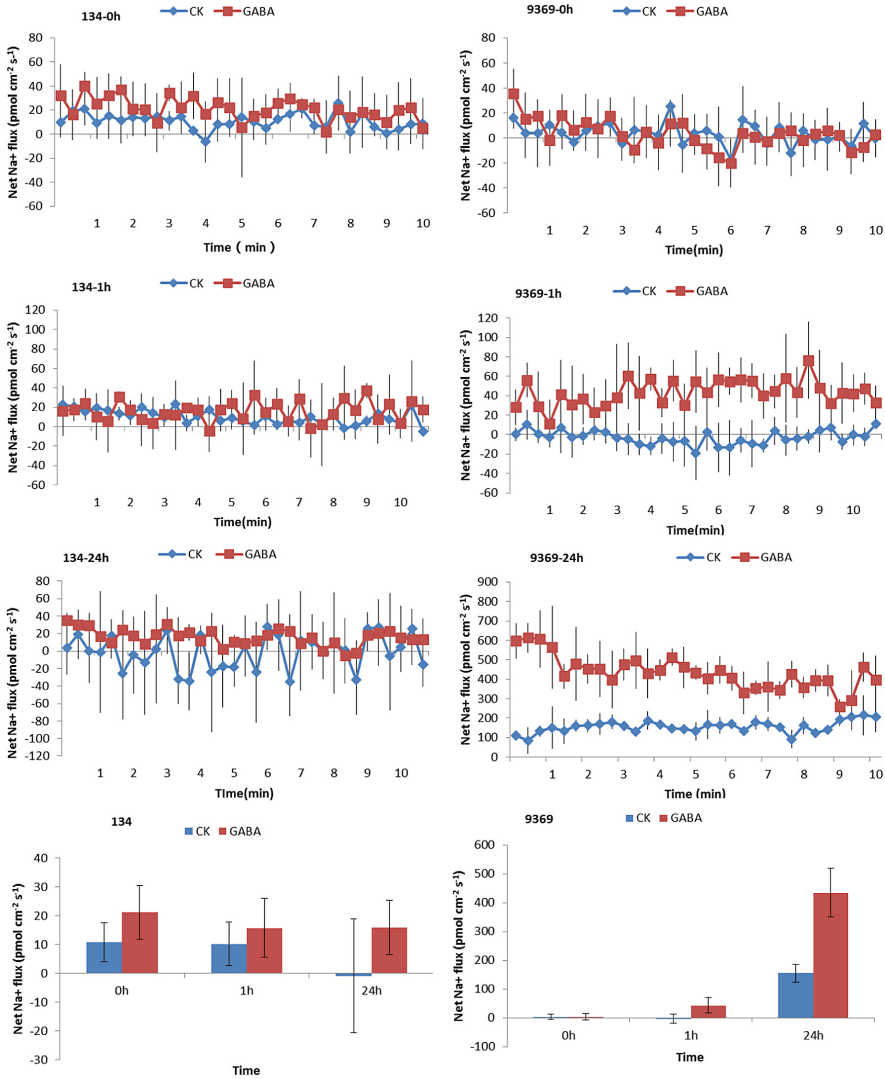


Fig. 6. Na⁺ fluxes measured from mature zone (10 mm from root tip) of two wheat cultivars in response to 150 mM NaCl treatments (0 h, 1 h, 24 h) (“+” response Na⁺ efflux; “-” response Na⁺ influx)

After 24 h stress, the CK of salt tolerant wheat materials changwu134 Na^+ efflux sharply reduced, while the GABA treatment remain the same as 1 h salt stress. On the contrary, CK and GABA treat of zhouyuan9369 showed efflux largely, and GABA treated one showed efflux rate greater than CK.

4 Discussion

The influence of salt stress on growth were investigated as plant height and dry weight differences in changwu134 and zhouyuan9369 plants. In this study, plant compared with the control, big difference was observed between GABA and non-GABA treatments. The salt stress treatment induced an obvious decrease in the growths and weights of the seedlings and root. The application of GABA alleviated the inhibition in seedling growth under salt stress, dry weights and water content of plant, Especially, zhouyuan9369 was enhanced remarkably, which similar to the results of Kathiresan [15]. In his work, with increasing in GABA concentration in the culture, the stem length was increased, until a concentration of 250 μM was reached. It is know that GABA treatment enhanced their endogenous GABA levels over control plants [15, 26]. Which indicated that endogenous GABA accumulation could be influence the stem elongation and the accumulation of dry mass.

According to the reports that when plant root subjected to salt stress, electrochemical gradient was established get through the plant membrane, and the ion homeostasis was disrupted by change of transported and accumulated of salt ions, and then the plant was injury [27–29]. In order to obtain a clear study of the GABA mechanisms essential, we focused only on the ion homeostasis in our work, to identify the effects of GABA to salt stress in wheat seedlings. In this study, a prominent K^+ efflux was observed in root after 1 h and 24 h of salinity treatment (Fig. 5), as reported by for rice [30] and broad bean [31]. Meanwhile, wheat roots excluded Na^+ mightly after 1 h and 24 h of salt stress (Fig. 6), which consistent with most of reports by Sun and others for *P. euphratica* [32], Cuin and others for wheat [33], and Xie for cotton [34]. As same as changes of K^+ flux, the content of K^+ in seedlings and root after 24 h stressed reduced by 21%–58% compared with that in the CK (Fig. 3). Although wheat roots excluded Na^+ after 1 h of salt stress, and to become stronger after 24 h of salt stress, but Na^+ accumulation in seedlings and root under salt treatment increased by 6.94–14.75 fold compared with the normal treatment after 24 h salt stress (Fig. 4). However, pretreatment with GABA further increased the Na^+ efflux, and decreased K^+ efflux compared with that of non-GABA treated seedlings under 150 mM NaCl stress. Therefore, compared with the non-GABA treated, the Na^+ content in the seedlings after 24 h stressed was remarkably decreased, whereas the K^+ content was obviously increased in the seedlings. This result suggested that the uptake of Na^+ can be limited by wheat seedling under short-time NaCl stress conditions. But the root had to absorb Na^+ and accumulated in leaves, when the salt stress prolong to 24 h (Fig. 4). So the Na^+/K^+ ratio in salt-stressed seedlings was increased. The salt tolerance plant depends on maintain a low Na^+/K^+ ratio in the cytoplasm, via to regulated the ion-selective of absorption and transport [35]. GABA decreased the Na^+ accumulation and increased the K^+ contents, especially in zhouyuan9369 which is not a salt-tolerant variety;

therefore, the Na^+/K^+ ratio was decreased. Accordingly, we hypothesize that exogenous GABA improved the seedling salt-tolerance by regulating the ion channels with high selectivity for K^+ over Na^+ to maintain a modest accumulation of Na^+ in the seedlings and to maintain a high K^+/Na^+ ratio.

5 Conclusion

In conclusion, our results showed that GABA improved seedling growth and alleviated the inhibition due to salt stress of wheat by altered ion balance, especially to the common variety (zhouyuan9369). Exogenous GABA can restrained transportation of salt ions to leaves and sustained normal function of leaves. But the role of GABA in plant under salt stress need make further study.

Acknowledgements. The authors are thankful for the funding from the National Natural Science Foundation of China (61571443), and Scientific and Technological Innovation Team of Beijing Academy of Agricultural and Forestry Sciences (JNKYT201604).

References

1. Bhatnagar-Mathur, P., Vadez, V., Sharma, K.K.: Transgenic approaches for abiotic stress tolerance in plants: retrospect and prospects. *Plant Cell Rep.* **27**, 411–424 (2008)
2. Munns, R., Tester, M.: Mechanisms of salinity tolerance. *Annu. Rev. Plant Biol.* **59**, 651–681 (2008)
3. Yang, J.: Development and prospect of the research on salt-affected soils in China. *Pedol. Sin.* **45**, 837–845 (2008). (in Chinese)
4. Lobell, D.B., Ortiz-Monsterio, J.I., Gurrrola, F.C., Valenzuela, L.: Dentification of saline soils with multiyear remote sensing of crop yields. *Soil Sci. Soc. Am.* **71**, 777–783 (2007)
5. Flowers, F.J.: Improving crop salt tolerance. *J. Exp. Bot.* **55**, 307–319 (2004)
6. Ford, C.W.: Accumulation of low molecular weight solutes in water-stressed tropical legumes. *Phytochemistry* **23**, 1007–1015 (1984)
7. Wang, H., Miyazaki, S., Kawai, K., Deyholos, M., Galbraith, D.W., Bohnert, H.J.: Temporal progression of gene expression responses to salt shock in maize roots. *Plant Mol. Biol.* **52**, 873–891 (2003)
8. Shelp, B.J., Bown, A.W., McLean, M.D.: Metabolism and functions of gamma-aminobutyric acid. *Trend in Plant Sci.* **4**(11), 446–452 (1999)
9. Narayan, V.S., Nair, P.M.: Metabolism, enzymology and possible roles of 4-aminobutyrate in higher plants. *Phytochemistry* **29**, 367–375 (1990)
10. Serraj, R., Shelp, B.J., Sinclair, T.R.: Accumulation of γ -amniobutyric acid in nodulated soybean in response to drought stress. *Physiol. Plant.* **102**, 79–86 (1998)
11. Shelp, B.J., Van Cauwenberghe, O.R., Bown, A.W.: Gamma aminobutyrate: from intellectual curiosity to practical pest control. *Can. J. Bot.* **81**, 1045–1048 (2003)
12. Koppitz, H., Dewender, M., Ostendorp, W., Schmieder, K.: Amino acid as indicators of physiological stress in common reed *Phragmites australis* affected by an extra flood. *Aquatic Bot.* **79**, 277–294 (2004)
13. Bown, A.W., Zhang, G.J.: Mechanical stimulation 4-aminobutyric acid (GABA) synthesis and growth inhibition in soybean hypocotyls tissue. *Can. J. Bot.* **78**, 119–123 (2000)
14. Kathiresan, A.: Gama-aminobutyric stimulates ethylene biosynthesis in sunflower. *Plant Physiol.* **115**(1), 129–135 (1997)

15. Kathiresan, A.: γ -aminobutyric acid promoted stem elongation in *Stellaria longipes*: the role of ethylene. *Plant Growth Regul.* **26**, 131–137 (1998)
16. Talannova, V.V., Akimova, T.V., Titov, A.F.: Effects of whole plant and local heating on the ABA content in cucumber seedling leaves and roots and on their heat tolerance. *Plant Physiol.* **50**, 90–94 (2003)
17. Bouche, N., Lacombe, B., Fromm, H.: GABA signaling: a conserved and ubiquitous mechanism. *Trends in Cell Biol.* **13**(12), 607–610 (2003)
18. Beuve, N., Rispaill, N., Laine, P., Clquet, J.B., Ourry, A., Deunff, E.L.: Putative role of γ -aminobutyric acid (GABA) as a long-distance signal in up-regulation of nitrate uptake in *Brassica napus* L. *Plant Cell Environ.* **27**, 1035–1046 (2004)
19. Palanivelu, R., Brass, L., Edlund, A.F., Preuss, D.: Pollen tube growth and guidance is regulated by *POP2*, an Arabidopsis gene that control GABA levels. *Cell* **114**, 47–59 (2003)
20. Xiang, L., Hu, L., Hu, X., Pan, X., Ren, W.: Response of reactive oxygen metabolism in melon chloroplasts to short-term salinity-alkalinity stress regulated by exogenous γ -aminobutyric acid. *Chin. J. Appl. Ecol.* **26**(12), 3746–3752 (2015). (in Chinese)
21. Salvatierra, A., Pimentel, P., Almada, R., Hinrichsen, P.: Exogenous GABA application transiently improves the tolerance to root hypoxia on a sensitive genotype of *Prunus* rootstock. *Environ. Exp. Bot.* **125**, 52–66 (2016)
22. Cuin, T.A., Shabala, S.: Exogenously supplied compatible solutes rapidly ameliorate NaCl-induced potassium eZux from barley roots. *Plant Cell Physiol.* **46**, 1924–1933 (2005)
23. Cuin, T.A., Shabala, S.: Amino acids regulate salinity-induced potassium efflux in barley root epidermis. *Planta* **225**, 753–761 (2007)
24. Wang, B.S., Zhao, K.F.: Comparison of extractive methods of Na^+ and K^+ in wheat leave. *Plant Physiol. Commun.* **31**(1), 50–52 (1995). (in Chinese)
25. Ma, R., Wang, C., Ma, Q., Hou, P.C., Wang, X.D.: Ion response of sunflower at sprouting stage to mixed salt stress. *Chin. J. Eco-Agric.* **25**(5), 720–729 (2017). (in Chinese)
26. Aghdam, M.S.: Impact of exogenous GABA treatments on endogenous GABA metabolism in anthurium cut flowers in response to postharvest chilling temperature. *Plant Physiol. Biochem.* **106**, 11–15 (2016)
27. Zhu, J.K.: Salt and drought stress signal transduction in plants. *Annual Rev. Plant Biol.* **53**, 247–273 (2002)
28. Sun, J., et al.: NaCl-induced alternations of cellular and tissue ion fluxes in roots of salt-resistant and salt-sensitive poplar species. *Plant Physiol.* **149**, 1141–1153 (2009)
29. Silva, P., Facanha, A.R., Tavares, R.M., Geros, H.: Role of tonoplast proton pumps and Na^+/H^+ antiport system in salt tolerance of *Populus euphratica* oliv. *Plant Growth Regul.* **29**, 23–34 (2010)
30. Coskun, D., et al.: K^+ efflux and retention in response to NaCl stress do not predict salt tolerance in contrasting genotypes of rice (*Oryza sativa* L.). *PLOS ONE.* **8**, 1–16 (2013)
31. Percy, W.J., Shabala, L., Breadmore, M.C., Guijt, R.M., Bose, J., Shabala, S.: Ion transport in broad bean leaf mesophyll under saline conditions. *Planta* **240**, 729–743 (2014)
32. Sun, J., et al.: H_2O_2 and cytosolic Ca^{2+} signals triggered by the PM H^+ -coupled transport system mediate K^+/Na^+ homeostasis in NaCl-stressed *Populus euphratica* cells. *Plant Cell Environ.* **33**, 943–958 (2010)
33. Cuin, T.A., et al.: Assessing the role of root plasma membrane and tonoplast Na^+/H^+ exchangers in salinity tolerance in wheat: in planta quantification methods. *Plant Cell Environ.* **34**, 947–961 (2011)
34. Xie, Z., Duan, L., Li, Z., Wang, X., Liu, X.: Dose-dependent effects of coronatine on cotton seedling growth under salt stress. *J. Plant Growth Regul.* **34**, 651–664 (2015)
35. Ashraf, M.: Salt tolerance of cotton: some new advances. *Crit. Rev. Plant Sci.* **21**, 1–30 (2002)



Development of Portable Dynamic Ion Flux Detecting Equipment

Peichen Hou^{1,2}, Cheng Wang^{1,2}, Xiaodong Wang¹, Aixue Li¹,
Peng Song¹, Bin Luo¹, Ye Hu¹, and Liping Chen¹(✉)

¹ Beijing Research Center of Intelligent Equipment for Agriculture,
Beijing Academy of Agriculture and Forestry Sciences, Beijing 100097, China
{houpc, wangc, wangxd, liax, songp,
luob, huy, chenlp}@nercita.org.cn

² Beijing Research Center for Information Technology in Agriculture,
Beijing Academy of Agriculture and Forestry Sciences, Beijing 100097, China

Abstract. Non-destructive testing of plant organs, tissues, and cells has important implications in studying the immediate physiological status of plants. The portable dynamic ion flux test equipment (PDIFTE) was developed based on Fick's first law of diffusion and the Nernst equation to achieve the ion flux measurement in $\text{pmol cm}^{-2}\text{s}^{-1}$. This equipment integrates micro-imaging, micro-signal processing, automation and control, and biosensor technologies with the original signal acquisition and conditioning module, the motion control module, the macro 3D automatically control platform, micro digital imaging system, electrostatic shielding coating, ion-selective microelectrode, and other components. PDIFTE can detect H^+ , K^+ , Na^+ , Mg^{2+} , Ca^{2+} , Cd^{2+} , Cl^- , NO_3^- , and NH_4^+ . This device can be used in the physiological mechanism research of salt-resistant, drought-resistant, cold-tolerant, heavy metal-resistant, and disease-resistant plants. It can also be used in the research on plant nutrition, ion channel-related gene function, and crop resistant breeding screening.

Keywords: Portable dynamic ion flux test equipment (PDIFTE)
Ion-selective microelectrodes · Liquid ion exchanger (LIX) · Ion flux

1 Introduction

Ion absorption is a marker of the normal life activity of plants. Detecting the absorption of external ions is essential in studying the physiology, anti-adversity, disease resistance, and nutrition of plants.

In the past, ion content in plants was detected using atomic absorption spectrophotometer [1], qualitative analysis by detecting the distribution of ions in plants using laser confocal fluorescent probe [2], or using the patch clamp technique to analyze the characteristics of single cell ion channels [3]. These static detection methods can be used to analyze the content, distribution, and absorption characteristics of ions in plants, but they cannot achieve lossless, dynamic, and long-term detection.

The development in physics, chemicals, mathematics, and other basic disciplines makes it possible to detect the dynamic absorption/transportation of ions in organisms

(transmembrane ion flux). Neuroscientist Lionel F. Jaffe of the US Marine Biological Laboratory put forward the initial model of ion flux detection technique by realizing the ion flux detection outside the cell or organization using Fick's law of diffusion and Nernst equation and the electrical principle of ion/molecule diffusion [4]. Newman of the University of Tasmania investigated the ion flux detection technique equipment and published an article on ion-selective microelectrodes detection of the velocity of H^+ and K^+ in the root tips of corn [5]. In 1995, Smith of the MBL published an article in *Nature* that detailed the detection of transmembrane flux transportation with the ion flux detection technique and reviewed the development of the ion flux detection technique [6]. In 2002, Franklin *et al.* of the University of Massachusetts established the buffer suitable for detecting ions and the research strategy by studying the velocity of H^+ in pollen tube [7]. In 2001, Newman elucidated the significance of ion detection in the gene function research [8]. In 2006, Davies reviewed the achievements of ion flux detection technique in the past years and their application status [9]. In recent years, ion flux detection technique has been used as an important solution for ion transport in many areas of plant research, such as plant physiology [10], plant water stress [11], plant salt stress [12], plant anti-heavy metals stress [13, 14], plant nutrition [15], and other fields [16–18]. With the continuous progress of technology and application of the continuous expansion of the ion flux detection technique, the United States Younger company and the AE company developed ion flux detection techniques for commercial products, such as the Younger model BIO-001B and the AE company model RP-1 ion flux detection technique system. The drawback of the equipment is that it is bulky and unsuitable for handling and field operation, thus limiting the use of the instrument only in the laboratory.

To overcome the shortcomings of the existing dynamic ion current detection equipment and its unsuitability for field operation, we developed the portable dynamic ion flux test equipment (PDIFTE) for laboratory and field environments. This equipment is fitted with a high-performance battery to ensure power supply, which effectively avoids the electrical signal acquisition interference of the alternating current and provides stable signal acquisition performance in the laboratory and field operation. Verified experimental results confirmed the data of PDIFTE and BIO-001B (Younger USA Sci. & Tech. Corp., USA) have very good consistency.

2 Basic Principle of the Dynamic Ion Flux Detection Equipment and System Scheme Design

2.1 Basic Principle of the Dynamic Ion Flux Detection Technique

The principle of the dynamic ion flux detection equipment is based on Fick's law of diffusion and the Nernst equation. Charged ions in the solution follow the law of diffusion from high concentration to low concentration. With the change in the electrochemical potential from high to low, the gradient can be detected. The diffusion velocity of ions in the solution can also be calculated. Finally, the concentration change rate of ions absorbed or released on the surface of the plant material in the solution can be calculated.

2.2 System Scheme Design

The dynamic ion flux detection equipment adopts the portable scheme design to develop original signal acquisition and modulation module, signal gathering and motion control module, macro 3D automatically controlled platform, micro digital imaging system, electrostatic shielding coating, ion-selective microelectrode design and preparation technique, and carried out the software design and development, finally realize the system integration and application after modulation (Fig. 1).

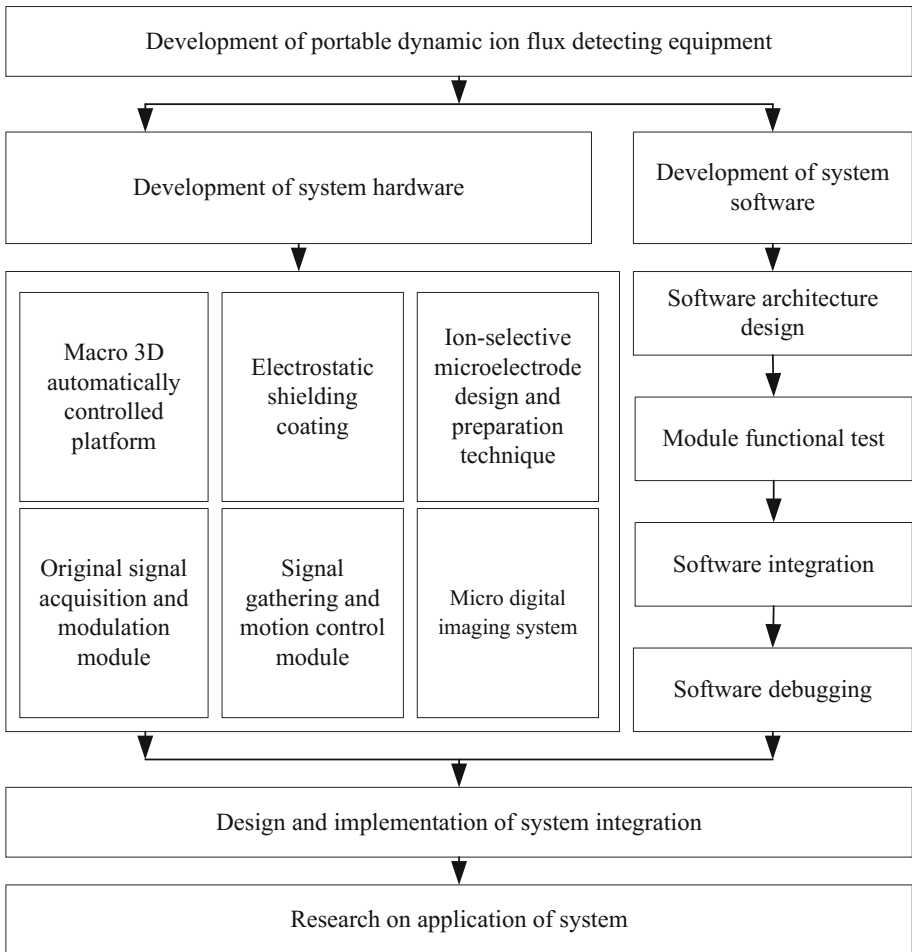


Fig. 1. System scheme design sketch

2.3 Hardware Design

2.3.1 System Structure

The dynamic ion flux detection equipment determines the locations of the tested material, reference electrode, and ion-selective microelectrode using a small inverted

microscope and high-resolution charge-coupled device (CCD) imaging. It controls the 3D modulation and movement of ion-selective microelectrodes using the high-precision macro 3D automatically controlled platform and the movement of the macro 3D automatically controlled platform using high-performance industrial computer. The system software realizes signal gathering and processing, CCD image presentation, and data analysis (Fig. 2).

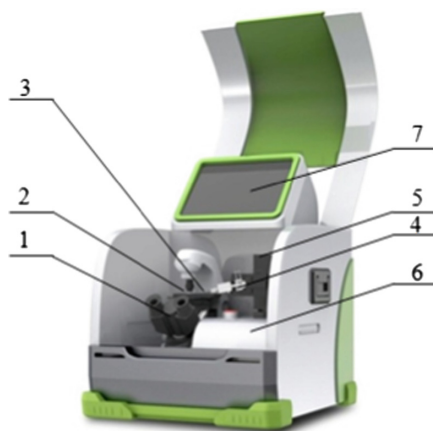


Fig. 2. System structure chart: 1. Microscope and CCD imaging module; 2. Detection pond; 3. Ion-selective microelectrode; 4. First signal amplifier; 5. Macro 3D automatically controlled platform; 6. Signal gathering/motion control/data analysis modules; 7. Touchscreen.

2.3.2 Hardware Components and Functions

The microscope and CCD imaging module comprises an inverted biological microscope eyepiece (15X and 20X; objective: 4X, 10X, and 25X). CCD is the colorful picture with the maximum resolution of 1024×768 . The sensor is a Sony CCD with an optical size of 1/3 in. and a maximum frame rate of 18 FPS. The AD conversion accuracy is 10 digits, and the exposure time is $1/15000 \text{ s}$ – 2 s using 12 V 1 W LED light source.

The detection pond is composed of a petri dish and buffer solution for testing. The components of the buffer solution vary because of the different target ions.

The ion-selective microelectrode has a length of 50 mm, tip diameter of 2–5 μm , outer diameter of the terminal of 1.5 mm, inside diameter of 1.05 mm, thickness of pipe wall at 0.225 mm, time resolution at 300 ms, space resolution at 5 μm , and tip-filled liquid ion exchanger (LIX).

The reference electrode comprises an isoplast pipe wall with a diameter of 2 mm embedded with Ag/AgCl electrode and filled with 3 M KCl with a resistance of 2.7 $\text{k}\Omega$.

The first signal amplifier comprises an input resistance of the initial signal acquiring module $\geq 10 \text{ T}\Omega$, with a minimum gain of $\times 10$ and a frequency response of DC $\sim 10 \text{ Hz}$.

The macro 3D automatically controlled platform has a micromanipulator with a moving precision of 0.5 μm , moving distance of driver at 1.25"/2.00" (30 mm/50 mm), no-load download speed of 2 mm/s, position precision at 0.2% of the moving distance, two-way repeatability at 1.0 μm , 400 paces per circle at a distance of 1.2598 for each pace.

The signal gathering/motion control/image gathering/data analysis module comprises Intel Atom N2600 low consumption industrial motherboard, 2G industrial INNODISK memory, 500G hardware, 9 V–30 V input 60 W broadband power module, signal processing, data gathering, motion control, and data analysis software developed based on Lab VIEW development environment.

The touchscreen is made of 12 in. of industrial capacitance touch screen with a resistance of $\geq 100 \text{ M}\Omega/25 \text{ V (DC)}$.

The electrostatic shielding coating adopts an electrostatic shielding paint with a density of 1.04 g/cm^3 and surface resistance of $<0.25 \text{ }\Omega/\text{cm}^2$.

2.4 Software Design

2.4.1 System Software Design

The system software interface consists of microscope control module, electrode control module, solution calibration module, data acquisition module, and system configuration module. The system software can control the hardware system, such as the microscope, CCD camera, and macro 3D automatically controlled platform. It can gather, process, and analyze the electrical signals and finally calculate the ion flux per $\text{pmol cm}^{-2}\text{sec}^{-1}$ (Fig. 3).

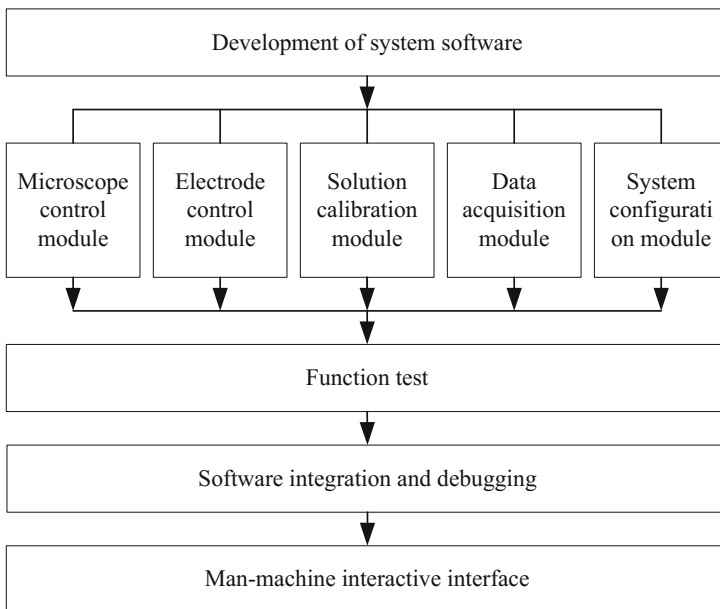


Fig. 3. Software design

2.4.2 Hardware Control and Data Gathering of the System

The microscope control module controls the LED light and the automatic focusing. The CCD module is integrated into the microscope and facilitated the real-time imaging, image recording, and management of the detection process using a colorful industrial CCD. The electrode control module of the macro 3D automatically controlled platform facilitates the serial port communication, motion command confirmation, accurate localization, and reciprocating motion of the ion-selective microelectrode. The solution calibration module performs the two-point calibration or the three-point calibration of the ion-selective microelectrode to ensure that the ion-selective microelectrode calibration value has a reasonable slope and intercept. The data acquisition module collects electrical signals and performs voltage difference processing and ion flux calculation. The system configuration module achieves different language switching and data export (Fig. 4).

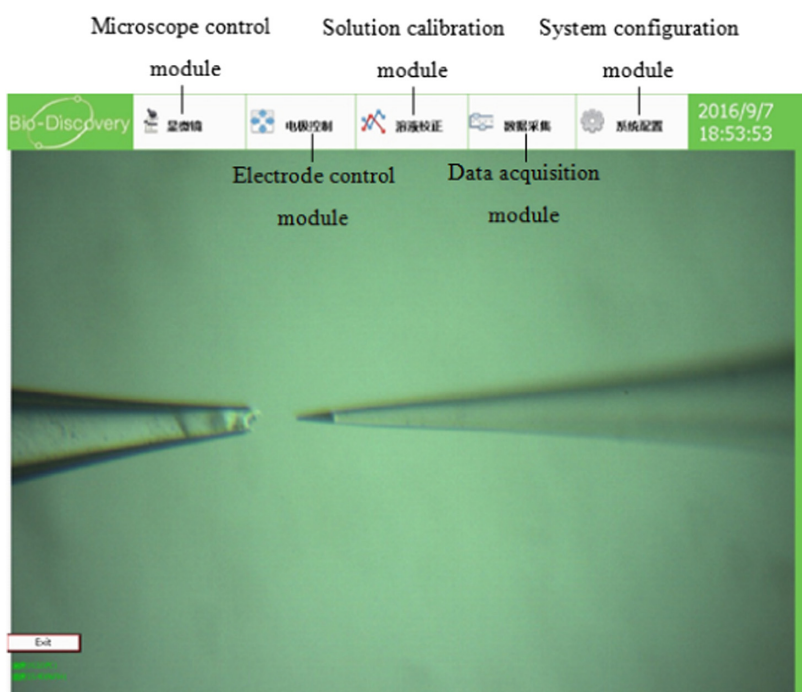


Fig. 4. Software interface

3 Verification of Results of the Dynamic Ion Current Testing Equipment and Commercial Ion Current Detection Instrument

3.1 Verification Method and Content

The ion source electrode was used as a proven ion-stable release source after the ion source electrode is dissolved by the internal components boiling at 1ml1MKCl and

9 ml 0.1% low melting agarose. Devices used to verification the experiment include PDIFTE and a commercialized ion flux detection technique system BIO-001B. K^+ LIX: Potassium ionophore I-cocktail A, Sigma–Aldrich, St. Louis, MO 63103, USA; backend filled LIX: 100 mM KCl; K^+ test buffer: 0.1 mM KCl; and 0.1 mM $CaCl_2$, 0.1 mM $MgCl_2$, 0.5 mM NaCl, 0.2 mM Na_2SO_4 , and 0.3 mM MES are used to detect K^+ and adjust pH 6.0 using KOH and HCl. The constant volume is 200 ml; the filling buffer is 100 mM KCl; the K^+ standard solution comprises 0.1 mM and 1 mM KCl; and the ion-selective microelectrode tip is 2–4 μm in diameter [12].

The filling liquid is pumped into the lumen from the back end of the ion-selective microelectrode and filled the electrode tip. Under micro-operation, the K^+ liquid ion exchanger was injected into the ion-selective microelectrode tip by negative pressure adsorption at a length of about 150 μm . Three K^+ ion-selective microelectrodes were made in the same manner. These ion-selective microelectrodes are used for BIO-001B and PDIFTE detection data comparison verification. The K^+ ion-selective microelectrode was calibrated with 0.1 mM and 1 mM KCl.

The K^+ ion source electrode was adhered at the center of the bottom of the detection pond using tape. The detection pond was filled with K^+ test buffer and placed on the inverted microscope 10X objective lens. The tip of the ion source electrode was located in the field of view of the display, and the ion-selective microelectrode movement is driven by the macro 3D automatically controlled platform, which finds the ion-selective microelectrode tip in the display field of view. The ion-selective microelectrode tip was moved to a position 20 μm from the tip of the ion source electrode (Fig. 4). BIO-001B and PDIFTE tested the ion source electrode to release K^+ ion flux at an uninterrupted test time of 5 min.

3.2 Validation Results

The results show that PDIFTE and BIO-001B continuously detected a stable release of K^+ flux from the K^+ ion source electrode. The data did not show abnormal fluctuations (Fig. 5). The released K^+ net flux detected by PDIFTE from the K^+ ion source electrode was 3.50274 $pmol\ cm^{-2}s^{-1}$. The BIO-001B detection of the K^+ ion source electrode showed a released K^+ net flux of 3.498082 $pmol\ cm^{-2}s^{-1}$. A test comparison of the K^+ ions released by the K^+ ion source electrodes at a distance of 20 μm by both devices confirms that PDIFTE and BIO-001B can achieve near-consistent data results (Fig. 6).

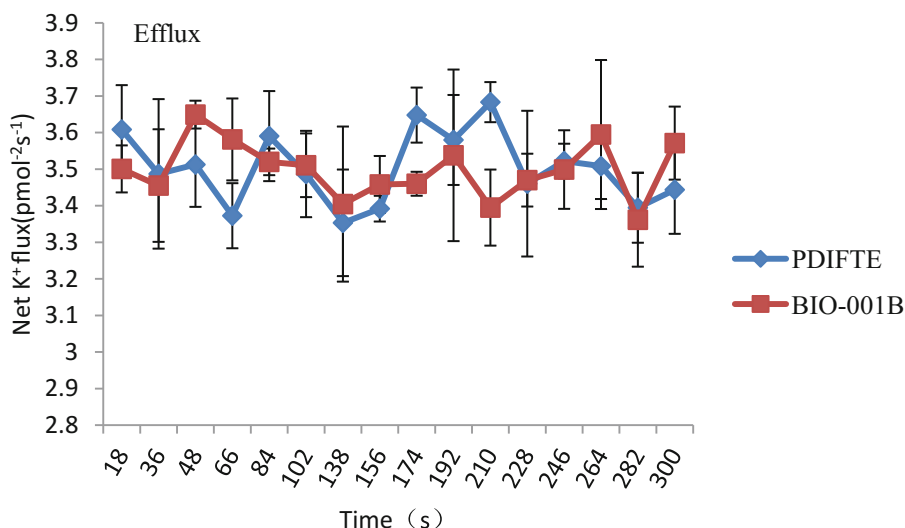


Fig. 5. Changes in the stable release of K^+ ion flux detected by PDIFTE and BIO-001B from the ion source electrode. The tip of the K^+ ion-selective microelectrode is 20 μm from the ion source electrode tip. The data acquisition of the K^+ ion flux was done continuously for 5 min. Each point represents the mean of three individual K^+ ion-selective microelectrodes detected. The bars represent the standard error of the mean.

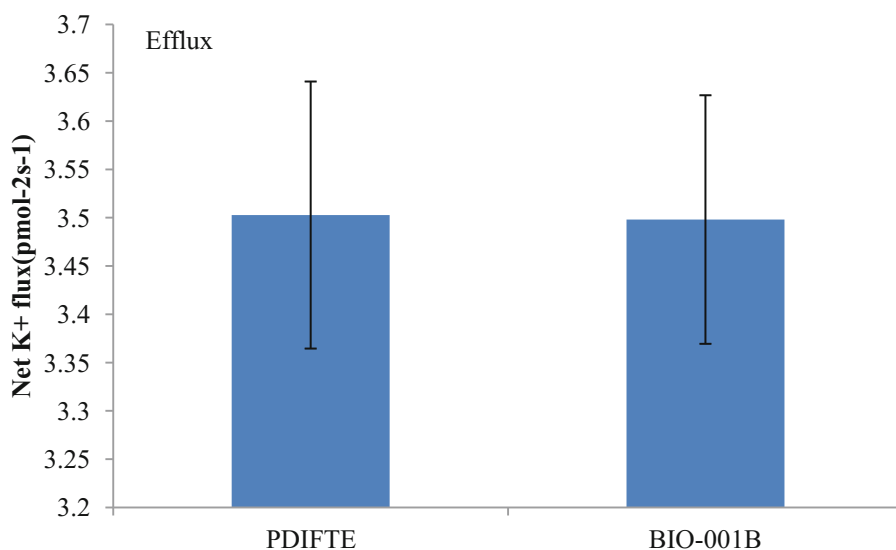


Fig. 6. Comparison of the stable release of K^+ net ion flux detected by PDIFTE and BIO-001B from the K^+ ion source electrode. The tip of the K^+ ion-selective microelectrode is 20 μm from the ion source electrode tip. Data acquisition of the K^+ ion flux was done continuously for 5 min. Each column represents the mean of three individual K^+ ion-selective microelectrodes detected. The bars represent the standard error of the mean.

4 Results and Discussion

The dynamic ion flux detection equipment solved the weak electrical signal gathering of the modulation technique under complex laboratory and field operation environments. Power to all parts of the system was supplied by battery, thus avoiding the interference of the AC in the signal gathering. The small size and structure satisfy the in-situ, real-time, and non-destructive detection and analysis of plant tissues, organs, and other dynamic ion fluxes in the laboratory and field environments. PDIFTE can be used in the physiological mechanism research of salt-resistant, drought-resistant, cold-tolerant, heavy metal-resistant, and disease-resistant plants. It can also be used in the research on plant nutrition, ion channel-related gene function, and crop resistant breeding screening. The test result data of PDIFTE and BIO-001B have very good consistency. The signal detected by PDIFTE was more stable and can be applied for target material ion flux detection.

Acknowledgments. This research was supported by the Postdoctoral Funding from Beijing Academy of Agriculture, Scientific and Technological Innovation Team of Beijing Academy of Agricultural and Forestry Sciences (JNKYT201604, and Fundings from the National Natural Science Foundation of China (Grant No.61571443).

References

1. Welz, B., Sperling, M.: Atomic Absorption Spectrometry. Wiley, Hoboken (2008)
2. Denk, W., Strickler, J.H., Webb, W.W.: Two-photon laser scanning fluorescence microscopy. *Science* **248**(4951), 73–76 (1990)
3. Li, J., Long, Y., Qi, G.N., Xu, Z.J., Wu, W.H., Wang, Y.: The Os-AKT1 channel is critical for K⁺ uptake in rice roots and is modulated by the rice CBL1-CIPK23 Complex. *Plant Cell* **26**(8), 3387–3402 (2014)
4. Jaffe, L.F., Nuccitelli, R.: An ultrasensitive vibrating probe for measuring steady extracellular currents. *J. Cell Biol.* **63**(2), 614–628 (1974)
5. Newman, I.A., Kochian, L.V., Grusak, M.A., Lucas, W.J.: Fluxes of H⁺ and K⁺ in corn roots characterization and stoichiometries using ion-selective microelectrodes. *Plant Physiol.* **84**(4), 1177–1184 (1987)
6. Smith, P.J.: Non-invasive ion probes—Tools for measuring transmembrane ion flux. *Nature* **378**(6557), 645 (1995)
7. Franklin-Tong, V.E., Holdaway-Clarke, T.L., Straatman, K.R., Kunkel, J.G., Hepler, P.K.: Involvement of extracellular calcium influx in the self-incompatibility response of *Papaver rhoeas*. *Plant J.* **29**(3), 333–345 (2002)
8. Newman, I.A.: Ion transport in roots: measurement of fluxes using ion-selective microelectrodes to characterize transporter function. *Plant Cell Environ.* **24**(1), 1–14 (2001)
9. Davies, E.: Electrical signals in plants: facts and hypotheses. In: Volkov, A.G. (ed.) *Plant Electrophysiology*, pp. 407–422. Springer, Heidelberg (2006). https://doi.org/10.1007/978-3-540-37843-3_17
10. Tang, B., Yin, C., Wang, Y., Sun, Y., Liu, Q.: Positive effects of night warming on physiology of coniferous trees in late growing season: leaf and root. *Acta Oecol.* **73**, 21–30 (2016)

11. Xu, W., et al.: Abscisic acid accumulation modulates auxin transport in the root tip to enhance proton secretion for maintaining root growth under moderate water stress. *New Phytol.* **197**(1), 139–150 (2013)
12. Sun, J., et al.: NaCl-induced alternations of cellular and tissue ion fluxes in roots of salt-resistant and salt-sensitive poplar species. *Plant Physiol.* **149**(2), 1141–1153 (2009)
13. Zhang, Y., et al.: Paxillus involutus-facilitated Cd^{2+} influx through plasma membrane Ca^{2+} -permeable channels is stimulated by H_2O_2 and H^+ -ATPase in ectomycorrhizal populus \times canescens under cadmium stress. *Front. Plant Sci.* **7**, 1975 (2016)
14. Wang, F., et al.: Different responses of low grain-Cd-accumulating and high grain-Cd-accumulating rice cultivars to Cd stress. *Plant Physiol. Biochem.* **96**, 261–269 (2015)
15. Han, Y.L., et al.: Nitrogen use efficiency is mediated by vacuolar nitrate sequestration capacity in roots of *Brassica napus*. *Plant Physiol.* **170**(3), 1684–1698 (2016)
16. Nemchinov, L.G., Shabala, L., Shabala, S.: Calcium efflux as a component of the hypersensitive response of *Nicotiana benthamiana* to *Pseudomonas syringae*. *Plant Cell Physiol.* **49**(1), 40–46 (2008)
17. Shabala, S., et al.: Plasma membrane Ca^{2+} transporters mediate virus-induced acquired resistance to oxidative stress. *Plant Cell Environ.* **34**(3), 406–417 (2011)
18. Tang, W., et al.: The calcium sensor GhCaM7 promotes cotton fiber elongation by modulating reactive oxygen species (ROS) production. *New Phytol.* **202**(2), 509–520 (2014)



Study on Intelligent Monitoring Technology for Composting of Agricultural and Livestock Wastes

Hualong Li^{1,2}, Miao Li^{1(✉)}, Xuanjiang Yang^{1,2}, Zelin Hu¹,
Zhirun Ma¹, and Xianwang Liu³

¹ Institute of Intelligent Machines, Chinese Academy of Sciences,
Hefei 230031, Anhui, China

lihualong2007@163.com, mli@iim.ac.cn

² University of Science and Technology of China, Hefei 230026, Anhui, China

³ Anhui Agricultural University, Hefei 230026, Anhui, China

Abstract. Composting is a harmless treatment process of agricultural and livestock wastes are widely used for grass-roots livestock farms. Composting temperature control is the key technical condition in composting process. In most current production process, the mechanical artificial temperature measuring devices were adopted to measure the composting temperature, which could not monitor the composting process resulting in the dumping delay. Meanwhile, the pathogenic microorganisms in compost could not be inactivated effectively. To solve this problem, an intelligent monitoring device was designed to realize the on-line monitoring of the whole process of composting. Users can query the compost temperature in real time by smart phone so as to dump in time to improve the inactivation efficiency of pathogenic microorganisms and reduce the loss of compost nutrients. The composting monitoring experiments showed that the system could monitor the composting process on-line and will have broad application in the field of livestock waste recycling.

Keywords: Intelligent monitoring · Agricultural and livestock waste
Harmless treatment · Composting temperature

1 Introduction

Aerobic composting is the process of absorption, oxidation and decomposition of organic compounds and pathogenic microorganisms in wastes such as livestock, sludge and straw with oxygen and bacteria. In the whole process, the composting temperature directly affect the inactivation of pathogenic microorganisms and the decomposition of organic compounds. Therefore, the composting temperature control is the key technical issue of the composting process [1, 2]. In most current production process, the mechanical artificial temperature measuring devices were adopted to measure the composting temperature, which could not monitor the composting process in real time, and would result in the dumping delayed, so that the pathogenic microorganisms in compost could not be inactivated effectively [3, 4].

To solve this problem, an intelligent monitoring device was designed to realize the real-time monitoring of the whole process of composting with the temperature sensor, which had the advantages of high temperature measurement accuracy, simple operation. Compared with the traditional use of mechanical temperature measuring instrument, the data support for scientific composting can be provided. Users could query the temperature of the compost online by web page or smartphone APP, and then dump in time, which could save the cost of composting and reduce the loss of compost nutrients.

2 The Design of Monitoring Systems

As Fig. 1, the system consisted of three parts: data acquisition terminal, server and client. The data acquisition terminal included a data collector and the composting temperature sensor. The sensor was connected to the data collector by RS-485 bus. STM32F103VB (ARM 32-bit Cortex-M3 CPU) was used as the core processor in the data collector, which could achieve the local storage and remote transmission of the data. The server was developed based on the Web platform, SQL Server 2008 and ASP.NET. And it was used to receive data storage and processing. The clients contained two parts: Web query and Android mobile client [5].

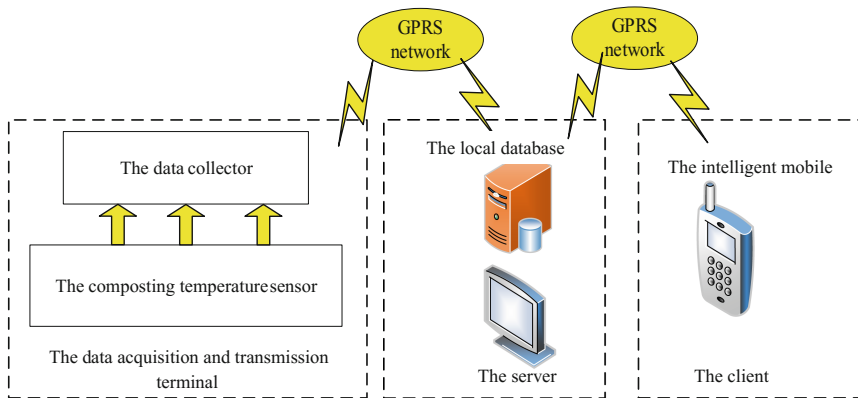


Fig. 1. The diagram of intelligent compost monitoring device

2.1 The Hardware Design

The data collector adopted the low power consumption microprocessor STM32F103VBT6 as CPU. The system function modules included the RS-485 data acquisition, GPRS wireless data sending, real-time clock, SD card data storage, human-computer interaction and power management (Fig. 2).

The RS-485 data acquisition module was used to connect with the composting temperature sensor (CG-01, Hefei heinford Electronic Technology Co. Ltd. The measurement range of air temperature: $-40\text{ }^{\circ}\text{C} - +85\text{ }^{\circ}\text{C}$, with the measurement accuracy: $\pm 0.3\text{ }^{\circ}\text{C}$). The GPRS wireless data sending module could accomplish the real-time transmission of the composting temperature data to the remote server. Combining with SD card data storage module and the real-time clock module, the temperature data was stored in SD card. This design could effectively solve the data loss which due to the instability of signal transmission and improve the reliability of the real-time monitoring [6].

Human-computer interaction module included a 4.3-inch LCD and a keyboard. The composting temperature could be displayed in real-time on the LCD. The LCD power could be turn off or open automatically, which can reduce system power consumption and extend the LED working life. The keyboard was used for setting of the periodic sampling, filtering and the controlling mode of data transmission. Power management module included a DC12V 48AH large capacity cell group and the corresponding power conversion circuit.

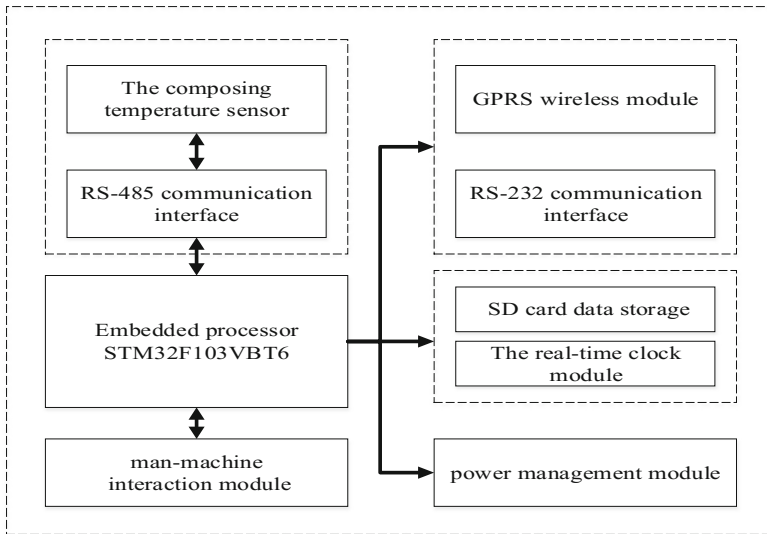


Fig. 2. The data structure diagram of the data collector

2.2 The Software Design

The Software Design of Data Collector. The monitoring terminal software was written in C language mainly to complete the collection of environment data and send them to the GPRS network by using Keil integrated development environment as software programming and debugging platform (Fig. 3).

When the system started, the data collector first determined whether the acquisition time reached, and sent the data acquisition command to the composting temperature sensor. If not, it continued to wait. Then the data collector received the composting temperature data from the sensor after three milliseconds delay, and performed CRC check. If the check result was correct, the data would be sent to the GPRS network. Otherwise the data acquisition instruction would be sent again.

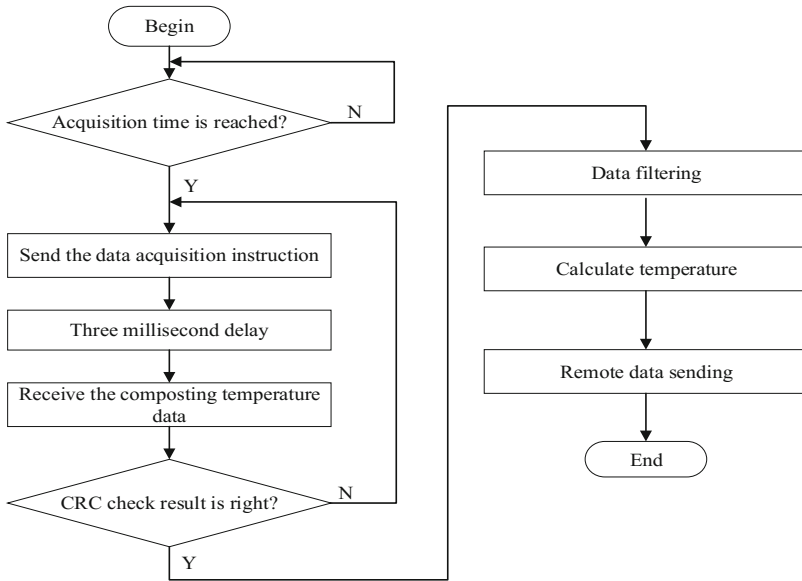


Fig. 3. The data structure diagram of the data collector

To improve the reliability of the sensor measurement and reduce the measurement error caused by interference, the average filtering algorithm of anti-impulse interference was used to process the received temperature data. The average filtering method had the advantages of simple calculation, less time consumption and less storage, which was very suitable for embedded system.

The Software Design of Monitoring System. The software of monitoring system platform included three parts: the server-side monitoring centre software, visual system software and the data query android APP.

The server-side monitoring centre software program was developed in Visual Studio 2010 with C# programming, which ran on the backend of the server. The service monitoring program established a communication connection with GPRS-DTU unit to accomplish two-way communication between the embedded terminal and the server. After the connection was established, the service monitor would parse the package data sent by the embedded device and store the parsed data in the SQL Server 2008 database. The specific process of the service monitoring centre software was shown in Fig. 4 [7, 8].

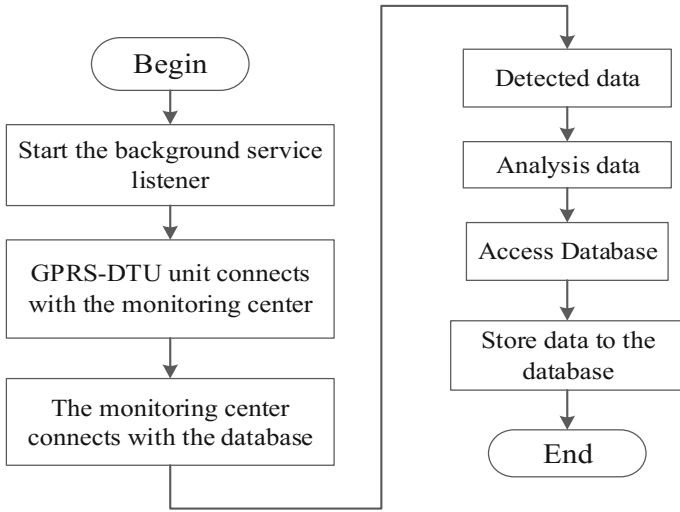


Fig. 4. The software design of data monitoring center

Data visualization platform mainly accomplished the function of data query, data download, data graphical display and remote control of monitoring device. The design process was shown in Fig. 5 and the compost temperature monitoring platform web page was shown in Fig. 6.

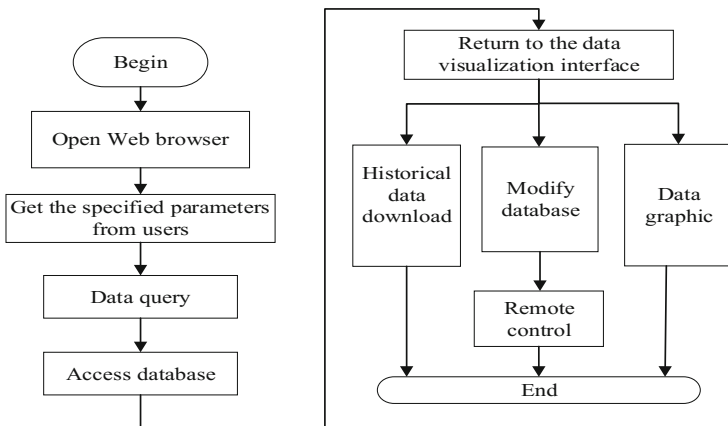


Fig. 5. The software design process of visual system



Fig. 6. The compost temperature monitoring platform web page

The data query android APP was developed based on eclipse. The android SDK plug-in was installed in eclipse. With android widget, Android clients could be quickly developed. In addition, the web service program was written on the server side to open the corresponding service port, so that the users could access the database from the Android client. The design process was shown in Fig. 7.

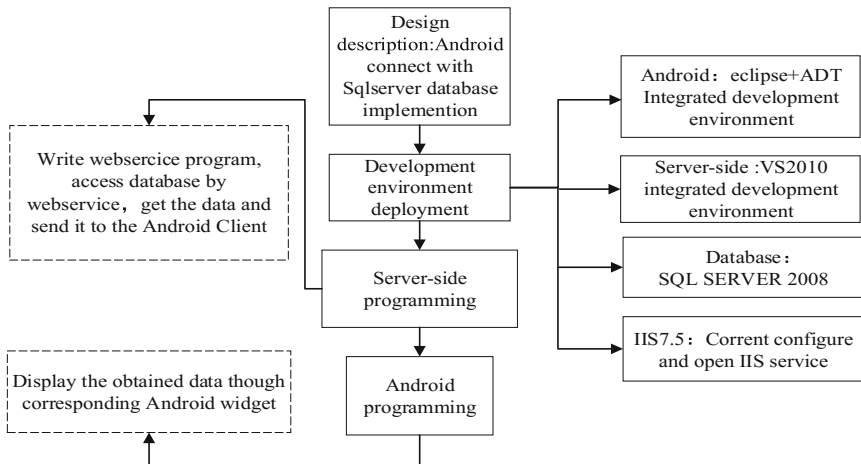


Fig. 7. The Android APP design process

3 Design of Composting Monitoring Experiments

The composting monitoring experiments were carried out from January 13 to February 22, 2017, in Linquan Quanyou breeding pig farm, Fuyang city, Anhui Province. Pig manure was taken from this pig farm, with C/N: 13: 1 and the moisture content: 70%.

The corn stalk was taken from the Zhangguan town of Linquan county, with C/N: 53: 1 and the moisture content: 12%. First, the corn straw was crushed into 2 cm length, and fresh pig manure was treated by the processing of wet and dry separation. Second, pig manure and corn straw were mixed according to the proportion of 4:1 and the water content of the pile was 65%–75%. Then mixed with inoculum (*Bacillus* 0.3%). Finally, divided into two piles which were named No. 1 compost and No. 2 compost with each weighed about 500 kg. No. 1 composting temperature was collected every ten minutes with the intelligent composting process monitoring device. No. 2 composting temperature was measured at 12:00 noon every day with the mechanical artificial temperature measuring device. Two composting temperature measure devices were inserted in the middle of each compost down at 30 cm. No. 1 compost was turned once every 3 days after the temperature rose to 55 °C. No. 2 compost was turned once every 4 days [9–11].

4 Results and Discussion

In Fig. 8, we could see clearly that the temperature of the compost rose rapidly after composting, and it reached the high temperature degradation stage of composting from fifth days (>50 °C). Then the temperature of 55 °C or more lasted for 17 days. According to the U.S. Environmental Protection Agency (USEPA) reported the composting temperature was maintained at 55 °C 3 days or 50 °C for more than 7 days, the pathogenic bacteria could be effectively killed and the sanitary standard of fecal harmless for static aerobic composting could be conformed [12–14]. After 22 days of fermentation, composting entered the cooling stage. By 34 days, the composting temperature was close to the environment temperature indicating that the compost had been basically rotted [15].

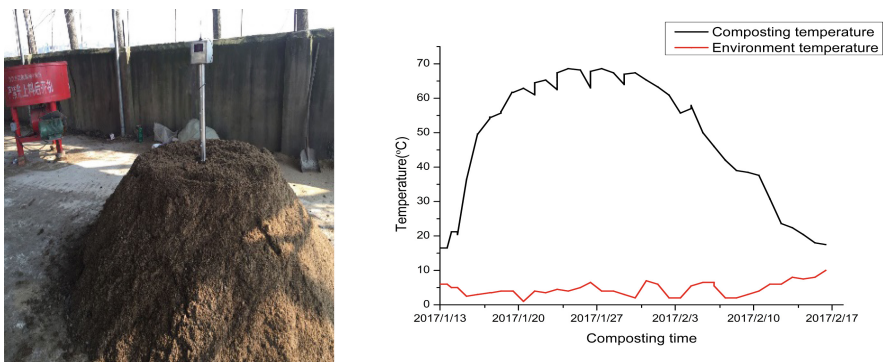


Fig. 8. No. 1 compost and its temperature change

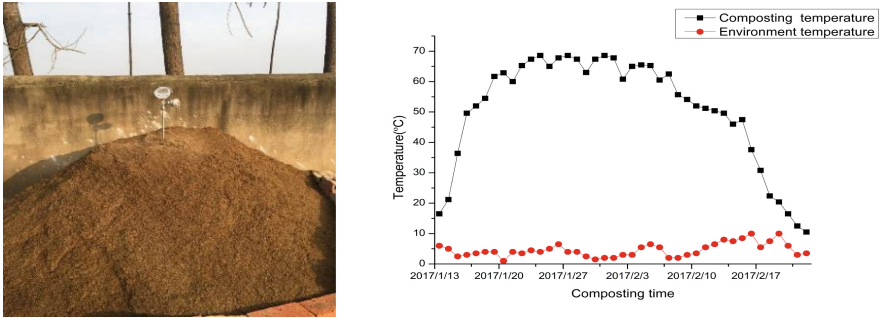


Fig. 9. No. 2 compost and its temperature change

However, in Fig. 9, there were about 21 days of the maintenance time at the temperature of 55 °C or more for No. 2 compost. After 25 days of fermentation, the compost entered the cooling stage, and the composting temperature was not close to the environmental temperature until the fortieth day. From these two sets of composting, it could be seen that the intelligent composting process monitoring device could be used to monitor the whole process of composting. Accordingly, the users could do the dump in a timely manner, which could reduce the composting time. In this compost experiments, No. 1 compost took about 6 days less than No. 2 compost.

5 Conclusions

In conclusion, an intelligent monitoring system was proposed in this paper, which could achieve the real-time monitoring of the whole process of composting. Users can query the temperature of the compost by web page or smartphone APP with the advantages of high temperature measurement accuracy, simple operation. Accordingly, the users can do the dump in time to improve the inactivation efficiency of pathogenic microorganisms and reduce the loss of compost nutrients. Therefore, this monitoring technology can significantly shorten the composting cycle, improve the compost quality, and have great potential.

Acknowledgments. The authors thank the financial support by the National High Technology Research and Development Program (SS2013AA102302); National Key Research and Development Program (2016YFD0800901-03); National Key Technology Research and Development Program of the Ministry of Science and Technology of China (2014BAD08B11). And thank Linquan Quanyou breeding pig farm (Fuyang city, Anhui Province) for providing experimental conditions.

References

1. Cesaro, A., Belgiorno, V., Guida, M.: Compost from organic solid waste: quality assessment and European regulations for its sustainable use. *Resour. Conserv. Recycl.* **94**, 72–79 (2015)
2. Park, K.: Composting of food waste and mixed poultry manure inoculated with effective microorganisms. *Eng. Agric. Environ. Food.* **4**(4), 106–111 (2011)
3. Khelil, O., Cheba, B.: Thermophilic cellulolytic microorganisms from Western Algerian sources: promising isolates for cellulosic biomass recycling. *Proc. Technol.* **12**, 519–528 (2014)
4. Xu, T., Li, L., Zhen, C., Sun, L., Fu, H., Zhang, X.: Effects of different microorganism consortiums on composting process of pig manures and their nutrient status. *Transect. Chin. Soc. Agric. Eng.* **24**(11), 217–221 (2008)
5. Li, H., et al.: Intelligent monitoring system for laminated henhouse based on internet of things. *Trans. Chin. Soc. Agric. Eng.* **31**(Supp. 2), 210–215 (2015)
6. Troubleyn, E., Moerman, I., Demeester, P.: QoS challenges in wireless sensor networked robotic. *Wirel. Pers. Commun.* **70**(3), 1059–1075 (2013)
7. Sharma, V., Kumar, R.: A cooperative network framework for multi-UAV guided ground Ad Hoc networks. *J. Intell. Robot. Syst.* **77**(3/4), 629–652 (2015)
8. Li, Q., Wang, X.C., Zhang, H.H., Shi, H.L., Ngo, H.H.: Characteristics of nitrogen transformation and microbial community in an aerobic composting reactor under two typical temperatures. *Bioresour. Technol.* **137**, 270–277 (2013)
9. Tandy, S., Healey, J.R., Nason, M.A., Williamson, J.C., Jones, D.L., Thain, S.C.: FT-IR as an alternative method for measuring chemical properties during composting. *Bioresour. Technol.* **101**(14), 5431–5436 (2010)
10. Zhou, J., Wang, L., Xu, Q., Jiang, X.: Optimum ratio of pig manure to edible fungi residue improving quality of organic fertilizer by composting. *Transect. Chin. Soc. Agric. Eng.* **31**(7), 201–207 (2015)
11. Shi, L., et al.: Improving enzyme activity by compound microbial agents in compost with mixed fruit tree branches and pig manure during composting. *Transect. Chin. Soc. Agric. Eng.* **31**(5), 244–251 (2015)
12. Wang, H., et al.: Investigation of livestock and poultry manure composting treatment to eliminate parasites and eggs. *J. Southwest Univ. Nat.* **39**(03), 307–310 (2013)
13. China National Standardization Management Committee: Sanitary standard for the non-hazardous treatment of night soil (GB7959-2012). Standards Press of China, Beijing (2013)
14. Cao, Y., Chang, Z., Huang, H., Xu, Y., Li, C., Wu, H.: Effect of compost inoculation on pig manure composting. *Transect. Chin. Soc. Agric. Eng.* **31**(21), 220–226 (2015)
15. Huang, X., Han, Z., Shi, D., Huang, X., Wu, W., Liu, Y.: Nitrogen loss and its control during livestock manure composting. *Chin. J. Appl. Ecol.* **21**(1), 247–254 (2010)



Optimization and Simulation of Fertilizer Guide Device Parameters Based on EDEM Software

Hai Ding^{1,2}, Xiaofei An^{2,3}(✉), Guangwei Wu^{2,3}, Liwei Li^{2,3},
and Qingzhen Zhu^{1,2,3}

¹ College of Mechanical and Electronic Engineering,
Northwest A&F University, Yangling 712100, China

² Beijing Research Center of Information Technology in Agriculture,
Beijing 100097, China
anxf@nercita.org.cn

³ National Research Center of Information Technology in Agriculture,
Beijing 100097, China

Abstract. In order to match the fertilizer line and seed line, fertilizer application should be homogeneous enough. A new fertilizer guide device was designed. It was consisted of fertilizer guide groove, shunted parts and cover plate. According to the theoretical analysis and practical experience, the main parameters affecting the effect of applying fertilizer were specified, including groove installation angle, the angle and the position of shunt part. With the single factor simulation experiment, the optimization and simulation of fertilizer guide device parameters were carried out based on EDEM software. The selected parameter interval was determined firstly. And then 10 set experiment results were obtained within the determined range. When the angle of diverter component was 33°, the distance was 25 mm, and the angle of guide groove installation was 37°, the best fertilizer application result was obtained. The simulation experiment provided a reference for the guide flow device design.

Keywords: Fertilizer diversion · Precision fertilization · EDEM · Simulation

1 Introduction

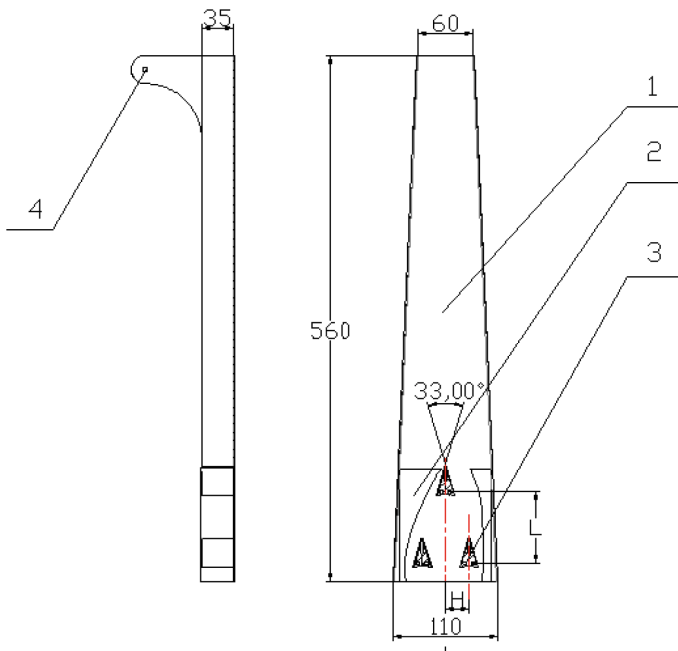
Fertilizer application was an important part in wheat growth period. In order to match the fertilizer line and seed line, uniform fertilizer distribution was the first step. At present, it has the phenomenon of accumulation or uneven distribution in the fertilizer application. Domestic and foreign scholars have researched on fertilizer mechanism parameter to improve the fertilizer effect [1–8]. Zeng [4] proposed that appropriate agricultural policies should be adopted and the level of agricultural machinery should also be improved. Wei Guojian [5] designed 1GF-200 rice rotary tillage fertilizer applicator, with the rectangular tube and sector fertilizer export, which could help improve fertilizer uniformity in the rice field. By testing experimental prototype, within 50 m, the uniformity coefficient of horizontal fertilization was 21%; the apiece row consistency variability coefficient was 2.28%; the stability variability coefficient of the full fertilizer quantity was 1.09%. Experimental results showed that it had a rational

design and reliable function and its working quality could be easily applied to agricultural requirement. Dun Guoqiang designed fertilizer allocation device to layered fertilization, which was typical of fertilizer uniform distribution device and Fertilizer adjustable ratio device to achieve the uniform of application. And by the simulation and the experimental verify, the qualified coefficient was 0.928 and the Fluctuation coefficient was 78. So the device was a rational design and could improve use efficiency of fertilizer. But referring to lots of research, the literature of wheat fertilizer guide device could not be found. As a result, it was needed to design a new kind of fertilizer guide device to improve the uniformity of fertilizer distribution.

The purpose of this study was to design a new fertilizer guide device to improve the uniformity of the base fertilizer application. And then the fertilizer simulation analysis was carried out to obtain the optimization parameter based on EDEM software.

2 Structure and Principle

The fertilizer guide device was consisted of fertilizer guide groove, shunt parts and cover plate. Figure 1 showed the device model. The fertilizer was discharged with three parts by the shunt parts. The cover plate could prevent fertilizer from splashing. We designed pattern draft for the guide device to make fertilizer discharged smoothly. The three triangular shunt parts were installed at the bottom of the device. The triangle configuration made it running smoothly. The cover plate size could cover the shunt parts. Otherwise, fertilizer would be blocked.



1 Fertilizer guide device 2 Cover plate 3 Shunt parts 4 Mounting hole

Fig. 1. Assembly drawing of fertilizing device

3 Key Component Parameter Designing

(1) Fertilizer guide groove designing

The total length of the fertilizer guide groove was 560 mm. The diameter of the fertilizer outlet was 40 mm. And the width of the top of the fertilizer guide groove was 60 mm. There were eight fertilizer outlets on the fertilizer mechanism. The total width of fertilizer mechanism was 2.0 m. Limited by the dimensions of fertilizer mechanism, the base of the fertilizer guide groove was determined about 110 mm. The installation angle of the fertilizer guide device had influence on the effect of fertilizer distribution. After the preliminary simulation, the angle was determined by the range of 30° – 50° (Fig. 2).

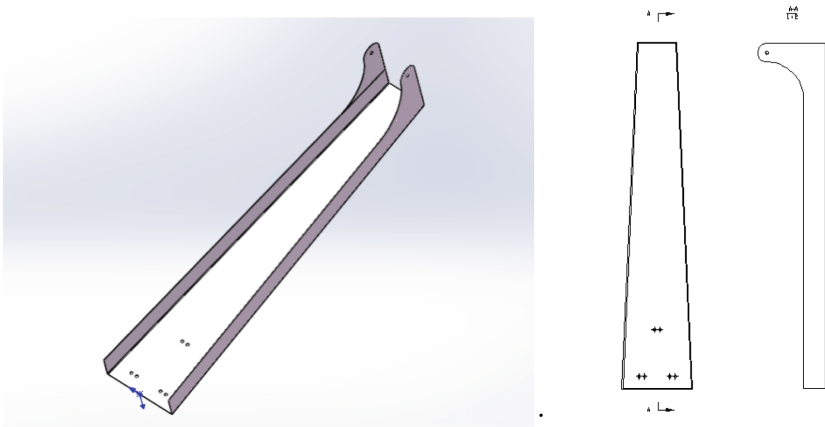


Fig. 2. Fertilizer guide device

(2) Shunt part designing

The shunt part was designed as triangle structure method, with fillet of the head, installed with M4 bolts. The opening angle of the shunt component was an important factor affecting the distributary effect of the fertilizer. If the opening angle was too large, as a result, fertilizer would be blocked. The pretreatment result showed that the middle export discharged 7.05 g when the opening angle was up to 42° and both sides were 13.1 g and 13.7 g under condition of 1000 particles. The side total weight was twice than that of the middle. So the shunt parts opening angel should be less than 42° . Meanwhile it should be greater than 30° on the consideration of the mounting hole size (Fig. 3).

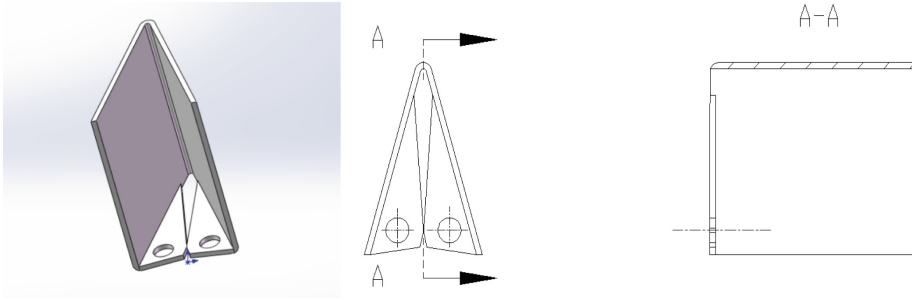


Fig. 3. The shunt part

(3) Cover plate designing

The cover plate was used to prevent fertilizer from splashing. It was need to cover the shunt parts exactly. As for the width, the cover plate shall be fully fitted to the inner wall of the fertilizer guide device in order to prevent the fertilizer from escaping from both sides. There was mounting hole on the cover. Its position was equal to the shunt parts. The adjustable vertical distance of the installation hole was longer than the transverse. And the two installation hole were symmetrical distribution (Fig. 4).

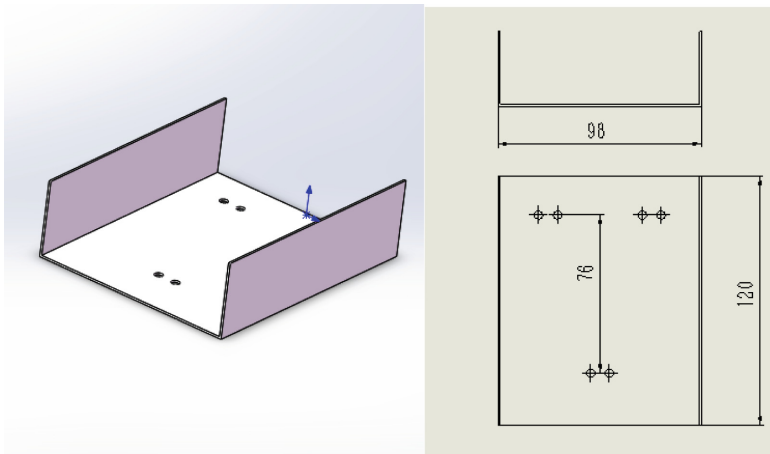


Fig. 4. The cover plate

4 Simulation Experiment of Parameter Optimization for Fertilizer Device

The effect of fertilizer distribution was closely related to the installation angle of the fertilizer guide device, the opening angel and position of the shunt parts. The simulation model of device was established based on EDEM software.

4.1 Simulation Parameter Setting

(1) Experimental Parameter Setting

Referring to the relevant research [9–11], the Le Sol compound fertilizer was selected as experiment material. Subsequently, thirty particles were selected to determine the average diameter of fertilizer and the mass of particle. Table 1 was the particle statistic data with the 30 selected particles. The final average mass was 0.0335 g.

Table 1. Particle parameter statistics

Particle parameters	Values
Average mass/g	0.0335
Mass standard deviation/g	0.0171
Average radius/mm	1.6405
Radius standard deviation/mm	0.1526

The fertilizer particles were modeled by sphere. The following equation was material density of the fertilizer particles.

$$\rho_f = \frac{m_f}{V_f} = \frac{m_f}{\frac{4}{3}\pi\left(\frac{D_f}{2}\right)^3} = \frac{6m_f}{\pi D_f^3} \quad (1)$$

ρ_f was particle density, g/cm³; m_f was particle mass, g; V_f was particle volume, mm³; D_f was average particle diameter, mm, average particle density $\rho_f = 1.861$ g/cm³; bulk density of fertilizer particle was 0.982 g/cm³.

(2) Model variable parameter setting

Hertz-mindlin (no-slip) model was adopted to simulate the collision of particle to particle, particle to grooved and box. Table 2 was detail pre-treatment parameter value. The simulation particle diameter was 1.64 mm. The quality attributes of fertilizer particles were calculated automatically by EDEM software.

Table 2. Pre-treatment parameter setting

Item	Property	Value
Particles	Poisson ratio	0.25
	Shear modulus/Pa	1.0×10^7
	Density/(kg · m ⁻³)	1861
Grooved wheel, housing	Poisson ratio	0.394
	Shear modulus	3.189×10^8
	Density/(kg · m ⁻³)	1335
Particle-particle	Coefficient of restitution	0.6
	Coefficient of static friction	0.4
	Coefficient of kinetic friction	0.01
Particle-grooved wheel, housing	Coefficient of restitution	0.5
	Coefficient of static friction	0.5
	Coefficient of kinetic friction	0.01

We used solidworks 2012 to establish 3D geometry model. At the same time, three storage boxes were designed at the bottom of device export to collect three parts of fertilizers from the outlet. And then simulate and measure the total quality of the three regions of fertilizers, respectively (Fig. 5).

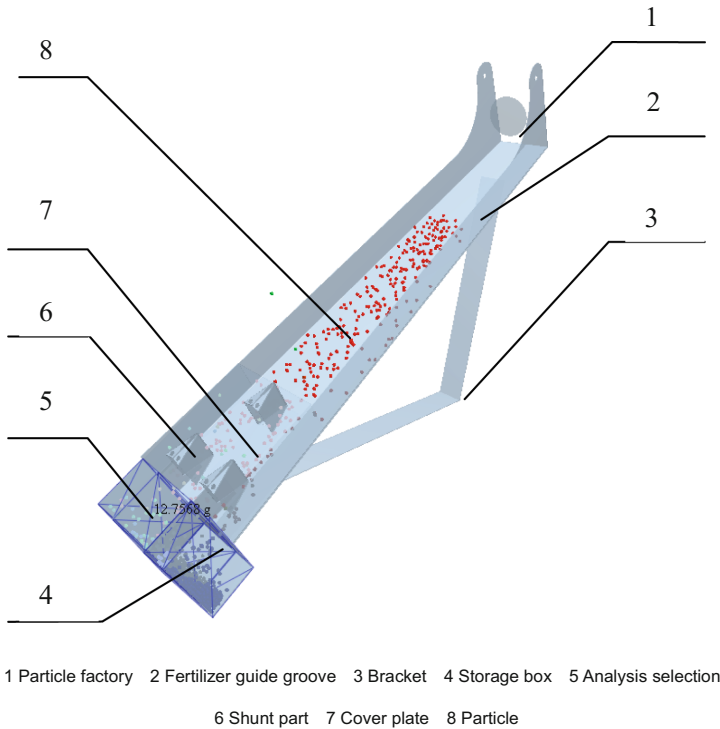


Fig. 5. EDEM simulation model of fertilizer application

The 3D model was saved in IGS format and was imported into the EDEM software. The total amount of particles was set to 1000 and the rate of product was 1000 particles per second. The gravitational acceleration was -9.81 m/s^2 . The simulation step was 1.53×10^{-5} . Total simulation time was 2 s.

4.2 Simulation Analysis and Parameter Optimization

(1) Simulate shunt part opening

In order to certain the optimal shunt part opening angle, ten groups of opening angle sample, from 30° to 40° were selected with interval of 1° . According to Tables 1 and 2, all the parameters were set. The corresponding simulated result was shown in the Fig. 6.

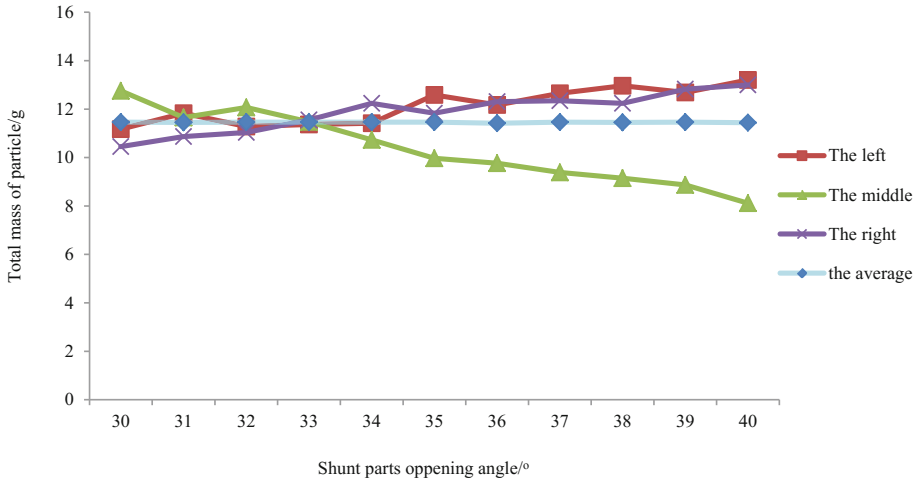


Fig. 6. Simulation of shunt parts opening

With the increase of the shunting part opening angle, the fertilizer amount at both sides of the outlet increased, while on the contrary, the fertilizer amount in the middle row decreased.

When the angle was smaller than the 33° , the total mass of the middle export was almost greater than the both of sides. When the angle was 33° , the left export total mass was 11.36 g; the middle one was 11.47 g; the right was 11.55 g and the average was 11.46 g. The value difference between the left and the average was 0.8%; the middle and the average was 0.08%; the right and the average was 0.7%. The total mass of both sides kept increasing and be greater than the middle export from 34° – 40° . At the same time, the both sides line kept same increasing trend and almost overlap, because the both sides was symmetry with each other. There was a similar variation between the middle of export and the sides export.

As a result, the most optimal parameter was 33° , which could be the fixed shunt part angle in the next experiment.

(2) Shunt part simulation analysis

The position of the shunt parts was divided into vertical and horizontal directions. In vertical direction, a single factor simulation experiment was designed. The L was used to denote the variable parameter in vertical direction. The test evaluation index was the total quantity of the three exports, respectively (Fig. 7).

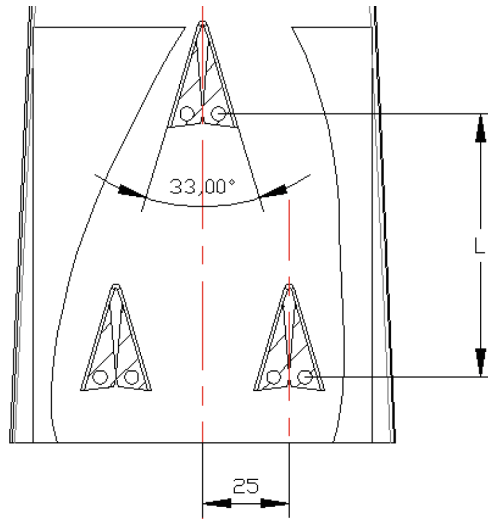


Fig. 7. Vertical distribution variable parameter

The vertical distance, L 's variable range was between 50 mm and 90 mm, and the interval was 5 mm. Simulation times was 2 s. The figure has shown as the increase of vertical distance, the both sides of the fertilize amount increased gradually, while the middle fertilize amount decreased gradually (Fig. 8).

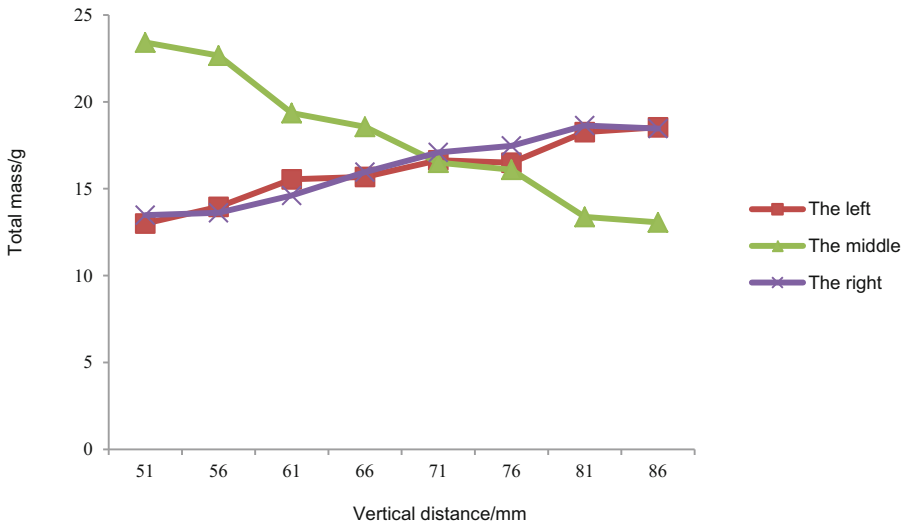


Fig. 8. Simulation analysis of vertical position

When the distance was smaller than the 71 mm, the total mass of the middle export was greater than the both sides. When the L was 71 mm, the left export total mass was 16.64 g; the middle one was 16.50 g; the right was 17.09 g and the average was 16.8 g. The value difference between the left and the average was 0.9%; the middle and the average was 1.8%; the right and the average was 1.7%. The total mass of both sides kept increasing and be greater than the middle export from the 76 mm. That was a similar situation when the L was between 71 mm and 76 mm. At the same time, the both sides line kept the same increase trend and almost overlap, because the both sides was symmetry with each other. There was a similar variation between the middle of export and the sides export. So the vertical distance obtained an optimal range. But consider of the true error, the L should be equal to 76 mm.

Then the horizontal position simulation was carried out. Two of shunt parts at the end shall be symmetrically distributed with the centerline of the device. The other one was on the centerline. The H was used to denote the variable parameter at the horizontal direction position (Fig. 9).

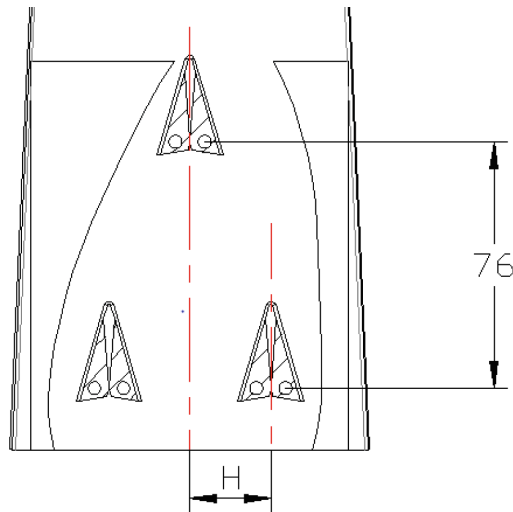


Fig. 9. Horizontally distributed parameter variable

Among the eleven groups of parameters, the variable range was from 23 to 27, with interval of 0.5 mm. The other two parameters were 27 mm and 29 mm. The corresponding simulated result was shown in Fig. 10.

With the increase of the center distance, the fertilizer amount on both sides exports gradually reduced, and the amount of fertilizer in the middle row of fertilizer increased gradually.

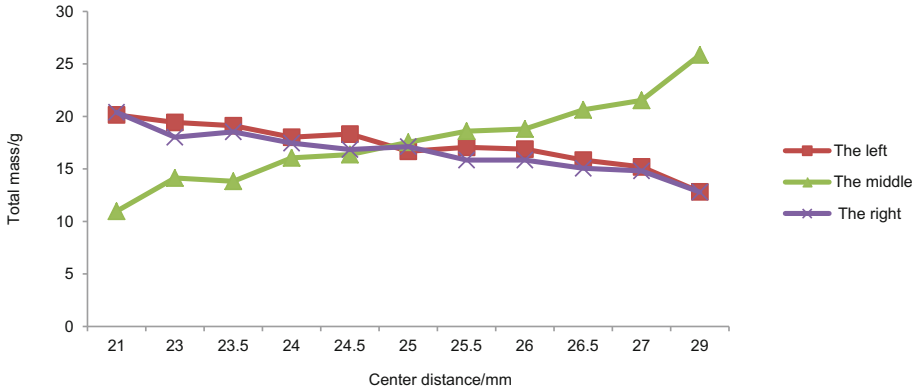


Fig. 10. EDEM simulation analysis of horizontal position

When the distance was smaller than the 25 mm, the total mass of the middle export was smaller than the both sides. When the distance was the 25 mm, the left export total mass was 16.67 g; the middle one was 17.53 g; the right was 17.12 g and the average was 17.11 g. The value difference between the left and the average was 2.6%, the middle and the average was 2.3%, the right and the average was 0.05%. The total mass of both sides kept increasing and being smaller than the middle export from 25 mm to 29 mm. At the same time, the both sides line kept the same decreasing trend and almost overlapping, because the both sides was symmetry with each other. As a result, 25 mm was the most optimal parameter among the all of Horizontal position parameters.

(3) Simulation of installation angle of fertilizer guide device

The angle between the fertilizer guide groove and the horizontal surface was also a variable parameter. The fertilizer guide device was arranged between the 30° angle to 50°. The simulation angle was from 32° to 41°, with interval of 1° and 50° (Fig. 11).

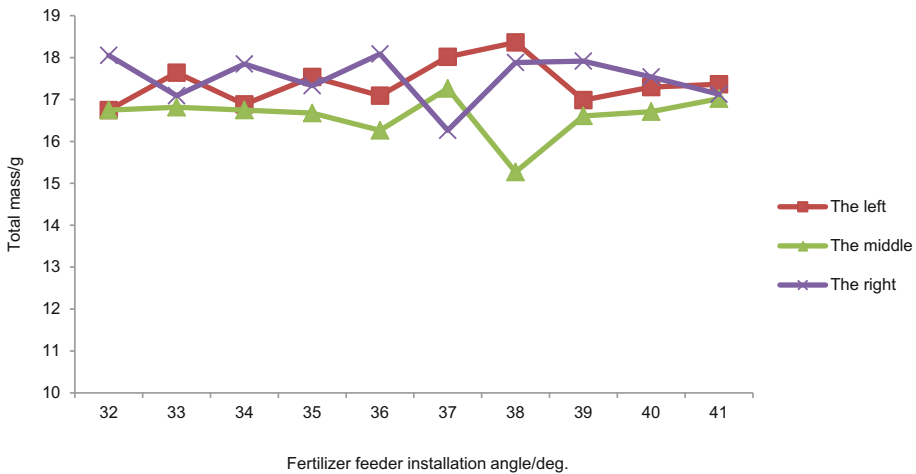


Fig. 11. EDEM simulation analysis of fertilizer feeder installation angle

With the increase of the installation angle of the fertilizer guide groove, the fertilizer amount of the three outlets has no obvious increase or decrease, All of three exports total mass vary from 16 g to 18 g, which remain constant from 32°–41°. And from the line chart, the three lines almost overlapped with each other and had no quite fluctuation. So there was no influence between the installation angle of the fertilizer guide device with the uniformity of fertilizer distribution. Meanwhile, the figure showed that quantity of the middle export was slightly lower than the both sides when all the parameters were the most optimal respectively. So in practical work, the shunt part opening angle or its position could be modified slightly to achieve the most optimal situation.

5 Conclusion

Through the above experiments and simulation, the following conclusions could be obtained.

- (1) A new fertilizer guide device was designed. It could improve the fertilizer application evenly and accurately.
- (2) When the shunt part opening angle was 33°, split between parts of vertical spacing was 76 mm, the horizontal spacing was 25 mm, the uniformity of the fertilizer distribution was best. The simulation results provided a reference for the design of the actual fertilizer guide device.

Acknowledgement. This study was supported by the Key Research and Development Program of Shandong Province (2016CYJS03a01-1), Special Fund for Agro-scientific Research in the Public Interest (201303103), and the BAAFS youth foundation project (QNJJ201529).

References

1. Parish, R.L., Bracy, R.P., Morris Jr., H.F.: Broadcast vs. band applications of fertilizer on vegetable crops. American Society of Agricultural Engineers (1997)
2. Yildirim, Y., Parish, R.L.: Band application performance of single-disc rotary fertilizer spreaders. *Appl. Eng. Agric.* **29**(2), 149–153 (2013)
3. Guifen, C., Li, M., Hang, C.: Research status and development trend of precision fertilization technology. *J. Jilin Agric. Univ.* **35**(3), 253–259 (2013)
4. Zeng, M., Wang, C., Yang, J.: A preliminary overview of site-specific fertilization and its application strategy in China. *J. Sichuan Agric. Univ.* **22**(4), 336–380 (2004)
5. Li, J.: Current situation and thinking of mechanized fertilization technology development. *Jiangsu Agric. Mechanization* **5**(5), 31–32 (2014)
6. Xu, X., Zhang, H., Xi, L., et al.: Decision-making system for wheat precision fertilization based on WebGIS. *Trans. CSAE* **27**(Supp. 2), 94–98 (2011)
7. Wan, H., Chen, H., Ji, W.: Anti-blocking mechanism of type 2BMFJ-3 no-till precision planter for wheat stubble fields. *Trans. Chin. Soc. Agric. Mach.* **44**(4), 64–70 (2013)
8. Pokrajac, D., Obradovi, C.Z.: Neural network-based software for fertilizer optimization in precision farming. *Neural Netw.* **3**(1), 2110–2115 (2001)

9. Dun, G., Chen, H., Feng, Y., et al.: Parameter optimization and test of key parts of fertilizer allocation device based on EDEM software. *Trans. Chin. Soc. Agric. Eng.* **32**(7), 36–42 (2016)
10. Wang, F., Shang, J., Liu, H., et al.: Application of EDEM particles simulation technology on seed-metering device research. *J. Northeast. Agric. Univ.* **44**(2), 110–114 (2013)
11. Zhou, W., Wei, H.: Simulation and analysis of belt conveyor based on EDEM software. *Coal Mine Mach.* **34**(5), 89–90 (2013)



Development of an Automated Guidance System for Tracked Combine Harvester

Fangming Zhang^{1(✉)}, Wenbin Wu², and Yunfei Zhu³

¹ Ningbo Institute of Technology, Zhejiang University, Ningbo, China
fangmingzhang@126.com

² Ningbo Microagri Technology Ltd., Ningbo, China
1979534947@qq.com

³ Thinker Agricultural Machine Ltd., Huzhou, China
642992007@qq.com

Abstract. An automated guidance system for tracked combine harvesters had been developed. A kinematics model for the harvester is constructed. A conventional and a X-turn path planning methods were provided. The system was successfully controlled speed, direction, and header of 2 modified harvesters, which had harvested 16 acres of rice land in December of 2015 and 2016. Results showed these machines can accurately cut along the edge of the cut/uncut, and cut all crops in every working path. The lateral offset is less than 5 cm in row following stage. In future, cutter, threshing roller, and other important working parts must be monitored to realize unmanned technology.

Keywords: Tracked combine harvester · Guidance system · Speed control
Path planning

1 Introduction

Rubber tracked combine harvesters are widely used for harvesting rice in China, however the work condition is filled with loud noise and flying dust, which results in short of labours in recent years. Farmers have great thirst for unmanned technology for combines. The domestic and overseas scholars had done a lot researches on automated guidance technology for tractors [1–5] and transplanters [6, 7], thus computer aided steering system for tractors have been commercial applied for nearly 15 years. He et al. [8] developed an automatic steering system for a tracked construction machinery through a remote control, whose functions were turning control, speed control, braking control with electro-hydraulic control system, but it lacks the ability of autonomous navigation.

Bound by weight, the volume of a harvester container is around 1200 L only, that is the harvester must unload grains after working 300 m. When working in a paddy field with length of 150 m, the harvester surrounds an area with some width, that it harvests from outer U-ring to inner ones till all crops inside this area are cut. The machine keeps

repeating the process from the outside to the inside in the rest of the land, which is the demand should be satisfied by an automatic guidance system. The objective of this research is to develop an automated guidance system for labour saving of tracked combine harvesters that computer will replace human operator to drive a combine to move forward or backward, to stop, to lift or drop the header.

2 Experiments and Methods

2.1 Kinematics Model and the Navigation System

As tracked vehicles use the principle of differential speeds between two rubber tracks to rectify any deviation, the kinematics model is drawn in Fig. 1. If position of the vehicle is (x_k, y_k) , moving in the path P_n , the kinematic equation is:

$$x_{k+1} = x_k + Tv_k \sin \psi_k \tag{1}$$

$$y_{k+1} = y_k + Tv_k \cos \psi_k \tag{2}$$

where T is acquisition cycle of attitude data, which is 0.2 s here, and v_k is speed of the central point, and ψ_k is heading angle.

A Kalman filter can be established like Ref. [7], whose state vector is $X = [x_k, y_k, v_k, \psi_k]^T$, and measurement vector is $Y = [x_{GPS}, y_{GPS}, v_{GPS}, \psi_{GPS}]^T$. Lateral deviation and heading deviation could get after comparing with path P_n .

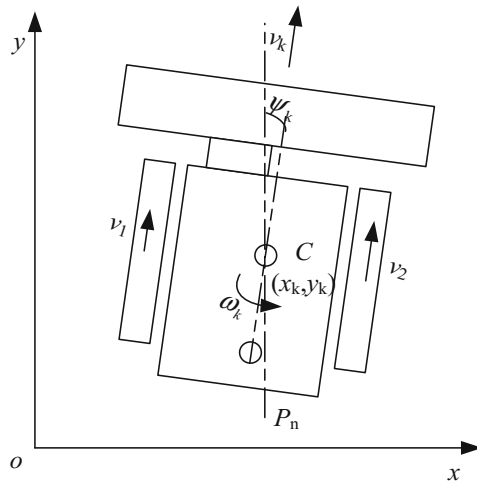


Fig. 1. The kinematics model of a tracked combine harvester

The guidance system consists of an electronic system and mechanical parts, shown in Fig. 2. The electronic system includes a navigation controller, 3 ECUs, a RTK-GPS receiver (Beidou, BD683), and a gyro (Luche, ASV940). The mechanical parts are an electro-hydraulic valve and a motor-driven speeder. The navigation controller adopts Arm-Cortex board (Emtrix, EM335X) and embedded Linux operating system platform, whose software is divided into man machine interface (MMI) and guidance control software(GCS). The ECU1 transfers the data of RTK-GPS and gyro, and the ECU2 controls the electro-hydraulic valve, and the ECU3 controls the motor driven speeder. The double antenna of the RTK-GPS produces precise heading angle with $0.2^{\circ}/m$. The gyro provides pitch and roll angles for positioning correction on uneven paddy land [7].

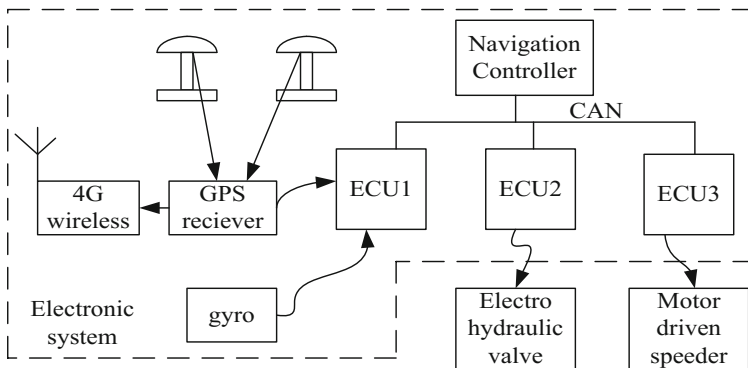
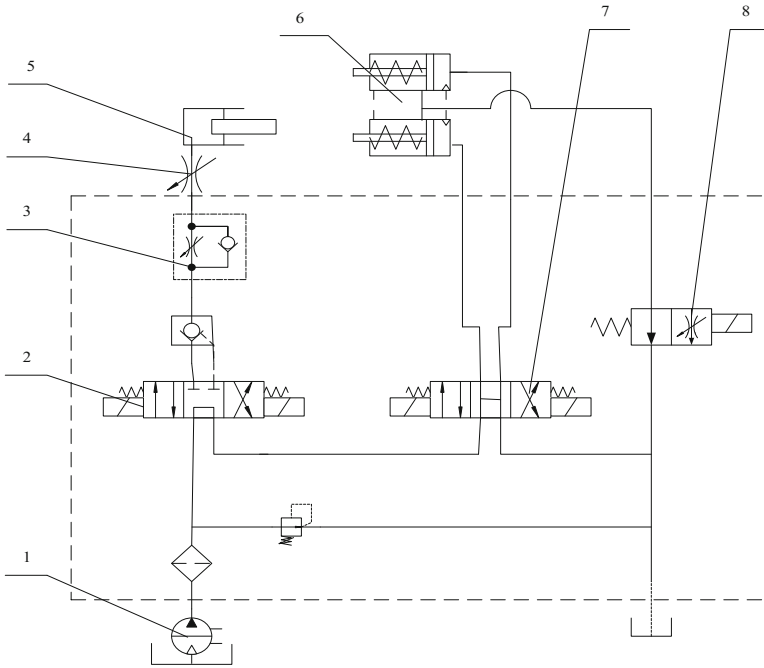


Fig. 2. System structure

2.2 The Electro-Hydraulic System for Steering Control

A new integrated electro-hydraulic valve, consists of components inside dotted-line rectangle as shown in Fig. 3, was installed into the harvester to control the steering cylinder and the head cylinder. When all valves are in normal position, oil flows through back to oil tank directly, and the head cylinder (5) keeps the header, and the steering cylinder (6) is in its initial position. When the valve A (2) acts, the header cylinder lifts up the header or descends it steadily. When the valve B (7) acts, the steering cylinder pushes the left or right clutch, which produces left turning or right turning. When the solenoid valve (8) is in normal position, a steering command makes a big turning, otherwise, the throttling pathway makes a small turning, whose heading regulating is relatively small and smooth, mainly used in row following control.



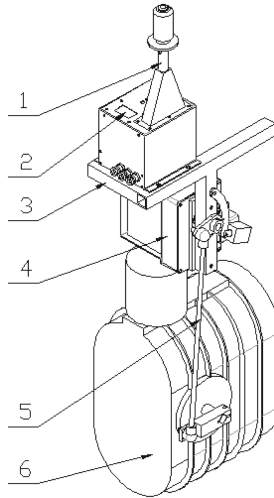
1. pump, 2. electro-four-way three-position directional valve A, 3. one-way throttle valve, 4. manual throttle valve, 5. head cylinder, 6. steering cylinder, 7. electro-four-way three-position directional valve B, 8. solenoid valve

Fig. 3. Diagram of electro-hydraulic steering control

2.3 The Motor-Driven Speeder

Speed control of harvester, aiming at reduced the labor strength and increased the harvesting efficiency, attracted some Chinese scholars to do research. Such as Chen et al. [9] built multivariate fusion reference models under adaptive control and the fuzzy control rules to control the speed. The objective of speed control of this project is realizing unmanned driving, that is the harvester needs to change speed, stop and reverse in the course of automated guidance control. It made use of infinitely variable speed control of HST (HydroStatic Transmission).

The motor-driven speeder, shown in Fig. 4, consists of electronic joystick, step motor reducer and a crank connecting rod mechanism. Inside the electronic joystick, the ECU3 controls the rotation of the step motor, thus changes rotation angle of extended shaft of HST. The speeder is initialized with manual control, that the joystick could control vehicle speed with its different position. The speeder could also controlled by commands through the CAN interface of the ECU3.



1. electronic joystick, 2. digital display, 3. frame, 4. step motor reducer, 5. crank connecting rod mechanism 6.HST

Fig. 4. HST electric control system

2.4 Path Planning

In theory harvesting crops is a coverage task with sequential operation without any repetition. Galceran [10] presented a survey on coverage path planning methods. However, paths at each end of roads have to be overlapped for higher efficiency. Figure 5 shows a conventional path planning for combine harvester. Here, a local coordinate system is set up after measuring point “A”, “B”, and “C”. The original point is point “A”, and the y axis is overlapped with path P_{F0} , and x axis is in right direction. The length and width of this subregion are:

$$L_A = L_{GPS} + L_R + L_F + R \quad (3)$$

$$W_A = 2N \cdot L_W \quad (4)$$

Where L_A is Length of the subregion, and W_A is width, and L_{GPS} is distance from point A to point B, and R is turning radius of this vehicle, and L_F and L_R are distance between the GPS to head, back of the vehicle respectively, and N is number of coverage cycles, usually is set to 4–8 rings.

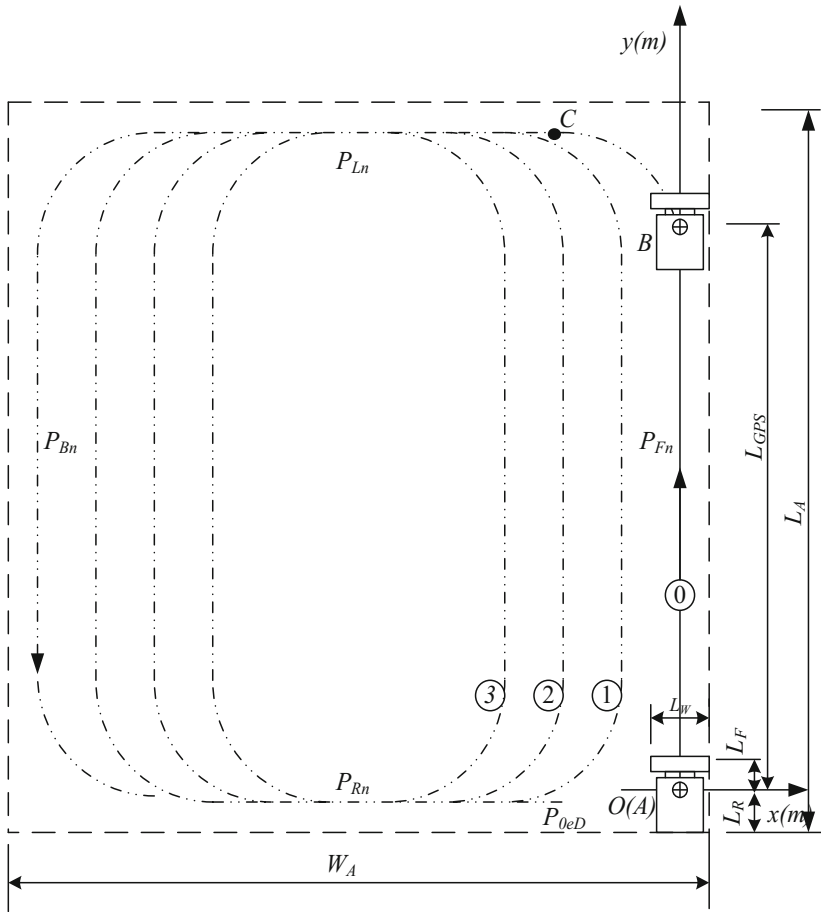


Fig. 5. Coverage path planning

The forward and backward paths changed when the number of ring increasing, while the values of y coordinate of the leftward and rightward paths are fixed. The four paths are list as following:

$$P_{Fn} = -n \cdot L_W \tag{5}$$

$$P_{Bn} = -(2N - n - 1) \cdot L_W \tag{6}$$

$$P_{Ln} = L_{GPS} + R + L_F \tag{7}$$

$$P_{Rn} = -L_R \tag{8}$$

Where $P_{Fn}, P_{Bn}, P_{Ln}, P_{Rn}$ are paths of forward, backward, leftward, and rightward in the n^{th} ring.

2.5 Navigation Control Process

The GCS executed the control process in step by step. GPS data, arriving every 200 ms, are the 1st step of every control process. Latitude and longitude data were then converted into x and y value of the local coordinate system. Together with speed and heading angle, these data constructed the measurement vector of the Kalman filter. In the 2nd step, the Kalman filter estimated state vector and produced smoothed data, positioning data. In the 3rd step, the GCS did rectifying or turning action depended on which state the vehicle was currently in, row following or turning state. If the machine was in a row following state, it got current path and calculated deviation. A PID function produced control value for the electro-hydraulic valve, and then sent to the ECU2 to make a steering operation, which is an end of the 3rd step. If the remaining distance before the end point of this path was less than turning radio R , the GCS sent a command of 90° turning to the ECU2, meanwhile, it changed over to turning state. If the machine was in turning state, the software monitored heading angle. When the accumulated heading angle was 90°, it finished the 3rd step too, and wait the next GPS data. After the machine crawled a cycle of forward, leftward, backward, and rightward, the cycles number added 1, and it began to harvest the inner subregion. The head cylinder dropped down in forward and backward paths, and lifted up in leftward and rightward paths.

2.6 Auxiliary Control Function

The guidance system also includes a pair of wireless data transmission modules (433 MHz, transmitting with bps of 9600, distance less than 600 m): one is inside the ECU1 and another is inside a remote control. The remote controller consists of a radio module, a LCD touch screen, and a microcomputer board, which is used for artificial intervention or control in some special cases, such as manually control the machine to get away from a muddy place, load into, or unload from a heavy truck. It also makes a operator completely leave the harvester, while stand near the machine to monitor its operation.

3 Results and Discussion

The guidance system was installed into two combine harvesters (a XG988SE and a XG988Z, Thinker agricultural machinery). The system had been tested not only on cement road, but also on paddy fields in Dec. of 2015 and 2016, that it harvested rice crops about 16 acres at Huzhou and Ningbo. Figure 6 is a scene of harvesting.



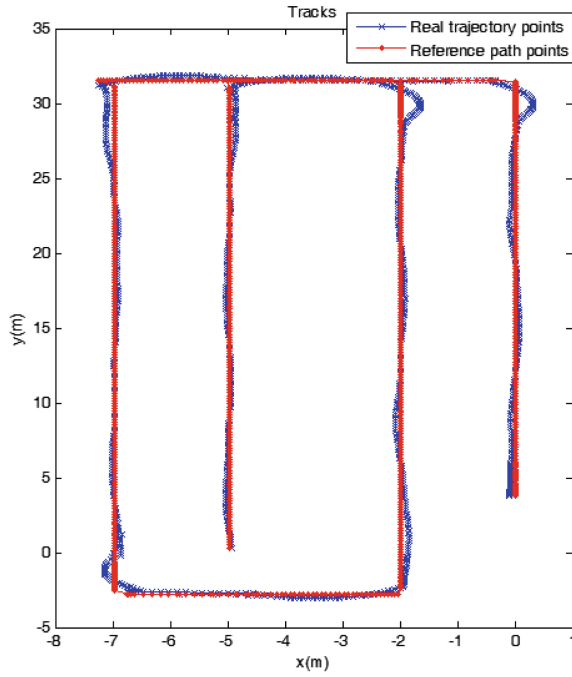
Fig. 6. The prototype of automated guided combine

3.1 Effect of Conventional Path Planning and Improved Turning Method

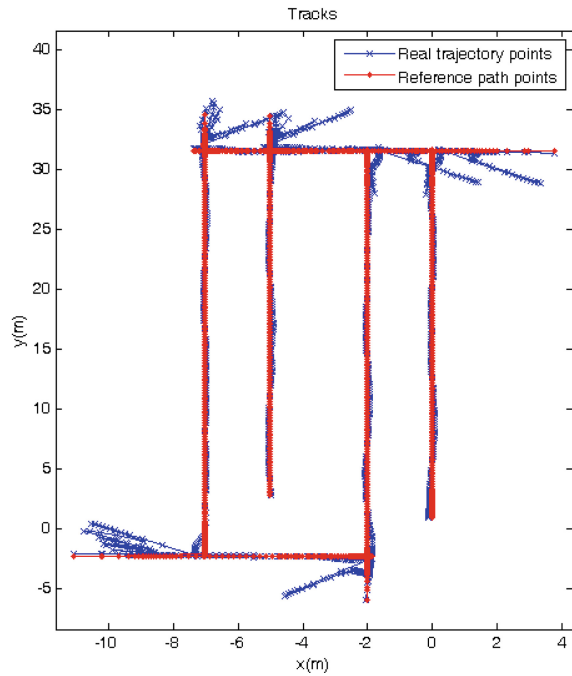
Field experiments showed that the guidance system has advantages over manual operation. Firstly, trajectories became a perfect straight line, that the header can be accurately cut along the edge of the cut/uncut. Secondly, path planning made a full harvest in the last path of every subregion, which improved the overall efficiency. Thirdly, the driver could stand far away from the noise and dusty machine while monitor it. Figure 7(a) plots a trajectory of the harvesting operation, showing the advantages mentioned above. However, soil is rather muddy in some rice fields, which results in difficulty to turn 90° at end of paths. Therefore the turning method was improved, called “X-turn”: the harvester turned anticlockwise for 3 s, then it went forward straightly for 1 s. It would not stop this cycle until a 45° of heading angle changed. The harvester stopped, and then retreated with clockwise turning for 3 s, then went backward straightly for 1 s. It would not stop this cycle until a 45° of heading angle changed, that a total 90° of turning happened. Figure 7(b) shows the trajectory of this operation. Experiments show that this method made the harvester could work in all kinds of rice crop lands.

3.2 Control Method for Rubber Track

Track control is one of key technology in this project. It shows that its control method is quite different with wheeled machinery. Firstly, the control frequency of wheeled agricultural machinery can be 5 Hz or more, while a tracked harvester became a matador at this frequency, and it can not meet the requirements of the smoothly harvesting operation. One solution is reducing the control frequency. Effect of different control frequency was recorded, from time interval of 0.8 s to 2 s. In these experiments, the automatic control started from point “C”, and ended at the rightward path. Average offset and standard deviation of offset in row following is listed in Table 1. Results show that average offset are very close in all tests, ranged from 0.4 cm to 4.6 cm from time interval of 0.8 s to 1.6 s, and so to standard deviation. It seems the minimal average offset come from time interval of 1.2 s, and minimal standard



(a) trajectory of 90° turning



(b) trajectory of X-turn

Fig. 7. Trajectory of 2 cycles with different turning methods

Table 1. Effect of different control frequency

Time interval (s)	Average offset (cm)			Standard deviation of offset (cm)			After turning, distance when lateral deviation is less than 10 cm (m)		
	Leftward	Backward	Rightward	Leftward	Backward	Rightward	Leftward	Backward	Rightward
0.8	-2.1	-3.9	1.6	3.7	6.6	4.7	0.0	0.87	0.0
1.0	2.9	-4.6	1.6	5.9	7.8	4.7	2.43	4.5	0.0
1.2	2.2	0.4	2.9	6.6	4.8	3.6	1.01	6.75	0.0
1.6	-0.4	-3.8	2.0	5.8	2.4	4.1	1.17	0.57	0.0

deviation come from 1.6 s, and the fastest arriving to objective path come from 0.8 s. When we continued to ascend time interval to 1.8 s or 2 s, the control performance was significantly worse. According to the experimental data, the time interval of 1.2 s is a suitable control frequency.

3.3 Parameters of PID Control

Tracked harvesters actually has higher efficiency on rectifying a deviation than wheeled vehicles. Heading angle of the body rotated has a linear positive relationship with the duration operated time to the electro-hydraulic valve. By using the conventional PID control algorithm, trajectories were recorded through a serial of row following experiments to evaluate effect of different PID parameters. Table 2 gives the experimental results. The results show that the appropriate value of proportional coefficient, K_p is between 0.6–0.8, where standard deviation is relatively small, and the average deviation is relatively small too, which means correction effect is obvious. The differential coefficient, K_d , should not be set too big. The standard deviations are relatively large when the K_d was set to 0.4, or 0.5.

Table 2. Effect of different PID parameters

$K_p:K_d:K_i$	Average offset (cm)	Standard deviation of offset (cm)
4:2:2	-4.6	6.0
4:5:1	-3.5	9.6
5:3:2	-5.5	5.4
5:4:1	-0.8	9.4
6:2:2	-3.7	2.0
6:3:1	-1.0	4.3
7:1:2	-1.2	3.3
8:1:1	-1.8	3.1
8:2:0	-2.8	4.2

4 Conclusions

An automated guidance control system had been developed for tracked combine harvesters. It shows that a traditional tracked harvester could be transformed into a robot harvester after adding a guidance system and a motor-driven speeder. The lateral deviation is less than 5 cm when steering in row following state. Helped by path planning and automated control, the header could cut full crops in every working path, so automated tracked harvester has higher efficiency than traditional harvester.

However, the automatic guided harvester may cause unevenness of the land in end of paths. In the future, some improvement should do on this type harvesters. (1) new crawler chassis structure should be developed that one track could crawl forward while the another track crawl backward when the machine need turning a 90° or more. This will reduce destruction of land; (2) main rotating parts, grain container, conveying channel should be monitored for unmanned operation.

Acknowledgment. Funds for this research was provided by the Yinzhou Science and Technology Plan Projects (2015), Ningbo Science and Technology Plan Projects (2014C100016).

References

1. Tillett, N.D., Hague, T.: Computer-vision-based hoe guidance for cereals—an initial trial. *J. Agric. Eng. Res.* **74**(3), 225–236 (1999)
2. Han, S., Zhang, Q., Ni, B., Reid, J.F.: A guidance directrix approach to vision-based vehicle guidance systems. *Comput. Electron. Agric.* **43**(3), 179–195 (2004)
3. Kise, M., Zhang, Q., Rovira Más, F.: A stereovision-based crop row detection method for tractor-automated guidance. *Biosyst. Eng.* **90**(4), 357–367 (2005)
4. Chen, J., Torisu, R., Zhu, Z.: Study on automatic guidance for tractor on grassland. *Trans. CSAM* **36**(7), 104–107 (2005). (in Chinese)
5. Noguchi, N., Reid, J.F., Zhang, Q., Will, J.D., Ishii, K.: Development of robot tractor based on RTK-GPS and gyroscope. In: 2001 ASAE Annual International Meeting, pp. 01–1195 (2001)
6. Zhang, Z., Luo, X., Zhou, Z., Zang, Y.: Design of GPS navigation control system for rice transplanter. *Trans. CSAM* **37**(7), 95–98 (2006). (in Chinese)
7. Zhang, F., Shin, B., Feng, X., Li, Y.: Development of a prototype of guidance system for Rice-transplanter. *J. Biosyst. Eng.* **38**(4), 255–263 (2013)
8. He, Z., Chen, H., Tao, G., Wu, S.: Remoted Automatic driving control system of crawler type vehicle. *Constr. Mach. Equip.* **10**, 3–7 (2003). (in Chinese)
9. Chen, J., Ning, X., Li, Y.: Fuzzy adaptive control system of forward speed for combine harvester based on model reference. *Trans. CSAM* **45**(10), 87–91 (2014). (in Chinese)
10. Galceran, E., Carreras, M.: A survey on coverage path planning for robotics. *Robot. Auton. Syst.* **61**, 1258–1276 (2013)



Research on the Internet of Things Platform Design for Agricultural Machinery Operation and Operation Management

Qian Zhou, Jiandong Jiang^(✉), Zhangfeng Zhao, Jiang Zhong,
Bosong Pan, Xiao Jin, and Yuanfang Sun

School of Mechanical Engineering, Zhejiang University of Technology,
Hangzhou 310014, China
1151221032@qq.com, jiangjd@zjut.edu.cn

Abstract. With the deepening of the agriculture and rural land reform, In China which is in the transition from traditional agriculture to modern agriculture, and the application of agricultural machinery networking technology is still in the preliminary application stage. This paper introduces the technology of Internet of things into the operation and operation and management of agricultural machinery, the technology integrates with Internet of things, cloud computing, and big data, then had optimized. So the managers can manage the agricultural machinery remotely, monitor the state of the machine at any time. The paper also discusses the core data management system of the platform, and gives the algorithm analysis of the rules such as the collection and excavation of the agricultural machinery operation and operation and maintenance process, and will improve the intelligent level of China's agricultural machinery to a certain extent.

Keywords: Agricultural machinery · Internet of things
Operation and maintenance management · Large data · Cloud platform

1 Introduction

The agricultural mechanization is an important part of agricultural production technology transform, and is an important manifestation of agricultural production technology progress. Since ancient times, agriculture is the first hand-operated, and then developed to semi-mechanized operations, and to the back of large-scale mechanized agriculture, The agricultural productivity has been improved. In recent years, with the relevant state-department attention on the agricultural mechanization development and the level of science and technology improved, the development of agricultural machinery has gradually become intelligent, saving, precision and large. However,

Zhejiang Province Science and Technology Project: R & D of portable multi-purpose tea machinery and equipment - intelligent testing of tea processing and equipment and quality decision-making control system integration research and production line application demonstration (2017C02027). National Science Fund subsidized project (51375456).

there are still many shortcomings in the management of agricultural machinery in China, which have resulting in poor quality of operation, low efficiency and high operating costs. This specific performance is the low utilization rate of agricultural machinery, waiting for or the idle in the process of agricultural operation, and far away from the transportation of agricultural materials or agricultural products, the operating machine walking route is not economical, repetitive operations or excessive operations, and other non-value-added activities with resulting in loss of crop losses and other operations waste.

In Europe, the United States, etc. other developed countries, the agricultural machinery products not only to achieve the agricultural operations, the operation and maintenance of real-time monitoring, but also to have the gradual realization of intelligent control in some mainstream products. The foreign agricultural operations, agricultural production are base on the positive information and big data after the realization of the digital [1]. Therefore, in this context, the development on Internet of Things provides an opportunity to improve intelligent agriculture. Agriculture is an important application area of Internet of Things technology. The deep integration of Internet of Things technology and agricultural production, management, management and service industry is of great significance to the transformation of the traditional agriculture and the promotion of agricultural modernization [2]. With the use of Internet of things technology and the computer, Internet, cloud computing and other technologies, to establish a combination of agricultural operation and maintenance management platform to strengthen the management of agricultural operations, to reduce or eliminate the existence of waste in the operation process for improving China's farming industry crop mechanization process operation and maintenance management level and improving operational efficiency, is of great significance.

2 Status and Problems of Operation and Maintenance of Agricultural Machinery at Home and Abroad

With the development of the agricultural machinery and equipment in foreign advanced industrialized countries. In the 1970s, the foreign advanced agricultural machinery and equipment has begun to integrate with the modern microelectronics technology, the instrumentation and control technology, the information and communication technology, and have the rapid development in the direction about the digital, information, automation. Intelligent.

Globally, American agriculture is leading the way in using the Internet of things technology. In 1995, the United States began to equip the united harvester with a global positioning system, in which using electronic sensors and satellites for precise positioning. As the world's agricultural machinery industry leading enterprises, John Deere of the United States, advocates JDLINK system, has many functions, such as online querying working location, working data, working efficiency and working costs of agricultural machinery. the managers can monitor online in the office to manage the work of agricultural machinery, to do the precision management of agricultural machinery work. John Deere's 60 Series harvester has been using the Green-Star system, equipped with the relevant sensors and control system, achieving the automatic

control of feed quantity and automatically drawing the yield and grain moisture graphs, the terrain and other high-map, etc. on. At present, some large farms, in Europe and the United States, have also begun to establish and use the management information system for data exchange through the wireless communication between the computer and mobile operating machinery in the agricultural production office. Through the management information system for data exchange through wireless communication the managers can enable to monitor and manage agricultural machinery, to work in field with the computers in the farm management center. The field working data can be remotely recalled and stored directly in the corresponding database, greatly improving the efficiency of data collection, the analysis and application; when the mechanical failure, the mechanical users can also make use of the computer techniques to analysis and diagnostic, or to take targeting processing procedures of precision agriculture, which is basing on GPS, GIS, RS Technology for urging on the agricultural production to be changed more scientific and refined [3, 4].

In China, the overall situation of agricultural equipment's development is: small agricultural machinery occupies the dominant position with a large number and a single function; the large and medium-sized mechanical costs are higher, and their degree of intelligence are low; the agricultural machinery product surplus and shortage of coexist, traditional farming machinery market is almost saturated, the product structure is irrational, the number of cultivated and harvested machinery about some new crops is little and the level is low. There are also many problems, such as the system is imperfect in the agricultural management, the managers are not professional and so on [5]. And "island-style" information technology investment of the current Chinese agricultural machinery networking cannot form a network model, and cannot have economies of scale effect. Therefore, it is better to study the advanced management and operation technology of the agricultural machinery, and to build a national advanced, low-cost, easy-to-use and dynamic agricultural data platform for improving the operating and managing level of the crop mechanization process in China's farming industry, then can greatly play the effectiveness of agricultural machinery, which is of great significance for serving the country [6].

3 The Overall System Architecture

The system model integrates many technologies such as the Internet, the mobile Internet, the cloud computing and the Internet of Things, and deeply integrates the Internet of things with the cloud computing big data. The cloud computing can help the intelligent cloud platform to realize the distributed storage of information storage resources and computing power. The information processing capacity of big data will provide support for the massive information processing and utilization, and rely on a variety of the sensor nodes and network environment, through the agricultural intelligence cloud platform operations large data information, environmental information,

geographic information, soil information, crop information and other big data mining, it establishes decision-making system to achieve the intelligent perception of agricultural operations environment, intelligent early warning, intelligent decision-making, intelligent data analysis, quality control and so on, to provides visualization and precision management to agricultural operations and operation and maintenance, for reducing human operations, improves agricultural efficiency, and timely having complete operation and maintenance fault detection and diagnosis. The following figure shows the intelligent agricultural management system map (Fig. 1).

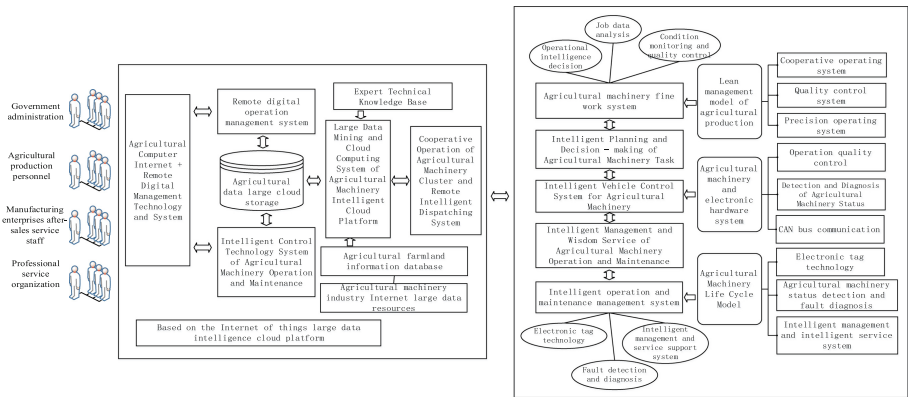


Fig. 1. Intelligent agricultural management system map

The subsystems of the intelligent agricultural machine management system:

(1) Agricultural machinery Internet digital management system

The intelligent monitoring terminal acquires the agricultural working environment temperature and humidity, agricultural fuel consumption, operating normally or abnormally and the information of location through collecting the signal of the sensor output. The intelligent monitoring terminal makes a reasonable analysis and judgment through the data processing, data operations, Data analysis, and conveys to the government official, agricultural production personnel, production and after-sales staff and professional organization service personnel by the monitoring side (client). Meanwhile real-time, the field monitoring terminal have uploading the data stably and quickly, which is collected in to the server to achieve data sharing and agricultural intelligence.

(2) Cooperative operation and remote intelligent dispatching technology and system of agricultural machinery group

The sub-modules in cooperative operation and remote intelligent dispatching system of the agricultural machinery group including the agricultural remote control system, the big data cloud storage system, the remote operation and maintenance

control technical support, the expert technical service library, the remote collaborative operating system and the information base. The system needs big data and the support of decision-making system, first we need to establish data mining models and algorithms in the wisdom cloud platform big data mining system. According to the real-time monitoring and reporting of agricultural working location, crop category, working area, working speed, working conditions and other parameters, and combining with the matching knowledge base among the agricultural machinery, through the agricultural intelligence cloud platform's extraction of big data, model provides decision-making data. Meanwhile, we study the multi-device concurrent access control technology and database service technology to formulate the plan of the cooperative work and remote intelligent scheduling scheme for the agricultural machinery cluster. To research and develop the agricultural operations scheduling system, to release agricultural scheduling information facing to the agricultural operations management personnel, to achieve agricultural machinery cluster operations and remote intelligent scheduling.

(3) The fine management technology and system of agricultural machinery work

The sub-modules is made up the system including the fine operating system, the intelligent planning and decision-making of task, intelligent vehicle control system, intelligent management, intelligent service and intelligent operation and maintenance management system. The system integrates the key technologies such as mobile communication, Internet technology, global positioning system and detection sensor and so on. It obtains the information such as the geographical position, operation information, fault information, running trajectory, bulletin information, transmitter status, work statistics and so on. Then it use mobile network technology to send data to the data management center to the implement data processing and analysis to achieve the target machine identification, location determination, voice communications, network information query, data transmission, the realization of agricultural operations remote monitoring and agricultural scheduling management. Users and agricultural management departments can monitor the platform or the mobile client APP to monitor and understand the operation of the agricultural machinery, query the area of agricultural operations, and monitor the status of agricultural machinery and other operations' quality condition.

4 Agricultural Machinery Operation and Maintenance Management Technology Road the Map and the Core of the Two Model Design

4.1 Key Technical Solutions and Implementation Methods

The technical route of the agricultural machine operation, based on the big data intelligent cloud platform, and the operation and maintenance intelligent management on Internet platform is shown in the figure below (Fig. 2).

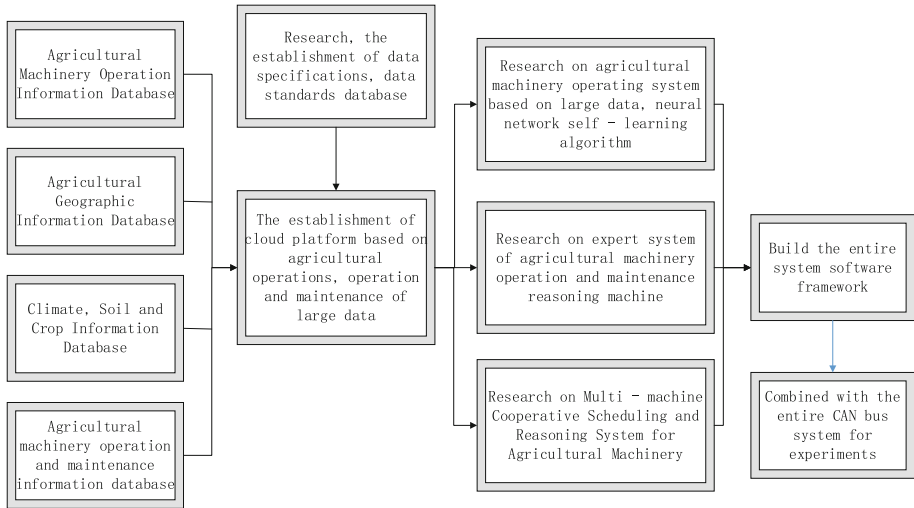


Fig. 2. Intelligent route of agricultural machinery operation and operation and maintenance based on big data intelligent cloud platform

The technical roadmap builds up the scheduling model of the database, in the process of agricultural machinery operation, and sets the target for the selection of hardware and software components and algorithms in the whole scheduling reasoning management organization, which lays the foundation for the design of the whole Internet of Things platform.

On the Internet of Things platform, the core technology is data processing, including three major parts: data collection, data analysis and mining, service of the data in the operation and maintenance, this instructions will be given in the design of the following core models [7, 8].

4.2 Design of Monitoring Platform for Agricultural Machinery

The agricultural big data intelligent cloud platform, based on the Internet of things, which's construction need the help of the raw data acquisition and storage support, therefore the first thing need to be done is the constructions of the agricultural machinery networking Monitoring platform, and the Monitoring platform mainly consists of the positioning system, mobile client, Internet of Things monitoring center system, Data management storage center, cloud computing modules and other components. The core part of Monitoring platform is the airborne data management module, which includes the data collection, analysis and data applications. The system topology diagram of the Monitoring platform is shown at the following (Fig. 3).

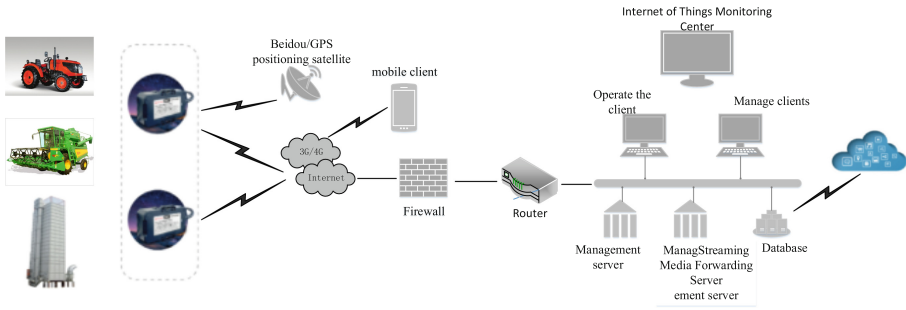


Fig. 3. Agricultural machinery and equipment network monitoring system topology

The data collected by the monitoring system mainly includes the job location information, the job status information, the fault detection information and the trajectory of the agricultural machinery. After the corresponding information is obtained by the sensor, the mobile network technology is used to send the data to the data management center of the platform in real time, to do the implement data Processing and analysis. The agricultural machinery data acquisition system should meet the needs of modern intelligent information management, effective management of historical data information, and can move towards the direction of development of higher precision, faster processing speed, more real-time, greater storage capacity and greater integration. The main acquisition technology included in the real-time data collection of agricultural machinery is shown in the following Fig. 4.

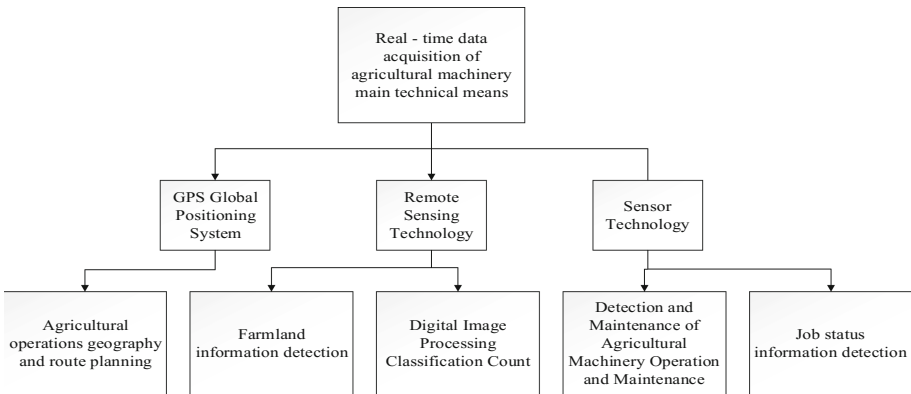


Fig. 4. Real - time data acquisition of agricultural machinery main technical means

The monitoring system can receive the information produced in the operation process of agricultural machinery by using the Internet of things RFID technology and the wireless sensor technology together, which can achieve intelligent management of agricultural machinery and real-time monitoring.

4.3 Intelligent Management System for Agricultural Machinery Operation and Operation Based on Big Data Intelligent Cloud Platform

As an organic combination of big data technology, the big data platform have multiple functions such as data collection, data storage, data processing, data analysis and so on, which can provide a strong support for the applications of big data. Nowadays. In the aspects of big data processing, the general process method is distributed Map Reduce, and stored in the form of pair of key/value, which reading process is also different from the traditional way. By using the data mining technology, the data mining in the agricultural operation and the maintenance management system can dig out the effective information from the agricultural work data, thereby to guide the operation and maintenance of the agricultural machinery. In this paper, the data mining system function diagram is designed as follows (Fig. 5).

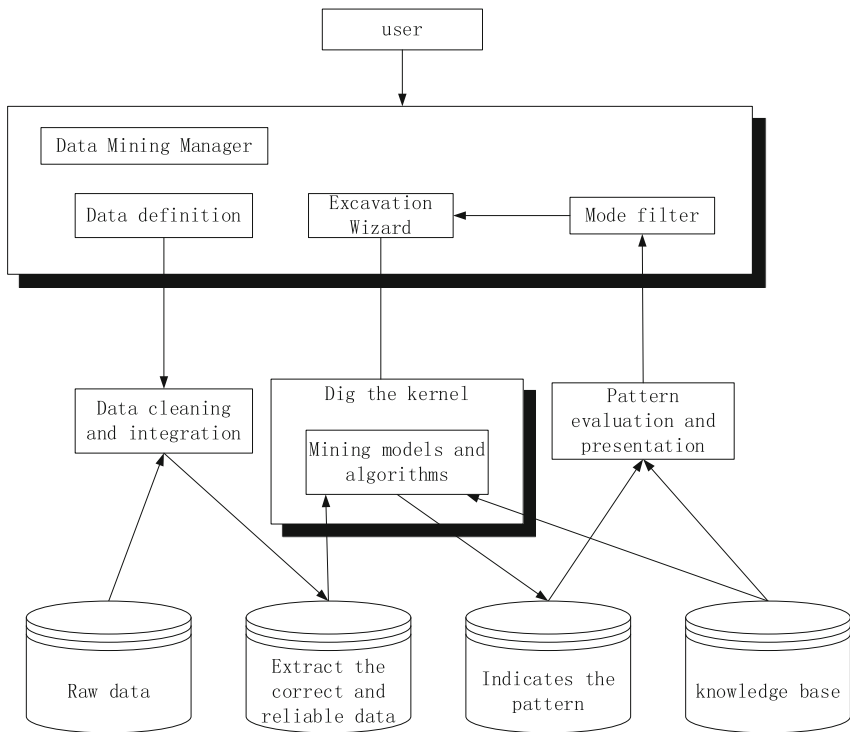


Fig. 5. Data mining system function diagram

The core part of the data mining system is the establishment of mining models and algorithms. The data mining of massive data group, generated in the operation process of the agricultural machinery, which depends on the ability of mapping the real world and the ability of processing the data. The current mainstream distributed data mining

platform is Hadoop, which use the distributed file system HDFS to save the file, and use the MapReduce to deal with the data of distributed file system, therefore can ensure the efficacy on the data analysis and processing [9, 10].

HDFS can store the large files produced by the operation and maintenance, proceed the effectively access the mode of writing once and reading many times, and can carry out the streaming data access. The architecture of HDFS is shown below (Fig. 6).

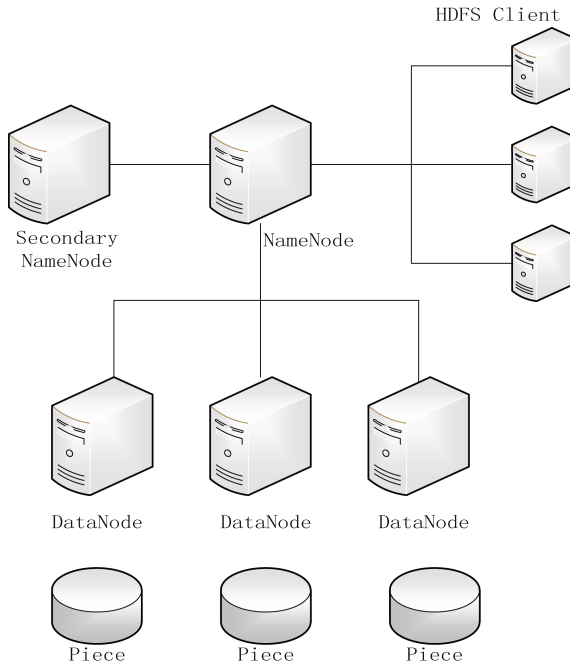


Fig. 6. HDFS architecture

The computer cluster has achieved the mutual communication among the cluster and data transmission. As the brain of the cluster in the HDFS, NameNode is used to store the metadata of the entire file system, the real data is stored in the blocks of the DataNode. HDFS determines whether the data collected is corrupted by using the checksum technology, DataNode is responsible for verifying the checksum of the received data, and the HDFS client also verifies the checksum when it reads data from the DataNode and compares them with the checksum stored in the DataNode. Not only the client will verify the checksum when reading data and writing data. Each DataNode will also run a DataBlockScanner in a background thread to periodically validate all the data blocks stored in this DataNode. And HDFS can also repair damaged data blocks [11].

The key about the operation and operational data of agricultural machinery is to excavate the relationship between the real-time status information of agricultural machinery and its operation and maintenance. Moreover the aim on improving the

parallel algorithm is to get the information that the agricultural machinery manager and the producer can use it to know the running status and the fault detect of the agricultural machinery better, therefore can solve the problem timely. Because the amount of data is very large, and in the process of generating candidate items, the traditional parallel Apriority algorithm will lead to data processing in the calculation process is slow or lack of memory. Therefore, it is necessary to improve the algorithm of Apriority, improve the efficiency on the algorithm implementation, and can reduce the size of candidate items with the implementation of algorithms, also make the calculation nodes independently perform the mining of the items, thus solve the problem of insufficient memory [12].

On the design of the cloud platform the operation and operation and maintenance of the data management system is developed, which will provide the effectively support for the store and the mining of massive data produced in the operation process of agricultural machinery.

5 Conclusion

This paper aims at solving the problem on the backward development of the agricultural machinery, such as poor quality of operation, low efficiency and high-difficulty of operation supervision, by comparing the development of agricultural machinery at home and abroad. and introducing the design of the agricultural machinery operation and operation and maintenance management network.

This paper gives the design framework of the intelligent agricultural management system map, the core is the design of the network monitoring platform for the agricultural machinery and the intelligent management system design on the agricultural machinery operation and operation and maintenance, based on the large data intelligence cloud platform. The platform establishes the field locomotive database and the query System, as well as the data collection, mining, etc. So we can facilitate query, add, delete and save and other operations of varieties of agricultural machinery and equipment data. At the same time, it can improve the positioning accuracy and stability of agricultural machinery system, and can monitor and diagnose the failure of agricultural machinery in real time, not only can improve the efficiency of production operation, but also can promote the development of intelligent and the precise development of agricultural machinery.

Acknowledgements. This paper is accomplished under the guidance of careful of my mentor-professor Jiang Jiandong. His serious scientific attitude, rigorous scholarship, the work style of excellence has been inspired me to keep forward. From the choice of the subject of the topic and the overall idea to the final completion of the paper, Jiang teacher has been given my patient guidance and support, I would like to extend my sincerely thanks to the professor Jiang. Secondly, I would also like to thank the students in the process of completing the process to give me support and help students, because of your patient help and relentless support, I can continue to overcome the problems encountered and confused to complete this paper. Finally, I would like to express my sincerely thanks for experts and teachers who take times out of their busy schedule to review my paper.

References

1. Wenzhong, Z.: Development status of intelligent agricultural machinery and equipment at home and abroad. *Mod. Agric. Mach.* **06**, 4–8 (2015)
2. Study on the application of internet of things in intelligent agriculture. Zhengzhou University (2012)
3. Archambault, S.: Ecological modernization of the agriculture industry in southern Sweden: reducing emissions to the Baltic Sea. *J. Clean. Prod.* **12**, 491–503 (2004)
4. Yokijiro, Y., Latan, V.: Agricultural development of the international analysis, p. 17. China Agriculture Press (2005)
5. Liu Jinlong, L., Kang, X.L.: Intelligent and development trend of agricultural machinery. *Sci. Technol. Innov.* **07**, 123–124 (2017)
6. Fei, M., Xiangzhi, K.: Overall situation and future orientation of agricultural modernization in China. *Reform* **10**, 9–21 (2012)
7. Technology of crop planting environment based on mobile GIS. *J. Agric. Mech.* (09), 325–334 (2015)
8. Liang, P.: Design and implementation of real-time data acquisition system. Southwest Jiaotong University (2015)
9. Zhang, M.: Study and research on data mining algorithm based on Hadoop. Kunming University of Science and Technology (2012)
10. Pruganti, S., Ding, Q., Tabrizi, N.: Exploring Hadoop as a platform for distributed association rule mining. In: *The Fifth International Conference on Future Computational Technologies and Applications, FUTURE COMPUTING 2013*, pp. 62–67 (2013)
11. Yu, H., Wang, D.: Mass log data processing and mining based on Dadoop and cloud computing. In: *2012 7th International Conference on Computer Science and Education (ICCSE)*, pp. 197–202. IEEE (2012)
12. Zhou, B.: Study on mining method of massive engineering data association planning based on Hadoop. Beijing Jiaotong University (2016)



Understanding the Consumer Satisfaction of the “Last-Mile” Delivery of E-Business Services

Shujun Liu¹, Yan Li¹(✉), Jingqi Huang¹, and Xin Zhao²

¹ International College, China Agricultural University,
Beijing 100083, People’s Republic of China
liushujun_cherie@163.com, icbliyan@cau.edu.cn,
376138979@qq.com

² College of Humanities and Development Studies,
China Agricultural University, Beijing 100083, People’s Republic of China
Zhaoxin_phd@cau.edu.cn

Abstract. With the rapid development of e-business and modern logistics, people put more and more attention on the service of the express delivery industry. The “last mile” delivery is regarded as the most important link between logistics companies and customers, which deeply affects consumers’ satisfaction on the companies’ services. Concerning the non-linear relationship between production supply and consumer meet, Kano model is widely adopted to evaluate the satisfaction from consumers in the e-business services. This research aims to figure out the factors that influence the consumer satisfaction on the service of the “last mile” by using Kano model. According to the result analysis, some suggestions are raised up to meet customers’ needs to enhance the quality of service of the “last mile” delivery of e-business service.

Keywords: Consumers satisfaction · Kano model · The “last mile” delivery

1 Introduction

1.1 Development of E-Business and Express Delivery Industry in China

Because of the low-cost, efficient, speedy alternative offers, Chinese market is going rapidly. E-business makes the handling of channel speedier and logistics functions more convenient, for instance inventory handling and delivery, order processing. Online shopping are becoming crucial in people’s daily life. As the China Electronic Commerce Research center reported, at the first half of 2016, China e-business’ transactions amount, which is up to 10 trillion and 500 billion RMB. It is an year-on-year growth increase of 7.2% [1]. Furthermore, B2B market transaction grows to 7 trillion and 900 billion RMB, and online retail market transaction is 2 trillion and 300 billion RMB.

New online tools construct a closer, personalized, interactive customer relationship. However, the rapid development and the severe competition bring some problems and challenges. One of the most serious challenges is express delivery. In 2016, the

amount of Chinese express delivery company has been 13.25 Billion Pieces, up 56.7% year on year [2]. The high speed of development of the express delivery industry requires scientific management and efficient distribution, which could undertake the pressure from e-business.

1.2 Development of the “Last Mile”

Express delivery can be divided into four stages. They are solicitation, sorting, transfer, and delivering. Delivering, which is the last part of distribution, is the most important part in this industry. It is because delivering is the only access for express delivery companies to contact the customers. In order to improve the service quality in the last part, express delivery industry develops the “last mile” strategy, which is particularly used to illustrate the interaction between people and goods from transportation centre to homes [3].

Express delivery companies have came up with two models for the “last mile”. The first one is joint distribution, which means one company will collect the products from different express logistic companies, then distribute them uniformly. The second one is that customers pick up the goods autonomously. The second model also can be divided into two categories. First, express delivery company could cooperate with convenience store. They put goods in the convenience store, customers are able to pick up them with certain message. The another one is that company build specialized pick-up points in communities or universities.

1.3 Jinlinbao Express

Jinlinbao is a typical and famous company that build the pick-up locations. It acts as a platform to provide service in the last mile. It offers intelligent express mail box for customers. Express delivery companies would put the packages in the mail box, then customers are able to pick up package according to certain cell phone message. Jinlinbao has been introduced in Beijing, Shanghai, Tianjin and other 20 cities. In addition, more than 1,000 communities and 100 colleges have Jinlinbao pick-up locations [4]. Because of the leading market share, Jinlinbao is the representative of this model. This model saves time, improves efficiency of distribution, and protects customers’ privacy. What’s more, it provides mobile app and official account of Wechat, which enlarge its coverage and allows mobile phone remote operation.

2 The Problems of the “Last Mile” Delivery

Compared with developed countries, it is no doubt that China still has a supply and demand problem on developing express delivery. The fast developing online business in China requires the higher quality of express delivery’s service. They highly focus on the “last mile” because it directly affect customer’s satisfaction for the shopping experience. “Considered the goods have to be transported to each consumer’s home eventually, they cannot be stand still in any freight station or port. However, in reality, the last leg of the supply chain is sometimes inefficient, literally up to 28% of the total

cost for moving goods, which is known the “last mile problem [5, 6].” According to it, we can know that “last mile” still exists some serious problems that drag on the development of e-business. Hence, the following part explains the most remarkable problems of the “last mile” delivery.

2.1 Low Quality of Distribution Services

Low quality of distribution services in the “last mile” can be reflected in three aspects. First, delivery man cannot distribute the packages to the customer in time, so the efficiency of distribution is pretty low. Second, customer may get the packages that are damaged during transportation. Third, the bad attitude of delivery man also lowers the quality of distribution services [7].

2.2 Low Traceability of Distribution Information

Nowadays, most express delivery companies still use labors to delivery and distribute packages. Therefore, the level of informatization is low. The information about when the packages are delivered to customers, or whether customers sign for the packages can be imprecise. It prevents companies and customers from following the track of their packages. Sometimes, express delivery companies even cannot discover the loss of products until customers complain about it.

3 Kano Model

We use Kano model to analyze customers satisfaction in our experience. This model consists of three attributes which are necessary attribute, attractive attribute, and value-added attribute. Necessary attribute is the basic requirement, and customers will be dissatisfied if company doesn’t provide it. Attractive attribute has Linear relationship with customers satisfaction, and more attractive attributes are provided, more satisfied customers would be. For value-added attribute, customers will be surprised and very satisfied if companies provide it, and not be dissatisfied without it.

Kano model requires a two side research questions which will be mentioned in next part. According to customers’ answers to question 1 and 2, Table 1 may record each consumer’s attitude about the classification of those factors. For each factor, most of consumer’s answers suggest it to be which attribute, we then classify it to be that attribute. After that, Kano model requires to calculate SI (satisfied influence) and DSI (dissatisfied influence) value according to the percentage of consumers’ A, O, M, I answers. The following two are the SI and DSI equations.

$$SI = (A + O) / (A + O + M + I)$$

$$DSI = -1 \times (O + M) / (A + O + M + I)$$

A unit square is drawn, and its one side represents SI value while the adjacent side represents DSI value. We also draw a circle with center of the intersection vertex of those two sides and its radius is half the length of the square’s diagonal. After that, we

label the attributes on the square according to their SI and DSI value. If the points are in the circle, it means they are less sensitive, can be put away temporarily. And the further the points from the center of the circle, the larger affects they have on customers satisfaction.

Table 1. Quality attributes categories of Kona model

With/without the attributes of service	Like	Must-be	Neutral	Live with	Dislike
Like	Q	R	R	R	R
Must-be	A	I	I	I	R
Neutral	A	I	I	I	R
Live with	A	I	I	I	R
Dislike	O	M	M	M	Q

4 Design of Duestionnaire and the Investigation of Consumers

4.1 Design of Questionnaire

In order to collect the data accurately, the questionnaire can be divided into two parts. The first part mainly investigates the demographic information of relevant customers, which contains gender, age, the use Jinlinbao, and the frequency for using Jinlinbao. Another part of is the express service-related attributes, a total of 10 pairs of entries, each of which is designed as the Table 2. The following chart illustrates each entry stand for what attribution about express delivery service. This part integrates the Kona model and traditional 5 scale survey method [8]. Therefore, participants will be asked to select answer from “like”, “muse be”, “neutral”, “live with”, and “dislike”. According their answers for each pair of questions, we can divide the attributions of express delivery service into five quality factors that the Table 1 already shows.

Table 2. Attributes and the benefits of express service

Service attributes	Description of logistic attributes	Benefit provided for customers
<i>f1</i>	Time difference between goods in distribution center and goods in pick up point is short	Fast
<i>f2</i>	Received goods are undamaged	Safe
<i>f3</i>	Customers can pick up goods in appointed place	Safe
<i>f4</i>	Arrive at next day	Fast
<i>f5</i>	Location for pick up point is reasonable, which saves time	Convenient
<i>f6</i>	Services for 24 h	Convenient
<i>f7</i>	Communicate with delivery staff easily	Cheerful
<i>f8</i>	Delivery staff dress clean and tidy uniform	Cheerful
<i>f9</i>	Have certain VIP activities	Value-added
<i>f10</i>	Have special activities for holidays	Value-added

4.2 The Distribution and Collection of Questionnaire

The questionnaire is distributed and collected from February 20, 2017 to April 15, 2017. Over the roughly 2 months, 400 questionnaires were collected in total, among which 365 are effective through the soft-ware testing. According to the statistical result, the characteristics of the personal information in the sample are as follows: 49.86% are males, 50.14% are females; 25.75% are freshman, 29.86% are sophomore, 21.92% are junior, 22.47% are senior; 30.68% seldom receive or send express, 35.07% receive and send 1–3 express one week, 34.25% receive and send more than 3 express one week.

In general, the male female ratio is fairly reasonable and the distribution of informants’ grade and the frequency of receive and send express are considered as normal distribution, which means that each index conform to the discipline of normal statistics.

4.3 The Analysis of Reliability of Questionnaire

Reliability represents the consistency and stability of a scale. In social science area, Cronbach’s Alpha is the most common standard to test a scale’s reliability. A high value of Cronbach’s Alpha suggests a high reliability of the scale and less error of the measurement. By using the PASW Statistics18.0, the result suggests that the Cronbach’s Alpha of all 21 questions in the second part is 0.835. Under normal circumstances, when the Cronbach’s Alpha is greater than 0.8, it suggests that the reliability of the scale is ideal. Therefore, it means that the collected data is consistent and stable which is very reliable, and it can satisfies the general requirement of the research.

5 Results and Discussion

5.1 Results

The mean satisfaction level of 365 customers is calculated, which is 2.9. Table 3 shows the independent variables classification results. It indicates that factor “fast” and “convenient” are classified into one-dimensional quality attribute, while “value-added” and “cheerful” factors belong to attractive quality attribute. Meantime, the factor “safe” is belonging to must-be quality attribute.

Table 3. Independent variables classification results

Independent variables	A	O	M	I	R	Q	Classification result (%)
Fast	19.2	32.5	22.5	24.5	0.2	1.1	O
Safe	14.2	11.5	26.4	45.2	0.8	1.9	M
Convenient	15.8	49.8	30.1	2.5	0.6	1.2	O
Valued-added	55.8	26.6	13.8	2.1	0.7	1	A
Cheerful	33.2	29.8	12.5	18.6	0.9	1	A

After classifying the attribute quality of these most important factors for express delivery industry, the SI (Satisfied influence) and DSI (Dissatisfied influence) are also analyzed, according to the formulas:

$$SI (\text{satisfied influence}) = (A + O) / (A + O + M + I) \tag{1}$$

$$DSI (\text{dissatisfied influence}) = -1 \times (O + M) / (A + O + M + I) \tag{2}$$

Table 4. Result for SI and DSI

	SI	DSI
Fast	0.52	-0.56
Safe	0.26	-0.39
Convenient	0.67	-0.81
Value-added	0.29	-0.41
Cheerful	0.67	-0.45

Table 4 represents the SI and DSI for each factor. According to the results for SI and DSI, Fig. 1 is drawn and it shows the sensitiveness of each factor. Figure 1 pictures that if one factor is in the circle, this factor is less sensitive for customers, which can be put away temporarily. While the customers are very sensitive for the factor that is out of circle. Figure 1 shows that “convenient”, “fast”, and “cheerful” are the most sensitive and influential factors.

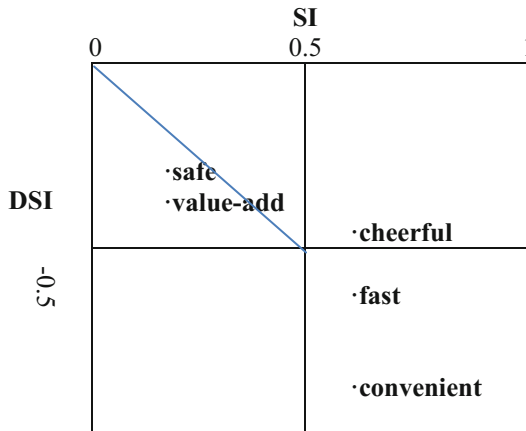


Fig. 1. Sensitiveness of factors

5.2 Discussion

Logistics enterprises may gain much more precious data on customer needs, providing kano model applies [9]. As the results state, the consumers’ satisfaction for Jinlinbao are not so high. About 55% customers think that the Jinlinbao’s service is generic or below. Therefore, some problems exists of Jinlinbao about its “last mile” delivery. Jinlinbao company needs to understand what customers think and adjust their service. The Kano model gives us a good way to know what service of express industry can satisfy their need. Therefore, express delivery companies are supposed to introduce appropriate policies to enhance the service quality according to the various service attributes.

From the statistical analysis in Fig. 1, we can conclude that most customers regard “safe” as must-have attribute, which means that safe is the most basic service that express delivery company should provide in the “last mile”. The “fast” and “convenient” are the attractive attributes. It hints that if the “last mile” could quickly deliver goods to customers and customers can take goods from pick-up points conveniently, customers will be satisfied with its delivery service. The one-dimension attribute includes staffs with clean cloth and special promotions. These kind of services would not drive customers away if companies don’t provide them. However, offering these services would have advantage than other companies, and attract more consumers. We find that “convenient” has the biggest influence on customers satisfaction and the following two are “fast’ and “cheerful”.

6 Conclusions

Based on the former research, it is conspicuously said that intensive interaction exists between consumers and companies, which constructs an ethical system, and the last mile, which I believe is a form of margin embedded in the system containing the both subjects. Therefore, since we concern the consumers’ satisfaction, sellers’ rights and obligations cannot be neglected.

First, rules must be established to constrain the acts of company workers. Now that safety is the most basic element in the “last mile”, according to our research, proper article shall stipulate that workers have the obligation to take accurate measures to preserve the goods safety, and they shall fix the cabinet if it does not work ensuring the regular service.

Secondly, institution of sales back or escrow shall be properly established to make sure the efficiency use of every locker. However, to prevent the abuse of such rights, companies must have the obligation to announce the consumer fetching goods, and leave a reasonable time for them.

Eventually, considering the fast and convenient factors, more picking up places could be set in one relatively close but big area, like universities or communities. Consumers can conveniently choose where to fetch by using Apps; on the other hand, to release the crowed at the same time.

References

1. China's e-Commerce Research Center: China E-business Report 2016, February 2017
2. China's e-Commerce Research Center: China Express Delivery Industry Report 2016 (2016)
3. Prickett, K.: What is The Last Mile for E-Commerce? Prospress, July 2014. <https://prospress.com/what-is-the-last-mile/>. Accessed 29 Jun 2017
4. Sun, H., Wang, X., Li, H., He, Y.: The analysis of the new distribution model: last mile. *J. Liaoning Univ. Technol. (Soc. Sci. Ed.)* **04**(19), 1–5 (2013). <https://doi.org/10.15916/j.issn1674-327x.2017.04>
5. Rodrigue, J.-P., Comtois, C., Slack, B.: The “Last Mile” in Freight Distribution. *The Geography of Transport Systems*, 2nd edn, p. 212. Routledge, London (2009)
6. Scott, M., Anderka, S., O'Donnell, E.: Improving Freight Movement in Delaware Central Business Districts. Institute for Public Administration, University of Delaware (2009)
7. Yang, J., Yang, C., Yao, X.: Research on the “Last-Mile” issue in the E-commerce logistics system. *J. Bus. Econ.* **04**(207), 17–20 (2014)
8. Meng, Q., Zhou, N., Tian, J., Chen, Y., Zhou, F.: Analysis of logistics service attributes based on quantitative Kano model: a case study of express delivering industries in China. *J. Serv. Sci. Manag.* **04**(01), 42–51 (2011)
9. Tang, Y., Meng, Q., Wang, X., Zhang, X., Wang, J.: Detection analysis of logistics services based on Kano model. *Value Eng.* 19 (2011)



The State of Motion Stereo About Plant Leaves Monitoring System Design and Simulation

Jiangchuan Fan^{1,2,3}, Xinyu Guo^{1,2,3(✉)}, Chuanyu Wang^{1,2,3},
Xianju Lu^{1,2,3}, and Sheng Wu^{1,2,3}

¹ Beijing Research Center for Information Technology in Agriculture,
Beijing 100097, China

² National Engineering Research Center for Information Technology
in Agriculture, Beijing 100097, China

{fanjc, guoxy, ralf.wangcy, luxj, wus}@nercita.org.cn

³ Beijing Key Lab of Digital Plant, Beijing 100097, China

Abstract. A binocular stereo vision plant leaf motion monitoring system was proposed in this paper, the system includes a binocular camera, horizontal movement module, the vertical movement module, the image acquisition card, and a computer. The supporting structure holds camera above the measured maize leaf, the camera is able to capture image pair at 30 fps, An image processing program is installed in computer, the program includes image acquisition, image pre-processing, markers extraction, sub-pixel edge refinement, 3D reconstruction and other modules. A fluorescent ball (diameter 0.35 cm) with high reflectivity was chosen as a marker, and its intensity is higher than the background environment which makes it easier to extract contour of ball out of background. The spherical marker will keep its circular shape more or less after perspective projection. In order to further improve the accuracy of stereo matching, a sub-pixel edge detection method based on gradient magnitude was adopted, in the initial position of the edge, a set of reference points was selected according to the gradient magnitude threshold along gradient direction, the x and y coordination of reference points sum up weighted by gradient magnitude, the mean of weighted sum is the increments of initial edge in sub-pixel form. In the simulation experiment, the camera is set away from the measured object about 50 cm, the system measurement accuracy can reach to 0.0139 cm, it is able to detect the small changes of leaf position. In field experiments, the actual measurement of the movement leaf caused by growth and physiological responses achieved the desired results, this study provide a solution to continuous, non-destructive, non-contact acquire crop growth information in three-dimensional space.

Keywords: Binocular stereo vision · Plant leaf · Growth monitoring
Image processing · Sub-pixel

1 Introduction

With the improvement of technology, the observation and research of the life phenomenon have further to an fine, quantitative development. In agricultural areas, some monitoring methods integrated light, machine, electricity and other various techniques

have played a key role in the production, scientific research and other key links. Among them, machine vision technology have achieved very good results in the quality detection of agricultural products, crop growth condition monitoring of agricultural machinery and automatic navigation of agricultural machinery, identification of crop diseases and insect pests for it's rapid, nondestructive, non – contact [1–9].

Machine vision technology can obtain the digital information of plant growth in real time and continuously [10, 11], and it plays an important role in the understanding of plant growth and the formulation of reasonable control measures. Ma et al. [12] used machine vision and image processing technology to monitor the growth information of many plants. It was found that in the process of image processing, the EEC (Estimation Error Cancel) image analysis method based on sub pixel and region matching can improve the detection accuracy effectively. Using this system to monitor the growth of chrysanthemum, we can see that the growth rate of the chrysanthemum in the day was lower than that at night.

Plant growth in the three-dimensional world, while uses the method of two-dimensional image monitoring of crop growth in the case that the crop biomass is small, the change of morphology is little can play a better role. However, for the crop organs with complex form such as corn leaves, it is difficult to ensure that the motion of the monitored blade is in the plane of the camera's projection.

The basic principle of binocular stereo vision technology is to observe the same object from two points of view in order to obtain the stereo image pair and match the corresponding image points, which can calculate the parallax and obtain the 3D information [13–17].

The difficulty of the binocular stereo vision technology is stereo matching of left and right two images. The stereo matching method based on feature points in Ref. [13] is difficult to get a dense 3D point cloud and obtain the 3D coordinates of the target points. References [16, 17] used the global matching methods based on the imulated annealing algorithm and dynamic programming to obtain the dense 3D point cloud of the maize leaf. However, the error of the solution is large, and the subtle movement of the corn leaves can not be well identified. The method presented in Ref. [14, 15] is special, and is not suitable for the folding and rolling of the blade edge. According to the shortage of these methods above, in order to realize the motion state monitoring of maize leaves, this paper present a method that attach the fluorescent light beads in maize leaves as markers, to simplify the complexity of stereo matching algorithm, and improve the precision of the 3D reconstruction of target.

2 System Design

Monitoring system includes the hardware support structure and the back-end image processing algorithm. The main function of hardware support structure is to create a relatively stable image acquisition environment in the corn canopy, while the back-end software algorithm is mainly used to complete the image processing, 3D reconstruction, visualization and so on.

2.1 Composition and Function of the System Hardware

The system is composed of a binocular camera, a sliding shaft, a sliding rod, a bracket, an image acquisition card, a data line and a computer. Image acquisition using binocular camera of Beijing microview MVC1000SAM-GE30ST and the 8.5 mm Pentax lens, which effective pixel is 1280 × 1024. The sensor size is 1/2 in. and the pixel size is 5.2 * 5.2 μm. Move the binocular camera to the top of the monitored blade through a sliding shaft when image is being acquired. The vertical height of camera is adjusted by the tripod of the supporting sliding rod. The distance 30–50 cm of the camera and blade is better. During image acquisition camera internal and external parameters remains the same and try to choose a better light sunny day using a larger aperture can ensure the images with a good depth of field (Fig. 1).

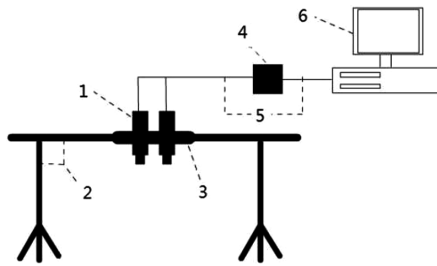


Fig. 1. Binocular stereo vision system. 1. A binocular camera 2. A sliding rod 3. A bracket 4. An image acquisition card 5. A data line 6. A computer.

2.2 Principle of Binocular Stereo Vision

Set a point M (X, Y, Z) in the marker. M1 (x1, Y1), M2 (X2, Y2) are the image coordinates of the M point’s projection in the left and right two images and the projection matrix of the left and right cameras is Pi:

$$P_i = \begin{bmatrix} a_{11}^i & a_{12}^i & a_{13}^i & a_{14}^i \\ a_{21}^i & a_{22}^i & a_{23}^i & a_{24}^i \\ a_{31}^i & a_{32}^i & a_{33}^i & a_{34}^i \end{bmatrix} \quad (i = 1, 2) \tag{1}$$

and so

$$w_i \begin{bmatrix} x_i \\ y_i \\ 1 \end{bmatrix} = P_i \begin{bmatrix} X \\ Y \\ Z \\ 1 \end{bmatrix} \quad (i = 1, 2) \tag{2}$$

where (x1, y1, 1), (x2, y2, 1) are the homogeneous coordinates of m1 and m2 in their respective images, (X, Y, Z, 1) is the homogeneous coordinates of M (X, Y, Z) points in the world coordinate, wi is nonzero parameter, akmn (k = 1, 2; m = 1, 2, 3; n = 1, 2, 3, 4) is the element in the projection matrix Pi (i = 1, 2), representing the intrinsic

matrix (focal length, distortion) and external parameters matrix (translation and rotation) of the camera. According to the coordinates $m1 (x1, y1)$, $m2 (x2, y2)$ of the measured point M on the camera image and formula (2), we can seek out the world coordinates (X, Y, Z) of unknown point M .

$$\begin{bmatrix} (a_{11}^i - a_{31}^i x_i) & (a_{12}^i - a_{32}^i x_i) & (a_{13}^i - a_{33}^i x_i) \\ (a_{21}^i - a_{31}^i y_i) & (a_{22}^i - a_{32}^i y_i) & (a_{23}^i - a_{33}^i y_i) \end{bmatrix} \begin{bmatrix} X \\ Y \\ Z \end{bmatrix} = \begin{bmatrix} x_i a_{14}^i \\ y_i a_{24}^i \end{bmatrix} \quad (3)$$

The camera projection matrix P_i is obtained by Zhang plane template calibration method [18]. It isn't described due to the limited space.

2.3 Image Processing Algorithm

The computer used in the algorithm development adopted the Pentium (R) D processor, whose memory is 2.0 GB. Software is written by C++ language and the computer vision library is OpenCV. Using the binocular stereo vision system to collect data and the image can be get at the speed of 30 frame/s supported by the system. After the experiment, the collected data were processed to obtain the state information of plant growth. The flow chart of the blade motion monitoring algorithm is shown in Fig. 2.

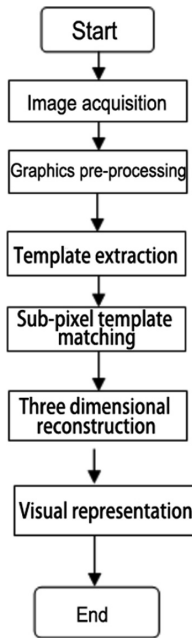


Fig. 2. Flow chat of the image processing

2.3.1 Image Acquisition and Preprocessing

In plant growth monitoring, a template with fixed form was placed on the surface of the tested plant, and the change of the position of the plant was indicated by the movement of this template. Considering the complex environment of the field and the plant itself, this paper put the diameter 0.35 cm fluorescent beads as landmarks and fluorescent beads attached in a black disk, which are convenient for placing maize leaves in different parts. According to the different monitoring purposes, one or more marks can be placed. Move the binocular camera to the appropriate position, to make the tag template in the visual field of the left and right two cameras. Set the image acquisition time interval is 60 s, the image is automatically stored in the computer to prepare for subsequent processing.

The initial image contains information about the leaves, marks, and soil background, as shown in Fig. 3.



Fig. 3. Maize leaf image

As the redundant information, the soil background will affect the subsequent image processing. There are many methods to remove it in the image of green plants, such as the threshold method using the difference of gray color between soil and plant, the super green method, which is said that the green plants meet this condition $2G > (B + R)$. We should also reserve the marker area at the same time. The traditional method will remove a part of the mark, and affect the final calculation accuracy. In this paper, the decision surface method is used to segment the image, which can keep the blade and mark pixels. The decision surface algorithm can be described as

$$C = \frac{R^2}{V^2} + \frac{(1 - G)^2}{(YB + U)^2} \quad (4)$$

where R, G, B is the intensity values of there colors red, green and blue after normalization and the values range from 0 to 1. The original values of the original color intensity red R, green G, blue B is from 0 to 255, corresponding to the normalized $R = r/255$, $G = g/255$, $B = b/255$. V, Y, U are parameters describing the curved

surface shape. Among of them V is the maximum intensity of the red when the green can be perceived. In this time $B = 0$, $G = 1$. Y is the tilt index of surface boundary in the plane of red and green. U is the difference between the maximum green strength value and the minimum value when the blue and red channels are both zero and the green can be sensed. V , Y , U are the constant value and here $V = 0.85$, $Y = -0.37$, $U = 0.74$. Put the normalized R , G , B value into the decision surface algorithm can calculate the C value. If the C value is greater than or equal to 1, this pixel belongs to the blade region, should be retained. If not, this pixel belongs to the soil background region, should be discarded.

There are still sporadic isolated island pixels in the soil background with the image binarization after segmentation, and it can be removed by area threshold filtering. The final image contains only the target area, as shown in Fig. 4.



Fig. 4. Background pixels removed image

2.3.2 Marker Extraction

Mark the brightness was significantly higher than that of the surrounding environment such as leaves, by edge detection algorithm to obtain fluorescence ball marker profile, if the ball to orthographic cameras, then ball image contour is round, but maize leaves have a larger bending, makes some fluorescence ball contour on the image oval. On a step of image using Canny operator for edge detection, and then use the following criteria, ellipse markers identification of fluorescent balls

- (1) Whether the edge is closed. The mark points edge is a closed curve, which removes the non closed curve caused by the texture, shadow, and so on by finding the closed contour.
- (2) The brightness of the marker is higher than that of the background, and the closed curve of the dark region is removed by the gray level threshold.
- (3) Contour area. Mark objects in the image pixel size is relatively fixed, which can remove the noise background contours of objects and smaller silhouettes.

- (4) To judge the roundness. Circular markers due to the visual distortion formed elliptic, compared with the images of natural objects contour closer to circular, judge whether the region as a marker by judge closed curve roundness. Like a circle method of calculating $D^2/(4\pi A)$, where D is the perimeter of the region, a area in the region for the calculated value is close to 1 the region shape is nearly circular.

By using these conditions, the image of the last step is restricted to get the two value image which contains the mark point, as shown in Fig. 5.

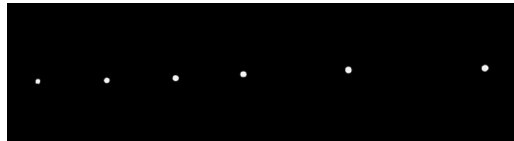


Fig. 5. The binary image of template

2.3.3 Markers of Sub-pixel Refinement

Get the logo pixels on the edge of the material, the edge pixels of the center of gravity as the left and right two pieces of stereo image of matching points. According to the prior calibration of the intrinsic and extrinsic parameters of the camera can obtain the three-dimensional coordinates of the point. A step for take marker edge are rough, directly used to calculate the results will appear larger error and some movement of the blade is small, this error will influence perception on the leaf fine motor. In order to further improve the accuracy, using sub-pixel edge refinement algorithm, first sub-pixel edge location, and then use the ladder of amplitude method of edge point adjusted so as to obtain the sub-pixel edge.

Gradient amplitude specific process: (1) at each pixel edge computing the gradient components of X and Y direction, each edge point and the gradient magnitude $G(x, y)$ and the gradient direction $\alpha(x, y)$ is calculated by the two components. Specific calculation method:

$$\text{gradient magnitude} \quad G(x, y) = \sqrt{G_x^2 + G_y^2} \tag{5}$$

$$\text{gradient direction} \quad \alpha(x, y) = \arctan(G_y/G_x) \tag{6}$$

Count G_x and G_y the specific form of the convolution template used in the time is shown in Fig. 6

-1	0	1
-1	0	1
-1	0	1

1	1	1
0	0	0
-1	-1	-1

Fig. 6. Gradient convolute template

(2) according to the $G(x, y)$ and a given threshold value T , the gradient direction is determined to meet the $G(x, y) > T$ value range.

Assuming the pixel edge points (x, y) , gradient direction for $\alpha(x, y)$, when $\alpha < \alpha(x, y) < \beta$ (Fig. 7 $\alpha = \text{Pi}/2 + \arctan(1/3)$, $\beta = -\arctan(1/3)$), along the gradient direction and the reverse direction judgment adjacent two points $(x - 1, Y - 1)$ and $(x + 1, y + 1)$, is greater than the threshold value T and obtains the distance component.

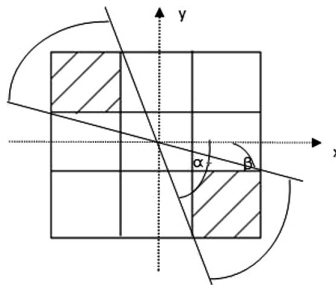


Fig. 7. Points in the direction of grads

(3) By using the gradient component G_x and G_y as the weight of the pixel edge, the edge pixels are obtained, Correction formula for:

$$\Delta d_x = \sum_{i=1}^n G_{x_i} d_{x_i} / \sum_{i=1}^n G_{x_i} \quad \Delta d_y = \sum_{i=1}^n G_{y_i} d_{y_i} / \sum_{i=1}^n G_{y_i} \tag{7}$$

Among, d_{x_i} —The distance between the pixel points along the gradient direction and the rough edge points X component product

d_{y_i} —The distance between the pixel points along the gradient direction and the rough edge points Y component product

G_{x_i} —X directional gradient component

G_{y_i} —Y directional gradient component

n —The number of pixels in the $G(x, y) > T$ along the gradient direction.

As shown in Fig. 8 after subpixel refinement markers of template image edge, edge to describe the boundary of the position of object and background in image logo, obtained by the edge of the center of gravity of the matching points matching accuracy is further improved. Figure 8(a) is sub-pixel refinement template edge, the edge in the lower left is a concave regions, corresponding to 8(b) image position of the same pixel gray than normal fluorescent spheres regional low, this may is caused by the processing defect of fluorescent balls, sub-pixel refinement algorithm to identify the defects, and can correct the edge extraction.

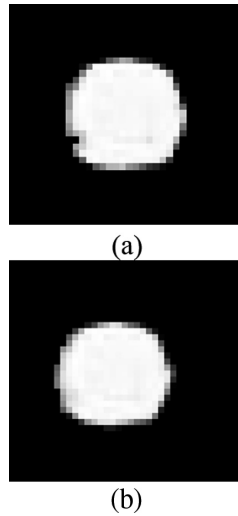


Fig. 8. Template edge after sub-pixel refine. (a) Template edge after sub-pixel refine processing, (b) Template edge before sub-pixel refine processing

3 Measurement and Result Analysis of Motion Information of Maize Leaf

3.1 Measurement Accuracy Analysis

From the experiments, the accuracy of the measuring precision of binocular stereo vision system of measurement accuracy is affected by many factors, such as the camera resolution and measurement of the object distance, two cameras into the angle calibration algorithm. It is difficult to through the theoretical derivation and calculation for a particular stereo vision system for the test of binocular stereo vision system accuracy and reliability, designed a special environment, such as Fig. 9 shows, with signs of blackboard is vertically placed in the horizontal displacement, the displacement in stepping motor to drive the horizontal motion and binocular camera is placed horizontally toward and blackboard vertical displacement platform is arranged at the lower

part of the ruler. At the beginning of the binocular camera and blackboard The P, p + 2 cm, p + 3 cm, p + 5 cm, p + 7 cm, p + 9 cm, and p + 1 cm, are moved from the blackboard to the following default position points.

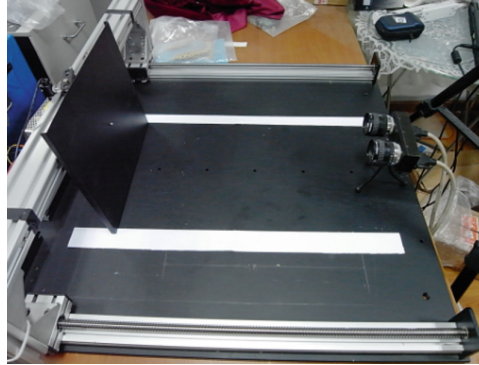


Fig. 9. Schematic of accuracy testing

In several preset position marking point 3D coordinates were calculated. Results are shown in Table 1 shows, X, Y, and Z preset three-dimensional coordinate value, the distance value for each preset point to the distance of the binocular camera coordinate system origin, the relative distance to the preset point to the first preset point distance.

Table 1. Result of simulation computation

Test point	X	Y	Z	Distance	Relative distance
p	0.621522	1.02058	-14.2087	14.25886	0
p+1 cm	0.641343	1.10705	-14.5564	14.61252	0.353659
p+2 cm	0.728676	1.13624	-14.8969	14.95793	0.699071
p+3 cm	0.776305	1.15987	-15.2637	15.32738	1.068519
p+5 cm	0.800921	1.21335	-16.0012	16.06711	1.808254
p+7 cm	0.813348	1.27049	-16.7475	16.8153	2.556446
p+9 cm	0.788134	1.32617	-17.4523	17.52035	3.261492

Calculated from Table 1 data and real world 0.358102 1 cm and binocular camera coordinate relative should. Distance between adjacent points of measurement error, the mean absolute value is 0.00498, corresponding to the real world 0.0139 cm test camera and sign in initial position and the distance of 50 cm, the measurement error in the range system has reached 0.0139 cm can meet the maize leaf movement monitoring required measurement accuracy.

3.2 Corn Leaf Growth Monitoring

Tested materials for maize varieties to educating 3352013.6.17 sowing date, density of 60000 plant/hm², normal water and fertilizer treatment. Select 13 leaf stage of maize plant growth monitoring experiment. At this time the growth of maize leaves is very strong, plant the rapid expansion of the volume, dry weight increased dramatically. Choose a unfolding visible leaf as experimental material, will mark the paste on the blade, using the system for continuous monitoring of plant growth, with 1H intervals calculated the time period of markers in three-dimensional space displacement (*l*). The results as shown in Fig. 10.

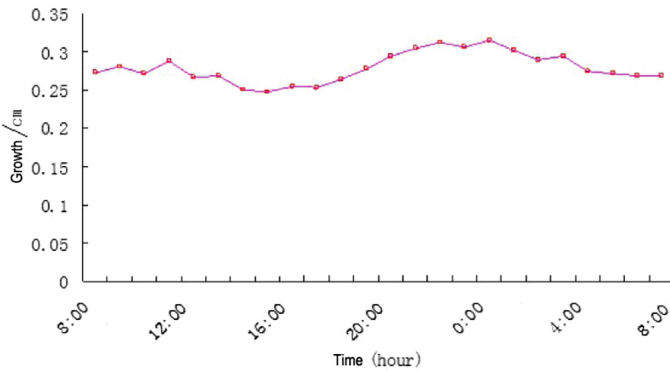


Fig. 10. The time course of leaf movement

3.3 Corn Leaf Movement Monitoring in One Day

Silking, ear of corn on a leaf of choose to do as the observation object, try to choose no wind conditions. From the leaves in the upper to tip six landmark points are uniformly arranged, mark points in the 8:00 time for initial state were recorded mark point position 10:00, 14:00, 16:00, calculation and the initial condition of the marker distance of 3D point position. Calculations such as shown in Fig. 11.

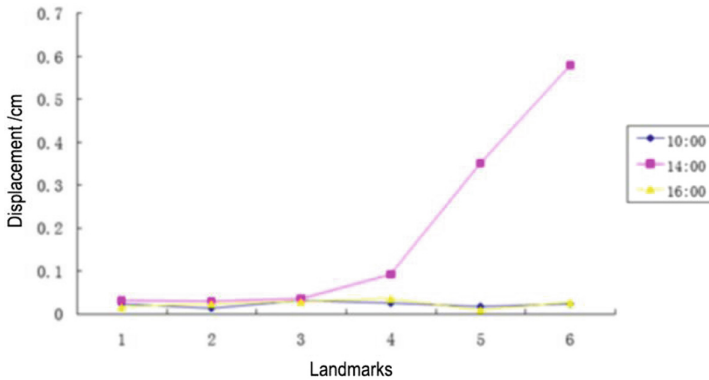


Fig. 11. The leaf movement in one day

From the figure can be seen mark points 14:00 and 8:00 landmarks near the blade tip of three points, large displacement, reaching the point of tip 0.579 cm, and 10:00 and 16:00 data with no obvious change of position. The reason, may is due to the midday leaf transpiration reached maximum, the cells of leaf water loss overall downward drooping, and 10:00 and 16:00 PM due to high temperature, transpiration have yet to make leaf water loss sag. In the central region of the corn leaf veins of leaves to a supporting role, especially lower in leaves, resulting in the loss of water drop phenomenon More pronounced at the tip of the blade.

4 Conclusions

Design and implementation of a for maize leaf movement monitoring of hardware structure and software algorithm, using fluorescent beads do as a marker to simplify the image processing algorithms, an increase of binocular stereo vision 3D coordinate measuring accuracy. Simulation experiment system measurement precision can reach 0.0139 cm, pass over field experiments demonstrate the movement monitoring system feasibility of leaves in three-dimensional displacement information acquisition, for further analysis of blade space attitude reflects the crops growth and physiological changes provides data acquisition means.

By the principle of binocular vision technology limited, if the measured object changes in the morphology of the larger, such as caused by the wind blade retroflexion and displacement, making the sign bit disappear from the camera's field of view, measurement accuracy will have great effect on.

References

1. Howarth, M.S., Brandon, J.R., Searcy, S.W., et al.: Estimation of tip shape for carrot classification by machine vision. *J Agri. Eng. Res.* **53**, 123–139 (1992)
2. Szczypiński, P.M., Zapotoczny, P.: Computer vision algorithm for barley kernel identification, orientation estimation and surface structure assessment. *Comput. Electron. Agric.* **87** (9), 32–38 (2012)
3. Pearson, T.C., Schatzki, T.F.: Machine vision system for automated detection of aflatoxin contaminated pistachios. *Agric. Food Chem.* **46**(6), 2248–2252 (1998)
4. Ni, B., Paulsen, M.R., Reid, J.F.: Size grading of corn kernels with machine vision. *Appl. Eng. Agric.* **14**(5), 567–571 (1998)
5. Linker, R., Cohen, O., Naor, A.: Determination of the number of green apples in RGB images recorded in orchards. *Comput. Electron. Agric.* **81**(2), 45–57 (2012)
6. Wang, Q., Wang, H., Xie, L., et al.: Outdoor color rating of sweet cherries using computer vision. *Comput. Electron. Agric.* **87**(9), 113–120 (2012)
7. Confalonieri, R., Foi, M., Casa, R., et al.: Development of an app for estimating leaf area index using a smartphone trueness and precision determination and comparison with other indirect methods. *Comput. Electron. Agric.* **96**(8), 67–74 (2013)
8. Ahmad, I.S., Reid, J.F.: Evaluation of colour representations for maize images. *J. Agric. Eng. Res.* **63**, 185–196 (1996)

9. Romero, J.R., Roncallo, P.F., Akkiraju, P.C., et al.: Using classification algorithms for predicting durum wheat yield in the province of Buenos aires. *Comput. Electron. Agric.* **96** (8), 173–179 (2013)
10. Kacira, M., Sase, S.: Optimization of vent configuration by evaluating greenhouse and plant canopy ventilation rates under wind induced ventilation. *Trans. ASAE* **47**(6), 2059–2067 (2004)
11. Ishizuka, T., Tanabata, T., Takano, M., Shinomura, T.: Kinetic measuring method of rice growth in tillering stage using automatic digital imaging system. *Environ. Control Biol.* **43**, 83–96 (2005)
12. Ma, Z., Hiroshim, S., Gu, S.: Non-destructive measurement system for plant growth information based on machine vision. *Trans. CSAE* **26**(9), 203–209 (2010)
13. Kise, M., Zhang, Q.: Reconstruction of a virtual 3D field scene from ground-based multi-spectral stereo imagery. In: 2006 ASABE Annual International Meeting Presentation, ASABE, 063098. ASABE, Portland (2006)
14. Jeon, H.Y., Tian, L.: Stereovision system and image processing algorithms for plant specific application. In: 2009 ASABE Annual International Meeting Presentation, ASABE, 090047. ASABE, Reno (2009)
15. Wang, C., Zhao, M., Yan, J.: Measurement of maize seedling morphological traits based on binocular stereo vision. *Trans. Chin. Soc. Agric. Mach.* **40**(5), 144–148 (2009)
16. Lati, R.N., Filin, S., Eizenberg, H.: Estimating plant growth parameters using an energy minimization-based stereovision model. *Comput. Electron. Agric.* **98**(10), 260–271 (2013)
17. Andersen, H.J., Reng, L., Kirk, K.: Geometric plant properties by relaxed stereo vision using simulated annealing. *Comput. Electron. Agric.* **49**(2), 219–232 (2005)
18. Zhang, Z.: A flexible new technique for camera calibration. *IEEE Trans. Pattern Anal. Mach. Intell.* **22**(11), 1330–1334 (2000)



Research on Agricultural Scientific and Technological Information Dissemination System Based on Complex Network Technology

Hang Chen¹, Guifen Chen^{2(✉)}, Ying Zhang², and HongJun Gu²

¹ Jilin Research Institute of Science and Technology Information,
Changchun, China

Chenhang0811@163.com

² College of Information Technology, Jilin Agricultural University,
Changchun, China

Guifchen@163.com,

1208973938@qq.com, 330837495@qq.com

Abstract. In view of the complexity of information dissemination in agriculture and the uncertainty of farmers' demand for scientific and technological information, this paper makes a comprehensive and accurate analysis for the dissemination network of scientific and technological information of agriculture based on complex network technology. Firstly, this paper researches the characteristics of the peak degree distribution, average path length and clustering coefficient of a complex network established by the agricultural information dissemination network. Through the research on the three basic characteristics, this paper confirms that the agriculture information dissemination network has the characteristics of scale-free network and small-world network. The method of node research is analyzed by using a complex network. That is that this paper makes a comprehensive analysis for the information propagation speed, scope, analysis and application of dissemination network of agricultural scientific and technological information from degree centrality, betweenness centrality and relationship strength theory. The research results show that the degree centrality can accelerate the information dissemination and be conducive to the accuracy of the information; the betweenness centrality can quickly expand the information dissemination and accurately grasp the degree of control for information resources; the relationship strength theory can reduce the cost of information dissemination and improve the degree of information adoption. This conclusion proves that the application of the analysis method of complex network can effectively improve the speed and quality of agricultural information dissemination network and better serve the agricultural production and farmers' life.

Keywords: Complex network
Dissemination of scientific and technological information
Centrality · Relationship strength

1 Introduction

In the study of the dissemination of information content, people frequently discussed the spread of infectious viruses in the crowd, the spread of computer viruses in the network and viral marketing activities. China is a big agricultural country, but the study of information dissemination in agriculture is comparatively scarce [1]. The basic position of agriculture in the development of our national economy can not be ignored. It is the source of people's food and clothing and the basis condition for survival. In real life, the majority of the population in China is in the rural areas [2–4]. The development of agriculture is directly related to the improvement of the living standards of farmers and the stability of the rural society. Every year, our country will accumulate a large amount of agricultural information. The specific agricultural information data include crop emergence information, soil information, fertilizer information, irrigation information, insects information, weather information, various disaster information, etc. [5]. However, in rural areas, the information is often blocked and the farmers can't understand various information timely, which will seriously restrict the development of rural social economy [6]. Therefore, now people should urgently study and solve the problems that how to improve the farmers' ability to obtain information and how to quickly and locally transmit the information to farmers to promote the rapid development of agriculture.

2 The Complex Network Characteristic of the Dissemination of Scientific and Technological Information of Agriculture

2.1 Distribution of the Degree of Network

The degree distribution of network nodes is one of the important statistical characteristics of complex networks. The degree of a node is usually defined as the number of adjacent nodes and the number of edges connected to the node. The average degree of a network refers to the average value of the degree of all nodes in the whole network, which is usually referred to as $\langle K \rangle$. When the nodes with the same degree are counted separately, a distribution diagram of the degree of network nodes can be obtained. We can use the distribution function $P(k)$ to describe the distribution situation of the degree [7]. It represents that when any node was selected in network, the degree of it is exactly the probability of K . Through the practice of a large number of researchers, it is proved that many networks in real life have power-law distribution, such as Internet network, scientific collaboration networks, protein interaction networks, etc. Such networks usually have the scale-free properties, also known as scale-free networks.

Researches show that the interpersonal relationship network has two statistical characteristics in real life, namely small world characteristics and scale-free characteristics. In rural areas, the rural information dissemination network also has scale-free network characteristics like the complex network [8].

2.2 The Average Path Length

The average path length is the another important statistical characteristic in a complex network. The distance between two nodes in a network has many different definitions. The most commonly used statistical method is to compute the number of edges in the shortest path that connects the two nodes. As shown in Fig. 1, the node A is directly connected to the node B and the distance between the node A and B is 1. As shown in Fig. 2, if node A wants to connect to the node B, it must pass through the node C, and the distance between node A and B is 2. As shown in Fig. 3, there are two paths A-C-B and A-C-D-B to connect node A and node B. If we want to calculate the distance between node A and B, we should adopt the path of A-C-B, so the distance between the node A and B is 2. Network diameter is defined as the maximum distance between two selected nodes in the network. The average path length of a network is defined as the average minimum distance between all node pairs in a network. The average path length and diameter measure the transmission performance and efficiency of the network. In different network structures, the average path length is given different meanings. For example, in urban traffic network, the average path length is often defined as the distance between traffic stations.

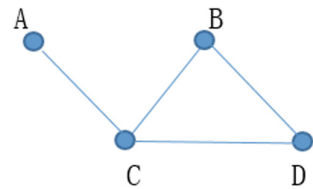
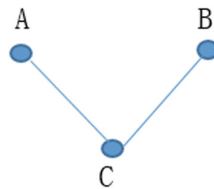


Fig. 1. Direct connection

Fig. 2. Connection with a midpoint

Fig. 3. Multipath connection

2.3 Clustering Coefficient

In a complex network, the clustering coefficient of a node is defined as the ratio between the number of edges between all nodes which are adjacent to this node and the maximum number of edges between these adjacent nodes. Suppose that there is a node i , and there are K_i nodes connected with it, then the clustering coefficient of the node(i) is:

$$C = \frac{2E_i}{k_i(k_i - 1)}, i = 1, 2, \dots, N \tag{1}$$

In the formula, E_i is the actual number of edges that exist between the k_i nodes. The average clustering coefficient of a network is defined as the average value of the clustering coefficients of all nodes contained in the network. In the case of (1), the maximum number of connected edges between k_i nodes is $k_i(k_i - 1)/2$, then the average clustering coefficient of the network is

$$C = \frac{1}{N} \sum_{i=1}^N C_i \quad (2)$$

The average clustering coefficient of the network reflects the aggregation of the network. For example, in a friend relationship network, a person's two friends are likely to be friends with each other. The aggregation coefficient of a network is essentially the study of the probability that the two adjacent nodes of the same node are still the adjacent nodes in the network. It clearly reflects the local characteristics of the complex network.

3 The Role of Complex Network Technology in the Dissemination of Scientific and Technological Information of Agriculture

3.1 Degree Centrality

For a node, the more the number of nodes which are directly associated with it, the stronger the central position of it, the higher the degree centrality of it. In complex networks, most of the nodes which are less directly related to other nodes are in the edge position. Such nodes have very little informal power and influence in the network. The behavior of such actors is usually limited by the actors in the central position [9].

Survey shows that rural big-specialized-households of crop and animal productions have the strongest demand for information resources, followed by the intermediary organization, marketing businesses, wholesale market personnel, agricultural entrepreneurs. The general farmers have the lowest demand for information. People such as the big-specialized-households of crop and animal productions and marketing businesses have higher knowledge level than the general farmers, and can accurately interpret and apply the acquired information. In general, ordinary villagers will have a process to re-read the information they receive. The information transmitted by the mass media is broad and the dissemination content lacks the pertinence, moreover has the strong specialty. For the ordinary farmers in low cultural level, it is difficult to achieve the understanding of the same level. Therefore, these big-specialized-households of crop and animal productions in high cultural level play a crucial role, they can translate the information they receive into the language that ordinary farmers can understand.

They have a high educational level, have a strong ability to receive and acquire information and their horizon is broadened, so they can deliver valuable information to ordinary farmers. Therefore, they have high prestige among the farmers. They can be regarded as "opinion leaders" in the eyes of ordinary farmers, and have a high influence on the attitude and behavior of farmers to accept information. In rural areas, people who can be regarded as "opinion leaders" are locally recognized as the people who have a high cultural level and have a certain prestige among the masses.

In the rural information dissemination network, the general farmers and “opinion leaders” are regarded as nodes in the network, the connection between the general farmers and general farmers, between the general farmers and “opinion leaders” and between the “opinion leaders” and “opinion leaders” are the edges between nodes in the network. In this complex network, the majority of farmers occupy the marginal position, but the “opinion leaders” occupy the central position. The opinion leaders have a high degree centrality in the whole complex network. Therefore, in the process of information dissemination, new information can be first transmitted to the local “opinion leaders” and then transmitted by “opinion leaders” to the ordinary farmers affected by them. By using this transmission mode from the node with a high degree centrality to the node with a low degree centrality, the speed of information dissemination can be accelerated and the scope of information dissemination also can be increased. It is also conducive to the accurate interpretation and application of information.

3.2 Betweenness Centrality

In a complex network, the degree centrality of nodes refers to the degree of difficulty and ease of the resource from one node to another. The betweenness centrality of nodes measures the control degree of this node for the resource in the network. The betweenness centrality means that in a network, if the two nodes want to have an association, they must establish a connection through another node. If a node is on the shortest path between the two nodes, then the node is considered to have a high betweenness centrality. The actor with high betweenness centrality can use more opportunities to speed up the dissemination of information. He has a strong ability to control the flow of information. This also shows that he has an important position in the network, because he decides whether or not the other two actors could communicate with each other and also affects whether information resources in the network can spread a large area. Therefore, nodes with high betweenness centrality have the obvious media role in the network transmission.

The rural interpersonal network is a common phenomenon. Figure 4 shows a typical model of rural interpersonal network. Through the connection among nodes, we can analyze the characteristics of information dissemination in rural areas and the path of information dissemination. According to the nodes and the content of connection, the network can be divided into several different sub networks, such as the village head network, well-informed man network and home core personnel network. The dotted portion in Fig. 4 is a small network combined by four nodes which are connected with each other. The people in this network usually have the common interests and hobbies and share information with each other. In this typical rural interpersonal network, it can be expanded according to the blood relationship, geographical relationship and occupation relationship to form a more complicated rural interpersonal interaction network.

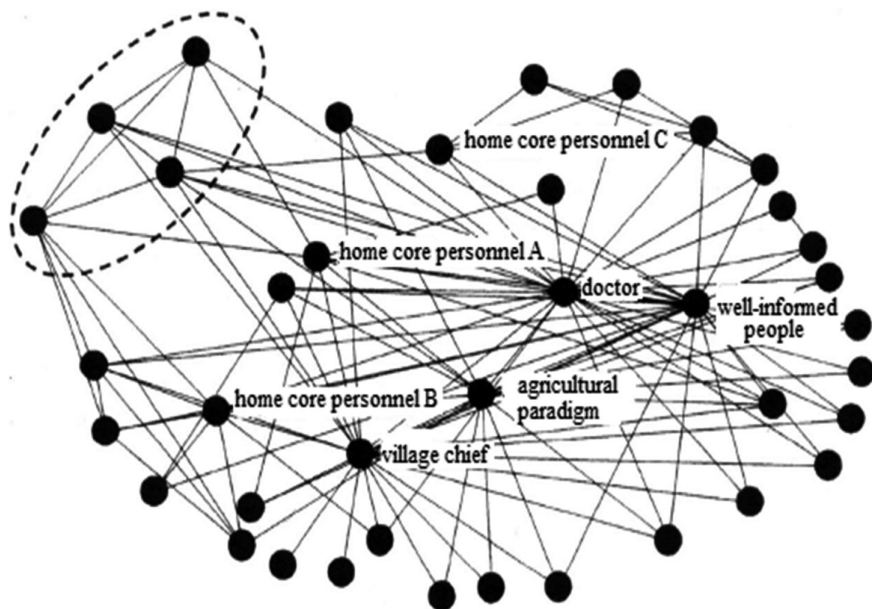


Fig. 4. Rural interpersonal network model

The people who promote the expansion of the network may be the village chief, well-informed people, agricultural demonstration households, or the general villagers in the network. In the network, he may be at the center or on the edge. Such villagers are very important, because they have an important place in the information dissemination network. Such nodes are called the intermediate nodes in complex networks because they directly affect the change of network size. The villagers who are similar to intermediary nodes should be paid enough attention in the process of information dissemination. The approval degree of such villagers for information and their willingly attitude of transmitting information directly determine the stability and scale of the information dissemination network. In the rural information dissemination network, the higher the betweenness centrality of farmers, the more important his position, the greater the impact on the scope of information dissemination. Therefore, the application of the analysis strategy of betweenness centrality of a complex network in the information dissemination of farmers can better control the diffusion range and accurately master the degree of control of information resources.

3.3 Relationship Strength

Strong relationship and weak relationship have different functions in the process of formation and operation of an information dissemination network [10]. Strong relationship will usually form a closed ring in the information dissemination network. The members in the ring network generally contact with each other directly. The information obtained by them is often what they have already known. In that way,

information will be transmitted repeatedly and shared deeply. The weak relationship will form a non-closed linear relation. The redundancy of information and the cohesiveness of the structure in such network are very low. Therefore, the main role of the strong relationship is to maintain the stability of information dissemination network, improve the cohesion within the organization and deepen the trust and sense of belonging of the organization members to the organization. The weak relationship exists among the people with different interests, so the information shared among them can't be repeated. Therefore, the weak relationship plays a "bridge" role in the dissemination of information in the network. It can transfer the information resources to another person who is not familiar with this information resources group.

As a ubiquitous group phenomenon, relationship strength theory also exists in the complex network of rural information dissemination. Due to the specific rural blood relationship, geographical relationship and occupation relationship, a small closed group with strong relationship will be formed easily among villagers. They have a common recognition, high sense of understanding and comply with the arrangement of the same system. Under the guidance of the high cohesion and behavior coordination of villagers, the cost of information dissemination can be reduced to a greater extent. Through the loose indirect contact, weak connection can integrate more villagers in other groups into the relationship network that it exists. In that way, it can not only be conducive to the villagers to acquire the information with high quality and low repetition rate in a larger scope, but also expand the scope of the dissemination of information.

The relationship strength theory should be applied to the rural information dissemination network. The villagers in strong relationship group should contact new villagers to form the weak relationship, and in this relationship, they should increase interaction frequency, deepen the emotion and enhance the intimacy, so as to strengthen the weak relationship and transform it into the strong relationship. Farmers are busy in spring and autumn. In summer and winter, they are mostly idle, so they have more leisure time to participate in various activities, create the opportunities to communicate with each other and deepen their feelings. Because of the unique lifestyle in rural areas, it is very beneficial to develop new relationships, and the cycle of transforming the weak relationship into the strong ones is also very short. Therefore, the application of the analysis method of relationship strength theory in rural information dissemination network can reduce the cost of information dissemination, accelerate the speed of information dissemination, expand the scope of information dissemination and improve the degree of information adoption.

4 Conclusion

From the original agriculture to the ancient traditional agriculture, and then to the modern agriculture today, the agricultural development of our country has lasted for thousands of years. Rural information dissemination involves the information flow at different levels and in many fields, such as agriculture, farmers and rural areas. According to the above research results, we can analyze that:

The first one is that because of the rural special geographical relationship, blood relationship and occupation relationship, rural information dissemination network has a small average path length and a large clustering coefficient. The information dissemination network of agriculture has scale-free network characteristics and small world network characteristics.

The second one is that the application of degree centrality theory in rural information dissemination network, the attention of “opinion leaders” effect and the adoption of mode of information dissemination from the villagers with high degree centrality to the villagers with low degree centrality can accelerate the speed of information dissemination, and be conducive to the accurate interpretation and application for the information.

The third one is that the analysis theory of betweenness centrality should be applied to the rural information dissemination network to analyze the villagers with intermediary nature. These villagers should be paid highly attention, their recognition for the information should be enhanced and their enthusiasm of information dissemination should be mobilized. In that way, the scope of information dissemination can be expanded quickly.

The fourth one is that by using the theory of relationship strength, the relationship between villagers can be divided into strong relationship and weak relationship. The strong relation can be used to develop new relation, that is the weak relation, and then the weak relation can be transformed into the strong relation. Because of the unique work and rest rules in rural areas, this transformation can be completed quickly. The application of relationship strength theory can reduce the cost of information dissemination cost, accelerate the speed of information dissemination, expand the scope of information dissemination and improve the adoption of information.

Acknowledgements. The authors wish to express their gratitude to the national spark program project: Precise operation technology integration and demonstration of corn (No. 2015GA660004) for its generous support of this work.

References

1. Zhou, T., Zhang, Z.K., Chen, G.R., et al.: *J. Univ. Electron. Sci. Tech. China* **43**(1), 1 (2014). (in Chinese)
2. Xu, X., Zhang, Q., Zhang, Y.L., et al.: *J. Ningbo Univ.* **36**(6), 89 (2014). (in Chinese)
3. Song, Y., Tian, A.K., Zhang, Y.: *Comput. Sci.* **41**(11), 204 (2014) (in Chinese)
4. Kuang, H.Y.: *J. Anhui Agri. Sci.* **43**(20), 376 (2014). (in Chinese)
5. Song, X.X., Liu, M.M., Zhao, X.: *Inf. Sci.* **35**(5), 42 (2017). (in Chinese)
6. Zhang, R.: *J. Mod. Inf.* **36**(4), 26 (2016). (in Chinese)
7. Li, M., Ma, Y.F., Jiang, X., et al.: *Comput. Mod.* **1**, 104. (in Chinese)
8. Pan, Y.H., Yan, Z.J., Liu, W.Y.: *Trans. Beijing Inst. Technol.* **35**(8), 872 (2015) (in Chinese)
9. Gou, Z.J., Fan, M.Y., Wang, G.W.: *J. Chengdu Univ. Inf. Technol.* **29**(5), 458 (2014). (in Chinese)
10. Tian, Z.W., Sui, Y.: *Libr. Inf. Serv.* **56**(8), 42 (2016). (in Chinese)



An Illumination Invariant Maize Canopy Structure Parameters Analysis Method Based on Hemispherical Photography

Chuanyu Wang^{1,2}, Xinyu Guo^{1,2(✉)}, and Jianjun Du^{1,2}

¹ Beijing Research Center for Information Technology in Agriculture,
Beijing, China

{wangcy, guoxy, dujj}@mercita.org.cn

² Beijing Key Lab of Digital Plant, Beijing 100097, China

Abstract. Hemispherical photography (HP) has already proven to be a powerful indirect method for measuring various components of canopy structure. In this paper an illumination invariant multiple exposure images fusion and mapping method was proposed in order to squash negative impact of variant illumination. Firstly, a series of multiple exposure maize canopy hemispherical images was captured under natural light condition. Secondly, the multiple photographs fused into a single radiance map whose pixel truncated in shadowed and lighted parts of original images expended to higher range. We were able to determine the irradiance value at each pixel, the pixel values are proportional to the true irradiance values in the scene. The pixel values, exposure times, and irradiance values form a least squares problem. Finally, we also employed a histogram equalisation method to map irradiance values to RGB color space. The comparison results show that canopy gaps fraction of HP acquired at 14:00 and 17:00 with threshold value 180 has difference of 15.4% percent, and our method reduces the difference up to 2.8%. Results of regression analysis shows that our method have a high consistency with canopy structure parameter direct surveying method, the correlation coefficient between two methods hit 0.94. The line slope was 1.463, our method measurement values were lower than direct surveying method. Our method expands the HP canopy structure parameters acquire timing, provides an automatic monitoring solution.

Keywords: Canopy structure · Hemispherical photography · Image fusion
Image mapping · Variant illumination

1 Introduction

Maize is one of the main planting crops in the world, and its production has a great influence on food security. Maize yield formation mainly comes from the accumulation of photosynthetic assimilation products in the canopy, and the accumulation of assimilation products is an exchanging process with substances and energy in the external environment through a series of physiological and biochemical reaction in the canopy. The strength of the physiological function of the canopy is mainly limited by the internal structure form of the canopy [1]. Canopy structure is a visual indicator of a

community appearance, directly reflecting the crop growth, cultivation conditions, as well as water and fertilizer measures. In many canopy structure parameters, the leaf area index (leaf area index, LAI) shows how much plant leaf area is on a unit surface of the field, while the mean leaf Angle (mean leaf Angle, MLA) expresses the spatial orientation of canopy leaves, in which the canopy structure plays a decisive role.

The parameter acquisition methods of canopy structure are divided into two categories, the direct method and indirect method. The so-called direct method is to measure the direct part of the involved indicators in the structural parameters, for example, by measuring the plant leaf areas in the sample zone and then summing (LAI) [2, 3]. The direct method needs a wide range of destructive sampling, consuming a large amount of manpower, and the subjective dependence in measuring is strong. So some indirect methods based on growth model, radiation model and canopy porosity had extensive development [4–7], of which hemisphere image (hemispherical photography), which can obtain crop growing and appearance data such as morphology, density, growth period while recording canopy porosity, was studied and applied by a great number of scholars.

Through the hemisphere image geometric correction, Huanhua et al. [8] established the parameter layer, and overlaid it on the classified vegetation canopy layer and conducted mathematical operations to extract the vegetation canopy structure parameters such as canopy widths, canopy area and canopy circumference etc. After comparing the leaf area index calculation method of the hemisphere image with other indirect methods, Tong et al. [9] pointed out that artificially setting threshold to the image segmentation is a major cause of the errors, and the accuracy is also affected by the sampling time and space because incorrect sampling time and space will bring certain errors to the LAI calculation. While Valerie Demarez et al. [10] applied the leaf area index of hemisphere image of three kinds of crops wheat, corn, sunflower, and introduced the cluster index (clumping index) into Poisson model of the hemisphere image, which made the value from LAI calculation is more close to the actual value. Gonsamo et al. [11] developed multi-platform calculation software package CIMES, using command line mode, based on canopy structure parameters of hemisphere image, which realized a variety of LAI calculation methods such as the Miller, Lang and Campbell etc. Baret et al. [12] applied the images obtained from 57.5° with the ground to simulate the zenith angle corresponding information of hemisphere image, proved the feasibility of this method through crop virtual 3d model, and took the results obtained by calculation as input parameters of the leaf surface calculation model. Confalonieri [13], and etc. developed an image acquisition device for canopy structure parameters based on handheld devices, using the angle sensors on the handheld device to acquire the canopy images at 57.5° . Verification results show that the measurement results from it have a high consistency with the ones from LAI2000, AccuPAR and other canopy analysis equipment, and the low price and portability extends its application conditions.

In related studies, whether using commercial equipment (such as: Hemiview, LAI - 2000, CI - 110), or equipment researchers developed by themselves, to obtain the hemisphere images, the requirements to light conditions are very strict: generally, 1 h after sunrise or before sunset within 1 h (less direct light, and more scattered light). The main reasons for Limiting the image acquisition time are, on the one hand, imaging

equipment in different light conditions adopts different exposure strategies, which causes great differences in colors and brightness of images obtained at different times and thus, the image segmentation threshold is difficult to unity; On the other hand, plant leaves to sunlight has a certain role in the transmission. Under the condition of strong direct light, the images at the top of the blades often display as excessive exposure, while, due to the influence of the blade shadows cast over, the images of the blades at the bottom are often underexposed.

To sum up, the hemisphere image method is a kind of important indirect calculation method of canopy structure parameters. Due to the influence of field changing light conditions, this method can only be used in certain light conditions, so the restrictions on image acquisition time greatly affect the practical application of the method. In this paper, we adopted the fusion mapping method based on multiple exposure images, removing the influences of image light and shade, highlights and shadows due to the light changes in fields, and greatly increased the scope of the hemisphere image technology.

2 Materials and Methods

2.1 Hemisphere Image Acquisition Device and Method

The lens was prime fishieye lens “(SIGMA) 8 mm F3.5 EX DG FISHEYE”, which were able to provide vision range images of level 360° and vertical 180°. The Canon full frame camera (Canon EOS 5 d Mark III) was adopted. The camera was placed in the bottom of the canopy, the vertical to ground and towards the sky. To quickly switch fixed number aperture setting, exposure time, exposure for more than a canopy hemisphere image sequence, Sample image is shown in Fig. 1.

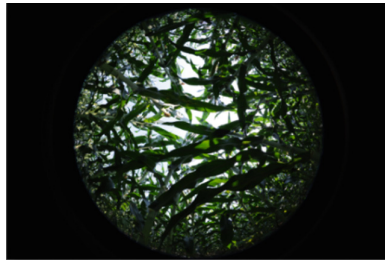


Fig. 1. Hemispherical photography sample of maize canopy

Image processing program is developed by Visual Studio 2010, using the image processing open-source library OpenCV 2.3. The program was running on PC, CPU core frequency 3.4 GHZ, memory 4 GB.

2.2 Hemisphere Image Processing Process

In this paper, the image processing algorithm process includes six steps, as shown in Fig. 2:

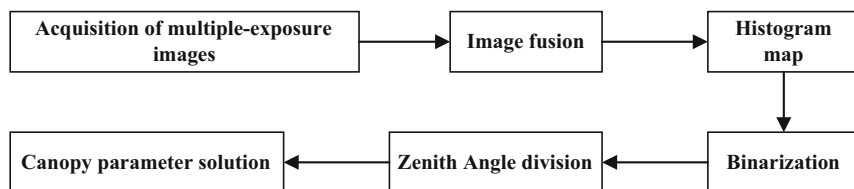


Fig. 2. Flowchart of image processing

2.3 Multiple-Exposure Image Fusion

The segmentation accuracy of plant pixels and non-plant pixels of the hemisphere images has a great influence on calculation of canopy porosity and the leaf area index. The brightness of the canopy hemisphere image varies with the acquisition time. The pixel brightness of the canopy top is high, and the pixel brightness of the canopy bottom is low, which causes 2 major effects on later image processing: (1) the fixed threshold to image segmentation can't be chosen; (2) the blade pixels in too bright and too dark areas can wrongly be divided into background pixels. Jeon and Lati [14, 15] pointed out that under the field illumination conditions, specular reflections and shadows on plants is a great challenge for image segmentation. Liu and Panneton [16, 17] tried to use the optimized color space (such as: RGB HSV Lab) in the plant image segmentation, but segmentation thresholds for different plant color spaces need artificial selection to adjust. Woebbecke and Burgos [18, 19] using the feature of plant leaves containing chlorophyll, put forward the green component reinforcement method (ExG), which assumed that the plant pixels and background pixels after linear transformation can be projected onto different space planes, then divided planes according to the beforehand thresholds. But the threshold selection in this method is affected by the light intensity. In order to solve the influence of illumination changes, Ruiz and Zheng [20, 21] used machine learning classification method to distinguish plant pixels and background pixels, taking multiple color features as vectors. Experiments show that this method has a higher degree of automation, but still the images with highlights and shadows have higher rate of wrong points.

Using multiple exposure image fusion, images with relatively uniform brightness [22] are able to be obtained under varied illumination conditions. By capturing the image light radiation intensity in the scene for correction and normalization to the image brightness, the effects on the image segmentation from light transform can be overcome. The mathematical relationship between the image brightness and scene light radiation intensity is shown below.

$$F(I_{ij}) = \ln E_i + \ln \Delta t_j \tag{1}$$

In the formula, E is light radiation intensity values of a point in the scene (dimensionless); Δt is the exposure time of images (s); i is a sampling point on an image, value range (I, n) ; J stands for an image in an image sequence with different exposure and value range $[I; m]$; $F(I)$ is the response function of the camera to light radiation intensity in the scene. The meaning of the formula (1) as follows: the light radiation intensity at some point in the scene of is E_i ; the camera uses Δt of exposure time; the brightness value of the image point is $F(I_{ij})$. In the digital image, the pixel luminance values are in the range of 0 to 255, so the formula (1) can be discretization, a least squares problem. As shown in formula (2):

$$D = \sum_{i=1}^n \sum_{j=1}^m F(I_{ij}) - \ln E_i - \ln \Delta t_j \tag{2}$$

After the camera response function is calculated, according to the formula (3), the light radiation intensity values of a point in the scene can be calculated by the pixel gray value and the image exposure time, completing the fusion of multiple exposure image sequence.

$$\ln E_i = \left\{ \sum_{j=1}^m F(I_{ij}) - \ln \Delta t_j \right\} / m \tag{3}$$

Figure 3 shows the image sequence of different exposure time. Figure 4 is the pseudo color image of light radiation intensity in the fused sequence (from blue to red, a gradual increase in values). It can be seen from the Fig. 3 that, affected by the pixel value range, the detailed light levels of the dark shadows and highlights in the images are not rich, with the top blades high brightness and the bottom blades low brightness under the direct sunlight. Through fusing the pixels of the multiple exposure images to

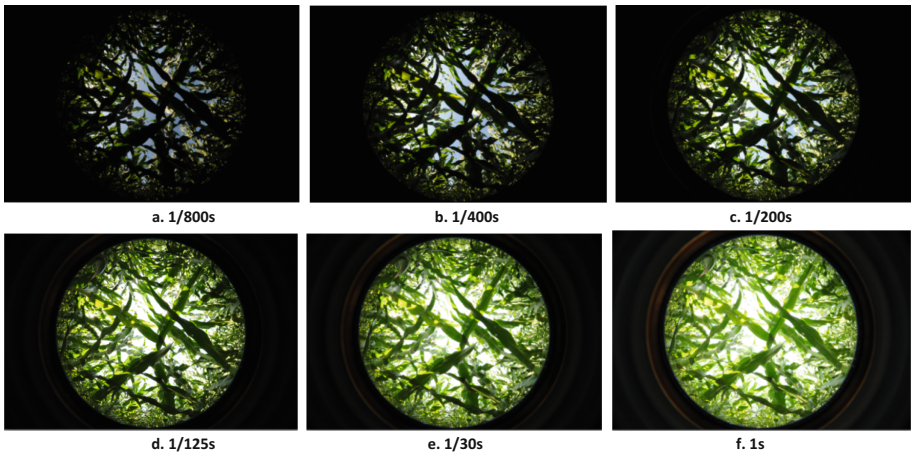


Fig. 3. Maize canopy hemispherical images with different exposure times

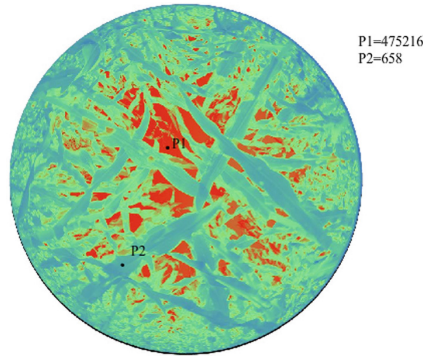


Fig. 4. Fusion image of irradiance value (Color figure online)

light radiation intensity spaces, the image value range has been increased. As shown in Fig. 4, P1 and P2 have a difference of 3 orders of magnitude in the light radiation intensity images. Compared with the original image, the light radiation intensity of the image has a wider value range, with the light radiation intensity image with highlights and dark areas in the original images rendering more details.

2.4 Light Radiation Intensity Image Map

Light radiation intensity map expands the range of the original RGB image and contains information of specular reflection and shadow regions in the image sequence with different exposure. In order to make the brightness distribution of the light radiation intensity images of different times tend to be more consistent and uniform, the light radiation intensity images need to be compressed mapping. In this paper, by using the idea of histogram equalization, while compressing the light radiation intensity image, the brightness differences of the images shot at different times of the day were corrected. The specific methods are as follows: a certain value V_0 was found in a numerical interval of the light radiation intensity images to make the formula (4) the minimum value. In this article, the value is 1.0, 2 kinds of effects can reflect; $H(x)$ is the histogram function;

$$\frac{(V_0 - 0.5(L_{\max} + L_{\min}))^2}{L^2} + \frac{\alpha((\sum_{x=0}^{V_0} h(x) - 0.5N)^2)}{N^2} \quad (4)$$

In the formula, L is the value range of light radiation intensity map; L_{\max} and L_{\min} are the maximum and the minimum; α is the condition parameter, whose range $[0, \infty]$ influences the mapping transformation effects; the closer to 0 it is, the closer to the linear transformation the mapping effects are, and the closer to ∞ it is, the closer to the histogram equalization the mapping effects are. In this article, the value is 1 and 0, both of the 2 kinds of effects can be reflected; N stands for the pixel numbers of the interval; value V_0 is calculated from formula (4). L can be divided into two intervals, on which

formula (4) is used again to calculate and gain V_{I0} , V_{I1} . The entire interval is divided into four, repeat the operation above until the entire range is divided into 256, and set up a mapping relation between the light radiation intensity images and 256 color images. The method diagram is as shown in Fig. 5.

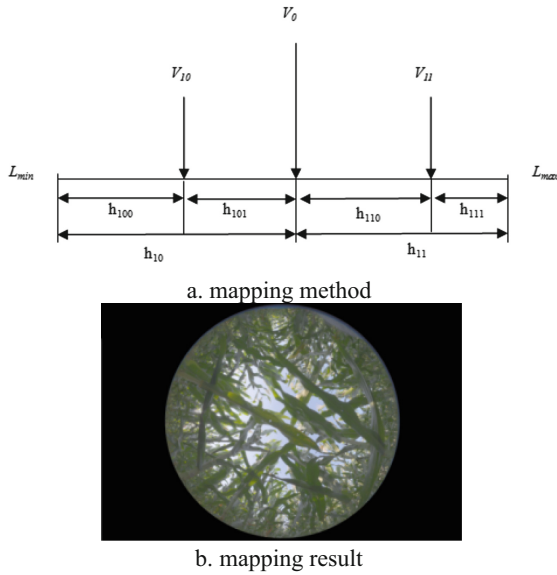


Fig. 5. Image mapping based on histogram equalisation method

2.5 Hemisphere Image Calculating Leaf Area Index and Average Leaf Inclination Angle

Monsi and Saeki [23] introduced the Beer - Lambert’s law of light propagation in homogeneous medium into the light propagation model of the crop canopy. The specific formula is as below

$$I/I_0 = e^{-k \cdot LAI} \tag{5}$$

In the formula, I stands for the radiation intensity at the bottom of the canopy (unit: lux); I_0 for the radiation intensity above the canopy (unit: lux); LAI for the leaf area index (dimensionless). Under the condition of only considering the direct light, I/I_0 can be expressed in canopy porosity T , and the value of k is related to the angle of the incident light and the leaf inclination angle distribution of the canopy itself [24]. The calculation method is as follows:

$$k = G(\theta, \alpha) / \cos \theta \tag{6}$$

In the formula, θ is the incidence angle of the light, namely zenith angle; α is the average leaf inclination angle; $G(\theta, \alpha)$ is the projection function; that is, a unit leaf area at a leaf inclination angle α is the projection area in the direction of θ . Accordingly, extinction coefficient has something with the light incident angle, blade orientation (in the form of leaf inclination angle). From formulas (5) and (6), the general formula is derived for calculating the leaf area index of crop canopy in hemisphere images.

$$T(\theta) = e^{-G(\theta, \alpha)LAI/\cos \theta} \tag{7}$$

in the formula, $T(\theta)$ is the canopy porosity under the zenith angle θ . The calculation of leaf area index is as formula (8)

$$LAI = -\ln T(\theta) \cdot \cos \theta / G(\theta, \alpha) \tag{8}$$

In it, the projection function $G(\theta, \alpha)$ has two features, (1) when the zenith angle from view angle is 57° , $G(\theta, \alpha) = 0.5$, a constant value [25]; (2) while $25^\circ < \theta < 65^\circ$, $G(\theta, \alpha)$ can be thought as linear function of θ , the slope can be calculated through the leaf inclination angle [26], formula (8) can be simplified as

$$LAI = -\ln T(57^\circ) \cdot \cos(57^\circ) / 0.5 \tag{9}$$

In the formula, $T(57^\circ)$ is the canopy porosity obtained from hemisphere image at zenith angle $\theta 57^\circ$. Canopy porosity calculation formula is

$$T(\theta) = P_L(\theta) / P_S(\theta) \tag{10}$$

$P_L(\theta)$ is the hemisphere leaf number of pixels on the image at zenith angle θ , and $P_S(\theta)$ is the number of ring pixels which the zenith angle is corresponding to.

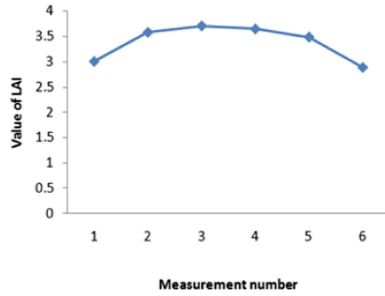
The leaf area index of a canopy can be calculated by the formula (9), and the average leaf inclination angle can be obtained by LAI indirect calculation. The porosity $T(25^\circ) - T(65^\circ)$ of the zenith angle $25^\circ - 65^\circ$ can be extracted from the hemisphere images, and the series of $G(25^\circ) - G(65^\circ)$ can be calculated by the formula (8). The series data of θ and $G(\theta)$ meet linear relationship, the straight slope D can be fitted, and thus the average leaf inclination angle MLA can be calculated through the polynomial about D .

$$MLA = 56.63 + 2.521 \times 10^3 D - 141.471 \times 10^{-3} D^2 - 15.59 \times 10^{-6} D^3 + 4.18 \times 10^{-9} D^4 + 442.83 \times 10^{-9} D^5 \tag{11}$$

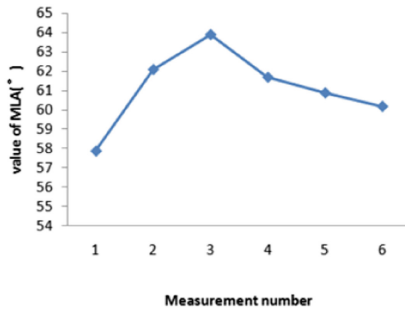
3 Results and Analysis

The calculation of LAI and MLA to the test materials was carried out using the method described in this article. The test materials was Xianyu 335 and sowing time was on June 5, 2013, with planting density of 60000 plants/ha and normal water management

measures. The hemisphere images of the canopy, which were separately obtained on August 6, August 13, August 19th, August 22, August 26, and September 12, were processed and analyzed. The LAI and MLA results are shown in the figure below (Fig. 6).



a. Time-varying value of Measured LAI



b. Time-varying value of MLA

Fig. 6. The experiment result of canopy structure

August 20 or so was 20 days after silking, and the plant growth reached maximum at this time. In the measurement results, the LAI 3.71 in the measurement results on August 19 was the peak for the whole measuring sequences, and consistent with the observed results. MLA measured values and the LAI values both have the same changing trend, with the growth to maximum, uplift degree of the upper leaves on the plants increased on the vertical so as to increase the transmittance rate of solar radiation on the upper canopy. With plant leaf senescence, leaf shapes gradually let loose, and MLA presents downtrend in the later stage.

In order to further validate the measuring precision and accuracy of the method described in this article, obtain the corn leaf area by using the direct method, and then the real LAI values were calculated. The measurement method of leaf area is as shown in the figure below. The blades were dismantled and paved one by one to shoot the images, and the number of the green leaf pixels in the images was converted into leaf areas. Limited by the length, the image processing algorithm is no longer here (Figs. 7 and 8).

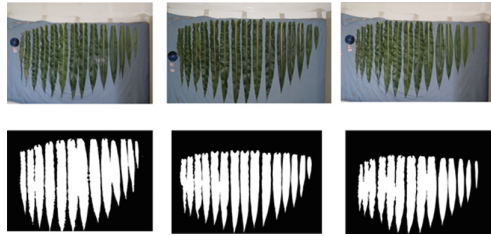


Fig. 7. The direct method of LAI measurement

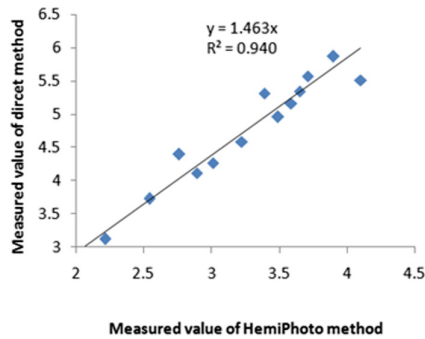


Fig. 8. The result of linear fitting of our method and direct method

An equation of straight line was fitted using the measured values from the method as described in this article as well as the ones from the direct method, it is shown that the closer to 1 the slope of the linear equation is, the better the accuracy of the method described in this article is, and it is also shown that the closer to 1 the value R is, the greater the relevance of the two is. From the results, the slope of the equation is 1.463, which indicates that the measured values from the method in the article is generally lower than the measured values from direct method; the value R was 0.940, indicating that both have a high correlation, and that the method in the article has a higher consistency on the trend with the direct method. Later, the accuracy of the method in the article can be improved by increasing the correction coefficient.

4 Discussion

The precision and stability of canopy structure parameters obtained through the hemisphere image method is mainly affected by light conditions when imaging. In the previous researches, changing the aperture and exposure time is often adopted to respond to the light changes, but in practice, overly relying on experience, it is difficult to acquire the hemisphere images with uniform brightness. The literature [27] pointed out that the canopy porosities of the hemisphere images with different exposure times may differ by 20%. The other way to eliminate the influence from changing light is to

acquire images under the condition of near sunset with more scattered light, the differences in light conditions at this time are relatively small, which can reduce the direct light transmission forming light spots and shadows on blades. The lighting conditions at the time of acquisitions limit the application scope of the hemisphere image method, and there is a big inconvenience in practical application, especially in some cases of timing continuous monitoring, the lighting changes are inevitable.

The fusion mapping method on the multiple exposure images described in this article, to a certain extent, eliminates the image brightness differences caused by the light change, and it is facilitated for the image processing program later to choose the same stable threshold for image segmentation. The multiple exposure images fusing increases the range of the image brightness values, as well as the magnitude order differences of different brightness pixel values. Mapping algorithm transforms the fused images to ordinary images, completing the compression to the brightness ranges of images. Observed from the images, light areas in the original images are suppressed, and dark areas are promoted and thereby the objective of reducing the light change effects on the image brightness has been achieved.

5 Conclusion

In this article, the hemisphere image method was used to acquire corn canopy structures parameters indirectly, and against the problem that hemisphere image method is easily affected by light changes, the fusion algorithm was proposed based on the multiple exposure images, which made the brightness of the images obtained at different times relatively uniform and stable, while eliminating the blade glossy reflections and shadows. The experiments show that, compared with the direct measurements, the method described in this article has a higher consistency, and provides a new means and a research idea for the study of the canopy structure parameter acquisition from the hemisphere images.

Acknowledgement. This work is supported by Nature Science Foundation of China (31501226).

References

1. Li, X., Wang, J.: *Vegetation Optical Remote Sensing Models and Vegetation Structure Parameterization*. Science Press, Beijing (1995)
2. Li, Y.: *Theory and Application of Vegetation Radiative Transfer*. Nanjing Normal University Press, Nanjing (2005)
3. Kvet, J., Marshall, J.K.: Assessment of leaf area and other assimilating plant surfaces. In: Sestak, Z., Catsky, J., Jarvis, P.G., et al. *Plant Photosynthetic Production: Manual of Methods*, The Hague, The Netherlands, pp. 517–574 (1971)
4. Song, G.Z.M., Doley, D., Yates, D., et al.: Improving accuracy of canopy hemispherical photography by a constant threshold value derived from an unobscured overcast sky. *Can. J. For. Res.* **44**(1), 17–27 (2013)

5. Leblanc, S.G., Fournier, R.A.: Hemispherical photography simulations with an architectural model to assess retrieval of leaf area index. *Agric. For. Meteorol.* **194**(6), 64–76 (2014)
6. Woodgate, W., Jones, S.D., Suarez, L., et al.: Understanding the variability in ground-based methods for retrieving canopy openness, gap fraction, and leaf area index in diverse forest systems. *Agric. For. Meteorol.* **205**(3), 83–95 (2015)
7. Foster, I., Kesselman, C., Nick, J., Tuecke, S.: The physiology of the grid: an open grid services architecture for distributed systems integration. Technical report, Global Grid Forum (2002)
8. Peng, H., Zhao, C., Feng, Z., et al.: Extracting the canopy structure parameters using hemispherical photography method. *Acta Ecol. Sin.* **31**(12), 3376–3383 (2011)
9. Wu, T., Ni, S., Li, Y.: A comparison on the algorithms for retrieval of LAI based on gap fraction of vegetation canopy. *J. Nanjing Norm. Univ. (Nat. Sci.)* **29**(1), 111–115 (2006)
10. Zarate-Valdez, J.L., Whiting, M.L., Lampinen, B.D., et al.: Prediction of leaf area index in almonds by vegetation indexes. *Comput. Electron. Agric.* **85**(5), 24–32 (2012)
11. Gonsamo, A., Jmn, W., Pellikka, P.: CIMES: a package of programs for determining canopy geometry and solar radiation regimes through hemispherical photographs. *Comput. Electron. Agric.* **79**(2), 207–215 (2011)
12. Baret, F., Solan, B.D., Lopez-Lozano, R., et al.: GAI estimates of row crops from downward looking digital photos taken perpendicular to rows at 57.5° zenith angle: theoretical considerations based on 3D architecture models and application to wheat crops. *Agric. For. Meteorol.* **150**(11), 1393–1401 (2010)
13. Confalonieri, R., Foi, M., Casa, R., et al.: Development of an app for estimating leaf area index using a smartphone. Trueness and precision determination and comparison with other indirect methods. *Comput. Electron. Agric.* **96**(12), 67–74 (2013)
14. Jeon, H.Y., Tian, L.F., Zhu, H.: Robust crop and weed segmentation under uncontrolled outdoor illumination. *Sensors* **11**(6), 6270–6283 (2011)
15. Lati, R.N., Filin, S., Eizenberg, H.: Robust methods for measurement of leaf-cover area and biomass from image data. *Weed Sci.* **59**(2), 276–284 (2011)
16. Liu, Y., Mu, X., Wang, H., et al.: A novel method for extracting green fractional vegetation cover from digital images. *J. Veg. Sci.* **23**(3), 406–418 (2012)
17. Panneton, B., Brouillard, M.: Colour representation methods for segmentation of vegetation in photographs. *Biosyst. Eng.* **102**(4), 365–378 (2009)
18. Woebbecke, D.M., Meyer, G.E., Von Bargen, K., Mortensen, D.A.: Color indices for weed identification under various soil residue and lighting conditions. *Trans. ASAE* **38**, 259–269 (1995)
19. Woebbecke, D.M., Meyer, G.E., Von Bargen, K., et al.: Color indices for weed identification under various soil, residue, and lighting conditions. *Trans. ASAE* **38**(1), 259–269 (1995)
20. Ruiz Ruiz, G., Gómez Gil, J., Navas Gracia, L.M.: Testing different color spaces based on hue for the environmentally adaptive segmentation algorithm (EASA). *Comput. Electron. Agric.* **68**(1), 88–96 (2009)
21. Zheng, L., Shi, D., Zhang, J.: Segmentation of green vegetation of crop canopy images based on mean shift and fisher linear discriminant. *Pattern Recogn. Lett.* **31**(9), 920–925 (2010)
22. Song, H., He, D., Gong, L.: Crops image fusion in different light conditions based on Contourlet transform. *Trans. Chin. Soc. Agric. Eng. (Trans. CSAE)* **30**(11), 173–179 (2014)
23. Monsi, M., Saeki, T.: The light factor in plant communities and its significance for dry matter production. *Jpn. J. Bot.* **14**(1), 22–52 (1953)

24. Kucharik, C.J., Norman, J.M., Gower, S.T.: Measurements of leaf orientation, light distribution and sunlit leaf area in a boreal aspen forest. *Agric. For. Meteorol.* **91**(1), 127–148 (1998)
25. Campbell, G.S.: Derivation of an angle density function for canopies with ellipsoidal leaf angle distributions. *Agric. For. Meteorol.* **49**(90), 173–176 (1990)
26. Lang, A.R.G.: An instrument for measuring canopy structure. *Remote Sens. Rev.* **5**(1), 61–71 (1990)
27. Ning, H., Chuangen, L., Kemin, Y., et al.: Inversion of rice canopy construction parameters from the hemispherical photograph. *Acta Gronomica Sin. A* **40**(8), 1443–1451 (2014)



Application of DBSCAN Algorithm in Precision Fertilization Decision of Maize

Yang Li^{1,2}, Guowei Wang^{1,2,3}, Yu Chen^{1,2}, Yang Jiao⁴, Haijiao Yu⁵,
and Guogang Zhao⁵(✉)

¹ School of Information Technology, Jilin Agricultural University,
Changchun 130118, China

547229667@qq.com, 41422306@qq.com, 123929697@qq.com

² Jilin Province Research Center, Changchun 130118, China

³ School of Biological and Agricultural Engineering, Jilin University,
Changchun 130022, China

⁴ Sixth Middle School in Changchun, Changchun 130000, China
61516131@qq.com

⁵ The City College of JLU, Changchun 130000, China
haihai951kl@163.com, zhaog2010@foxmail.com

Abstract. In the current era of big data, information technology is developing quite rapidly, the most important data mining technology in information technology is also widely used, and now it is applied to the field of agricultural production, what can solve many problems such as agricultural production, fertilization and so on. In this paper, data mining technology is applied to the process of corn fertilization, because in corn production, effective and reasonable amount of fertilizer can make corn grow better, however, if there is no specific fertilization according to the soil properties of the corn, it will lead to the soil which needs fertility can not be with enough fertility, and the soil without fertility will be added more and more. In view of this problem, the soil planted with corn was graded and treated with different levels of soil, so as to achieve the purpose of effective utilization of soil fertility. In this paper, the DBSCAN algorithm in clustering analysis is used to classify the soil, the DBSCAN algorithm to this field have not been reported so far. By applying the nutrient balance method, the amount of soil fertilizer was calculated at each level, and the fertilizer was targeted according to the amount of fertilizer. Through the pilot application in Nong'an County of Jilin province Chen hometown, compared with the traditional fertilization results, Fertilizer reduced by 25%, corn production increased by about 15%, effectively reducing the input of chemical fertilizer and increasing the output of crops.

Keywords: Data mining · Cluster analysis · Soil classification
DBSCAN algorithm

1 Introduction

Precision agriculture developed in the early 1980, and precision agriculture is a subject jumping. Precision agriculture is the main system of modern agricultural production operation according to the spatial location, timing, spatial variability and quantitative to achieve, it is mainly the information technology to support, most of the data mining technology [1].

© IFIP International Federation for Information Processing 2019

Published by Springer Nature Switzerland AG 2019

D. Li and C. Zhao (Eds.): CCTA 2017, IFIP AICT 546, pp. 453–459, 2019.

https://doi.org/10.1007/978-3-030-06179-1_45

Precision agriculture is mainly composed of intelligent decision-making technology, field information collection technology, and intelligent equipment technology. Through the collection of farmland information for digital analysis and processing, intelligent decision-making, mechanization of farmland information and application of information, can increase crop production, increase efficiency and increase the income of farmers [2]. The main idea of precision agriculture is that agricultural production can be adjusted according to local conditions. It can be reasonably invested, not wasted, and managed scientifically. Precision agriculture has achieved orderly management in space and time, and improved the efficiency of agricultural production. Through the use of modern agricultural machinery operation scale, improve the agricultural production efficiency and the efficiency of agricultural production, greatly changed the peasant workers will always work hard in the fields only in traditional agriculture, backward production mode and the “inspiration” extensive industry management [3].

The productivity of the soil is mainly composed of soil fertility, soil fertility mainly refers to organic matter, nutrient content, soil texture, soil thickness and other factors in the soil, these factors have different effects on soil fertility, and have different constraints on soil fertility.

For the study of soil fertility classification, there are several situations that appear below: Zhang et al. [4] applied the mathematical method of principal component analysis and discriminant function discriminant to classify soil fertility. In addition to the mathematical model approach, quantification of soil fertility has also been studied, so far, however, quantitative indicators have not appeared, so that the size of soil fertility cannot be calculated. Liu and Liu [5] proposed that the soil per unit area under general conditions should be used to measure the amount of soil formed by plants to measure soil fertility. Because of the different types of soil use, the annual crop yield of the farming soil; the annual growth of timber for the forest soil; the grassland soil is measured by the annual grass growth, from an ecological point of view, soils of all types of use can be measured by solar energy (Joules), which is fixed by plants in the unit area throughout the year.

2 DBSCAN Algorithm

2.1 DBSCAN Algorithm Concepts

DBSCAN algorithm is a density based clustering analysis method. The algorithm defines clusters as the largest set of points connected by density, and divides the regions with high density into clusters. The kernel idea of clustering is to measure the density of the space of the point with the neighbor number in the neighborhood of a point [6]. For example, the object p is the center, and epsilon is the radius of the region, that is, within the epsilon neighborhood of p , including at least one positive integer Minpts objects, and p is the core object, fields containing Minpts objects are clusters, otherwise p is on the boundary of a cluster and is called boundary point [7, 8]. The following explains the relevant definitions:

2.1.1 Directly Density-Reachable

If the p is the core point, q in the ϵ -neighborhood of p , the p direct density of up to q (Fig. 1).

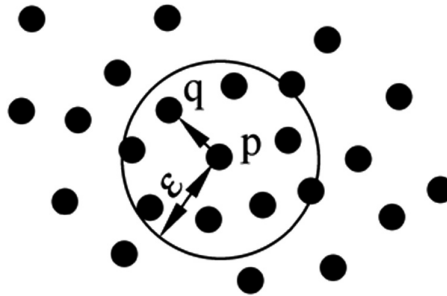


Fig. 1. Directly density-reachable

2.1.2 Density-Linked

If an object o exists in the object set D , which causes the object p and q to be reachable from the object o about epsilon and $Minpts$, then the object p and q are connected to epsilon and $Minpts$ density [9].

The definitions are parsed using Fig. 2 below, in Fig. 2, given the radius of the field epsilon, the minimum number is $Minpts = 3$. According to the above definition, point m , o , p , and r core objects because there are at least 3 objects in their respective epsilon fields. In addition, it is also observed that m is directly accessible from p and vice versa. q is direct density reachable from m , but m is not directly reachable from q , because q is not the core object. The density from q to m is up to m , and the direct density of p from p can reach up to q so that the density is reachable. Similarly, p and s are density reachable from o , and o is density accessible from r .

As a result, o , r , and s are density-reachable between each other.

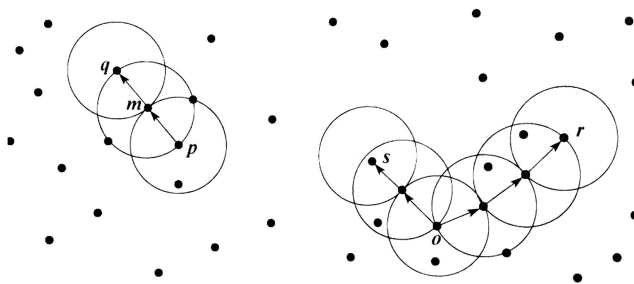


Fig. 2. Density-reachable and density-linked

2.2 DBSCAN Algorithm Progress

Input: n data objects, radius epsilon, minimum number Minpts.

Output: all clusters that reach the density requirement.

Algorithm processing flow:

Step1 Extracts an unprocessed point from the data object;

Step2 IF points out is the core point, THEN finds all objects reachable from the point density, forming a cluster;

Step3 ELSE The point that you take is the edge point (non core object). Jump out of this loop and look for the next point;

Step4 Loop Step1 to Step3 until all points are processed [10].

3 Maize Precision Fertilization

3.1 Data Acquisition

In Nong'an County of Jilin province Chen hometown pilot application, access to land information using the 3S technology, grid according to the distance of 40 m * 40 m. Soil sampling was carried out in the divided mesh, and 152 sampling points were obtained, which were collected for soil nutrient content, including four values of organic matter, available phosphorus, available nitrogen and available potassium.

3.2 Data Standardization

Since different data has different dimensions, it needs a unified dimension to compare the data, that is to standardize the data. normalization formula is:

$$g = \frac{G - \min}{\max - \min} \quad (1)$$

3.3 Soil Fertility Grading

The DBSCAN algorithm is used to cluster the processed data, that is, to classify the soil fertility, and each soil grade is called the cluster. In this paper, WAKA data mining tools are used to download DBSCAN data management package, set (field radius) 0.5, Minpts (epsilon field minimum point) is 10 of the cluster, the soil is divided into six cluster classes, that is, six levels.

According to the number of soil plots at each level, the four attributes of all soils in different levels are calculated, the average value is summed, and sorted according to the size of the sum, and the bigger one is ranked, and so on.

According to the sum of the average values of the attributes in the six clusters, the soil classification results are shown in Table 1.

Table 1. Soil classification result

Soil level	Included sample points
Class A	a140 a83 a80 a3 a22 a54 a21 a131 a51 a90 a19 a20 a57
Class B	a40 a31 a11 a6 a149 a28 a314 a119 a64 a13 a151 a16
Class C	a70 a142 a100 a148 a109 a121 a47 a95 a96 a62 a116 a44 a39 a146 a10 a33 a38 a88 a7 a9 a147 a86 a130 a138 a14 a8 a139 a108 a144 a45
Class D	a35 a17 a145 a120 a23 a97 a71 a41 a143 a123
Class E	a1 a63 a133 a18 a89 a69 a84 a15 a50 a106 a60 a4
Class F	a55 a53 a81 a43 a59 a103 a105 a120 a78 a124 a75

3.4 Calculation of Fertilizer Application

A fertilizer calculation model was established, and the nutrient balance method was used to calculate the amount of fertilizer needed for the nutrient content in different soil levels. We calculate the average of four attributes in different soil levels and substitute them into the formula of nutrient balance method, the required values here are the raw values before data processing, and the data values are shown in Table 2.

Table 2. Average properties of different soil classification

Soil level	Organic mean	Available phosphorus mean	Available nitrogen mean	K mean
Class A	32.295	19.042	132.538	314.846
Class B	30.785	23.004	116.083	241.583
Class C	27.912	18.092	115.500	157.333
Class D	28.765	16.480	111.700	142.400
Class E	27.577	15.304	98.083	138.750
Class F	26.289	13.850	98.182	137.000

Calculation of nutrient balance fertilization model by fertilizer application rate (2):

$$sf = \frac{cl \times xs - cd \times ys}{hl \times ly} \quad (2)$$

- sf: Fertilization; cl: Corn yield target;
 xs: Grain corn nutrient absorption amount per 100 kg;
 cd: Soil nutrient determination;
 ys: Soil available nutrient conversion factor;
 hl: Fertilizer nutrient content;
 ly: Fertilizer utilization season.

Taking the mathematical model of fertilizer application rate as an example (The content of P₂O₅ was 46% in the application of diammonium phosphate):

$$\text{Phosphate fertilizer} = \frac{\text{Corn target amount} * 0.07 - 0.03 * \text{Soil nutrient content} * \text{Soil available nutrient conversion factor}}{0.46 * \text{Fertilizer utilization rate}}$$

$$\text{Soil available nutrient conversion factor} = \begin{cases} \frac{1578.8 * \text{Soil nutrient content}^{-0.98}}{100} \\ \frac{1068 * \text{Soil nutrient content}^{-0.832}}{100} \\ \frac{732 * \text{Soil nutrient content}^{-0.749}}{100} \end{cases}$$

$$\text{Blank area yield} = \frac{0.3 * \text{Soil nutrient content} * \text{Soil available nutrient conversion factor}}{0.022}$$

$$\text{Fertilizer utilization rate} = \begin{cases} \frac{(43.4-0.024) * \text{Blank area yield}}{100} \\ \frac{(36.6-0.025) * \text{Blank area yield}}{100} \\ \frac{(4.6-0.035) * \text{Blank area yield}}{100} \end{cases}$$

$$\text{Yield} = 10000 \text{ kg/hm}^2$$

According to the nutrient balance method, the data of Table 2 are replaced by (2), and the specific amount of soil fertility at each level of soil as shown in Table 3 can be obtained.

Table 3. Soil nutrient fertilizer rate

Soil level	N amount of fertilizer (kg/hm ²)	P amount of fertilizer (kg/hm ²)	K amount of fertilizer (kg/hm ²)
Class A	440.063	565.009	327.032
Class B	440.158	564.844	327.171
Class C	440.161	565.053	327.398
Class D	440.185	565.135	327.451
Class E	441.160	565.200	327.465
Class F	440.276	565.287	327.471

4 Conclusions

In this paper, the DBSCAN algorithm is used to classify the soil, and the classification results are applied to the corn precision fertilization decision, The experimental results of demonstration and application in Nong'an County of Jilin province Chen hometown.

The average amount of fertilizer is 560 kg/hm^2 (the average amount of fertilizer is calculated by the total amount of fertilizer divided by the total area), compared with the traditional fertilizer 608.42 kg/hm^2 , saving fertilizer 48.42 kg/hm^2 ; The average yield of the experiment is 8313 kg/hm^2 , which is 930 kg/hm^2 higher than that of the traditional output (the traditional values are derived from the statistical yearbook of China). Indeed, the purpose of reducing chemical fertilizer input, improving soil environment, increasing production and increasing income has been achieved.

Acknowledgment. The study was conducted by 2016 jilin province rural special project supported by the modern agricultural development «Demonstration and Application of Traceable System of Quinoa Products Based on Internet of Things and 3S Technology», Jilin science and technology development plan project, «Research on precision control and control technology for high quality and high efficiency production of major grain crops» (20170204020NY).

References

1. Miao, Y.: Research and application of intelligent agricultural production measurement system. Shanghai Jiao Tong University, Shanghai (2003)
2. Chen, G., Yu, H., Cao, L., Ma, L.: Data mining and precision agriculture intelligent decision system. Science Press, Beijing (2011)
3. National Research Council: Precision Agriculture in the 21st Century, Geospatial and Information Technologies in Crop Management. National Academic Press, Washington (1997)
4. Zhang, Y.: Preliminary study on soil fertility classification using numerical analysis method. *J. Shenyang Agric. Univ.* **17**(3), 49–55 (1986)
5. Liu, C., Liu, L.: Study on quantitative classification of soil fertility. *Guizhou Agric. Sci.* **27**(4), 20–22 (1999)
6. Zeng, Y., Xu, H., Bai, S.: Improved OPTICS algorithm and its application in text clustering. *Chin. J. Inf.* **22**(1), 22–24 (2008)
7. Wu, X., Zhang, Q., Li, H.: The value of clustering analysis and principal component analysis in the study of anthropology. *J. Anthropol.* **29**(4), 35–37 (2007)
8. Wu, S.: Further thinking on classification method of fuzzy clustering. *J. North China Inst. Sci. Technol.* **5**(1), 108–110 (2008)
9. Ester, M., Kriegel, H.P., Sander, J., Xu, X.: A density-based algorithm for discovering clusters in large spatial database. In: Knowledge Discovery and Data Mining (KDD 1996), pp. 226–231 (1996)
10. Ester, M., Kriegel, H.P., et al.: A density based algorithm for discovering clusters in large spatial data-bases with noise. In: Proceedings of the 2nd International Conference on Knowledge Discovery and Data Mining (KDD-96), Portland, Oregon (1996)



Location and Recognition Fruit Trees Based on Binocular Stereo Vision

Xueguan Zhao^{1,2}, Yuanyuan Gao^{1,2}, Songlin Wang^{1,2},
Xiu Wang^{1,2}(✉), Pengfei Fan^{1,2}, and Qingcun Feng^{1,2}

¹ Beijing Research Center of Intelligent Equipment for Agriculture,
Beijing, China

² National Research Center of Intelligent Equipment for Agriculture,
Beijing, China

{zhaoxg, gaoyy, wangsl, wangx, wangxiu,
fanpf, fengqc}@nercita.org.cn

Abstract. In order to improve pesticide utilization rate and reduce the environmental pollution caused by pesticide ground loss, this paper proposes to use binocular vision to recognize the contour and distance information of fruit trees. To improve the recognition accuracy and speed, focusing on the optimization of SIFT stereo matching algorithm. A method for matching the feature points of left and right images base on cosine distance and the vector modulus is proposed. On this basis, two stereo matching algorithms are compared, The accuracy of the Improved SIFT stereo matching algorithm is improved by 1.53%. With this method, the recognition time is almost unchanged, And the stability of depth measurement is analyzed. When the target distance sensor is 180 cm–220 cm, the standard deviation is 1.3592 cm, can meet the requirements of the work.

Keywords: Image recognition · Binocular vision · Stereo match
Visual location

1 Introduction

The misuse of pesticide application is very common in the actual process of agricultural production. Excessive application of will not only cause the waste of pesticide, but also bring pollution to the environment. Automatic target spray technology of fruit trees is an important way to achieve high efficiency and low pollution. The realization of target spray based on machine vision technology has become a research hotspot in the field of precision spray technology at home and abroad due to its high flexibility and low equipment development cost.

Target technology mainly uses sensors for target detection, such as infrared sensors, ultrasonic sensors, laser radar, image sensors (CCD) and so on. Li Li et al. designed a target spraying control system [1], in which the infrared sensor was used to judge whether the target was available or not, and a green sensor was used to judge whether the target was green, so as to achieve the goal of applying pesticide only to green crops, thereby further reducing the waste of pesticides. However, because of the small

detection area of infrared sensor, some switch jitter may be caused by the space between the branches and leaves. As the ultrasonic sensor could detect surfaces, it could solve the similar problem effectively. Gil et al. designed a multi nozzle sprayer consists of 3 ultrasonic sensors and 3 solenoid valves in early 2007 [3]. It could realize variable spraying according to the variation of grape leaves and save 58% pesticide compared with traditional spraying method.

Changyuan Zhai et al. built a target contour detection platform based on the ultrasonic sensor [2, 4], and some target detection experiments were carried out on the regular crown and cherry trees. Good results were obtained, which proved the feasibility of the ultrasonic target detection. Solanelles et al. applied ultrasonic sensors and proportional control valves to the air blower and controlled the spray flow according to the measured tree width, thereby greatly saving the pesticide [5]. Although the cost of CCD image sensor is higher and the processing speed is slower, it can also detect crop diseases and insect pests with a certain image processing technology. Honghui Rao et al. used CCD image sensors to collect target information, and sprayed the target by controlling motor movement after images processing from CCD sensors [6]. In 2010, Tianxiang Hu et al. studied the application of binocular vision technology in intelligent target spray, and further improved the accuracy and efficiency of spray [7].

Zacharie, Doerr used two-dimensional laser radar and GPS as sensors, and successfully developed a tractor autonomous navigation system for orchard operations. The accuracy of the system was higher [8, 9].

We can see that the application and research of machine vision in agriculture and forestry have entered the stage of development, and various theoretical and practical results emerge in an endless stream. But the accuracy of ultrasonic sensors and infrared sensors is poor, and laser ranging is expensive, at the same time target detection of machine vision is mainly used in weed identification in the field, and the research of target detection in orchard based on machine vision is still very few. At the same time, as the nerve center of target spraying system, the vision detection decision system needs to be further improved at the speed and accuracy of the detection algorithm.

2 Real - Time Precision Target System

The hardware of Precision target spray decision system mainly include: Daheng CCD camera, PC (host computer), indoor fruit tree test stand. Image analysis development based on Microsoft Visual Studio 2012, It mainly to achieve image acquisition, segmentation, measurement, ranging, intelligent decision-making and sending results and other functions. The image acquisition function is completed by the CCD camera. The image of the fruit tree collected by the CCD camera is stored in the form of an image sequence to the computer for subsequent image processing.

The image acquisition function is completed by CCD camera, and the fruit images collected by the CCD camera are stored in the form of image sequences for the computer to be used for subsequent image processing The applicable image

segmentation, recognition and measurement algorithm is sought and develop software used for image segmentation and processing, realize description of fruit tree by gravity, perimeter, shape complexity, depth and other parameters. And can recover the real object of fruit tree from the image information to lay the foundation for the precise application of pesticides, functional flow chart shown in Fig. 1.

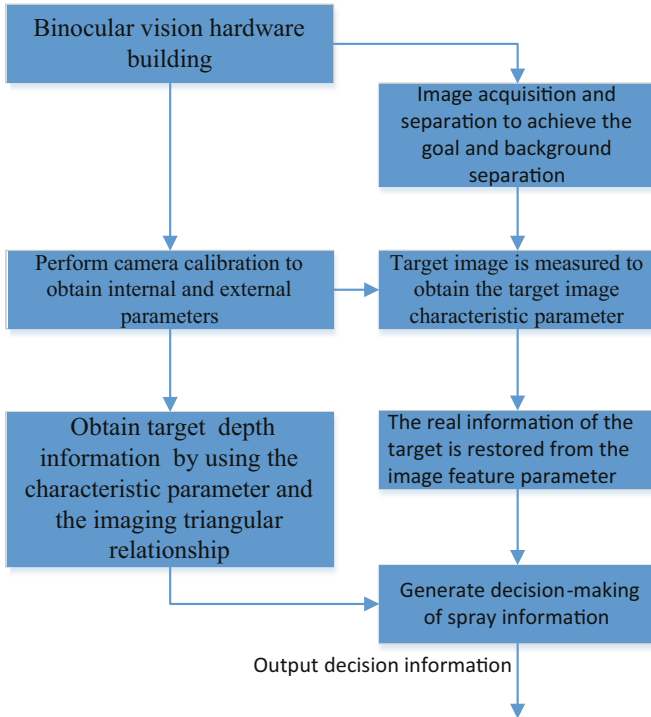


Fig. 1. Functional flow chart

3 System Calibration

MATLAB camera calibration toolbox has higher calibration accuracy, and the calibration method is simple, therefore this paper uses MATLAB to about camera calibration, the mercury series Daheng camera MER-500-7UC, 2592*1944 resolution, spatial position and binocular vision sensor calibration plate as shown in Fig. 2:

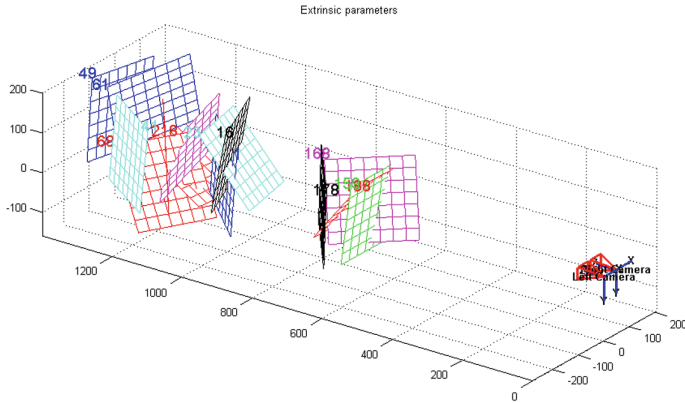


Fig. 2. Spatial position of calibration board and binocular vision sensor

MATLAB's camera calibration toolbox has a high calibration accuracy [10, 11], and calibration method is simple, so use MATLAB to calibrate the left and right cameras in this paper, and the calibration results are as follows, the internal parameters of the left and right camera are:

$$A = \begin{bmatrix} 3503.12 & 0 & 1207.31 \\ 0 & 3504.61 & 967.84 \\ 0 & 0 & 1 \end{bmatrix} \quad B = \begin{bmatrix} 3511.25 & 0 & 1198.93 \\ 0 & 3511.71 & 960.13 \\ 0 & 0 & 1 \end{bmatrix}$$

The equivalent focal length of the camera in the X direction is f_x , the inner parameter matrix of the left camera obtained from the test shows that the f_x of the left camera is 3503.12, This article adopts Computer brand 8 mm focal length lens, the physical dimensions of a camera pixel in the X direction have been given by the camera: $dx = 2.2 \mu\text{m}$. According to $f_x = f/dx$, can get $f_l = 7.706 \text{ mm}$, the same can get $f_r = 7.724 \text{ mm}$, A computer series of 8 mm focal length lenses are used. Which can be obtained left and right camera calibration error were 0.37% and 0.34% respectively. Then the rotation matrix and the translation matrix are calculated according to the common feature points, and R and T are

$$R = \begin{bmatrix} 0.0220 & 0.6674 & 0.7446 \\ 0.9964 & -0.0759 & 0.0386 \\ 0.0822 & 0.7408 & -0.0666 \end{bmatrix}$$

$$T = [-166.1646 \quad -84.2903 \quad 955.0699]$$

The obtained R and T results represent the matrix required for the left camera and the right camera to achieve coplanar, write R and T as XML files for `cvStereoRectify` function calls in Opencv for stereo correction, the results of the stereo correction are shown in Fig. 3:

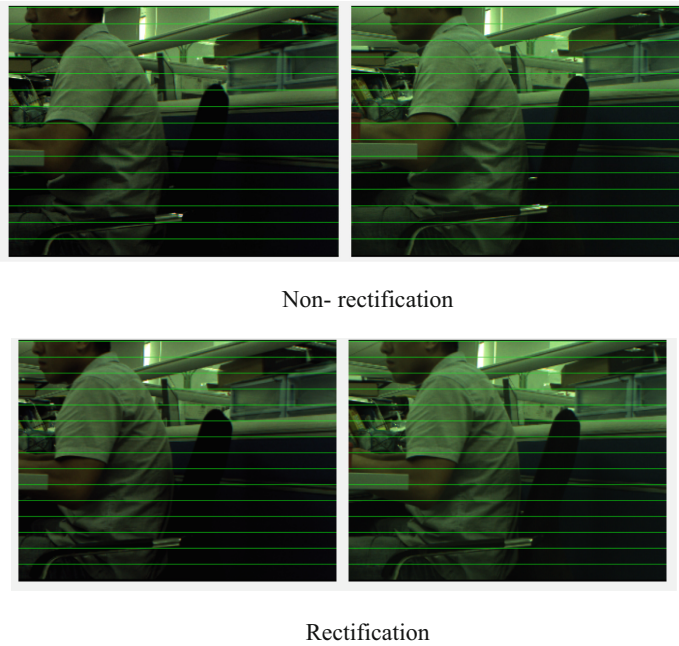


Fig. 3. Image before and after the rectification

4 Location

According to the principle of stereo vision, the simplest binocular stereo vision model is a stereo camera made up of two parallel lenses to capture the same scene image, as shown in Fig. 4. Since there is a distance between the two lenses (Fig. 4b), the target perceived through these two lenses will produce bias in the captured image (Fig. 4, dl, dr). According to the triangulation principle [12, 13], these deviations are proportional to the distance between the camera and the target (Z in Fig. 4), so that these deviations can be used to calculate the depth information of the target.

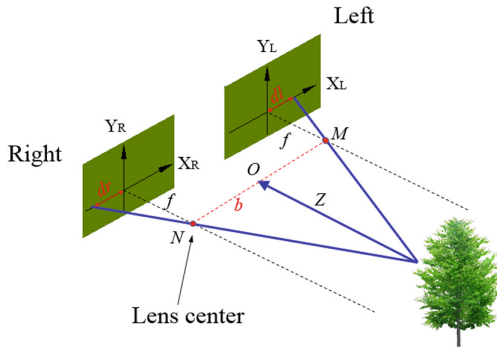


Fig. 4. Parallel optical axis geometric model of fruit trees Stereoscopic vision

b represents the horizontal distance between the two cameras, the baseline of the stereo vision system, the F is focal length, and the Z is depth. The parallax d can be calculated according to the formula (2-1) once the deviation (dl and dr) of the horizontal direction of the two images is determined.

$$d = d_l - d_r \tag{1}$$

See from the coordinates in Fig. 4, the dr is negative, so in fact the parallax d is the sum of dl and dr. Where the relevant parameters from the triangular similarity relationship can be obtained from the baseline mathematical expression:

$$b = (d_l + d_r) \cdot \frac{Z}{f} = d \cdot \frac{Z}{f} \tag{2}$$

Considering the relationship between length and pixels, the unit unity of parallax and depth calculation results is:

$$Z_{[mm]} = \frac{b_{[mm]} \cdot f_{[mm]}}{k_{[mm/pixel]} \cdot d_{[pixels]}} \tag{3}$$

In Eq. (3), Z, b, f units are mm, d is represented by pixels, and k is the size of each pixel.

5 Binocular Matching

Identification of fruit trees in the environment in real time and accurately, it is the key to the target spraying vision system, and the essence of object recognition is image segmentation. In this study, indoor simulation experiments were conducted to collect images of fruit trees [14]. Because there is a big difference between the surface color and the background color of fruit trees, there are different distribution characteristics in color space, so that image segmentation can be used to extract the target fruits and vegetables from the background. In this paper, 2G-R-B is used as a partition factor of the super green method. The picture of the fruit tree captured by the binocular vision system is shown in Fig. 5.



Fig. 5. A Pair of original stereo images

5.1 SIFT Feature Point Matching Algorithm

The appearance of fruit trees is complicated and prone to mismatching. Due to a hypothetical of region matching in the space plane is the plane, which is parallel to the camera plane, in the actual orchard scene there are a lot of non-positive planes, so people began to consider the use of some of the more significant feature points (points of interest) to match, this method can also be called feature matching method [15, 16].

SIFT feature matching algorithm is an image local feature description algorithm based on scale space, invariance to image scaling, rotation, and even affine transformations, therefore, it is widely used in matching technology. Because the number of feature points detected by SIFT feature point detection algorithm is larger, and each feature point descriptor is a vector of 128 dimensions. The feature utilization rate of the algorithm is not very high, it takes longer time, and there are some problems such as matching error or repetition.

5.2 Improved Stereo Matching Strategy

As the most common distance measurement standard, “euclidean distance” is also used as a matching criterion for SIFT based matching, and good results are obtained. However, there are still problems such as matching errors or repetitions. From the analysis of the eigenvector itself: if the direction of the two vectors is the same, the smaller the angle is, on the basis of that, the modulus of the vector is taken into account. If the modulus is equal or close, the two vectors are considered equal. To determine whether the two vectors are in the same direction, it is necessary to use the cosine theorem to compute the angle of the vector. The cosine similarity of vector a and B is calculated as follows

$$\cos \theta = \frac{a \cdot b}{|a||b|} \quad (4)$$

From the above SIFT feature descriptor, we can see that the dimension of vectors a and b is $a = (a_1, a_2, \dots, a_n)^T$, $b = (b_1, b_2, \dots, b_n)^T$, then the cosine of vectors a and b is:

$$\cos \theta = \frac{\sum_{i=1}^n a_i b_i}{\sqrt{\sum_{i=1}^n a_i^2 \sum_{i=1}^n b_i^2}} \quad (5)$$

Compared to Euclidean distance, cosine distance pays more attention to the difference of the two vectors in the direction. If we compare the length of the two vectors on the basis of the direction, we can accurately extract the feature matching points, the length of the vector, that is, the norm of the vector:

$$\|x\| = \sqrt{x_1^2 + x_2^2 + \dots + x_n^2} \quad (6)$$

The specific implementation steps of the proposed stereo matching strategy are as follows: Firstly, the key feature points of the left/right image are extracted, and the image with the key feature points is used as the reference image, and the image with

less key feature points is used as the image to be matched. The vector matrix of the K1 critical feature points of the baseline image is X, the vector matrix of the K2 critical feature points of the matched image is Y, X and Y are shown below:

$$X = \begin{bmatrix} x_{1,1} & x_{1,2} & x_{1,3} & x_{1,4} \\ x_{2,1} & x_{2,2} & x_{2,3} & x_{2,4} \\ \vdots & \vdots & \vdots & \vdots \\ x_{k1,1} & x_{k1,2} & x_{k1,3} & x_{k1,4} \end{bmatrix} \quad Y = \begin{bmatrix} y_{1,1} & y_{1,2} & y_{1,3} & y_{1,4} \\ y_{2,1} & y_{2,2} & y_{2,3} & y_{2,4} \\ \vdots & \vdots & \vdots & \vdots \\ y_{k2,1} & y_{k2,2} & y_{k2,3} & y_{k2,4} \end{bmatrix} \quad (7)$$

Take the first row vector of A $[x_{1,1} \ x_{1,2} \ x_{1,3} \ x_{1,4}]$, that is, the first critical feature point vector of the reference image, calculates cosine distance from all row vectors in B and takes inverse cosine, obtain an angle sequence of two vectors $\{\theta_1, 1, \theta_1, 2, \theta_1, 3, \dots, \theta_1, k\}$. To increase robustness,

Take the minimum value of the sequence of five values corresponding to the vector for norm comparison, take X first row feature vector and Y line k feature vector as an example:

$$\delta = abs(||a|| - ||b||) = |\sqrt{x_{1,1}^2 + x_{1,2}^2 + \dots + x_{1,n}^2} - \sqrt{y_{k,1}^2 + y_{k,2}^2 + \dots + y_{k,n}^2}| \quad (8)$$

Take the vector corresponding to the minimum of the δ as the feature point. And so on, until all of the row vectors in A have been completed in turn to calculate the cosine distance of all row vectors in B, and the comparison of the norm. That is, all the key K1 feature points of the reference image are matched with all the K2 key feature points of the image to be matched.

5.3 Key Feature Point Matching Contrast Experiment

According to the research scheme described in this paper, the application of improved SIFT algorithm in stereo matching is studied, and simulation experiments are carried out to verify and analyze the feasibility of the improved stereo matching strategy. Computer configuration in the test are: CPU core i5-2410 M, Memory is 2 GB, the operating system is Win7, and simulation platform is Matlab 2013. According to this method, the key feature points of left and right images are generated based on the improved SIFT algorithm, and the feature vectors extracted from the key feature points of left and right pictures are shown in Fig. 6(a) and (b).

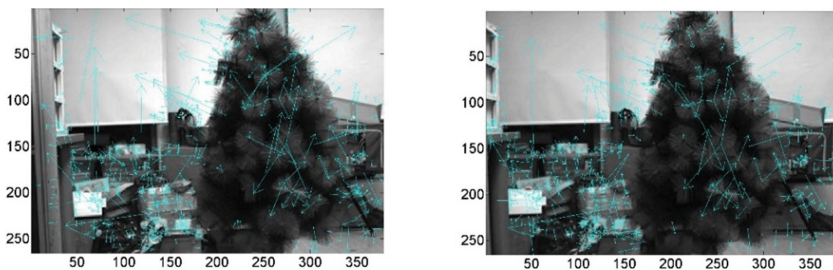
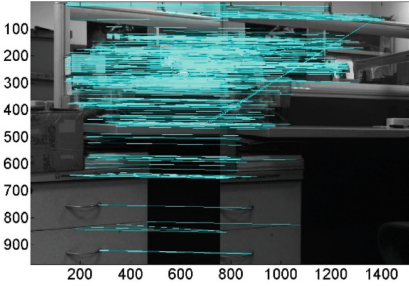
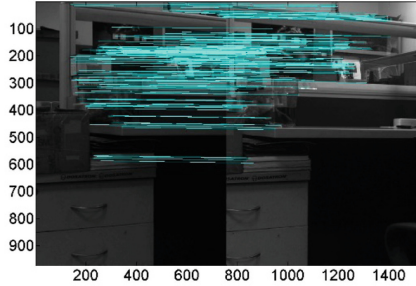


Fig. 6. Feature extraction result of the key feature points of the left/right image

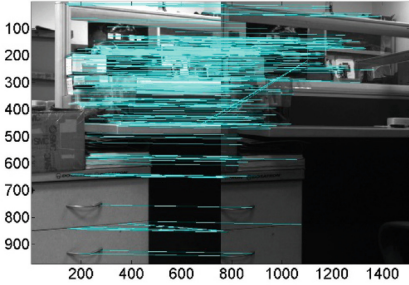
In this paper, the indoor environment image is selected, and the improved SIFT algorithm is tested under the illumination changes, scale changes and rotation changes. The matching results are shown in Fig. 7.



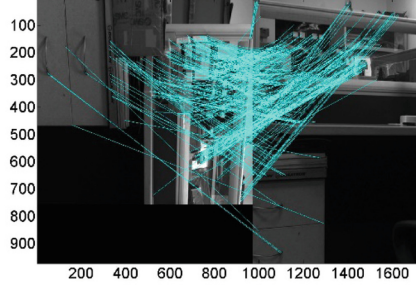
Control group



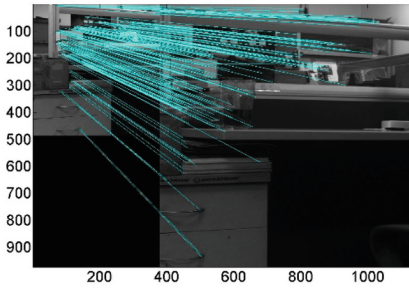
light is reduced by 30%.



light is increased by 30%.



Rotate 90 °



Scaling 50%

Fig. 7. Matching results of improved SIFT algorithm

Table 1. Statistical results of feature point matching

Matching method	Number of key feature points		Number of feature points matching	Number of error matching points	Correct matching rate/%	Matching time/ms
	Left	Right				
SIFT matching algorithm	490	498	206	7	96.60	697.21
Improved SIFT matching algorithm	490	498	214	4	98.13	702.63

In order to compare the difference in matching time between the improved SIFT algorithm and the SIFT algorithm, about 20 of the image acquisition in contrast, rotation, zoom, change of illumination conditions, using SIFT algorithm and improved SIFT matching algorithm for feature matching results statistics, statistical results from 20 on average of the image, as shown in the Table 1. The improved rule matching, stereo matching method increases the matching number, improve the matching efficiency, matching repetition or error reduce 1.53%, it is more advantageous to 3D reconstruction and localization of robot vision system.

5.4 Binocular Stereo Vision Experiment

The distance between the fruit tree and the camera is between 1.5 and 2.5 m, the length of the baseline of the two camera is 50 mm, and the algorithm is used to match. The matching effect is as Fig. 8:

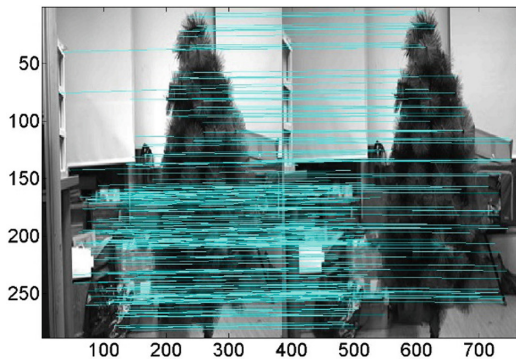


Fig. 8. Matching result of fruit tree binocular image

5.5 Test Results and Discussions

In order to further observe the influence of matching region selection on the region matching effect, the SIFT matching algorithm and the improved SIFT matching algorithm are tested respectively. The binocular vision sensor is used to reconstruct the fruit tree, and then the width, height and depth of the fruit tree are measured in space, and the comparison is made. In order to test the accuracy of the binocular vision sensor in space reconstruction at different depths from the target, the distance between binocular camera and fruit tree from 1.5 m to 2.5 m is measured every 0.05 m. The measurement results are shown in Fig. 9.

According to the three-dimensional reconstruction method, combined with the camera's internal and external parameters and parallax images, the 3D point cloud is measured at different angles, to get the height, width of the fruit trees and the depth in the vertical direction of the image plane. Where AB is the connection between vertex and diameter center of stem, The CD is the corners of the vertical line at 1/8 of the AB line. and the outer contour, 1 is the center of the AB line, 2 is the 1/8 at one end of the AB line, 3,4, respectively, at both ends 1/6 of the CD, the results shown in Table 1.

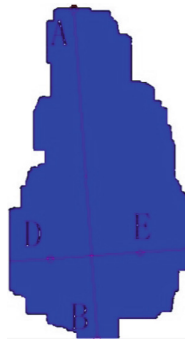


Fig. 9. Test point distribution

The actual distance between the lens and the target 1 points(cm)	Measured value					
	Height (cm)	Width	Target point A	Target point B	Target point D	Target point E
150	120.0	45.5	136.4	147.6	168.6	173.3
160	119.9	46.7	147.3	148.7	176.1	179.7
170	120.4	45.2	159.4	164.5	190.7	194.5
180	121.8	47.1	177.8	182.0	208.2	207.5
190	122.1	48.4	186.6	192.4	219.6	219.2
200	121.4	48.1	210.4	212.8	227.1	241.6
210	120.9	47.8	221.2	224.3	244.0	252.6
220	122.0	48.8	228.9	230.8	260.3	261.9
230	122.1	49.1	236.6	246.8	274.4	271.9

(continued)

(continued)

The actual distance between the lens and the target 1 points(cm)	Measured value					
	Height (cm)	Width	Target point A	Target point B	Target point D	Target point E
240	124.5	49.6	258.9	261.0	287.5	287.1
250	123.2	50.3	273.8	274.9	302.6	302.4
True value	121.5	48.0	-	-5.4	+20.3	+22.7

The true value of the target 2–4 points is the relative depth of the target 1, and the “+” represents the direction of great depth.

In order to analyze the stability of the depth measurement, the difference between the target A and the mean value of target D, E as the length, the difference between the target D and the target E is half of the width, from the three-dimensional reconstruction of the measurement results can be found, compared to its height and width, length and manual measurement results, the standard deviation was 1.3805, 1.6224, 3.6081. And length value corresponds to the depth value in space, and its beating is greater compared with the width and height, the, and the width and height than the beating larger, When the sensor is away from the target at 180 cm–220 cm, the standard deviation is 1.174, relatively stable, so in the actual positioning of the apple space, the Deviation range of distance from visual sensor to the target 1 point range should be measured within the 40 cm (Fig. 10).



Fig. 10. Real-time measurement results

Through a lot of test analysis, the error is mainly due to the accuracy of the depth information acquisition and several factors related to: the distance between the trees and the camera; the uniformity of light on the regional matching is also greater, due to the uneven light resulting in the match is not accurate, easy to cause the depth of information error, coupled with the impact of random noise, image segmentation results will be biased, affecting the results of distance measurement.

Acknowledgement. This research was financially supported by the National Key R&D Program of China (2016YFD0200604).

References

1. Li, L., Li, H., He, X., et al.: Development and experiment of automatic detection device for infrared. *Trans. Chin. Soc. Agric. Eng.* **28**(12), 159–163 (2012)
2. Zhai, C., Zhao, C., Wang, X., et al.: Probing method of tree spray target profile. *Trans. CSAE* **26**(12), 173–177 (2010)
3. Gile, E., Rosell, J.R., et al.: Variable rate application of plant protection products in vineyard using ultrasonic sensors. *Crop. Prot.* **26**(8), 1287–1297 (2007)
4. Stajanko, D., Berk, P., Lešnik, M., et al.: Programmable ultrasonic sensing system for targeted spraying in orchards. *Sensors* **12**(11), 15500–15519 (2012)
5. Solanelles, F., Escola, A., Planas, S., et al.: An electronic control system for pesticide application proportional to the canopy width of tree crops. *Biosyst. Eng.* **95**(4), 473–481 (2006)
6. Rao, H.: Study on crop spraying control based on machine vision. *J. Nanjing Agric. Univ.* **30**(1), 120–123 (2007)
7. Hu, T., Zheng, J., Zhou, H.: Distance measurement of tree images based on binocular vision. *Proc. Agric. Mech. Soc.* **41**(11), 158–162 (2010)
8. Cai, J., Sun, H., Li, Y.: Three dimensional information acquisition and reconstruction based on binocular stereo vision. *Chin. J. Agric. Mach.* **43**(3), 152–156 (2012)
9. Doerr, Z., Lague, C.: Evaluating the ability to detect foreign objects in crops using range scanners mounted on agricultural vehicles. In: ASABE Annual International Meeting, Nevada, 21–24 June 2009
10. Zou, L., Li, Y.: A method of stereo vision matching based on Open CV. In: Proceedings of 2010 International Conference on Audio Language and Image Processing (ICALIP), pp. 185–190. IEEE, Piscataway (2010)
11. Spampinato, G., Lidholm, J., Ahlberg, C., et al.: An embedded stereo vision module for industrial vehicles automation. In: 2013 IEEE International Conference on Industrial Technology (ICIT), pp. 52–55. IEEE, Piscataway (2013)
12. Ganganath, N., Leung, H.: Mobile robot localization using odometry and Kinect sensor. In: 2010 IEEE International conference on Emerging Signal Processing Applications (ES-PA), NJ, USA, pp. 91–94 (2010)
13. Bradley, D., Heidrich, W.: Binocular camera calibration using rectification error. In: 2010 Canadian Conference on Computer and Robot Vision (CRV), pp. 183–190. IEEE (2010)
14. Shuai, Z.: Research on the Error Theory of Binocular Vision measurement system on Non-cooperative Targe. Changchun: Changchun Institute of Optics, fine Mechanics and Physics, Chinese Academy of Sciences (2014)
15. Ravari, A.R.N., Taghirad, H.D., Tamjidi, A.H.: Vision-based fuzzy navigation of mobile robots in grassland environments. In: Proceedings of International Conference on Advanced Intelligent Mechatronics.[S. I.]. IEEE/ASME Press (2009)
16. Song, T., Tang, B., Zhao, M., et al.: An accurate 3-D fire location method based on sub-pixel edge detection and non-parametric stereo matching. *Measurement* **50**, 160–171 (2014)



The Realization of Pig Intelligent Feeding Equipment and Network Service Platform

Weihong Ma^{1,2,3,4}(✉), Jinwei Fan¹, Chunjiang Zhao^{2,3,4},
and Huarui Wu^{2,3,4}

¹ College of Mechanical Engineering and Applied Electronics Technology,
Beijing University of Technology, Beijing 100124, China

mawh@nercita.org.cn

² National Engineering Research Center for Information Technology
in Agriculture, Beijing 100097, China

³ Key Laboratory of Agri-Informatics, Ministry of Agriculture,
Beijing 100097, China

⁴ Beijing Engineering Research Center of Agriculture Internet of Things,
Beijing 100097, China

Abstract. Proper feeding of pigs can increase the litter size and improve the disease resistance level. In recent years, intelligent and automatic equipment, which can collect feeding times, feed intake, feed time and growth conditions, have been applied to the pig feeding. Most equipment can feed both manually and automatically. Not enough attention has been paid to one pig's health condition, living environment, and dietary status, which should be considered together in order to make an accurate decision on the feed intake of each pig. At the same time, there are not many network service platforms in China which can effectively manage the intelligent and automatic equipment remotely and simultaneously. To improve pigs' productivity and enhance the intelligent management of pigs, wireless sensor network, intelligent sensors, network service platform, and reasoning and decision-making technology have been utilized in the management of pigs in multiple areas throughout China. Single feed intake, living environment information, fitness, and weight for pigs throughout China with different conditions were collected in the network service platform by using the intelligent feed equipment which had several different sensors. Meanwhile, the network service platform could recognize the identity of each pig and provide accurate feed remotely. The network service platform would send a text message or an audible and visual alarm to inform the pig keeper whether the pig's feed intake was proper. According to the reasoning and decision-making model we built in the network service platform, we can remotely obtain through the platform more accurate information within seconds as to each pig's feeding status. Moreover, the experiment showed that the feeding container was the key factor that influenced the precision of feeding, and the measured value was closely approximate to the target value with error correction.

Keywords: Management of pigs · Internet of things · Monitoring and warning Reasoning and decision-making · Network service platform

1 Introduction

Proper feeding is an important way to improve pig productivity, which increases litter size and improves disease resistance [1]. The feeding status of pigs is a very important index of health monitoring. Abnormal feeding behavior can be a sign of epidemic disease [2].

Considering the disadvantages of traditional livestock farms, such as being time-consuming, laborious and having low accuracy [3], Zhong et al. used RFID, GPRS and embedded technology to collect and analyze each pig's feeding times, feed intake, and growth status in large-scale pig farms. They proposed a new method based on RFID and ARM embedded technology to monitor pigs' daily behavior. Although this method can be used to collect each pig's feeding times, food intake, and growth state, there is no monitoring of a pig's health information and living environment information, no comprehensive analysis and reasoning with health information, no living environment information and feed intake, and no network service platform which could provide an effective way of managing pigs from multiple areas. Hence, this method cannot remotely provide accurate feeding information. Moreover, the multiple intelligent feeders from multiple areas cannot be centrally monitored and managed. We used Wireless Sensor Network, intelligent sensors, network service platform technology, and remote reasoning and decision-making [4] to achieve accurate feeding and precision management of pigs from multiple areas, which improved their productivity level.

2 System Composition

The system we built comprised two parts which were (a) the pig intelligent feeding equipment and (b) the pig health monitoring and management network service platform. The network management of the pig feeding equipment and the remote monitoring and managing of useful information, such as living environment, health information and daily feeding amount of pigs from multiple areas, was realized by using the Internet of things technology [5, 6]. Through cameras installed in pig farms in multiple areas, users could have a remote view of the pig farm and were able to remotely control the pig feeding equipment through the network service platform via mobile phone and PC [7].

The decision-making model [8] was used in the pig health monitoring and managing network service platform to obtain the precise feed amount. Then, the platform sent instructions to the feeding equipment to control the pig feeding motor to feed the precise amount. The intelligent feeding equipment from multiple areas was centrally managed through the pig health monitoring and managing network service platform via the wireless transmission network, as shown in Fig. 1. Meanwhile, users were able to access the platform service through mobile phone and PC at any time and from anywhere.

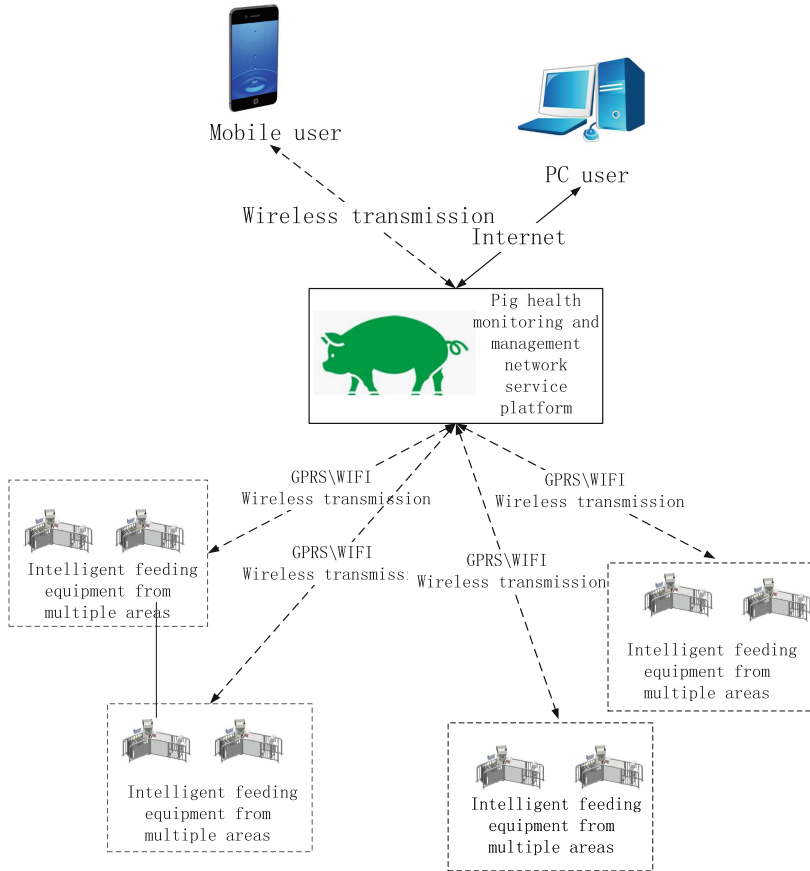


Fig. 1. The whole system structure

3 Pig Intelligent Feeding Equipment

3.1 Hardware of Pig Intelligent Feeding Equipment

The hardware of the feeding management equipment was composed of the core processing unit, environmental monitoring unit, process monitoring unit, health monitoring unit, execution unit, and the wireless transmission unit. The core processing unit was composed of the core processor and its peripheral circuit. The main function of the core processing unit was to manage the equipment's other units. The sensors in the environmental monitoring unit were an ambient temperature sensor, humidity sensor, ammonia sensor [9], carbon dioxide sensor, and hydrogen sulfide sensor [10], all monitoring the gas concentration of the pigs' living environment.

There was an entrance and exit detection in the process monitoring unit with infrared sensors which used infrared detection to determine whether a pig had passed. The RFID identifier was used to identify the identity of each pig in order to make the

intelligent feeding equipment feed accurately. The RFID identifier sent the radio frequency modulation signal to the label through the antenna. At the same time, it received the RF signal which contained information from the label through the antenna [11]. Then, the RF signal was processed to be transmitted to the core processor.

The sensors in the health monitoring unit were a material level monitoring sensor, electronic scale sensor, non-contact infrared temperature measuring sensor [12], and animal ultrasonic thickness sensor [13]. The material level monitoring sensor was used to monitor the actual amount of the hopper in order to obtain the pig’s effective feeding intake. The electronic scale was used to measure the pig’s weight before feeding. Hence, the electronic scale enabled the equipment to record pig weight daily. The non-contact infrared temperature sensor was used to monitor the pig’s body temperature before eating. In addition, the temperature and humidity compensation algorithm was used to make the pig’s body temperature measurement more accurate [14]. The ultrasonic thickness sensor, which uses ultrasound to measure the thickness of mammals, was applied in our experiment.

The execution unit comprised of the hopper feed motor, entrance door motor, and exit door motor whose function was feeding, opening and closing the door of the equipment. The main function of the wireless transmission unit was to transmit the real-time data of the intelligent feeding equipment to the network service platform [15] and at the same time accept the instructions from the network service platform to collect data, feed, open and close the door, etc. The equipment hardware is shown in Fig. 2.

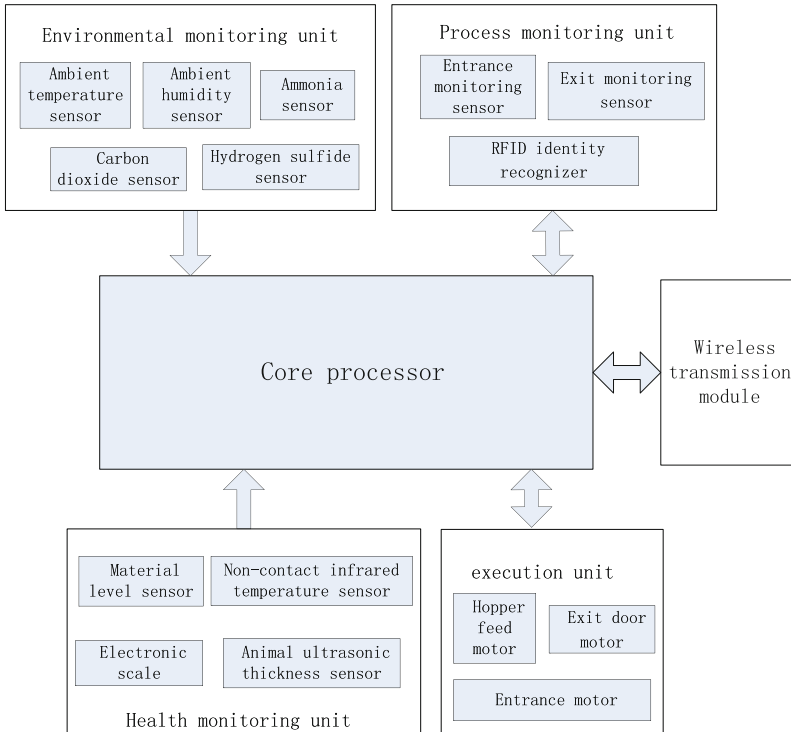


Fig. 2. The hardware of pig intelligent feeding equipment

3.2 Software Process of Pig Intelligent Feeding Equipment

The intelligent feeding equipment first initialized and then opened the entrance door to allow the pigs to enter one by one. The equipment used the entrance door sensor to detect whether a pig had entered the entrance door. When the pig entered, the core processor activated the RFID identifier to identify the electronic earmark of the pig. As the distance of the identification of the electronic earmark was relatively close, when the RFID recognized the pig ear, it meant that the pig had entered the dietary channel. At the same time, the equipment closed the entrance door to prevent other pigs from entering into the dietary channel. If other pigs were able to enter the dietary channel, then the equipment would not be able to tell which electronic ear tag belonged to the pig. When the core processor received the electronic ear tag information, then the electronic scales, non-contact infrared temperature, and fat thickness sensors began to collect data. Sensor data and environmental information together with the identity information of the RFID and the current time were then transmitted to the server through the wireless transmission module [16].

After the server received the sensor data and the other information, it then obtained the result from the forward inference [17, 18] of the server platform to determine the feeding amount of the recognized pig. The network service platform [19] sent the feeding amount instruction to the core processor module of the feeding device through the wireless module. After replying to the instruction, the core processor operated the material level motor to feed according to the amount of the instruction. During the pig's feeding time, the core processor worked with the material level sensor to monitor whether there was residual feed. If the monitoring result was still surplus, the material level sensor would continue to monitor whether the material level was still reducing 10 min later. If the material level was still reducing, it indicated that the pig was still feeding. Then the material level sensor would keep monitoring the material level until the material level was no longer reduced, which meant that the pig had finished feeding this time. The actual feed intake would be uploaded to the platform server. Finally, the equipment would open the exit door. When the exit door sensor detected that the pig had left the exit door, the equipment would close the exit door and open the entrance door, waiting for the next pig to enter to feed. The software flow chart of the intelligent feeding equipment is shown in Fig. 3.

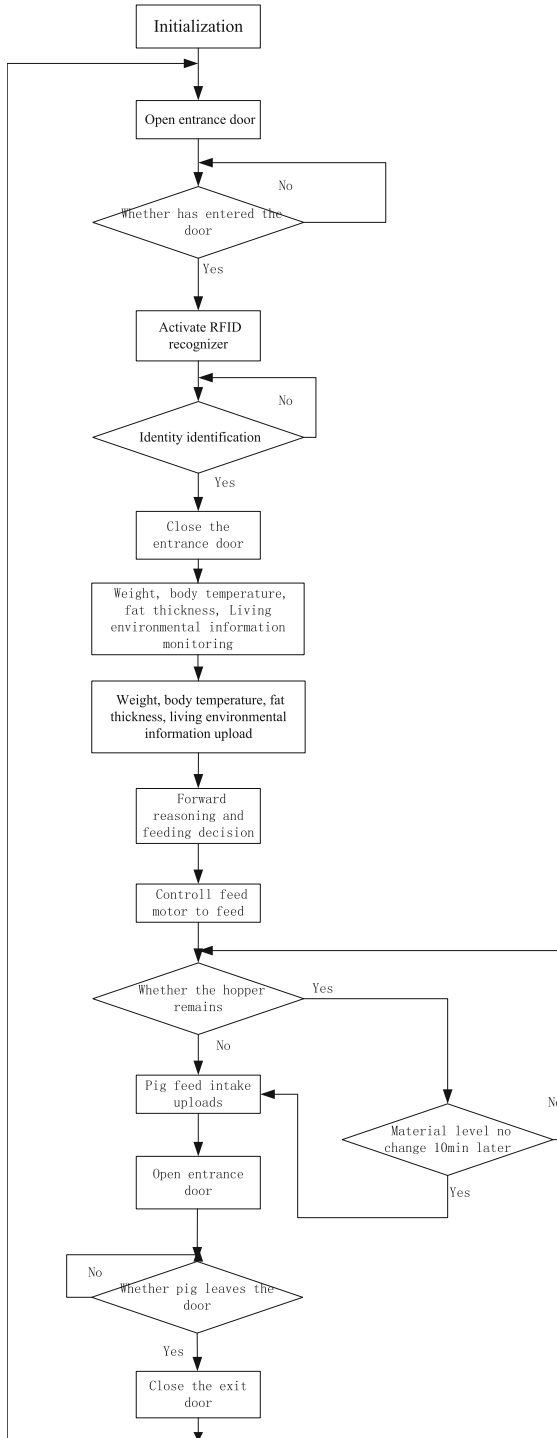


Fig. 3. The software flow chart of intelligent feeding equipment

4 Pig Network Service Platform

4.1 Network Service Platform Structure

The function of the network service platform was to monitor and manage pig health, which included basic information management, environmental information monitoring, reasoning and decision-making, and user management, as shown in Fig. 4.

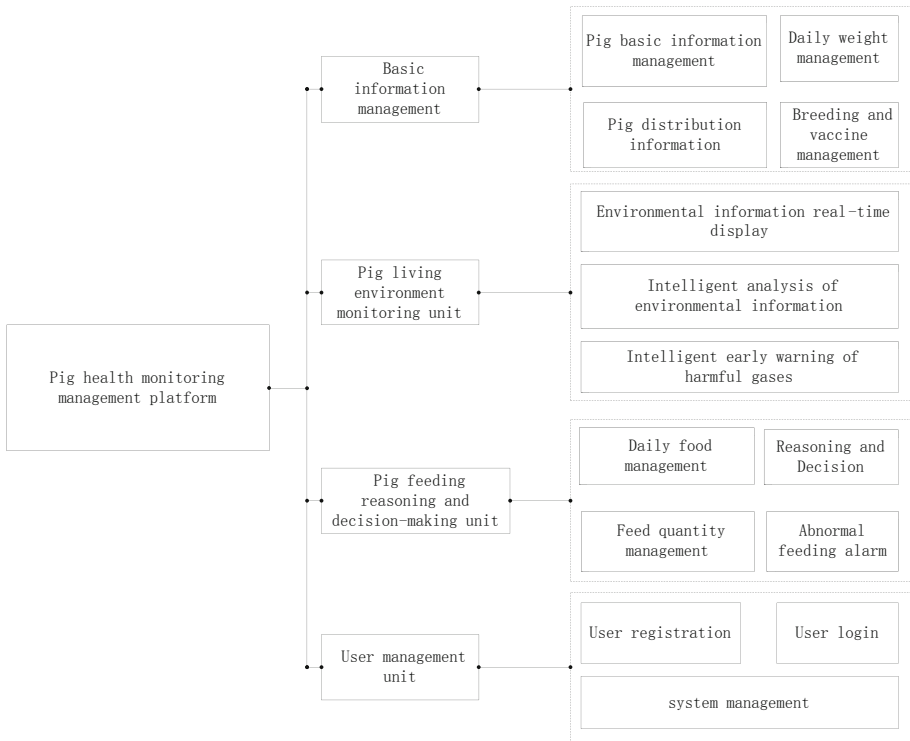


Fig. 4. Network service platform structure

Users from multiple areas viewed the network service platform installed in the remote server either through mobile phone or PC. The network service platform was developed by using the Eclipse 8.0 development platform [20]. The foreground page and background program were written using Java language [21, 22]. The management of the relational database was realized by MySQL [23, 24], which has the most comprehensive set of advanced features, management tools, and technical support to achieve the levels of MySQL scalability, security, reliability, and uptime.

4.2 Reasoning and Decision-Making

Considering that the control targets, living environment, and growth data of individual pigs were different, it was not a simple process to determine the feed intake of

individual pigs. Previous feeding methods did not consider the multiple control targets taken into account by our team. They also did not refer to expert opinion and historical data to determine the correct feed intake of a typical pig. The intelligent feeding system based on the expert system reasoning machine [25, 26] linked together the living environment, growth status, growth parameters, and growth stage by case matching, fuzzy reasoning, and decision-making to derive the pigs' best diet condition, so as to effectively apply expert opinion and historical parameters to control the pigs' diet.

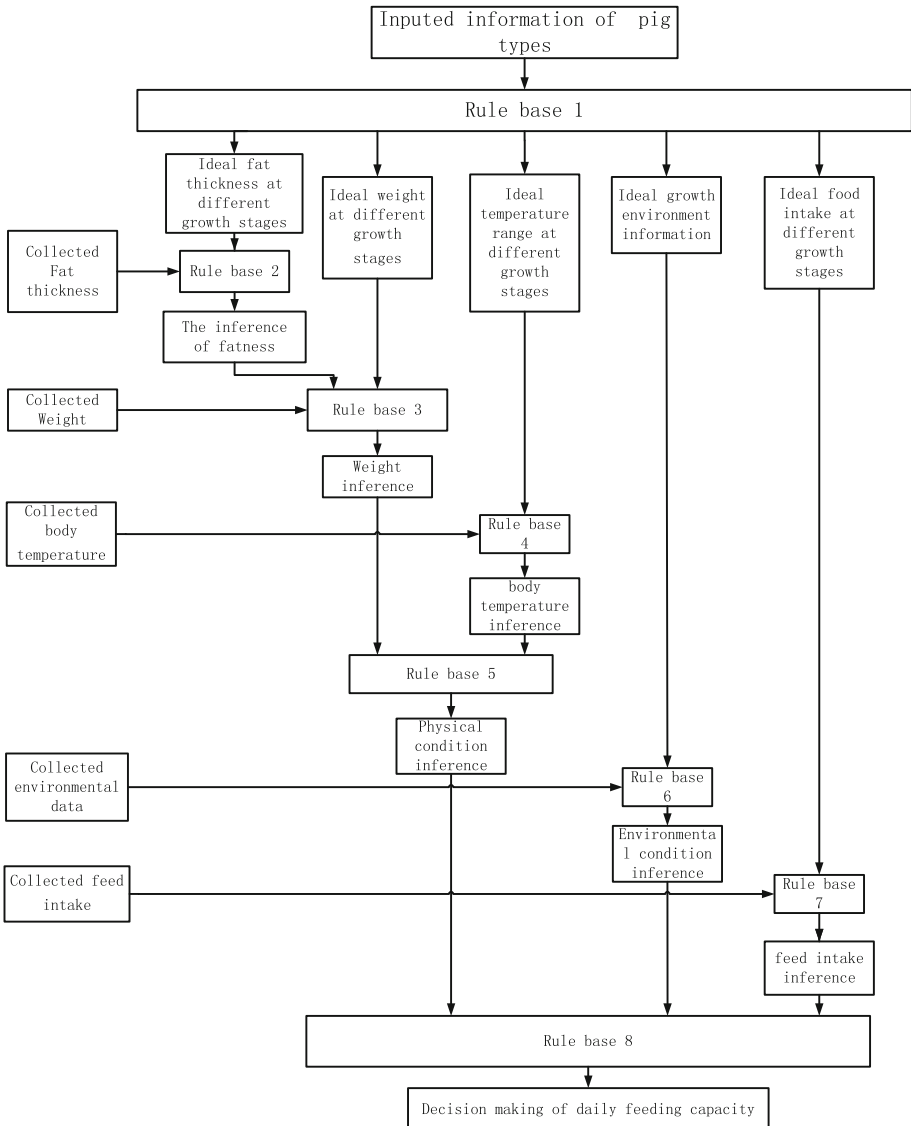


Fig. 5. Expert system inference engine

Reasoning and decision-making were made by the inference engine [27, 28], which used certain reasoning methods and strategies in the dynamic database [29] for working memory. According to the current content of the dynamic database, the corresponding reasoning control strategy was used by the inference engine to decide how to use the knowledge in the knowledge base.

At the same time, the rules in the rule base were controlled to match the data and facts in the dynamic database. When the match was a success, the corresponding rules were triggered to modify the dynamic database. Using the decision-making model, the final result was obtained. Expert system inference engine [30] was used in this paper, as shown in Fig. 5.

5 Experiment

5.1 Feeding Accuracy Experiment for Pig Feeding Equipment

Experiment equipment: Pig intelligent feeding equipment, high-precision electronic scale.

Measured material: Powder concentrated feed.

Experimental purpose: To detect the feeding accuracy of pig intelligent feeding equipment.

Considering the intake amount of a pig is about 2 kg–4 kg per day, we set the feed target values as 2 kg, 3 kg and 4 kg, which were each measured 5 times using a high-precision electronic scale whose precision is 0.2 g and range 10 kg. The target value was the theoretical value computed according to the relationship between design volume and pulse equivalent. There was some error of drop feeder assembly and pulse equivalent, which is inevitable. After correcting the error by the averaging algorithm, the actual value and target value were as follows (Table 1):

Table 1. Target value, measured value and average value

Target value (Kg)	a (Kg)	b (Kg)	c (Kg)	d (Kg)	e (Kg)	Average value (Kg)
2	1.98	1.90	1.97	2.03	2.05	1.97
3	2.90	2.91	2.98	3.03	3.05	2.97
4	4.09	4.05	3.96	3.92	4.03	4.01

It was obvious that the average value was approximate to the target value, concluding that the feeding container was the key factor that influenced the precision of the intelligent feeding equipment.

5.2 Reasoning and Decision-Making Test

The experiment was carried out by pig intelligent feeding equipment on one pig. The decision-making was obtained through the network service platform. The server received a pig's electronic ear tag information, DBZRSQU3041. After comparing the

ear tag information to the database on the server, the equipment derived the following information: the large white variety, pregnancy status, and gestational age of 20 days. The data collected by the sensors were: body weight, 95 kg; body temperature, 38.7 °C; and fat thickness, 16 mm. The living environment parameters were: temperature, 30 °C; humidity, 25%; ammonia concentration, 25 ppm; CO₂ concentration, 356 ppm; and hydrogen sulfide concentration, 3 ppm. According to the information on pig varieties and breeding stages of pigs, the network service server obtained the knowledge base of the ideal physical parameters: body weight, 90 kg–100 kg; body temperature, 38.3–39.1 °C; and fat thickness, 15.0–21.0 mm. The ideal living environment parameters were: temperature, 25°; humidity 50%–60%; ammonia concentration, 0–30 ppm; carbon dioxide concentration in the air, 300–450 ppm; and hydrogen sulfide concentration, less than 10 ppm. After comparing the physical parameters and preset parameters, the reasoning and decision-making model concluded that weight, body temperature, fat thickness, and physical condition were normal. After comparing the collected environmental parameters to the ideal environmental parameters, the reasoning and decision-making model concluded that the temperature was high, humidity was low, and gas concentration was normal. Hence, the environment parameters were not suitable for this pig. Thus, when the forward reasoning and the contrast of the knowledge base model were finished, the forward reasoning machine model in the network service platform made a decision that the current recommended intake was 2.8 kg.

6 Conclusion

Proper feeding is an important condition for the growth of pigs. The difference in the growth period, health status, and environmental parameters make the daily intake of feed of each pig different. Proper feeding can effectively avoid the waste of feed and maintain pigs' health condition. At present, there is a lack of an effective health monitoring network service platform for large-scale and multiple areas pigs' precision feeding. Previous research did not do an effective reasoning and analysis based on pigs' living environment and physical status. Previous research also did not use an effective reasoning and decision-making model that considered pigs' living environment and physical status. We combined with the Internet of things technology, network service platform technology, sensor technology, and reasoning and decision making to make an intelligent feeding equipment and network service platform which can provide a convenient and intelligent feeding method as well as multiple areas pig management. The average value of the equipment was approximate to the target value, which meant that the accuracy of the equipment was high, and the feeding container was the key factor that influenced the precision of the intelligent feeding equipment. Decision-making was obtained through the network service platform which was able to monitor and manage the health status of pigs. In the future, on the basis of the accumulation of data, we can use machine learning to analyze big data to enrich and improve the reasoning and decision-making model and forecast the future of pigs' feeding status.

Acknowledgment. This work is partially funded by the National Natural Science Foundation of China, (project number F010407). We thank Dr. Tina Giannoukos for her English-language editing.

References

1. Hall, A.D., Hill, W.G., Bampton, P.R.: Genetic and phenotypic parameter estimates for feeding pattern and performance test traits in pigs. *J. Anim. Sci.* **68**(1), 43–48 (1999)
2. Maselyne, J., Saeys, W., Van, N.A.: Review: quantifying animal feeding behaviour with a focus on pigs. *J. Physiol. Behav.* **138**, 37–51 (2015)
3. Latruffe, L., Balcombe, K., Davidova, S.: Technical and scale efficiency of crop and livestock farms in Poland: does specialization matter? *J. Agric. Econ.* **32**(3), 281–296 (2015)
4. Pomar, J., Pomar, C.: A knowledge-based decision support system to improve sow farm productivity. *Expert Syst. Appl.* **29**(1), 33–40 (2005)
5. Botta, A., Donato, W.D., Persico, V.: Integration of cloud computing and internet of things. *J. Future Gen. Comput. Syst.* **56**(C), 684–700 (2016)
6. Li, S., Xu, L.D., Zhao, S.: The internet of things: a survey. *J. Inf. Syst. Front.* **17**(2), 243–259 (2015)
7. Yerunkar, M., Rangnekar, A., Reshamwala, A.: Implementing methodologies for achieving a communication channel between a mobile phone and a remote computer. *J. Int. J. Comput. Sci. Inf. Technol. Secur.* **2**(2), 293–298 (2012)
8. Wang, Y.J.: A fuzzy multi-criteria decision-making model based on simple additive weighting method and relative preference relation. *J. Appl. Soft Comput. J.* **30**(C), 412–420 (2015)
9. Timmer, B., Olthuis, W., Berg, A.V.D.: Ammonia sensors and their applications—a review. *J. Sens. Actuators B Chem.* **107**(2), 666–677 (2005)
10. Olson, K.R.: Hydrogen sulfide as an oxygen sensor. *J. Antioxid. Redox Signal.* **22**(5), 377–397 (2015)
11. De Souza, K.G., Woodward, S., Fare, J.W.D., Schott, S.H.: Check fraud detection process using checks having radio frequency identifier (RFID) tags and a system therefor. US, US20040000987 (2004)
12. Yoo, W.J., et al.: Infrared fiber-optic sensor for non-contact temperature measurements. In: 3rd International Conference on Sensing Technology, pp. 500–503 (2008)
13. Tong, A., Newman, J.A., Martin, A.H., Fredeen, H.T.: Live animal ultrasonic measurements of subcutaneous fat thickness as predictors of beef carcass composition. *J. Can. Vet. J. La Revue Veterinaire Canadienne* **61**(2), 483–491 (1981)
14. Wang, Z.: The influence of environmental temperature and humidity on the body temperature and water content of *chorthippus dubius* (zub). *Acta Entomologica Sinica* (1989)
15. Puskala, T.: System and method for transmission of predefined messages among wireless terminals accessing an on-line service, and a wireless terminal. US, US20020165024 (2002)
16. Liu, B., Zhang, X., Ren, X.: Wireless data transmission between iOS client and web server. In: International Conference on Computer Science & Education, pp. 351–354. IEEE (2014)
17. Hansen, S.T., Hauberg, S., Hansen, L.K.: Data-driven forward model inference for EEG brain imaging. *J. Neuroimage* **139**, 249–258 (2016)
18. Penny, W.D., Zeidman, P., Burgess, N.: Forward and backward inference in spatial cognition. *J. Plos Comput. Biol.* **9**(12), e1003383 (2013)

19. Kato, Y., Narita, M., Akiguchi, C.: The network service platform for real-world data. In: International Conference on Advanced Information Networking and Applications Workshops, pp. 55–60. IEEE Computer Society (2009)
20. Norton, B.: Eclipse as a development platform for semantic web services. Eclipse Technology Exchange (2004)
21. Gosling, James: The Java Language Specification. China Machine Press, Beijing (2006)
22. Gosling, J., Joy, B., Steele, G., Bracha, G.: The Java Language Specification, 3 edn. (2005). *J. Java*, 14(2–3), 133–158
23. Linksvayer, T., Mikheyev, A.: Data tables from MySQL database for gene expression analysis. *J. Dev.* **130**(25), 6221–6231 (2015)
24. Bell, C., Kindahl, M., Thalmann, L.: MySQL High Availability: Tools for Building Robust Data Centers. O’Reilly Media Inc., Sebastopol (2010)
25. Chen, X.Y.: Study and realization of uncertain reasoning machine base on expert system. *Manuf. Autom.* **33**, 78–80 (2011)
26. Liu, H.M., Chen, X.Y.: The study and realization of an uncertain reasoning machine in the expert system platform. *J. Nanyang Inst. Technol.* **2**, 17–20 (2010)
27. Zou, Y., Finin, T., Chen, H.: F-OWL: an inference engine for semantic web. In: Hinchey, M.G., Rash, J.L., Truszkowski, W.F., Rouff, C.A. (eds.) FAABS 2004. LNCS, vol. 3228, pp. 238–248. Springer, Heidelberg (2004)
28. Su, H., Wen, Z., Wu, Z.: Study on an intelligent inference engine in early-warning system of dam health. *J. Water Resour. Manag.* **25**(6), 1545–1563 (2011)
29. Zhang, S., Zhang, J., Zhang, C.: EDUA: an efficient algorithm for dynamic database mining. *J. Inf. Sci.* **177**(13), 2756–2767 (2007)
30. Tzafestas, S., Palios, L., Cholin, F.: Diagnostic expert system inference engine based on the certainty factors model. *J. Knowl.-Based Syst.* **7**(1), 17–26 (1994)



Improvement of Regional Spatial Interaction Based on Spatial Traffic System Accessibility: A Case Study in Shandong Province, China

Yu Zhang¹(✉), Shouzhi Xu², Fengguang Kang¹, and Shihua Yin³

¹ Chinese Academy of Surveying and Mapping, Beijing, China
Zhangyu6242@163.com, Kangfg@casm.ac.cn

² National Calibration Center for Surveying Instruments, Beijing, China
xushouzhi@126.com

³ Liaoning Technology University, Fuxin, Liaoning, China
2830554908@qq.com

Abstract. In order to quantitatively analyze the spatial interaction among regions, a new approach on reconstruction of intercity spatial interactional model based on spatial traffic system accessibility was proposed in this paper. Multi-indicators were used to comprehensively measure urban quality instead of a single demographic or economic index. Time distance combined with traffic distance was made as the final distance instead of Euclidean distance. The coefficient of the model is modified considering the proportion of passenger quantity and freight capacity, and the shortest travel time and so on. And then an example of reconstruction of intercity gravity model in Shandong Province has been done. The results showed that Qingdao has the most comprehensive strength, while Jinan has the highest spatial interaction. Although the comprehensive development level of a city has a great influence on its radiation capacity, the accessibility of the transportation system between cities also plays a certain role. The results prove that traffic accessibility has a guide significance to the spatial interaction among regions, and the new model is fit for the actual than the older one. It is a reasonable and effective method to analysis and research the capability of spatial interaction among cities.

Keywords: Spatial interaction · Traffic system accessibility · Gravity model Shandong Province · City

1 Introduction

Cities are playing an important role in the regional and national development, as they are an agglomeration center of population, political, economic and cultural center. Since the 21st century, cities have entered a stage of rapid development in China, and the engine role they are playing has become more prominent in regional and national development. There are three expressions of urban spatial interaction, including urban attraction, urban radiation, and urban intermediation. They are important indicators used to measure the strength of urban spatial interaction. Spatial interaction refers to the mutual transmission process of population, commodity and information, technology,

capital, labor and other factors occurring between regions [1]. And separated regions are combined into an organism with certain structure and function by spatial interaction [2]. The processing of spatial interaction is extremely complex. In the main body of the role, including cities and regions, it should also include commercial outlets, cultural facilities, green gardens and other service facilities within cities and regions; in the form of role, it is expressed as an exchange, connection and interaction, usually A kind of action is also expressed; in the geographical space, it is integrated into the division of the geographic entity's action space, which can be expressed by attracting ranges [3].

In a region, spatial flows such as people flow, logistics, information flow, technology flow, and capital flow occur frequently, in two-way or multi-directional flow. This has an important impact on the structure, function and development of regions. The spatial interaction has the characteristics of distance attenuation, and then Newton's universal gravitation formula was used to express the interaction [4]. In 1929, Reilly WJ conducted a field trip to more than 200 urban trade markets in Texas and then proposed the "retail gravity model" (also known as the "Ryley model"). In this model, the number of retail customers is proportional to the size of the urban population, and is inversely proportional to the distance of retail customers to the trade market. This model was used to divide the boundaries of retailers' control market in geospatial space [5, 6]; Next year, Converse P.D proposed the concept of breakpoint based on the Reilly model. This concept was used to determine the extent of space impact and to divide economic zones [7, 8]. In 1964, Huff D.L. proposed the Huff model based on large-scale retail stores. This model is used to measure the likelihood that a consumer is to spend in retail stores at a particular location [9]. In 1967, Wilson A.G. derived a gravity model from the theory of maximum entropy for quantitative analysis of interaction strength [10]. In 1991, Wang et al explained the spatial interaction as the macroscopic representation of population, information, capital, etc. in the two-dimensional space, and proposed the oral particle model to describe the spatial interaction [3, 11]. In the past, the distance in the model was directly expressed by the spatial Euclidean distance, not considering the importance of accessibility to population, goods, and capital flows. Due to the imbalance of social and economic development, the flow of people, goods and money between regions is more dependent on the transportation system [12]. The higher the accessibility of the transportation system is, the more convenient the connection between the two places is. The traffic system accessibility refers to the convenience of reaching a place of activity from a given location by traffic system [13]. Hansen first proposed the concept of reachability, defined it as the opportunity of interaction between nodes in the traffic network, and used gravity method to study the relationship between accessibility and land use in cities [14, 15]. The related indicators include distance, time, cost, etc. [16]. The model distance parameter is modified by the weight, time cost, and monetary cost of various modes of transportation between the two places [1, 4] to express the conventional distance in some studies [17]. However, both time distance and cost distance are difficult to accurately acquire and measure, and sometimes contradictory [18, 19]. For example, in terms of ground transportation, high-speed rail is the fastest means of transportation, but the corresponding travel cost is also very high [20]. Dong et al. [12] took this problem into consideration, and used the traffic volume and other indicators to correct the distance parameters. At the same time, the interaction coefficient was

improved by using the comprehensive traffic indicators such as daily average train times and shortest travel time.

Although the gravitation model is used widely now, but it is still just a basic model converted over from the Formula of universal gravitation [21]. In order to reflect influence the characteristics, rules and influential factors of urban influence, it should be amended. Based on the research results of Dong et al. [12], to better reflect urban influence of Shandong Province, we do some revision and reconstruction the quality, distance and coefficients of gravitation model and build the potential model to reflect the membership degree of the urban influence. In this paper, revision model and empirical analysis were made based on the traditional spatial interaction model according to the special traffic conditions in the study area (Shandong Province), and then the externalities of various cities in Shandong Province was calculated. In order to reflect influence the characteristics, rules and influential factors of urban influence, it should be amended. To better reflect urban influence of Shandong Province, on the base of the law of gravitation, affected by lots of comprehensive factors, we do some revision and reconstruction the quality, distance and coefficients of gravitation model and build the potential model to reflect the membership degree of the urban influence. Then we define the strength and direction of urban influence area and make analysis for spatial influence variance. In addition, the rationality and feasibility of the modified model are proved by comparing with the analysis results of the traditional spatial interaction model.

2 Reconstructing the Gravitation Model for Urban Spatial Interaction

The gravitation model is a spatial interaction model used widely, which is the mathematical equations that can be used to analyze and predict the form of spatial interaction. It has been continuously used to study urban influence.

In 1687, Newton put forward the famous gravitation model in physics. Namely, the interaction between any two objects (gravitation) in size is proportional to its mass and inversely proportional to the square of the distance.

The research status for the gravitation model and the urban region circumstance was analyzed in this paper, and the quality, distance and coefficients of gravitation model were revised and reconstructed.

$$F = \frac{K_{ij}M_iM_j}{d^2} \quad (1)$$

The city, as a principal part of the economic activity, has various influencing factors. It is apparent unconvincing to use urban GDP and the total urban populations to evaluate urban development level, especially for some of the characteristic economic cities. These measuring approaches caused limitations and deviations. Therefore, a number of cities have started to be focused on assessments of the importance of urban comprehensive quality currently. Twenty three key indicators of 17 prefecture-level cities of Shandong province were selected in this paper by using PCA algorithm to get urban quality (M).

It is more complicated to determine the coefficient of gravitation model. In general, to simplify model calculation, research scholars regard the coefficient of gravitation model as a constant that is 1. To be better improving the model performance, the urban influence coefficient was modified as follow:

$$K_{ij} = \varphi \left\{ \frac{H_i}{\sum_i^j H} + \frac{C_i}{\sum_i^j C} \right\} \tag{2}$$

Where, φ is assumed urban conversion coefficient between comprehensive quality and volume of traffic, and represented in comprehensive strength and the total value of passenger and freight traffic of each city; H_i represents cargo of the i st city; C_i represents the passenger volume of the i st city.

With all the modern means of transport development, urban road network accessibility between the existing situations between the influences of urban factors. So that the railway line in Shandong Province on behalf of the city can be basically the link between the influences. The distance d was regard as the average Shortest time (hours) by EMU.

3 The Processing of Measuring Urban Spatial Interaction

3.1 Quality of Urban Integrated Assessment Model

In this paper, several initial indicators were selected from the Shandong Statistical Yearbook. Then Pearson correlation analysis and principal component analysis methods were used to eliminate correlations and the indicators with a commonality less than 0.9. These 23 indicators that meet the conditions are used to comprehensively measure the quality of cities in Shandong Province.

(1) Select Initial Variables According to the Research Topic ($n = 17, p = 23$).

$$X = \begin{pmatrix} X_{11} & X_{12} & \cdots & X_{1p} \\ X_{21} & X_{22} & \cdots & X_{2p} \\ \cdots & \cdots & \cdots & \cdots \\ X_{n1} & X_{n2} & \cdots & X_{np} \end{pmatrix} \tag{3}$$

(2) Normalize the raw data with Z-score method formula, on the one hand is to eliminate the effect on the analysis results that the different indicators have different dimension, and on the other hand is to eliminate the impact that different indicators have different magnitudes with the analysis results;

$$Z_{ij} = \frac{X_{ij} - \bar{X}}{S_j^2} \tag{4}$$

Where, $\bar{X} = \frac{\sum_{i=1}^n X_{ij}}{n}$ is the mean For the J th variable, $S_j^2 = \frac{1}{n} \sum_{i=1}^n (X_{ij} - \bar{X}_j)^2$ is the sample variance for the J th variable. The results standardized (omitted).

(3) Solve the correlation coefficient matrix. According to the relationship established by analyzing the original variable characteristics, the formula below:

$$R = (r_{ij})_{p \times p} \tag{5}$$

Which $r_{ij} = \frac{1}{n} \sum_{k=1}^n Z_{ki}Z_{kj}$, Where $i = 1, 2, 3, \dots; j = 1, 2, 3, \dots$

(4) Calculate eigenvectors and eigenvalues for the correlation coefficient matrix. The principal component matrix can explain the meaning of each composite factor (principal component). The first principal component mainly reflects urban economic development level; the second component mainly reflects the social development level of each city; the third component mainly reflects the urban natural resource status; the fourth component reflects the urban location conditions. For the verification, the above-mentioned four principal component factors were extracted. From the obtained results, the contribution rate of the factors (principal component) has exceeded 85%, so the above four principal components are sufficiently representative (Table 1).

Table 1. Eigenvalue, principal component and the cumulative rate of the principal component

Component	Initial eigenvalues			Extraction sums of squared loadings		
	Total	% of Variance	Cumulative %	Total	% of Variance	Cumulative %
1.000	13.084	56.887	56.887	13.084	56.887	56.887
2.000	4.655	20.240	77.127	4.655	20.240	77.126
3.000	2.325	10.108	87.235	2.325	10.108	87.234
4.000	1.213	5.272	92.507	1.213	5.272	92.506
5.000	0.561	2.437	94.944			
6.000	0.371	1.614	96.558			
7.000	0.235	1.023	97.581			
8.000	0.184	0.800	98.381			
9.000	0.112	0.488	98.869			
10.000	0.091	0.396	99.265			
11.000	0.071	0.308	99.573			
12.000	0.050	0.217	99.790			
13.000	0.023	0.099	99.889			
14.000	0.019	0.081	99.970			
15.000	0.052	0.023	99.993			
16.000	0.015	0.064	100.000			
17.000	0.044	0.019	100.000			
18.000	0.037	0.016	100.000			
19.000	0.023	0.010	100.000			
20.000	0.055	0.024	100.000			
21.000	0.040	0.018	100.000			
22.000	-0.025	-0.011	100.000			
23.000	-0.038	-0.017	100.000			

(5) Carry out the linear combination to gain the comprehensive evaluation indicators function, with the variance of each principal component contribution rate as a weight, calculate the integrated scores for each principal component, and test the reliability of the scores.

(6) Array the scores according to the value and the load factor matrix tested in the sixth step. Then take a comprehensive evaluation for the 23 economic indicators for these cities (Table 2).

Table 2. Urban comprehensive quality in Shandong

Ranking	City	Quality value	Ranking	City	Quality value	Ranking	City	Quality value
1	Qingdao	100	7	Jining	29.57	13	Liaocheng	14.56
2	Jinan	70.47	8	Weihai	20.32	14	Binzhou	12.76
3	Yantai	52.62	9	Tai'an	19.17	15	Zaozhuang	11.07
4	Weifang	44.88	10	Heze	16.58	16	Rizhao	8.86
5	Linyi	34.78	11	Dongying	15.92	17	Laiwu	0.85
6	Zibo	30.98	12	Dezhou	15.5			

3.2 Correction of the Coefficient for Urban Influence

The route and navigation data in Shandong Province are difficult to obtain. Therefore, according to the regional accessibility characteristics, the transportation system composed of train and automobile in the reconstruction of spatial interaction model were mainly considered in this paper. The urban road and traffic data [22] in 2015 for 17 cities in Shandong was collected. According to the formula (2), the coefficient K_{ij} was calculated. Moreover, the final coefficients were calculated by the coefficients K_{ij} multiplied with 100. The coefficient of gravitation model was as follows (Table 3):

Table 3. The coefficient of gravitation model

City	Coefficient	City	Coefficient
Jinan	3.869	Heze	0.324
Qingdao	2.378	Weihai	0.233
Zibo	1.108	Dezhou	0.230
Yantai	0.860	Tai'an	0.172
Jining	0.837	Liaocheng	0.131
Linyi	0.794	Laiwu	0.039
Weifang	0.724	Dongying	0.022
Rizhao	0.697	Binzhou	0.010
Zaozhuang	0.569		

3.3 Measuring the Impact of the Economic Distance Among Cities

The traditional concept of distance has being a serious challenge. In a region with convenient transportation, the time, transportation costs and currency costs were used to measure economic distance among cities gradually. In Shandong province, the urban railway lines is the main transport way, and most cities have the railway lines and national highway. First, the OD cost matrix analysis tool in ArcGIS10.2 software is used to calculate the traffic distance between two cities. The average shortest time (hours) by EMU from the one to another is showed below (Table 4).

4 Results and Analysis

According to the quality, distance and coefficient from the model of urban spatial interaction, gravitation model was constructed and the visualization results are shown as follows. Jinan, Qingdao, Zibo, Weifang have a greater potential, which form a city chain along Jiaoji railway. Jinan and Qingdao have the strongest spatial interaction, while Jinan has the highest comprehensive radiation level. Spatial radiation intensity in Laiwu and Binzhou are relative minimal. Jinan, as the political, cultural and technology education center of Shandong Province, is also a communications hub and the economic center of Midwest of Shandong Province. This city lies at the junction of the Jinghu, Jingfu, Jiqing, Jitai and Jiliao railways (Fig. 1).

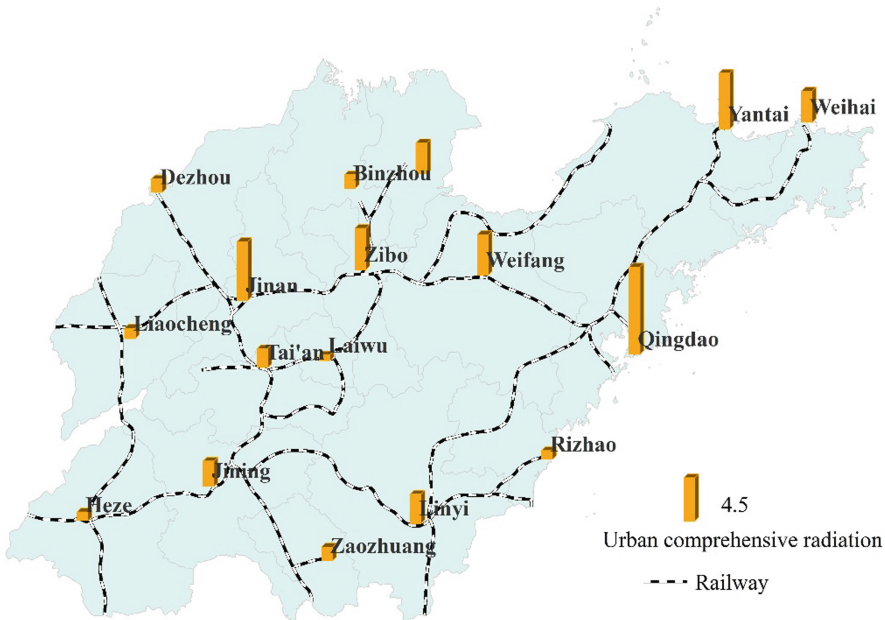


Fig. 1. The degree of the urban spatial interaction in potention model for 17 cities in Shandong province

Therefore, Jinan has a relative disperse influence among all the cities, but has the higher radiation on the cities along the Jiaoji railway. Qingdao is an international port and tourist city. As the development of modern manufacturing and modern services, Qingdao has a certain scientific research strength, so the spatial influence of Qingdao on other cities is also relative large. In Shandong province, four vertical and four horizontal trunk railways will be focused on and the railway will cover most cities, important ports and major industrial and mining enterprises. In addition, more facility construction in passenger and cargo hub of Jinan and Qingdao will be increased, and Qingdao, Rizhao and Yantai railway will be connected into three ports for accelerating the seamless transfer of passenger and cargo (Fig. 2).

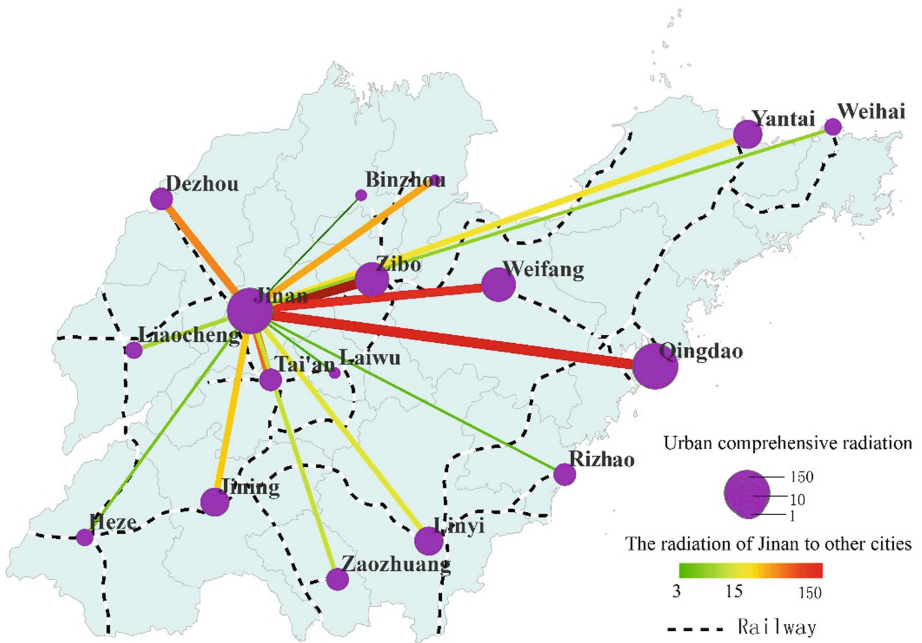


Fig. 2. The spatial interaction strength of Jinan to the other cities

5 Discussion and Conclusions

The distance parameter was modified and a new economic gravitation model was then reestablished with GIS technology. Seventeen municipalities in Shandong province were selected in this paper, and then the strength and direction of urban spatial influence and comparing the differences characteristics between them were measured. We can conclude that Qingdao has the most comprehensive strength, while Jinan has the highest spatial influence. And the factors which affect the strength and direction of cities were analyzed. The spatial orientation of the economic development for cities were made clear, and the links and cooperation in economic between cities coordinated

and the channel of economic will be built. Besides for offering decision-making references for integration of urban space and spatial diffusion of outside space, the reference value for the development of urban regional integration and the plan to build urban spatial construction will be also provided. They are mainly characterized by the following:

Based on the gravity law, the various indicators were integrated and the model was reconstructed. The PCA algorithm was used to evaluate the urban comprehensive quality. This made up for the shortcomings of the previous model and the deviation caused by the single indicator measurement.

Urban influence and overall urban strength are closely related to the transportation system accessibility. The cities around Jiaozhou Railway and Intercity Railway have a strong spatial interaction. However, some important factors affecting the connection between cities are difficult to quantify, such as urban historical background, political factors, and urban structural characteristics. The scale of spatial interactions in each city varies widely. As a socio-economic entity, a city is different from a simple physical entity. The influence between cities varies with the size of the city and the strength of the city.

The spatial distance between cities is not the determining factor of the size of inter-city influence. Through this study above, Qingdao is closer to Weihai than Yantai. However, compared with the later, the degree of spatial interaction of Weihai is greater than the former. And we can see that the inter-city strength are affected by many factors, such as traffic conditions, resources, environment, population exchanges and others.

Transportation is the supporting system of regional economic linkages. The spatial interaction between cities satisfies the distance attenuation. The improvement of road network will increase the influence of the city on the strength and scope, and thus can determine the interaction of urban space in depth and width. The intensity of spatial interactions between cities increases with time and distance.

In this paper, the distance and space interaction coefficients are modified, and the urban spatial interaction model of Shandong Province is reconstructed, and the comprehensive radiation amount of 17 cities in Shandong Province is calculated. It can be seen from the results that the comprehensive radiation ranking of each city is not completely consistent with the urban quality ranking. That is to say, although the comprehensive development level of a city has a great influence on its radiation capacity, the accessibility of the transportation system between cities also plays a certain role. It can be seen from the study that urban influence is static, but it is different essentially. So we handle urban influences calculated as time series data, and we will evaluate scientifically the strength of urban influence in the later research. In the model reconstruction process, it is a thorny problem to amend the parameters. As for how to make the modified parameters better, more rational and more scientific in modeling reconstruction will be made in a further study.

Acknowledgements. This study is supported by the National Natural Science Foundation of China (No. 71773117) and Basic Research Fund of Chinese Academy Surveying and Mapping (No. 7771718). We would also like to acknowledge Prof. Xizhi Wu with his generous support for this research.

References

1. Li, J.S., Luo, H.S., Wang, X.R.: Application of reconstruction of gravitation model in the space reciprocity between the city zone and the suburb. *World Reg. Stud.* **18**(2), 6 (2009)
2. Wang, H.J., Miao, C.H., Ru, L.F.: The spatial framework and change of Chinese provincial region economic links. *Econ. Geogr.* **7**(32), 18–23 (2012)
3. Yan, W.Y., Wang, F.Z., Qin, Y.C.: Analysis of the principle and evolvement of the theoretic models of urban spatial interaction. *Prog. Geogr.* **28**(4), 511–518 (2009)
4. He, S., Tang, C.L., Zhou, G.L.: Research on spatial interaction of the urban agglomeration in the middle reaches of the Yangtze river. *Econ. Geogr.* **4**(34), 46–53 (2014)
5. Reilly, W.J.: *Methods for the study of retail relationships*. Bureau of Business Research, Research Monograph, The University of Texas, Austin, Texas (1929)
6. Reilly, W.J.: *The Laws of Retail Gravitation*. Knickerbocker Press, New York (1931)
7. Anderson, S.J., Volker, J.X., Phillips, M.D.: Converse's breaking-point model revised. *J. Manag. Mark. Res.* 1–10
8. Meng, D.Y., Yu, L.L.: Strength and direction of regional economic linkage in Jiangsu province based on gravitation model. *Prog. Geogr.* **28**(5), 697–704 (2009). The measurement of spatial interaction among cities in Jiangsu province based on highway network
9. Sandıkcioglu, M., Ali, O.G., Sayin, S.: A new gravity model with variable distance decay. In: *International Conference*, pp. 376–380 (2008)
10. Berzins, M., Wilson, A.G.: Spatial interaction models and fisher information: a new calibration algorithm. **5**(5) (2003)
11. Liu, K., Shen, Y.M.: Review of research on regional spatial interaction at home and abroad. *World Reg. Stud.* **1**(23), 73–83 (2014)
12. Dong, C., Zhang, Y.: An approach on reconstruction of intercity spatial interaction model based on spatial traffic system accessibility. *World Reg. Stud.* **2**(22), 34–42 (2013)
13. Deng, Y., Cai, J.M., Yang, Z., Wang, H.: Measuring time accessibility with its spatial characteristics in urban areas of Beijing. *Acta Geogr. Sin.* **2**(67), 169–178 (2012)
14. Liu, H., Shen, Y.M., Meng, D.: The city network centrality and spatial structure in the Beijing-Tianjin-Hebei metropolitan region. *Econ. Geogr.* **8**(33), 37–45 (2013)
15. Hansen, W.G.: How accessibility shapes land use. *J. Am. Inst. Plan.* **25**, 73–76 (1959)
16. Taaffe, E.J.: City level - air passenger clearance. In: *Economic Geography*, pp. 11–14 (1962)
17. Geertman, S.C.M., Ritsema Van Eck, J.R.: GIS and models of accessibility potential: an application in planning. *Int. J. Geogr. Inf. Syst.* **9**(1), 67–80 (1995)
18. Keum, K.: Tourism flows and trade theory: a panel data analysis with the gravity model. *Ann. Reg. Sci.* **44**(3), 541–557 (2010)
19. Dock, J.P., Wei, S., Jia, L.: Evaluation of dine-in restaurant location and competitiveness: applications of gravity modeling in Jefferson County, Kentucky. *Appl. Geogr.* **60**, 204–209 (2015)
20. Dahyann, A., Marc, J.M., Neil, S., Meriwether, W., Danilo, C.: A spatial fuzzy logic approach to urban multi-hazard impact assessment in concepción, Chile. *Sci. Total Environ.* **576**, 508–519 (2015)
21. Kerkman, K., Martens, K., Meurs, H.: A multilevel spatial interaction model of transit flows incorporating spatial and network autocorrelation. *J. Transp. Geogr.* **60**, 155–166 (2017)
22. China Statistics Press: *China Statistical Yearbook 2016* (2016)



Research on the Key Techniques of Semantic Mining of Information Digest in the Field of Agricultural Major Crops Based on Deep Learning

Hao G. J. M. Gong, Yunpeng Cui^(✉), and Ping Qian

Agricultural Information Institute of CAAS, Beijing, China
flygongh hao@163.com, {cuiyunpeng, qianping}@caas.cn

Abstract. Nowadays application scopes of deep learning research in the machine learning subfield have been gradually expanded, mainly in the field of computer vision and natural language processing. However, in the latter NLP field, there is very little semantic excavation research on agricultural literature data. This paper bases on the attempting to combine relevant paradigms of semantic mining techniques and characteristics of agricultural digest data, for the service of providing new methods and technologies of information acquisition and analysis in the agricultural information domain. Data cleaning methods and data mining experiment are mainly based on deep learning algorithms, which are Seq2Seq and attention mechanism. Finally, through qualitative evaluation and quantitative evaluation of the experimental results, which based on the ROUGE evaluation index system, the experiment shows that the semantic mining model has reached the optimal level of model evaluation in the certain range.

Keywords: NLP · Semantic mining · Deep learning · ROUGE

1 Introduction

Now the network and other mediums produce more and more text contents, which include substantial agricultural science and technology information. Traditionally, agricultural researchers generally find a bunch of related agriculture literatures through web search engines, but the topics that they may contain may be more than just one, and the article may discuss the interactions and relationships between different themes. Those require researchers to have to browse the abstract of each article and even the entire contents, which stretches out searching time, makes the accuracy of access to information questionable and so on. Then, in the era of the gradual development of the natural language processing field, how to exactly grasp the gist of agricultural science and technology articles, accurately understand the themes of that, and better provide the knowledge service to the researchers become the research mainstream.

Although lack of rigorous theoretical basis, deep learning algorithms significantly reduce the threshold of application for the machine learning technology to bring the

practice of engineering convenience. As for why it is popular at this time, there may be three basic reasons. First, the current development of the algorithm is more mature.

Second, different from the past, there are huge quantities of datasets right now. Third, computer hardware computing capacity is more powerful. Why not use Chinese abstract information for semantic mining is that the original automatic word segmentation and part of speech are in the initial stage of Chinese analysis and understanding process. It should provide initial information for the next step of syntactic and semantic analysis. But they need some sort of syntactic and semantic knowledge to be completed. In this way, automatic word segmentation needs to rely on certain results of syntactic and semantic analysis as a condition. The reason why this “circular argument” arises is that this research are using a mechanical process to simulate a human language process that is far from the real language of mankind and is too superficial for current level of research this research can make qualitative progress on this issue, so the automatic word segmentation and part of speech in Chinese automatically mark such a seemingly basic and simple problem, in a short time Chinese NLP researchers can not get to stand the test, and widely recognize results.

This paper will focus on the use of deep neural network techniques combined with the characteristics of information digest in the field of agricultural major crops to provide new methods and technologies of information acquisition and analysis in the agricultural information field.

2 The Relevant Theories of This Semantic Mining Research

2.1 Recursive Neural Network

Direct extraction of important sentences of the extraction method is relatively simple, such as PAM algorithm realizing (TextRank). While generating sentences (re-generate a new sentence) is more complex, but its effect is not satisfactory. In the traditional forward neural network, there exists basically no way to remember the state of a certain period of time. This is a problem when research needs to deal with timing activities, such as dealing with the state memory of sentence sequence in a segment, which is why researchers use recursive neural networks.

2.1.1 Simple Recursive Neural Network

A neural network takes a sequence x_0, \dots, x_N as input. Each element in the sequence is processed by the same node, and the node is called a state vector in a memory space and memorizes useful information. Then, during the output or all the time to end, this memory space is used to produce a solution to the problem. It can also be said that for each time step t , RNN has the state vector to be calculated:

$$h_t = \sigma(U * x_t + W * h_{t-1}) \quad (1)$$

Here is a non-linear function, such as sigmoid function, tanh function or ReLU (modified linear unit) function, is initialized to a value, U and W are two weight vectors.

Then, an output can be calculated using the state vector at time t :

$$output_t = softmax(V * h_t) \quad (2)$$

V is the weight vector. Sometimes, only the final output will be used. Here, RNN normally takes the softmax normalization function. It is effective to use probability distributions between hierarchies. For example, if research has a set of terms, it will get the probability distribution of the group of words, and then choose one of them. More formally, if RNN has the K layer, each layer is represented by j , and then these terms are converted into the following probability:

$$softmax(z)_j = \frac{exp(z_j)}{\sum_{i=1}^K exp(z_i)} \quad (3)$$

Softmax function can be understood to be derived from the fact that if it is significantly larger than the other terms, then it is only one that needs to be considered (which has a value close to 1). It is one of the probability largest functions.

2.1.2 LSTM

LSTM (long and short memory network, Hochreiter et al. 1997) authors believe that the traditional RNN will be hidden as a model of the memory module, and other parts of the network has a direct connection, not only makes the model to expand the number of layers, resulting in the disappearance of the gradient problem, and make the effective historical information by a steady stream of new input data and can not save for a long time. LSTM redesigned the RNN memory module, consisting of a memory cell and a plurality of gate gates. LSTM uses the state of the memory cell to hold the history information. The use of input data for states updates and the operation of outputting state information are controlled by input gate and output gate respectively. When the input gate is closed, the history information is not disturbed by the new input data and is saved as is (constant error carousel). Similarly, only the output gate is opened and the historical information in the memory cell is active.

2.1.3 Seq2seq (Sequence to Sequence)

Seq2seq is formally introduced in 2014 (Cho et al. 2014). The basic idea is to use the recursive unit to convert the input sequence into an output sequence. For example, this article is to enter a sequence of words or characters from the text of the article, which are converted into a summary of the paragraph (title sequence or small snippet of the summary). Seq2seq can be decomposed into two parts in general. The first part is called the encoding part, which translates the input into a separate vector (which can be understood as encoding the input), which is generated by using, for example, GRUs or LSTMs (Fig. 1).

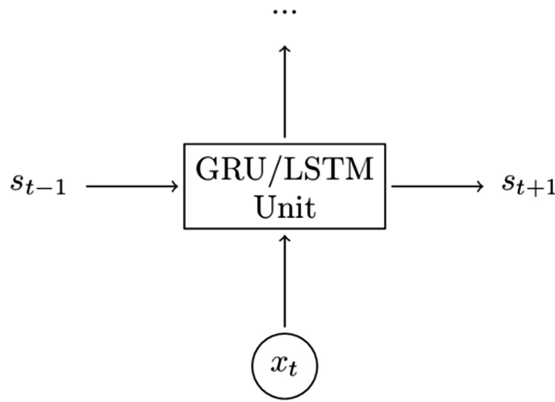


Fig. 1. Encoding input sequence x_t

The input is divided into several representations (in general terms), each representing an input as a gate. Then, once this research get the vector at the end of the encoding, this research assign it to the decoding section. The encoding part also has a recursive neural network, whose initial state is the final state of the code, and its input is the last generated output. Each recursive unit produces an output until the end of the sequence is generated. It should be noted that the coding part does not produce an output for each step. Instead, it enters a word at each step until the input sequence is entered, and then the semantic correlation information betthis researchen the sequences is captured in its internal state memory. The final hidden layer’s state vector is called a context vector or a “think” vector, which should be a semantic-related summary of the input sequence.

If x represents the length of the input sequence, the encoding function is represented as f (representing a gate), then a hidden layer state can be calculated as follows:

$$h_i = f(h_{i-1}, x_i) \tag{4}$$

Here will h_0 be set to a fixed value (for example, 0 vector), and the decoding part will be the initial state. Then this research can compute the functions g and k :

$$p(y_i|y_1, \dots, y_{i-1}, x) = g(y_{i-1}, s_i) \tag{5}$$

Here $s_i = k(s_{i-1}, y_{i-1})$, y represents the output sequence. Seq2seq model can adapt to different sequence structure, and the current more popular attention mechanism can also be applied to them. After adding the attention distribution mechanism, Decoder can generate the new Target Sequence to get the hidden information vector Hidden State of each character before the Encoder coding phase, so that the accuracy of generating the new sequence is improved (Fig. 2).

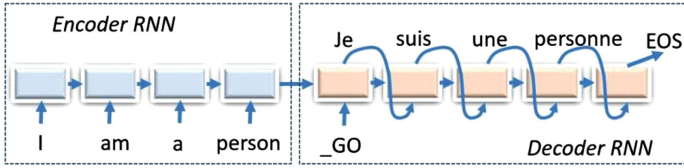


Fig. 2. An english to french translator with encoder and decoder Seq2Seq expansion, showing the flow of information (Source: <https://esciencegroup.com/2016/03/04/fun-with-recurrent-neural-nets-one-more-dive-into-ctnk-and-tensorflow/>)

2.2 Attention Mechanism

One problem that Seq2seq might exist is that it may not be able to effectively summarize the entire input sequence into a separate vector (this vector will be treated as a decoder input). In particular, the long term dependency may be more difficult to model, the solution is that refers to the “attention” mechanism. The basic idea is simple: to replace the sentence to build a vector, this research will keep the entire input sequence, and then in the recursive neural network every step to produce an output. What researchers are trying to do is to focus on the information that is useful to us in the input sequence at every time step, and this depends on the output of all the previous recursive neural networks.

“Attention” is a mechanism for machine translation proposed by Bahdanau for 2014. The “attention” mechanism does not directly use the input sequence, but directly uses the state vector, and then the state vector is combined with the weight produced by the previous step. This step, only useful information will be retained.

The state vector may be expressed exactly as (representing the length of the input sequence), which may be created from the input sequence using a bi-directional recurrent neural network such as the one mentioned above. Through these state vectors, the “attention” mechanism is used to construct the context vector at each time step of the output neural network. Enter a weight for the state vector and are:

$$c_i = \sum_{i=1}^{T_m} \alpha_{i,t} h_i \tag{6}$$

Then, the recursive neural network output layer uses this state vector. If it is recursive neural network state vector, but the output, this research can function f and h said as follows:

$$p(y_i|y_1, \dots, y_{i-1}, x) = g(y_{i-1}, s_i, c_i) \tag{7}$$

Where

$$s_i = f(s_{i-1}, y_{i-1}, c_i) \tag{8}$$

As mentioned above, the context vector is the weight of the input state vector that relies on all the forward output (by outputting the state vector). Thus, s (representing the “attention” vector) can be calculated by finding the probability of each state vector

at each time step. Thanks to a function called a alignment model a , which is essentially a forward neural network (Fig. 3):

$$e_{i,t} = a(s_{t-1}, h_i) \tag{9}$$

Thanks to the softmax function, researchers can transfer $e_{i,t}$ to a probability α_s

$$\alpha_{i,t} = \frac{\exp(e_{i,t})}{\sum_j \exp(e_{j,t})} \tag{10}$$

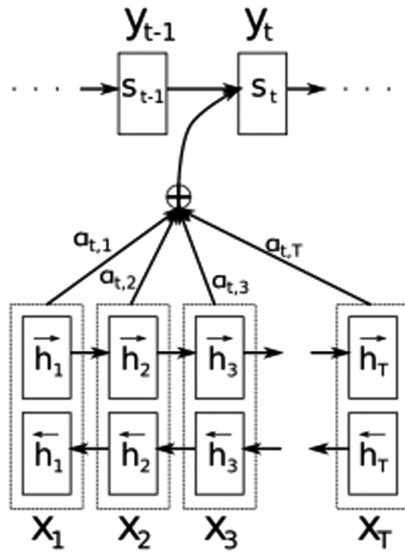


Fig. 3. Input sequence is tackled by bidirectional recurrent neural network, and ‘attention’ mechanism (Source: <http://www.wildml.com/2016/01/attention-and-memory-in-deep-learning-and-nlp/>)

3 Research Methodology of Semantic Mining on Agricultural Major Corps

NLP used the seq2seq and attention mechanism to solve the problem is in the field of sequence generating, which has been swept through a number of other methods.

The seq2seq model is generally structured as follows (Fig. 4):

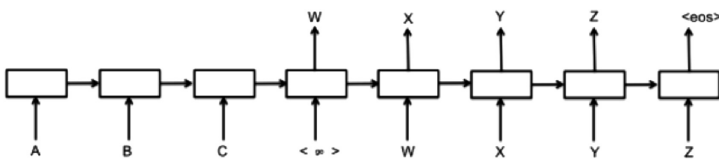


Fig. 4. Encoding-decoding model

The encoder section encodes the input with a single layer or multiple layers of RNN/LSTM/GRU, and the decoder section is a language model used to generate the digest. This kind of generative problem can be summed up as a conditional probability problem $P(\text{word} \mid \text{context})$. Under the context condition, the probability of each word in the vocabulary is calculated, and the word with the highest probability is used word, and then generate all the words in the summary. The key here is how to express context, the biggest difference between each model is the context of the difference, where the context may either be the expression of the encoder, or be the expression of attention and encoder. The decoder part usually uses the beam search algorithm to do the build.

The research methodology in this paper is based on data-intensive machine learning techniques. Based on the deep learning theory mentioned in Sect. 2, the Seq2Seq and Attention mechanism is combined with specific methods to perform the agricultural science abstracts data processed in Sect. 4. Then use Objective function cross-entropy loss training and gradient descent algorithm to update parameters, adapt neural network parameters of the model to agricultural abstract corpus collection, and finally perform qualitative and quantitative model evaluation. The specific process is as follows:

- (1) Initially setting the model hyper parameter values, according to the Seq2Seq neural network model structure, completing the scripting, then defining the loss function, and selecting the optimization direction and optimization method;
- (2) Model initialization, model training and model parameter adjustment to achieve model benchmarks;
- (3) Model assessment, based on the qualitative assessment of the project carried out by the research team, and the next section will introduce the relevant assessment criteria for the implementation of qualitative assessment and ISI's ROUGE indicator system for quantitative assessment.

4 Model Experiment

4.1 The Corpus of Agricultural Science and Technology Information and Its Processing

4.1.1 The Dataset Composition

Based on the principle of research and implementation of cutting-edge technologies that have covered recent years, we selected English scientific and technological digest information on crop cultivation, molecular breeding, phenotypomics, and new variety breeding harvested by the laboratory, which in the form of title, abstract, keywords, authors and institutions, and a total of 54,659 articles we captured. Where the article is originally marked with XML format, each article starts and ends with the `<paper> ... </paper>` tag, and the document number begins with the `<doc_id> </doc_id>` tag. The same article number is `<paper_id>` The journal number is `<journal_id>`, the title is `<title>`, the abstract is `<abstract>`, the keyword is `<keyword>`, the classification number is `<classification>`, the author is `<authorlist>` and so on.

Extract the original data set into the formatted “Title # Summary # Keyword/Keyword/Keyword ... Author/Author/Author ... # Organization /Organization ...”, where the ellipsis represents there may be a number, and there will be no The item is marked as None; for example, an organization does not exist: “Title # Summary # Keywords/Keywords ... Author/Author ... # None”. Which is the size of the abstract because of the different content of the length of the abstract, the title is also due to the lack of effective enough manpower and field experts (including agricultural rice field related to the technical vocabulary, to the corresponding human experts to mark the data is unlikely), So we chose to keep the data with a relatively objective summary of the article and the title to generate the training corpus and discard the remaining ones so that the data set with the title plus the abstract can be generated, taking into account the same as in the future Look at the application, I used the abstract, title and keyword to generate the vocabulary Vocab.

The title of the article as the target, the first sentence of the abstract and the second sentence as the source, preprocessing, including: lower case, word, extract punctuation from the word, the end of the title and the end of the text will add a custom end tag <eos> , that no title or no content or title of the content less than 10 tokens or text over 50 tokens will be filtered out, the occurrence frequency sorted token, take the top 200,000 tokens as a dictionary, a low-frequency word symbol <unk> replaced.

4.1.2 Python’s Natural Language Approach

Here the introduction of the relevant scientific data processing toolkit, needing to import the package numpy and collections, to use Stanford Natural Language Processing Toolkit to deal with the relevant statement information.

Because this research use the neural network model to carry out unregulated data processing, so here to simplify the relevant natural language processing methods, related to the pronunciation of the annotation, block, naming body recognition, relationship extraction and analysis of sentence structure and grammar and other omissions, only involved To the data segmentation and unrecognized vocabulary labeling and other simple natural language processing work, the remaining work to the model training and tuning skills. The data is placed in the path of the relevant file, and then converted using the encapsulated method, the data is abstracted as tensor can recognize the tensor, for example, the data stored in the previous step is converted to the corresponding textsum model. Need to read the binary file format, for example, using the command ‘python textsum_data_convert.py --command text_to_binary -in_directories thesisdata / --out_files shuidao-train.bin, shuidao-validation.bin, shuidao-test.bin --split 0.8, 0.15, 0.05 ’. Save the previous data set in proportion to the ratio of 8: 1.5: 0.5 to save the training binary file, verify the file and test set files. Here is the script to convert the binary file ANSI into an easy-to-read UTF-8 format, using the script data_convert_example.py conversion.

Among them, the model needs to read the sequence is marked as a sign of abstract, the value of the “ = ” behind the string, the output value is the value of the title tag, which contains the sequence <d> <p> <s> </s> </p> </d> mark the article, paragraph, sentence. Where the labels are separated by tabs and abstract. Likewise, generating a

validation set and a test set from the dataset. In this way, the data set can be used to complete the automatic generation of abstracts, title generation or article classification and so on.

4.2 Research Progress of Data Mining Semantic Mining Model

Research model code is built on the open source code of the Tensorflow project. This research changes session part of training code, part of the model in the `textsum/seq2seq_attention.py`, and make support for multi-core CPU by running `tf.ConfigProto`. In the model script running, Google's open source code is also vigorously pursuing its bazel run, this research makes one of the bazel running environments changed, to supported lab CPUs to run the thread unlocking protocol, so the terminal command changes from the original '`$ bazel build -c opt --config = cuda textsum / ...`' to '`$ bazel build -c opt --copt = -mavx --copt = -mavx2 -copt = -mfma -copt = -mfpmath = both --copt = -msse4.2 -copt = -march = native -config = opt textsum / ...`' to support more acceleration protocols AVX, SSE4.2 and so on. Finally, in order to show the data flow graph of our model in tensorboard dashboard, we added `sess.graph` to the original `tf.train.FileWriter` builder, and of course researchers can use the `add_graph` method of `tf.train.FileWriter` builder to build the project data flow chart.

Here follows the model configuration (Table 1):

Table 1. Model parameter configuration.

Function	Purpose	Setting
Mode	Train, test, decode	Train
Working_directory	Vocabulary files and training, verification and test file storage addresses	data/
Pretrained_model	-	-
Batch_size	Data bundle size for training	64
Bidirection Encoding layer	The number of bidirectional RNN layers in the encoding section	3
Article length	The maximum acceptable article input sequence length	120
Summary length	Generated sequence maximum length	30
Word embedding size	Word vector dimension size	128
LSTM hidden units	Number of LSTM hidden units	192
Sample softmax	Final normalization function using units	4096
Vocabulary size	Vocabulary for generating, taking the word frequency top 200k	200 k

4.3 Study on Experimental Results of Model

Model of the original training step is 10,000,000 steps, but if the amount of data is not large enough, many steps are likely to cause too much training. The sample volume of

Google original data is about 10,000,000, which is marked Gigaword English news dataset (also can used DUC2004 dataset to test), in each server is 4 core K series graphics card and a total of 10 servers, running a week, in view of the inability to achieve its experimental environment, this research will apply the moderate quantity of standard experimental agricultural major crops digest corpus to the changed models, and the training steps temporarily transferred to the 130500 steps, the effect shown in figure (Fig. 5).

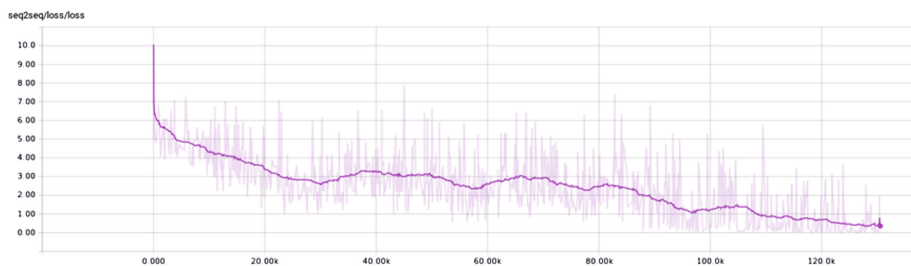


Fig. 5. Textsum model loss value trend on agricultural science and technology dataset. Smooth coefficient 0.88

This is agricultural corps digest data training renderings, after 9 days more than total recursive training about 130,500 steps, the loss value reached a standard level with the standard data set (below 1.0).

The following example illustrates the textum automatic digest model to generate the title sequence effect.

Article. To study whether the biomass of soil microorganisms in a boreal *Pinus sylvestris*-*Vaccinium vitis-idaea* forest was limited by the availability of carbon or nitrogen, we applied sucrose from sugar cane, a C-4 plant, to the organic mor-layer of the C-3-C dominated soil. We can distinguish between microbial mineralization of the added sucrose and respiration of endogenous carbon (root and microbial) by using the C-4-sucrose as a tracer, exploiting the difference in natural abundance of C-13 between the added C-4-sucrose ($\delta(13)C$ -10.8 parts per thousand) and the endogenous C-3-carbon ($\delta(13)C$ -26.6 parts per thousand). In addition to sucrose, NH_4Cl (340 kg N ha⁻¹) was added factorially to the mor-layer. We followed the microbial activity for nine days after the treatments, by in situ sampling of CO₂ evolved from the soil and mass spectrometric analyses of $\delta(13)C$ in the CO₂. We found that microbial biomass was limited by the availability of carbon, rather than nitrogen availability, since there was a 50% increase in soil respiration in situ between 1 h and 5 days after adding the sucrose. However, no further increase was observed unless nitrogen was also added. Analyses of the $\delta(13)C$ ratios of the evolved CO₂ showed that increases in respiration observed between 1 h and 9 days after the additions could be accounted for by an increase in mineralization of the added C-4-C. (Data source: Ekblad et al. 2002).

Ref. Is growth of soil microorganisms in boreal forests limited by carbon or nitrogen availability? (Data source: Ekblad et al. 2002).

Decode. The effects of organic manure nutrient on the leaching by acid movement of soil.

This is the result of the abstractive automatic summary model decoder part training from the agricultural main corpus corpus. The input sequence is article contents, the target sequence, title contents, is marked with Ref, and the output sequence is the decode flag (Table 2).

Table 2. Textual automatic digest model ROUGE value contrast.

Model	ROUGE-1	ROUGE-2
ABS (Rush et al. 2015)	30.88	12.22
ABS+	31.00	12.65
Char Level (Golub et al. 2016)	11.31	2.65
COMPRESS (Clarke et al. 2008)	19.63	5.13
TextRank (Mihalcea et al. 2004)	31.10	9.03
Textsum	36.99 (up to 38.27)	19.68 (up to 20.58)

Rouge (Recall-Oriented Understudy for Gisting Evaluation), the basic idea is to use the abstract generated by the model and the n-tuple contribution statistic of the reference abstract as the basis for judging.

It can be seen that the higher the ROUGE value, the better the effect of generating the abstract on behalf of the model, and conclusion from the table is that the textum model is superior to the current majority of text automatic summary models.

5 Related Research Progress

In academia, deep learning begins to receive attention from 2006, because in the tens of thousands of samples of medium-scale datasets, the deep learning learnt from the new sample at that time more than many popular algorithms and generalized better. Soon after, the deep learning in the industry has received more attention, because it provides a scalable way to train large data sets on the nonlinear model. LeCun, Bengio & Hinton, leaders in deep learning, are looking forward to the future development of deep learning in journal Nature (Lecun et al. 2015): first, although the recent unsupervised learning was restrained and supervised learned to snatch the limelight, but in the long run, unsupervised learning is still a more important issue, and Michael et al. also hold this idea (Michael et al. 2015). Second natural language processing will be the depth of learning in the future to achieve significant breakthroughs in the field, to better “understand” statements and text semantic system will appear. Third, combination of deep learning and symbolic artificial intelligence will bring revolutionary changes in the field of artificial intelligence.

Direct extraction of important sentences of the extraction method is relatively simple, such as PAM algorithm realizing TextRank, while generating (re-generating a new sentence) is more complex, and the effect is not satisfactory. At present, the more

popular Seq2Seq model, proposed by Sutskever et al., based on the structure of an Encoder-Decoder, the source sentence first is encoded into a vector of fixed dimension D , and then generate the target sentence one character at a time using the decoder part. After adding the ‘Attention’ mechanism, decoder can generate the new target Sequence to get the hidden information vector Hidden State of each character before the Encoder coding phase, so that the accuracy of generating the new sequence is improved. The increase in end-to-end training in neural networks has led to significant changes in many areas, including speech recognition, computer vision, and natural language processing. Recent work has shown that neural networks can do more than any sort of task, and they can be used to map complex structures to another complex structure. For example, a sequence is directly translated into another sequence, which has a direct application in natural language understanding (Luong et al. 2014).

6 Conclusion

The main advantage of this model is that when matches or transcends the current optimal benchmark, it requires little feature processing and specific domain-specific knowledge. This advantage, in my opinion, is to allow researchers to focus on tasks in certain unknown areas or in areas where it is too difficult to design artificial rules (e.g. ontology, etc.). This research will be devoted to the development of the automatic digest extraction system of semantic mining of agricultural science and technology literatures, and make a modest contribution to the development of semantic excavation of this field.

References

- Hochreiter, S., Schmidhuber, J.: Long short-term memory. *Neural Comput.* **9**(8), 1735–1780 (1997)
- Cho, K., Van Merriënboer, B., Gulcehre, C., et al.: Learning Phrase Representations using RNN encoder–decoder for statistical machine translation. *Empirical Methods Nat. Lang. Process.* **2**, 1724–1734 (2014)
- Rush, A.M., Chopra, S., Weston, J., et al.: Neural attention model for abstractive sentence summarization. *Empirical Methods Nat. Lang. Process.* **2**, 379–389 (2015)
- Golub, D., He, X.: Character-level question answering with attention. *arXiv preprint arXiv:1604.00727* (2016)
- Clarke, J., Lapata, M.: Global inference for sentence compression: an integer linear programming approach. *J. Artif. Intell. Res.* **31**, 399–429 (2008)
- Mihalcea, R., Tarau, P.: TextRank: bringing order into texts. *Emnlp.* **6**, 404–411 (2004)
- Luong, M.T., Sutskever, I., Le, Q.V., et al.: Addressing the rare word problem in neural machine translation. *Bull. Univ. Agric. Sci. Vet. Med. Cluj-Napoca.* **27**(2), 82–86 (2014)
- Ekblad, A., Nordgren, A.: Is growth of soil microorganisms in boreal forests limited by carbon or nitrogen availability? *Plant Soil* **242**(1), 115–122 (2002)
- Lecun, Y., Bengio, Y., Hinton, G.: Deep learning. *Nature* **521**(7553), 436 (2015)
- Michael, I., Mitchell, T.: Machine learning: trends, perspectives, and prospects. *Science* **349**, 255–260 (2015)



COPS: A Real-Time Cross-Domain Object Part Segmentation System

Xueqing He^(✉)

China Agricultural University, No. 17 Qinghua East Road,
Beijing 100083, People's Republic of China
2015314060617@cau.edu.cn

Abstract. Although the object part segmentation is widely applied to surveillance video analysis and smart recommendation and so on, however, it does not show a good performance in cross-domain testing. This means the segmentation model has to label various data in different scenarios and it is costly due to the time and labor cost. Accordingly, in the paper, we would like to propose a real-time cross-domain object part segmentation system (COPS) based on the work of *Cross-domain Human Parsing via Adversarial Feature and Label Adaptation* [2]. Several vital techniques are applied in this real-time cross-domain object part segmentation system, including object detection, object tracking, and cross-domain adaptation object part segmentation. Taking an unconstrained benchmark dataset with rich pixel-wise labeling as the source domain, the real-time cross-domain object part segmentation system aims to segment frames of target domain videos without any additional manual labeling in real-time. Compared with the traditional approaches, this system is demonstrated to be a highly efficient and useful one among most practical applications, and the exploration on the challenging issue will contribute our real-time cross-domain object part segmentation system and push human parsing into next step. Therefore, we would like to present the details of our real-time cross-domain object part segmentation system in the following parts.

Keywords: Cross-domain · Object part segmentation · Real-time system

1 Introduction

Semantic segmentation is understanding an image at pixel level i.e., and we want to assign each pixel an object class in the image [8]. Scene parsing and object parsing, as types of semantic segmentation, are widely used in autonomous driving and surveillance video analysis. However, pixel-level labeling is costly, and semantic segmentation models tend to be poorly generalized across domains. A well-trained model based on the database of one scene always performs poorly in the data from other scenes.

Object part segmentation, which refers to an object decomposed into several semantic parts, enables a computer to understand an image deeply as well as automatically. It takes a significant part in various practical product applications such as face beauty fication, virtual reality and so on. However, we generally use to train a model using a lot of data with annotations, and it will cost a high annotation expense

both in time and labor [1]. Consequently, we expect to create a superior model trained with labeled data from source domain to segment data of any target domain. Nevertheless, a trained object part segmentation model often turns out to be bad results in application due to the shift between source domain and target domain. As a consequence, we are focused on solving this new problem: taking an unrestrained benchmark dataset with rich pixel-wise labels as the source domain and our real-time cross-domain object part segmentation system seems to be necessary and promising. But how to acquire an ideal parser that can annotate automatically by the system itself for the target domain is the remaining problem.

In this paper, we would like to put forward a real-time cross-domain object part segmentation system so as to solve the problem. This system consists of four modules, namely video capturing module, object capturing module, object segmentation module and result displaying module. Object segmentation module, the core module, applies the cross-domain human parsing method. It consists of two new compensation components, adversarial feature adaptation component and adversarial structured label adaptation component. The feature adaptation component is aimed at minimizing the feature distinctions between different domains, while the structured label adaptation is used for maximizing the label map universalities across the domains. The outcomes conformably corroborate our system an ideal one with efficient data and excellent performance for the challenging cross-domain human parsing problem. Meanwhile, we will continue to extend this approach to cross-domain object part segmentation as well. In addition, we presume that the exploration of the challenging issue will contribute our real-time cross-domain object part segmentation system to be more useful one among various practical applications.

The superiorities of this created system are summarized as follows. For one thing, the real-time cross-domain object part segmentation system can segment any target domain without any annotation just through transforming a source domain with rich pixel-wise annotation. For another, the capability of the system outperforms the state-of-art cross-domain approaches by two novel compensation components. Moreover, the system can segment 25 frames per second using NVIDIA GeForce GTX 1080, almost in real-time, and it can also be applied among the practical scenes in many fields.

2 Related Work

Although for many situations, we can find sufficient good performance on some correlating domains, extending the semantic segmentation model to a large variety of areas has many advantages, especially the real-time cross-domain area. Current statistical parsers tend to perform well only on their training domain and nearby genres [5]. We explore this issue as a new mission—taking an unconstrained benchmark dataset with rich pixel-wise labeling as the source domain. With the following techniques object detection, object tracking and cross-domain adaptation object part segmentation, our system aims to segment frames of target domain videos without any additional manual labeling in real-time. When the system is applied to a certain scene, we only need to collect the data of that scene, and then it can be used as the training data of our system

without any labeling. Once the training is completed, it can be applied to this scene, which can save a lot of time and labor costs. Compared with the traditional approaches, this resulting system shows obvious advantageous and presents to be a highly effective one among most practical applications, and the exploration on the challenging problem will contribute our real-time cross-domain object part segmentation system to be a more useful one among practical applications. Therefore, we are able to display the value of the real-time cross-domain object part segmentation system.

Object Parsing. The semantic object parsing problem has aroused people's interest in exploring general object parsing, person part segmentation, as well as human parsing. Combining CNNs and CRFs is one method for capturing the rich structure information based on the advanced CNN architecture [4].

Domain Adaptation. Deep domain adaptation focuses on transferring model learnt in one labeled source domain to one target domain in the deep learning framework. The exploration on this topic has been carried out along three various dimensions: unsupervised adaptation, supervised adaptation and semi-supervised adaptation. Unsupervised domain adaptation refers to the setting when the labeled target data is not available [9].

Domain Adaptation Method for Segmentation. The closely related work to ours is [2], where the adversarial feature and structured label adaptation method is firstly put forward and developed to learn to diminish the cross-domain feature distinctions and increase the label universalities across the two domains. Most mainstream fashion parsing model concentrates on parsing high resolution and clean images. However, parsers that directly apply benchmarks for high-quality samples to particular applications in the field often exhibit unsatisfactory performance because of the domain shifts. The authors propose a new cross-domain human parsing model to diminish the cross-domain distinctions in terms of visual appearance and environment conditions and fully increase universalities across domains. The model they proposed explicitly explores a feature compensation network, and it is focused on diminishing the cross-domain distinctions. The outcomes consistently confirm data efficiency and excellent performance of the proposed method for the challenging cross-domain human parsing issue. The superiorities of the cross-domain human parsing model can be concluded as follows. Not only does this model firstly explore the cross-domain human parsing problem, but it means putting forward a cross-domain human parsing framework with the new feature adaptation and structured label adaptation network as well. Since no manual labeling in the target domain is needed, the new method is very useful and practical in terms of fully considering both feature invariance and label structure regularization in their cross-domain work. We have made the authors' original method of the paper into a training-predictive integration system. And the authors' original model and work guarantee sufficient preparation for the reality of our real-time cross-domain object part segmentation system.

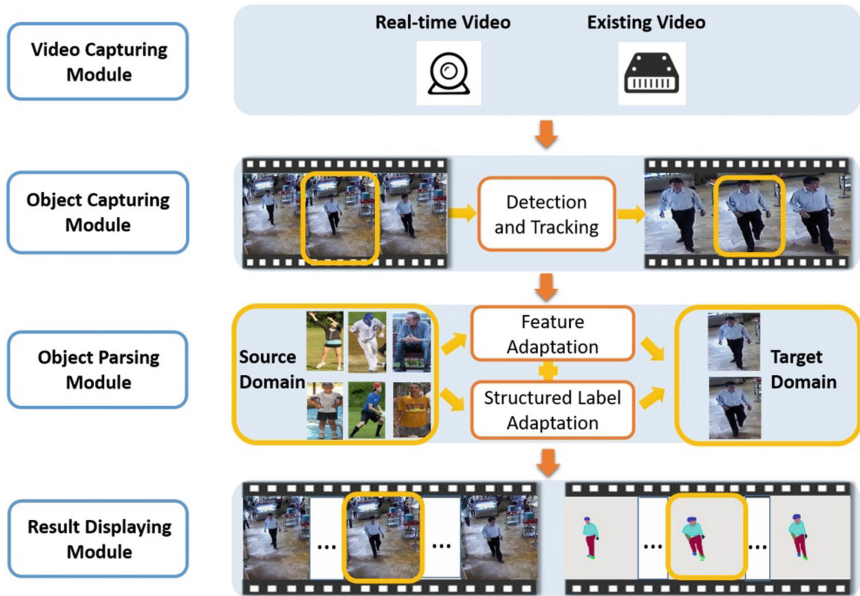


Fig. 1. The architecture of COPS system

3 System

Figure 1 displays the architecture of COPS system. As we can see, it contains four modules, including video capturing module, object capturing module, object part segmentation module and result displaying module. In the video capturing module, a video can be filmed by a real-time camera or loaded from the disk offline. After acquiring the video frames, detection [7], and tracking technique [3] are adopted. Detection technique is used in object capturing module to detect the main objects in the first frame, while tracking technique is used to track the detected objects in the following frames. Then, the core module, object part segmentation module, generates the segmentation results of the test video frames through a model trained in a source domain and transformed by adversarial feature adaptation and adversarial structured label adaptation. After finishing these steps, the result displaying module will finally show the live video and corresponding segmentation results on the screen at the same time. These four modules all work together and play their significant role in the whole system.

Moreover, we would like to highlight the third module, object part segmentation. From the third row of Fig. 1, the following universalities and distinctions across the source domain and target domain can be found, where the universalities are expected to be fully utilized, and the distinctions are what we need to overcome and eliminate. As for distinctions, they own various viewpoint, tone, illumination, object scale, object posture, resolution and degree of blurry. For instance, the light in the target domain is much darker than the light in the source domain. Besides, object scale from target

domain is smaller than the source domain's. The people from both domains exist the intrinsic universalities, such as the similar structure of human parts. Taking a detail as an example, in both domains, according to human being's common sense, the body is below the head, but in the middle of both arms. The approach we adopted is to use the universalities and to overcome distinctions for domain adaptation. As a consequence, the distinctions of the features by adversarial feature adaptation are diminished, while the universalities of the structured labels by adversarial structured label adaptation are increased in this system. Plus, the system extremely improves the performance of segmentation.

We try to elaborate the details of adversarial feature adaptation component and adversarial structured label adaptation component. The real-time cross-domain object part segmentation system contains five networks, namely feature extractor, pixel-wise labeler, feature compensation network, feature adversarial network, and structured label adversarial network. Firstly, for feature adversarial network, we define one adversarial objective function that is adopted to measure the distance between the distribution of features of target domain and the distribution of the combined features including features of source domain and the output of feature compensation network. Secondly, for structured label adversarial network, another adversarial objective function is adopted for measuring the distance between the distribution of predicted label of target domain and the distribution of ground truth of source domain. Finally, the system can be trained jointly through the approach of LSGAN (least squares generative adversarial networks) that alternates between optimizing feature adaptation component and adversarial structured label adaptation component [6].

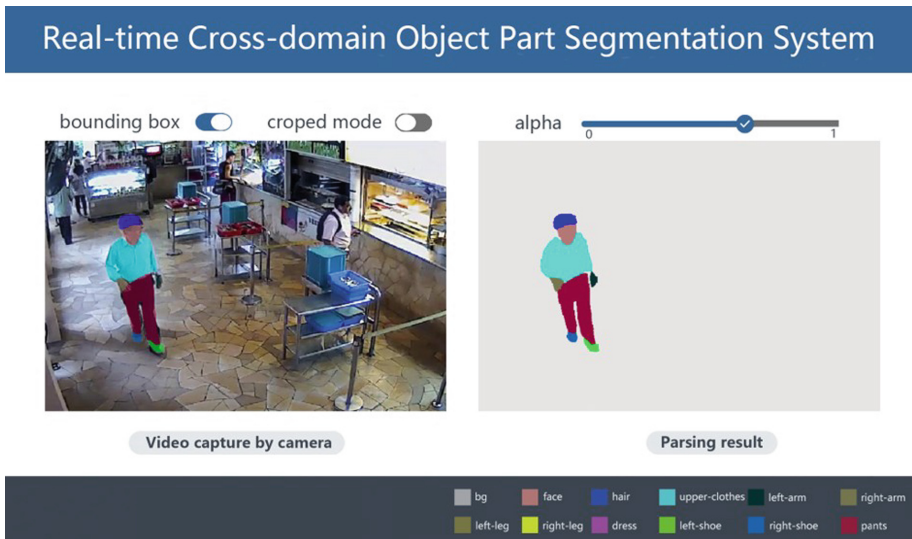


Fig. 2. The user interface of COPS system.

4 Demonstration

In order to attest the performance of the real-time cross-domain object part segmentation system, the demonstration needs a laptop, a video camera as well as a large screen. The laptop processes the frames captured by the video camera or loaded from disk and then the segmentation results are shown on the screen.

When selecting a local video file or the live video filmed by the real-time camera whose user interface is displayed in Fig. 2, this video is going to be shown on screen in the left side, while the outcome of object part segmentation module will also be presented on screen in the right side during system execution. Meanwhile, users can choose whether to present bounding box of the object or crop the object from video. Alpha denotes the degree of mergence between the video and the segmentation result and it can be adjusted as well.

We present the comparisons of experimental results human parsing both with domain adaptation and without adaptation respectively in Fig. 3. The cross-domain adaptation human parsing model can predict the details of the pictures so that these running results are more robust and adapted to the target domain. Overall, the real-time cross-domain object part segmentation system shows good performance and can be more advantageous for practical applications.

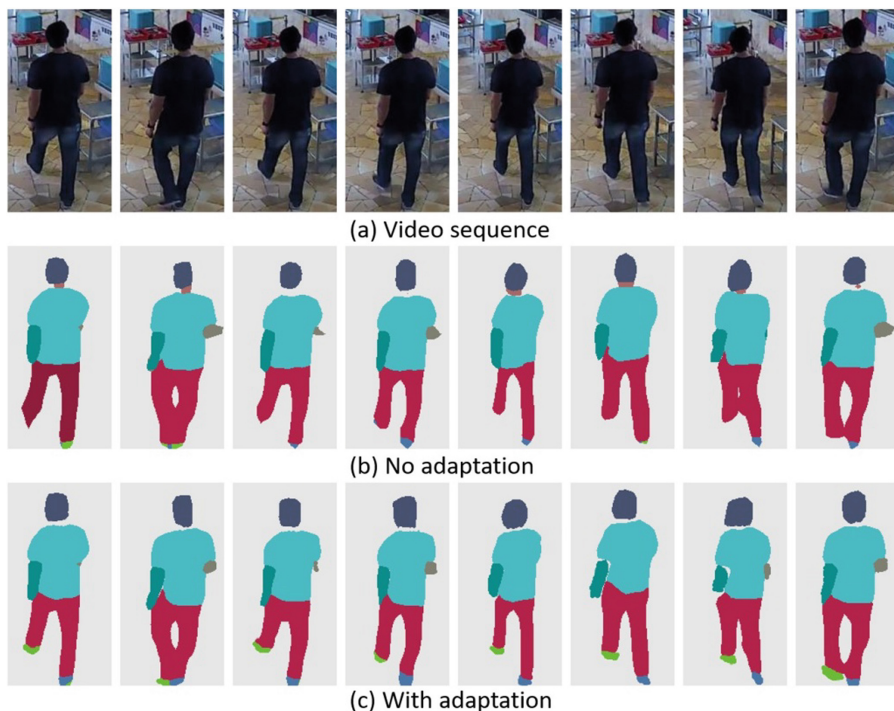


Fig. 3. Qualitative results on video sequence from target domain.

5 Discussion

Substantial benefit is obvious to applying our system over existing approaches. Using the cross-domain human parsing model without any additional manual labeling in real-time gives rise to excellent performance in practice. Additionally, our system tries to combine the human parsing and cross-domain feature transformation and a future direction is to learn these two jointly. Nowadays, our work focuses on challenging the issue, how to acquire an ideal parser that can annotate automatically by the system itself for the target domain. Not only the human parsing field, we also intend to extend our approach to scene parsing field. Scene semantic segmentation can be used as the core technology in various fields such as autonomous vehicles and smart home, and the cross-domain adaptive techniques tend to be extremely essential for these applications.

6 Conclusion

As mentioned above, we address the problem of taking an unconstrained benchmark dataset with rich pixel-wise labeling as the source domain and the real-time cross-domain object segmentation system is put forward to solve the challenging issue. The system is demonstrated to be an excellent one with higher practical advantages and more suitable applications. And according to the demonstration, an adversarial feature and structured label adaptation method are adopted to the object part segmentation module of the real-time cross-domain object segmentation system and they can jointly guarantee a precise and stable parser. Apart from the work we have done, we plan to continue researching on this approach and updating the domain adaptation technology to improve performance of our real-time cross-domain object part segmentation system of various fields in the network.

Acknowledgments. This work was performed and supported by the China Agricultural University. And we also would like to thank Defa Zhu for his technical and theoretical help.

References

1. Chen, L.C., Papandreou, G., Kokkinos, I., Murphy, K., Yuille, A.L.: DeepLab: semantic image segmentation with deep convolutional nets, atrous convolution, and fully connected CRFs. arXiv preprint [arXiv:1606.00915](https://arxiv.org/abs/1606.00915) (2016)
2. Liu, S., et al.: Cross-domain human parsing via adversarial feature and label adaptation. In: AAAI (2018)
3. Liu, S., Zhang, T.Z., Cao, X.C., Xu, C.S.: Structural correlation filter for robust visual tracking. In: CVPR (2016)
4. Liang, X., Shen, X., Feng, J., Lin, L., Yan, S.: Semantic object parsing with graph LSTM. In: Leibe, B., Matas, J., Sebe, N., Welling, M. (eds.) ECCV 2016. LNCS, vol. 9905, pp. 125–143. Springer, Cham (2016). https://doi.org/10.1007/978-3-319-46448-0_8
5. McClosky, D., Charniak, E., Johnson, M.: Automatic domain adaptation for parsing. In: ACL (2010)

6. Mao, X.D., Li, Q., Xie, H.R., Lau, R.Y., Wang, Z., Smolley, S.P.: The grid: least squares generative adversarial networks. [arXiv:1611.04076](https://arxiv.org/abs/1611.04076) (2016)
7. Ren, S.Q., He, K.M., Girshick, R., Sun, J.: Faster R-CNN: towards real-time object detection with region proposal networks. In: NIPS (2015)
8. Sasank, C.: <http://blog.qure.ai/notes/semantic-segmentation-deep-learning-review>
9. Zhang, Y.: Fully convolutional adaptation networks for semantic segmentation. In: CVPR (2018)

Author Index

- An, Xiaofei II-377
- Bai, Chenrui I-540
Bai, Jie II-251
Böhmer, Dennis I-31
- Cao, Qimin II-283
Chang, Liu II-154
Changchun, Li II-321
Chen, Guifen I-9, II-1, II-21, II-56, II-119, II-432
Chen, Hang II-432
Chen, Jing I-1
Chen, Lan I-98
Chen, Lei I-416
Chen, Liping II-358
Chen, Meixiang I-40
Chen, Yu II-453
Chen, Zhen I-116
Chen, Zhili I-486
Cong, Yue I-507, I-517
Cui, Bei I-316, II-94, II-283
Cui, Yun-peng I-54
Cui, Yunpeng II-496
- Deng, Leilei I-365
Ding, Hai II-377
Ding, Jinfeng II-127
Ding, Wen I-194, I-462
Dong, Hongtu II-347
Dong, Shiwei I-134, I-159
Dong, Yingying I-316
Du, Jianjun I-31, II-340, II-440
Duan, Qiguo II-185
- Fa, Lei I-159
Fan, Jiangchuan II-218, II-419
Fan, Jinwei II-473
Fan, Pengfei II-460
Fan, Wang I-499
Fan, Xin I-87
Fan, Xinrui I-468
- Fang, Xiaoyi I-143
Feng, Haikuan I-65, II-45, II-139, II-173, II-194, II-231, II-241, II-271, II-301
Feng, Jianying II-109
Feng, Qingcun II-460
Feng, Wenjie I-333
Fu, Jingying II-271
Fu, Siwei II-1, II-56, II-119
Fu, Weiqiang I-440, I-507, I-517
Fu, Yuanyuan II-45, II-139
Fuqin, Yang II-321
- Gao, Bingbo I-134
Gao, Fei I-341
Gao, Xiaojing II-251
Gao, Yanhu I-143
Gao, Yi II-75
Gao, Yuanyuan II-460
Geng, Xia II-86
Gong, Hao G. J. M. II-496
Gong, He II-100
Gong, Wenwen I-87
Gu, HongJun II-432
Guijun, Yang II-321
Guo, Hui I-159
Guo, Qiang I-98
Guo, Shuxia I-440
Guo, Wei I-143
Guo, Wenshan II-127
Guo, Xinyu I-31, I-108, I-244, II-67, II-162, II-218, II-340, II-419, II-440
Guomin, Zhou I-253, I-269
- Haikuan, Feng II-154, II-321
Han, Xue I-24
Hao, Junmeng I-87, I-529
Hao, Peng I-232
Haojie, Pei II-321
He, Jin I-170
He, Lulu II-347
He, Xueqing II-508
Hongchun, Zhu II-154

- Hou, Peichen II-347, II-358
Hou, Xuehui I-116, II-13
Hu, Shupeng I-440, I-517
Hu, Ye I-476, II-358
Hu, Yu II-109
Hu, Ze Lin II-75
Hu, Zelin II-368
Huang, Dong-yan I-285, I-293
Huang, Haihong II-225
Huang, Jingqi II-411
Huang, Wenjiang I-316, II-283
- Jäck, Ortrud I-206
Jia, Haifeng I-9
Jia, Lijuan I-24
Jian, Wang I-253, I-269
Jiang, Jiandong II-400
Jiang, Xinhua II-251
Jianwen, Wang II-154
Jiao, Weijie I-24
Jiao, Yang I-1, II-453
Jin, Chenyue I-395
Jin, Xiao II-400
Jingchao, Fan I-253, I-269
- Kang, Fengguang II-485
- Lai, Zhiyu I-395
Li, Aixue I-476, II-358
Li, Changchun II-139, II-194, II-301
Li, Chenxiao I-428, II-100
Li, Chunwei II-218
Li, Chunyan II-127
Li, Gen I-206
Li, Heli II-173
Li, Hongwen I-170
Li, Hua Long II-75
Li, Hualong II-292, II-368
Li, Junying II-292
Li, Liwei I-302, II-377
Li, Miao II-75, II-292, II-368
Li, Ming I-40
Li, Mingxin I-395
Li, Qingxue I-232
Li, Shijuan I-217
Li, Shuqin I-217
Li, Wenyong I-40
Li, Xiaochen I-24
Li, Yan II-411
- Li, Yang II-453
Li, Yinglun II-21
Li, Yonglin I-468
Li, You I-440, I-517
Li, Zhemin I-452, II-31
Li, Zhenhai II-139, II-231, II-241, II-301
Li, Zhihua I-126
Liang, Shouzhen I-116
Liang, Yong I-87, I-529
Liao, Qinzhong I-152
Lin, Chan I-1
Lin, Hu I-253, I-269
Lin, Kai I-98
Ling, Shouzhen II-13
Liu, Chang II-173, II-241
Liu, En-ping I-54
Liu, Hailong I-217
Liu, Hai-qing I-54
Liu, Jianping I-341
Liu, Long II-162
Liu, Min I-24
Liu, Mingxing II-194, II-301
Liu, Peng II-310
Liu, Qifeng I-404
Liu, Qing II-263
Liu, Shengping I-217, I-452, II-31
Liu, Shi-hong I-54
Liu, Shujun II-411
Liu, Siyu I-507
Liu, Tao I-116, II-13
Liu, Wenzheng I-170
Liu, Xianwang II-292, II-368
Liu, Yang I-285, I-293
Liu, Yangchun I-384
Liu, Yonghong I-143
Liu, Yuanyuan II-100
Lou, Yue I-404
Lu, Caiyun I-170, I-302
Lu, Xianju I-108, II-67, II-218, II-419
Luan, Qingzu I-143
Luo, Bin II-358
Luo, Changhai I-440
Luo, Chaorong I-404
Luo, Sheng II-218
Lv, Chengxu I-384, I-540
- Ma, Liming I-31, II-340
Ma, Shumin I-159
Ma, Wei II-109

- Ma, Weihong II-473
 Ma, Xinming II-185
 Ma, Yinchu I-194, I-462
 Ma, Zhi Run II-75
 Ma, Zhirun II-368
 McHugh, Allen D. I-170
 Menegat, Alexander I-206
 Meng, Xiaotian I-428
 Meng, Zhijun I-302, I-517
 Mingxing, Liu II-321
 Mu, Weisong II-109
- Nie, Chenwei I-65
 Nina, Sun I-170
 Niu, Hongfei I-352
 Niu, Kang II-208
 Niu, Luyan I-333
 Niu, Qinglin II-139, II-231
- Pan, Bosong II-400
 Pan, Rui I-507
 Pan, Xiaodi I-31, II-340
 Pan, Yuchun I-134
 Pei, Haojie II-139, II-194, II-231, II-301
 Pei, Shunxiang I-159
 Ping, Gan II-154
- Qi, Yan I-395
 Qian, Ping II-496
 Qian, Shuan II-225
 Qu, Yonghua I-194
- Ren, Chang I-384
- Shang, Yehua I-507, I-517
 Shao, Meng I-31
 Shen, Hongzheng I-468
 Shi, Lei II-185
 Shi, Yang I-76
 Shouzhi, Xu II-321
 Song, Huan II-109
 Song, Lihong II-185
 Song, Peng II-358
 Song, Qian II-100
 Song, Shide I-416
 Song, Xiaoyu I-316
 Song, Yufa II-218
 Sui, Xueyan I-116, II-13
 Sun, Chengming I-452, II-31
- Sun, Chuanheng I-40, I-98
 Sun, Juanying I-24
 Sun, Shijun I-352
 Sun, Xiang I-232
 Sun, Xiudong II-94
 Sun, Yu I-1
 Sun, Yuanfang II-400
- Tang, Fuquan II-173, II-241
 Tao, Liu I-452, II-31
 Tao, Shuanghua I-24
 Tian, Dong II-109
- Wang, Bin II-310
 Wang, Caiyuan I-352
 Wang, Cheng I-476, II-347, II-358
 Wang, Chuanyu II-419, II-440
 Wang, Chunlan II-251
 Wang, Dongxue II-21
 Wang, Duo I-404
 Wang, Fengyun I-333
 Wang, Guowei I-1, II-453
 Wang, Hao I-468
 Wang, Huifang I-143
 Wang, Jian I-54, I-341
 Wang, Jianwen II-241
 Wang, Jinglu I-31, II-340
 Wang, Junchan I-452, II-31
 Wang, Lei I-333
 Wang, Lin I-40
 Wang, Meng I-116, II-13
 Wang, Qingjie I-170, I-302
 Wang, Ruimei II-109
 Wang, Rujing I-76
 Wang, Sida II-263
 Wang, Songlin II-460
 Wang, Xiaodong II-347, II-358
 Wang, Xindong I-428
 Wang, Xiu I-206, I-302, II-460
 Wang, Yan II-94
 Wang, Yangren I-468, II-263
 Wang, Yongjian I-108
 Wang, Yubing I-76
 Wang, Zeng-hui I-285, I-293
 Wang, Zhenghao I-365
 Wang, Zhuqing I-87
 Wei, Caoyuan I-341
 Wei, Liguo I-540
 Wen, Changji I-404

- Wen, Weiliang I-108, I-244, II-67, II-162
 Wu, Di I-159
 Wu, Guangwei II-377
 Wu, Huarui I-232, I-375, I-486, II-473
 Wu, Kaihua II-310
 Wu, Qiulan I-529
 Wu, Quan I-24
 Wu, Sha I-159
 Wu, Sheng I-244, II-162, II-419
 Wu, Wenbin II-389
 Wu, Zhichao II-194, II-301
- Xiao, Boxiang I-244, II-162
 Xiao, Enze II-1, II-56, II-119
 Xiaobin, Xu II-154
 Xin, Xuebing I-159
 Xing, Huimin II-271
 Xingang, Xu II-154
 Xiong, Mingyang II-185
 Xiuming, Guo I-253, I-269
 Xu, Bo II-301
 Xu, Daming I-98
 Xu, Shouzhi II-485
 Xu, Xiangying II-127
 Xu, Xingang II-271
 Xu, Yanlei I-428, II-100
 Xu, Ying I-404
 Xue, Heru II-251
 Xue, Xia I-253, I-269
- Yan, Hao II-225
 Yan, Wu I-499
 Yang, Fuqin II-231
 Yang, Guijun I-65, II-45, II-139, II-173,
 II-194, II-231, II-241, II-271, II-301
 Yang, Liwei I-384
 Yang, Qingfeng I-507
 Yang, Xiaodong I-65
 Yang, Xin II-225
 Yang, Xuan Jiang II-75
 Yang, Xuanjiang II-368
 Yao, Huimin I-116, II-13
 Ye, Huichun I-316, II-283
 Ye, Lantao II-263
 Yin, Shihua II-485
 Yu, Haijiao I-1, II-453
 Yu, Zetao I-108, II-67
 Yuan, Yanwei I-384, II-208
- Yuan, Yuan I-416
 Yun, Qiu I-253, I-269
- Zhan, Kai II-292
 Zhang, Chuanhong I-1
 Zhang, Chunlan II-173, II-241
 Zhang, Dalei I-529
 Zhang, Fangming II-389
 Zhang, Fujie I-507
 Zhang, Guilan I-341
 Zhang, Jingcheng I-65, II-310
 Zhang, Jinjing I-462
 Zhang, Jinwei I-206
 Zhang, Juanjuan II-185
 Zhang, Junning I-384, I-540, II-208
 Zhang, Junxiong I-440
 Zhang, Liyan II-241
 Zhang, Qi I-428
 Zhang, Qiuting II-86
 Zhang, Shirui I-352
 Zhang, Shuo I-143
 Zhang, Song I-98
 Zhang, Xin I-352
 Zhang, Xuexue II-310
 Zhang, Ying I-31, II-340, II-432
 Zhang, Yu II-485
 Zhang, Zhiqiang I-170
 Zhangzhong, Lili I-352
 Zhao, Bo I-384, I-540
 Zhao, Chuanqi I-529
 Zhao, Chunjiang I-486, I-507, II-45, II-473
 Zhao, Guogang I-1, II-453
 Zhao, Shan II-1, II-56, II-119
 Zhao, Xiande I-194
 Zhao, Xin I-126, II-411
 Zhao, Xueguan II-460
 Zhao, Yan-jun I-285, I-293
 Zhao, Zhangfeng II-400
 Zheng, Jiye I-333
 Zheng, Wengang I-352
 Zhenhai, Li II-154, II-321
 Zhong, Jiang II-400
 Zhong, Xiaochun I-452, II-31
 Zhou, Chao I-98
 Zhou, Guomin I-341
 Zhou, Hang II-347
 Zhou, Hui I-365
 Zhou, Liming I-540, II-208

Zhou, Qian [II-400](#)
Zhou, Yanhua [II-94](#)
Zhou, Yanqing [II-251](#)
Zhu, Huaji [I-375](#)
Zhu, Qingzhen [II-377](#)

Zhu, Xinkai [II-127](#)
Zhu, Xinyao [I-395](#)
Zhu, Yeping [I-217](#)
Zhu, Yunfei [II-389](#)
Zhuang, Li [I-253, I-269](#)